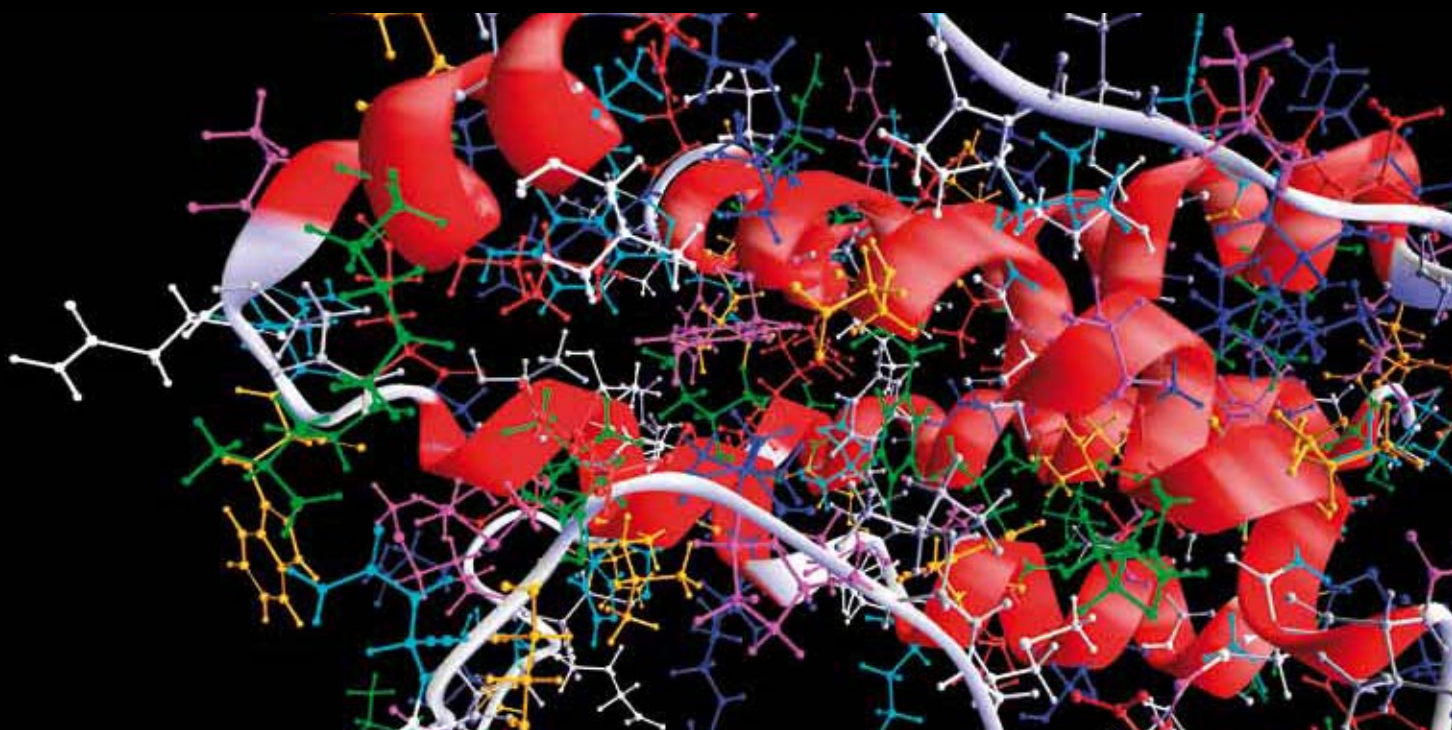


MATHEMATICAL METHODS IN BIOMEDICAL IMAGING

GUEST EDITORS: WENXIANG CONG, KUMAR DURAI, AND PENG FENG





Mathematical Methods in Biomedical Imaging

Computational and Mathematical Methods in Medicine

Mathematical Methods in Biomedical Imaging

Guest Editors: Wenxiang Cong, Kumar Durai, and Peng Feng



Copyright © 2013 Hindawi Publishing Corporation. All rights reserved.

This is a special issue published in “Computational and Mathematical Methods in Medicine.” All articles are open access articles distributed under the Creative Commons Attribution License, which permits unrestricted use, distribution, and reproduction in any medium, provided the original work is properly cited.

Editorial Board

Emil Alexov, USA
Georgios Archontis, Cyprus
Dimos Baltas, Germany
Chris Bauch, Canada
Maxim Bazhenov, USA
Thierry Busso, France
Carlo Cattani, Italy
Sheng-yong Chen, China
William Crum, UK
Ricardo Femat, Mexico
Alfonso T. García-Sosa, Estonia

Damien Hall, Australia
Volkhard Helms, Germany
Seiya Imoto, Japan
Lev Klebanov, Czech Republic
Quan Long, UK
C-M Charlie Ma, USA
Reinoud Maex, France
Michele Migliore, Italy
Karol Miller, Australia
Ernst Niebur, USA
Kazuhisa Nishizawa, Japan

Hugo Palmans, UK
David James Sherman, France
Sivabal Sivaloganathan, Canada
Nestor V. Torres, Spain
Nelson J. Trujillo-Barreto, Cuba
Gabriel Turinici, France
Kutlu O. Ulgen, Turkey
Edelmira Valero, Spain
Guang Wu, China
Henggui Zhang, United Kingdom

Contents

Mathematical Methods in Biomedical Imaging, Wenxiang Cong, Kumar Durairaj, and Peng Feng
Volume 2013, Article ID 932794, 2 pages

The Approach to Steady State Using Homogeneous and Cartesian Coordinates,
D. F. Gochberg and Z. Ding
Volume 2013, Article ID 729236, 5 pages

Research on Calculation of the IOL Tilt and Decentration Based on Surface Fitting, Lin Li, Ke Wang,
Yan Yan, Xudong Song, and Zhicheng Liu
Volume 2013, Article ID 572530, 7 pages

Bayesian Hierarchical Modeling for Categorical Longitudinal Data from Sedation Measurements,
Erol Terzi and Mehmet Ali Cengiz
Volume 2013, Article ID 579214, 6 pages

**Multiple Active Contours Driven by Particle Swarm Optimization for Cardiac Medical Image
Segmentation**, I. Cruz-Aceves, J. G. Aviña-Cervantes, J. M. López-Hernández, and S. E. González-Reyna
Volume 2013, Article ID 132953, 13 pages

Spatiotemporal Quantification of Local Drug Delivery Using MRI, Morgan B. Giers, Alex C. McLaren,
Jonathan D. Plasencia, David Frakes, Ryan McLemore, and Michael R. Caplan
Volume 2013, Article ID 149608, 12 pages

Rotation Covariant Image Processing for Biomedical Applications, Henrik Skibbe and Marco Reisert
Volume 2013, Article ID 931507, 19 pages

Nonrigid 3D Medical Image Registration and Fusion Based on Deformable Models, Peng Liu,
Benjamin Eberhardt, Christian Wybranski, Jens Ricke, and Lutz Lüdemann
Volume 2013, Article ID 902470, 10 pages

Attenuation Correction for Small Animal PET Images: A Comparison of Two Methods,
Daniela D'Ambrosio, Federico Zagni, Antonello E. Spinelli, and Mario Marengo
Volume 2013, Article ID 103476, 12 pages

Simulation of Intra-Aneurysmal Blood Flow by Different Numerical Methods, Frank Weichert,
Lars Walczak, Denis Fisseler, Tobias Opfermann, Mudassar Razzaq, Raphael Münster, Stefan Turek, Iris
Grunwald, Christian Roth, Christian Veith, and Mathias Wagner
Volume 2013, Article ID 527654, 10 pages

Encoding Scratch and Scrape Features for Wear Modeling of Total Joint Replacements, Karen M. Kruger,
Nishant M. Tikekar, Anneliese D. Heiner, Thomas E. Baer, John J. Lannutti, John J. Callaghan,
and Thomas D. Brown
Volume 2013, Article ID 624267, 12 pages

Acceleration of Early-Photon Fluorescence Molecular Tomography with Graphics Processing Units,
Xin Wang, Bin Zhang, Xu Cao, Fei Liu, Jianwen Luo, and Jing Bai
Volume 2013, Article ID 297291, 9 pages

**Automated Detection of Healthy and Diseased Aortae from Images Obtained by Contrast-Enhanced
CT Scan**, Michael Gayhart and Hiroshi Arisawa
Volume 2013, Article ID 107871, 7 pages

Sparse Constrained Reconstruction for Accelerating Parallel Imaging Based on Variable Splitting

Method, Wenlong Xu, Xiaofang Liu, and Xia Li

Volume 2013, Article ID 605632, 10 pages

Improved Compressed Sensing-Based Algorithm for Sparse-View CT Image Reconstruction,

Zangen Zhu, Khan Wahid, Paul Babyn, David Cooper, Isaac Pratt,
and Yasmin Carter

Volume 2013, Article ID 185750, 15 pages

Development of Image Segmentation Methods for Intracranial Aneurysms, Yuka Sen, Yi Qian,

Alberto Avolio, and Michael Morgan

Volume 2013, Article ID 715325, 7 pages

**Numerical Study of Magnetoacoustic Signal Generation with Magnetic Induction Based on
Inhomogeneous Conductivity Anisotropy,** Xun Li, Sanqing Hu, Lihua Li,

and Shan'an Zhu

Volume 2013, Article ID 161357, 13 pages

***In Vivo* Imaging-Based Mathematical Modeling Techniques That Enhance the Understanding of**

Oncogene Addiction in relation to Tumor Growth, Chinyere Nwabugwu, Kavya Rakhra, Dean Felsner,
and David Paik

Volume 2013, Article ID 802512, 8 pages

**Optimization of Contrast-to-Tissue Ratio by Adaptation of Transmitted Ternary Signal in Ultrasound
Pulse Inversion Imaging,** Sébastien Ménigot and Jean-Marc Girault

Volume 2013, Article ID 297463, 6 pages

Differential Diagnosis Tool for Parkinsonian Syndrome Using Multiple Structural Brain Measures,

Miho Ota, Yasuhiro Nakata, Kimiteru Ito, Kouhei Kamiya, Masafumi Ogawa, Miho Murata, Satoko Obu,
Hiroshi Kunugi, and Noriko Sato

Volume 2013, Article ID 571289, 10 pages

**A General Framework for Modeling Sub- and Ultraharmonics of Ultrasound Contrast Agent Signals
with MISO Volterra Series,** Fatima Sbeity, Sébastien Ménigot, Jamal Charara, and Jean-Marc Girault

Volume 2013, Article ID 934538, 9 pages

Ultrasound Common Carotid Artery Segmentation Based on Active Shape Model, Xin Yang,

Jiaoying Jin, Mengling Xu, Huihui Wu, Wanji He, Ming Yuchi, and Mingyue Ding

Volume 2013, Article ID 345968, 11 pages

Group Factor Analysis for Alzheimer's Disease, Wei-Chen Cheng, Philip E. Cheng, and Michelle Liou

Volume 2013, Article ID 428385, 8 pages

A Semiautomatic Segmentation Algorithm for Extracting the Complete Structure of Acini from

Synchrotron Micro-CT Images, Luosha Xiao, Toshihiro Sera, Kenichiro Koshiyama, and Shigeo Wada

Volume 2013, Article ID 575086, 10 pages

Piecewise-Constant-Model-Based Interior Tomography Applied to Dentin Tubules, Peng He, Biao Wei,
Steve Wang, Stuart R. Stock, Hengyong Yu, and Ge Wang

Volume 2013, Article ID 892451, 8 pages

A Fusion Algorithm for GFP Image and Phase Contrast Image of Arabidopsis Cell Based on SFL-Contourlet Transform, Peng Feng, Jing Wang, Biao Wei, and Deling Mi
Volume 2013, Article ID 635040, 10 pages

Nonrigid Medical Image Registration Based on Mesh Deformation Constraints, XiangBo Lin, Su Ruan, TianShuang Qiu, and DongMei Guo
Volume 2013, Article ID 373082, 8 pages

A 3D Visualization Method for Bladder Filling Examination Based on EIT, Wei He, Peng Ran, Zheng Xu, Bing Li, and Song-nong Li
Volume 2012, Article ID 528096, 9 pages

Two-Dimensional Matrix Algorithm Using Detrended Fluctuation Analysis to Distinguish Burkitt and Diffuse Large B-Cell Lymphoma, Rong-Guan Yeh, Chung-Wu Lin, Maysam F. Abbod, and Jiann-Shing Shieh
Volume 2012, Article ID 947191, 8 pages

Wavelet-Based Color Pathological Image Watermark through Dynamically Adjusting the Embedding Intensity, Guoyan Liu, Hongjun Liu, and Abdurahman Kadir
Volume 2012, Article ID 406349, 10 pages

Modified Global and Modified Linear Contrast Stretching Algorithms: New Colour Contrast Enhancement Techniques for Microscopic Analysis of Malaria Slide Images, Aimi Salihah Abdul-Nasir, Mohd Yusoff Mashor, and Zeehaida Mohamed
Volume 2012, Article ID 637360, 16 pages

Editorial

Mathematical Methods in Biomedical Imaging

Wenxiang Cong,¹ Kumar Durairaj,² and Peng Feng³

¹ Biomedical Imaging Center, Department of Biomedical Engineering, Rensselaer Polytechnic Institute, Troy, NY 12180, USA

² Department of Electrical and Electronics Engineering, Periyar Maniammai University, Vallam, Thanjavur 613403, India

³ Department of Optoelectronics Engineering, Chongqing University, Chongqing 400044, China

Correspondence should be addressed to Wenxiang Cong; cong@vt.edu

Received 8 October 2013; Accepted 8 October 2013

Copyright © 2013 Wenxiang Cong et al. This is an open access article distributed under the Creative Commons Attribution License, which permits unrestricted use, distribution, and reproduction in any medium, provided the original work is properly cited.

Biomedical imaging is a rapidly growing field to provide a state-of-the-art tool for preclinical biomedical research and clinical applications, in view of its ability to noninvasively reveal subtle structural variations of biological tissues and visualize in vivo physiological and pathological processes at the cellular and molecular levels. Mathematical methods are involved with imaging theories, models, and reconstruction algorithms in biomedical imaging. X-ray computed tomography (CT) was a successful application of mathematical method in medical imaging. The CT mathematical model can be reduced to a Radon transform. The inverse transform of Radon transform is invented by Radon in 1917. Magnetic resonance imaging (MRI) is a versatile medical imaging modality. MRI can provide more diagnostic information than any of the existing imaging techniques. It does not involve the use of ionizing radiation, hence free from associated harmful effects. Inverse Fast Fourier Transform (IFFT) is a standard method of image reconstruction in MRI from uniformly sampled K-space data. From nonuniform K-space data, iterative algorithms can improve image quality of image reconstruction for MRI. In the optical molecular imaging, the radiative transport equation (RTE) is the fundamental equation to describe photon propagation in biological tissues. The forward solution predicts photon propagation in the optical molecular imaging. The inverse solution can reconstruct molecular probe distribution in a small animal for providing unique insights into disease pathogenesis, drug development, and responses of therapy. The solutions for RTE usually involve analytical methods, Monte Carlo (MC) method, diffusion approximation (DA) method, simplified spherical harmonics method, and some numerical methods.

In this special issue, each paper was reviewed by at least two reviewers and revised according to review comments. This special issue covered most of common biomedical imaging models and various image processing methods, such as registration, segmentation, and so forth, were involved. For Positron Emission Tomography (PET) imaging model, two attenuation correction methods based on X-rays CT (CTAC method) and segmentation of emission images (SE-AC method) were simulated with Monte Carlo method and compared. For synchrotron Micro-CT imaging model, a semiautomatic segmentation algorithm for extracting the complete structure of acini has been proposed. For ultrasound imaging model, a common carotid artery segmentation scheme based on active shape model can get better result and promote the translation of carotid 3D US to clinical care for the monitoring of the atherosclerotic disease progression and regression. For MRI model, a mesh-deformation constraints based image registration algorithm was carefully investigated. Also the development of image segmentation for intracranial aneurysms and rotation covariant image processing method for biomedical applications are summarized. Furthermore, in order to accelerate the parallel imaging, a sparse constrained reconstruction approach with variable splitting methods was proposed and verified: total variation (TV)-minimization interior tomography algorithm, dynamic and robust blind watermarking scheme to resist against common distortions, modified global and modified linear contrast stretching techniques for identification of various stages and species of malaria, a 3D surface-based deformable model as guidance for nonrigid 3D medical image registration and fusion, mathematical or computational modeling

for oncogene inactivation, a group factor analysis model for neuroimaging applications by assigning separate factor patterns to control and patient groups yielding more reasonable factor scores and patterns, different MISO Volterra methods to model simulated ultrasound contrast agents signals, an automated process that determines whether an aortic object in a slice is a candidate for aortic dissection or PAU based on contrast enhanced CT data, image-based computational techniques to quantify the severity and directionality of individual scratches and scrapes, combination of genetic algorithm and closed loop to obtain optimal ternary command which maximized the contrast to tissue ratio, and magnetoacoustic tomography with magnetic induction (MATMI) for generating electrical conductivity images of biological tissues with high spatial resolution. An acceleration strategy for fluorescence molecular tomography (FMT) with early photons is proposed using graphics processing units (GPUs). The fluorescence molecular tomography (FMT) with early photons can efficiently improve the spatial resolution and fidelity of the reconstructed results. An efficient compressed sensing-based algorithm is proposed for CT image reconstruction from few-view data to suppress the streak artifact. The compressed sensing (CS) algorithm shows the potential to accurately recover images from highly undersampled data. The discriminant analysis techniques are discussed using MRI to identify the correlative pattern of brain changes for differentiating parkinsonian syndromes. A hybrid multiscale and multilevel image fusion algorithm for green fluorescent protein (GFP) image and phase contrast image of Arabidopsis cell is proposed. This algorithm uses different fusion strategies for different detailed subbands, which include neighborhood consistency measurement (NCM) that can adaptively find balance between color background and gray structure. A detrended fluctuation analysis (DFA) method is applied to image analysis to investigate the characteristic of different type of simulated and lymphoma image. A method is presented to estimate the tilt and decentration of intraocular lens (IOL) more accurately. The Bayesian hierarchical model for the analysis of categorical longitudinal data is investigated from sedation measurement for MRI and CT. In vivo MRI of local drug delivery is discussed to visualize and quantify the time resolved distribution of MRI contrast agents.

These papers represent an insightful observation into the state of the art, as well as future topics in this biomedical imaging field. We hope that this special issue would attract a wide attention of the peers.

*Wenxiang Cong
Kumar Durairaj
Peng Feng*

Research Article

The Approach to Steady State Using Homogeneous and Cartesian Coordinates

D. F. Gochberg^{1,2} and Z. Ding¹

¹ Department of Radiology and Radiological Sciences, Vanderbilt University Institute for Imaging Science (VUIIS), Vanderbilt University, Nashville, TN 37232-2675, USA

² Department of Physics, Vanderbilt University Institute for Imaging Science (VUIIS), Vanderbilt University, Nashville, TN 37232-2675, USA

Correspondence should be addressed to D. F. Gochberg; daniel.gochberg@vanderbilt.edu

Received 21 December 2012; Revised 5 July 2013; Accepted 7 July 2013

Academic Editor: Wenxiang Cong

Copyright © 2013 D. F. Gochberg and Z. Ding. This is an open access article distributed under the Creative Commons Attribution License, which permits unrestricted use, distribution, and reproduction in any medium, provided the original work is properly cited.

Repeating an arbitrary sequence of RF pulses and magnetic field gradients will eventually lead to a steady-state condition in any magnetic resonance system. While numerical methods can quantify this trajectory, analytic analysis provides significantly more insight and a means for faster calculation. Recently, an analytic analysis using homogeneous coordinates was published. The current work further develops this line of thought and compares the relative merits of using a homogeneous or a Cartesian coordinate system.

1. Introduction

A recent paper by Nazarova and Hemminga [1] analyzed the signal arising from repeated identical RF pulses using a formalism based on homogeneous coordinates. Unlike the conventional Cartesian coordinates, homogeneous coordinates allow T_1 relaxation to be treated in a manner similar to RF field-induced rotations, that is, by matrix multiplication. Signals from repeated identical RF pulses are an issue, most notably, in steady-state free precession (SSFP) fast imaging [2] techniques, where the lack of gradient or RF spoiling leads to complicated dynamics when the repetition time $< T_2$. The formalism can also be applied to any repeated sequence of pulses, such as those, for example, that arise in pulsed saturation magnetization transfer methods [3].

In this paper, we will expand on the work of Nazarova and Hemminga to show a simple way to calculate the steady-state magnetization, and we will relate the properties of the homogeneous matrices and calculations to those that arise in a more traditional Cartesian representation of magnetization. Specifically, we explicitly establish algebraic relations between the two systems, thus facilitating understanding of the pros

and cons of each representation. We will employ the same notation as Nazarova and Hemminga, except as noted.

2. Background

Consider a pulse sequence made up of RF pulses and magnetic field gradients repeated every τ seconds (see Figure 1). The conventional representation of the magnetization is a 3×1 vector \mathbf{M} with equilibrium value \mathbf{M}_{eq} and components M_x , M_y , and M_z in the rotating frame. RF pulses with field strengths $= B_1 \gg 1/(\gamma T_2)$ and angular frequency offset $\Delta\omega_0$ can be represented by a 3×3 rotation matrix $R_{x,y}(\alpha)$, where T_2 is the transverse relaxation rate and γ is the gyromagnetic ratio. Likewise, off-resonance precession and the scaling effect of relaxation can also be represented by matrices. For example, precession about the z direction and the decay of magnetization can be represented as follows:

$$\mathbf{R}_z(\Delta\omega_0\tau) = \begin{bmatrix} \cos \Delta\omega_0\tau & \sin \Delta\omega_0\tau & 0 \\ -\sin \Delta\omega_0\tau & \cos \Delta\omega_0\tau & 0 \\ 0 & 0 & 1 \end{bmatrix},$$

$$\mathbf{S}(\tau, T_1, T_2) = \begin{bmatrix} e^{-\tau/T_2} & 0 & 0 \\ 0 & e^{-\tau/T_2} & 0 \\ 0 & 0 & e^{-\tau/T_1} \end{bmatrix}. \quad (1)$$

Similarly, a gradient pulse can be modeled by making the precession position dependent. In distinction, the effect of T_1 relaxation to a nonzero thermal equilibrium value cannot be represented by a 3×3 matrix. It is instead equivalent to an additive translation.

Nazarova and Hemminga use this approach to give the relation for magnetization after n repeated α pulses about the x -axis:

$$\mathbf{M}_n = \mathbf{R}_z(\Delta\omega_0\tau) \mathbf{S}(\tau, T_1, T_2) \mathbf{R}_x(\alpha) \mathbf{M}_{n-1} + (1 - e^{-\tau/T_1}) \mathbf{M}_{\text{eq}}, \quad (2)$$

where \mathbf{M}_n is the magnetization after the n th repetition (initial condition = \mathbf{M}_0). The general form for the repetition of an arbitrary pulse sequence is

$$\begin{aligned} \mathbf{M}_n &= \mathbf{C}\mathbf{M}_{n-1} + \mathbf{D}\mathbf{M}_{\text{eq}}, \quad \text{for } n \geq 1, \\ \mathbf{M}_n &= \mathbf{M}_0, \quad \text{for } n = 0. \end{aligned} \quad (3)$$

Note that \mathbf{D} is scalar only when a single RF pulse is repeated.

An alternative approach is to use homogeneous coordinates where T_1 relaxation enters in the same way as do rotations:

$$\begin{aligned} \mathbf{M}_n &= \mathbf{A}\mathbf{M}_{n-1}, \quad \text{for } n \geq 1, \\ \mathbf{M}_n &= \mathbf{M}_0, \quad \text{for } n = 0. \end{aligned} \quad (4)$$

\mathbf{M} is now a 4×1 vector with components M_x, M_y, M_z , and 1, and \mathbf{A} is a 4×4 matrix whose upper left portion matches the 3×3 rotations and scalings discussed above and whose far right column represents the T_1 relaxation towards \mathbf{M}_{eq} . For example,

$$R_z(\Delta\omega_0\tau) = \begin{bmatrix} \cos \Delta\omega_0\tau & \sin \Delta\omega_0\tau & 0 & 0 \\ -\sin \Delta\omega_0\tau & \cos \Delta\omega_0\tau & 0 & 0 \\ 0 & 0 & 1 & 0 \\ 0 & 0 & 0 & 1 \end{bmatrix}. \quad (5)$$

And T_1 relaxation for a period τ is represented by

$$T = \begin{bmatrix} 1 & 0 & 0 & 0 \\ 0 & 1 & 0 & 0 \\ 0 & 0 & 1 & M_{\text{eq}}(1 - e^{-\tau/T_1}) \\ 0 & 0 & 0 & 1 \end{bmatrix}. \quad (6)$$

\mathbf{M}_{eq} in this notation is represented by

$$\begin{bmatrix} 0 \\ 0 \\ M_{\text{eq}} \\ 1 \end{bmatrix}. \quad (7)$$

(Note the corrections to Nazarova and Hemminga in (6) and (7)).

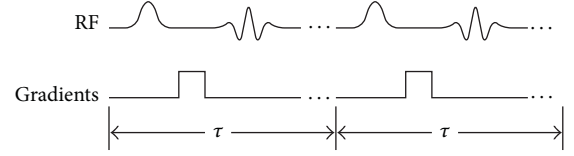


FIGURE 1: An arbitrary sequence of pulses repeated every τ seconds.

3. Homogeneous and Cartesian Representations

Both homogeneous and conventional representations have identical underlying math and therefore will give equivalent results. However, their differences in formalism have small consequences in computation time, and they provide different notational approaches.

The solution in the homogeneous case is

$$\begin{aligned} \mathbf{M}_n &= \mathbf{A}^n \mathbf{M}_0 \\ &= p_{A1} \lambda_{A1}^n \mathbf{v}_{A1} + p_{A2} \lambda_{A2}^n \mathbf{v}_{A2} + p_{A3} \lambda_{A3}^n \mathbf{v}_{A3} + p_{A4} \lambda_{A4}^n \mathbf{v}_{A4}, \end{aligned} \quad (8)$$

where \mathbf{v}_{Ai} and λ_{Ai} are the i th eigenvector and eigenvalue, respectively, of \mathbf{A} and p_{Ai} is the corresponding projection of \mathbf{M}_0 onto \mathbf{v}_{Ai} . The second form of the solution can be derived in two ways: (1) by rewriting \mathbf{A}^n as $(\mathbf{V}_A \mathbf{\Lambda}_A \mathbf{V}_A^{-1})^n = \mathbf{V}_A \mathbf{\Lambda}_A^n \mathbf{V}_A^{-1}$, where the columns of \mathbf{V}_A are \mathbf{v}_{Ai} , $\mathbf{\Lambda}_A$ is diagonal with elements λ_{Ai} , and \mathbf{p}_A (with elements p_{Ai}) equals $\mathbf{V}_A^{-1} \mathbf{M}_0$ and (2) by rewriting \mathbf{M}_0 as $p_{A1} \mathbf{v}_{A1} + p_{A2} \mathbf{v}_{A2} + p_{A3} \mathbf{v}_{A3} + p_{A4} \mathbf{v}_{A4}$ and applying (4) n times. (Note that in Nazarova and Hemminga \mathbf{V}_A is called \mathbf{B}).

The conventional Cartesian case has the less intuitive solution to (3):

$$\begin{aligned} \mathbf{M}_n &= \mathbf{C}^n \mathbf{M}_0 + \left(\sum_{i=0}^{n-1} \mathbf{C}^i \right) \mathbf{D} \mathbf{M}_{\text{eq}}, \quad \text{for } n \geq 1 \\ &= \mathbf{C}^n \mathbf{M}_0 + \left(-\sum_{i=n}^{\infty} \mathbf{C}^i \mathbf{D} + \sum_{i=0}^{\infty} \mathbf{C}^i \mathbf{D} \right) \mathbf{M}_{\text{eq}} \\ &= \mathbf{C}^n \mathbf{M}_0 + (-\mathbf{C}^n + \mathbf{I}) \sum_{i=0}^{\infty} \mathbf{C}^i \mathbf{D} \mathbf{M}_{\text{eq}} \\ &= \mathbf{C}^n (\mathbf{M}_0 - (\mathbf{I} - \mathbf{C})^{-1} \mathbf{D} \mathbf{M}_{\text{eq}}) + (\mathbf{I} - \mathbf{C})^{-1} \mathbf{D} \mathbf{M}_{\text{eq}} \\ &= \mathbf{V}_C \mathbf{\Lambda}_C^n \mathbf{V}_C^{-1} (\mathbf{M}_0 - (\mathbf{I} - \mathbf{C})^{-1} \mathbf{D} \mathbf{M}_{\text{eq}}) + (\mathbf{I} - \mathbf{C})^{-1} \mathbf{D} \mathbf{M}_{\text{eq}} \\ &= p_{C1} \lambda_{C1}^n \mathbf{v}_{C1} + p_{C2} \lambda_{C2}^n \mathbf{v}_{C2} + p_{C3} \lambda_{C3}^n \mathbf{v}_{C3} + (\mathbf{I} - \mathbf{C})^{-1} \mathbf{D} \mathbf{M}_{\text{eq}}, \end{aligned} \quad (9)$$

where the columns of \mathbf{V}_C are the eigenvectors \mathbf{v}_{Ci} of \mathbf{C} , the elements of the diagonal matrix $\mathbf{\Lambda}_C$ are the eigenvalues λ_{Ci} , and \mathbf{p}_C (with elements p_{Ci}) equals $\mathbf{V}_C^{-1} (\mathbf{M}_0 - (\mathbf{I} - \mathbf{C})^{-1} \mathbf{D} \mathbf{M}_{\text{eq}})$.

Often, one only cares about the steady-state solution, which is the solution that is independent of n and is approached as $n \rightarrow \infty$. We can solve this condition by

solving \mathbf{M}_n when $\mathbf{M}_n = \mathbf{M}_{n-1}$. For the homogeneous notation (4),

$$\mathbf{M}_n = \mathbf{A}\mathbf{M}_{n-1} = \mathbf{A}\mathbf{M}_n. \quad (11)$$

That is, the steady-state solution is the eigenvector of \mathbf{A} with eigenvalue = 1.

In the conventional formalism, we again solve for a steady-state solution ($\equiv \mathbf{M}_{ss}$) by setting $\mathbf{M}_n = \mathbf{M}_{n-1}$, this time in (3):

$$\mathbf{M}_{ss} = (\mathbf{I} - \mathbf{C})^{-1} \mathbf{D}\mathbf{M}_{eq}, \quad (12)$$

(another option is to take $n \rightarrow \infty$ in (9) with $\mathbf{C}^n \rightarrow 0$ due to the relaxation terms on the diagonal). Since taking an inverse takes \sim dimension³ operations, while finding an eigenvector via row reduction takes $\sim 1/3$ dimension³ operations [4], finding the steady-state via the homogeneous equation may provide a slightly more efficient method, though no rigorous evaluation of the computation time has been made. The computation time is normally not essential but may be so in certain problems, such as least squares fitting of magnetization transfer parameters [3].

4. Relations between Homogeneous and Cartesian Representations

In general, \mathbf{A} has the form

$$\mathbf{A} = \begin{bmatrix} \mathbf{C} (3 \times 3) & \mathbf{D}\mathbf{M}_{eq} (3 \times 1) \\ 0 & 1 \end{bmatrix}. \quad (13)$$

From this form it follows that

$$\begin{aligned} \lambda_{Ai} &= \lambda_{Ci}, \quad \text{for } i = 1, 2, 3, \\ \lambda_{A4} &= 1, \\ \mathbf{v}_{Ai} &= \begin{bmatrix} \mathbf{v}_{Ci} \\ 0 \end{bmatrix}, \quad \text{for } i = 1, 2, 3, \\ \mathbf{v}_{A4} &= \begin{bmatrix} \mathbf{M}_{ss} \\ 1 \end{bmatrix}. \end{aligned} \quad (14)$$

5. An Example

Consider a simple example: a single short (relative to T_2) 90° pulse repeated every τ seconds. To keep the illustration as analytically simple as possible, we assume $T_1 = T_2$ and a system starting at thermal equilibrium. This gives (from Nazarova and Hemminga with corrections)

$$\mathbf{A} = \begin{bmatrix} E \cos \theta & 0 & E \sin \theta & 0 \\ -E \sin \theta & 0 & E \cos \theta & 0 \\ 0 & -E & 0 & M_{eq}(1-E) \\ 0 & 0 & 0 & 0 \end{bmatrix}, \quad (15)$$

where $E = \exp(-\tau/T_1) = \exp(-\tau/T_2)$ and $\theta = \Delta\omega_0\tau$. We can solve \mathbf{M}_n using (8) and then convert back to Cartesian

coordinates, or we can use (13) to get \mathbf{C} and $\mathbf{D}\mathbf{M}_0$ and then use (10). With help from Mathematica, we get

$$\begin{aligned} \mathbf{M}_n &= \frac{M_{eq}}{1 + E^2 + 2E\gamma} \begin{bmatrix} 2E\sqrt{\gamma(1-\gamma)} \\ E(1-E-2\gamma) \\ 1 + E(-1+2\gamma) \end{bmatrix} \\ &+ (-E)^n \left(\gamma + i\sqrt{1-\gamma^2} \right)^n \\ &\times \frac{Ei\sqrt{1-\gamma^2} \left(i\sqrt{1-\gamma^2} + E + \gamma \right) M_{eq}}{(1+\gamma)(1+E^2+2E\gamma) \left(-1 + \gamma + i\sqrt{1-\gamma^2} \right)} \\ &\times \begin{bmatrix} \frac{2\sqrt{\gamma(1-\gamma)}}{-1 + \gamma - i\sqrt{1-\gamma^2}} \\ \gamma + i\sqrt{1-\gamma^2} \\ 1 \end{bmatrix} \\ &+ E^n \left(-\gamma + i\sqrt{1-\gamma^2} \right)^n \\ &\times \frac{Ei\sqrt{1-\gamma^2} \left(-i\sqrt{1-\gamma^2} + E + \gamma \right) M_{eq}}{(1+\gamma)(1+E^2+2E\gamma) \left(1 - \gamma + i\sqrt{1-\gamma^2} \right)} \\ &\times \begin{bmatrix} \frac{2\sqrt{\gamma(1-\gamma)}}{-1 + \gamma + i\sqrt{1-\gamma^2}} \\ \gamma - i\sqrt{1-\gamma^2} \\ 1 \end{bmatrix}, \end{aligned} \quad (16)$$

where $\gamma = (1 - \cos\theta)/2$ (not to be confused with the gyromagnetic ratio). Note that even though it is calculated from complex eigenvectors and eigenvalues, for every n , \mathbf{M}_n has real components. (We have chosen to keep the solution in a form where its connection to (8) is clear.) One of the eigenvalues = 1, corresponding to the steady-state solution. Since one of the p components equals zero, there are only two eigenvectors that contribute, thereby ensuring that \mathbf{M}_n travels in a plane as n increases. If there is no relaxation ($E = 1$), then this plane is perpendicular to the steady-state vector, as can be seen by taking the dot product of the steady-state vector with the other two eigenvectors. (In this case the “steady-state” vector is never actually reached, as discussed below.)

If instead $\mathbf{M}_0 \neq \mathbf{M}_{eq}$, then none of the p components are equal to zero. Therefore, an additional eigenvector contributes, and the path is no longer planar. The additional eigenvector is

$$\begin{bmatrix} \sqrt{\frac{\gamma-1}{\gamma}} \\ -1 \\ 1 \end{bmatrix} \quad (17)$$

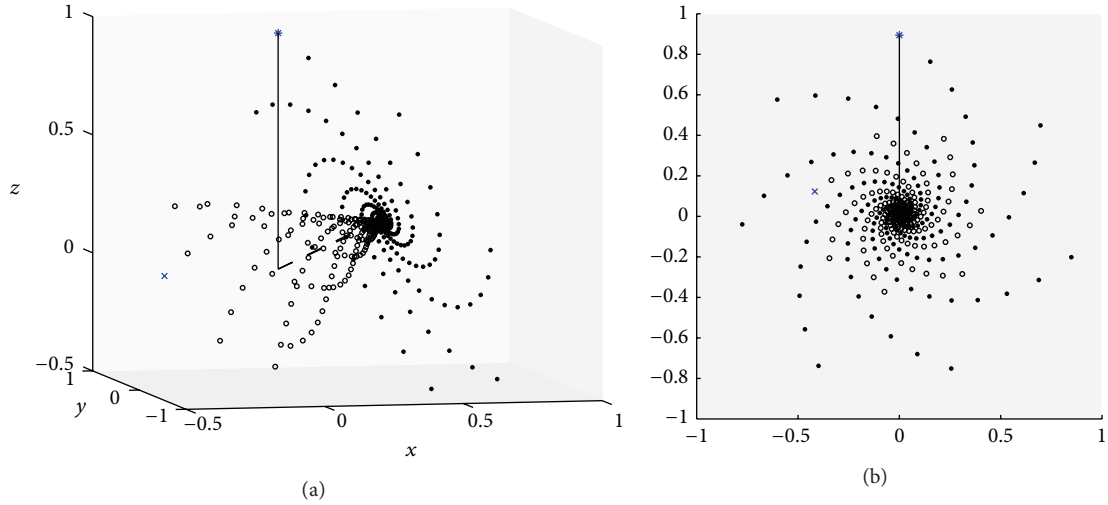


FIGURE 2: \mathbf{M}_n for $n = 0, 1, \dots, 200$. $\alpha = 90^\circ$, $\theta = 60^\circ$, and $E = 0.98$ with two different initial conditions: $\mathbf{M}_0 = [0 \ 0 \ 1] = \mathbf{M}_{\text{eq}}$ (solid circles starting at $*$) and $[-0.4472 \ -0.2236 \ 0]$ (open circles starting at \times). The solid line is along the +z-axis and the dashed line is the steady-state magnetization \mathbf{M}_{ss} . (a) and (b) are two different views, with (b) looking down along the direction of \mathbf{M}_{ss} .

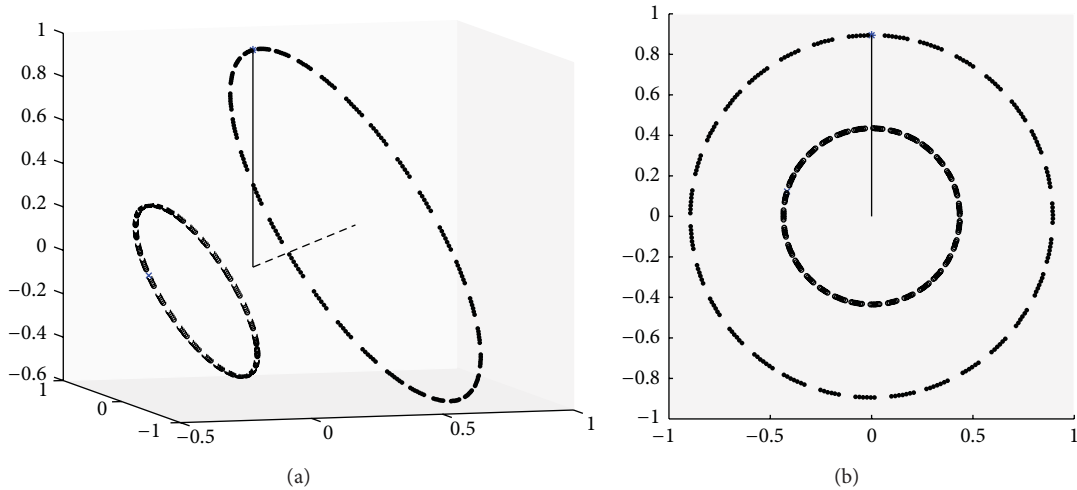


FIGURE 3: Identical to Figure 2, but with $E = 1$. Note that the “steady-state” vector is never actually reached and that it is perpendicular to the plane containing the circular trajectory.

with corresponding eigenvalue E . Since this eigenvalue is real, it cannot contribute to a rotational trajectory, as will be illustrated below.

6. Numerical Methods

Figure 2 plots the case for a repeated 90° pulse with $E = 0.98$, $\theta = 60^\circ$, and with two different initial conditions \mathbf{M}_0 . Figure 2(a) illustrates that when $\mathbf{M}_0 = \mathbf{M}_{\text{eq}}$, the path is a planar spiral, as expected. When $\mathbf{M}_0 \neq \mathbf{M}_{\text{eq}}$ (reached by magnetization preparations), the spiral instead wraps around a cone. The head-on view in Figure 2(b) indicates that the spirals rotate at the same angular rate, which follows from the additional eigenvalue being real. The conditions in Figure 3

are the same as in Figure 2 except that $E = 1$. With no relaxation, there is no decay and the “steady-state” solution is never reached; it is perpendicular to the plane containing the trajectory.

7. Discussion

The homogeneous and Cartesian coordinates provide two equivalent ways of representing magnetization. In pulsed repetition experiments, homogeneous coordinates lead to a simpler equation for the dynamics and steady state, but with a less intuitive connection to the measured magnetization. The choice of which system to use is in the end one of personal preference.

Acknowledgments

The authors would like to thank Martin Lepage for discussions concerning steady-state solutions. This work was supported by a Vanderbilt University Medical Center Discovery Grant.

References

- [1] I. Nazarova and M. A. Hemminga, “Analytical analysis of multi-pulse NMR,” *Journal of Magnetic Resonance*, vol. 170, no. 2, pp. 284–289, 2004.
- [2] M. L. Gyngell, “The steady-state signals in short-repetition-time sequences,” *Journal of Magnetic Resonance*, vol. 81, no. 3, pp. 474–483, 1989.
- [3] J. G. Sled and G. B. Pike, “Quantitative interpretation of magnetization transfer in spoiled gradient echo MRI sequences,” *Journal of Magnetic Resonance*, vol. 145, no. 1, pp. 24–36, 2000.
- [4] G. Strang, *Linear Algebra and Its Applications*, Harcourt Brace Jovanovich, Orlando, Fla, USA, 3rd edition, 1988.

Research Article

Research on Calculation of the IOL Tilt and Decentration Based on Surface Fitting

Lin Li,¹ Ke Wang,¹ Yan Yan,¹ Xudong Song,² and Zhicheng Liu¹

¹ School of Biomedical Engineering, Capital Medical University, Beijing 100069, China

² Beijing Tongren Hospital Affiliated to Capital Medical University, Beijing 100730, China

Correspondence should be addressed to Zhicheng Liu; zcl_55@163.com

Received 21 December 2012; Accepted 2 June 2013

Academic Editor: Wenxiang Cong

Copyright © 2013 Lin Li et al. This is an open access article distributed under the Creative Commons Attribution License, which permits unrestricted use, distribution, and reproduction in any medium, provided the original work is properly cited.

The tilt and decentration of intraocular lens (IOL) result in defocussing, astigmatism, and wavefront aberration after operation. The objective is to give a method to estimate the tilt and decentration of IOL more accurately. Based on AS-OCT images of twelve eyes from eight cases with subluxation lens after operation, we fitted spherical equation to the data obtained from the images of the anterior and posterior surfaces of the IOL. By the established relationship between IOL tilt (decentration) and the scanned angle, at which a piece of AS-OCT image was taken by the instrument, the IOL tilt and decentration were calculated. IOL tilt angle and decentration of each subject were given. Moreover, the horizontal and vertical tilt was also obtained. Accordingly, the possible errors of IOL tilt and decentration existed in the method employed by AS-OCT instrument. Based on 6–12 pieces of AS-OCT images at different directions, the tilt angle and decentration values were shown, respectively. The method of the surface fitting to the IOL surface can accurately analyze the IOL's location, and six pieces of AS-OCT images at three pairs symmetrical directions are enough to get tilt angle and decentration value of IOL more precisely.

1. Introduction

The operations of congenital lens subluxation have mostly implanted posterior chamber intraocular lens (IOL) through scleral suture fixation or capsular tension ring to combine with the capsular bag. Serious IOL dislocation has been controlled, but it is difficult to avoid the tilt and decentration of IOL [1–3]. Therefore, to obtain the reliable tilt and decentration of IOL could play an important role in the evaluation of the different operation schemes and effective treatment of postoperative complications.

Ultrasound biomicroscopy (UBM), Purkinje imaging system, anterior segment optical coherence tomography (AS-OCT), and Scheimpflug imaging system are the methods used for measurements of the IOL tilt and decentration in clinical practice. The Purkinje imaging system is simple, but it depends on the radius of curvature of the IOL surfaces. The III image by Purkinje meter can only show parts of the IOL anterior and posterior surfaces. This can have an effect on the radius of curvature and the results of IOL tilt

and decentration [4–7]. By UBM, operators can clearly see whether the IOL has tilt and decentration, but the tilt and decentration cannot be directly measured. Moreover, it is a contact inspection method and the deformation of the eyeball extruded by water in bath cup may affect the measured results [8, 9]. Scheimpflug imaging system can rapidly obtain the IOL tilt and decentration values, but it requires pupil dilation, which can cause the deviation of the pupil center. So, the IOL decentration measured by the system should be a distance between the IOL center and the nonreal pupil axis, thus the result measured is not accurate and the method has limitations [6, 10–12].

AS-OCT is a noninvasive and noncontact imaging method of measuring the IOL tilt and decentration and has been widely used in clinical practice. AS-OCT instrument can scan the eyeball at the rotated axis which is the line (called a baseline) passed through the anterior cornea center and the pupil center, and a lot of images can be scanned by AS-OCT at every scanned angle [13, 14]. According to each piece of scanned images, the IOL tilt and decentration are given by

AS-OCT instrument. The maximum value of IOL tilts and decentrations obtained from all the images are taken as the IOL tilt and decentration, respectively. In clinical practice, the IOL tilt degree is an angle between the IOL optical axis and the baseline, and the IOL decentration value is the vertical distance from the IOL center to the baseline [6, 11, 15]. Geometrically, the IOL tilt and decentration are two values independent with images. However, we have found that the IOL tilt and decentration values measured on different images at the same scanned angle were not the same. It is possible to result in errors of IOL tilt and decentration.

Due to the fact that IOL surface is similar to the spherical [6, 16], we assumed anterior and posterior surfaces of IOL to be spherical surfaces. The equations of the IOL anterior and posterior surfaces were calculated through the AS-OCT image registration and the surface fitting method, and then the IOL tilt and decentration were calculated.

2. Materials and Methods

2.1. Image Obtaining. In this study, AS-OCT images of 12 eyes of 8 patients with congenital subluxation lens were provided by the Ophthalmic Research Center of Beijing, Tongren Hospital. The system takes 2000 A scans per second and has an axial resolution of $18 \mu\text{m}$ and transverse resolution of $60 \mu\text{m}$. Moreover, it has a scan speed of 2000 times/second, scan time of 0.125 s/row and frame rate of 30 Hz [9, 13, 14, 17]. For each eyeball, the AS-OCT instrument provides 2-3 pieces of images at a degree from 0° to 180° with periods of 15° , Figure 1 shows a piece of these images. Image format is RGB and image size is 816×553 .

2.2. Image Registration. Because the center locations of the corneal anterior surface may be different among images, we need to use image registration for all the images from each scanned angle. The center of the corneal anterior surface is regarded as a reference point defined by the intersection point of corneal anterior surface and perpendicular bisector of the line joining scleral spurs, which is also regarded as reference line (Figure 1). Each picture can be made rigid transformation. Figure 2 gives one piece of registered images. After image transformation, the pixel values of the center of the corneal anterior surface in images were read to verify the correctness and validity of the rigid body transformation image again.

2.3. Collecting IOL Surface Data. From each piece of AS-OCT images, we can obtain two-dimensional pixel coordinates of points of the IOL anterior and posterior surfaces. In order to obtain the three-dimensional coordinates of points of the IOL surface data, Cartesian coordinate system is needed. We set the horizontal direction (alar to zygomatic direction) parallel to X axis, the vertical direction (nasal bone to the jaw bone direction) parallel to the Y axis, and the ocular axial is set as the Z axis. The center of the corneal anterior surface is as the origin of coordinates. Assuming that the two-dimensional coordinate of point A is (x, y) , and the three-dimensional



FIGURE 1: The AS-OCT image at 30 degrees scanned angle. Points A and B are scleral spurs. Point P is the intersection point of perpendicular bisector (L) and corneal anterior surface.

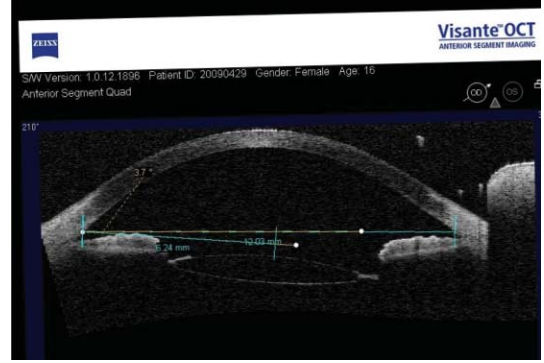


FIGURE 2: The registered image at 30 degrees scanned angle.

coordinate is (x', y', z') , the relations between them are as follows:

$$x' = x \cos \alpha, \quad y' = x \sin \alpha, \quad z' = y, \quad (1)$$

where α is scanned angle of AS-OCT.

2.4. The Tilt and Decentration of IOL Calculated by Geometric Method. From Figure 3, θ , known as tilt of IOL, is an angle between visual axis and optical axis of IOL. β , defined as tilt at the horizontal direction, is an angle between optical axis of IOL and X-axis. γ , defined as tilt at vertical direction, is an angle between optical axis of IOL and Y axis, and we know the following

$$\cos \theta = \frac{|c_2 - c_1|}{r_d}, \quad \cos \beta = \frac{|a_2 - a_1|}{r_d},$$

$$\cos \gamma = \frac{|b_2 - b_1|}{r_d}, \quad r_d = \sqrt{(a_2 - a_1)^2 + (b_2 - b_1)^2 + (c_2 - c_1)^2}. \quad (2)$$

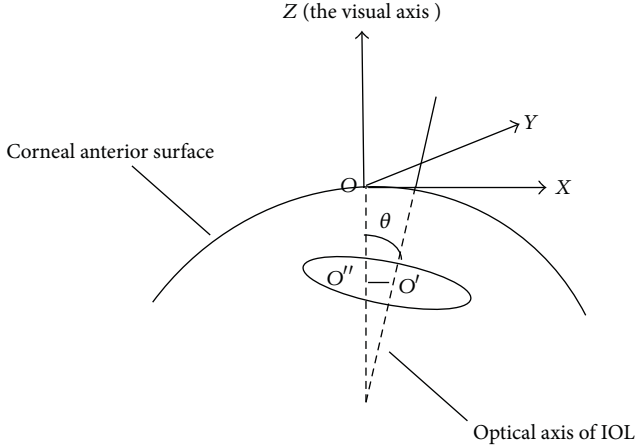


FIGURE 3: The geometrical definition of IOL tilt and decentration.

Decentration equation is as follows:

$$d = \sqrt{d_1^2 + \left[\left(\frac{b_2 - b_1}{a_2 - a_1} \right) d_1 + \frac{a_2 b_1 - a_1 b_2}{a_2 - a_1} \right]^2}, \quad (3)$$

$$d_1 = \frac{1}{2} \left(\frac{(a_2 - a_1)^2 (r_1^2 - r_2^2)}{r_d^2} + a_2 + a_1 \right),$$

where (a_1, b_1, c_1) and (a_2, b_2, c_2) are the coordinates of the spherical center of the fitted IOL anterior and posterior surface with radius of r_1 and r_2 , respectively.

2.5. IOL Tilt Calculated When the Different Scanned Angles. The IOL tilt and decentration at different scanned angles were calculated based on the equations of the IOL anterior and posterior surface. For the AS-OCT image with scanned angle of α , one can get the IOL tilt, denoted by $\omega(\alpha)$, from the following:

$$\cos \omega(\alpha) = \frac{|c_2 - c_1|}{\sqrt{r_d^2 - ((b_2 - b_1) \cos \alpha - (a_2 - a_1) \sin \alpha)^2}}. \quad (4)$$

Apparently, as $((b_2 - b_1) \cos \alpha - (a_2 - a_1) \sin \alpha)^2 = 0$, $\cos \omega(\alpha_0) = |c_2 - c_1|/r_d$ attains its minimum value, and $\omega(\alpha_0)$ is a maxima, which is exactly equal to tilt. Therefore, the tilt (θ) should take the maximum value from the tilts calculated at the different scanned angles.

For a piece of AS-OCT image with scanned angle of α (Figure 4), point E is the projection point of image center of IOL, and point F is the projection point of real center of IOL on XOY plane (coordinate plane, Figure 3). If there were not any decentration, three points O , E , and F were the same one. The length of segment OF is the IOL decentration, denoted by d . If there were not any IOL tilt, we know $EF \perp OE$. Defining, $\alpha = \angle XO E$, $\rho = \angle XO F$, and the equation of line OE is $y = x \tan \alpha$, for the AS-OCT image with scanned angle of α , the IOL decentration, denoted by $d_2(\alpha)$, can be obtained

$$d_2(\alpha) = \cos(\alpha - \rho) d. \quad (5)$$

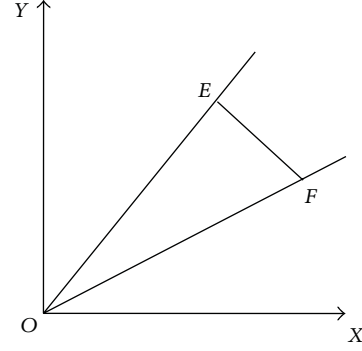


FIGURE 4: The projection of IOL center point in the plane at different scanned angles.

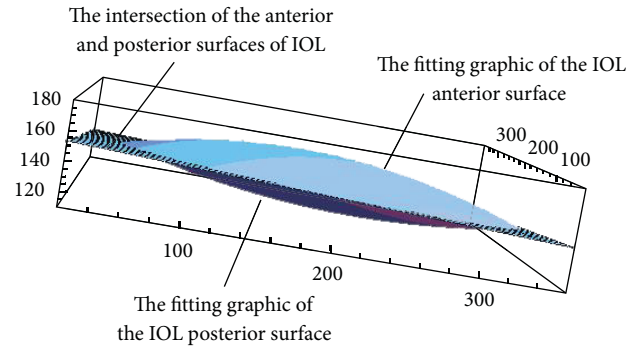


FIGURE 5: The image of IOL fitting surface and intersection of the anterior and posterior surfaces of IOL.

The IOL decentration $d_2(\alpha)$ attains its maximum value, the IOL decentration d , as long as $\cos(\alpha - \rho) = 1$. Therefore, the IOL decentration d is the maximum value of decentration $d_2(\alpha)$ calculated from all of different scanned angle images. If there is a tilt of IOL, segments EF and OE are nearly orthogonal; then the maximum of $d_2(\alpha)$ is close to the IOL decentration d .

3. Results

Figure 5 shows the IOL fitting surface of case 11. Table 1 gives the IOL tilt and decentration calculated by the surface fitting approach and their values given by AS-OCT instrument. The eighth column of Table 1 gives the diameter of IOL computed by the method of surface fitting. The goodness-of-fit (correlation coefficient R^2), shown in the ninth-tenth column of Table 1, was between 0.85 and 0.97.

Figure 6 gives the graph of the tilt $\omega(\alpha)$ defined by formula (4) and provided by AS-OCT instrument for case 12. It is found that the trend of two curves is identical with respect to the change of scanned angle. But the data provided by AS-OCT instrument oscillates with a small amplitude. It definitely affects the estimation of tilt.

Figure 7 gives data of the decentration calculated by the method of surface fitting and provided by AS-OCT instrument for case 12. It is shown that the trend of two curves is inconsistent with respect to the change of scanned angle.

TABLE 1: The IOL tilt and decentration obtained by the method of surface fitting.

Case	The method of AS-OCT instrument			The method of surface fitting					
	Tilt/ $^{\circ}$	Decentration/mm	The IOL tilt (θ)/ $^{\circ}$	The tilt at horizontal direction/ $^{\circ}$	The tilt at vertical direction/ $^{\circ}$	Decentration/mm	Optical diameter/mm	R^2 (IOL anterior surface)	R^2 (IOL posterior surface)
1	7.90	1.01	7.52	86.19	83.53	0.88	5.82	0.67	0.81
2	4.30	0.83	3.35	87.82	87.46	0.71	5.91	0.89	0.91
3	3.30	0.73	2.13	89.30	87.98	0.29	5.87	0.87	0.93
4	4.90	0.85	2.79	87.80	89.13	0.80	5.81	0.85	0.86
5	6.90	0.67	5.86	88.04	84.47	0.28	5.77	0.86	0.86
6	4.20	2.33	3.92	86.23	88.94	1.08	5.85	0.86	0.83
7	3.60	0.77	1.76	88.59	88.94	0.67	6.12	0.93	0.88
8	3.30	0.51	2.2	88.18	88.77	0.45	5.91	0.83	0.89
9	5.40	0.78	2.13	88.24	88.80	0.76	5.96	0.90	0.85
10	5.20	0.73	4.08	87.85	86.54	0.27	6.15	0.97	0.87
11	6.80	0.71	5.85	89.07	84.21	0.44	6.21	0.91	0.85
12	5.40	0.74	4.55	86.40	87.22	0.63	6.06	0.93	0.83

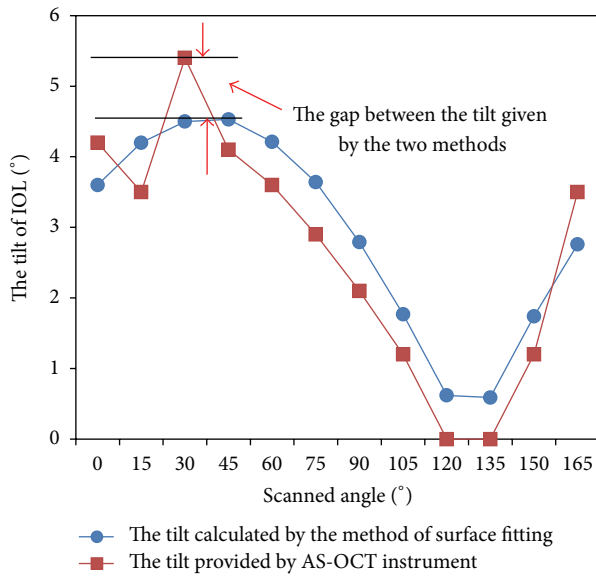


FIGURE 6: The relation with IOL tilts by the method of surface fitting and AS-OCT and scanned angles.

But the data provided by AS-OCT instrument oscillates with a large amplitude. According to formula (5), the decentration $d_2(\alpha)$ changes in accordance with cosine approximately. Clearly, the change of decentration $d_2(\alpha)$ calculated by our method is in accordance with cosine, but the decentration $d_2(\alpha)$ data provided by AS-OCT instrument is inconsistent with the previous trend.

Table 2 gives the results of the IOL tilt and decentration of three cases by two methods in different scanned angles (The “—” shown in the Table 2 means that this data is not available). The results of IOL tilt and decentration shown in Table 3 were calculated by surface fitting method based on 6, 7, 8, 9, 10, and 11 pieces of AS-OCT images, respectively.

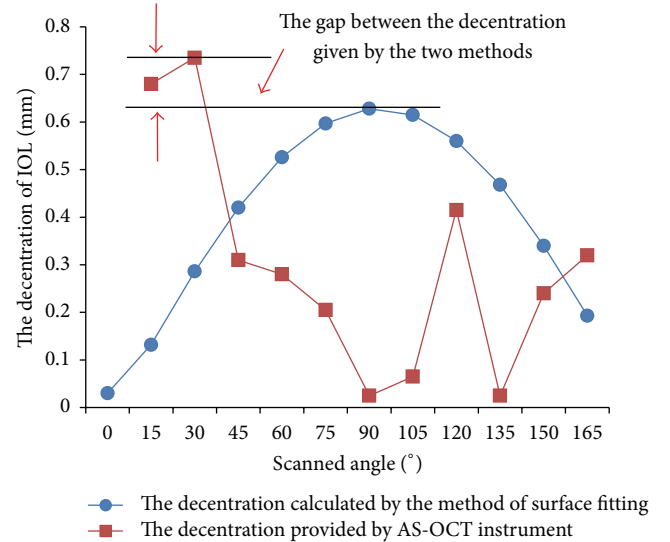


FIGURE 7: The relation with IOL decentration by the method of surface fitting and AS-OCT and scanned angles.

4. Discussion

According to AS-OCT images, the IOL tilt and decentration were calculated by collecting data of IOL surface and spherical fitting to the data of IOL anterior and posterior surfaces. The goodness-of-fit (R^2) is between 0.85 and 0.97.

Korynta et al. [18] showed that the drift and oblique astigmatism can be caused by the IOL decentration being more than 1 mm and the IOL tilt being more than 5 degrees. In our results, the decentration of one eye was greater than 1 mm and the tilts of 3 eyes were greater than 5 degrees. The IOL tilt and decentration of the other 8 eyes basically were within the normal range given by Korynta. It is noticed that most of the cases used in this study are successful in operations. This verified that our results were in accordance

TABLE 2: IOL decentration and tilt obtained from the image with different scanned angle.

Scanned angle/ $^{\circ}$	Tilt/ $^{\circ}$						Decentration/mm					
	Case 6		Case 4		Case 12		Case 6		Case 4		Case 12	
	Surface fitting	AS-OCT	Surface fitting	AS-OCT	Surface fitting	AS-OCT	Surface fitting	AS-OCT	Surface fitting	AS-OCT	Surface fitting	AS-OCT
0	2.72	3.60	2.21	2.50	3.60	4.20	0.18	1.86	0.15	0.01	0.03	—
15	3.93	1.50	1.70	3.40	4.20	3.50	0.68	1.69	0.35	0.85	0.13	0.68
30	3.82	1.90	1.47	4.10	4.50	5.40	0.44	1.39	0.52	0.79	0.29	0.74
45	3.41	3.20	1.21	2.00	4.53	4.10	0.17	1.32	0.66	0.78	0.42	0.31
60	2.83	1.30	0.40	0.50	4.21	3.60	0.11	2.40	0.75	0.33	0.53	0.28
75	2.03	4.20	0.30	0.50	3.64	2.90	0.38	1.67	0.80	0.67	0.60	0.21
90	1.1	2.00	0.92	1.60	2.79	2.10	0.63	2.16	0.78	0.16	0.63	0.03
105	0.04	0.00	1.40	1.00	1.77	1.20	0.83	2.34	0.72	0.59	0.62	0.07
120	0.98	2.40	1.85	2.10	0.62	0.00	0.98	2.34	0.61	0.31	0.56	0.42
135	1.13	3.10	2.21	2.70	0.59	0.00	0.87	—	0.45	0.03	0.47	0.03
150	2.74	2.40	2.40	3.50	1.74	1.20	1.07	1.94	0.26	0.03	0.34	0.24
165	3.38	2.30	2.35	4.90	2.76	3.50	1.01	1.77	0.06	0.77	0.20	0.32
IOL	3.92	4.20	2.37	4.90	4.55	5.40	1.08	2.40	0.80	0.85	0.63	0.74

TABLE 3: IOL tilt and decentration calculated by surface fitting method based on 6, 7, 8, 9, 10, and 11 pieces of AS-OCT images.

AS-OCT image	Case 5		Case 6		Case 1		Case 4	
	Tilt/ $^{\circ}$	Decentration/mm						
11	5.86	0.28	3.92	1.08	—	—	—	—
10	6.10	0.25	3.94	1.02	7.50	0.88	2.79	0.80
9	6.05	0.27	3.73	1.03	7.85	0.81	2.56	0.79
8	5.79	0.25	3.76	1.03	7.49	0.84	2.54	0.81
7	6.45	0.21	3.70	1.02	6.69	0.86	2.63	0.79
6	6.22	0.24	3.68	1.03	6.35	0.82	2.54	0.79

with results of the literatures and clinical. In addition, optical diameter of the IOL provided by the manufacturer is 5.5 mm–6 mm. The IOL optical diameter obtained in this study was basically in this range (Table 1). We noticed that the calculated IOL diameters are slightly larger than those provided by the manufacturer. The reason is that the edge of IOL was made with a smooth and certain thickness shape, but we have not taken into account this issue in the calculation (Figure 7).

The results of tilt calculated by surface fitting (Table 1, 1.76–7.52 degrees) were higher than those of Dhivya's study (0.04–3.6 degrees) [19]. Besides sample differences, the main reason is that the maximum value obtained from the four images (0 degrees, 90 degrees, 45 degrees, and 135 degrees [19]) is possibly less than the IOL tilt (see, (4)). Our results are consistent with those of Xue et al. (tilt, 5.48 ± 1.95 degrees; decentration 1.09 ± 0.65 mm) [20] and Baumeister et al. (tilt, 0.91–6.83 degrees; decentration 0.06 mm–0.51 mm) [21]. In fact, the IOL tilt and decentration were possibly involved in the difference of individuals, surgeons, and measurements.

Assume that IOL anterior and posterior surfaces are spheres. We give the formula of tilt $\omega(\alpha)$ and the approximate expression of decentration $d_2(\alpha)$ when the scanned angle is α . The two relationships display that both of tilt and

decentration continuously change in cosine law. The IOL tilt and decentration are the maximum values of the tilt $\omega(\alpha)$ and decentration $d_2(\alpha)$, respectively. However, the tilt and decentration given by AS-OCT instrument are the maximum value of $\omega(\alpha)$ and $d_2(\alpha)$ among of all scanned images, respectively. Figures 6 and 7 show that the errors of tilt and decentration produced by AS-OCT are large. In fact, each image contains errors. If these errors are not eliminated, the tilt $\omega(\alpha)$ and decentration $d_2(\alpha)$ calculated from each image could cause larger accumulation errors. In our method, the errors are eliminated by registration of images at different scanned directions and selecting as many as possible pixel points to a certain extent. So, the IOL tilt and decentration calculated with the method of surface fitting are accurate.

In order to reduce the pressure of clinical work, it is very significant to provide the method for calculating the more accurate tilt and decentration of IOL and saving the workload. Table 3 gives the results of IOL tilt and decentration calculated with 11, 10, 9, 8, 7, 6 AS-OCT images, respectively by the method. This problem is one of innovations of this study. Although the number of images used to obtain IOL tilt and decentration are 2 (90 degrees and 180 degrees) [6, 15], 4 (0 degrees, 45 degrees, 90 degrees, and 135 degrees) [19],

and 5 (five different directions) [22], their results are not verified. Table 3 shows that the IOL tilt and decentration become smaller with the decreasing of the number of images. The tilt and decentration changed in the range of 1 degree and 0.05 mm, respectively. If the errors were neglected in clinical practice. It is suggested that the method can calculate the more accurate tilt and decentration of IOL with scanned angles at the six symmetrical directions.

The IOL tilt measured by AS-COT instrument is the angle between the IOL optical axis and the line joining the centers of the anterior cornea and the pupil. Our method can not only give the IOL tilt, but also the tilt at the horizontal direction and the tilt at the vertical direction. To the knowledge of the authors, it has not been reported whether the horizontal and vertical angles can affect the recovery of vision and optical imaging quality. This may be related to the current methods in clinic leaving two angles unknown. Therefore, it should be studied that whether the horizontal and vertical angles have an impact on visual acuity and visual effect in future.

This study is limited in the following: because IOL was covered by iris and opaque tissues, the middle part of IOL is only displayed in the image, and the point near the IOL boundary cannot be obtained. In addition, artificial selection and obtaining pixel coordinates will bring the errors. This will affect the similarity of the fitting surface and the actual IOL surface. Therefore, it should be studied that the method can reduce errors in collecting data for improving the fitting goodness in future. In addition, this study assumed that the IOL surface was spherical. But the aspheric surface cannot be thought about. It is hoped that the IOL surface can be calculated with the method of aspheric fitting in future. Moreover, compared with two methods of spherical and aspheric fitting, the results calculated with two methods can be more close to the real values in clinical.

In conclusion, the method of the surface fitting to the IOL surface can accurately analyze the IOL's location, and six piece of AS-OCT images at three pairs symmetrical directions are enough to get tilt angle and decentration value of IOL more precisely.

Authors' Contribution

Lin Li and Ke Wang contributed equally to this work.

Acknowledgments

This work was financially supported by the National Natural Science Foundation of China (no. 31070840), the Beijing Natural Science Foundation (3122010), and Beijing Leading Academic Discipline Project of Beijing Municipal education Commission (PHR201110506).

References

- [1] M. Scherer, E. Bertelmann, and P. Rieck, "Late spontaneous in-the-bag intraocular lens and capsular tension ring dislocation in pseudoxfoliation syndrome," *Journal of Cataract and Refractive Surgery*, vol. 32, no. 4, pp. 672–675, 2006.
- [2] H. Saedon, W. H. Chan, and R. Radford, "Anterior dislocation of a Morcher capsular tension ring," *Journal of Cataract and Refractive Surgery*, vol. 37, no. 5, pp. 967–968, 2011.
- [3] F. Taketani, T. Matuura, E. Yukawa, and Y. Hara, "Influence of intraocular lens tilt and decentration on wavefront aberrations," *Journal of Cataract and Refractive Surgery*, vol. 30, no. 10, pp. 2158–2162, 2004.
- [4] D. L. Guyton, H. Uozato, and H. J. Wisnicki, "Rapid determination of intraocular lens tilt and decentration through the undilated pupil," *Ophthalmology*, vol. 97, no. 10, pp. 1259–1264, 1990.
- [5] U. Mester, T. Sauer, and H. Kaymak, "Decentration and tilt of a single-piece aspheric intraocular lens compared with the lens position in young phakic eyes," *Journal of Cataract and Refractive Surgery*, vol. 35, no. 3, pp. 485–490, 2009.
- [6] W. Zhang, Z. X. Ma, R. Y. Liu, and L. Zhang, "Spherical and aspheric intraocular lens tilt and decentration effect on Visual quality," *Chinese Journal of Practical Ophthalmology*, vol. 28, no. 11, pp. 1232–1235, 2010.
- [7] Y. Nishi, N. Hirnschall, A. Crnej et al., "Reproducibility of intraocular lens decentration and tilt measurement using a clinical Purkinje meter," *Journal of Cataract and Refractive Surgery*, vol. 36, no. 9, pp. 1529–1535, 2010.
- [8] M. Modesti, G. Pasqualitto, R. Appolloni, I. Pecorella, and P. Sourdille, "Preoperative and postoperative size and movements of the lens capsular bag: ultrasound biomicroscopy analysis," *Journal of Cataract and Refractive Surgery*, vol. 37, no. 10, pp. 1775–1784, 2011.
- [9] T. Dada, R. Sihota, R. Gadia, A. Aggarwal, S. Mandal, and V. Gupta, "Comparison of anterior segment optical coherence tomography and ultrasound biomicroscopy for assessment of the anterior segment," *Journal of Cataract and Refractive Surgery*, vol. 33, no. 5, pp. 837–840, 2007.
- [10] A. D. Castro, P. Rosales, and S. Marcos, "Tilt and decentration of intraocular lenses in vivo from Purkinje and Scheimpflug imaging. Validation study," *Journal of Cataract and Refractive Surgery*, vol. 33, no. 3, pp. 418–429, 2007.
- [11] Y. W. Fang, Y. Lu, and L. Wang, "Decentration and tilt of foldable intraocular lenses in the lens capsule," *Chinese Journal of Optometry & Ophthalmology*, vol. 10, no. 4, pp. 252–258, 2008.
- [12] M. Baumeister and T. Kohnen, "Scheimpflug measurement of intraocular lens position after piggyback implantation of foldable intraocular lenses in eyes with high hyperopia," *Journal of Cataract and Refractive Surgery*, vol. 32, no. 12, pp. 2098–2104, 2006.
- [13] D. A. Kumar, A. Agarwal, G. Prakash, S. Jacob, Y. Saravanan, and A. Agarwal, "Evaluation of intraocular lens tilt with anterior segment optical coherence tomography," *American Journal of Ophthalmology*, vol. 151, no. 3, pp. 406–412, 2011.
- [14] Q. Zhang, W. Jin, and Q. Wang, "Repeatability, reproducibility, and agreement of central anterior chamber depth measurements in pseudophakic and phakic eyes: optical coherence tomography versus ultrasound biomicroscopy," *Journal of Cataract and Refractive Surgery*, vol. 36, no. 6, pp. 941–946, 2010.
- [15] Y. L. Wang, J. Yang, Y. Wang, L. Luo, M. He, and Y. Liu, "Biometry of intraocular lenses using Pentacam Scheimpflug images," *Eye Science*, vol. 22, no. 2, pp. 119–123, 2006.
- [16] X.-J. Xing, X. Tang, H. Song, and W.-W. Li, "Comparison of tilt and decentration of four different kinds of aspheric intraocular lenses implantation," *Chinese Journal of Ophthalmology*, vol. 46, no. 4, pp. 332–336, 2010.

- [17] A. Koivula and M. Kugelberg, "Optical coherence tomography of the anterior segment in eyes with phakic refractive lenses," *Ophthalmology*, vol. 114, no. 11, pp. 2031–2037, 2007.
- [18] J. Korynta, J. Bok, J. Cendelin, and K. Michalova, "Computer modeling of visual impairment caused by intraocular lens misalignment," *Journal of Cataract and Refractive Surgery*, vol. 25, no. 1, pp. 100–105, 1999.
- [19] A. K. Dhivya, A. Amar, and P. Gaurav, "Evaluation of intraocular lens tilt with anterior segment optical coherence tomography," *American Journal of Ophthalmology*, vol. 151, no. 3, pp. 406–412, 2011.
- [20] W. J. Xue, X. D. Song, and Y. Yan, "Surgical treatment of congenital subluxated lense—a random controlled clinical trial. Chinese," *Journal of Practical Ophthalmology*, vol. 28, no. 6, pp. 615–618, 2010.
- [21] M. Baumeister, J. Bühren, and T. Kohnen, "Tilt and decentration of spherical and aspheric intraocular lenses: effect on higher-order aberrations," *Journal of Cataract and Refractive Surgery*, vol. 35, no. 6, pp. 1006–1012, 2009.
- [22] S. J. Yu, Y. Yan, and L. Li, "A geometry method for evaluating the values of intraocular lens tilt and decentration," in *Proceedings of the 4th International Conference on Biomedical Engineering and Informatics (BMEI '11)*, vol. 3, pp. 1462–1465, October 2011.

Research Article

Bayesian Hierarchical Modeling for Categorical Longitudinal Data from Sedation Measurements

Erol Terzi and Mehmet Ali Cengiz

Department of Statistic, Ondokuz Mayıs University, 55139 Samsun, Turkey

Correspondence should be addressed to Erol Terzi; eroltrz@omu.edu.tr

Received 20 December 2012; Accepted 17 June 2013

Academic Editor: Wenxiang Cong

Copyright © 2013 E. Terzi and M. A. Cengiz. This is an open access article distributed under the Creative Commons Attribution License, which permits unrestricted use, distribution, and reproduction in any medium, provided the original work is properly cited.

We investigate a Bayesian hierarchical model for the analysis of categorical longitudinal data from sedation measurement for Magnetic Resonance Imaging (MRI) and Computerized Tomography (CT). Data for each patient is observed at different time points within the time up to 60 min. A model for the sedation level of patients is developed by introducing, at the first stage of a hierarchical model, a multinomial model for the response, and then subsequent terms are introduced. To estimate the model, we use the Gibbs sampling given some appropriate prior distributions.

1. Introduction

Magnetic Resonance Imaging (MRI) and Computerized Tomography (CT) require the patient to lie still for periods of up to 60 min. These two diagnostic procedures also require strict immobility and sedation for a successful result. If a child cannot remain adequately still for examination, sedation may be necessary. Optimal sedation management of children before MRI and CT has received attention in the last decade [1, 2]. The sedation medications must be chosen carefully for children's safety and effectiveness. Many researches related to the comparison of different sedation medications have been performed successfully [3, 4]. In these studies, for each medication group sedation levels were obtained at different time points within the time up to 60 min. In addition to sedation level measurements, the other multiple assessments of the same patient were recorded, and the within subject ones, such as sedation levels at different time points for a given patient, were correlated. This case is an example when a longitudinal study is made with responses being measured repeatedly on the same patient across time. In medical studies, statistical analysis of the data set described earlier has been performed by many researchers, who use the known methods such as ANOVA, MANOVA, and Linear Models, assuming that the repeated observations from each patient

are uncorrelated. Since repeated observations are made on the same patient, observed responses are generally correlated. For robust analysis, this association must be accounted for. Weighted least squares model is used for repeated categorical data. This model works well for large sample size, no missing data, a small number of response variables, and discrete independent variables. Recent years have witnessed new statistical methods of analysing for data that do not meet these conditions.

Mathematical models for multiple regression, linear models, and time series are generally useful where random variables are approximately normal and can be explained by some linear structure. However, data can be clearly nonnormal when they represent categorical or frequency observations. Generalized Linear Models (GLMs) offer convenient and highly applicable tools for these kinds of data. They allow for more general structures and more general distributions than linear regression and ANOVA. Nelder and Wedderburn developed the concept of GLMs [5], and an extensive treatment was given by [6]. With the introduction of GLM, a much more flexible instrument for statistical modeling was created. As special cases, they include multiple linear regression, logit and probit models for quantal responses, and log linear response models for counts. Introduced Generalized

Estimating Equations (GEEs) [7] were developed to extend the GLM introduced by [5].

Longitudinal researches are defined as studies in which the response of each patient is observed on two or more occasions. They are often used in medical and health research. The methods used for the analysis of longitudinal data differ from the traditional regression analysis such as multiple regressions. Longitudinal data sets consist of repeated observations of an patient and a set of covariates for each of many patients which may be fixed or which may be changed with time. Longitudinal data sets are defined by the fact that repeated observations for a patient are correlated [8]. Therefore the modeling of the correlation structure is required. When the response variable is normal, a large class of linear models is available for analysis. However, when the response variable is categorical, other methods must be considered. In recent years, considerable effort has gone into the development of statistical methods for the analysis of longitudinal categorical response data. While much of this effort has focused on methods for binary or Poisson data, relatively little attention has been given to nominal categorical data.

More generally, hierarchical models describe efficiently complex datasets incorporating correlation or including other properties in our model. Hence, when multivariate or repeated responses are observed, correlation can be incorporated in the model via a common “random” effect for all measurements referring to the same individual. This introduces a marginal correlation between repeated data, while interpretation is based on the conditional means. Therefore, given the random effects, the structure and the interpretation are similar to common generalized linear models. Accordingly, hierarchical models naturally appear, for example, when modeling spatiotemporal data in which correlation between time and space can be added by using common random effects on adjacent (in time or space) responses. Hierarchical models can also be used to imply a complicated marginal distribution but (at the same time) keep the conditional structure as simple as possible [9].

Bayesian analyses of hierarchical linear models have been considered for at least forty years [10] and have remained a topic of theoretical and applied interest [11–14]. Reference [15] reviews much of the extensive literature in the course of comparing Bayesian and non-Bayesian inferences for hierarchical models. As part of their article, Browne and Draper consider some different prior distributions for variance parameters; here, we explore the principles of hierarchical prior distributions in the context of a specific class of models. Hierarchical (multilevel) models are central to modern Bayesian statistics for both conceptual and practical reasons. At a practical level, hierarchical models are flexible tools for combining information and partial pooling of inferences [16–18].

In this study, we use a Bayesian approach to fit several hierarchical models of increasing complexity to assess the significance of both fixed and random effects on sedation levels and investigate a Bayesian hierarchical model for the analysis of categorical longitudinal data from sedation measurement for MRI and CT. A model for the sedation level of patients is developed by introducing, at the first stage of

a hierarchical model, a multinomial model for the response and then subsequent terms are introduced.

2. Material and Method

There are several methods that may be used to estimate the determinants of sedation levels with categories $(1, \dots, 6)$.

First method we considered is the multinomial logit approach. The model

$$\Pr\left(Y_{it} = \frac{j}{X_{it}}\right) = \frac{\exp(X_{it}\beta_j)}{\sum_{k=1}^j \exp(X_{it}\beta_k)}, \quad (1)$$

where $\Pr(Y_{it} = j/X_{it})$ is the probability that patient i has outcome j at time t given covariates X_{it} of the patient at that time.

In our analysis the response has six levels ($j = 1, \dots, 6$). For identifiability, $j = 1$ is set as the reference category so that the parameters estimated from the multinomial logistic model are interpreted as the logarithm of the change in the odds of being outcome j relative to that of being outcome 2 for a one unit change in the corresponding explanatory variable at time t .

We investigate the relationship between sedation levels and both categorical and continuous explanatory variables by specifying a Bayesian hierarchical model for the multinomial response. We also include the lagged response variable in the model to assess the probability of transition between the times. Reference [19] considers a dynamic multinomial logit panel model with random effects to explain the labour market level of individuals in urban Mexico. The individual effects are assumed to be independent of the observed characteristics and to follow a multivariate normal distribution. We use a similar model for explaining the sedation levels of patients in which the selected covariates and sedation levels at the time of the previous time may influence the sedation levels of a patient.

Assume that patient $i (= 1, \dots, N)$ can be in any of j possible levels at time $t (= 1, \dots, T)$. In the first level of the Bayesian hierarchical model, the $y_{it} = (y_{it1}, \dots, y_{itj})$ are assumed to be distributed as multinomial random variables. The response takes the value $y_{itj} \in \{1, 2, 3, 4, 5, 6\}$. The model may be written as

$$y_{itj} \sim \text{multinomial}(P_{itj}, n_{it}), \quad (2)$$

where P_{itj} is the probability of patient i being in level j at time t .

The second level of the model relates the probabilities P_{itj} to the regression effects, lagged effects, and random effects such that

$$P_{itj} = \frac{\mu_{itj}}{\sum_j \mu_{itj}}, \quad (3)$$

$$\log it(\mu_{itj}) = X_{it}^T \beta_j + Z_{it}^T \gamma_j + \alpha_{ij},$$

where X_{it} is a matrix of explanatory variables, Z_{it} is a matrix of lagged level variables, β_j and γ_j are vectors of parameters

TABLE 1: The model used in this study.

Model	
1	$\log(\mu_{itj}) = X_{it}^T \beta_j + \alpha_{ij}$
2	$\log(\mu_{itj}) = X_{it}^T \beta_j + Z_{it}^T \gamma_j$
3	$\log(\mu_{itj}) = X_{it}^T \beta_j + Z_{it}^T \gamma_j + \alpha_{ij}$
4	$\log(\mu_{itj}) = X_{it}^T \beta_j + Z_{it}^T \gamma_{jt}$
5	$\log(\mu_{itj}) = X_{it}^T \beta_j + Z_{it}^T \gamma_{jt} + \alpha_{ij}$

to be estimated, and α_{ij} is a random effect reflecting time constant unobserved heterogeneity.

To identify the model, we choose first level of sedation to be reference level ($j = 1$) with β_1, γ_1 , and α_{i1} set to 0. It follows that $\log(\mu_{it1}) = 0$, and, hence,

$$\log\left(\frac{P_{itj}}{P_{it1}}\right) = \log\left(\frac{\mu_{itj}}{\mu_{it1}}\right) = \log(\mu_{itj}). \quad (4)$$

So $\log(\mu_{itj})$ can be interpreted as the log of the probability of being in level j relative to the probability of being in level 1.

The posterior distributions for all parameters are as follows

$$P(\beta, \gamma, \alpha, \Sigma | y) \propto P(y | \beta, \gamma, \alpha, \Sigma) \times P(\Sigma) \times P(\beta) \times P(\gamma), \quad (5)$$

where we have assumed that unknown parameters β , γ , and Σ are a priori independent and α depend only on Σ . MCMC methods are used to sample from the posterior distributions of the unknown parameters. We have used the WinBug software which uses the Gibbs sampling to form the posterior distribution for each unknown parameter by drawing samples from their full conditional distributions.

Our primary interest in modeling sedation levels is to investigate the effects of the some covariates as well as the transition from one sedation level to another as time since arrival progresses. To do this we consider five variations of the model in Table 1. The models contain combinations of terms to capture the covariate effects, the transition effects, and a random effects term to capture over dispersion in the form of between-subject variability.

In the model 1, given sedation level j , the regression effects remain constant but each individual i is considered as a cluster of responses over time ($t = 1, 2, 3$). A random intercept term α_{ij} which is allowed to vary between individuals, given level j , is included in the model to account for time constant unobserved variability. In the model 2, given sedation level j , this model includes constant regression effects β_j for the covariates X_{it} as well as constant regression effects γ_j for the lagged response variable Z_{it} . The term representing the lagged response may be useful in explaining the transition between sedation levels and absorb some of the unobserved variability between individuals. The model 3 is similar to model 2 with a random effect term α_{ij} included to capture any additional between-subject variation. In the model 4, given sedation level j , this model includes constant regression effects for the covariates but differs to model 2

TABLE 2: Descriptions of predictor values used in the analysis.

Predictor	Description
Group	M: Midazolam; D: Diazepam; L: Luminal; C: Cardiac Cocktail.
Age	Between 4 months old and 13 years old.
Weight	Between 6 kg and 46 kg.
Test	CT and MRI.
Sex	Male and female.
Disease	Diseased with neurological damage. Not diseased.
SBP	Systolic blood pressure.
PUL	Pulse.
OSAT	Oxygen saturation.
Comp	Complication: yes and no.

TABLE 3: Ramsay sedation scale.

Categories	Response
Sed1	Anxious or restless or both
Sed2	Cooperative, orientated, and tranquil
Sed3	Responding to commands
Sed4	Brisk response to stimulus
Sed5	Sluggish response to stimulus
Sed6	No response to stimulus

as it also includes time-varying effects γ_{jt} for the lagged response variable, Z_{it} . These effects are included to capture any change in the transition in sedation levels between the different times. The model 5 is similar to model 4 with a random effect term α_{ij} included to capture any additional between-subject variation.

The ability to fit complex hierarchical models using MCMC techniques presents a need for methods to compare alternative models. Standard model comparison techniques such as the Akaike Information Criterion (AIC) [20] and the Bayesian Information Criterion (BIC) [21] require the specification of the number of parameters in each model. For hierarchical models which contain random effects, the number of parameters is not generally obvious and so an alternative method of comparison is required. The Deviance Information Criterion (DIC) is a hierarchical modeling generalization of the AIC and BIC. It is particularly useful in Bayesian model selection problems where the posterior distributions of the models have been obtained by MCMC simulation. Like AIC and BIC it is an asymptotic approximation as the sample size becomes large.

DIC was developed by [22]. The DIC statistic is a measure of model complexity and fit and is defined as

$$DIC = \overline{D(\theta)} + p_D, \quad (6)$$

where $D(\theta)$ is the deviance given the model parameters θ , $\overline{D(\theta)}$ is the posterior mean of the deviance, $D(\bar{\theta})$ is the deviance evaluated at the posterior mean $\bar{\theta}$, and $p_D = \overline{D(\theta)} - D(\bar{\theta})$ is the effective number of parameters in the model.

TABLE 4: Posterior summaries for the effect on $\log[P(\text{Sed6})/P(\text{Sed1})]$ using Model 1.

Variables	Mean	Sd	MC error	%2.5	Median	%97.5	Start	Sample
Group								
C	-3,1681	4,172	0,0043	-1,121	-3,017	7,016	1000	10.000
D	-53,215	1,931	0,0011	-53,131	-52,911	-50,97	1000	10.000
L	17,312	10,171	0,0211	-21,431	16,951	23,71	1000	10.000
Age	0,017	0,021	0,0001	-0,015	0,021	0,038	1000	10.000
Sex [male]	-0,312	0,295	0,003	-0,773	-0,331	0,121	1000	10.000
Disease [1]	-0,215	0,211	0,015	-0,328	-0,231	0,174	1000	10.000
Weight	-0,1311	0,0111	0,001	-0,151	-0,1417	-0,1317	1000	10.000
Comp (yes)	0,087	0,0095	0,002	0,065	0,081	0,093	1000	10.000
Test (1)	0,137	0,131	0,021	-0,021	0,136	0,141	1000	10.000
Sps	-0,016	0,003	0,003	-0,6171	-0,015	-0,0139	1000	10.000
Pul	-0,0121	0,002	0,0001	-0,0729	-0,012	-0,011	1000	10.000
OSAT	-0,117	0,011	0,0002	-0,018	-0,013	0,011	1000	10.000

TABLE 5: Estimated posterior means and %95 intervals.

Variables	Model 1	Model 2	Model 3	Model 4	Model 5
Group					
C	-3,017 (-4,121; 7,016)	-2,981 (-3,115; 6,812)	-2,17 (-2,29; 5,61)	-4,21 (-5,51; 9,82)	-3,81 (-6,61; 3,43)
D	-52,911 (-53,131; -50,97)	-48,17 (-52,16; -46,13)	-37,4 (-48,1; -29,8)	-41,4 (-53,1; -26,1)	-43,5 (-51,4; -31,5)
L	16,931 (-21,431; 23,71)	15,81 (-21,03; 21,74)	10,71 (-5,03; 15,2)	13,15 (-4,81; 27,16)	17,51 (-3,85; 21,12)
Age	0,021 (-0,025; 0,039)	0,018 (-0,074; 0,041)	0,17 (-0,43; 0,48)	0,07 (-0,29; 0,61)	0,11 (-0,41; 0,23)
Sex	-0,331 (-0,773; 0,121)	-0,365 (-0,443; 0,141)	-0,91 (-1,21; 0,78)	-0,45 (-1,54; 1,131)	-0,71 (-1,13; 1,45)
Disease	-0,231 (-0,328; 0,174)	-0,261 (-0,317; 0,161)	-0,98 (-1,67; 0,71)	-0,631 (-1,27; 0,617)	-0,73 (-1,11; 0,62)
Weight	-0,1417 (-0,151; 0,1317)	-0,1321 (-0,1617; -0,117)	-0,67 (-0,87; -0,25)	-0,24 (-0,43; 0,12)	-0,34 (-0,84; -0,17)
Comp	0,081 (0,065; 0,093)	0,076 (0,051; 0,113)	0,162 (0,101; 0,312)	0,151 (0,09; 0,27)	0,101 (0,06; 0,17)
Test	0,136 (-0,221; 0,141)	0,121 (-0,114; 0,151)	0,671 (-1,21; 0,83)	0,541 (-1,51; 1,19)	0,337 (-1,17; 0,98)
Sps	-0,015 (-0,0171; -0,0139)	-0,013 (-0,031; -0,009)	-0,065 (-1,11; -0,03)	-0,047 (-1,76; -0,04)	-0,018 (-0,29; -0,03)
Pul	-0,012 (-0,0729; -0,011)	-0,015 (-0,021; -0,008)	-0,023 (-0,045; -0,012)	-0,014 (-0,21; -0,04)	-0,091 (-1,21; -0,02)
OSAT	-0,013 (-0,018; 0,011)	-0,021 (-0,033; 0,016)	-0,156 (-0,211; 0,06)	-0,11 (-0,35; -0,04)	-0,17 (-0,29; -0,13)
Sed-level (1, $t - 1$) [Sed1]					
Sed2		5,43 (3,98; 6,83)	4,91 (3,71; 5,61)		
Sed3		5,65 (2,68; 7,26)	4,73 (3,86; 5,12)		
Sed4		5,21 (3,12; 5,93)	5,13 (4,67; 5,37)		
Sed5		5,85 (3,29; 6,81)	4,88 (4,21; 5,17)		
Sed6		5,43 (4,71; 4,81)	5,13 (4,91; 5,61)		
Sed-level (2, $t - 1$) [Sed1]					
Sed2				5,13 (4,81; 5,61)	5,41 (4,71; 5,91)
Sed3				5,29 (4,61; 5,79)	5,16 (4,51; 5,56)
Sed4				5,41 (4,71; 4,81)	5,23 (4,91; 5,61)
Sed5				5,35 (4,91; 5,81)	5,44 (5,01; 5,96)
Sed6				5,25 (4,12; 5,93)	5,23 (4,67; 5,37)
Sed-level (3, $t - 1$) [Sed1]					
Sed2				5,29 (4,87; 5,65)	5,96 (5,26; 6,36)
Sed3				5,17 (4,67; 5,81)	5,91 (5,31; 6,31)
Sed4				5,27 (4,71; 5,67)	5,77 (5,27; 6,28)
Sed5				5,13 (4,55; 5,87)	5,85 (5,11; 6,51)
Sed6				5,31 (4,71; 5,81)	5,33 (4,91; 5,61)

TABLE 6: The DIC values for model comparisons.

Effect	Model	DIC	DIC*
log [P (Sed6) /P (Sed1)]	1	28,71	72,17
	2	30,81	63,15
	3	30,76	62,17
	4	30,14	63,28
	5	30,95	63,17
log [P (Sed5) /P (Sed1)]	1	26,16	74,85
	2	29,64	67,61
	3	29,71	66,75
	4	29,67	66,81
	5	29,17	66,37
log [P (Sed4) /P (Sed1)]	1	26,73	75,11
	2	28,95	67,91
	3	28,72	67,54
	4	28,67	67,17
	5	28,81	67,18
log [P (Sed3) /P (Sed1)]	1	25,03	73,71
	2	28,75	67,55
	3	28,19	68,01
	4	28,63	67,85
	5	28,85	67,47
log [P (Sed2) /P (Sed1)]	1	26,25	72,19
	2	29,37	65,16
	3	29,85	64,18
	4	29,67	65,93
	5	29,17	65,41

* Shows the DIC value at times 2 and 3.

The quantities $\overline{D(\theta)}$ and $D(\overline{\theta})$ are easily computed from an MCMC simulation chain.

3. Application to Sedation Data

A part of the data was used by [23]. They compared the effects of Midazolam, Diazepam, Luminal, and Cardiac Cocktail in terms of sedation level. Also 127 children who received MRI and CT were included in this study. Group M ($n = 30$) received Midazolam, Group D ($n = 31$) received Diazepam, Group L ($n = 32$) received Luminal, and Group C ($n = 34$) received Cardiac Cocktail. Systolic Blood pressures, Pulse rates, the number of breathe, and oxygen saturation were monitored. The other measurements, which may affect the sedation level, such as weight, disease status, test status, complication status, age, and adaptation status, were also recorded. Descriptions of predictor values used in the analysis are given in Table 2.

Models in Table 1 were constructed according to the assumption that sedation levels are distributed as a multinomial random variables with the six possible categories as in Table 3. Sedation levels were maintained in the range of Ramsey Scale from 1 to 6 for the 15th minute, 30th minute, and 60th minute. The Ramsay Sedation Scale was given in Table 3.

The models were constructed according to the assumption that sedation levels are distributed as multinomial random variables with the six possible categories. Since there is little information available about the parameters, we choose noninformative prior distributions for the parameters. For regression parameters $\beta \sim \text{Normal}(0, 10^3)$ and $\gamma \sim \text{Normal}(0, 10^3)$, we assume that the random effects α_i are drawn from a multivariate normal distribution with zero mean and a variance-covariance matrix Σ . Noninformative uniform priors were determined for the individual elements of Σ . Σ_{11} and Σ_{22} were given uniform $(0, 100)$ priors and $\Sigma_{12} = \Sigma_{21}$ was assigned uniform $(-\sqrt{\Sigma_{11}\Sigma_{22}}, \sqrt{\Sigma_{11}\Sigma_{22}})$ prior.

Gibbs sampler was run for 10.000 iterations with the first 1000 as burn-in. Convergence for the posterior distributions of all models was achieved. We set up five multinomial models with six possible sedation levels for each model in Table 1. Therefore 30 models were constructed. Posterior calculations were calculated for all models. As an example posterior summaries for the effect on $\log[P(\text{Sed6})/P(\text{Sed1})]$ using model 1 are represented in Table 4.

It is easy to say from Table 4 that there are associations between the response and some explanatory variables. The explanatory variable group D, weight, comp, SPS, and PUL have significant effect on $\log[P(\text{Sed6})/P(\text{Sed1})]$. We have the similar posterior results for all thirty models. Estimated posterior means and %95 intervals for the effects of all explanatory variables in Table 2 on the log of the probability of a patient being in Sed6 relative to the probability of being in Sed1 from models 1, 2, 3, 4, and 5 were obtained. They are given in Table 5. The variable Sed-lev.($t - 1$) refers to the sedation levels of the patient in the previous time. The corresponding effect in the model is averaged over the 2 steps between times. The variable Sed-lev.($s, t - 1$) refers to the previous sedation levels at time s for $s = 2, 3$.

From Table 5, we can say that the explanatory variable group D, weight, comp, SPS, and PUL have significant effect on $\log[P(\text{Sed6})/P(\text{Sed1})]$ for models 1, 2, 3, 4, and 5. We also certainly state that there is relationship between the current sedation level and the sedation level at the previous time of measurements for all models.

For model comparisons, DIC values for all effect for each model were calculated. The DIC values were given in Table 6.

Firstly, Deviance Information Criteria (DIC) value was obtained at three times for all models with different effect. Table 6 compares the models when the deviance is obtained at three times. Model 2 and Model 4 are log models and essentially condition time 1 and model 1 explains time 1, with model 1 which explain time 1. We also calculate the DIC* at times 2 and 3. Therefore we focus on prediction of these times only.

4. Conclusions

Results in Table 6 show that the DIC for model is smaller than the DIC for the other models. Model 1 which contains a random effects term for each patient and sedation level over time shows better performance than the other models.

Model 2, which includes a transition variable, shows the similar performance with models 3, 4, and 5. If we are

concerned with the prediction of times 2 and 3 only, model comparisons results in Table 6 show that the DIC* for models 2, 4, and 5 is smaller than model 1. Models 2, 4, and 5 provide better understanding of the effect of the changes over the three waves than Model 1. For this aim, we prefer to consider models 2, 3, 4, and 5.

For models 4 and 5, Table 6 shows that there is a significant difference between the transitions in sedation levels for times 1 to 2, and from times 2 to 3. Therefore we may prefer models 4 and 5 to the other models for the transitions.

We say that an important characteristic of hierarchical models is that each parameter referring to a specific group from the corresponding parameters of the other group.

Using Bayesian approach makes hierarchical model more flexible than classic hierarchical models. That is why they describe the data better. Bayesian hierarchical approach simplifies the interpretation and computation of the model.

References

- [1] J. Pershad, J. Wan, and D. L. Angheliescu, "Comparison of propofol with pentobarbital/midazolam/fentanyl sedation for magnetic resonance imaging of the brain in children," *Pediatrics*, vol. 120, no. 3, pp. e629–e636, 2007.
- [2] S. A. Godambe, V. Elliot, D. Matheny, and J. Pershad, "Comparison of propofol/fentanyl versus ketamine/midazolam for brief orthopedic procedural sedation in a pediatric emergency department," *Pediatrics*, vol. 112, no. 1 I, pp. 116–123, 2003.
- [3] J. P. Cravero and G. T. Blike, "Review of pediatric sedation," *Anesthesia and Analgesia*, vol. 99, no. 5, pp. 1355–1364, 2004.
- [4] C. Heard, F. Burrows, K. Johnson, P. Joshi, J. Houck, and J. Lerman, "A comparison of dexmedetomidine-midazolam with propofol for maintenance of anesthesia in children undergoing magnetic resonance imaging," *Anesthesia and Analgesia*, vol. 107, no. 6, pp. 1832–1839, 2008.
- [5] J. A. Nelder and R. W. M. Wedderburn, "Generalized linear models," *Journal of the Royal Statistical Society A*, vol. 135, pp. 370–384, 1972.
- [6] P. McCullagh and J. A. Nelder, *Generalized Linear Models*, Chapman and Hall, London, UK, 2nd edition, 1989.
- [7] K. Y. Liang and S. L. Zeger, "Longitudinal data analysis using generalized linear models," *Biometrika*, vol. 73, no. 1, pp. 13–22, 1986.
- [8] P. J. Diggle, K. Y. Liang, and S. L. Zeger, *Analysis of Longitudinal Data*, Oxford University Press, Oxford, UK, 2nd edition, 1994.
- [9] I. Ntzoufras, "Gibbs variable selection using BUGS," *Journal of Statistical Software*, vol. 7, pp. 1–19, 2002.
- [10] G. Tiao and A. Zellner, "On the Bayesian estimation of multivariate regression," *Journal of the Royal Statistical Society B*, vol. 26, pp. 277–285, 1964.
- [11] G. Box and G. Tiao, *Bayesian Inference for Statistical Analysis*, Wiley, New York, NY, USA, 1973.
- [12] A. Gelman and J. Hill, *Data Analysis Using Regression and Multilevel Hierarchical Models*, Cambridge University Press, New York, NY, USA, 2006.
- [13] B. Carlin, "Hierarchical longitudinal modelling," in *Markov Chain Monte Carlo in Practice*, W. Gilks, S. Richardson, and D. Spiegelhalter, Eds., pp. 303–320, Chapman & Hall, Suffolk, UK, 1996.
- [14] X. L. Meng, "Posterior predictive p-values," *Annals of Statistics*, vol. 22, pp. 1142–1160, 1994.
- [15] P. J. Brown, M. Vannucci, and T. Fearn, "Multivariate Bayesian variable selection and prediction," *Journal of the Royal Statistical Society B*, vol. 60, no. 3, pp. 627–641, 1998.
- [16] J. De Leeuw and E. Meijer, *Handbook of Multilevel Analysis*, Springer, New York, NY, USA, 2008.
- [17] D. Spiegelhalter, K. Abrams, and J. Myles, *Bayesian Approaches to Clinical Trials and Health-Care Evaluation*, Statistics in Practice, Wiley, Chichester, UK, 2004.
- [18] B. Carlin and T. Louis, *Bayes and Empirical Bayes Methods for Data Analysis*, Texts in Statistical Science, Chapman & HaWCRC, New York, NY, USA, 2000.
- [19] A. Gelfand and D. Dey, "Bayesian model choice: asymptotic and exact calculations," *Journal of the Royal Statistical Society B*, vol. 56, pp. 501–514, 1994.
- [20] H. Akaike, "Information theory and an extension of the maximum likelihood principle," in *Proceedings of the 2nd International Symposium on Information Theory*, B. Petrov and F. Csaki, Eds., pp. 267–281, Akademiai Kiado, Budapest, Hungary, 1973.
- [21] R. Kass and A. Raftery, "Bayes factors," *Journal of the American Statistical Association*, vol. 90, pp. 773–795, 1995.
- [22] D. J. Spiegelhalter, N. G. Best, B. P. Carlin, and A. Van Der Linde, "Bayesian measures of model complexity and fit," *Journal of the Royal Statistical Society B*, vol. 64, no. 4, pp. 583–616, 2002.
- [23] M. A. Cengiz, T. Şenel, Y. Terzi, N. Murat, and N. Savaş, "Comparing different sedation medications using generalized estimating equations approach," *African Journal of Pharmacy and Pharmacology*, vol. 4, no. 4, pp. 130–134, 2010.

Research Article

Multiple Active Contours Driven by Particle Swarm Optimization for Cardiac Medical Image Segmentation

I. Cruz-Aceves, J. G. Aviña-Cervantes, J. M. López-Hernández, and S. E. González-Reyna

Universidad de Guanajuato, División de Ingenierías, Campus Irapuato-Salamanca, Carretera Salamanca, Valle de Santiago km 3.5+1.8, Comunidad de Palo Blanco, 36885 Salamanca, GTO, Mexico

Correspondence should be addressed to I. Cruz-Aceves; i.cruzaceves@ugto.mx

Received 21 December 2012; Revised 8 April 2013; Accepted 9 April 2013

Academic Editor: Peng Feng

Copyright © 2013 I. Cruz-Aceves et al. This is an open access article distributed under the Creative Commons Attribution License, which permits unrestricted use, distribution, and reproduction in any medium, provided the original work is properly cited.

This paper presents a novel image segmentation method based on multiple active contours driven by particle swarm optimization (MACPSO). The proposed method uses particle swarm optimization over a polar coordinate system to increase the energy-minimizing capability with respect to the traditional active contour model. In the first stage, to evaluate the robustness of the proposed method, a set of synthetic images containing objects with several concavities and Gaussian noise is presented. Subsequently, MACPSO is used to segment the human heart and the human left ventricle from datasets of sequential computed tomography and magnetic resonance images, respectively. Finally, to assess the performance of the medical image segmentations with respect to regions outlined by experts and by the graph cut method objectively and quantifiably, a set of distance and similarity metrics has been adopted. The experimental results demonstrate that MACPSO outperforms the traditional active contour model in terms of segmentation accuracy and stability.

1. Introduction

Computed tomography (CT) scanning and magnetic resonance imaging (MRI) are effective and widely used modalities in clinical practice for the diagnosis of cardiac disease. The process carried out by a cardiologist is based on a visual examination of the images followed by a manual delineation of the human organ. This process can be subjective, time-consuming, and susceptible to errors. According to the above process, the accurate medical image segmentation by computational techniques plays an essential role.

Image segmentation is an important and challenging task in computer vision and image processing areas with different applications including medical image analysis, video surveillance, biology, and militar, systems. In recent years, numerous approaches have been introduced for this purpose based only on information available in the image such as wavelet transform [1], rule optimization with region growing [2], enhanced suppressed fuzzy c-means [3], improved watershed transform [4], multithreshold using artificial immune systems [5], graph cut [6, 7], and active contour models (ACM) [8, 9]. This latter technique was introduced by [10],

and it is an energy-minimizing spline that consists of control points known as snaxels. The spline will evolve through the evaluation of internal and external forces according to the shape of the object of interest. ACM has been widely used in medical applications including segmentation of breast lesions [11], breast tumors [12], human prostate [13], and intravascular, ultrasound images [14], to name a few.

There are two main drawbacks in the traditional implementation of active contour models. Firstly, initialization of control points must be close to the object of interest; otherwise, failure of convergence will occur. Secondly, the snake is prone to stagnate in local minima and results in an inaccurate convergence to the boundaries of the object. To address these drawbacks, many researchers have suggested to adapt different techniques to work together with the active contour models including waterballoons [15], statistical methods [16, 17], graph cut [18], genetic algorithms [19], differential evolution [20], and particle swarm optimization (PSO) [21] where static large searching windows are dynamically generated depending on the initial position of the interactive control points. Similarly, in [22], a snake model hybrid was proposed by adapting the PSO velocity equation to the active contour

model. The performance of both PSO approaches is very suitable according to the tests since the active contour model becomes more robust in local minima problem.

PSO has become very popular to solve optimization problems in continuous spaces [23, 24]. PSO is similar to evolutionary computation techniques since it handles a set of randomly initialized potential solutions known as swarm instead of population. These potential solutions are referred to as particles rather than individuals, and they are evaluated using a fitness function. This computational intelligence technique provides a mechanism inspired by the cognitive and social behavior of bird flocking or fish schooling to exchange information between particles flown through hyperspace based on two main ways generally. Firstly, all the particles are guided by the best particle of the swarm, and, secondly, each particle keeps track of its best solution found through iterations, which is an advantage with regard to some evolutionary computation techniques. As PSO is not computationally expensive and it is highly efficient, it has been used in medical applications such as branch-cut phase unwrapping of MRI data [25] and tumor classification [26].

In this paper, we introduce a new method based on multiple active contours driven by particle swarm optimization (MACPSO) to segment an object of interest by dividing the search space into polar sections. Each polar section has a swarm of particles composed of control points, which performs a strategy search with the aim of finding the optimal control point (snaxel) in its particular constrained space. MACPSO method is able to overcome in a very suitable way the inaccurate convergence to the concave boundaries of the object and the drawback of initialization of the traditional ACM. In addition, the proposed method also addresses the problem of segmenting datasets of sequential CT and MR images which contain the human heart and the human left ventricle, respectively. Finally, to visualize the sequential CT segmentations obtained from MACPSO, a 3D reconstruction approach of the human heart is presented.

The structure of this work is as follows. In Section 2, the basics of active contour model and particle swarm optimization are presented. In Section 3, the proposed MACPSO method is introduced, along with a set of similarity metrics to assess its performance. The experimental results are discussed in Section 4, and from the numerical analysis, conclusions are presented in Section 5.

2. Background

In this section, the fundamentals of the active contour model and particle swarm optimization are explained in detail.

2.1. Active Contour Model. Active contour model (ACM), also called snake, is a parametric curve that can move within a spatial image domain where it was defined. The snake is described by $p(s, t) = (x(s, t), y(s, t))$, $s \in [0, 1]$, where t is the time-related changing aspect. This curve evolves through time to minimize the total energy function given by the following:

$$E_{\text{snake}} = \int_0^1 [E_{\text{int}}(p(s, t)) + E_{\text{ext}}(p(s, t))] ds. \quad (1)$$

The defined energy function consists of two components, E_{int} and E_{ext} that represent the internal and external energies, respectively. The internal energy presented in the following is used to maintain the search within the spatial image domain and the shape modification of the parametric curve:

$$E_{\text{int}}(p(s, t)) = \frac{1}{2} \left[\alpha(s) \left| \frac{\partial p(s)}{\partial s} \right|^2 + \beta(s) \left| \frac{\partial^2 p(s)}{\partial s^2} \right|^2 \right]. \quad (2)$$

Internal energy is represented by the first derivative of $p(s)$ controlled by curve tension parameter $\alpha(s)$ and the second derivative of $p(s)$ guided by rigidity parameter $\beta(s)$.

The external energy presented in the following is defined by the particular features of the image, where $\nabla I(p(s))$ is the surface gradient calculated at $p(s)$ and γ is the weight parameter of this force:

$$E_{\text{ext}}(p(s)) = -\gamma |\nabla I(p(s))|^2. \quad (3)$$

The optimal solution is acquired by solving the following Euler equation, that is, when external and internal forces become stable:

$$\nabla E_{\text{ext}} - \alpha \frac{\partial^2 p(s)}{\partial s^2} + \beta \frac{\partial^4 p(s)}{\partial s^4} = 0. \quad (4)$$

The computational implementation of ACM is conformed by a set of n discrete points $\{p_i \mid i = 1, 2, \dots, n\}$. The discrete formulation of internal energy is computed by (5), and the external energy is approximated by (6). In both external and internal energies, $(q_{i,j})$ is the control point (p_i), and (j) is the index in the searching window. In addition, the local energy function given by (7) is iteratively evaluated in order to minimize the k_i index by using (8), where W_i represents the predefined searching window for the control point p_i [21]:

$$E_{\text{int}} = \frac{1}{2} \left[\alpha(s) |q_{i,j} - p_{i-1}|_2^2 + \beta(s) |p_{i-1} - 2q_{i,j} + p_{i+1}|_2^2 \right], \quad (5)$$

$$E_{\text{ext}} = -\gamma |\nabla I(q_{i,j})|_2^2, \quad (6)$$

$$E_{i,j} = E_{\text{int}} + E_{\text{ext}}, \quad (7)$$

$$E_{\text{snake}} = \sum_{i=1}^n E_{i,k_i}, \quad k_i = \arg \min_j (E_{i,j}), \quad j \in W_i. \quad (8)$$

The traditional ACM has two main drawbacks: firstly, sensitivity to the initial position of the control points. Secondly, the control points are prone to stagnate in local minima due to the presence of noise in the image deflecting the curve of the optimum edge. A suitable alternative to overcome the local minima drawback is to use a robust optimization technique as particle swarm optimization, which is described in Section 2.2.

2.2. Particle Swarm Optimization. PSO is a population-based computational intelligence technique developed by [23, 24]

to solve optimization problems. As in evolutionary computation techniques, the population (referred to as swarm in PSO) consists of a number of potential solutions known as individuals (called particles in PSO) to the optimization task. Each particle moves through hyperspace to a new position according to the following velocity equation:

$$v_i(t+1) = \varphi v_i(t) + \kappa r_1 (p_{\text{best}} - x_i(t)) + \kappa r_2 (p_{g_{\text{best}}} - x_i(t)), \quad (9)$$

where $v_i(t)$ is the current velocity of the particle $x_i(t)$, t denotes the time step, φ is the inertia weight, κ represents the learning factor, $r_1, r_2 \sim U(0, 1)$ where U is a uniform distribution, p_{best} is the current best solution found by the present particle, and $p_{g_{\text{best}}}$ is the current best solution found by the best particle of the whole swarm. Assuming that the new velocity of the particle has been updated, its new position is computed by using the following:

$$x_i(t+1) = x_i(t) + v_i(t+1). \quad (10)$$

According to the previous description, the PSO algorithm can be implemented by using the following procedure.

- (1) Set the swarm size and initialize each particle by generating random candidate solutions and velocities.
- (2) Evaluate each particle in the predefined fitness function and update its p_{best} only if the current fitness is better.
- (3) Find the particle that has the best fitness in the whole swarm and update $p_{g_{\text{best}}}$ only if the fitness value found is better.
- (4) If the stopping criterion is satisfied (e.g., stability or number of iterations), then stop.
- (5) Update velocity and position of all the particles according to (9) and (10), then repeat steps (2)–(5).

In Section 3, the proposed image segmentation method is described in detail.

3. Proposed Image Segmentation Method

The proposed MACPSO method based on particle swarm optimization and multiple active contours is described in Section 3.1. Additionally, to evaluate the performance of the proposed method, the set of similarity metrics is explained in Section 3.2.

3.1. Multiple Active Contours Driven by Particle Swarm Optimization (MACPSO). Due to the two main drawbacks of the traditional ACM discussed above, PSO is adopted to drive multiple active contours dividing the object of interest into a polar optimization problem. Since the methodology of the proposed MACPSO method makes it possible to apply the traditional implementation of PSO, some advantages are inherently acquired such as robustness, low computational time, and efficiency. The procedure of the proposed segmentation method is illustrated in Figure 1, and it is described below.

In the preprocessing stage of MACPSO, we first remove the noise of the image by utilizing a 2D median filter (3×3 window size). Subsequently, the Canny edge detector ($\sigma = 1.3$, $T_l = 10.0$, and $T_h = 30.0$) is used to detect the edge between the background and regions of interest. In the final step of this stage, in order to perform the minimization process, the Euclidean distance map is produced. The second stage is the MACPSO initialization on the resulting distance map, where the origin point of the coordinate system can be determined by the user in an interactive way or it can be generated automatically inside the region of interest. The generated coordinate system divides the region or object of interest through $\theta = 2\pi/g$, where g denotes the degrees of each constrained polar section S . On the other hand, the n initial contours can be created in a circular or elliptical shape according to the pattern of the region of interest and assuming that this region is within their spatial domain. After the n contours are produced, n control points (snaxels) are generated and assigned as particles for each constrained polar section S_i , in which one edge sectional solution and one swarm of particles O_i must exist. The segmentation process is performed by applying the PSO strategy in each section S_i separately in order to be placed on its corresponding edge sectional solution. For each section, the particles are evaluated according to the fitness function corresponding to external energy derived from (6), and through iterations the best particle (g_{best}) of each swarm is updated only if a best value is found in its search space. When the optimization process for each swarm is finished, the resulting segmented object is acquired by connecting the g_{best} particle of each swarm to each other.

This proposed method has three main advantages in the initialization process. Firstly, the initial contours can be automatically initialized in a circular or elliptical shape. Secondly, the number of snaxels can be adjusted directly by modifying the number of sections in which the object of interest is divided. These two features must be considered to adapt this method according to the shape of the object of interest and obtain a more accurate segmentation without affecting the PSO performance. The third advantage is the origin point created interactively by the user, which is used to generate automatically all the snaxels on the spatial domain of the object of interest. Due to this advantage, the proposed method is easy to extend in the segmentation of sequential CT and MR images by just reproducing the origin point through the set of images.

The procedure of the proposed MACPSO image segmentation method is described as follows.

- (1) Initialize coordinates (x, y) from the origin point, degrees g , and number of snakes.
- (2) Initialize parameters of PSO algorithm: number of iterations, inertia weight, and learning factor.
- (3) Generate one swarm for each polar section S_i assigning the current snaxels as particles.
- (4) For each swarm O_i , initialize velocities and assign the initials p_{best} and g_{best} .

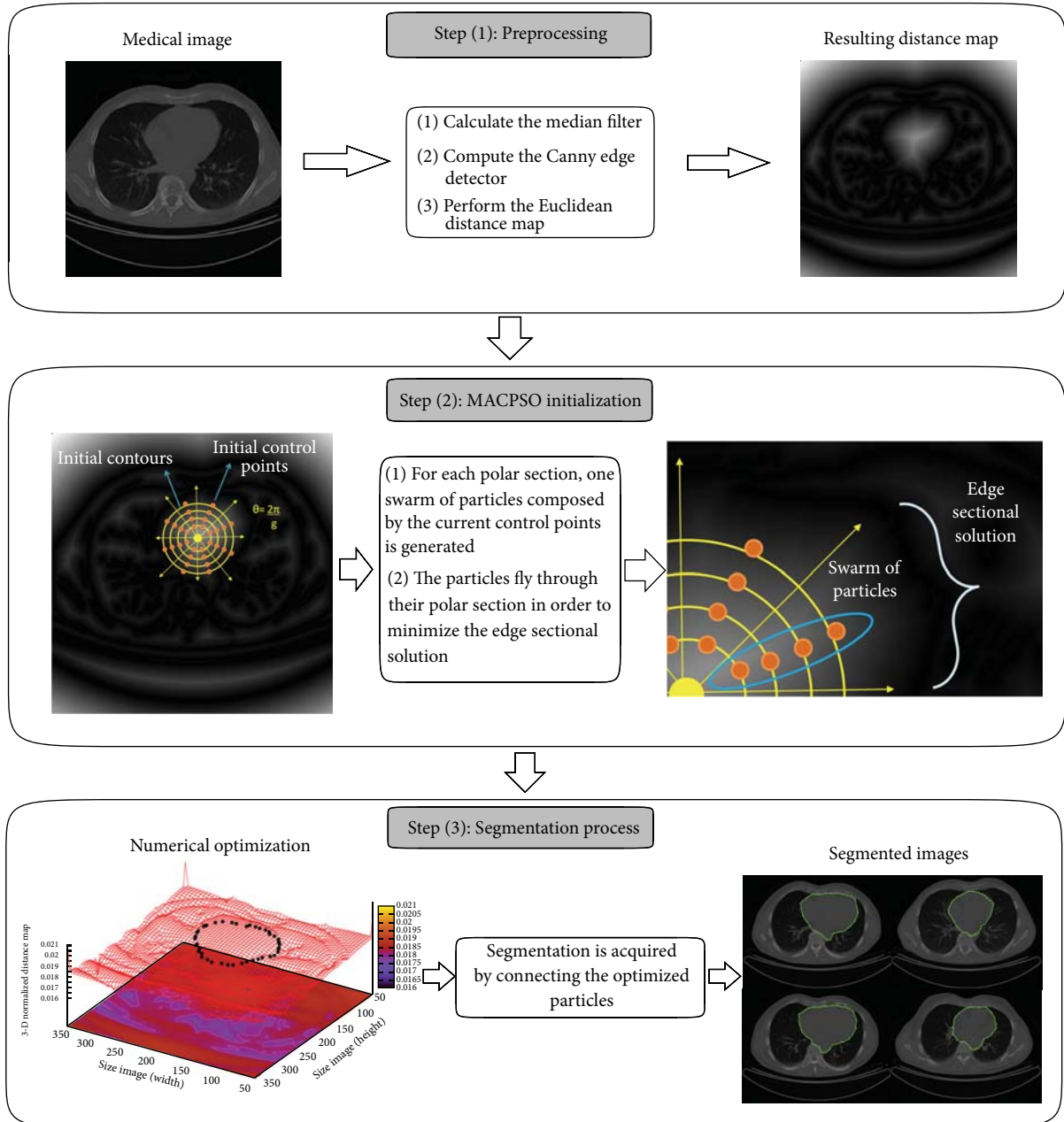


FIGURE 1: Process of the proposed MACPSO image segmentation method.

- (a) Apply restriction of the search space to ignore improper particles.
 - (b) Evaluate each particle in fitness function.
 - (c) Update p_{best} and g_{best} if better particles are found.
 - (d) Apply (9) and (10), respectively.
 - (e) If the stopping criterion is satisfied (e.g., stability or number of iterations), then stop; otherwise, go to step (a).
- (5) Stop MACPSO.

3.2. Validation Metrics. To assess the performance of the proposed method in medical image segmentation, the Jaccard index, the Dice index, the Hausdorff distance, and area and perimeter metrics have been adopted to be compared with the traditional ACM and the regions outlined by two experts.

The Jaccard index $J(A, B)$ and the Dice index $D(A, B)$ are similarity measures situated in the range $[0, 1]$ used for binary variables [4]. These indexes are calculated by using (11) and (12), respectively. In our tests, A represents the segmented region by computational methods (MACPSO and traditional active contour model separately) and B represents the region outlined by the experts. In both indexes, if regions A and B

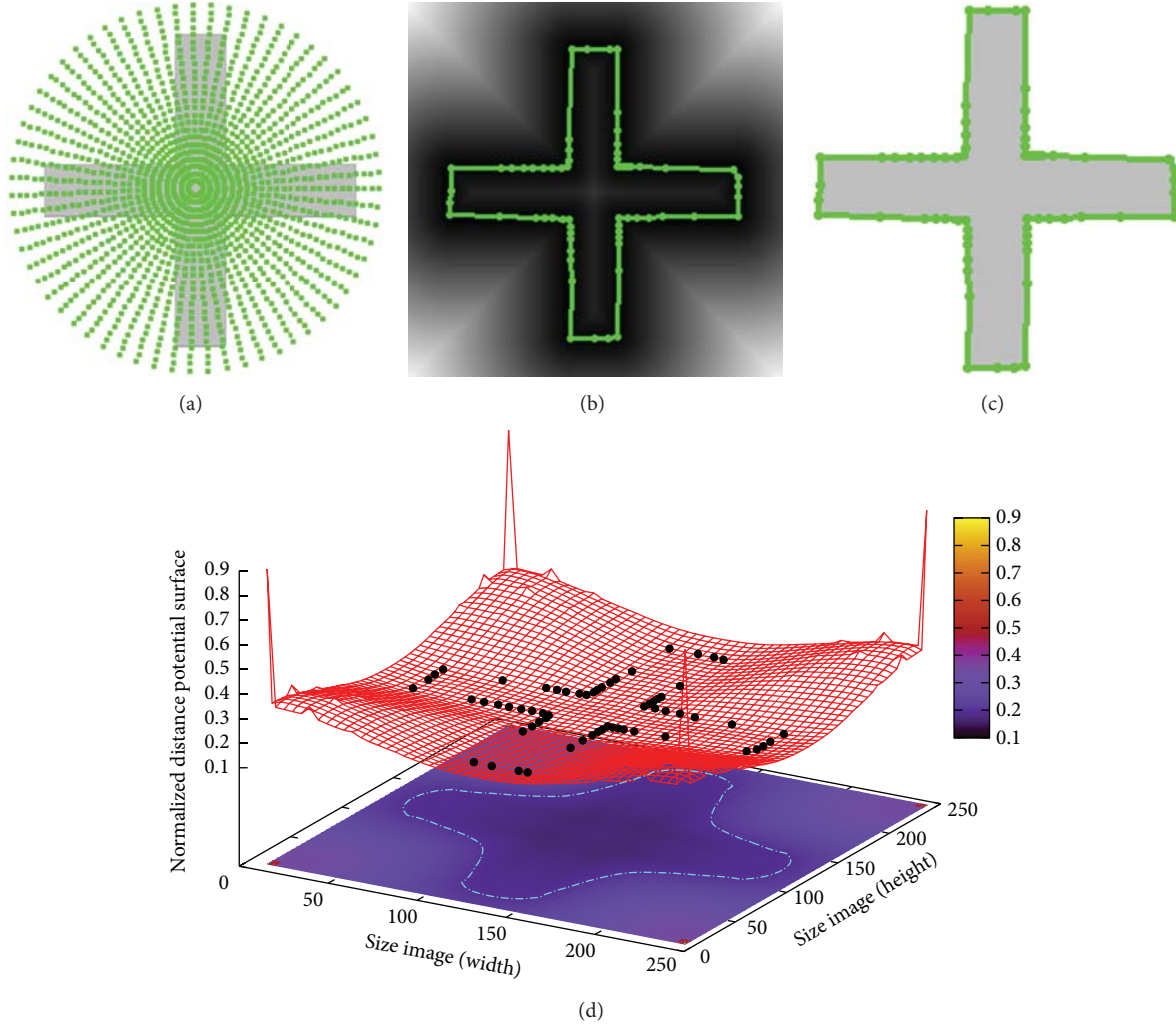


FIGURE 2: Symmetrical cross: (a) initialization of the proposed method, (b) result of MACPSO on the Euclidean distance map derived from cross-object, (c) result of MACPSO implementation, and (d) result of optimization process on the distance potential surface.

are entirely overlapping, the obtained result is 1, and 0 it is when these two regions are completely different:

$$J(A, B) = \frac{A \cap B}{A \cup B}, \quad (11)$$

$$D(A, B) = \frac{2(A \cap B)}{A + B}. \quad (12)$$

The Hausdorff distance is a commonly used metric for shape matching in medical image segmentation. It measures the degree of similarity between two superimposed sets and it is calculated by the following, where a and b are points defined in sets A and B , respectively, and $\|a - b\|$ is some underlying distance (Euclidean distance in our tests):

$$H(A, B) = \max_{a \in A} \min_{b \in B} \|a - b\|. \quad (13)$$

In Section 4, the segmentation results in different synthetic and medical images using the proposed MACPSO method and being analyzed by the validation metrics are presented.

4. Experimental Results

In this section, we evaluate the performance of the proposed MACPSO method for segmenting objects on different medical and synthetic images. The computational implementations presented in this section are performed using the gcc compiler version 4.4.5 running on Debian GNU/Linux 6.0, Intel Core i3 with 2.13 Ghz and 4 Gb of memory.

4.1. Application on Synthetic Images. The results of segmenting synthetic images are shown in Figures 2, 3, and 4, which are a symmetrical cross, circle with Gaussian, noise and a star object, respectively. The three synthetic images have been used to test the performance of other approaches such as [21, 22] which are described below.

In Figure 2, the result of applying MACPSO on a symmetrical cross-image of size 256×256 pixels is presented. In Figure 2(a), the initialization of the proposed method is shown. This simulation is performed by using the next parameters: 20 iterations, 0.8 of inertia weight, 0.5 of learning

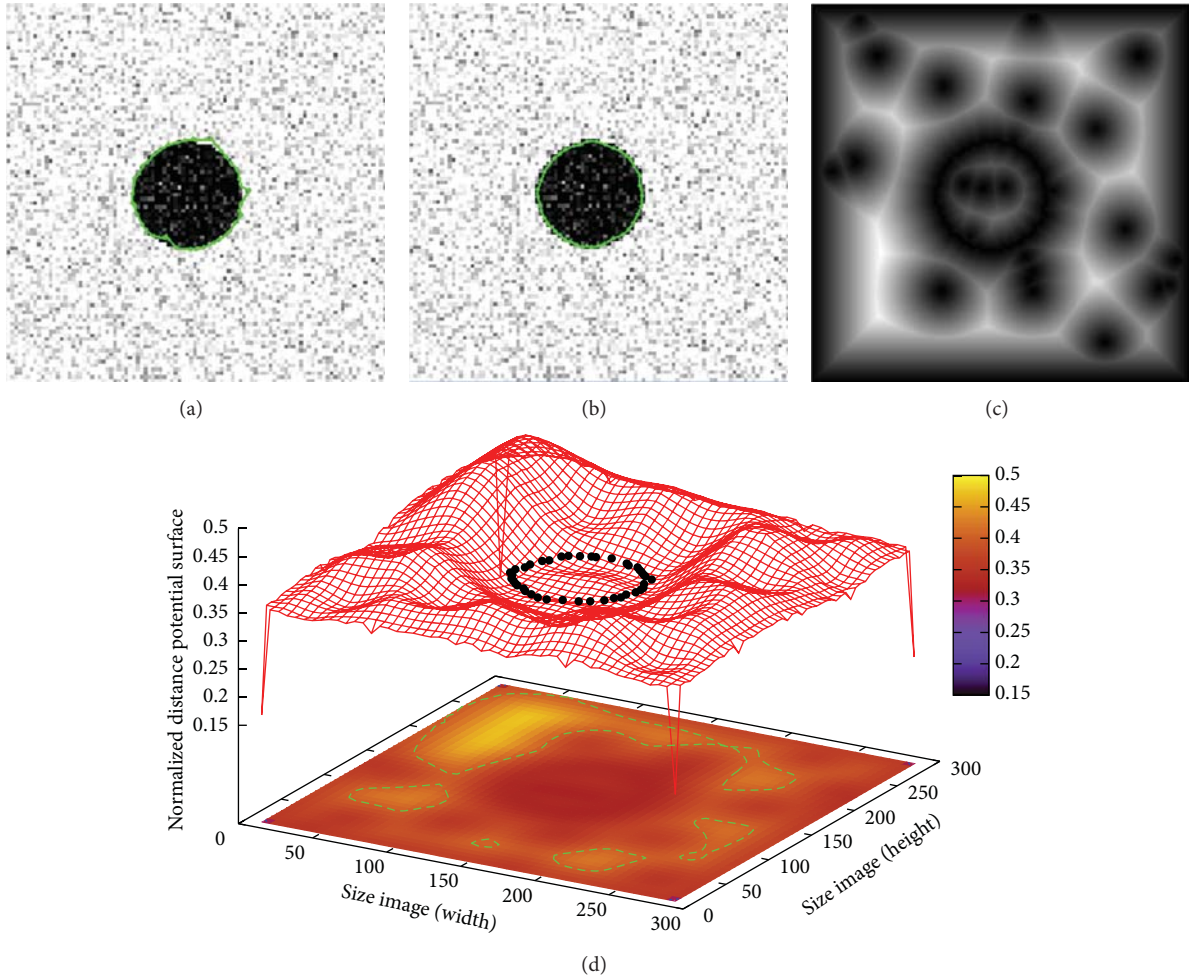


FIGURE 3: Noisy circle: (a) result of traditional ACM, (b) result of MACPSO implementation, (c) Euclidean distance map of the image, and (d) result of optimization process on the distance potential surface.

factor, 25 snakes, and 63 control points per snake obtained since the value of g is 10. Additionally, after the preprocessing stage, the Euclidean distance map (EDM) is derived from the image to perform the segmentation process. In Figure 2(b), the result of applying MACPSO on the EDM is presented, which, in Figure 2(c), is shown on the original test image. This segmentation process must be viewed as an optimization task since the snaxels (particles) work on the 3D distance map also called distance potential surface computed from the EDM in order to minimize the shape of the object of interest. The resulting particles on the distance potential surface when the optimization process is finished are shown in Figure 2(d) where these particles are subsequently connected to obtain the final segmentation result previously introduced in Figure 2(c). In this test image, the MACPSO method can overcome the concavity problem and converge into a correct way to the cross-edge on the image in 0.277 s.

Figure 3 presents a synthetic image of size 300×300 pixels containing a circle with Gaussian noise (mean = 0 and variance = 0.04). As shown in Figure 3(a), the result

of applying the traditional implementation of active contour model cannot overcome the Gaussian noise to fit the object boundary accurately. The curve tension α , rigidity β , and weight external energy γ parameters remain constant according to experiments performed by [21], where similar segmentation problems have been effectively addressed. The traditional AC parameters in this simulation are set as $\alpha = 0.01$, $\beta = 0.9$, $\gamma = 0.05$, and 42 control points giving an executing time of 0.104 s. Moreover, as shown in Figure 3(b), the proposed method is robust in the presence of noise and it is able to locate the circle boundary in an accurate way. The inertia, learning factor, and iteration parameters of MACPSO are statistically adjusted to promote local exploitation, while the number of snakes has been considered to enclose the object of interest, and number of snaxels to smooth and fit the resulting contour. In this simulation, MACPSO parameters are set as iterations = 20, inertia weight = 0.8, learning factor = 0.5, number of snakes = 15, and 42 snaxels per snake since g -value = 15 with an executing time of 0.159 s. In Figure 3(c), the Euclidean distance map after the preprocessing stage

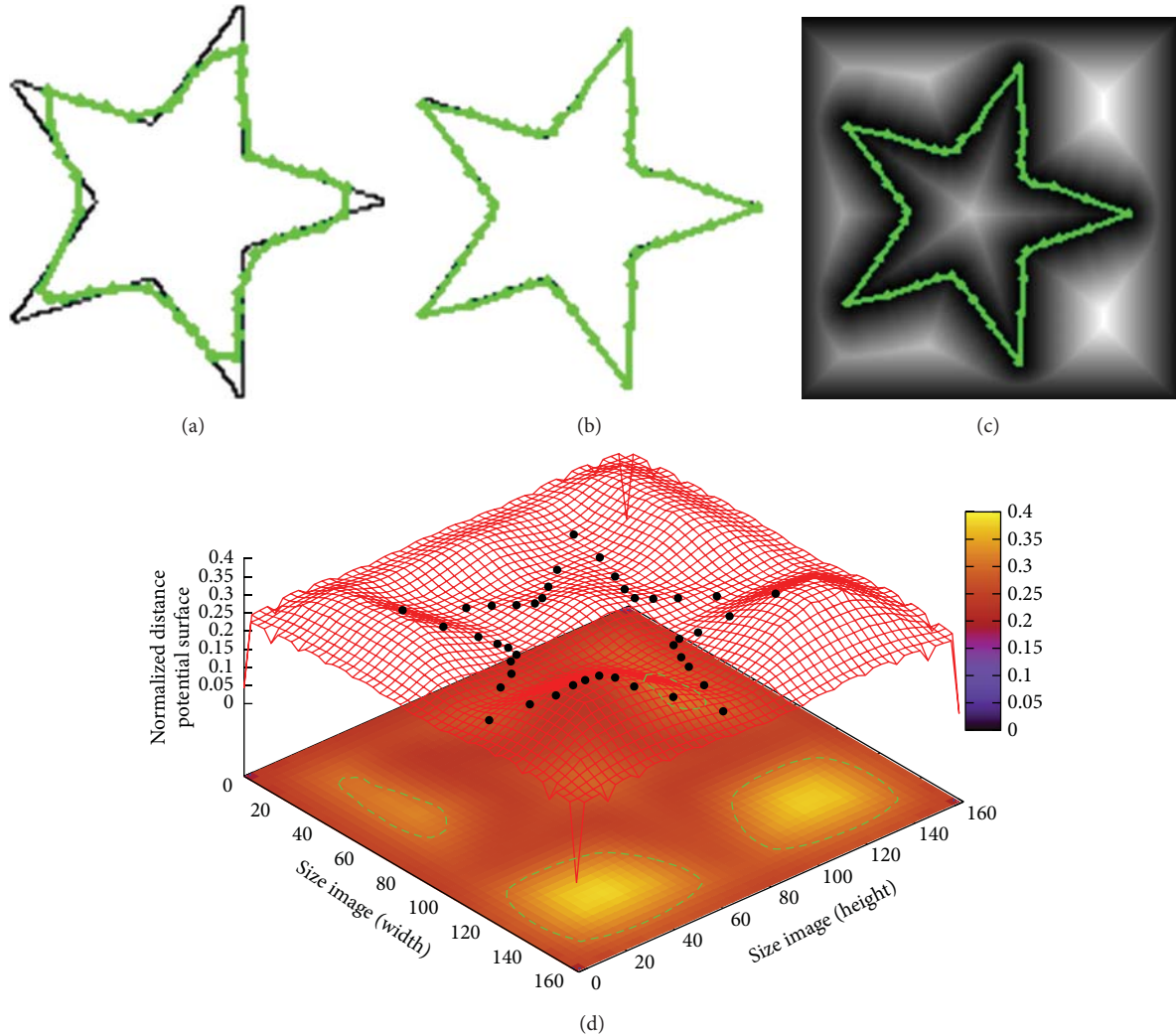


FIGURE 4: Synthetic star: (a) result of traditional ACM, (b) result of MACPSO implementation, (c) result of MACPSO on the Euclidean distance map, and (d) result of optimization process on the distance potential surface.

is presented and the distance potential surface with the resulting optimized control points is shown in Figure 3(d).

In Figure 4, a synthetic image of size 160×160 pixels with an artificial shape of a star is introduced. Figure 4(a) presents the resulting segmentation obtained with the traditional implementation of ACM using the parameters as $\alpha = 0.01$, $\beta = 0.9$, $\gamma = 0.05$, and 42 control points giving an executing time of 0.090 s. In this figure the traditional ACM is not able to fit the concavities of the object boundary accurately. This drawback is solved with the proposed method by overcoming the concavity problem and fitting the correct boundary as shown in Figure 4(b). In this simulation, the MACPSO parameters are set as iterations = 20, inertia weight = 0.8, learning factor = 0.5, number of snakes = 15 and 42 snaxels per snake since the value of g is equal to 15 with an executing time of 0.125 s. On the other hand, derived from the star object, in Figures 4(c) and 4(d), the resulting segmentation on the Euclidean distance map and the convergence of the optimized particles on the distance potential surface are illustrated.

The quality of the segmented objects through MACPSO in the three different synthetic test images has demonstrated

that the proposed method is more stable and accurate than the traditional implementation of ACM. The robustness of MACPSO is due to the process of convergence carried out by particle swarm optimization instead of the traditional ACM. Even though the computational time of the proposed method is comparable to the traditional ACM, MACPSO capabilities, such as avoiding local minima and fitting to the boundary of the objects, improve the quality of the obtained segmentations.

In Section 4.2, based on the performance of MACPSO on synthetic images, a set of cardiac medical images has been introduced to prove the accuracy of the proposed method through different distance and similarity measures.

4.2. Application on Medical Images. The proposed method has been applied in the segmentation of datasets from sequential CT and MR images which contain the human heart and the human left ventricle, respectively. These medical images have been provided by the Mexican Social Security Institute and by the Auckland MRI Research Group, University of Auckland.

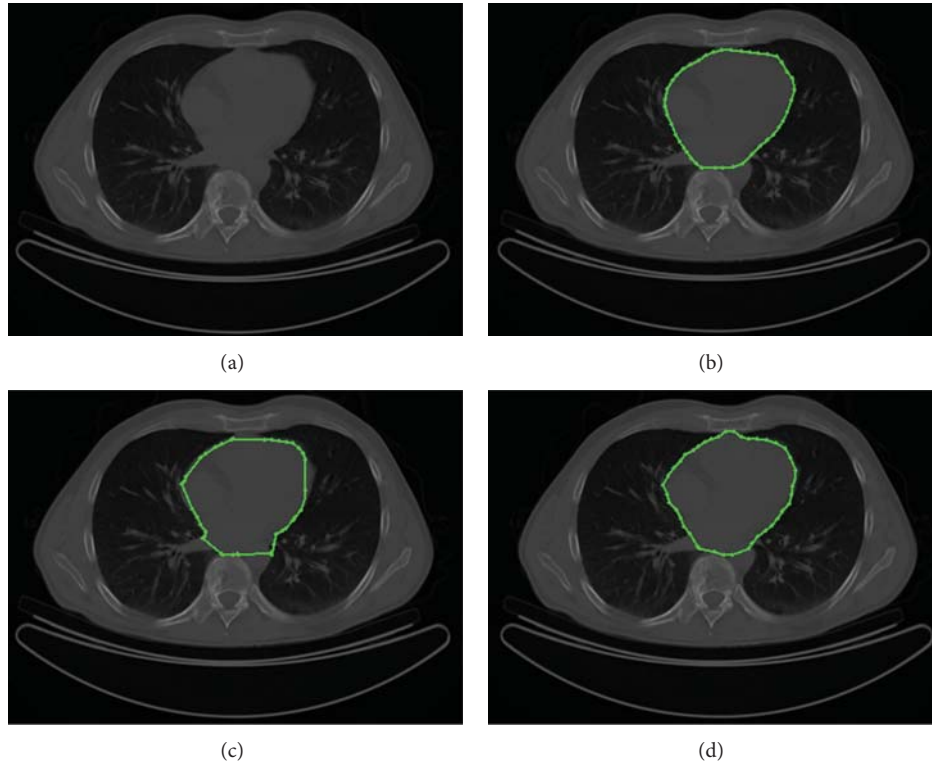


FIGURE 5: CT image: (a) test image, (b) the human heart outlined by experts, (c) result of traditional ACM and (d) result of MACPSO implementation.

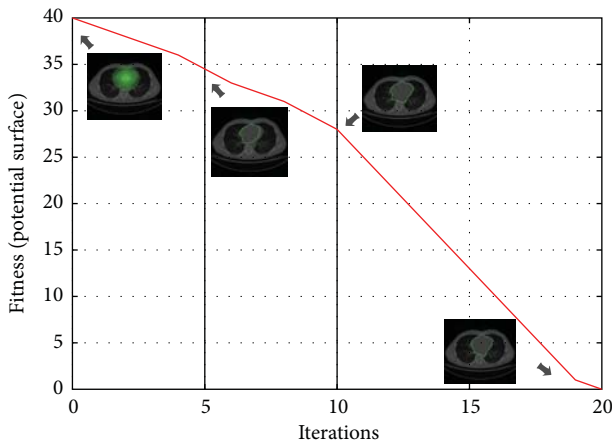


FIGURE 6: Convergence of the human heart segmentation through PSO iterations in CT image.

Figure 5(a) shows a medical image of size 512×512 pixels acquired from a CT scanning with the aim of segmenting the present human heart. In Figure 5(b), the human heart outlined by cardiologists is presented. In addition, Figure 5(c) illustrates the segmented region through the traditional implementation of ACM with the next parameters: 42 control points, $\alpha = 0.01$, $\beta = 0.9$, and $\gamma = 0.05$ in 0.087 s. As shown in Figure 5(d), the human heart segmentation by using the proposed MACPSO method fits the heart boundary accurately. The parameters in this simulation are set as iterations = 20, inertia weight = 0.8, learning factor = 0.5,

number of snakes = 15, and g -value = 15 (obtaining 42 snaxels per snake) with an executing time of 0.127 s.

Figure 6 shows the process of convergence of the MACPSO on CT test image. The convergence measure is given by the fitness value which is computed from the average of the control points on the distance potential surface and it is iteratively minimized through the 20 predefined iterations to improve the human heart segmentation.

Figure 7(a) shows a low-contrast, 512×512 pixels medical image acquired from the MR procedure with the aim of segmenting the present human left ventricle. In Figure 7(b), the Euclidean distance map derived from the test image is presented to increase the perception of the segmentation task. On the other hand, in Figures 7(c) and 7(d), the human left ventricle outlined by expert 1 and expert 2 is presented. Figure 7(e) shows the resulting segmented region through the traditional implementation of ACM with the next parameters: 42 control points, $\alpha = 0.01$, $\beta = 0.9$, and $\gamma = 0.05$ in 0.085s. Figure 7(f) illustrates the resulting segmentation by using the proposed MACPSO method locating the boundary human left ventricle accurately. The parameters in this simulation are set as iterations = 20, inertia weight = 0.8, learning factor = 0.5, number of snakes = 9, and g -value = 15 (obtaining 42 snaxels per snake) with an executing time of 0.108 s.

Figure 8 illustrates the process of convergence of the MACPSO on an MR test image by using the average of the control points as a fitness value evaluated on the distance potential surface on each iteration. This convergence is performed with the same parameters used in Figure 7.

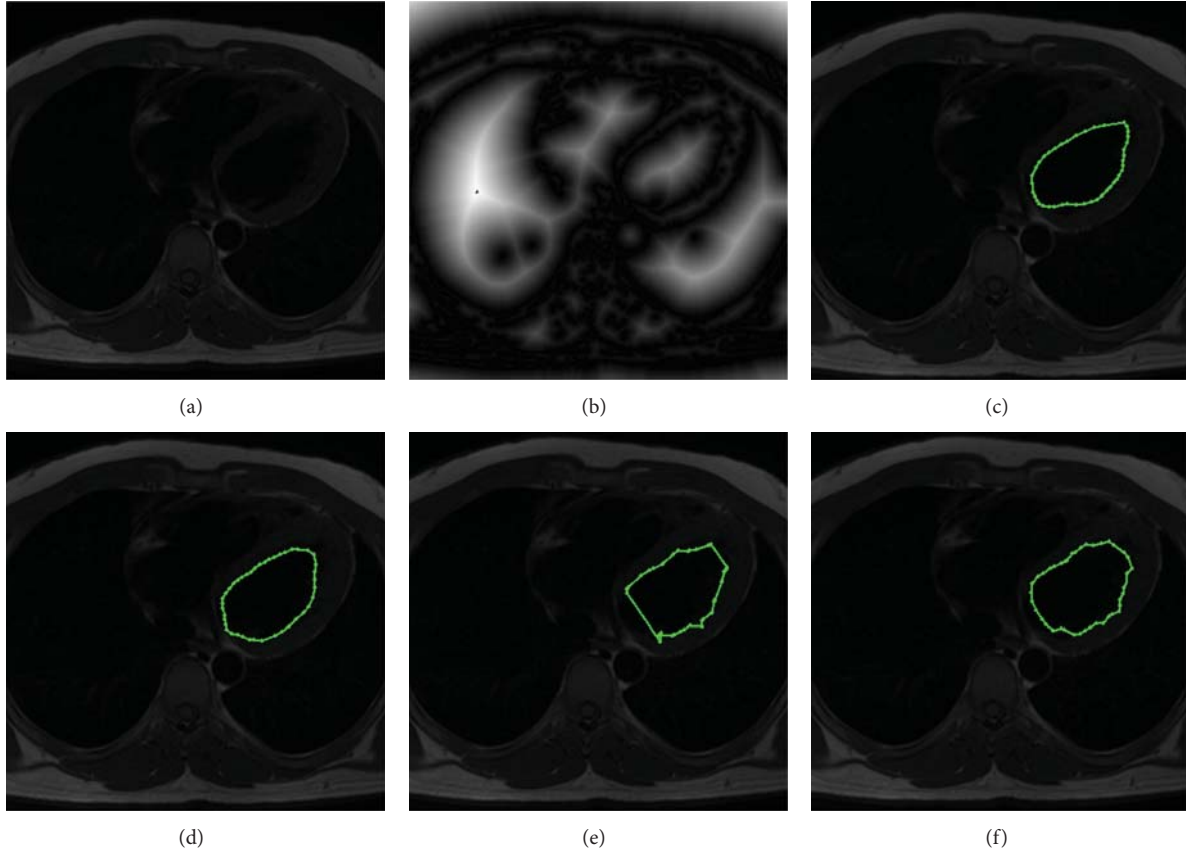


FIGURE 7: MR image: (a) test image, (b) Euclidean distance map of test image, (c) the human left ventricle outlined by expert 1, (d) the human left ventricle outlined by expert 2, (e) result of traditional ACM, and (f) result of MACPSO implementation.

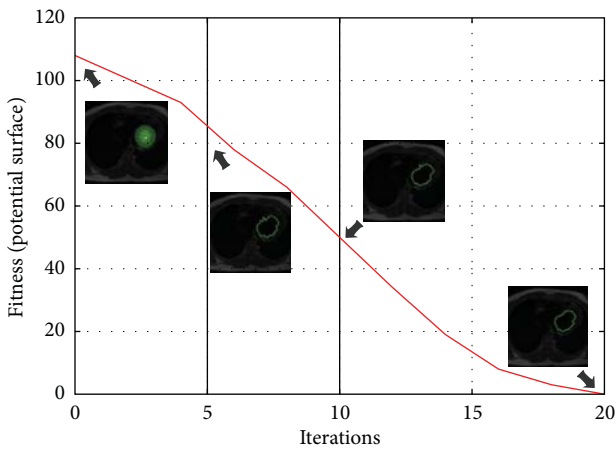


FIGURE 8: Convergence of the human left ventricle segmentation through PSO iterations in MR image.

Due to the initialization methodology of MACPSO, this method can be easily extended to work with datasets of sequential images just reproducing the coordinates (x, y) of the origin point and the initial parameters in the whole set of images. This initialization process is an advantage over the traditional implementation of ACM, since only one user interaction is needed to generate automatically all of

snaxels to the segmentation process, while in traditional ACM each snaxel has to be provided interactively, which is time consuming.

In Figure 9 the results of segmenting a subset of CT images containing the human heart are presented. These images have been extracted from a segmented dataset consisting of 144 sequential CT images from different patients where each image is of size 512×512 pixels. In Figure 9(a), the resulting segmentations of applying the traditional ACM are presented, in which the fitting problem is shown. The parameters of ACM are set as 42 control points, $\alpha = 0.01$, $\beta = 0.9$, and $\gamma = 0.05$ with an executing time of 9.168 s. Figure 9(b) presents the segmentation results obtained through the interactive graph cut method, which were computed in 10.065 s. In this method, the experts defined areas (human heart and background seeds) that should be separated by the segmentation. Moreover, in Figure 9(c), the segmented images by using MACPSO show in a very suitable way the boundary of the human heart. In this simulation, the parameters of the proposed method are set as iterations = 20, inertia weight = 0.8, learning factor = 0.5, number of snakes = 15, and g -value = 15 (obtaining 42 snaxels per snake) with an executing time of 11.152 s.

From the previously dataset of CT images described above, in Table 1 the average of the resulting segmentations performed by two experts, traditional ACM, graph cut, and

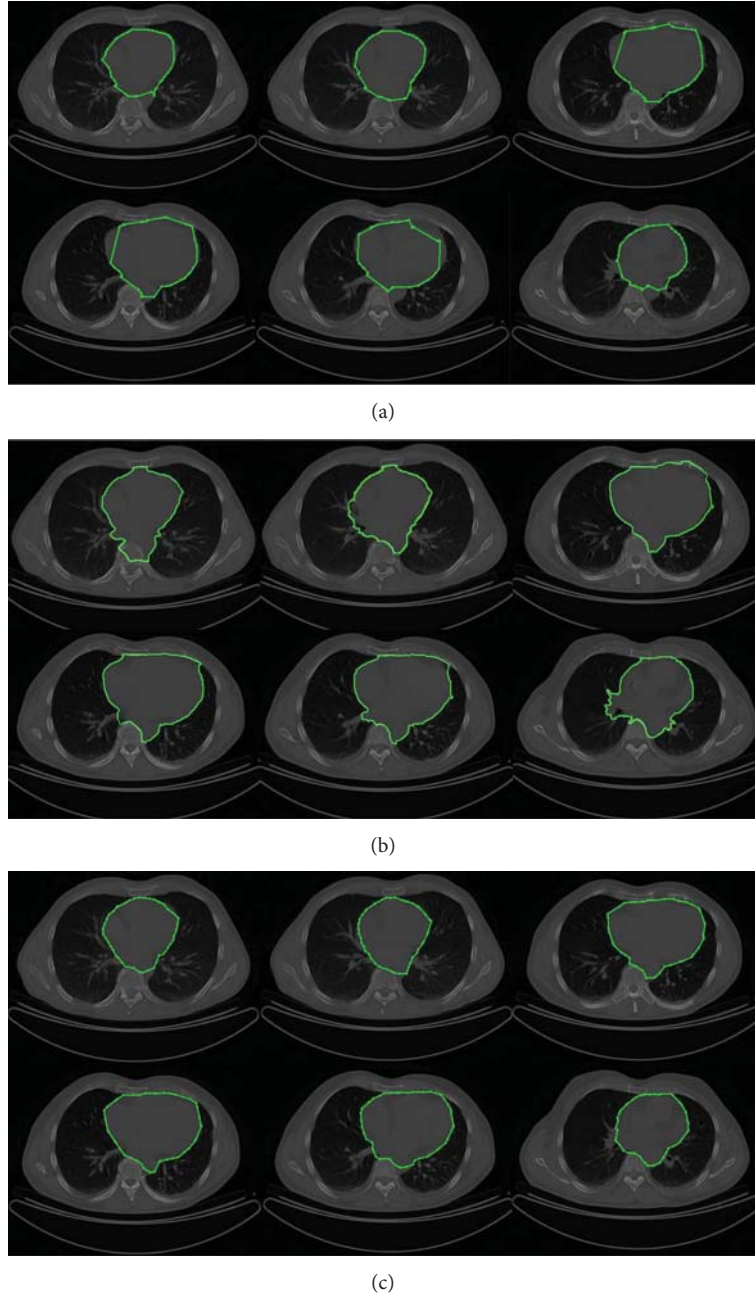


FIGURE 9: CT images (human heart segmentation): (a) results of traditional ACM, (b) results of graph cut method, and (c) results of MACPSO implementation.

the MACPSO method is listed. The comparative results suggest that the MACPSO method is promising in human heart segmentation.

In Figure 10, the results of segmenting a subset of MR images containing the human left ventricle are presented. These images have been extracted from a segmented dataset with 23 sequential MR images of a patient where each image is of size 512×512 pixels. Figure 10(a) shows the resulting segmentations of applying the traditional ACM, where the resulting snake cannot adjust to the correct left

ventricle boundary. The parameters of ACM are set as 42 control points, $\alpha = 0.01$, $\beta = 0.9$, and $\gamma = 0.05$ with an executing time of 4.183 s. To perform the graph cut method, the experts defined the human left ventricle and background seeds. In Figure 10(b), the segmentation results acquired by the interactive graph cut method, which were obtained in 3.726 s, are illustrated. On the other hand, in Figure 10(c), the segmented images via MACPSO show in an appropriate way the boundary of the human left ventricle. In this simulation, the parameters of the proposed method are

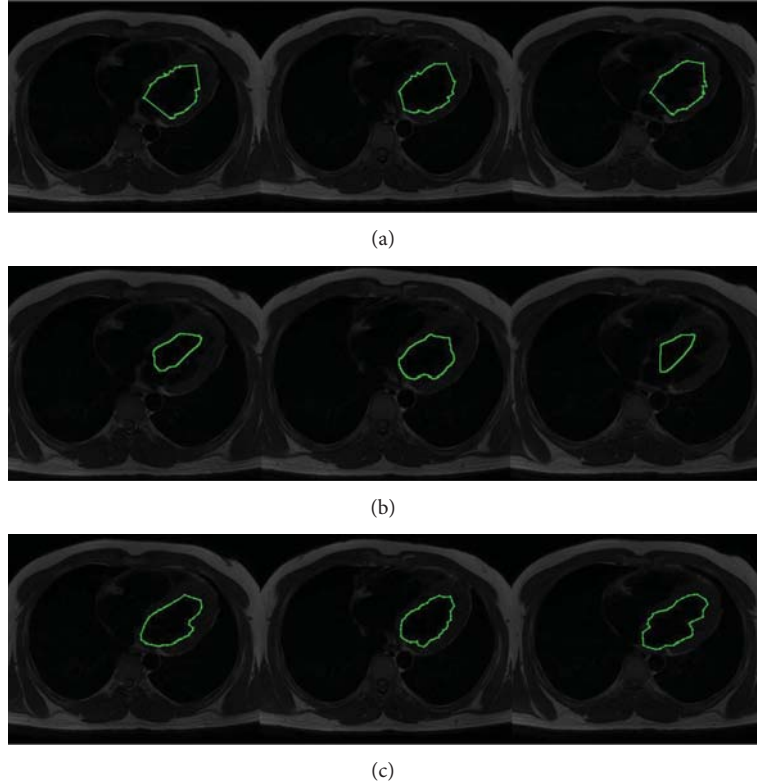


FIGURE 10: MR images (human left ventricle segmentation): (a) results of traditional ACM, (b) results of graph cut method, and (c) results of MACPSO implementation.

TABLE 1: Average similarity measure with the Jaccard index, the Dice index, and the Hausdorff distance among the regions segmented by the traditional ACM, graph cut method, our proposed method (MACPSO), and the regions outlined by two experts of the set of CT images.

Comparative studies	Distance/similarity measure		
	Hausdorff (H)	Jaccard's index (J)	Dice's index (D)
ACM versus Expert 1	7.071	0.5272	0.6904
ACM versus Expert 2	5.0	0.5	0.6666
Graph cut versus Expert 1	4.2426	0.7142	0.8333
Graph cut versus Expert 2	3.1622	0.6153	0.7619
MACPSO versus Expert 1	2.0	0.8260	0.9047
MACPSO versus Expert 2	1.4142	0.9090	0.9523

TABLE 2: Average similarity measure with the Jaccard index, the Dice index, and the Hausdorff distance among the regions segmented by the traditional ACM, graph cut method, our proposed method (MACPSO), and the regions outlined by two experts of the set of MR images.

Comparative studies	Distance/similarity measure		
	Hausdorff (H)	Jaccard's index (J)	Dice's index (D)
ACM versus Expert 1	7.615	0.377	0.5476
ACM versus Expert 2	15.231	0.4	0.5714
Graph cut versus Expert 1	6.236	0.5555	0.7142
Graph cut versus Expert 2	6.782	0.5272	0.6904
MACPSO versus Expert 1	6.708	0.7142	0.8333
MACPSO versus Expert 2	7.071	0.6153	0.7619

set as iterations = 20, inertia weight = 0.8, learning factor = 0.5, number of snakes = 9, and g -value = 15 (obtaining 42 snaxels per snake) with an executing time of 5.179 s.

Moreover, to quantify the resulting segmentations from the dataset of sequential MR images described above, Table 2 presents comparative results through the Hausdorff distance, the Jaccard index, and the Dice index. This similarity analysis shows that the proposed method is very suitable in left ventricle segmentation. Additionally, area and perimeter measures have been adopted to compare in a quantitative way

the segmented regions performed by two experts, traditional ACM, graph cut, and MACPSO method, which are shown in Table 3.

As shown in Table 1, compared to segmentations made by experts, the distance and similarity measures indicate that MACPSO is promising in human heart segmentation on CT images since the Jaccard and Dice indexes show a high accuracy (90% and 95% with expert 2) and the Hausdorff distance is low with respect to the traditional ACM and graph cut method. Besides, Table 2 shows that

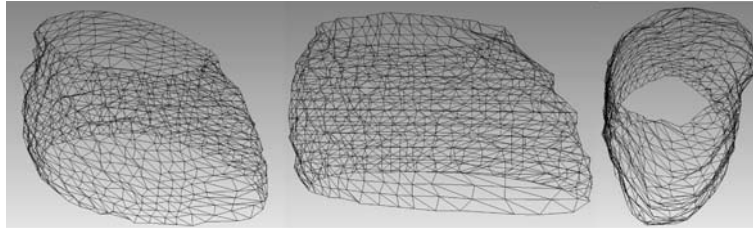


FIGURE 11: 3D reconstruction of human heart from the segmented cardiac CT images.

TABLE 3: Average of the area and perimeter in pixels obtained from the traditional ACM, graph cut method, our proposed method (MACPSO), and the regions outlined by two experts from the sets of CT and MR images.

Method	Set of CT images		Set of MR images	
	Area	Perimeter	Area	Perimeter
Expert 1	9904.5 pix.	355.209 pix.	5796.0 pix.	291.645 pix.
Expert 2	10369.5 pix.	370.137 pix.	6250.5 pix.	310.13 pix.
ACM	9529.5 pix.	367.634 pix.	7283.5 pix.	350.734 pix.
Graph cut	10036.5 pix.	410.673 pix.	7405.0 pix.	383.992 pix.
MACPSO	10439.5 pix.	376.902 pix.	6385.5 pix.	308.009 pix.

the performance of MACPSO in human left ventricle is more sensitive due to the low contrast and the presence of noise in MR images achieving an acceptable accuracy of 83%. The area and perimeter measures have also shown that MACPSO is more stable than ACM and graph cut, since the values of the proposed method are located in the range of the values acquired by the experts.

Since MACPSO has proved a suitable efficiency in the segmentation of sequential cardiac images, a potential application of the proposed method is the 3D reconstruction of human organs. The quality of the reconstruction depends on the number of sequential images considered. In Figure 11, a 3D reconstruction approach of the human heart is presented, which is achieved by superimposing the resulting contours according to the image acquisition order, and triangulation is performed through the snaxels of each contour to obtain a complete mapping. This 3D reconstruction consists of 18 CT images previously selected by the experts and segmented via the proposed MACPSO method.

5. Conclusions

In this research, a new image segmentation method based on multiple active contours driven by particle swarm optimization (MACPSO) has been presented. MACPSO divides the search space in polar sections to overcome the sensitivity to initial contour position and the local minima drawbacks of the traditional active contour model (ACM). In a first stage of this paper, to evaluate the performance of the proposed method and to compare it to the traditional ACM, some experiments with synthetic images have been introduced. Subsequently, in the second stage, experiments with cardiac medical images acquired from the computed tomography

and magnetic resonance procedures have been used. The experimental results revealed that the proposed method can lead to more efficiency and stability in the presence of noise and concavities than the traditional ACM. This advantage made it possible to obtain a high accuracy and effectiveness in the human heart and human left ventricle segmentations compared to those outlined by the experts and by the graph cut method according to the evidence of similarity metrics. Additionally, the experimental results have also shown that the local exploitation of polar sections through the constant parameters of MACPSO is highly suitable for medical image applications, including segmenting datasets of sequential medical images within an appropriate computational time.

Acknowledgments

This research has been partly supported by the National Council of Science and Technology of México (CONACYT) under Grant no. 241224-218157. The authors would like to thank Dr. R. Mendoza-Gómez and Dr. F. J. Solórzano-Zepeda at the Cardiology Department of the Mexican Social Security Institute, UMAE TI León, for their precious clinical advice and assistance during data collecting. The authors thank the Auckland MRI Research Group, University of Auckland and Cardiac Atlas Website for the valuable collaboration providing us the sources of Magnetic Resonance Imaging. The authors thank Ehsan Shahamatnia at Universidade Nova de Lisboa for kindly supplying them the source of the symmetrical cross and noisy circle test images, respectively.

References

- [1] H. Castillejos, V. Ponomaryov, L. N. de Rivera, and V. Golikov, "Wavelet transform fuzzy algorithms for dermoscopic image segmentation," *Computational and Mathematical Methods in Medicine*, vol. 2012, Article ID 578721, 11 pages, 2012.
- [2] P. Davuluri, J. Wu, Y. Tang et al., "Hemorrhage detection and segmentation in traumatic pelvic injuries," *Computational and Mathematical Methods in Medicine*, vol. 2012, Article ID 898430, 12 pages, 2012.
- [3] A. Nyma, M. Kang, Y. Kwon, C. Kim, and J. Kim, "A hybrid technique for medical image segmentation," *Journal of Biomedicine and Biotechnology*, vol. 2012, Article ID 830252, 7 pages, 2012.
- [4] W. Hsu, "Improved watershed transform for tumor segmentation: application to mammogram image compression," *Expert Systems With Applications*, vol. 39, no. 4, pp. 3950–3955, 2012.
- [5] E. Cuevas, V. Osuna-Enciso, D. Zaldivar, M. Perez-Cisneros, and H. Sossa, "Multithreshold segmentation based on artificial

- immune systems,” *Mathematical Problems in Engineering*, vol. 2012, Article ID 874761, 20 pages, 2012.
- [6] Y. Boykov and M. Jolly, “Interactive organ segmentation using graph cuts,” in *Proceedings of the Medical Image Computing and Computer-Assisted Intervention*, pp. 276–286, 2000.
- [7] F. R. Schmidt, E. Töppe, and D. Cremers, “Efficient planar graph cuts with applications in computer vision,” in *Proceedings of the IEEE Computer Society Conference on Computer Vision and Pattern Recognition Workshops (CVPR Workshops '09)*, pp. 351–356, June 2009.
- [8] D. R. Chen, R. F. Chang, W. J. Wu, W. K. Moon, and W. L. Wu, “3-D breast ultrasound segmentation using active contour model,” *Ultrasound in Medicine and Biology*, vol. 29, no. 7, pp. 1017–1026, 2003.
- [9] A. Jumaat, W. Rahman, A. Ibrahim, and R. Mahmud, “Segmentation of masses from breast ultrasound images using parametric active contour algorithm,” *Procedia Social and Behavioral Sciences*, vol. 8, pp. 640–647, 2010.
- [10] M. Kass, A. Witkin, and D. Terzopoulos, “Snakes: active contour models,” *International Journal of Computer Vision*, vol. 1, no. 4, pp. 321–331, 1988.
- [11] Y. Pang, L. Li, W. Hu, Y. Peng, L. Liu, and Y. Shao, “Computerized segmentation and characterization of breast lesions in dynamic contrast-enhanced mr images using fuzzy c-means clustering and snake algorithm,” *Computational and Mathematical Methods in Medicine*, vol. 2012, Article ID 634907, 10 pages, 2012.
- [12] L. Gao, X. Liu, and W. Chen, “Phase- and gvf-based level set segmentation of ultrasonic breast tumors,” *Journal of Applied Mathematics*, vol. 2012, Article ID 810805, 22 pages, 2012.
- [13] X. Liu, M. Haider, and I. Yetik, “Unsupervised 3d prostate segmentation based on diffusion-weighted imaging mri using active contour models with a shape prior,” *Journal of Electrical and Computer Engineering*, vol. 2011, Article ID 410912, 11 pages, 2011.
- [14] X. Zhu, P. Zhang, J. Shao, Y. Cheng, Y. Zhang, and J. Bai, “A snake-based method for segmentation of intravascular ultrasound images and its in vivo validation,” *Ultrasonics*, vol. 51, no. 2, pp. 181–189, 2011.
- [15] I. Dagher and K. E. Tom, “Waterballoons: a hybrid watershed balloon snake segmentation,” *Image and Vision Computing*, vol. 26, no. 7, pp. 905–912, 2008.
- [16] L. Wang, L. He, A. Mishra, and C. Li, “Active contours driven by local gaussian distribution fitting energy,” *Signal Processing*, vol. 89, no. 12, pp. 2435–2447, 2009.
- [17] B. Liu, H. Cheng, J. Huang, J. Tian, X. Tang, and J. Liu, “Probability density difference-based active contour for ultrasound image segmentation,” *Pattern Recognition*, vol. 43, no. 6, pp. 2028–2042, 2010.
- [18] X. Chen, J. Udupa, U. Bagci, Y. Zhuge, and J. Yao, “Medical image segmentation by combining graph cuts and oriented active appearance models,” *IEEE Transactions on Image Processing*, vol. 21, no. 4, pp. 2035–2046, 2012.
- [19] M. Talebi, A. Ayatollahi, and A. Kermani, “Medical ultrasound image segmentation using genetic active contour,” *Journal of Biomedical Science and Engineering*, vol. 4, pp. 105–109, 2011.
- [20] J. Novo, J. Santos, and M. Penedo, “Topological active models optimization with differential evolution,” *Expert Systems With Applications*, vol. 39, no. 15, pp. 12165–12176, 2012.
- [21] C. C. Tseng, J. G. Hsieh, and J. H. Jeng, “Active contour model via multi-population particle swarm optimization,” *Expert Systems with Applications*, vol. 36, no. 3, pp. 5348–5352, 2009.
- [22] E. Shahamatnia and M. Ebadzadeh, “Application of particle swarm optimization and snake model hybrid on medical imaging,” in *Proceedings of the 3rd International Workshop on Computational Intelligence in Medical Imaging (CIMI '11)*, pp. 1–8, IEEE service center, 2011.
- [23] R. Eberhart and J. Kennedy, “New optimizer using particle swarm theory,” in *Proceedings of the 6th International Symposium on Micro Machine and Human Science*, pp. 39–43, October 1995.
- [24] Y. Shi and R. Eberhart, “Modified particle swarm optimizer,” in *Proceedings of the IEEE International Conference on Evolutionary Computation (ICEC '98)*, pp. 69–73, May 1998.
- [25] W. He, Y. Cheng, L. Xia, and F. Liu, “A new particle swarm optimization-based method for phase unwrapping of mri data,” *Computational and Mathematical Methods in Medicine*, vol. 2012, Article ID 475745, 9 pages, 2012.
- [26] M. J. Abdi, S. Hosseini, and M. Rezghi, “A novel weighted support vector machine based on particle swarm optimization for gene selection and tumor classification,” *Computational and Mathematical Methods in Medicine*, vol. 2012, Article ID 320698, 7 pages, 2012.

Research Article

Spatiotemporal Quantification of Local Drug Delivery Using MRI

Morgan B. Giers,¹ Alex C. McLaren,^{1,2} Jonathan D. Plasencia,³ David Frakes,³
Ryan McLemore,^{1,2} and Michael R. Caplan¹

¹ Center for Interventional Biomaterials, School of Biological and Health Systems Engineering, Arizona State University, P.O. Box 879709, Tempe, AZ 85287, USA

² Banner Good Samaritan Medical Center, 901 E Willetta Street, 2nd Floor, Phoenix, AZ 85006, USA

³ Image Processing Application Laboratory, School of Biological and Health Systems Engineering, Arizona State University, P.O. Box 879709, Tempe, AZ 85287, USA

Correspondence should be addressed to Michael R. Caplan; michael.caplan@asu.edu

Received 20 December 2012; Revised 25 March 2013; Accepted 26 March 2013

Academic Editor: Wenxiang Cong

Copyright © 2013 Morgan B. Giers et al. This is an open access article distributed under the Creative Commons Attribution License, which permits unrestricted use, distribution, and reproduction in any medium, provided the original work is properly cited.

Controlled release formulations for local, *in vivo* drug delivery are of growing interest to device manufacturers, research scientists, and clinicians; however, most research characterizing controlled release formulations occurs *in vitro* because the spatial and temporal distribution of drug delivery is difficult to measure *in vivo*. In this work, *in vivo* magnetic resonance imaging (MRI) of local drug delivery was performed to visualize and quantify the time resolved distribution of MRI contrast agents. Three-dimensional T_1 maps (generated from T_1 -weighted images with varied T_R) were processed using noise-reducing filtering. A segmented region of contrast, from a thresholded image, was converted to concentration maps using the equation $1/T_1 = 1/T_{1,0} + R_1C$, where $T_{1,0}$ and T_1 are the precontrast and postcontrast T_1 map values, respectively. In this technique, a uniform estimated value for $T_{1,0}$ was used. Error estimations were performed for each step. The practical usefulness of this method was assessed using comparisons between devices located in different locations both with and without contrast. The method using a uniform $T_{1,0}$, requiring no registration of pre- and postcontrast image volumes, was compared to a method using either affine or deformation registrations.

1. Introduction

Controlled release formulations for local drug delivery are of growing interest to device manufacturers, research scientists, and clinicians. There are many current and potential applications for controlled release devices, including cancer treatment [1], pain management [2, 3], tissue engineering [4], and infection treatment [5]. For decades, orthopaedic infection management has relied on the use of antimicrobials delivered from bone cement at the infection site [6]. There are an estimated 112,000 total orthopaedic infections of arthroplasties and fracture-fixation devices per year [7], and this number is expected to increase as the projected number of arthroplasties will likely increase by several fold over the

next 18 years [8]. Approximately \$1.8 billion is spent annually on increased medical costs due to orthopaedic infection of total joint arthroplasties in the USA [7]. Orthopaedic implant infections result from common human skin microbes, such as *Staphylococcus epidermidis* and *Staphylococcus aureus*, and are often complicated by biofilm formation. Biofilm residing microbes are not only protected by transport-limiting polysaccharide matrix, but are more resistant to antimicrobials [9]. Antimicrobial concentration of 100–1000 times the usual minimum inhibitory concentration (MIC) used to treat planktonic microbes are required to treat infections with biofilm effectively [10, 11]. Intravenous delivery to achieve these antimicrobial levels will cause serious systemic toxicity for most of the antimicrobials used to treat implant infections.

Local drug delivery at the site of orthopaedic infection is used to achieve effective concentration of antimicrobial without systemic toxicity.

Even though antimicrobial loaded bone cement (ALBC) is intended for *in vivo* use, most release studies of antimicrobials from ALBC have been performed *in vitro*. For instance, researchers commonly characterize drug elution profiles from controlled release formulations by placing samples of known geometry under near infinite sink conditions, such as a large volume of frequently exchanged fluid [12, 13]. While release studies give valuable information necessary for directly comparing different controlled release formulations, it does not represent how or where the drugs will distribute when the device is implanted. Infinite sink conditions produce the greatest possible release of drug which represents the potential release capability not the actual elution profiles likely to be achieved *in vivo*, where mass transport resistances from the surrounding tissue are likely to decrease the rate of release. *In vivo* studies have been performed [14–17], but none provide comprehensive information on the spatial and temporal distribution of drug delivery. *In vivo* tests frequently focus on efficacy, such as infection control [17], but do not provide details regarding how the antimicrobial is distributed because this is difficult, expensive, and time consuming to measure. *In vivo* animal experiments that do consider spatial distribution of antimicrobial commonly utilize tissue biopsies near implants and collect fluids, such as seroma, blood, and urine [14–16]. These techniques are time consuming to analyze, not comprehensive (e.g., resolution is low due to limited number of samples), and of limited clinical applicability to humans due to their invasiveness and requirements for multiple sampling.

Magnetic resonance imaging (MRI) has been used to visualize distribution of drugs delivered locally in several clinically relevant applications; however, in most of these studies, either concentration of the drug is not calculated or is not defined spatially. Sampson and coworkers deliver MRI contrast agents to brain tumors, but no quantification of the agent's concentration is performed [18, 19]. Krauze et al. [20] and Port et al. [21] imaged liposomal Gd-DTPA delivery, but neither quantified concentration. Fritz-Hansen et al. calculated bulk concentration of contrast in arterial blood, but, was not concerned with spatial distribution [22]. Other studies have considered other aspects of the MRI contrast/concentration relationship based on *in vitro* tests [23–29].

Some studies of imaging drug delivery have calculated local concentration of drug, but each has limitations. Sarntinoranont and coworkers have studied delivery of gadolinium diethylenetriaminepentaacetic acid (Gd-DTPA) delivery to brain tumors [30], and they calculate concentration of the Gd-DTPA using a method validated in an agarose phantom [31]. Sarntinoranont et al.'s studies seem to accurately calculate concentration with good spatial resolution; however, in our attempts to utilize a similar method for a different area of the body, additional studies into the potential sources of error and methods to minimize and quantify that error are warranted. Kim et al. quantified the distribution of drugs delivered from an ocular implant using MRI [32];

however, the function used by Kim et al. to convert MR intensity to concentration is similar in shape to a parabola and thus results in two valid concentrations for most MR intensity values—one concentration being high and the other being low; thus, the user must infer which concentration is more likely based on proximity to the depot. Several groups have calculated concentrations of contrast agent *in vitro* [23, 33–36]; however, their methods of quantification are not validated *in vivo* to determine sources of error or to quantify the error likely in their *in vivo* measurements.

In this work, we provide detailed methods for *in vivo* MR imaging of local delivery of Gd-DTPA in an orthopaedic model which provides a rigorous test of the method's ability to distinguish contrast agent from anatomical features, thus, also provides a rigorous test of the method's ability to accurately calculate concentration of the Gd-DTPA. In this model MRI images of Gd-DTPA, delivered from polymethyl methacrylate (PMMA) bone cement, were converted to Gd-DTPA concentration to provide time-resolved maps of Gd-DTPA concentration. The contrast agent, Gd-DTPA, was chosen because of its similar solubility and diffusion coefficient ($4.0 \times 10^{-6} \text{ cm}^2/\text{sec}$) [37] to the antimicrobials Vancomycin ($3.64 \times 10^{-6} \text{ cm}^2/\text{sec}$) [38] and Gentamicin ($2.08 \times 10^{-6} \text{ cm}^2/\text{sec}$) [39], which are common choices to treat infected orthopaedic implants. This paper presents a detailed protocol for performing this method on an animal model. Further, sources of error are discussed and quantified when possible. Finally, methods of image volume registration are demonstrated and compared to the method proposed here (average value of precontrast T_1 applied to all voxels).

2. Methods

2.1. Implant Formulation. PMMA bone cement was formed using Simplex P bone cement (Stryker, Kalamazoo, MI, USA). Control implants, with no contrast agent, were made according to the manufacturer's instructions. Experimental implants were made identically with the addition of either (a) an additional 2.1%v (2.9%w) Gd-DTPA, an MRI contrast agent; 8.8%v (11.4%w) xylitol, a particulate porogen used to increase release rate and amount; and 89.1%v (85.7%w) PMMA and polymerized MMA or (b) an additional 1.1%v (1.4%w) Gd-DTPA, 9.9%v (12.9%w) xylitol, and 89%v (85.7%w) PMMA and polymerized MMA. Implants of all compositions were formed into 3 mm diameter \times 7 cm long rods using a red rubber catheter (Covidien, Mansfield, MA, USA) as mold.

2.2. Surgical Procedure. All procedures were compliant with the National Institutes of Health guidelines for the care and use of laboratory animals and approved by the Institutional Animal Care and Use Committee. All studies were performed using New Zealand White rabbits ($n = 18$). Animals were sedated using ketamine (35 mg/kg), xylazine (5 mg/kg), and butorphanol (0.1 mg/kg), and anesthesia was maintained by administering 2% isoflurane during the procedure.

ALBC was implanted in four different ways to study the effect of different sizes/shapes of implants and effect

of implant location on distribution of Gd-DTPA from the implant. The rationale for these different implantations and comprehensive discussion of the similarities and differences of resulting Gd-DTPA distribution is published elsewhere [40, 41]. In the first set of procedures, ALBC rods were implanted in either muscle, intramuscular rod (IMR), or the intramedullary canal of the femur, intraosseous rod (IOR) [40]. Briefly, the right quadriceps of each animal received a cement rod of either the experimental (2.1%v Gd-DTPA, 8.8%v xylitol, 89.1%v PMMA, and polymerized MMA) or control (no Gd-DTPA, no xylitol) cement composition. The left femur of each animal received a cement rod of either the experimental (1.1%v Gd-DTPA, 9.9%v xylitol, 89%v PMMA and polymerized MMA) or control composition. In the second set of procedures, either a partial thickness section of muscle (PTM) or a full thickness section of muscle and bone (FTMB) was removed and replaced with bone cement [41]. For the FTMB wound, muscle tissue was removed from the mid quadricep, and a femoral circumference window was created in the anterolateral cortex of the femur. The defect was filled with ALBC (composition as in IMR) or control. In the PTM model, muscle was removed, the dead space was filled with cement of either experimental or control composition (compositions as in IMR).

2.3. Image Acquisition. A series of T_1 -weighted rapid acquisition with relaxation enhancement (RARE) scans were taken at repetition times (T_R) of 1463, 2000, 3000, and 5000 ms (RARE = 2, no averages) on a Bruker Biospin 7-T MRI (Bruker Biospin, Billerica, MA, USA) every 15 minutes for 4–6 hours (Figure 1(a)). A 15 cm quadrature transceiver coil was used. Flip angle of the RF pulse was calibrated by the Bruker software before each scan, and the images were checked to ensure no ghosting artifacts were present. The images were taken with coronal slices from knee to hip, 42 slices total (field of view = 12 cm), with a voxel size of $0.3 \text{ mm} \times 0.3 \text{ mm} \times 2 \text{ mm}$, where the slice thickness was 2 mm and resultant matrix size was $256 \times 256 \times 42$. This imaging sequence required approximately 14 minutes.

The series of T_1 -weighted images at different T_R was used by the Bruker software to construct a longitudinal relaxation time, T_1 , map based on the solution to the Bloch equation:

$$S(T_R) = S_0 \left(1 - e^{-T_R/T_1}\right), \quad (1)$$

$$S_0 = k\rho e^{-T_E/T_2}, \quad (2)$$

where S is the signal intensity, T_R is repetition time (time between RF pulses), T_1 is the longitudinal relaxation time, and S_0 is defined by (2), where k is the proportionality constant based on instrument factors, ρ is the spin density, T_E is the echo time, and T_2 is the transverse relaxation time [42]. The estimated error of this process was calculated by taking the residuals of the curve fitting process for 1 pixel. In a T_1 -weighted image, contrast and fat appeared bright, whereas, cement and bone appeared dark as seen in Figure 1(a). In the T_1 map, fat appeared bright, whereas, contrast, bone, and cement appeared dark as seen in Figure 1(b).

2.4. Image Processing. The T_1 maps were imported into MATLAB (Mathworks, Natick, MA, USA). In MATLAB each slice of the T_1 map was separately treated with a noise-reducing filter which changes a pixel to the median value of itself and the 4 in-plane neighbors that share an edge with the pixel. The filtering results are shown in Figure 1(c). Subsequently, a binary mask of the leg area was made by morphologically opening the filtered T_1 -weighted image slice, applying a binary threshold, filling holes, and removing groupings of pixels less than 100, then morphologically closing the image slice. The binary mask of the leg area was used to mask noise from outside of the legs in the T_1 map (Figure 1(c)). A histogram of this image was then calculated. The portion of the histogram to the right of the peak (values with T_1 equal to or greater than the peak) was duplicated to the left of the peak to make the histogram symmetric (excluding pixels containing contrast agent) enabling calculation of a standard deviation for determination of a suitable threshold for segmentation. After this, both the T_1 -weighted and T_1 map image slices were exported from MATLAB as a series of TIFF files. The TIFF images were imported into Mimics (Materialise, Leuven, Belgium), where the T_1 map was thresholded to a value of T_1 at one standard deviation less than the peak value of the histogram. This threshold level (one standard deviation less than peak of histogram) matched the segmentation performed by several expert users.

We then employed a semiautomatic gradient flow detection algorithm in Mimics to create the 3D representation of areas containing Gd-DTPA. First, all pixels within the muscle tissue of the leg were segmented from the thresholded region. Then, all the pixels connected to the implant in this region were segmented. This gave a region of all the pixels connected to the implant within the muscle of the leg, which included the cement implant and contrast agent. After muscle implants and contrast were segmented, several steps were performed to segment contrast within the intramedullary canal of the femur. The intramedullary canals of both femurs (both legs) were segmented from the T_1 -weighted image volume using a semiautomatic gradient flow detection algorithm, which is similar to the method shown by Karasev et al. [43]. The mask of the segmented region from the femur without contrast (one of two legs contained a PTM experiment which does not contain ALBC in the intramedullary space) was imported into MATLAB, where a symmetric histogram was created for the intramedullary space as described above. The peak value and standard deviation of the symmetric histogram were calculated. In Mimics, the masked intramedullary space of the femur containing an implant and contrast agent was thresholded to T_1 one standard deviation less the peak value of the histogram. All pixels connected to the cement implant within this thresholded region were segmented.

Additionally, to provide anatomical reference in the 3D images, the exterior of the cortex of the femur was segmented using a semiautomatic gradient flow detection algorithm in Mimics, manual correction, and a 3D object smoothing function. The legs were also segmented for an anatomical reference using thresholding, manual correction, and 3D object smoothing. The segmented femur, legs, and contrast

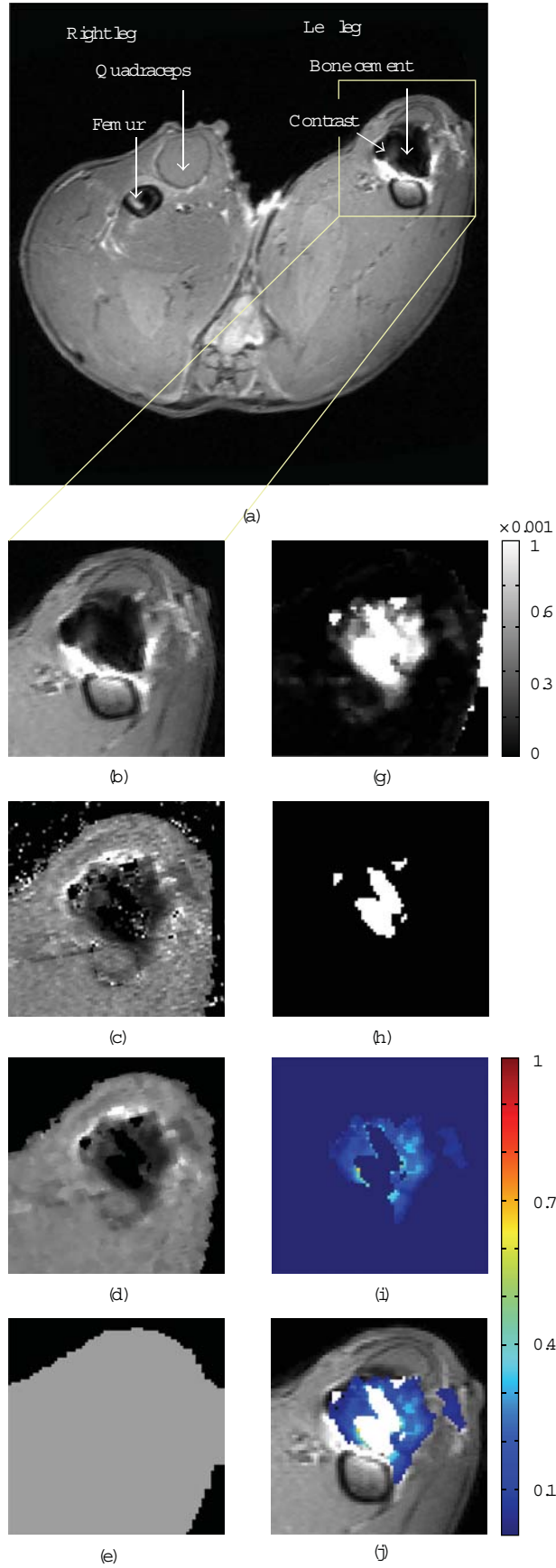


FIGURE 1: Continued.

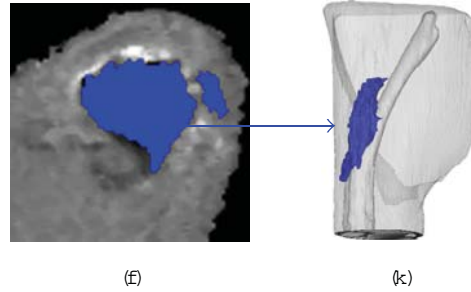


FIGURE 1: (a) T_1 -weighted image, (b) ROI of the T_1 -weighted image, (c) original T_1 Map, (d) filtered and masked T_1 map, (e) $T_{1,0}$ calculated as one standard deviation less than peak of histogram, (f) segmented region of contrast, (g) $1/T_1 - 1/T_{1,0}$ values plotted, (h) region where $T_1 = \text{NA}$, (i) concentration map where the scale is in mM, (j) concentration map superimposed onto T_1 -weighted image, (k) 3D reconstruction from Mimics.

were plotted together as 3D objects using Mimics as shown in Figure 1(h).

The segmented regions of contrast and cement were exported as a series of mask images in a bitmap format. The bitmaps were imported back into MATLAB where they were transformed into a binary image mask. The binary image mask was multiplied by the T_1 map to give a map in only the area of contrast (Figure 1(d)). This region was transformed into a concentration map (Figures 1(e) and 1(f)) using the following:

$$\frac{1}{T_1} = \frac{1}{T_{1,0}} + r_1 C, \quad (3)$$

(see [28, 31, 33]), where $T_{1,0}$ is a precontrast T_1 map value and T_1 is the postcontrast T_1 map value. For (3), the peak value from the histogram for the appropriate tissue (muscle or intramedullary canal) was used for $T_{1,0}$. Relaxivity (r_1) of the contrast agent was set to $0.0038 \text{ mM}^{-1} \text{ s}^{-1}$ which is consistent with reported values from several literature studies using 3–7T MRIs, including Rohrer et al. who obtained this particular value for Gd-DTPA in serum using a 4.7T MRI [27]. The concentration map was superimposed onto a T_1 -weighted image to provide the anatomical details as shown in Figure 1(g).

To evaluate the validity of the use of a single $T_{1,0}$ value rather than a pixel-by-pixel $T_{1,0}$ value achieved by image registration, histograms of 5 precontrast rabbits (rabbits no. 1, 8, 9, 15, 18 in the series) were composed. We then used the standard deviations from these histograms to perform sensitivity analysis on the concentrations calculated for different T_1 values using the peak $T_{1,0}$ value with $T_{1,0}$ one standard deviation greater than and less than the mean $T_{1,0}$. To evaluate if one $T_{1,0}$ value could be used for multiple tissue types, histograms were calculated for the femur and the muscle separately. We also compare/contrast the accuracy of the above technique with using T_1 values from an image in which no contrast is present. This requires that the image volumes with no contrast be spatially registered to the image volumes with contrast present. Such a registration was completed for one image set. First, a 3D rigid body affine registration

was performed in which matching points on the femur in precontrast and postcontrast images were chosen by a user. A transformation matrix was created and optimized using singular value decomposition similar to a method outlined by Eggert et al. [44]. The precontrast image volume was transformed using a 3D linear interpolation algorithm, which used Delaunay triangulation to handle the scattered data points. Then a 3D deformation registration was performed by picking points from the affine registered precontrast image and postcontrast image. A transformation map was generated by calculating the difference between current and desired point location for the points chosen, then interpolating all the surrounding pixel values using linear interpolation. The image volume was transformed using the same linear interpolation algorithm as in the affine registration.

Although varying concentration of the contrast agent does effect the magnetic susceptibility and thus the relaxivity of the contrast agent, (3) seems to accurately calculate concentration using a constant value of r_1 ($0.0038 \text{ mM}^{-1} \text{ s}^{-1}$) between approximately $100 \mu\text{M}$ and 5 mM (shown in Figure 3). Data in Figure 3 were acquired by scanning a series of vials containing known concentrations of Gd-DTPA in 2%w agarose, plotting $1/T_1$ versus concentration, and comparing to (3) (dashed line).

2.5. Image Analysis. Volumes of segmented contrast, including the cement implant, were calculated. These were adjusted by subtracting the volume of cement implanted, as calculated from the weight of the implant (see details of the surgical insertion). The volumes of the region where $T_1 = \text{NA}$, which includes the cement implant and a region of extremely high concentrations of contrast ($>50 \text{ mM}$), were calculated. Total mass of contrast agent was calculated by summing all concentrations from pixels with a real T_1 value and multiplying by voxel volume ($0.18 \mu\text{L}$).

Volumes and total mass were analyzed for significance by two-way ANOVA (wound types and presence of contrast agent: experimental IMR, experimental IOR, control IMR, and control IOR) using Minitab (Minitab Inc., State College, PA, USA). Post hoc t -tests were performed when $P < 0.05$ by ANOVA.

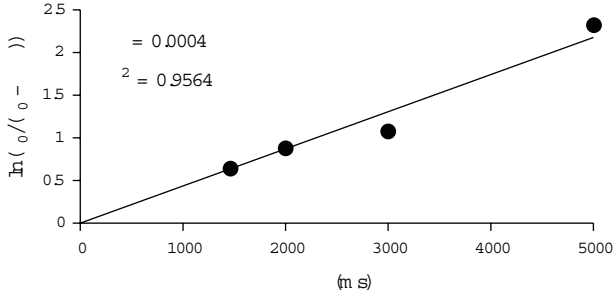


FIGURE 2: A plot of signal intensity from the T_1 -weighted images at different T_R , for one pixel, used to determine T_1 value.

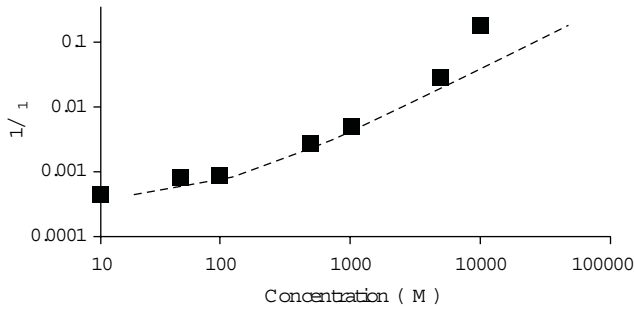


FIGURE 3: T_1 maps were acquired for a series of different concentrations of Gd-DTPA prepared in agarose gel. The plot shows the difference between actual concentration (squares) and concentration calculated using (3) (dashed line).

3. Results and Discussion

Equations (1) and (2) were used to calculate T_1 from the intensity values from a set of T_1 -weighted images taken at different relaxation times (T_R). The fitting is performed pixel-by-pixel. There is noise in the T_1 -weighted images; thus, there is noise in the T_1 value obtained. The noise in the T_1 values depends on the signal-to-noise ratio (SNR) of the image acquisition method used. $\ln(S_0/(S_0 - S_\infty))$ is plotted versus T_R for a single pixel in the muscle of specimen 4 (Figure 2); the inverse of the slope is the T_1 value, and an estimate of the error can be determined from the residuals (Figure 2). This algorithm results in $T_1 < 1$ ms for some pixels, and these pixels are set to $T_1 = \text{NA}$ (not applicable). For the pixel in Figure 2, the T_1 value is 2500 ms, and the residuals squared are 0.96, indicating that a good fit is achieved. Noise is visible as graininess in the T_1 map image (Figure 1(b)). Including more values of T_R decreases the error and improves the calculation, but this requires longer image acquisition time. The time required for the scan is also a function of the T_R values chosen, number of slices, and resolution desired. For the 4 T_R values used here (1463, 2000, 3000, and 5000 ms), 42 slices and $0.3 \text{ mm} \times 0.3 \text{ mm}$ resolution, a scan takes 14 minutes. Certain applications, such as imaging a beating heart, require a fast measurement time. In those cases, a 14-minute scan is unacceptable so a single T_1 -weighted image can be used in such cases [22, 33, 35]. These methods typically

result in greater error, but the error can be offset by acquiring a greater number of replicates.

Next, the T_1 map is filtered to decrease noise (Figure 1(c)). Filtering increases confidence that voxels included as containing contrast are not a product of noise, but filtering also reduces the ability to detect small features in the image. In order for a voxel to be included as having contrast, at least two neighboring pixels must also have contrast. Consequently, a single voxel that contains contrast will be changed to the median value of the surrounding pixels, thus losing the information in the voxel containing contrast. Other sharp features such as tissue planes and bone edges can be replaced (if less than one voxel thick) or thinned by the filtering technique. The order of the filtering technique affects the severity of these changes, with higher order (including more neighboring voxels) making the effects more severe. Here, a 5th-order filtering method is applied (pixel + 4 in-plane neighbors), and this seems to remove much of the noise while only losing very fine features in the image.

Next, the pixels containing contrast agent are identified (Figures 1(e) and 1(f)). In previous work by these authors, blinded reviewers chose areas of contrast from image slices thresholded at 1400 ms, and there was good agreement among reviewers (intraclass correlation coefficient = 0.92–0.96) [40]. In the present work, the method was made even more robust by thresholding at a level based on the longitudinal relaxation times within a single tissue (muscle or intramedullary canal), and including all voxels with T_1 less than the threshold using a semiautomated gradient flow detection algorithm employed in Mimics.

Concentrations were calculated by applying (3) to each pixel containing contrast agent. Pixels with a $T_1 = \text{NA}$ are excluded from this calculation and assumed to either contain high concentration of Gd-DTPA or be voxels containing cement which has a very low water content. Equation (3) relates T_1 with contrast concentration, but it is only accurate within a range of concentrations (100 μM to 5 mM). Within this range, (3) is not exact because the relaxivity (r_1) can vary depending on local variation of magnetic field strength, molecular microenvironment, binding to macromolecules, access to intracellular or extracellular water, and water exchange rates [28]. Thus, although Figure 3 shows that plotting $1/T_1$ versus concentration of samples with known concentrations of Gd-DTPA matches (3) well, it is possible that r_1 values *in vivo* (where more variation in microenvironment is likely) may vary more and cause error in the calculation of Gd-DTPA concentration using (3). At low concentrations, which produce T_1 values close to native tissue, the likely error between the calculated and actual concentrations is fairly large (Figure 3); however, the error is skewed so that the actual concentration is not likely to be much greater than the calculated value, but the actual concentration may be substantially less than the calculated value. When Gd-DTPA exceeds approximately 10–50 mM, an artifact occurs due to the transition of the material properties from paramagnetic to superparamagnetic. This change affects the ability of the MRI to encode spatial information through frequency encoding [42]. This results in $T_1 = \text{NA}$ not only in a pixel containing contrast greater than this concentration

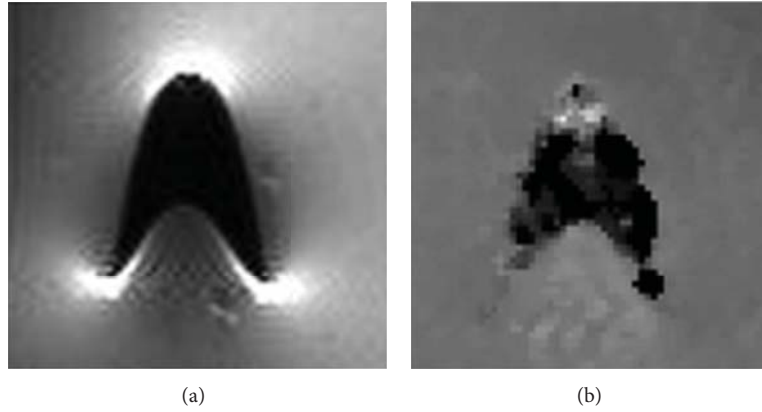


FIGURE 4: (a) T_1 -weighted image and (b) T_1 map of a vial of 100 mM Gd-DTPA which creates an artifact. The dark portion of the images should be round, and the dark portion of the T_1 -weighted image should be bright.

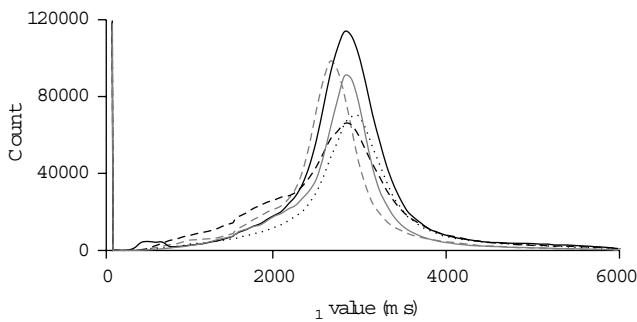


FIGURE 5: Histograms of 5 precontrast rabbit T_1 maps: rabbit 1 (dashed grey line), rabbit 2 (solid grey line), rabbit 3 (dotted black line), rabbit 4 (dashed black line), and rabbit 5 (solid black line).

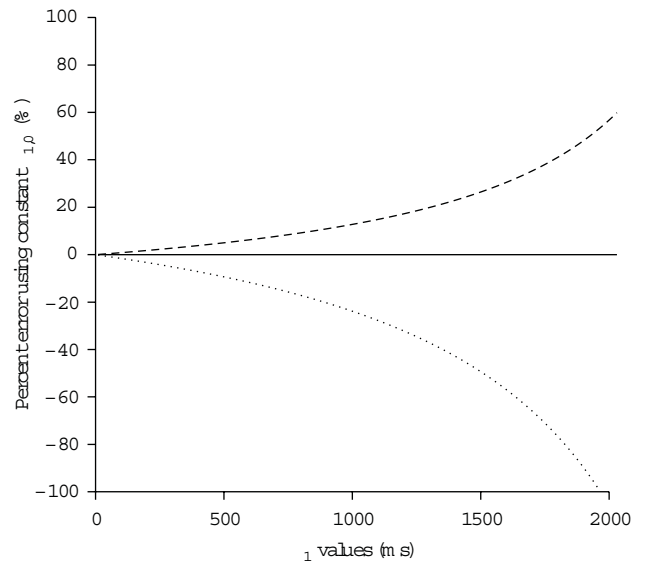


FIGURE 6: Estimation of sensitivity of concentration calculated using isotropic $T_{1,0} = 2817$ ms (mean of Figure 5 histograms, solid line), 3669 ms (one standard deviation greater, dashed line), and 1965 ms (one standard deviation less, dotted line).

but also in some nearby pixels due to this error in spatial encoding as shown in Figure 4. The range of concentration between these high (leading to artifact) and low ($100 \mu\text{M}$) values should be considered when choosing the amount of contrast agent to load into the drug delivery vehicle. The concentration of Gd-DTPA loaded into the ALBC in this study (67 mM) is great enough to allow for an artifact to occur. Most images are unaffected because the Gd-DTPA in the ALBC is not near water and, once it is released into the volume surrounding the ALBC, it quickly becomes diluted to less than the concentration causing artifacts; however, in some images, high concentrations near the femur cause spatial morphing indicating an artifact. The magnitude of this effect was estimated by comparing the volume of pixels where $T_1 = \text{NA}$ between control and experimental implants. If there were a significant amount of artifact or superthreshold gadolinium near the implant in the images with contrast, the volume of pixels where $T_1 = \text{NA}$ would be higher than in the control images. From the ANOVA, there is no statistically significant differences between the control and experimental ($P = 0.86$), indicating that artifacts present are not large enough to significantly affect the experiment and that the $T_1 = \text{NA}$ pixels are most likely pixels containing cement which has a very low water content. The possibility of artifacts must

be balanced against the necessity for visualization of contrast agent further away from the implant when choosing the Gd-DTPA loading amount.

The histograms of five precontrast image volumes were analyzed to find the mean T_1 value of tissue containing no contrast agent (2817 ± 852 ms) (Figure 5) for use on image volumes for which no precontrast image was taken, thus avoiding the need for image registration or using a unique value for each animal. This value, 2817 ± 852 ms, is based on both muscle and intramedullary canal tissue, and the analyses shown in Figures 5 and 6 are based on these unsegregated $T_{1,0}$ values. Our current technique for image analysis uses two different $T_{1,0}$ values: one for tissue outside of the femur and a separate $T_{1,0}$ for the intramedullary canal. The analyses in Figures 5 and 6 provide a quantitative

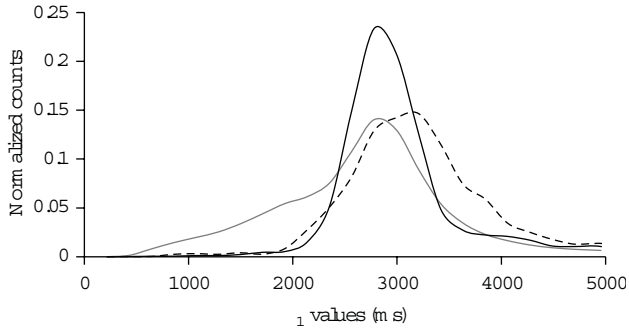


FIGURE 7: Histograms of the total image (solid grey line), the muscle tissue (solid black line), and the bone (dashed black line) in a precontrast T_1 map.

estimate of the error of using one value of $T_{1,0}$ to calculate concentration in an entire region of pixels based on the histogram of that tissue's precontrast T_1 values. Using tissue-specific T_1 values (e.g., for muscle and intramedullary canal) decreases the error in each tissue. The mean (2817 ± 852 ms) provided similar information to the histogram peak values (largest count number in the histogram) for the 5 rabbits shown (2815 ± 132 ms). Animal-to-animal variability can be assessed by comparing a single histogram's mean and standard deviation (2905 ± 834 ms) to the mean from the compounded 5-rabbit histogram (2817 ± 852 ms), whose deviation overlaps considerably. Despite the fact that $T_{1,0}$ values can vary with metabolic activity, the animal-to-animal variability is small relative to the spread of the histogram. Thus error from animal-to-animal variability is less than error due to differences within a single animal. This indicates that there is minimal error introduced by using the 2817 ms value for all animals rather than using a value determined for each animal.

To quantify error likely resulting from using an average value of $T_{1,0}$ rather than a registered precontrast image volume to provide a pixel-by-pixel value of $T_{1,0}$, we applied (2) to T_1 values between 0 and 1965 using $T_{1,0} = 2817$ ms (mean), 3669 ms (+1 standard deviation), and 1965 ms (-1 standard deviation) (Figure 6). This provides a reasonable estimate of the effect that large variability in observed T_1 would have on the calculation of concentration. Equation (2) applied to $T_1 = 1650$ ms results in a concentration of $66 \pm 22/40 \mu\text{M}$ (where the first error number is the difference calculated using $T_{1,0} = 3669$ ms and the second number is the difference calculated using $T_{1,0} = 1965$ ms). As can be seen in Figure 6, error becomes less as T_1 decreases (actual concentration increases). Note that the error is unequal above and below the concentration. For $T_1 = 1965$ ms, using $T_{1,0} = 3669$ ms calculates a concentration value 54% greater than that calculated using $T_{1,0} = 2817$ ms, whereas using $T_{1,0} = 1965$ ms calculates a concentration of $0 \mu\text{M}$ (100% error). The error is always greater for lower concentrations. At low values of T_1 (high concentrations), the error is minimal. For example, $T_{1,0} = 51.5$ ms results in a concentration of $5000 \pm 20/40 \mu\text{M}$ (0.4%/0.8%).

The uneven error results in concentrations that are more likely to be overestimated rather than underestimated. In other words, a pixel calculated to contain $41 \mu\text{M}$ contrast agent ($T_1 = 1965$ ms) may contain no contrast agent at all, but it is unlikely to contain any more than $62 \mu\text{M}$. Also, if a pixel has a T_1 value greater than the threshold (1965 ms) (thus is calculated to have no contrast agent present), it is unlikely to have concentration greater than $62 \mu\text{M}$. The concentration calculation error will be greater in some areas than in others. For example, the femur has a broader histogram distribution than the total image, as shown in Figure 7, so in the femur, error will be greater than the previous estimate. The muscle is more isotropic than the total image so the error for calculations performed in muscle will be slightly less than the previous estimate. Therefore, using an isotropic $T_{1,0}$ values can give accurate order of magnitude information, but specific values, especially low concentration values, should be considered with caution. One potential clinical application of this technique is codelivering Gd-DTPA with antimicrobials to determine if the infection is being treated effectively. For this application, the minimum effective concentration of antimicrobial is near the lower limit of detection of the isotropic $T_{1,0}$ technique (20–200 μM). At that lower limit, if a pixel shows as containing contrast ($T_1 \leq 1965$ ms), it may or not contain effective concentration of antimicrobial; however, if a pixel does not show as containing contrast ($T_1 > 1965$ ms), then it likely contains less than an effective concentration of antimicrobial. Therefore, it is unlikely that a patient would receive an additional intervention unnecessarily, but a patient requiring additional intervention could be evaluated to require no additional intervention allowing a risk that the infection could recur.

Next we compare and contrast results when a single isotropic value of $T_{1,0}$ is used (as described above) versus when $T_{1,0}$ values are taken from image volumes of the tissue prior to the addition of contrast agent. Images of a precontrast and postcontrast FTMB procedure are shown in Figure 8. Figure 8(a) (left) shows a precontrast image that has not been altered; Figure 8(b) (left) shows the same image but registered to the postcontrast image using an affine registration (rigid body registration); Figure 8(c) (left) shows the same image but registered to the postcontrast image using a deformation registration; and, finally, Figure 8(d) (left) shows the isotropic $T_{1,0}$ method in which a single value of $T_{1,0}$ is applied to all of the pixels in the region of interest. It is apparent in Figures 8(a)–8(c) (right) that the edges of the legs do not perfectly overlap (large red region in concentration map) in the unregistered, affine registered, or deformation registered images, but the isotropic $T_{1,0}$ concentration map (Figure 8(d), right) does not have significant patches of red surrounding the leg indicating that this is not a problem for the isotropic $T_{1,0}$ method. The rigid body transformation (Figure 8(b)) was performed by choosing points on the femur, which is a rigid anatomical feature. While the transformation worked well for the femur, the surrounding soft tissue is not registered using this technique. The registration with deformation was applied to register the soft tissue (Figure 8(c)); however, several factors made the registration with deformation method less capable of describing the transform well. It was difficult to

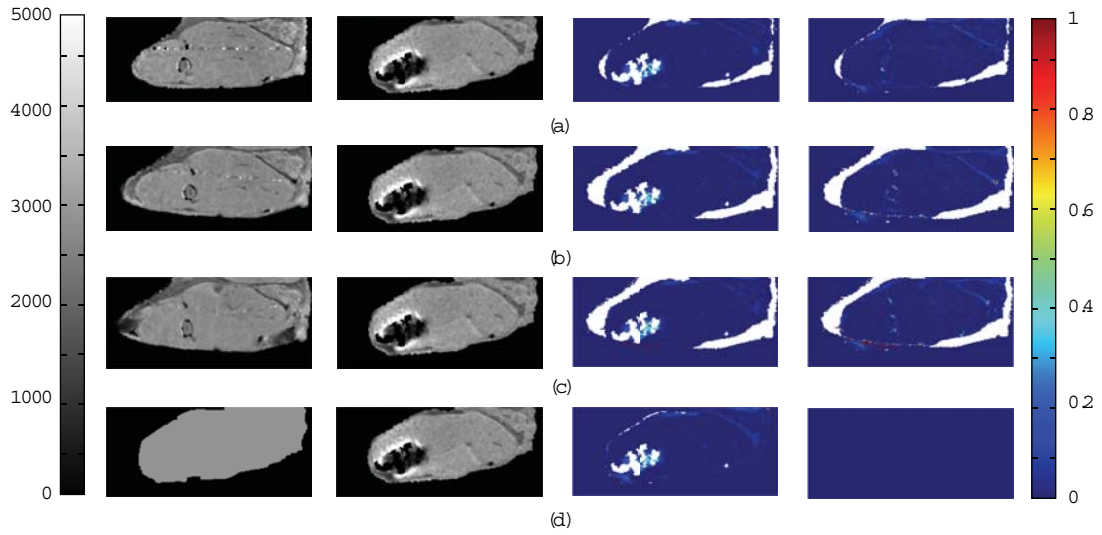


FIGURE 8: (a) The unregistered images, (b) affine registered images, (c) registration with deformation, (d) constant $T_{1,0}$, where the left image is $T_{1,0}$, 2nd column image is T_1 , the 3rd column image is the concentration map resulting from those $T_{1,0}$ and T_1 images, and the right image is the difference between concentration maps for (a), (b), or (c) with (d). White represents regions in which $T_1 = NA$ or for which concentration calculate is out of the range of the color bar (0 mM-1 mM).

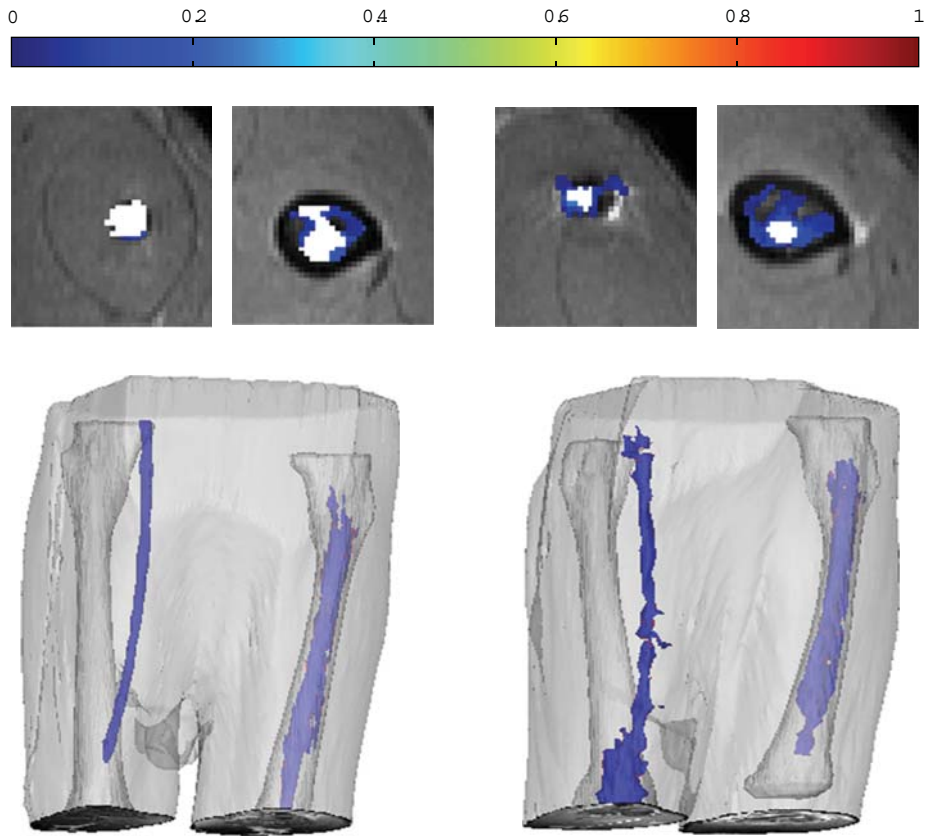


FIGURE 9: A comparison of concentration maps and 3D Mimics reconstructions of an IMR and IOR without (left) and with (right) contrast agent mixed into the ALBC. Color bar for concentration maps is from 0 mM to 1 mM; white represents region where $T_1 = NA$.

identify landmarks to register by in the muscle tissue and especially the fat marrow tissue. Furthermore, choosing the number of corresponding points necessary to obtain a better transform in 3D would be impractically time consuming (250 points takes ~4 hours). Even though the registration with deformation was not perfect, it seems to perform better than the isotropic $T_{1,0}$ method for some anatomic features having $T_{1,0}$ values different from the tissue mean. For example, in Figure 8(d) (right), fairly thick features appearing to have nonzero contrast agent concentration appear. These features also appear in the registered concentration maps (Figures 8(b), right and 8(c), right), but the features are generally fewer and thinner. This indicates that, for anatomical locations such as the brain, which is less isotropic than the muscle, registration may be more necessary and practical. The brain is simpler to register because of the lack of deformation and multiple landmarks to register by. There are many groups working on performing and automating registration techniques that could be useful if registration were required [45–50]. Regardless of the strengths and weaknesses of each method, within the region likely containing contrast agent (bottom left corner of the leg), all four methods seem to perform well, and no major differences are noted among the methods. There are slight differences in the concentrations calculated in the isotropic $T_{1,0}$ method near the edge of the leg; however, these differences are not likely to affect conclusions drawn from these data since animal-to-animal variability is likely greater than error due to the value of $T_{1,0}$ used. It should be noted that even though the registration and isotropic $T_{1,0}$ methods give similar results for this application, the isotropic $T_{1,0}$ method is far less time consuming and has the practical benefit of not requiring a precontrast image (which requires that the animal be scanned, removed from the scanner, and then implanted with the local drug delivery vehicle). For applications where the precontrast and postcontrast image could be obtained without removing the subject from the MRI, such as when the contrast or delivery vehicle is injected, the precontrast image could easily be used for $T_{1,0}$ without needing to perform a registration. Therefore, the practicality of a method for a specific anatomical region and the expected performance of a method for that anatomical region should be considered when choosing whether to use a registration technique or an isotropic $T_{1,0}$ method.

Figure 9 shows concentration maps and 3D reconstructions for an IMR and IOR of the control and experimental cement composition. Visual examination of the sagittal concentration maps from the dataset shows contrast above and below the IMR. The isotropic $T_{1,0}$ contrast concentration calculation method calculates a significant difference in volume of distribution between control and experimental animals with an IMR ($P < 0.0001$) (Figure 9); however, no significant difference is found between control and experimental IOR ($P \approx 0.5$). When the same implants were compared with total mass of contrast agent observed as the metric, the IMR again showed significance ($P < 0.005$) and the IOR showed no significance ($P \approx 0.8$). This likely indicates that, in the femur, it is more difficult to distinguish between pixels above the threshold containing contrast and not containing contrast. This is likely due to the broader distribution of precontrast

T_1 values ($T_{1,0}$) in the intramedullary canal; thus, the error in calculating concentrations in this region is greater.

4. Conclusions

This paper demonstrates a simple to use method for imaging local drug delivery and calculating its local concentration with good spatial and temporal resolution. This method has broad applications in the field of drug delivery, but here is shown applied to delivery from ALBC for the treatment and prevention of infection in orthopaedic applications. We identify and quantify sources of error in this method and suggest ways to minimize these errors. Specifically, we discuss how to generate images with T_1 values in the range that will yield accurate concentrations and avoid artifacts from excessive concentration of contrast agent, the strengths and weaknesses of several methods of generating $T_{1,0}$ values for use in converting from T_1 to concentration, and methods for using these data to statistically compare contrast agent distributions between wound models.

Acknowledgments

The authors of this paper did not accept any financial support from any 3rd parties likely to profit from the research conducted. Salaries of Morgan B. Giers, Jonathan D. Plasencia, David Frakes, and Michael R. Caplan were also supported by Arizona State University; salaries of Ryan McLemore and Alex C. McLaren were also supported by Banner Good Samaritan Medical Center and the Herbert Louis fund at Orthopaedic Research and Education Foundation. The authors have no financial interests in entities likely to profit from this research. The authors would like to thank G. Turner, PhD, and Q. Liu, PhD, at the Keller Center for Preclinical Imaging at St. Joseph's Hospital in Phoenix, and Chiao May Lee at Arizona State University for their contributions to this work. The authors would also like to thank V. Kodibagkar, PhD, for critical review of the procedure. This work was funded by Arizona Biomedical Research Commission Grant no. 1116. Morgan B. Giers received funding from the Ira A. Fulton Schools of Engineering and Achievement Rewards for College Scientists (we thank the Balster-Evani Family for their funding support). Jonathan D. Plasencia was also supported by the National Science Foundation Graduate Research Fellowship Program.

References

- [1] J. B. Wolinsky, Y. L. Colson, and M. W. Grinstaff, "Local drug delivery strategies for cancer treatment: gels, nanoparticles, polymeric films, rods, and wafers," *Journal of Controlled Release*, vol. 159, no. 1, pp. 14–26, 2012.
- [2] F. Coluzzi and C. Mattia, "OROS hydromorphone in chronic pain management: when drug delivery technology matches clinical needs," *Minerva Anestesiologica*, vol. 76, no. 12, pp. 1072–1084, 2010.
- [3] R. J. Hurlbert, N. Theodore, J. B. Drabier, A. M. Magwood, and V. K. H. Sonntag, "A prospective randomized double-blind controlled trial to evaluate the efficacy of an analgesic epidural

- paste following lumbar decompressive surgery,” *Journal of Neurosurgery*, vol. 90, no. 4, pp. 191–197, 1999.
- [4] K. Ladewig, “Drug delivery in soft tissue engineering,” *Expert Opinion on Drug Delivery*, vol. 8, no. 9, pp. 1175–1188, 2011.
 - [5] M. J. Dunbar, “Antibiotic bone cements: their use in routine primary total joint arthroplasty is justified,” *Orthopedics*, vol. 32, no. 9, p. 660, 2009.
 - [6] H. W. Buchholz, R. A. Elson, E. Engelbrecht, H. Lodenkämper, J. Röttger, and A. Siegel, “Management of deep infection of total hip replacement,” *Journal of Bone and Joint Surgery. British*, vol. 63, no. 3, pp. 342–353, 1981.
 - [7] R. O. Darouiche, “Treatment of infections associated with surgical implants,” *The New England Journal of Medicine*, vol. 350, no. 14, pp. 1422–1429, 2004.
 - [8] S. Kurtz, K. Ong, E. Lau, F. Mowat, and M. Halpern, “Projections of primary and revision hip and knee arthroplasty in the United States from 2005 to 2030,” *Journal of Bone and Joint Surgery. American*, vol. 89, no. 4, pp. 780–785, 2007.
 - [9] P. S. Stewart and J. W. Costerton, “Antibiotic resistance of bacteria in biofilms,” *The Lancet*, vol. 358, no. 9276, pp. 135–138, 2001.
 - [10] H. Ceri, M. E. Olson, C. Stremick, R. R. Read, D. Morck, and A. Buret, “The Calgary Biofilm Device: new technology for rapid determination of antibiotic susceptibilities of bacterial biofilms,” *Journal of Clinical Microbiology*, vol. 37, no. 6, pp. 1771–1776, 1999.
 - [11] M. Diefenbeck, T. Mückley, and G. O. Hofmann, “Prophylaxis and treatment of implant-related infections by local application of antibiotics,” *Injury*, vol. 37, no. 2, pp. S95–S104, 2006.
 - [12] J. Klekamp, J. M. Dawson, D. W. Haas, D. DeBoer, and M. Christie, “The use of vancomycin and tobramycin in acrylic bone cement: biomechanical effects and elution kinetics for use in joint arthroplasty,” *Journal of Arthroplasty*, vol. 14, no. 3, pp. 339–346, 1999.
 - [13] A. C. McLaren, M. Nugent, K. Economopoulos, H. Kaul, B. L. Vernon, and R. McLemore, “Hand-mixed and premixed antibiotic-loaded bone cement have similar homogeneity,” *Clinical Orthopaedics and Related Research*, vol. 467, no. 7, pp. 1693–1698, 2009.
 - [14] M. W. Nijhof, W. J. A. Dhert, P. B. J. Tilman, A. J. Verbout, and A. Fleer, “Release of tobramycin from tobramycin-containing bone cement in bone and serum of rabbits,” *Journal of Materials Science: Materials in Medicine*, vol. 8, no. 12, pp. 799–802, 1997.
 - [15] G. J. Sterling, S. Crawford, J. H. Potter, G. Koerbin, and R. Crawford, “The pharmacokinetics of Simplex-tobramycin bone cement,” *Journal of Bone and Joint Surgery. British*, vol. 85, no. 5, pp. 646–649, 2003.
 - [16] K. Adams, L. Couch, G. Cierny, J. Calhoun, and J. T. Mader, “In vitro and in vivo evaluation of antibiotic diffusion from antibiotic-impregnated polymethylmethacrylate beads,” *Clinical Orthopaedics and Related Research*, no. 278, pp. 244–252, 1992.
 - [17] G. Cierny III and D. DiPasquale, “Periprosthetic total joint infections: staging, treatment, and outcomes,” *Clinical Orthopaedics and Related Research*, no. 403, pp. 23–28, 2002.
 - [18] R. Raghavan, M. L. Brady, M. I. Rodríguez-Ponce, A. Hartlep, C. Pedain, and J. H. Sampson, “Convection-enhanced delivery of therapeutics for brain disease, and its optimization,” *Neurosurgical Focus*, vol. 20, no. 4, pp. 1–13, 2006.
 - [19] J. H. Sampson, R. Raghavan, M. L. Brady et al., “Clinical utility of a patient-specific algorithm for simulating intracerebral drug infusions,” *Neuro-Oncology*, vol. 9, no. 3, pp. 343–353, 2007.
 - [20] M. T. Krauze, J. Forsayeth, J. W. Park, and K. S. Bankiewicz, “Successful and safe perfusion of the primate brainstem: in vivo magnetic resonance imaging of macromolecular distribution during infusion,” *Pharmaceutical Research*, vol. 23, no. 11, pp. 2493–2504, 2006.
 - [21] R. E. Port, C. Schuster, C. R. Port, and P. Bachert, “Simultaneous sustained release of fludarabine monophosphate and Gd-DTPA from an interstitial liposome depot in rats: potential for indirect monitoring of drug release by magnetic resonance imaging,” *Cancer Chemotherapy and Pharmacology*, vol. 58, no. 5, pp. 607–617, 2006.
 - [22] T. Fritz-Hansen, E. Rostrup, H. B. W. Larsson, L. Søndergaard, P. Ring, and O. Henriksen, “Measurement of the arterial concentration of Gd-DTPA using MRI: a step toward quantitative perfusion imaging,” *Magnetic Resonance in Medicine*, vol. 36, no. 2, pp. 225–231, 1996.
 - [23] K. M. Donahue, D. Burstein, W. J. Manning, and M. L. Gray, “Studies of Gd-DTPA relaxivity and proton exchange rates in tissue,” *Magnetic Resonance in Medicine*, vol. 32, no. 1, pp. 66–76, 1994.
 - [24] J. L. Fleckenstein, R. C. Canby, R. W. Parkey, and R. M. Peshock, “Acute effects of exercise on MR imaging of skeletal muscle in normal volunteers,” *American Journal of Roentgenology*, vol. 151, no. 2, pp. 231–237, 1988.
 - [25] S. Noordin, C. S. Winalski, S. Shortkroff, and R. V. Mulkern, “Factors affecting paramagnetic contrast enhancement in synovial fluid: effects of electrolytes, protein concentrations, and temperature on water proton relaxivities from Mn ions and Gd chelated contrast agents,” *Osteoarthritis and Cartilage*, vol. 18, no. 7, pp. 964–970, 2010.
 - [26] A. M. Prantner, V. Sharma, J. R. Garbow, and D. Piwnica-Worms, “Synthesis and characterization of a Gd-DOTA-D-permeation peptide for magnetic resonance relaxation enhancement of intracellular targets,” *Molecular Imaging*, vol. 2, no. 4, pp. 333–341, 2003.
 - [27] M. Rohrer, H. Bauer, J. Mintorovitch, M. Requardt, and H. J. Weinmann, “Comparison of magnetic properties of MRI contrast media solutions at different magnetic field strengths,” *Investigative Radiology*, vol. 40, no. 11, pp. 715–724, 2005.
 - [28] G. J. Stanisz and R. M. Henkelman, “Gd-DTPA relaxivity depends on macromolecular content,” *Magnetic Resonance in Medicine*, vol. 44, pp. 665–667, 2000.
 - [29] G. Strich, P. L. Hagan, K. H. Gerber, and R. A. Stutsky, “Tissue distribution and magnetic resonance spin lattice relaxation effects of gadolinium-DTPA,” *Radiology*, vol. 154, no. 3, pp. 723–726, 1985.
 - [30] K. N. Magdoom, G. L. Pishko, J. H. Kim, and M. Sarntinoranont, “Evaluation of a voxelized model based on DCE-MRI for tracer transport in tumor,” *Journal of Biomechanical Engineering*, vol. 134, no. 9, Article ID 091004, 9 pages, 2012.
 - [31] X. Chen, G. W. Astary, H. Sepulveda, T. H. Mareci, and M. Sarntinoranont, “Quantitative assessment of macromolecular concentration during direct infusion into an agarose hydrogel phantom using contrast-enhanced MRI,” *Magnetic Resonance Imaging*, vol. 26, no. 10, pp. 1433–1441, 2008.
 - [32] H. Kim, M. R. Robinson, M. J. Lizak et al., “Controlled drug release from an ocular implant: an evaluation using dynamic three-dimensional magnetic resonance imaging,” *Investigative Ophthalmology and Visual Science*, vol. 45, no. 8, pp. 2722–2731, 2004.
 - [33] F. Xu, H. Han, H. Zhang, J. Pi, and Y. Fu, “Quantification of Gd-DTPA concentration in neuroimaging using T1 3D MP-RAGE

- sequence at 3.0 T," *Magnetic Resonance Imaging*, vol. 29, no. 6, pp. 827–834, 2011.
- [34] K. Hittmair, G. Gomiscek, K. Langenberger, M. Recht, H. Imhof, and J. Kramer, "Method for the quantitative assessment of contrast agent uptake in dynamic contrast-enhanced MRI," *Magnetic Resonance in Medicine*, vol. 31, no. 5, pp. 567–571, 1994.
- [35] L. Bokacheva, H. Rusinek, Q. Chen et al., "Quantitative determination of Gd-DTPA concentration in T 1-weighted MR renography studies," *Magnetic Resonance in Medicine*, vol. 57, no. 6, pp. 1012–1018, 2007.
- [36] J. Mørkenborg, M. Pedersen, F. T. Jensen, H. Stødkilde-Jørgensen, J. C. Djourhuus, and J. Frøkiær, "Quantitative assessment of Gd-DTPA contrast agent from signal enhancement: an in-vitro study," *Magnetic Resonance Imaging*, vol. 21, no. 6, pp. 637–643, 2003.
- [37] B. D. Foy and J. Blake, "Diffusion of paramagnetically labeled proteins in cartilage: enhancement of the 1-D NMR imaging technique," *Journal of Magnetic Resonance*, vol. 148, no. 1, pp. 126–134, 2001.
- [38] K. Bleicher, M. Lin, M. J. Shapiro, and J. R. Wareing, "Diffusion edited NMR: screening compound mixtures by affinity NMR to detect binding ligands to vancomycin," *Journal of Organic Chemistry*, vol. 63, no. 23, pp. 8486–8490, 1998.
- [39] C. A. Gordon, N. A. Hodges, and C. Marriott, "Use of slime dispersants to promote antibiotic penetration through the extracellular polysaccharide of mucoid *Pseudomonas aeruginosa*," *Antimicrobial Agents and Chemotherapy*, vol. 35, no. 6, pp. 1258–1260, 1991.
- [40] M. B. Giers, C. S. Estes, A. C. McLaren, M. R. Caplan, and R. McLemore, "Jeannette Wilkins Award: can locally delivered gadolinium be visualized on MRI? A pilot study," *Clinical Orthopaedics and Related Research*, vol. 470, no. 10, pp. 2654–2662, 2012.
- [41] M. B. Giers, A. C. McLaren, K. J. Schmidt, M. R. Caplan, and R. McLemore, "Magnetic resonance imaging drug distribution following local delivery in surgical wounds," submitted.
- [42] E. M. Haacke, R. W. Brown, M. R. Thompson, and R. Venkatesan, *Magnetic Resonance Imaging: Physical Principles and Sequence Design*, Wiley-Liss, 1st edition, 1999.
- [43] P. Karasev, I. Kolesov, K. Chudy, A. Tannenbaum, G. Muller, and J. Xerogeanes, "Interactive MRI segmentation with controlled active vision," in *Proceedings of the 50th IEEE Conference on Decision and Control and European Control Conference*, 2011.
- [44] D. W. Eggert, A. Lorusso, and R. B. Fisher, "Estimating 3-D rigid body transformations: a comparison of four major algorithms," *Machine Vision and Applications*, vol. 9, no. 5-6, pp. 272–290, 1997.
- [45] X. Zhuang, S. Arridge, D. J. Hawkes, and S. Ourselin, "A non-rigid registration framework using spatially encoded mutual information and free form deformations," *IEEE Transactions on Medical Imaging*, vol. 30, no. 10, pp. 1819–1828, 2011.
- [46] T. Boehler, F. Zoehrer, M. Harz, and H. K. Hahn, "Breast image registration and deformation modeling," *Critical Reviews in Biomedical Engineering*, vol. 40, no. 3, pp. 235–258, 2012.
- [47] D. Loeckx, P. Slagmolen, F. Maes, D. Vandermeulen, and P. Suetens, "Nonrigid image registration using conditional mutual information," *IEEE Transactions on Medical Imaging*, vol. 29, no. 1, pp. 19–29, 2010.
- [48] D. Rueckert, L. I. Sonoda, C. Hayes, D. L. Hill, M. O. Leach, and D. J. Hawkes, "Nonrigid registration using free-form deformations: application to breast MR images," *IEEE Transactions on Medical Imaging*, vol. 18, no. 8, pp. 712–721, 1999.
- [49] L. Zhe, D. Deng, and W. Guang-Zhi, "Accuracy validation for medical image registration algorithms: a review," *Chinese Medical Sciences Journal*, vol. 27, no. 3, pp. 176–181, 2012.
- [50] D. H. Frakes, L. P. Dasi, K. Pekkan et al., "A new method for registration-based medical image interpolation," *IEEE Transactions on Medical Imaging*, vol. 27, no. 3, pp. 370–377, 2008.

Research Article

Rotation Covariant Image Processing for Biomedical Applications

Henrik Skibbe^{1,2} and Marco Reisert²

¹ Graduate School of Informatics, Kyoto University, Gokasho, 611-0011 Uji, Kyoto, Japan

² Department of Diagnostic Radiology, Medical Physics, University Medical Center, Breisacher Street 60a, 79106 Freiburg, Germany

Correspondence should be addressed to Henrik Skibbe; henrik.skibbe@gmail.com

Received 21 December 2012; Accepted 21 March 2013

Academic Editor: Peng Feng

Copyright © 2013 H. Skibbe and M. Reisert. This is an open access article distributed under the Creative Commons Attribution License, which permits unrestricted use, distribution, and reproduction in any medium, provided the original work is properly cited.

With the advent of novel biomedical 3D image acquisition techniques, the efficient and reliable analysis of volumetric images has become more and more important. The amount of data is enormous and demands an automated processing. The applications are manifold, ranging from image enhancement, image reconstruction, and image description to object/feature detection and high-level contextual feature extraction. In most scenarios, it is expected that geometric transformations alter the output in a mathematically well-defined manner. In this paper we emphasize on 3D translations and rotations. Many algorithms rely on intensity or low-order tensorial-like descriptions to fulfill this demand. This paper proposes a general mathematical framework based on mathematical concepts and theories transferred from mathematical physics and harmonic analysis into the domain of image analysis and pattern recognition. Based on two basic operations, spherical tensor differentiation and spherical tensor multiplication, we show how to design a variety of 3D image processing methods in an efficient way. The framework has already been applied to several biomedical applications ranging from feature and object detection tasks to image enhancement and image restoration techniques. In this paper, the proposed methods are applied on a variety of different 3D data modalities stemming from medical and biological sciences.

1. Introduction

The analysis of three-dimensional images has gained more and more importance in recent years. Particular in the medical and biological sciences, new acquisition techniques lead to an enormous amount of 3D data calling for automated analysis. In this paper, we show how the harmonic analysis of the 3D rotation group offers a convenient and computationally efficient framework for rotation covariant image processing and analysis. Most of the state-of-the-art techniques rely on “low”-order features such as intensities, gradients of intensities, or second order tensors like the Hessian matrix or the structure tensor [1]. For example, consider a lesion detection/segmentation problem in a T_1 -weighted magnetic resonance image. A typical procedure for solving such a task would rely on a local image feature extraction step such as the computation of a Laplacian- or a Gaussian-pyramid. Once the feature images are computed, a healthy group of volunteers is used to determine the distribution of such features for subjects in a healthy condition.

From such a distribution, we can estimate the probabilities for the absence or presence of lesions in a voxel-by-voxel manner. Instead of solely using 0-order features, such as the Laplacian-pyramid, higher order tensor fields can be used to derive further scalar valued quantities. Such features can be the smoothed intensity gradient magnitudes (1-order features), or the eigenstructures of a Hessian matrix field or a structure tensor field (2-order features). However, due to their mathematical and computational complexity, features of order three or even higher order are rarely used. This paper proposes a unified framework that can cope with high-order features in a systematic way. The proposed framework is based on the harmonic, irreducible representations of the 3D rotation group. This guarantees the most sparse tensor representation. Consequently, in comparison with ordinary Cartesian tensor analysis, the algorithms and the handling are operationally clearer and more efficient.

Given a Cartesian tensor t_{i_1, \dots, i_n} of rank n , such a tensor can be the result from a simple projection onto moment functions or from a differentiation process (for instance,

a gradient is a tensor of order 1, and a Hessian matrix is a tensor of order 2). A tensor can be considered as a feature describing an object in a rotation covariant way; that is, if the original object is rotated by a rotation matrix \mathbf{R} , the tensor rotates in the following manner:

$$(gt)_{i_1, \dots, i_n} = \sum_{j_1, \dots, j_n} R_{i_1, j_1} \cdots R_{i_n, j_n} t_{j_1, \dots, j_n}, \quad (1)$$

where g denotes an element of the 3D rotation group. A tensor rotation is a common operation in many applications, for instance, steering a local image descriptor (a tensor) with respect to some data dependent reference frame. From a computationally point of view a Cartesian tensor rotation is quite inconvenient. Typically, there are symmetries with respect to index permutations (for instance, the Hessian matrix is a symmetric tensor). These symmetries have to be taken into account to provide an efficient computation. Another problem is that the tensor rotation matrix $R_{i_1, j_1} \cdots R_{i_n, j_n}$ is “full”; that is, all elements t_{j_1, \dots, j_n} mix under rotations. Spherical tensor analysis, where tensors appear in their irreducible representations, solves these problems, and, even more, it offers further advantages regarding tensor operations. Suppose that we aim at extracting rotation invariant features. Given a Cartesian tensor t , for Cartesian tensors, the basic operation is *tensor contraction*. The tensor is contracted down to a rank 0 tensor by repeatedly combining two indexes (with the Kronecker delta δ_{ij}), or three indexes (with the ϵ -tensor ϵ_{ijk}). This can be done in several ways, for example, linearly $\sum_{ii} t_{,i,i,i}$, quadratically $\sum_{ij} t_{,i,i,t,i}$, or even cubically $\sum_{ijk} \epsilon_{ijk} t_{,i,t,j,t,k}$. It is possible to combine different tensors as well. A problem that occurs is ambiguities; in the presence of symmetries, some ways might end up in the same result, some may not. In contrast, the spherical tensor analysis offers a systematic way of performing such operations. The Kronecker and ϵ products are replaced by one single *spherical product* which allows for multiplying spherical tensors of arbitrary rank. The even parity products are related to the Kronecker product, the odd parity products to ϵ products.

In this paper, we want to review the basics of spherical tensor analysis and how it can be applied to image processing problems. In Section 2, we introduce the basic concepts such as the notion of a spherical tensors. We define the spherical product and introduce its properties. We also show how spherical tensors are related to ordinary Cartesian tensors. In Section 3, the so-called spherical tensor derivative operators (shortly spherical derivatives) are introduced. The spherical derivative operators are able to connect spherical tensor fields of different rank. We discuss several properties and derive their representation in polar coordinates. We focus on two types of basis systems evolving from the spherical differentiation process: the Gauss-Laguerre functions and the spherical Gabor-functions. Both are known to be very important in pattern analysis. The differential relationships of these functions offer an efficient way to compute projections onto these type of functions. In Section 4, expansions in terms of tensorial harmonics are discussed, which are just the straight-forward generalization of ordinary scalar-valued

spherical harmonic expansions. Finally, in Section 5, several biomedical applications are reviewed and discussed.

2. Spherical Tensor Analysis

Let \mathbf{D}_g^j be the unitary irreducible representation of a $g \in SO(3)$ of order j with $j \in \mathbb{N}$. They are also known as the *Wigner D-matrices* (e.g., see [3]). The representation \mathbf{D}_g^j acts on a vector space V_j which is represented by \mathbb{C}^{2j+1} . We write the elements of V_j in bold face, for example, $\mathbf{u} \in V_j$, and write the $2j + 1$ components in unbolt face $u_m \in \mathbb{C}$ where $m = -j, \dots, j$. For the transposition of a vector/matrix, we write \mathbf{u}^T ; the joint complex conjugation and transposition is denoted by $\mathbf{u}^\top = \overline{\mathbf{u}^T}$. In this terms, the unitarity of \mathbf{D}_g^j is expressed by the formula $(\mathbf{D}_g^j)^\top \mathbf{D}_g^j = \mathbf{I}$.

Note that we treat the space V_j as a real vector space of dimensions $2j + 1$, although the components of \mathbf{u} may be complex. This means that the space V_j is only closed under weighted superpositions with real numbers. As a consequence of this, we always have that the components are interrelated by $\overline{u_m} = (-1)^m u_{-m}$. From a computational point of view, this is an important issue. Although the vectors are elements of \mathbb{C}^{2j+1} , we just have to store just $2j + 1$ real numbers.

We denote the standard basis of \mathbb{C}^{2j+1} by \mathbf{e}_m^j , where the n th component of \mathbf{e}_m^j is δ_{mn} . In contrast, the standard basis of V_j is written as $\mathbf{c}_m^j = ((1 + \mathbf{i})/2)\mathbf{e}_m^j + (-1)^m((1 - \mathbf{i})/2)\mathbf{e}_{-m}^j$. We denote the corresponding “imaginary” space by $\mathbf{i}V_j$; that is, elements of $\mathbf{i}V_j$ can be written as $\mathbf{i}\mathbf{v}$ where $\mathbf{v} \in V_j$. So, elements $\mathbf{w} \in \mathbf{i}V_j$ fulfill $\overline{w_m} = (-1)^{m+1} w_{-m}$. Hence, we can write the space \mathbb{C}^{2j+1} as the direct sum of the two spaces $\mathbb{C}^{2j+1} = V_j \oplus \mathbf{i}V_j$. The standard coordinate vector $\mathbf{r} = (x, y, z)^T \in \mathbb{R}^3$ has a natural relation to elements $\mathbf{u} \in V_1$ by

$$\begin{aligned} \mathbf{u} &= \frac{x-y}{\sqrt{2}} \mathbf{c}_1^1 + z \mathbf{c}_0^1 - \frac{x+y}{\sqrt{2}} \mathbf{c}_{-1}^1 \\ &= \begin{pmatrix} \frac{1}{\sqrt{2}}(x - \mathbf{i}y) \\ z \\ -\frac{1}{\sqrt{2}}(x + \mathbf{i}y) \end{pmatrix} = \mathbf{S}\mathbf{r} \in V_1. \end{aligned} \quad (2)$$

Note that \mathbf{S} is an unitary coordinate transformation. The representation \mathbf{D}_g^1 is directly related to the real-valued rotation matrix $\mathbf{U}_g \in SO(3) \subset \mathbb{R}^{3 \times 3}$ by $\mathbf{D}_g^1 = \mathbf{S}\mathbf{U}_g\mathbf{S}^\top$.

Definition 1. A function $\mathbf{f} : \mathbb{R}^3 \mapsto V_j$ is called a spherical tensor field of rank j if it transforms with respect to rotations as

$$(g\mathbf{f})(\mathbf{r}) := \mathbf{D}_g^j \mathbf{f}(\mathbf{U}_g^\top \mathbf{r}), \quad (3)$$

for all $g \in SO(3)$. The space of all spherical tensor fields of rank j is denoted by \mathcal{F}_j .

2.1. Spherical Tensor Coupling. Now, we define a family of bilinear forms that connect tensors of different ranks.

Definition 2. For every $j \geq 0$, we define a family of bilinear forms of type

$$\circ_j : V_{j_1} \times V_{j_2} \mapsto \mathbb{C}^{2j+1}, \quad (4)$$

where $j_1, j_2 \in \mathbb{N}$ has to be chosen according to the triangle inequality $|j_1 - j_2| \leq j \leq j_1 + j_2$. It is defined by

$$(\mathbf{e}_m^j)^\top (\mathbf{v} \circ_j \mathbf{w}) := \sum_{m=m_1+m_2} \langle jm \mid j_1 m_1, j_2 m_2 \rangle v_{m_1} w_{m_2}, \quad (5)$$

where $\langle jm \mid j_1 m_1, j_2 m_2 \rangle$ are the Clebsch-Gordan coefficients.

The characterizing property of these products is that they respect the rotations of the arguments.

Proposition 3. Let $\mathbf{v} \in V_{j_1}$ and $\mathbf{w} \in V_{j_2}$; then, for any $g \in \text{SO}(3)$,

$$(\mathbf{D}_g^{j_1} \mathbf{v}) \circ_j (\mathbf{D}_g^{j_2} \mathbf{w}) = \mathbf{D}_g^j (\mathbf{v} \circ_j \mathbf{w}) \quad (6)$$

holds.

Proof. The components of the left-hand side look as

$$\begin{aligned} & (\mathbf{e}_m^j)^\top ((\mathbf{D}_g^{j_1} \mathbf{v}) \circ_j (\mathbf{D}_g^{j_2} \mathbf{w})) \\ &= \sum_{\substack{m=m_1+m_2 \\ m'_1 m'_2}} \langle jm \mid j_1 m_1, j_2 m_2 \rangle D_{m_1 m'_1}^{j_1} D_{m_2 m'_2}^{j_2} v_{m'_1} w_{m'_2}. \end{aligned} \quad (7)$$

First one has to insert the identity by using orthogonality relation (B.1) with respect to m'_1 and m'_2 . Then, we can use relation (C.2) and the definition of \circ_j to prove the assertion. \square

Proposition 4. If $j_1 + j_2 + j$ is even, then \circ is symmetric, otherwise antisymmetric. The spaces V_j are closed for the symmetric product, and for the antisymmetric product this is not the case. Consider

$$\begin{aligned} j + j_1 + j_2 \text{ is even} & \implies \mathbf{v} \circ_j \mathbf{w} \in V_j, \\ j + j_1 + j_2 \text{ is odd} & \implies \mathbf{v} \circ_j \mathbf{w} \in \mathbf{i}V_j, \end{aligned} \quad (8)$$

where $\mathbf{v} \in V_{j_1}$ and $\mathbf{w} \in V_{j_2}$.

Proof. The proposition is proved by the symmetry properties of the Clebsch-Gordan coefficients (B.6). To show the closure property, consider

$$\begin{aligned} & (\mathbf{e}_m^j)^\top \overline{\mathbf{v} \circ_j \mathbf{w}} \\ &= \sum_{m=m_1+m_2} \langle jm \mid j_1 m_1, j_2 m_2 \rangle \overline{v_{m_1} w_{m_2}} \\ &= \sum_{m=m_1+m_2} (-1)^m \langle jm \mid j_1 m_1, j_2 m_2 \rangle v_{-m_1} w_{-m_2} \\ &= \sum_{m=m_1+m_2} (-1)^{m+j+j_1+j_2} \\ & \quad \times \langle j(-m) \mid j_1 m_1, j_2 m_2 \rangle v_{m_1} w_{m_2} \\ &= (-1)^{m+j+j_1+j_2} (\mathbf{e}_{-m}^j)^\top \overline{\mathbf{v} \circ_j \mathbf{w}}. \end{aligned} \quad (9)$$

Hence, we have for even $j + j_1 + j_2$ the ‘‘realness’’ condition complying to V_j and for odd $j + j_1 + j_2$ the ‘‘imaginariness’’ condition for $\mathbf{i}V_j$, which prove the statements. \square

We will later see that the symmetric product plays an important role, in particular, because we can normalize it in an special way such that it shows a more gentle behavior with respect to the spherical harmonics.

Definition 5. For every $j \geq 0$ with $|j_1 - j_2| \leq j \leq j_1 + j_2$ and even $j + j_1 + j_2$, we define a family of symmetric bilinear forms by

$$\mathbf{v} \bullet_j \mathbf{w} := \frac{1}{\langle j0 \mid j_1 0, j_2 0 \rangle} \mathbf{v} \circ_j \mathbf{w}. \quad (10)$$

For the special case $j = 0$, the arguments have to be of the same rank due to the triangle inequality. Actually in this case, the symmetric product coincides with the standard inner product

$$\mathbf{v} \bullet_0 \mathbf{w} = \sum_{m=-j}^{m=j} (-1)^m v_m w_{-m} = \mathbf{w}^\top \mathbf{v}, \quad (11)$$

where j is the rank of \mathbf{v} and \mathbf{w} .

The introduced product can also be used to combine tensor fields of different rank by point-wise multiplication.

Proposition 6. Let $\mathbf{v} \in \mathcal{T}_{j_1}$ and $\mathbf{w} \in \mathcal{T}_{j_2}$ and j chosen such that $|j_1 - j_2| \leq j \leq j_1 + j_2$; then,

$$\mathbf{f}(\mathbf{r}) = \mathbf{v}(\mathbf{r}) \circ_j \mathbf{w}(\mathbf{r}) \quad (12)$$

is in \mathcal{T}_j , that is, a tensor field of rank j .

In fact, there is another way to combine two tensor fields: by convolution. The advantage of the convolution is that the evolving product also is covariant with respect to translation; that is, the product is covariant to 3D Euclidean motion.

Proposition 7. Let $\mathbf{v} \in \mathcal{T}_{j_1}$ and $\mathbf{w} \in \mathcal{T}_{j_2}$ and j chosen such that $|j_1 - j_2| \leq j \leq j_1 + j_2$; then,

$$(\mathbf{v} \tilde{\circ}_j \mathbf{w})(\mathbf{r}) := \int_{\mathbb{R}^3} \mathbf{v}(\mathbf{r}' - \mathbf{r}) \circ_j \mathbf{w}(\mathbf{r}') d\mathbf{r}' \quad (13)$$

is in \mathcal{T}_j , that is, a tensor field of rank j .

Given a translation τ , the following two relations hold:

$$\begin{aligned} (\tau \mathbf{v}) \circ_j (\tau \mathbf{w}) &= \tau (\mathbf{v} \circ_j \mathbf{w}), \\ \mathbf{v} \tilde{\circ}_j (\tau \mathbf{w}) &= (\tau \mathbf{v}) \tilde{\circ}_j \mathbf{w} = \tau (\mathbf{v} \tilde{\circ}_j \mathbf{w}). \end{aligned} \quad (14)$$

Further important properties of the products are their associativity rules.

Proposition 8. The product \circ is associative as

$$\mathbf{v}^{j_1} \circ_\ell (\mathbf{w}^{j_2} \circ_{j_2+j_3} \mathbf{y}^{j_3}) = (\mathbf{v}^{j_1} \circ_{j_1+j_2} \mathbf{w}^{j_2}) \circ_\ell \mathbf{y}^{j_3} \quad (15)$$

holds if $j_1 + j_2 + j_3 = \ell$. And

$$\mathbf{v}^{j_1} \circ_{\ell} \left(\mathbf{w}^{j_2} \circ_{j_2-j_3} \mathbf{y}^{j_3} \right) = \left(\mathbf{v}^{j_1} \circ_{j_2-j_1} \mathbf{w}^{j_2} \right) \circ_{\ell} \mathbf{y}^{j_3} \quad (16)$$

holds if $\ell = j_2 - (j_1 + j_3) \geq 0$. And

$$\mathbf{v}^{j_2} \circ_{\ell} \left(\mathbf{w}^{j_1} \circ_{j_1+j_3} \mathbf{y}^{j_3} \right) = \left(\mathbf{v}^{j_1} \circ_{j_2-j_1} \mathbf{w}^{j_2} \right) \circ_{\ell} \mathbf{y}^{j_3} \quad (17)$$

with $\ell = j_2 - (j_1 + j_3) \geq 0$.

2.2. Spherical and Solid Harmonics. Due to their special properties, the spherical harmonics (see, Appendix A for definition) play the central role in spherical tensor analysis. One of the most important ones is that each \mathbf{Y}^j , interpreted as a tensor field of rank j , is a fix-point with respect to rotations; that is,

$$(g\mathbf{Y}^j)(\mathbf{r}) = \mathbf{D}_g^j \mathbf{Y}^j(\mathbf{U}_g^T \mathbf{r}) = \mathbf{Y}^j(\mathbf{r}). \quad (18)$$

Consequently,

$$\mathbf{Y}^j(\mathbf{U}_g \mathbf{r}) = \mathbf{D}_g^j \mathbf{Y}^j(\mathbf{r}). \quad (19)$$

The \mathbf{Y}^j form an orthogonal and complete basis of the functions defined on the 2-sphere. Hence, any real square-integrable scalar field $f \in \mathcal{S}_0$ can be written as

$$f(\mathbf{r}) = \sum_{j=0}^{\infty} \mathbf{a}^j(\mathbf{r})^T \mathbf{Y}^j(\mathbf{r}) = \sum_{j=0}^{\infty} \sum_{m=-j}^{m=j} a_m^j(\mathbf{r}) Y_m^j(\mathbf{r}). \quad (20)$$

A band-limited spherical harmonic representation of two images is illustrated in Figure 1.

The expansion coefficients of the rotated function $(gf)(\mathbf{r}) = f(\mathbf{U}_g^T \mathbf{r})$ are simply $\mathbf{D}_g^j \mathbf{a}^j(\mathbf{r})$, which can be concluded from the fix-point property. In the following, we always use Racah's normalization (also known as semi-Schmidt normalization); that is,

$$\begin{aligned} \langle Y_m^j, Y_{m'}^{j'} \rangle &= \int_{S^2} Y_m^j(\mathbf{s}) \overline{Y_{m'}^{j'}(\mathbf{s})} ds \\ &= \frac{4\pi}{2j+1} \delta_{jj'} \delta_{mm'}, \end{aligned} \quad (21)$$

where the integral ranges over a sphere using the standard measure. With this, the coupling of two spherical harmonics gives, again, a spherical harmonic

$$\mathbf{Y}^{j_1}(\mathbf{r}) \bullet \mathbf{Y}^{j_2}(\mathbf{r}) = \mathbf{Y}^j(\mathbf{r}). \quad (22)$$

From a computational perspective, this property can be used to efficiently compute higher order harmonics for lower ones.

Besides the spherical harmonics, the so-called solid harmonics, often appear in the context of harmonic analysis of the 3D rotation group. They are the homogeneous solutions of the Laplace-equation and are just related by $\mathbf{R}^j := r^j \mathbf{Y}^j$, and they are homogeneous polynomials of degree j ; that is, $\mathbf{R}^j(\lambda \mathbf{r}) = \lambda^j \mathbf{R}^j(\mathbf{r})$.

2.3. Relation to Cartesian Tensors. The correspondence of spherical and Cartesian tensors of rank 0 is trivial. For rank 1, it is just the matrix \mathbf{S} that connects the real-valued vector $\mathbf{r} \in \mathbb{R}^3$ with the spherical coordinate vector $\mathbf{u} = \mathbf{S}\mathbf{r} \in V_1$. For rank 2, the consideration gets more intricate. Consider a real-valued Cartesian rank-2 tensor $\mathbf{T} \in \mathbb{R}^{3 \times 3}$ and the following unique decomposition:

$$\mathbf{T} = \begin{pmatrix} t_{00} & t_{01} & t_{02} \\ t_{10} & t_{11} & t_{12} \\ t_{20} & t_{21} & t_{22} \end{pmatrix} = \alpha \mathbf{I} + \mathbf{T}_{\text{anti}} + \mathbf{T}_{\text{sym}}, \quad (23)$$

where $\alpha \in \mathbb{R}$, \mathbf{T}_{anti} is an antisymmetric matrix, and \mathbf{T}_{sym} a traceless symmetric matrix. In fact, this decomposition follows the same manner as the spherical tensor decomposition. A rank 0 spherical tensor corresponds to the identity matrix in Cartesian notation, while the rank 1 spherical tensor to a antisymmetric 3×3 matrix or, equivalently, to a vector. And finally, the rank 2 spherical tensor corresponds to a traceless, symmetric matrix. So, let us consider the spherical decomposition. For convenience, let $\mathbf{T}^s = \mathbf{S}\mathbf{T}\mathbf{S}^T$; then, the components of the corresponding spherical tensors \mathbf{b}^j with $j = 0, 1, 2$ are

$$b_m^j = \sum_{m_1+m_2=m} \langle 1m_1, 1m_2 | jm \rangle (-1)^{m_2} T_{m_1(-m_2)}^s, \quad (24)$$

where \mathbf{b}^0 corresponds to α , \mathbf{b}^1 to \mathbf{T}_{anti} and \mathbf{b}^2 to \mathbf{T}_{sym} . Explicitly, the relation to \mathbf{T} is

$$\begin{aligned} \mathbf{b}^0 &= \frac{-(t_{00} + t_{11} + t_{22})}{\sqrt{3}}, \\ \mathbf{b}^1 &= \begin{pmatrix} \frac{1}{2}(t_{20} - t_{02} + \mathbf{i}(t_{21} - t_{12})) \\ \frac{\mathbf{i}}{\sqrt{2}}(t_{10} - t_{01}) \\ \frac{1}{2}(t_{20} - t_{02} - \mathbf{i}(t_{21} - t_{12})) \end{pmatrix}, \\ \mathbf{b}^2 &= \begin{pmatrix} \frac{1}{2}(t_{00} - t_{11} + \mathbf{i}(t_{01} + t_{10})) \\ \frac{1}{2}((t_{02} + t_{20}) + \mathbf{i}(t_{12} + t_{21})) \\ \frac{-1}{\sqrt{6}}(t_{00} + t_{11} - 2t_{22}) \\ \frac{1}{2}(-(t_{02} + t_{20}) + \mathbf{i}(t_{12} + t_{21})) \\ \frac{1}{2}(t_{00} - t_{11} - \mathbf{i}(t_{01} + t_{10})) \end{pmatrix}. \end{aligned} \quad (25)$$

The inverse of this ‘‘Cartesian to spherical’’-transformation is

$$T_{m_1 m_2}^s = \sum_{j=0,2} \sum_{m=-j}^{m=j} \langle 1m_1, 1(-m_2) | jm \rangle (-1)^{m_2} b_m^j. \quad (26)$$

Note that for arbitrary ranked Cartesian tensor, the relations are not that trivial.

3. Spherical Derivatives

This section proposes the concepts of differentiation in the context of spherical tensor analysis. First, we will introduce

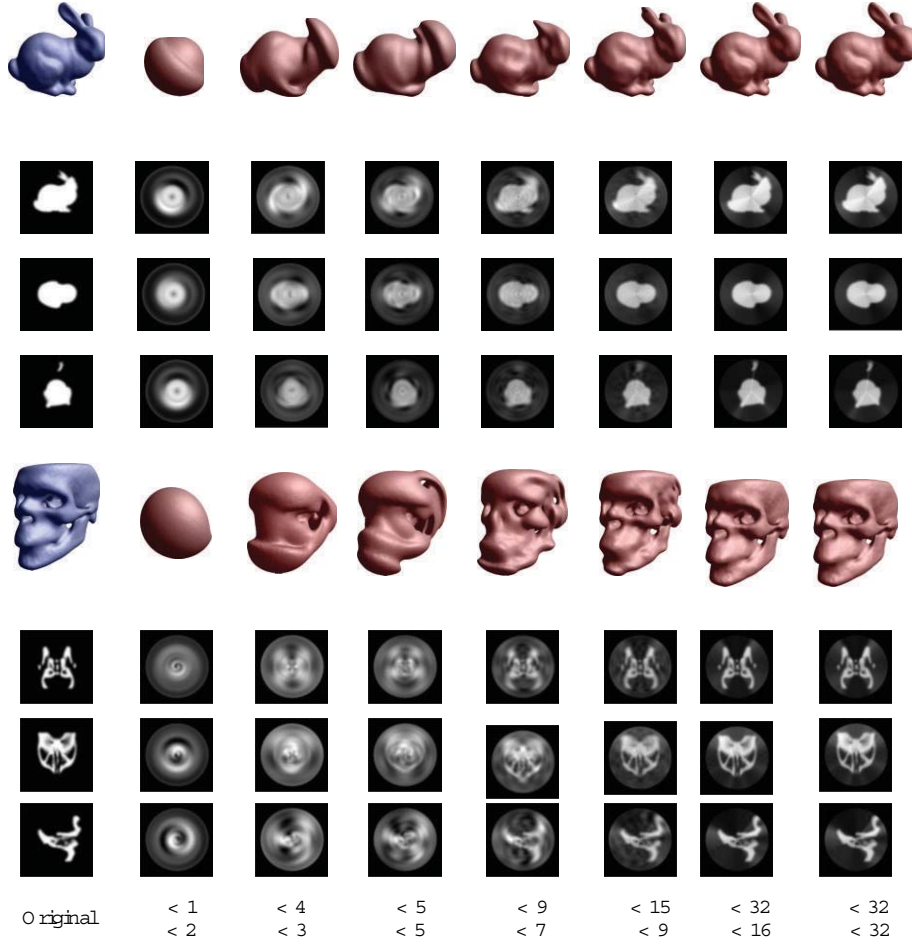


FIGURE 1: A spherical harmonic decomposition of images can be seen as some kind of frequency decomposition. A band limited expansion of a volumetric images is illustrated. We see that lower frequency components (right-hand side) are roughly representing the important characteristics of the objects. However, higher frequency components are necessary to represent the details. For the expansion here, we use a Fourier-like basis for representing the images in radial direction. Here, ℓ represents the order of the spherical harmonics and k the number of radial frequency components taken into account. The image shows an isosurface rendering together with the centered X , Y , and Z -slice. The interested reader is referred to [2].

the spherical derivative operator which connects spherical tensor fields of different ranks by differentiation. The basic idea is simple; formally replace the coordinates $\mathbf{r} = (x, y, z)$ appearing within the solid harmonics \mathbf{R}^j by the gradient operator $(\partial_x, \partial_y, \partial_z)$.

Proposition 9 (spherical derivatives). *Let $\mathbf{f} \in \mathcal{T}_\ell$ be a tensor field. The spherical up-derivative $\nabla^1 : \mathcal{T}_\ell \rightarrow \mathcal{T}_{\ell+1}$ and the down-derivative $\nabla_1 : \mathcal{T}_\ell \rightarrow \mathcal{T}_{\ell-1}$ are defined as*

$$\begin{aligned} \nabla^1 \mathbf{f} &:= \mathbf{R}^1(\nabla) \bullet_{\ell+1} \mathbf{f}, \\ \nabla_1 \mathbf{f} &:= \mathbf{R}^1(\nabla) \bullet_{\ell-1} \mathbf{f}, \end{aligned} \quad (27)$$

where ∇ is the gradient operator $(\partial_x, \partial_y, \partial_z)$.

In fact there are much more rotation covariant differential operators than the two defined previously. Given a tensor field \mathbf{f} , any field of the form $\mathbf{g} = \mathbf{R}^j(\nabla) \bullet_\ell \mathbf{f}$, which we obtain via differentiation, is a spherical tensor field, too.

But the up- and down-derivatives are from a computational point very attractive, because, as shown earlier, they allow an iterative computation of higher order differentials, which is computationally much more efficient than the direct way. For further discussion on the spherical tensor derivative operator, consider the spherical derivatives in the Fourier domain, where they act by point-wise \bullet -multiplications with a solid harmonic $\mathbf{i}\mathbf{k}\mathbf{Y}^1(\mathbf{k}) = \mathbf{i}\mathbf{R}^1(\mathbf{k}) = \mathbf{i}\mathbf{S}\mathbf{k}$ where $k = |\mathbf{k}|$ is the frequency magnitude.

Proposition 10 (Fourier representation). *Let $\tilde{\mathbf{f}}(\mathbf{k})$ be the Fourier transformation of some $\mathbf{f} \in \mathcal{T}_\ell$ and $\tilde{\nabla}$ representations of the spherical derivative in the Fourier domain that are implicitly defined by $(\tilde{\nabla}\tilde{\mathbf{f}}) = \tilde{\nabla}\tilde{\mathbf{f}}$; then,*

$$\tilde{\nabla}^1 \tilde{\mathbf{f}}(\mathbf{k}) = \mathbf{i}\mathbf{R}^1(\mathbf{k}) \bullet_{\ell+1} \tilde{\mathbf{f}}(\mathbf{k}), \quad (28)$$

$$\tilde{\nabla}_1 \tilde{\mathbf{f}}(\mathbf{k}) = \mathbf{i}\mathbf{R}^1(\mathbf{k}) \bullet_{\ell-1} \tilde{\mathbf{f}}(\mathbf{k}). \quad (29)$$

Proof. See [4]. \square

Both statements are direct consequences of the Fourier correspondences for the ordinary partial derivatives. For scalar fields, we can generalize this statement also for higher orders.

Proposition 11 (multiple spherical derivatives). *For $n \geq i$, he defines $\nabla_i^n : \mathcal{T}_0 \rightarrow \mathcal{T}_{n-i}$ by*

$$\nabla_i^n := \nabla_i \nabla_i^{n-1} := \underbrace{\nabla_1 \cdots \nabla_1}_{i\text{-times}} \underbrace{\nabla^1 \cdots \nabla^1}_{n\text{-times}}. \quad (30)$$

In the Fourier domain, these multiple derivatives act by

$$\left(\widetilde{\nabla_i^n f}\right)(\mathbf{k}) = (\mathbf{i})^{n+i} \mathbf{R}_i^n(\mathbf{k}) \widetilde{f}(\mathbf{k}). \quad (31)$$

Using this one can show that $\nabla_i^n = \nabla^{n-i} \Delta^i$, where Δ is the Laplace operator.

Proof. See [5]. \square

We want to emphasize that both statements only hold for scalar-valued fields, and generalizations to tensor-valued do not hold in general due to the nontrivial associativity rules.

Proposition 12 (product rule). *Let $\mathbf{f} \in \mathcal{T}_\ell$ and $h \in \mathcal{T}_0$; then, one has the product rules*

$$\begin{aligned} \nabla^1(h\mathbf{f}) &= \nabla^1 h \bullet_{\ell+1} \mathbf{f} + h \nabla^1 \mathbf{f}, \\ \nabla_1(h\mathbf{f}) &= \nabla^1 h \bullet_{\ell-1} \mathbf{f} + h \nabla_1 \mathbf{f}. \end{aligned} \quad (32)$$

It is well known that convolutions commute with differentiation, and actually there are generalized commutation rules for spherical tensor fields.

Proposition 13 (commuting property for convolutions). *Let $\mathbf{f} \in \mathcal{T}_k$ and $\mathbf{g} \in \mathcal{T}_j$ be arbitrary spherical tensor fields; then,*

$$\left(\nabla^\ell \mathbf{f}\right) \bullet_j \widetilde{\mathbf{g}} = \mathbf{f} \bullet_j \widetilde{\left(\nabla^\ell \mathbf{g}\right)}, \quad (33)$$

$$\left(\nabla^\ell \mathbf{f}\right) \bullet_L \widetilde{\mathbf{g}} = \mathbf{f} \bullet_L \widetilde{\left(\nabla^\ell \mathbf{g}\right)}, \quad (34)$$

where $J = j - (\ell + k)$ and $L = j + \ell + k$.

Proof. Both assertions are founded by the associativity of the spherical product. Consider the first statement in the Fourier domain by using (28) and then apply the associativity given in (17) as follows:

$$\begin{aligned} \left(\widetilde{\nabla^\ell \mathbf{f}}\right) \bullet_j \widetilde{\mathbf{g}} &= \left(\mathbf{R}^1 \bullet_{k+\ell} \left(\widetilde{\nabla^{\ell-1} \mathbf{f}}\right)\right) \bullet_j \widetilde{\mathbf{g}} \\ &= \left(\widetilde{\nabla^{\ell-1} \mathbf{f}}\right) \bullet_j \left(\mathbf{R}^1 \bullet_{j-1} \widetilde{\mathbf{g}}\right) \\ &= \left(\widetilde{\nabla^{\ell-1} \mathbf{f}}\right) \bullet_j \left(\widetilde{\nabla_1 \mathbf{g}}\right), \end{aligned} \quad (35)$$

where we abbreviated $\mathbf{R}^1 = \mathbf{R}^1(\mathbf{i}\mathbf{k})$. A repeated application of this proves the first assertion. For the second statement, it is similar but using the associativity as given in (15). \square

This proposition shows again the importance of the up- and down-derivatives. For general derivative operators $\mathbf{R}^j(\nabla) \bullet_\ell \mathbf{f}$, the previous commutations rules do not hold. The previous convolution property is of particular importance for the efficient covariant processing of 3D images. The major motivation is to compute convolutions with the spherical harmonic basis in an efficient way. Suppose that the goal is to compute

$$\mathbf{f} = \left(\mathbf{R}^j e^{-r^2/2}\right) * g, \quad (36)$$

where g is some arbitrary scalar image. In fact, as we will show in the next section, one can show that $\nabla^j e^{-r^2/2} = (-1)^j \mathbf{R}^j e^{-r^2/2}$. Together with the convolution theorem, we get

$$\mathbf{f} = \left(\mathbf{R}^j e^{-r^2/2}\right) * g = (-1)^j \nabla^j \left(e^{-r^2/2} * g\right) \quad (37)$$

which enables us to compute the convolution by an repeated application of the spherical derivatives, which is computationally much cheaper than a direct convolution (even by the use of the Fast Fourier Transform).

3.1. Spherical Derivatives in Polar Representation. To get a better understanding of what happens during the differentiation via spherical derivatives, we consider their properties in polar representations.

Lemma 14. *Given a spherical tensor field $\mathbf{f}^j \in \mathcal{T}_j$ whose angular and radial component are separable such that $\mathbf{f}^j(\mathbf{r}) = \mathbf{Y}^j(\mathbf{r}) f^j(r)$, where $f^j : \mathbb{R} \rightarrow \mathbb{C}$ denotes the function representing the radial component of \mathbf{f}^j , then the spherical up- and down-derivatives of \mathbf{f}^j can be computed by*

$$\left(\nabla^1 \mathbf{f}^j\right)(\mathbf{r}) = \mathbf{Y}^{j+1}(\mathbf{r}) r^j \frac{\partial}{\partial r} \frac{1}{r^j} f^j(r), \quad (38)$$

$$\left(\nabla_1 \mathbf{f}^j\right)(\mathbf{r}) = \mathbf{Y}^{j-1}(\mathbf{r}) \frac{1}{r^{j+1}} \frac{\partial}{\partial r} r^{j+1} f^j(r), \quad (39)$$

respectively.

Proof. See [7]. \square

3.2. Gauss-Laguerre Functions. Previously, we already stated that $\nabla^j e^{-r^2/2} = (-1)^j \mathbf{R}^j e^{-r^2/2}$ holds; in fact, there is a more general statement involving the so-called Laguerre polynomials. This offers the possibility to compute convolutions with the evolving functions in an iterative and efficient way. We denote by L_n^α the α associated Laguerre polynomial of order n (F.1). We further denote by

$$\mathcal{L}_n^j(\mathbf{r}) := \mathbf{R}^{j-n}(\mathbf{r}) L_n^{(j-n)+(1/2)}\left(\frac{r^2}{2}\right) \quad (40)$$

the spherical tensor valued polynomials $\mathcal{L}_n^j \in \mathcal{T}_{j-n}$. These polynomials are widely known as Laguerre Gaussian-type functions in the field of theoretical chemistry (e.g., see [8] or [9]). In the image processing community, these functions are known as generic neighborhood operators [10] and are used, for example, for key-point detection [11].

Theorem 15. *The Gaussian windowed polynomials $\mathcal{L}_n^j(\mathbf{r}) e^{-r^2/2}$ can be computed iteratively in terms of ∇_n^j starting with an isotropic Gaussian; namely,*

$$\mathcal{L}_n^j(\mathbf{r}) e^{-r^2/2} = \frac{(-1)^j}{n!2^n} \nabla_n^j e^{-r^2/2}. \quad (41)$$

Proof. See [7]. \square

3.3. Gabor Functions. Gabor functions, that is, Gaussian-windowed plane waves, play an important role in image processing due to the fact that the different frequency components of signals can be studied locally. This information is, for example, used for tracking [12] or feature extraction [6]. Thus, it is of particular interest to provide efficient methods to apply Gabor filters. One way is to explicitly represent a finite number of Gabor kernels, each representing a certain orientation of the plane-wave [13]. The problem is that the orientation space must be discretized. However, representing Gabor functions in terms of spherical derivatives offers a way to compute Gabor filter responses for the whole range of possible orientations. First, note that applying spherical derivatives on a plane wave gives a quite neat result as

$$\nabla^j e^{i\mathbf{k}^T \mathbf{r}} = (\mathbf{i})^j \mathbf{R}^j(\mathbf{k}) e^{i\mathbf{k}^T \mathbf{r}}. \quad (42)$$

Following the proof from Section 3.1, a similar result holds for the spherical Bessel function, which constitutes the radial part in the harmonic expansion of the plane wave as

$$\begin{aligned} \nabla^j j_0(kr) &= (k)^j \mathbf{Y}^j(\mathbf{r}) j_j(kr) \\ &= (k)^j \mathcal{B}^j(\mathbf{r}, k). \end{aligned} \quad (43)$$

In the following, we show that there exists a very similar way to represent the Gaussian windowed wave in terms of the derivatives of the Gaussian windowed Bessel functions. Let

$$\mathcal{B}_s^0(\mathbf{r}, k) := j_0(kr) e^{-r^2/(2s)} \quad (44)$$

be the Gaussian windowed 0-order Bessel functions. The parameter $s \in \mathbb{R}_{s>0}$ represents the size of the Gaussian window with respect to the wave. With (38) and (D.3), we can derive the higher order Gaussian windowed Bessel functions $\mathcal{B}_s^j := (-1)^j \nabla^j \mathcal{B}_s^0$.

Theorem 16. *The spherical derivatives \mathcal{B}_s^j of the Gaussian windowed 0-ordered Bessel functions \mathcal{B}_s^0 are given by*

$$\mathcal{B}_s^j(\mathbf{r}, k) = \mathbf{Y}^j(\mathbf{r}) \left[\sum_{i=0}^j \binom{j}{i} \left(\frac{r}{s}\right)^{j-i} (k)^i j_i(kr) \right] e^{-r^2/2s}. \quad (45)$$

Consider that $\mathcal{B}_s^j \rightarrow_{s \rightarrow \infty} \mathcal{B}^j$. The Gabor wave can now be represented by a superposition of Bessel functions \mathcal{B}_s^j , each representing a certain angular frequency; namely,

$$\begin{aligned} e^{i\mathbf{k}^T \mathbf{r}} e^{-r^2/2s} &\approx \sum_j (\mathbf{i})^j \alpha_j(k) \mathcal{B}_s^j(\mathbf{r}, k) \bullet_0 \mathbf{Y}^j(\mathbf{k}) \\ &= \sum_j (-\mathbf{i})^j \alpha_j(k) \nabla^j \mathcal{B}_s^0(\mathbf{r}, k) \bullet_0 \mathbf{Y}^j(\mathbf{k}), \end{aligned} \quad (46)$$

where $\alpha_j(k) \in \mathbb{R}$ are real-valued weighting factors.

Proof. See [7]. \square

4. Tensorial Harmonic Expansions

In most image processing applications, the data to be processed is of scalar nature; that is, for each voxel, we observe one single intensity value. But there are actually acquisition techniques, where the measurement itself is already a tensorial quantity. For example, in diffusion weighted magnet resonance imaging (DW-MRI), rank 2 tensors are common. Or, in phase contrast MRI velocity, vectors are measured. Thus, there is a great interest to represent these measurement in an appropriate way. In [14], we proposed to expand a spherical tensor field $\mathbf{f} \in \mathcal{T}_\ell$ of rank ℓ as follows:

$$\mathbf{f}(\mathbf{r}) = \sum_{j=0}^{\infty} \sum_{k=-\ell}^{k=\ell} \mathbf{a}_k^j(r) \circ_\ell \mathbf{Y}^j(\mathbf{r}), \quad (47)$$

where $\mathbf{a}_k^j(r) \in \mathcal{T}_{j+k}$ are expansion coefficients. For $\ell = 0$, the expansion coincides with the ordinary scalar spherical harmonic expansion. We can observe properties very similar to the ordinary SH expansion; that is,

$$\begin{aligned} (g\mathbf{f})(\mathbf{r}) &= \mathbf{D}_g^\ell \mathbf{f}(\mathbf{U}_g^T \mathbf{r}) \\ &= \sum_{j=0}^{\infty} \sum_{k=-\ell}^{k=\ell} \mathbf{D}_g^{j+k} \mathbf{a}_k^j(r) \circ_\ell \mathbf{Y}^j(\mathbf{r}). \end{aligned} \quad (48)$$

A rotation of the tensor field affects the expansion coefficients \mathbf{a}_k^j to be multiplied from the left with \mathbf{D}_g^{j+k} . So, the previous expansion shows the same, very convenient, rotation behavior like an SH expansion, which can be used, for example, to extract invariant local descriptors in a simple way. And in fact, the previous representation is orthogonal and complete. By setting $\mathbf{a}_k^j(r) = \sum_{m=-(j+k)}^{m=j+k} \mathbf{a}_{km}^j(r) \mathbf{e}_m^{j+k}$, we can identify the functional basis \mathbf{Z}_{km}^j as

$$\mathbf{f}(\mathbf{r}) = \sum_{j=0}^{\infty} \sum_{k=-\ell}^{k=\ell} \sum_{m=-(j+k)}^{m=j+k} \mathbf{a}_{km}^j(r) \underbrace{\mathbf{e}_m^{j+k} \circ_\ell \mathbf{Y}^j(\mathbf{r})}_{\mathbf{Z}_{km}^j}. \quad (49)$$

Proposition 17 (tensorial harmonics). *The functions $\mathbf{Z}_{km}^j : S^2 \mapsto V_\ell$ provide a complete and orthogonal basis of the angular part of \mathcal{T}_ℓ , that is;*

$$\int_{S^2} (\mathbf{Z}_{km}^j(\mathbf{s}))^\top \mathbf{Z}_{k'm'}^{j'}(\mathbf{s}) d\mathbf{s} = \frac{4\pi}{N_{j,k}} \delta_{j,j'} \delta_{k,k'} \delta_{m,m'}, \quad (50)$$

where

$$N_{j,k} = \frac{1}{2\ell + 1} (2j + 1) (2(j + k) + 1). \quad (51)$$

The functions \mathbf{Z}_{km}^j are called the tensorial harmonics.

4.1. Symmetric Tensor Fields. In this section, we discuss the properties of expansion coefficients of specific tensor fields, expanded in terms of tensorial harmonics. We show that symmetries in a tensor field are simplifying the tensorial harmonic expansion coefficients. This is similar to the ordinary spherical harmonic expansion. For example, the point symmetry $f(\mathbf{r}) = f(-\mathbf{r})$ of a scalar fields leads to vanishing spherical harmonic coefficients for odd j . In the following, we consider similar symmetries for tensorial harmonics.

The rotation symmetry of a spherical tensor field $\mathbf{f} \in \mathcal{T}_\ell$ around the z -axis is expressed algebraically by the fact that $g_\phi \mathbf{f} = \mathbf{f}$ for all rotation g_ϕ around the z -axis. Such fields can easily be obtained by averaging a general tensor field \mathbf{f} over all these rotations as

$$\mathbf{f}_s = \frac{1}{2\pi} \int_0^{2\pi} g_\phi \mathbf{f} d\phi. \quad (52)$$

It is well known that the representation $\mathbf{D}_{g_\phi}^j$ of such a rotation is diagonal; namely, $D_{g_\phi, mm'}^j = \delta_{mm'} e^{im\phi}$. Hence, the expansion coefficients a_{km}^j of \mathbf{f}_s vanish for all $m \neq 0$. Thus, we can write any rotation symmetric tensor field as

$$\mathbf{f}_s(\mathbf{r}) = \sum_{j=0}^{\infty} \sum_{k=-\ell}^{k=\ell} a_k^j(r) \mathbf{e}_0^{j+k} \circ_\ell \mathbf{Y}^j(\mathbf{r}). \quad (53)$$

We call such a rotation symmetric field torsion-free if $g_{yz} \mathbf{f}_s = \mathbf{f}_s$, where $g_{yz} \in O(3)$ is a reflection with respect to the yz -plane (or xz -plane). The action of such a reflection on spherical tensors is given by $D_{g_{yz}, mm'}^j = (-1)^m \delta_{m(-m')}$. Similar to the rotational symmetry, we can obtain such fields by averaging over the symmetry operation as

$$\mathbf{f}_{\text{stf}} = \frac{1}{2} (\mathbf{f}_s + g_{yz} \mathbf{f}_s). \quad (54)$$

Note that the mirroring operation for a spherical harmonic is just a complex conjugation; that is, $\mathbf{Y}^j(\mathbf{U}_{g_{yz}}^T \mathbf{r}) = \overline{\mathbf{Y}^j(\mathbf{r})}$. The consequence for (53) is that all terms where the $k + \ell$ are odd vanish. The reason for that is mainly Proposition 4 because with its help we can show that

$$\mathbf{D}_{g_{yz}}^\ell \left(\mathbf{e}_0^{j+k} \circ_\ell \mathbf{Y}^j \left(\mathbf{U}_{g_{yz}}^T \mathbf{r} \right) \right) = (-1)^{(k+\ell)} \left(\mathbf{e}_0^{j+k} \circ_\ell \mathbf{Y}^j(\mathbf{r}) \right) \quad (55)$$

holds.

Finally, consider the reflection symmetry with respect to the xy -plane. This symmetry is particularly important for fields of even rank. The symmetry is algebraically expressed by $g_{xy} \mathbf{f}_s = \mathbf{f}_s$ where $g_{xy} \in O(3)$ is a reflection with respect to the xy -plane, whose action on spherical tensors is given by $D_{g_{xy}, mm'}^j = (-1)^j \delta_{mm'}$. Averaging over this symmetry operation has the consequence that expansion terms with odd j are vanishing. For odd rank tensor fields, the reflection symmetry is not imperative. But there is typically an antisymmetry of the form $g_{xy} \mathbf{f}_s = -\mathbf{f}_s$. This antisymmetry lets the expansion terms vanish with even index j .

5. Applications

In the context of rotation covariant image processing, the applications of the proposed framework are manifold. The mathematical representation might appear unfamiliar, but the provided tools can be used quite easily. Basically, there are two types of operations: differentiation by spherical tensor derivatives and multiplication by spherical tensor products. The spherical derivatives can be used in two ways. On the one hand, the up-derivatives can be used to “create” new tensor fields out of existing fields by incorporating neighborhood relations. This can be regarded as a simple and efficient way to compute local meaningful image descriptors in a covariant way. On the other hand, the down-derivatives can be used to gather information from a local point neighborhood and form a lower ranked tensor field via superposition. Due to the tensorial nature, the information is able to interfere in a destructive or constructive way. The spherical products are the basic nonlinear ingredient in the framework. They can be used to combine tensor fields in a nonlinear, covariant manner.

Several principles in the image processing and pattern recognition [15–17] literature are based on the following principle: compute, in a first step, local descriptors at several image locations, make some inference based on this knowledge, and cast this information back by combining evidence from several locations. In fact, our framework is ideally suited to adopt this principle. First, local descriptors are densely computed by differentiation for *all* image locations. Then, the information is combined by using spherical products in a nonlinear and nontrivial way. Finally, we use again the spherical derivative to form neighborhood descriptors. The descriptors are then used for object or feature detection.

In the following, we give examples of the proposed framework in several application domains.

5.1. Implementation. For implementing the discrete spherical derivatives, we propose to utilize central differences of 4th order accuracy for computing the partial derivatives (see Figure 2(b)). We observed that this scheme is a good tradeoff between computational complexity and accuracy. We experienced that the standard Laplace operator (considering a six voxel neighborhood) is numerically very unstable (even if double precision numbers are used!). Therefore, we propose the usage of the scheme depicted in Figure 2(a) which performed significantly better regarding numerical stability in our experiments. This is illustrated in Figure 3. As an example, we show the expansion images obtained via the proposed schemes together with the images obtained via a standard scheme. For comparison, we also show explicitly computed expansion images. The example illustrates that the ordinary Laplace operator leads to strong artifacts after a few number of applications.

5.2. Tensor Voting. The Tensor Voting framework was originally proposed by [15] and has found several application in low-level vision in 2D and 3D. For example, it is used for perceptual grouping and extraction of line, curves, and surfaces. The key idea is to make unreliable measurements

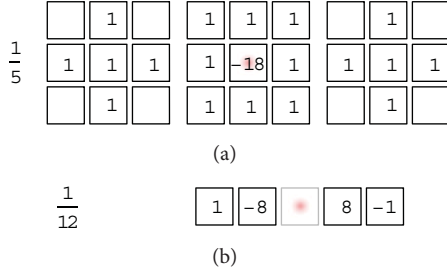


FIGURE 2: The discrete differential operators we use for realizing the discrete spherical derivative operators. On the left-hand side, the corresponding global weights are depicted. The red dot denotes the current image position.

more robust by incorporating neighborhood information in a consistent and coherent manner. Following [4], the key expression that has to be computed is

$$\mathbf{U}(\mathbf{r}) = \int_{\mathbb{R}^3} \mathbf{V}^{\mathbf{n}}(\mathbf{r}') (\mathbf{r} - \mathbf{r}') m(\mathbf{r}') d\mathbf{r}', \quad (56)$$

where $\mathbf{V}^{\mathbf{n}} : \mathbb{R}^3 \rightarrow V_\ell$ is the voting field, $m : \mathbb{R}^3 \rightarrow \mathbb{R}$ a scalar valued feature image giving evidence for the occurrence of the feature, and $\mathbf{n} : \mathbb{R}^3 \rightarrow \mathbb{R}^3$ the orientation of the feature of interest. In the following, we restrict ourselves to axial symmetric voting fields. Therefore, let f_s be a axial symmetric function, where the z -axis is the symmetry axis. Then, the voting field is

$$\mathbf{V}^{\mathbf{n}}(\mathbf{r}) = (g_{\mathbf{n}} \mathbf{f}_s)(\mathbf{r}), \quad (57)$$

where $g_{\mathbf{n}}$ is a rotation such that the z -axis is mapped onto the axis defined by the normalized vector \mathbf{n} . In [4], we have shown that (56) simplifies to

$$\mathbf{U}(\mathbf{r}) = \sum_{j=0}^{\infty} \sum_{k=-\ell}^{k=\ell} (\mathbf{E}^{j+k} \tilde{\omega}_\ell \mathbf{A}_k^j)(\mathbf{r}), \quad (58)$$

where

$$\mathbf{E}^j(\mathbf{r}) := m(\mathbf{r}) \mathbf{Y}^j(\mathbf{n}(\mathbf{r})) \quad (59)$$

are combined tensor-valued evidence images and

$$\mathbf{A}_k^j(\mathbf{r}) := a_k^j(r) \mathbf{Y}^j(\mathbf{r}) \quad (60)$$

is the harmonic expansion of the voting field $\mathbf{V}^{\mathbf{r}^z}$ steered in z -direction. The coefficients $a_k^j(r)$ can be obtained by a projection on the tensorial harmonics

$$a_k^j(r) = N_{j,k} \int_{S_\ell^2} (\mathbf{Z}_{k0}^j(\mathbf{r}))^\top \mathbf{V}^{\mathbf{r}^z}(\mathbf{r}) d\mathbf{r}. \quad (61)$$

Due to the symmetry of $\mathbf{V}^{\mathbf{r}^z}$, only \mathbf{Z}_{k0}^j are involved. Further information concerning a practical point of view can be found in [14].

5.3. Nonlinear Covariant Filters. In the following, we briefly show how to design trainable rotation covariant image filters which can be used for rotation invariant object or landmark detection. The idea is that expansion coefficients of a spherically expanded voting function are learned in a data driven way. The filter is mainly based on two steps. Rotation covariant image descriptors are densely computed in a voxel-by-voxel manner. Then, a weighted superposition of these image descriptors is used to form expansion coefficients of a spherical voting function. The expansion coefficients are formed such that each voting function votes for the presence or absence of landmarks or objects. The weights are found by a least square fit to a given training data set. For a fast implementation, we propose to use voting functions based on an expansion of spherical functions having a differential relationship in terms of spherical derivatives. In [18, 19], we used a spherical superposition of Gaussian windowed solid harmonics for representing the voting function. However, we are not restricted to them. For instance, we also can use the spherical plane-wave expansion leading to a voting function that is not only highly adaptable in angular direction, but also highly adaptable in radial direction, too; see the paper by [20]. The Fourier like voting function can be written as

$$V_c(\mathbf{r}) = \int_0^\infty \sum_{j=0}^{\infty} \mathbf{V}^j(\mathbf{c}, k) \bullet_0 \mathcal{B}^j(\mathbf{r} - \mathbf{c}, k) dk, \quad (62)$$

where $\mathbf{V}^j(k) \in \mathbb{C}^{2j+1}$ are the expansion coefficients of the filter and \mathcal{B}^j are spherical Fourier basis functions known as Bessel functions (see (43)). The filter response is a saliency map representing the evidence for the presence or absence of objects. The saliency map is computed by collecting all contributions (votes) utilizing simple scalar valued convolutions. The explicit expression of the filter is

$$\begin{aligned} \mathcal{H}\{f\}(\mathbf{r}) &:= \int_{\mathbb{R}^3} V_c(\mathbf{r}) d\mathbf{c} \\ &= \left(\sum_{j=0}^{\infty} \int_0^\infty (\mathcal{B}^j(k) \tilde{\omega}_0 \mathbf{V}^j(k)) dk \right) (\mathbf{r}) \\ &\quad \text{(using (33))} \\ &= \left(\int_0^\infty \mathcal{B}^0(k) * \sum_j^{\infty} \nabla_j \mathbf{V}^j(k) dk \right) (\mathbf{r}). \end{aligned} \quad (63)$$

For implementation we use a band-limited expansion (up to order $N \in \mathbb{N}$) and only take a small set of frequencies $(k_0, \dots, k_i, \dots, k_N) \in \mathbb{R}$ into account. We further make use of Gabor waves (see Theorem 16) to gain a filter that adapts and votes locally. In this case, the filter simplifies to

$$\mathcal{H}\{f\} \approx \sum_i \mathcal{B}_s^0(k_i) * \sum_j^N \nabla_j \mathbf{V}^j(k_i). \quad (64)$$

Trainable filters based on the Gabor waves have shown superior performance over the standard harmonic filters [20].

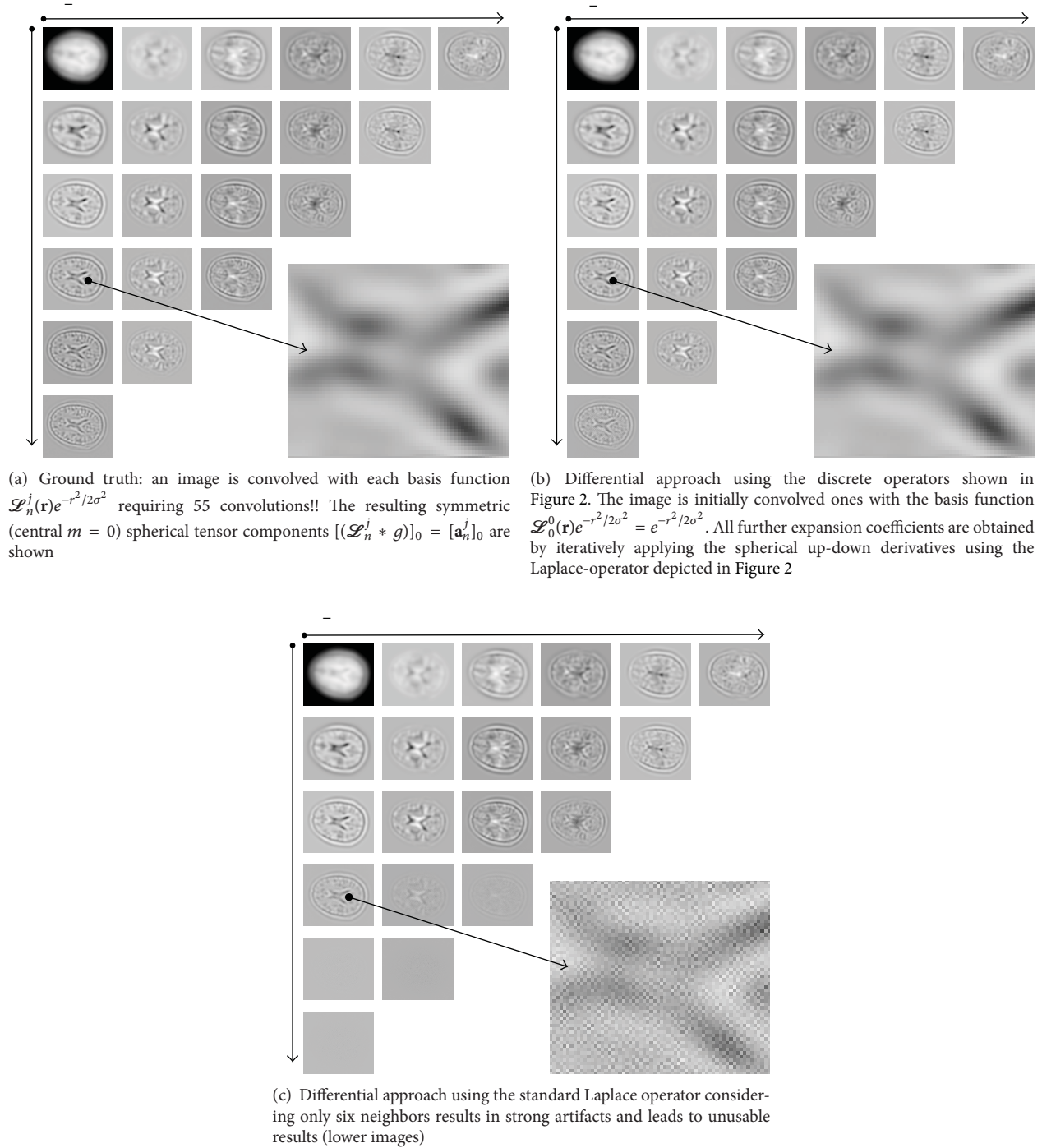
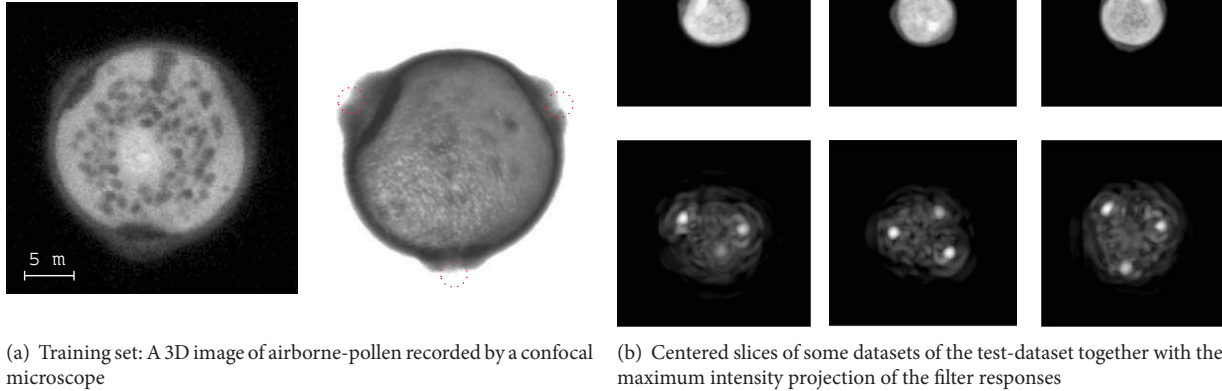


FIGURE 3: The theory in practice: Laguerre expansion of a volumetric image with $j+n \leq 5$ and a Gaussian width of $\sigma = 6$. For the experiments we use an image (size $144 \times 224 \times 256$) showing the T_1 -weighted MRT image of a human skull. In (a) we depict the center slice of the 3D volume showing the real-valued parts ($m = 0$) of the expansion coefficients computed explicitly by convolution of the image with the kernel functions ($[\mathbf{a}_n^j]_m(\mathbf{x}) = (g * [\mathcal{L}_n^j]_m e^{-r^2/2\sigma^2})(\mathbf{x})$). (b) Shows the same expansion coefficients obtained when using the proposed differential approach, with $[\mathbf{a}_n^j]_m(\mathbf{x}) = ((-1)^j/2^n n!) \bar{\nabla}^{j-n} \Delta^n (g * e^{-r^2/2\sigma^2})(\mathbf{x})$. (c) Shows that the choice of the discrete operator has a big influence of the result.

Figure 4 shows some qualitative results of an experiment where we detect the pores of airborne-pollen. The database contains 3D recordings of airborne-pollen acquired via a confocal laser scanning microscope. In Figure 4(a), we see the

training image. The three pores are marked by red circles. In Figure 4(b), we exemplary show three datasets belonging to the test set together with the maximum intensity projection of the filter response.



(a) Training set: A 3D image of airborne-pollen recorded by a confocal microscope

(b) Centered slices of some datasets of the test-dataset together with the maximum intensity projection of the filter responses

FIGURE 4: Filter response.

5.4. Voxel-Wise Classification. Especially in the field of biomedical imaging, the third dimension becomes more and more important due to the fact that organism can be studied in their natural constellation. Objects and organism can be located in any number at any position and, much more challenging, in any orientation. The third dimension does not only lead to larger datasets, but also the interrelation of neighboring intensity values becomes more complex. With a fast voxel-wise transformation of volumetric images into the harmonic domain, we are capable to compute rotation invariant image descriptors in an analytical way. In [6, 7], we used a fast Gabor transform to locally analyze images by decomposing local image patches into basic frequency components. For the experiments, we used confocal recordings of Arabidopsis root tips. We exemplarily aimed at detecting differentiated cells located in the root cap. They morphologically differ from the other cells by their nonroundish shape. For this experiment, two datasets were used: one dataset for training and one dataset for evaluation. All cells (about 3600 in each root) were manually labeled by an expert. We transformed the Gabor expansion coefficients into invariant features utilizing the spherical tensor product; we combine the expansion coefficients corresponding to the same angular frequency, but not necessarily the same radial frequencies, whereas

$$c^j(k_1, k_2) := (\mathbf{a}^j(k_1) \bullet_0 \mathbf{a}^j(k_2)), \quad (65)$$

where $c^j(k_1, k_2) \in \mathbb{C}$ are the rotation invariant image descriptors. It is worth mentioning that the combination of the same expansion coefficient coincides with the power-spectrum; namely, $c^j(k) = (\mathbf{a}^j(k) \bullet_0 \mathbf{a}^j(k)) = \|\mathbf{a}^j(k)\|^2$. In Figure 5(a), we depict the center slice of the training data together with the training samples. Based on the rotation invariant image descriptors representing the training samples, an SVM classifier is trained. We used the SVM to classify test-set in a voxel-by-voxel manner (Figures 5(b) and 5(c)). We classed each voxel into root-cap cell or non-root-cap cell. For further details regarding the experiment, we refer to [6, 7].

5.5. DTI Processing. Diffusion weighted magnetic resonance imaging (DWI) plays a substantial role in neuroscience and clinical applications. One field of interest is the investigation of the neuronal fiber architecture located in the brain white matter connecting different regions in the brain. The fibers themselves cannot be recorded directly. However, the data is usually recorded using the high angular resolution diffusion imaging (HARDI) technique [21], a specific kind of diffusion tensor imaging (DTI) technique. The resulting signal is an angular dependent, volumetric image. From such an image representation, the fiber architecture can be estimated (e.g., see [22]). Due to the angular dependency of HARDI signals, spherical harmonics are a common tool for signal representation. Therefore, in the context of DTI, there exist several applications worth considering spherical tensor algebra.

5.5.1. Tissue Classification. For the analysis of the fiber structure, a preprocessing step that identifies the brain white matter within the image is required. For group studies, the parcellation of the human brain into anatomical regions is of great interest. Preliminary results have been published in conference papers [23, 24].

We utilize the fact that the given recordings are tensor valued. We first transform the local measurements into the spherical harmonic domain (e.g., see [25]). Based on these rotation covariant image representations, we compute voxel-wise rotation invariant image features.

This is done by first comprising the voxels surrounding using the spherical down derivative operators. This can be seen as some kind of Taylor expansion of the given data. Then, we compute rotation invariant image features by computing the power spectrum of the resulting expansion coefficients. We finally use a random forest classifier [26] to learn the appearance of different kinds of brain regions and tissue types based on labeled training images. Such a parcellation might be for example, gray brain matter, white brain matter, and background signal. Qualitative results showing the resulting decisions of the random forest on an unclassified image are shown for the gray matter/white matter scenario in Figure 7.

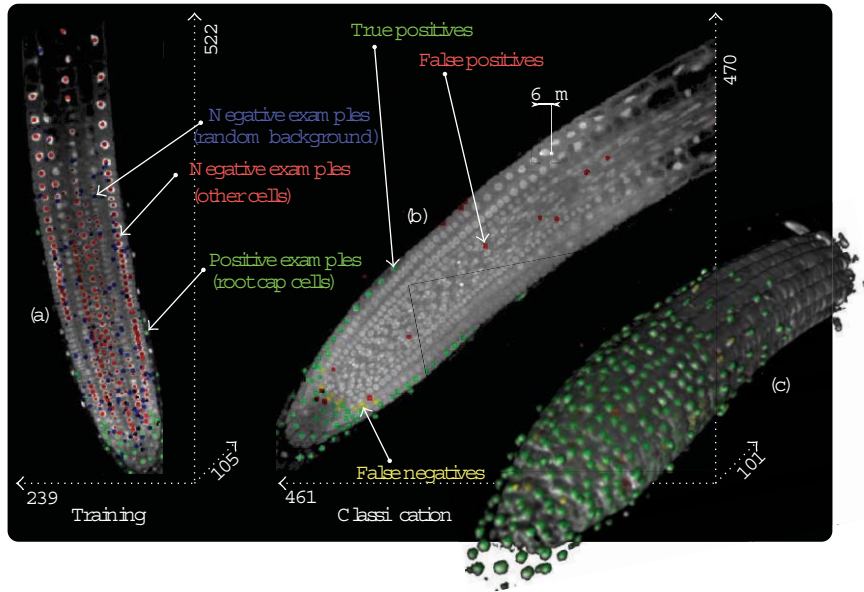


FIGURE 5: Voxel-wise classification of cells. For a voxel-wise classification, we first use a manually labeled image (a) for training a support vector machine (SVM) based on local rotation invariant image descriptors. Then, the SVM classifier is used to detect and classify cells in unclassified images (b). In (c) we depict an isosurface rendering of the classified root. Further details concerning the experiment can be found in [6].

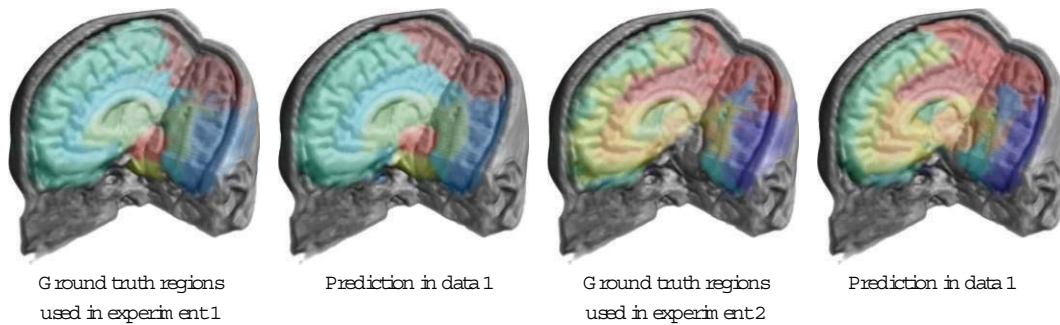


FIGURE 6: The ground truth regions that we used to train and evaluate our algorithm shown together with our algorithm's regions prediction. We can clearly see that our predictions are much more consistent with the data.

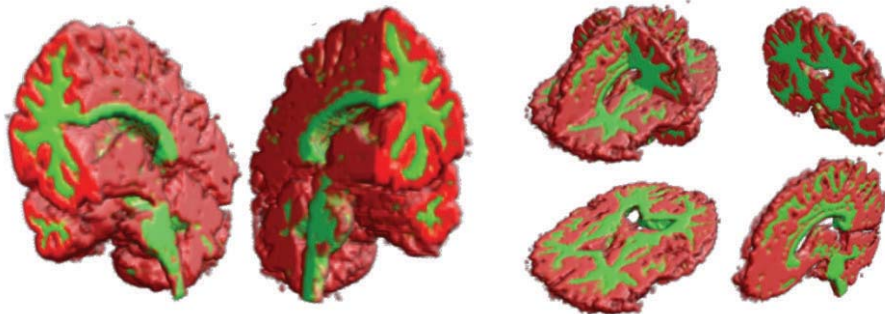


FIGURE 7: Isosurface showing the predictions for dataset 3 using GND and a random forest (RF) classifier. The classifier can distinguish between background, brain white matter (green), and gray matter (red).

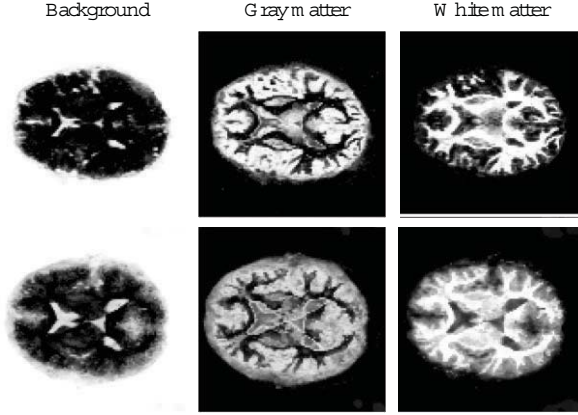


FIGURE 8: The confidence of the classifier represents the probability that a certain voxel belongs either to the background class, gray matter class, or the white matter class. The probability is represented by the intensity. A final decision is made by decision by majority (as shown in Figure 7).

Furthermore, the votes for a certain class can be used as a kind of evidence value in further processing steps. Examples for the three classes background, white matter, and gray matter are depicted in Figure 8.

In Figures 9 and 10, we show the probability map of different kinds of brain regions that have been detected within unlabeled test images via a random forest classifier. Figure 6 shows final predictions for one of the test sets.

5.5.2. Unique Point-Landmark Detection. Group studies often require the coregistration of images or partial image structures of different individuals. In such applications, the detection of characteristic landmarks is often an indispensable prerequisite.

Similar to [27], where features are used to find correspondences in scalar valued MR contrasts, we used tensor-based features in [28] offering a unique signature of a voxel's surrounding in tensor-valued HARDI signals. Thanks to these features, a large number of corresponding points can be reliably found in images of different individuals using a linear classifier. The features are computed in three steps. (1) We first entirely fit the HARDI signal to spherical harmonics. (2) The resulting fields are then efficiently expanded in terms of tensorial harmonics (Section 4) via tensor derivatives (see Section 3). (3) We obtain new covariant feature images which we use to form a trainable filter (see Section 5.3). The filter is used for the landmark detection task.

Second-order features which are sufficient for most applications are not providing enough information to solve the detection task in a human brain; they are invariant against reflection about an axis. Hence, they cannot distinguish the left and the right hemisphere. It is known that the spherical triple-correlation [29] yields complete rotation invariant features. Hence, they must solve this issue. Based on this idea we designed new 3rd order rotation invariant differential features fitting into our framework that are variant with respect to reflections about an axis. These features are additionally

included in the harmonic filter framework. The triple product is given by

$$\left((\mathbf{b}_a^{j_1} \circ_j \mathbf{b}_a^{j_2}) \circ_{j_4} \mathbf{b}_a^{j_3} \right), \quad j_1 + j_2 + j_3 + j_4 \text{ is odd,} \quad (66)$$

$$j_4, j \leq L,$$

where $\mathbf{b}_a^{j_1} \in \mathbb{C}^{2j_1+1}$, $\mathbf{b}_a^{j_2} \in \mathbb{C}^{2j_2+1}$, $\mathbf{b}_a^{j_3} \in \mathbb{C}^{2j_3+1}$ are the local tensorial harmonics expansion coefficients. A proof can be found in [28].

The resulting filter has shown very promising results on a training set of 7 and a test set of 14 images. For the experiment, we placed about 20000 landmarks within the brain gray and white matter in an equidistant manner. For each dataset, the computation of the features and the detection of all landmarks took about 5 minutes. We show some detection results in Figures 11, 12, 13, and 14.

Appendices

A. Spherical Harmonic Functions

The Schmidt seminormalized spherical harmonics $Y_m^j : S_2 \rightarrow \mathbb{C}$ are defined by

$$Y_m^j(\mathbf{r}) := \sqrt{\frac{(j-m)!}{(j+m)!}} P_j^m(\cos \theta) e^{im\phi}, \quad (A.1)$$

where P_j^m are the with m associated Legendre polynomials of order j [30]. The spherical harmonics build a complete orthogonal basis for functions on the 2-sphere, whereas

$$\langle Y_m^j, Y_{m'}^{j'} \rangle = \frac{\pi^4}{(2j+1)} \delta_{j,j'} \delta_{m,m'}. \quad (A.2)$$

B. Clebsch-Gordan Coefficients

Orthogonality

$$\sum_{j,m} \langle jm | j_1 m_1, j_2 m_2 \rangle \langle jm | j_1 m'_1, j_2 m'_2 \rangle \quad (B.1)$$

$$= \delta_{m_1, m'_1} \delta_{m_2, m'_2},$$

$$\sum_{j,m} \frac{2j+1}{2j_1+1} \langle j_1 m_1 | jm, j_2 m_2 \rangle \langle j_1 m'_1 | jm, j_2 m'_2 \rangle \quad (B.2)$$

$$= \delta_{m_1, m'_1} \delta_{m_2, m'_2},$$

$$\sum_{m=m_1+m_2} \langle jm | j_1 m_1, j_2 m_2 \rangle \langle j' m' | j_1 m_1, j_2 m_2 \rangle \quad (B.3)$$

$$= \delta_{j,j'} \delta_{m,m'},$$

$$\sum_{m_1, m_2} \langle jm | j_1 m_1, j_2 m_2 \rangle \langle jm | j_1 m_1, j'_2 m'_2 \rangle \quad (B.4)$$

$$= \frac{2j+1}{2j'_2+1} \delta_{j_2, j'_2} \delta_{m_2, m'_2}.$$

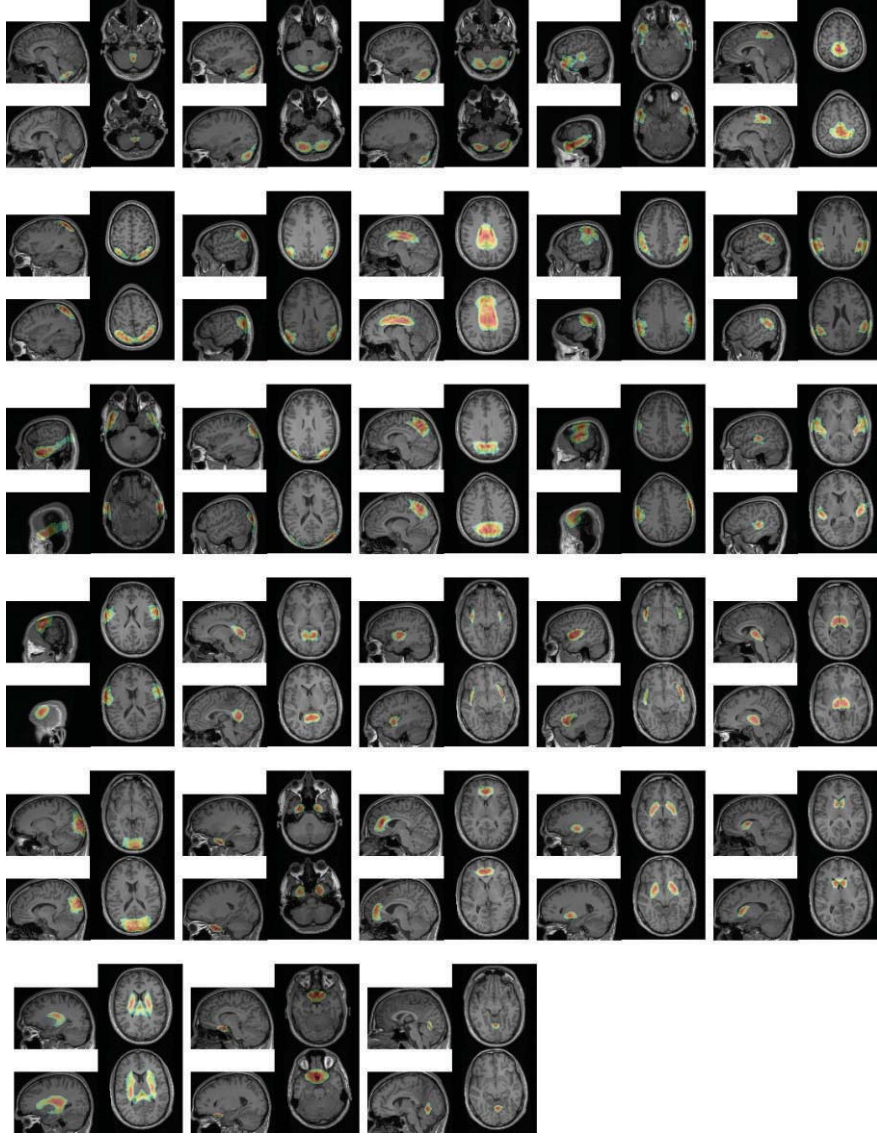


FIGURE 9: Heat maps representing the probability for all regions used in an experiment (continued in Figure 10).

Special values

$$\begin{aligned}
 & \langle \ell m \mid (\ell - \lambda)(m - \mu), \lambda \mu \rangle \\
 &= \left(\frac{\ell + m}{\lambda + \mu} \right)^{1/2} \left(\frac{\ell - m}{\lambda - \mu} \right)^{1/2} (2\ell)^{-1/2}, \\
 & \langle \ell m \mid (\ell + \lambda)(m - \mu), \lambda \mu \rangle \\
 &= (-1)^{\lambda + \mu} \left(\frac{\ell + \lambda - m + \mu}{\lambda + \mu} \right)^{1/2} \\
 & \quad \times \left(\frac{\ell + \lambda + m - \mu}{\lambda - \mu} \right)^{1/2} (2\ell + 2\lambda + 1)^{-1/2}.
 \end{aligned} \tag{B.5}$$

Symmetry

$$\begin{aligned}
 & \langle jm \mid j_1 m_1, j_2 m_2 \rangle = \langle j_1 m_1, j_2 m_2 \mid jm \rangle, \\
 & \langle jm \mid j_1 m_1, j_2 m_2 \rangle = (-1)^{j_1 + j_2} \langle jm \mid j_2 m_2, j_1 m_1 \rangle,
 \end{aligned}$$

$$\begin{aligned}
 & \langle jm \mid j_1 m_1, j_2 m_2 \rangle \\
 &= (-1)^{j_1 + j_2} \langle j(-m) \mid j_1(-m_1), j_2(-m_2) \rangle, \\
 & \langle jm \mid j_1 m_1, j_2 m_2 \rangle \\
 &= \sqrt{\frac{2j+1}{2j_2+1}} (-1)^{j_1 + m_1} \langle j_2 m_2 \mid jm, j_1(-m_1) \rangle.
 \end{aligned} \tag{B.6}$$

C. Wigner D-Matrix

The components of \mathbf{D}_g^ℓ are written D_{mn}^ℓ . They are called the Wigner D-matrix. In Euler angles ϕ, θ, ψ in ZYZ-convention, we have

$$D_{mn}^\ell(\phi, \theta, \psi) = e^{im\phi} d_{mn}^\ell(\theta) e^{in\psi}, \tag{C.1}$$

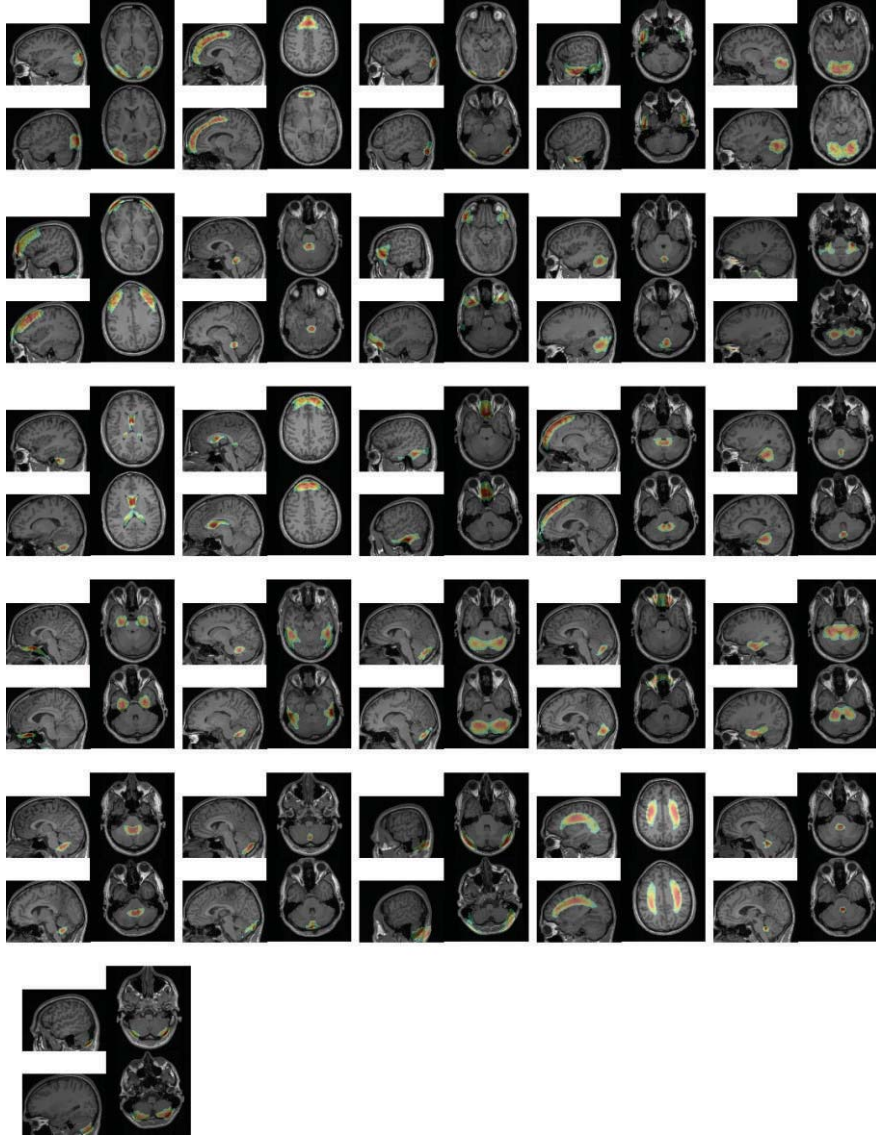


FIGURE 10: Heat maps representing the probability for all regions used an experiment (starting in Figure 9).

where $d_{mn}^\ell(\theta)$ is the Wigner d-matrix which is real-valued. Relation to the Clebsch-Gordan coefficients:

$$D_{mn}^\ell = \sum_{\substack{m_1+m_2=m \\ n_1+n_2=n}} D_{m_1 n_1}^{\ell_1} D_{m_2 n_2}^{\ell_2} \langle lm | l_1 m_1, l_2 m_2 \rangle \langle ln | l_1 n_1, l_2 n_2 \rangle, \quad (\text{C.2})$$

$$D_{m_1 n_1}^{\ell_1} D_{m_2 n_2}^{\ell_2} = \sum_{l, m, n} D_{mn}^\ell \langle lm | l_1 m_1, l_2 m_2 \rangle \langle ln | l_1 n_1, l_2 n_2 \rangle. \quad (\text{C.3})$$

D. Spherical Bessel Functions

The spherical Bessel functions $j_j : \mathbb{R}_{\geq 0} \rightarrow \mathbb{R}$ are related to the Bessel functions of the kind J_ν (e.g., see [30])

by $j_j(r) := \sqrt{\pi/2r} J_{j+1/2}(r)$ and are represented by the expansion

$$j_j(r) = r^j \sum_{m=0}^{\infty} \frac{(-1)^m}{2^m m! (2(j+m)+1)!!} r^{2m}, \quad (\text{D.1})$$

where

$$\int_0^\infty j_j(kr) j_j(k'r) r^2 dr = \frac{\pi}{2k^2} \delta(k - k'). \quad (\text{D.2})$$

For the spherical Bessel functions, we have the following differential relations [30]:

$$\frac{\partial}{\partial r} [r^{-\nu} j_\nu] = -r^{-\nu} j_{\nu+1}, \quad (\text{D.3})$$

$$\frac{\partial}{\partial r} [r^{\nu+1} j_\nu] = r^{\nu+1} j_{\nu-1}. \quad (\text{D.4})$$

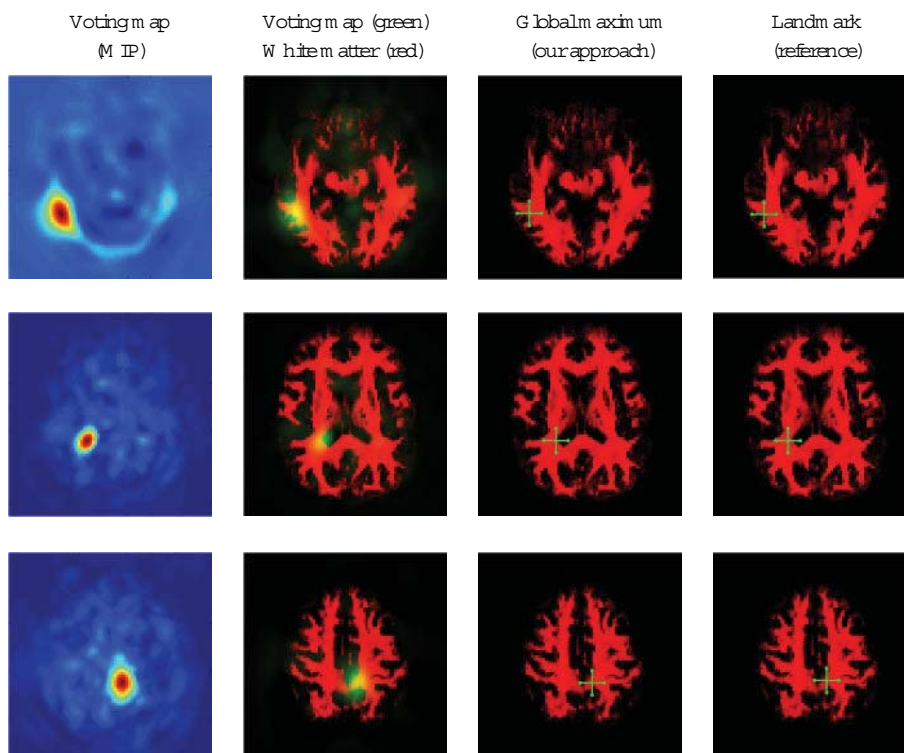


FIGURE 11: Differently weighted linear combinations of the feature images lead to different detection results.

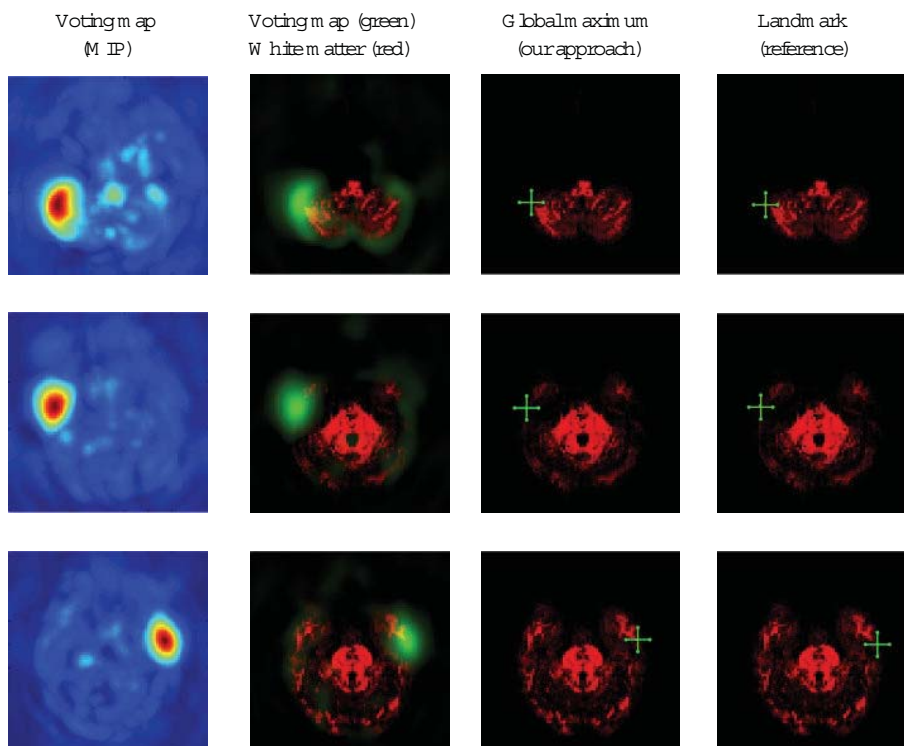


FIGURE 12: Differently weighted linear combinations of the feature images lead to different detection results.

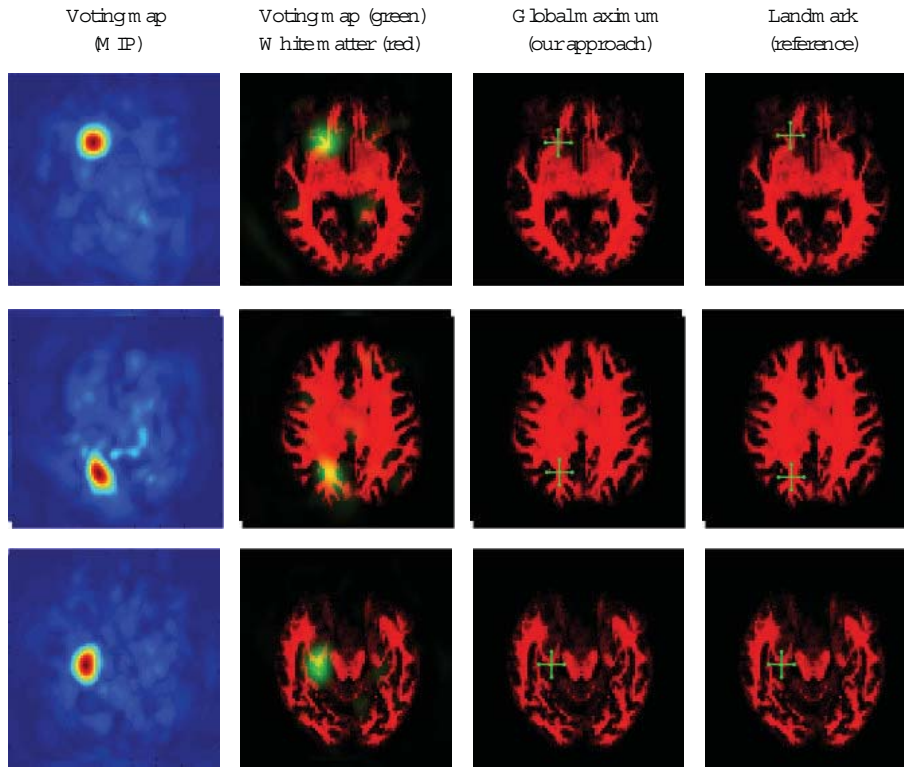


FIGURE 13: Differently weighted linear combinations of the feature images lead to different detection results.

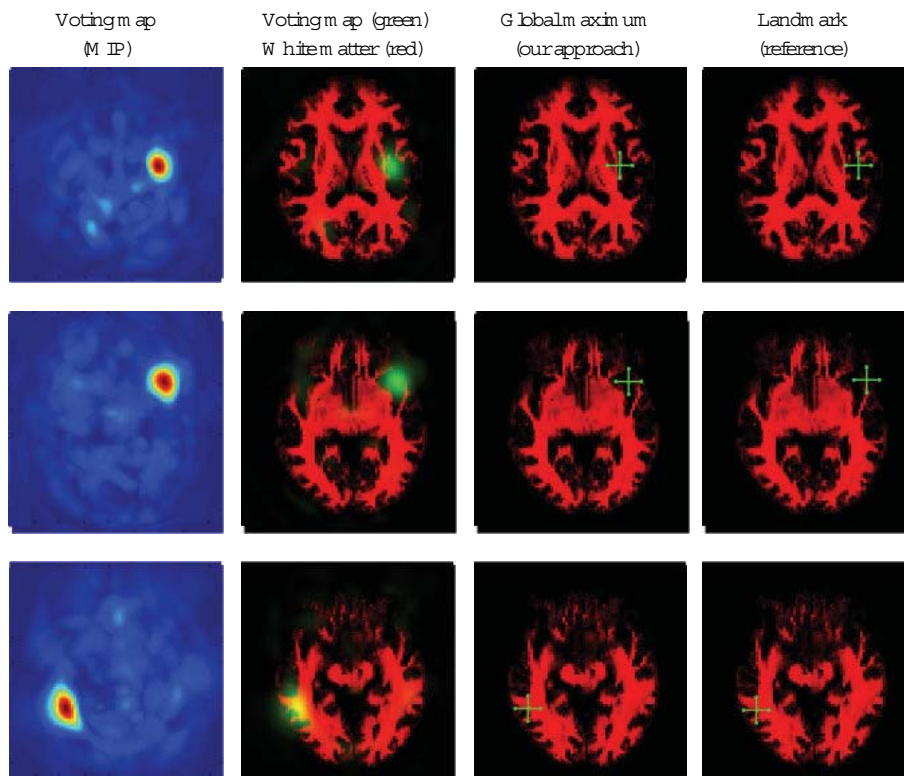


FIGURE 14: Differently weighted linear combinations of the feature images lead to different detection results.

The Hankel Transform [31] (also known as Fourier-Bessel transform) of order j in terms of the spherical Bessel functions is given by

$$\alpha_j(k) = \int_0^\infty f(r) j_j(kr) r^2 dr, \quad (\text{D.5})$$

and its corresponding inverse transformation is given by

$$f(r) = \frac{2}{\pi} \int_0^\infty \alpha_j(k) j_j(kr) k^2 dk, \quad (\text{D.6})$$

which both are directly a result of (D.2).

E. Plane Wave

Using the addition theorem of the spherical harmonics, we can express the spherical expansion of the plane wave (e.g., see [3, page 136]) in terms of the tensor product \bullet_0 leading to

$$e^{i\mathbf{k}^T \mathbf{r}} = \sum_j (i)^j (2j+1) j_j(kr) Y^j(\mathbf{r}) \bullet_0 Y^j(\mathbf{k}), \quad (\text{E.1})$$

where P_j are the Legendre polynomials [30] of order j and $Y^j = (Y_{-j}^j, \dots, Y_j^j)^T$ the semi-Schmidt normalized spherical harmonics written as vector.

F. Associated Laguerre Polynomials

The associated Laguerre polynomials [30] are defined by

$$L_n^k(x) = \sum_{i=0}^n (-1)^i \binom{n+k}{n-i} \frac{x^i}{i!}. \quad (\text{F.1})$$

The following 3-point-rule [30] is used in this work:

$$nL_n^k(x) = (n+k)L_{n-1}^k(x) - xL_{n-1}^{k+1}(x). \quad (\text{F.2})$$

We further need the the following differential equation [30]:

$$\frac{1}{m!} \frac{d^m}{dx^m} x^k L_n^k(x) = \binom{n+k}{m} x^{(k-m)} L_n^{(k-m)}(x). \quad (\text{F.3})$$

The polynomials L_n^k and $L_{n'}^k$ are orthogonal over $[0, \infty)$ with respect to the weighting function $x^k e^{-x}$ as

$$\int_0^\infty x^k e^{-x} L_n^k(x) L_{n'}^k(x) dx = \frac{\Gamma(n+k+1)}{n!} \delta_{n,n'}. \quad (\text{F.4})$$

For positive integers n , we have the following relation between the Gamma function and the double factorial [32, 33]:

$$\Gamma\left(n + \frac{1}{2}\right) = \frac{(2n-1)!!}{2^n} \sqrt{\pi}. \quad (\text{F.5})$$

Acknowledgments

M. Reisert and H. Skibbe are indebted to the Baden-Württemberg Stiftung for the financial support of this research project by the Eliteprogramme for Postdocs. This work was partly supported by Bioinformatics for Brain Sciences under the Strategic Research Program for Brain Sciences, by the Ministry of Education, Culture, Sports, Science, and Technology of Japan (MEXT).

References

- [1] W. F. Förstner, "A feature based correspondence algorithm for image matching," *International Archives of Photogrammetry and Remote Sensing*, vol. 26, no. 3, pp. 150–166, 1986.
- [2] H. Skibbe, M. Reisert, Q. Wang, O. Ronneberger, and H. Burkhardt, "Fast computation of 3D spherical Fourier harmonic descriptors—a complete orthonormal basis for a rotational invariant representation of three-dimensional objects," in *Proceedings of the 12th IEEE International Conference on Computer Vision Workshops (ICCV '09)*, pp. 1863–1869, Kyoto, Japan, October 2009.
- [3] M. Rose, *Elementary Theory of Angular Momentum*, Dover Publications, New York, NY, USA, 1995.
- [4] M. Reisert and H. Burkhardt, "Spherical tensor calculus for local adaptive filtering," in *Tensors in Image Processing and Computer Vision*, S. Aja-Fernández, R. de Luis García, D. Tao, and X. Li, Eds., Springer, 2009.
- [5] M. Reisert, "Spherical derivatives for steerable filtering in 3D," Tech. Rep. 3, Albert-Ludwigs-Universitt Freiburg, 2007.
- [6] H. Skibbe, M. Reisert, T. Schmidt, K. Palme, O. Ronneberger, and H. Burkhardt, "3D object detection using a fast voxel-wise spherical Fourier tensor transformation," in *Proceedings of the 32nd Symposium of the German Association for Pattern Recognition (DAGM '10)*, Lecture Notes in Computer Science, pp. 412–421, Springer, Darmstadt, Germany, 2010.
- [7] H. Skibbe, M. Reisert, T. Schmidt, T. Brox, O. Ronneberger, and H. Burkhardt, "Fast rotation invariant 3D feature computation utilizing efficient local neighborhood operators," *IEEE Transactions on Pattern Analysis and Machine Intelligence*, vol. 34, no. 8, pp. 1563–1575, 2012.
- [8] O. Matsuoka, "Molecular integrals over spherical Laguerre Gaussian-type functions," *The Journal of Chemical Physics*, vol. 92, no. 7, pp. 4364–4371, 1990.
- [9] L. Y. Chow Chiu and M. Moharerrzadeh, "The addition theorem of spherical Laguerre Gaussian functions and its application in molecular integrals," *Journal of Molecular Structure: THEOCHEM*, vol. 536, no. 2-3, pp. 263–267, 2001.
- [10] J. J. Koenderink and A. J. van Doorn, "Generic neighborhood operators," *IEEE Transactions on Pattern Analysis and Machine Intelligence*, vol. 14, no. 6, pp. 597–605, 1992.
- [11] L. Sorgi, N. Cimminiello, and A. Neri, "Keypoints selection in the gauss laguerre transformed domain," in *Proceedings of the British Machine Vision Conference (BMVC '06)*, pp. 539–547, Edinburgh, UK, 2006.
- [12] Z. Qian, D. N. Metaxas, and L. Axel, "Extraction and tracking of MRI tagging sheets using a 3D Gabor filter bank," in *Proceedings of the Annual International Conference of the IEEE Engineering in Medicine and Biology Society*, vol. 1, pp. 711–714, 2006.
- [13] J. Bigun, "Speed, frequency, and orientation tuned 3-D Gabor filter banks and their design," in *Proceedings of the 12th IAPR International Conference on Pattern Recognition (ICPR '94)*, pp. 184–187, 1994.
- [14] M. Reisert and H. Burkhardt, "Efficient tensor voting with 3D tensorial harmonics," in *Proceedings of the IEEE Computer Society Conference on Computer Vision and Pattern Recognition Workshops (CVPRW '08)*, pp. 1–7, June 2008.
- [15] G. Guy and G. Medioni, "Inferring global perceptual contours from local features," *International Journal of Computer Vision*, vol. 20, no. 1-2, pp. 113–133, 1996.

- [16] D. H. Ballard, "Generalizing the Hough transform to detect arbitrary shapes," *Pattern Recognition*, vol. 13, no. 2, pp. 111–122, 1981.
- [17] D. G. Lowe, "Distinctive image features from scale-invariant keypoints," *International Journal of Computer Vision*, vol. 60, no. 2, pp. 91–110, 2004.
- [18] M. Reisert and H. Burkhardt, "Harmonic filters for generic feature detection in 3D," in *Proceedings of the 31st Symposium of the German Association for Pattern Recognition (DAGM '09)*, vol. 5748 of *Lecture Notes in Computer Science*, pp. 131–140, Springer, Jena, Germany, 2009.
- [19] M. Schlachter, M. Reisert, C. Herz et al., "Harmonic filters for 3D multichannel data: rotation invariant detection of mitoses in colorectal cancer," *IEEE Transactions on Medical Imaging*, vol. 29, no. 8, pp. 1485–1495, 2010.
- [20] H. Skibbe, M. Reisert, O. Ronneberger, and H. Burkhardt, "Spherical Bessel filter for 3D object detection," in *Proceedings of the 8th IEEE International Symposium on Biomedical Imaging (ISBI '11)*, Chicago, Ill, USA, April 2011.
- [21] D. S. Tuch, R. M. Weissko, J. W. Belliveau, and V. J. Wedeen, "High angular resolution diffusion imaging of the human brain," in *Proceedings of the 7th Annual Meeting of the ISMRM*, Philadelphia, Pa, USA, 1999.
- [22] M. Reisert, I. Mader, C. Anastopoulos, M. Weigel, S. Schnell, and V. Kiselev, "Global fiber reconstruction becomes practical," *NeuroImage*, vol. 54, no. 2, pp. 955–962, 2011.
- [23] H. Skibbe, M. Reisert, and H. Burkhardt, "Gaussian neighborhood descriptors for brain segmentation," in *Proceedings of the 12th IAPR Conference on Machine Vision Applications (MVA '11)*, Nara, Japan, 2011.
- [24] H. Skibbe and M. Reisert, "Dense rotation invariant brain pyramids for automated human brain parcellation," in *Proceedings of the Workshop on Emerging Technologies for Medical Diagnosis and Therapy (Informatik '11)*, Berlin, Germany, 2011.
- [25] S. Schnell, D. Saur, B. W. Kreher, J. Hennig, H. Burkhardt, and V. G. Kiselev, "Fully automated classification of HARDI in vivo data using a support vector machine," *NeuroImage*, vol. 46, no. 3, pp. 642–651, 2009.
- [26] L. Breiman, "Random forests," *Machine Learning*, vol. 45, no. 1, pp. 5–32, 2001.
- [27] Z. Xue, D. Shen, and C. Davatzikos, "Determining correspondence in 3-D MR brain images using attribute vectors as morphological signatures of voxels," *IEEE Transactions on Medical Imaging*, vol. 23, no. 10, pp. 1276–1291, 2004.
- [28] H. Skibbe and M. Reisert, "Detection of unique point landmarks in hardi images of the human brain," in *Proceedings of the MICCAI Workshop on Computational Diffusion MRI (CDMRI '12)*, Nice, France, 2012.
- [29] R. Kondor, *Group theoretical methods in machine learning [Ph.D. thesis]*, Columbia University, 2008.
- [30] M. Abramowitz and I. A. Stegun, *Handbook of Mathematical Functions with Formulas, Graphs, and Mathematical Tables*, Dover, Gpo, New York, NY, USA, 9th-10th edition, 1964.
- [31] I. N. Bronshtein and K. A. Semendiyayev, *Handbook of Mathematics*, Springer, London, UK, 3rd edition, 1997.
- [32] E. W. Weisstein, "Double factorial," MathWorld—A Wolfram Web Resource, <http://mathworld.wolfram.com/Double-Factorial.html>.
- [33] E. W. Weisstein, "Gamma function," MathWorld—A Wolfram Web Resource, <http://mathworld.wolfram.com/Gamma-Function.html>.

Research Article

Nonrigid 3D Medical Image Registration and Fusion Based on Deformable Models

Peng Liu,¹ Benjamin Eberhardt,² Christian Wybranski,² Jens Ricke,² and Lutz Lüdemann¹

¹ Department of Radiotherapy, Universitätsklinikum Essen, Hufelandstraße 55, 45147 Essen, Germany

² Department for Radiology and Nuclear Medicine, Universitätsklinikum Magdeburg, Leipziger Straße 44, 39120 Magdeburg, Germany

Correspondence should be addressed to Lutz Lüdemann; lutz.luedemann@uk-essen.de

Received 18 January 2013; Accepted 26 March 2013

Academic Editor: Kumar Durai

Copyright © 2013 Peng Liu et al. This is an open access article distributed under the Creative Commons Attribution License, which permits unrestricted use, distribution, and reproduction in any medium, provided the original work is properly cited.

For coregistration of medical images, rigid methods often fail to provide enough freedom, while reliable elastic methods are available clinically for special applications only. The number of degrees of freedom of elastic models must be reduced for use in the clinical setting to archive a reliable result. We propose a novel geometry-based method of nonrigid 3D medical image registration and fusion. The proposed method uses a 3D surface-based deformable model as guidance. In our twofold approach, the deformable mesh from one of the images is first applied to the boundary of the object to be registered. Thereafter, the non-rigid volume deformation vector field needed for registration and fusion inside of the region of interest (ROI) described by the active surface is inferred from the displacement of the surface mesh points. The method was validated using clinical images of a quasirigid organ (kidney) and of an elastic organ (liver). The reduction in standard deviation of the image intensity difference between reference image and model was used as a measure of performance. Landmarks placed at vessel bifurcations in the liver were used as a gold standard for evaluating registration results for the elastic liver. Our registration method was compared with affine registration using mutual information applied to the quasi-rigid kidney. The new method achieved 15.11% better quality with a high confidence level of 99% for rigid registration. However, when applied to the quasi-elastic liver, the method has an averaged landmark dislocation of 4.32 mm. In contrast, affine registration of extracted livers yields a significantly ($P = 0.000001$) smaller dislocation of 3.26 mm. In conclusion, our validation shows that the novel approach is applicable in cases where internal deformation is not crucial, but it has limitations in cases where internal displacement must also be taken into account.

1. Introduction

In many clinical tasks it is necessary to acquire images using different modalities such as magnetic resonance imaging (MRI), positron emission tomography (PET), and computed tomography (CT), which often provide complementary information on anatomy and tissue function. Combination of these multimodal images can improve the diagnosis by providing synergistic information. Image registration is an important tool for fusion of medical images. It generates an image that simultaneously displays the information of the reference and the registered image. Image registration aims at identifying corresponding points in two images using spatial transform. Due to the spatial difference in the local coordinate systems of images acquired with different imaging modalities registration has to align the images.

Another application of image registration is serial imaging of a patient using the same imaging modality, which is often required for purposes such as treatment planning and monitoring [1], evaluation of disease development [2, 3], and tracking of contrast bolus propagation in perfusion studies [4–6]. Registration is required to correct for the motion caused by patient movement and respiration and to compensate for the displacement of structures resulting from different patient positions in serial imaging studies. Although many spatial displacements can be traced back to rigid movement and are easy to correct, elastic deformation is required to describe the movement of many anatomic structures such as the liver. Thus nonrigid registration is often required for both repeated acquisitions using the same image modality and examinations using different image modalities.

Rigid transformation, which allows translation and rotation, and affine registration, which allows shearing and

scaling, are widely used for image fusion in a clinical setting. However, since the human body is intrinsically deformable, rigid techniques often provide insufficient registration. Thus elastic or nonrigid methods are required to cope with local differences between images. While the number of parameters is limited to six for rigid transformation and to twelve for affine transformation, nonparametric elastic transformation requires a transformation vector for each voxel; that is, the number of parameters is three times that of image voxels. The huge number of parameters generates two basic problems for elastic transformation. First, the computing time is enormous. Second, the intrinsic image information is in general not sufficient to exactly and independently estimate the transformation vector of each voxel.

Therefore, elastic image registration uses models to limit the number of parameters. However, one can also benefit from the fact that the number of effective transformation parameters is actually much smaller. It is obvious that a tissue voxel in general cannot move independently of a neighboring voxel. Thus elastic registrations exploit the fact that the transformation field should be smooth [7, 8]. A smooth transformation field adequately describes the actual dislocation of most voxels. On the other hand, in some instances, the entire inner organ moves, while movement of organ voxels relative to each other is small. It was demonstrated that movement of organs such as the prostate [4], kidney [6], or liver [1] can be estimated, in a first approximation, by a rigid or affine transformation. In consequence, the transformation field for some inner organs is not smooth. The difference between the transformation vectors inside an organ is small, while the difference between the transformation vectors at the organ surface might be much larger.

Most approaches to elastic registration are based on matching signal intensities [9–12], which is limited to special applications [10, 11] or make use only of a smooth transformation field [7–9, 13, 14]. In our paper we introduce a novel geometry-based three-dimensional nonrigid registration approach. The method is based on the assumption that organ movement is primarily effective at the organ surface. We assume a smooth transformation field inside an organ and free transformation at the organ surface. Thus, our registration algorithm is a geometrical method based on segmentation. This kind of registration requires preliminary segmentation of the anatomical structure of interest on the reference or model image. Binary structures such as contours and surfaces can be generated by labeling them manually or (semi)automatically using an advanced algorithm. The basic idea is to use deformable models to guide image registration. With such models, nonrigid volume deformations are inferred from surface deformations. The transformation required for registration is then calculated by minimizing the distance of the contour points. Furthermore, a fusion technique based on the inferred volume deformation is introduced. Factors which may influence the performance of the method are discussed.

2. Theory

2.1. Concept. Our registration algorithm is a geometrical method based on segmentation. This kind of registration requires segmentation of the anatomical structure of interest on the reference or model image to generate a binary structure. Segmentation can be performed manually or (semi)automatically using an advanced algorithm. An active surface mesh is generated from the segmentation of the reference images. Since an active surface mesh is a 3D deformable model which extends active contours [15] to 3D and thus can be adapted to be applied to the edges of an edge map extracted from the complementary image of the registration or fusion, we believe that mesh displacement could indicate movement of the organ. In our approach, surface evolution in the edge map leads to surface deformations described by the displacement of surface mesh points. The resulting nonrigid volume deformation vector field for registration or fusion inside the region of interest (ROI) is predicted by solving the reverse problem of free-form deformation (FFD) [16]. FFD allows to obtain the first experimental result of prediction based only on geometrical knowledge.

2.1.1. Active Surface. Deformable models can be applied to image edges [17] with large image intensity gradients by using an optimization method. In our approach we use a 3D extension of active contours called active surfaces. While the level set method uses implicit surfaces [18, 19], we use explicit surfaces constructed from tetrahedres.

The basic concept of active models in general, and of active surfaces in particular, is to give the models physical characteristics in terms of energy. Internal energy and external energy are two widely used concepts in this context: internal energy E_{int} describes the internal deformation characteristics of the model, that is, the smoothness of the surface. External energy E_{ext} describes the environmental influence on the model. Here “environment” refers to images or their filtered forms, on which the models are settled and transformed. Basically, external energy is extracted from features such as object boundaries, where the image gradient has its local maximum and is often described as potential energy.

Based on the definition of energy, the segmentation process ideally minimizes the total energy, E_{total} , of the model:

$$E_{\text{total}} = E_{\text{int}} + E_{\text{ext}}. \quad (1)$$

As a result the active model will be attracted to the object boundary, where total energy is the lowest. To achieve this desired property of the model, the shape of the object of interest is supposed to be regular and smooth so that, at the object boundary, the bending energy, defined by rigid force \vec{F}_{rigid} , and the stretching energy, defined by elastic force \vec{F}_{elastic} , compensate for the potential energy that defines the external energy. This can also be seen as a state of

force balancing of the internal forces ($\vec{\mathbf{F}}_{\text{rigid}}, \vec{\mathbf{F}}_{\text{elastic}}$) and the external force ($\vec{\mathbf{F}}_{\text{ext}}$):

$$\vec{\mathbf{F}}_{\text{total}} = \vec{\mathbf{F}}_{\text{rigid}} + \vec{\mathbf{F}}_{\text{elastic}} + \vec{\mathbf{F}}_{\text{ext}} = 0. \quad (2)$$

Since the active surface moves during the energy-minimizing procedure, we thus describe the whole process as a surface evolution function of time:

$$\frac{\partial \mathbf{S}(s, t)}{\partial t} = \tau(t) \vec{\mathbf{F}}_{\text{total}}(t), \quad (3)$$

where S is the active surface defined as a set of surface mesh points s at time t . Vector $\tau(t)\vec{\mathbf{F}}_{\text{total}}(t)$ refers to the increment of surface movement at time t , where the time-dependent scale factor τ is used to control movement speed, ensuring numerical stability under the *Courant-Friedrichs-Lewy* (CFL) condition [20]. The steady state, in which total energy is at its minimum, is reached if the increment for optimization approximates zero.

2.1.2. Free-Form Deformation. Our method uses FFD to describe deformation of the object of interest, which is embedded in a control grid with a given resolution in three dimensions of $(l+1)(m+1)(n+1)$. Using its local coordinate system defined by unit vectors $\vec{\mathbf{S}}, \vec{\mathbf{T}},$ and $\vec{\mathbf{U}}$, a grid point $\vec{\mathbf{p}}_{ijk}$ of the FFD can be defined as

$$\vec{\mathbf{p}}_{ijk} = \vec{\mathbf{x}}_0 + \frac{i}{l}\vec{\mathbf{S}} + \frac{j}{m}\vec{\mathbf{T}} + \frac{k}{n}\vec{\mathbf{U}} \quad (4)$$

$(i \in [0, l], j \in [0, m], k \in [0, n]),$

where $\vec{\mathbf{x}}_0$, described by its global coordinates, is the origin of the local coordinate system. Using trivariate tensor product Bernstein polynomial, the position in the global coordinate system of any point $\vec{\mathbf{x}}$ inside the FFD grid can be interpolated via

$$\vec{\mathbf{x}} = \sum_{i=0}^l \sum_{j=0}^m \sum_{k=0}^n C_l^i C_m^j C_n^k (1-\chi)^{l-i} \chi^i (1-\psi)^{m-j} \psi^j \cdot (1-\omega)^{n-k} \omega^k \vec{\mathbf{p}}_{ijk}, \quad (5)$$

where $C_l^i, C_m^j,$ and C_n^k are the binomial coefficients in respect of $l, m,$ and n . Furthermore $\chi, \psi,$ and ω are the local coordinates of $\vec{\mathbf{x}}$, where

$$\begin{aligned} \chi &= \frac{\vec{\mathbf{T}} \times \vec{\mathbf{U}} \cdot (\vec{\mathbf{x}} - \vec{\mathbf{x}}_0)}{\vec{\mathbf{T}} \times \vec{\mathbf{U}} \cdot \vec{\mathbf{S}}}, \\ \psi &= \frac{\vec{\mathbf{S}} \times \vec{\mathbf{U}} \cdot (\vec{\mathbf{x}} - \vec{\mathbf{x}}_0)}{\vec{\mathbf{S}} \times \vec{\mathbf{U}} \cdot \vec{\mathbf{T}}}, \\ \omega &= \frac{\vec{\mathbf{S}} \times \vec{\mathbf{T}} \cdot (\vec{\mathbf{x}} - \vec{\mathbf{x}}_0)}{\vec{\mathbf{S}} \times \vec{\mathbf{T}} \cdot \vec{\mathbf{U}}}. \end{aligned} \quad (6)$$

Since all surface mesh points are settled inside the FFD grid, a surface point $\vec{\mathbf{s}}$ can be interpolated as well using the above interpolation function (5) by replacing $\vec{\mathbf{x}}$ with $\vec{\mathbf{s}}$. Since we

always take a set of points, in our case the active surface, into consideration, we use the matrix description of (5) for the whole surface \mathbf{S} :

$$\mathbf{S} = \mathbf{B} \cdot \mathbf{P}, \quad (7)$$

where \mathbf{S} is an $N \times 3$ matrix, \mathbf{B} is an $N \times (l+1)(m+1)(n+1)$ matrix, and \mathbf{P} is an $(l+1)(m+1)(n+1) \times 3$ matrix for a given number N of surface mesh points considered inside the FFD grid. Since \mathbf{B} solely describes the deformation for a given set of grid control points \mathbf{P} , it is normally referred to as deformation matrix. Based on the above matrix description (7) the following applies:

$$\mathbf{S}^* = \mathbf{B} \cdot \mathbf{P}^*, \quad (8)$$

where \mathbf{P}^* describes the set of displaced control points and \mathbf{S}^* refers to the deformed surface resulting from the right side of the function, given that \mathbf{B} is unchanged. This means, if we know the displacement of \mathbf{P} , we can calculate the deformation of \mathbf{S} . But note that our goal is to reversely solve the problem; that is, we have a set of deformed surface mesh points \mathbf{S}^* and wish to calculate \mathbf{P}^* in order to further use \mathbf{P}^* for interpolating the deformation of any point $\vec{\mathbf{x}}$ of the volume inside the surface as described in (5). Since the number of surface mesh points is much larger than that represented in the FFD control grid, using the pseudoinverse \mathbf{B}^+ of \mathbf{B} to solve

$$\mathbf{P}^* = \mathbf{B}^+ \mathbf{S}^* \quad (9)$$

will provide the solution to an overdetermined system rather than giving us a sufficient solution to the reverse problem in general. In our approach, we therefore solve the problem by using the Levenberg-Marquardt algorithm [21, 22], a method of least squares, in order to minimize the squared distance between \mathbf{S} and \mathbf{S}^* :

$$\mathbf{P}^* = \arg \min_{\mathbf{P}} \|\mathbf{S} - \mathbf{S}^*\|^2. \quad (10)$$

3. Material and Methods

3.1. Numerical Implementation. In our approach we use an active surface 3D deformable model to guide the registration. The active surface is generated through triangulation from a preliminary segmentation of the object of interest on the model image and later adapted to the edges of the reference image as a deformable model by defining the internal and external forces acting on it. The elastic force acting on a surface mesh point is the sum of tensile forces from its neighboring points. The rigid force is described as a linear prediction of the tensile forces from its neighboring points and their neighbors [23]. The active surface is optimized by applying the finite difference method (FDM) to an *inverse edge map* [24] of the reference image.

After minimizing the total energy a deformed version of the original surface is displayed at the boundary of the object of interest on the reference image. Thus we have a one-to-one mapping of the surface mesh points as well. Based on the mapping an FFD control grid wrapping the original active surface can be deformed by solving the inverse problem of

the FFD. We then use the computed deformation of the FFD control grid, along with the deformation matrix of the FFD, to transform the voxels inside the original surface of the model image onto the reference image; hence image information such as intensity saved in the object of interest of the model image can be transferred into the deformed object described by the deformed surface on the reference image, which fulfills the registration task.

Conversely the procedure can also begin with a preliminary segmentation on the reference image in order to adapt the initial surface mesh to the reference image on the model image, thereby transferring the volume deformation from the reference to the model image. Using the aforementioned FFD interpolation method, image intensity in the deformed FFD on the model image can be sampled and traced back to the original object of interest in the reference image. In this way, fusion is accomplished.

Our method has been implemented as AMIRA (<http://www.amira.com>) modules. AMIRA is an advanced 3D visualization software developed by Konrad-Zuse-Zentrum für Informationstechnik, Berlin (<http://www.zib.de/de/home.html>) and distributed by Visage Imaging, Berlin (<http://www.visageimaging.com>). AMIRA is highly modularized using C++ to offer visualization and image analysis pipelines based on modules. Since our method is a twofold approach consisting of segmentation and subsequent FFD computation, the AMIRA modules are implemented in two packages, *hxactcontour* and *hxffd*. Furthermore, an upper level package *hxsera* (*sera* stands for segmentation-based elastic registration algorithm.) wraps the two packages for user-friendly access to the entire procedure.

The computational complexity of the segmentation task is linearly dependent on the number of surface mesh points and can be described as $O(n)$ using big- O notation [25]. When performing kidney segmentation, for example, we in general had from 10,000 to 20,000 points to process. In comparison the complexity of FFD computation is $O(m \cdot n)$, where m is the number of FFD control points and n is the number of surface mesh points. The FFD grid we used typically had a resolution of $5 \times 5 \times 5$ to $10 \times 10 \times 10$. Thus the number of FFD control points is considerably smaller than that of surface mesh points.

3.2. Image Data. To test the feasibility of our approach we first applied it to two contrast-enhanced dynamic computed tomography (CT) examinations consisting of a total of 41 3D datasets of the kidneys obtained in two patients who underwent routine clinical evaluation of renal perfusion. Each CT series was acquired using 320 slices with a 512×512 voxel in-plane resolution. The CT examinations were performed on a *TOSHIBA Aquilion ONE* with a total acquisition time of 1 min for the complete dataset while the iodine contrast agent was administered as a bolus. To reduce the absorbed dose the tube current was minimized.

The first patient received 90 mL contrast medium and was examined with a CT scanner tube voltage of 120 kV and tube current of 150 mA. 24 3D CT datasets were acquired with a spatial resolution of $0.571 \text{ mm} \times 0.571 \text{ mm}$ and a slice

thickness of 0.5 mm. The second patient received 120 mL contrast medium and underwent CT scanning with a tube voltage and current of 100 kV and 100 mA, respectively. Seventeen 3D CT datasets were acquired with a spatial resolution of $0.702 \text{ mm} \times 0.702 \text{ mm} \times 0.5 \text{ mm}$. Due to the high signal noise of the low dose scans the effective spatial resolution was lower than the nominal resolution of the scans. Therefore, the 3D CT datasets were resampled to a resolution of $256 \times 256 \times 160$ for the study.

We further used our method for multimodal registration in patients undergoing imaging of the liver, which is a more elastic organ than the kidney. Twenty patients treated by routine clinical brachytherapy [26] were investigated. A 3D CT and a 3D MRI interventional dataset from each patient were acquired no later than 1 hour after brachytherapy catheter positioning. One of the two 3D datasets was used for therapy planning. Furthermore, follow-up MRI performed several months after treatment was available for all patients. Because of the long interval between the intervention and follow-up MRI, there may be considerable liver movement and deformation in the follow-up images compared with the initial planning 3D dataset.

All axial CT scans of the liver were acquired with a resolution of 512×512 , but the number of slices ranged from 31 to 322, resulting in severe partial volume effects in the CT scans acquired with a lower number of slices. The averaged spatial resolution of the CT scans is $0.743 \text{ mm} \times 0.743 \text{ mm} \times 3.04 \text{ mm}$ compared with $1.187 \text{ mm} \times 1.187 \text{ mm} \times 2.50 \text{ mm}$ for MRI, where an invariable slice thickness of 2.50 mm applies to all cases. T1-weighted volume-interpolated 3D gradient echo MR images were acquired during catheter positioning on an open bore Philips 1.0 Tesla MR with a more inhomogeneous signal distribution.

The following sequence parameters were used: echo time (TE) 2.14 ms, repetition time (TR) 4.3 ms, echo train length 104, 122 phase-encoding steps, flip angle 12° , image matrix 320×320 , FOV 360 mm, 58% sampling, 75 slices, slice thickness 5.0 mm, slice spacing 2.5 mm. Additional T1-weighted 2D GRE MR images were acquired 12 weeks after brachytherapy for assessing the response to treatment on a Philips Achieva 1.5 Tesla MR imager using the following sequence parameters: TE 5.0 ms, TR 110 ms, 192 phase-encoding steps, flip angle 7° , image matrix 512×512 , FOV 430 mm, 75% sampling, 70% phase FOV, 28 slices, slice thickness 8.0 mm, slice spacing 9.0 mm. MR images with incomplete depiction of the liver were excluded from evaluation.

3.3. Evaluation Methods. To validate our approach, we used empirical methods, which are subcategorized into discrepancy and goodness methods as described in [27]. Discrepancy methods depend on an optimal reference, which is generally known as the gold standard and has been verified by experts. Goodness methods do not need a reference but rather depend on some preferable characteristics to describe and thus judge the performance of the algorithm.

In our validation we investigated alignment of the volume and misalignment of contours by using two different kinds

of discrepancy features. The *Dice similarity coefficient* (DSC) [28, 29] was used to evaluate volume alignment

$$\text{DSC} = \frac{2|A \cap B|}{|A \cup B|}, \quad (11)$$

where A is the volume of the segment to be validated and B the volume of the gold standard. For contour misalignment, we evaluated the *Hausdorff distance* [30]

$$d_h(k_A, k_B) = \max \left(\max_i \{d(a_i, k_B)\}, \max_j \{d(b_j, k_A)\} \right) \quad (12)$$

$(a_i \in k_A, b_j \in k_B)$

with

$$d(a_i, k_B) = \min_j |b_j - a_i| \quad (13)$$

and the averaged contour misalignment

$$\bar{d}(k_A, k_B) = \frac{\sum_i \min_j |b_j - a_i|}{|k_A|}, \quad (14)$$

where k_A and k_B are sets of contour points of the segment to be validated and the gold standard, respectively, and a_i and b_j represent the contour points of sets k_A and k_B . Note that $\bar{d}(k_A, k_B)$ and $\bar{d}(k_B, k_A)$ are generally not equal [31], so that the combined average of the contour misalignment was used for evaluation.

Furthermore, two different goodness methods were used to validate the segmentation approach: the *intraregion uniformity* [32] and the *gray level contrast* [27]. Intraregion uniformity is based on the assumption that the regions that have been segmented should have a uniform distribution of gray levels, which means that variance within each region should be small. \bar{g}_j is defined by the signal intensity g_i of voxel i in region R_j that has been segmented with mean intensity in R_j as

$$\bar{g}_j = \sum_{i \in R_j} \frac{g_i}{V_j}, \quad (15)$$

where V_j describes the volume of R_j . The variance of R_j is defined as

$$\sigma_j^2 = \sum_{i \in R_j} \frac{g_i - \bar{g}_j}{V_j}. \quad (16)$$

Based on the intensity variance defined previously, uniformity is defined as

$$U = 1 - \sum_{R_j} \frac{V_j \sigma_j^2}{V_{\text{all}} \sigma_{\text{max}}^2}, \quad (17)$$

where V_{all} is the sum of all volumes that have been segmented and σ_{max}^2 is a normalization factor defined as

$$\sigma_{\text{max}}^2 = \frac{(g_{\text{max}} - g_{\text{min}})^2}{2}, \quad (18)$$

where g_{max} and g_{min} are the absolute maximum and minimum of the signal intensities from all segmented regions, respectively. In comparison, the signal contrast takes the intensity difference between the segmented region and its background into consideration and assumes that contrast should be large. For the averaged signal intensity of the segmented region, f_0 , and the averaged background signal intensity, f_b , signal contrast is defined as

$$\text{GC} = \frac{|f_0 - f_b|}{f_0 + f_b}. \quad (19)$$

Furthermore, to validate our final registration result, we used a goodness method based on our empirical study, assuming that the change in signal intensity should be small within the region of interest (ROI) but large between the ROI and its background. This means that an accurate registration should yield a small variance in intensity, while a poor registration should yield much greater variance. Here we measure the standard deviation of intensity of the registered image within the reference ROI that was segmented by experts as gold standard (see Appendix A).

3.4. Evaluation. As mentioned above, we first applied our approach to dynamically acquired renal CT scans because the kidneys are relatively rigid organs. Segmentation and registration were evaluated separately. The two patients are numbered $P.\#1$ and $P.\#2$, and their 3D datasets are numbered consecutively beginning with the first acquisition of the dynamic series.

To reduce intra- and interexpert variability gold standards were obtained for the discrepancy methods using an iterative *expectation-maximization* method [33, 34] with an expert performing five segmentations for each 3D dataset. To validate the registration result we used our goodness feature—the standard deviation of intensity—to compare our registration with an intensity-based affine registration using mutual information [35] as the optimization metric.

We further validated our method for multimodal registration of the liver, which is more elastic than the kidney. We compared our registration results with a quasigold standard based on a voxel-based affine registration using mutual information on the same datasets. The quasigold standard was generated using the approach in [1]; here the liver is first segmented by a radiologist, and the segmented images are then registered. Intrahepatic landmarks positioned at vessel bifurcations by an experienced radiologist in both datasets were used to compare registration accuracy by measuring dislocation of the landmarks after registration.

4. Results

4.1. Segmentation of Kidney. First, we evaluated the performance of our method in the segmentation of the kidney. The kidney moves several centimeters during breathing but is, in a first approximation, a rigid organ. Table 1 presents Dice similarity coefficients, averaged contour misalignment, and Hausdorff distances in relation to the gold standard as well as intraregion uniformity and gray level contrast. Our method

TABLE 1: Segmentation quality.

Image	DSC	\bar{d} (mm)	d_H (mm)	U	GC
t06 (P1)	0.958	0.575	4.482	0.927	0.311
t07 (P1)	0.966	0.450	3.153	0.928	0.311
t09 (P1)	0.971	0.351	2.104	0.921	0.248
t08 (P2)	0.960	0.628	4.275	0.910	0.144
t16 (P2)	0.966	0.517	3.512	0.918	0.151
Mean	0.964	0.504	3.505	0.921	0.233

DSC: dice similarity coefficient. \bar{d} : averaged contour misalignment. d_H : Hausdorff distance. U : intraregion uniformity. GC: gray level contrast.

TABLE 2: Comparison of segmentation quality between experts (averaged) and our program.

Expert	DSC	\bar{d} (mm)	d_H (mm)	U	GC
1	0.977	0.297	3.590	0.927	0.307
2	0.978	0.358	2.816	0.926	0.303
3	0.970	0.431	6.084	0.926	0.308
4	0.966	0.556	3.862	0.927	0.313
5	0.963	0.546	4.555	0.926	0.307
Mean	0.971	0.438	4.181	0.927	0.308
Program	0.958	0.575	4.482	0.927	0.311

DSC: dice similarity coefficient. \bar{d} : averaged contour misalignment. d_H : Hausdorff distance. U : intraregion uniformity. GC: signal contrast.

showed subvoxel accuracy with a mean averaged contour misalignment of 0.504 mm (Table 1), which is below the the voxel size after subsampling of over 1.00 mm.

Furthermore, the averaged Hausdorff distance of 3.505 mm (see Table 1) is quite acceptable. To show this, we compared the results achieved with our method with those of manual segmentation by experts in Table 2, where we used the same gold standard to measure the Dice similarity coefficient, averaged contour misalignment, and Hausdorff distance. Our method has a slightly higher misalignment of 4.482 mm compared with the experts average of 4.181 mm. However, this value is well within the subvoxel range.

To test the goodness features, which are independent of the gold standard, we compared the quality of our segmentation method directly with that of experts. The results are presented in Table 3. The paired t -test was used to investigate for significant differences. With a P value of 0.2466, we found no significant difference in intraregion uniformity. Performance of the program was significantly better ($P = 0.0028$) using signal contrast for evaluation.

4.2. Registration of Kidney. To compare our registration method with affine registration using mutual information, the paired t -test was used to estimate the level of reduction of standard deviation of image intensity after affine and elastic registration. As can be seen from Table 4 our method achieved a 15.11% better quality with a high confidence of 99%. This value corresponds approximately 1 mm correction of translation (see Figures 1 and 3).

TABLE 3: Comparison of intraregion uniformity and signal contrast between program and gold standards.

Image	U_g	U_{prg}	GC_g	GC_{prg}
t06 (P1)	0.9269	0.9265	0.3089	0.3108
t07 (P1)	0.9280	0.9278	0.3094	0.3109
t09 (P1)	0.9214	0.9214	0.2446	0.2475
t08 (P2)	0.9099	0.9099	0.1419	0.1443
t16 (P2)	0.9175	0.9176	0.1472	0.1508
Mean	0.9207	0.9206	0.2304	0.2329
P	0.2466		0.0028	

U_g : intraregion uniformity of gold standard. U_{prg} : intraregion uniformity of program. GC_g : signal contrast of gold standard. GC_{prg} : signal contrast of program. P : two-sided level of significance of the t -test for U_{prg} versus U_g and GC_{prg} versus GC_g .

TABLE 4: Comparison: rigid registration versus elastic registration.

Image pair	σ_v	σ_s	σ_e
t07 \rightarrow t09 (P1)	119.11	70.97	58.33
t20 \rightarrow t05 (P1)	93.47	77.89	52.26
t12 \rightarrow t20 (P1)	123.06	58.61	43.91
t09 \rightarrow t13 (P2)	130.52	78.83	75.99
t07 \rightarrow t05 (P2)	121.13	64.20	61.66
t11 \rightarrow t08 (P2)	152.16	97.06	92.26
t16 \rightarrow t01 (P2)	117.60	86.95	64.93
$\bar{\sigma}$	122.43	76.36	64.19
Reduction of $\bar{\sigma}$	37.63%		47.57%
P	0.01		

σ_v : standard deviation before registration. σ_s : standard deviation after rigid registration. σ_e : standard deviation after elastic registration. P : two-sided significance of t -test for σ_s versus σ_v and σ_e versus σ_v .

TABLE 5: Comparison of landmark dislocation with different registration methods.

Registration	CT to iMRI	CT to pMRI	iMRI to pMRI
$N_{p,A}$	20	20	20
$N_{l,A}$	76	76	77
\bar{d}_A (mm)	3.26	6.58	6.58
σ_A	1.25	3.31	3.25
$N_{p,E}$	20	15	14
$N_{l,E}$	76	56	53
\bar{d}_E (mm)	4.32	11.98	10.72
σ_E	1.94	5.62	5.60
P	0.000001	≈ 0	≈ 0

(iMRI: intrainterventional MRI, pMRI postinterventional MRI.) $N_{p,A}$: number of patients (affine registration). $N_{l,A}$: number of landmarks (affine registration). \bar{d}_A : averaged dislocation (affine registration). σ_A : standard deviation (affine registration). $N_{p,E}$: number of patients (elastic registration). $N_{l,E}$: number of landmarks (elastic registration). \bar{d}_E : averaged dislocation (elastic registration). σ_E : standard deviation (elastic registration). P : two-sided level of significance of t -test for d_A versus d_E in the same column.

4.3. Registration of Liver. The liver was investigated as an example of a deformable organ. Accuracy of registration of our new method was studied using up to four landmarks

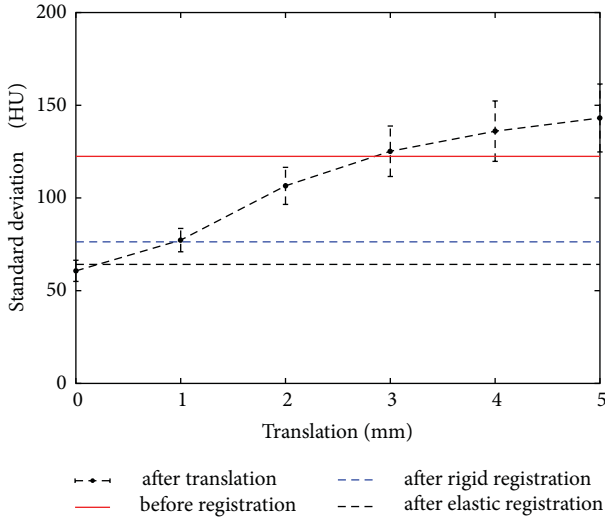


FIGURE 1: Comparison of rigid registration versus elastic registration (error bars: standard error).

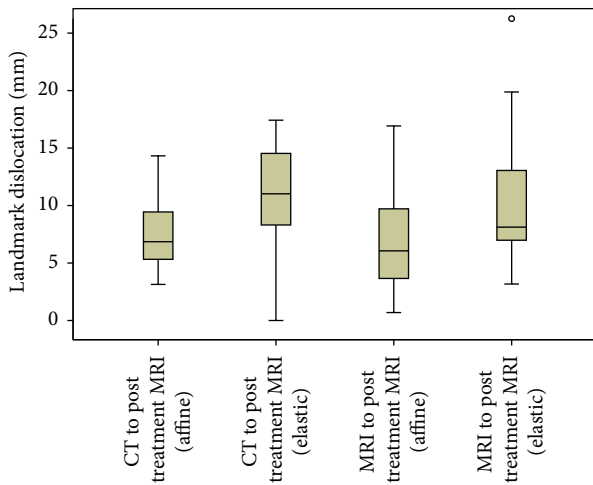


FIGURE 2: Boxplot of standard deviation of different registration methods to postinterventional MRI.

per liver. Interventional liver MRI and CT examinations were performed within one hour. The paired t -test was used to compare landmark dislocation between both registration methods. The first column of Table 5 shows that our method has an average landmark dislocation of 4.32 mm. Affine registration yields a significantly ($P = 0.000001$) smaller dislocation of 3.26 mm.

The difference between the two registration methods was also investigated using the Wilcoxon signed-rank test, where the correlation value between the two dislocation tests was also calculated. No significant correlation between the registration accuracy of both methods was found, with landmarks using the Wilcoxon signed-rank test. The correlation between landmark dislocations of affine and elastic registration was found to be 0.49. Therefore, registration accuracy did not significantly depend on individual image

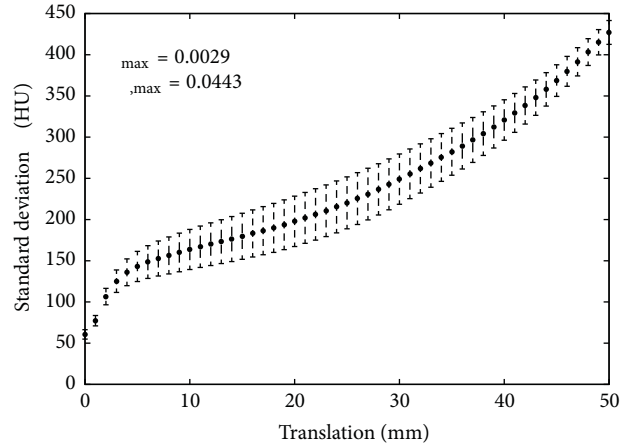


FIGURE 3: Characteristics of the standard deviation of image intensity differences after translation with the error bars demonstrating the standard error.

quality. This indicates that the landmarks were well set and are very well suited for our evaluation purpose.

Furthermore, the registration methods were compared using interventional and follow-up image datasets acquired 12 weeks later. The results for coregistration of CT to follow-up MRI and interventional MRI to follow-up MRI are presented in Table 5 and in the boxplot in Figure 2, respectively. There is a clear drop in quality for both affine and elastic registrations, which is attributable to greater deformation resulting from the long interval between the two examinations. In comparison to affine registration, our method shows nearly two times greater degradation in each case. Moreover, there are also some cases in which our method did not perform better (compare N_p and N_l in Table 5).

5. Discussion

This paper presents a novel approach of elastic registration based on the coregistration of surface and volume interpolation. An important feature of our approach is that volume deformation is interpolated solely from geometric changes of the surface. We validated our approach by comparison with affine registration as the gold standard. We performed a series of tests advancing from rigid objects (the kidney), to predominantly affinely deformed objects (liver with interventional images), to elastically deformed objects (liver with follow-up images). In the last test, the liver was definitely strongly deformed due to the localized effects of brachytherapy irradiation.

Applied to the kidney, our registration method significantly improves movement correction compared with affine registration. The kidney is a relatively rigid organ and there is relatively little deformation in the 4D CT time series due to short duration of image acquisition. The result indicates that our elastic registration method performs well based on effective first correction of affine registration and can adequately correct for displacement of rigid organs such as

the kidney when there is relatively little deformation inside the organ.

In contrast, for multimodal elastic registration of the liver, which is more elastic than the kidney and was deformed by irradiation in our tests, our method showed poorer performance in terms of quality compared with the twelve-parameter affine registration method. Landmark dislocation determined with affine registration seems to be a quasigold standard, which yielded 1.06 mm dislocation for quasi-simultaneously acquired interventional MRI and CT, 5.40 mm for interventional CT and a follow-up MRI, and 4.14 mm for interventional MRI and follow-up MRI. The poorer image quality of interventional MRI (signal-to-noise ratio, signal homogeneity, and spatial resolution) reduces registration accuracy for affine registration and especially for elastic registration. In principle, elastic registration should improve matching of a liver deformed by radiation treatment. The elastic registration method applied in the present study uses only information on the liver surface. In contrast, the affine registration method uses the image information of the entire liver, thus yielding a more accurate registration result. A technique using additional internal information beneath the surface might yield better results [10].

A limitation of the present study as well as of most studies using real medical images is the reliability of the validation method. Often, investigators use artificial image data for validation of their registration method, failing to take real registration problems into account. Several approaches have been proposed to validate registration accuracy; for example, Schnabel et al. validated their elastic registration method using a biomechanical model [36]. In the appendix to this paper, we demonstrate that the standard deviation in an ROI might also be a measure for comparing different coregistration methods, for example, comparison of affine registration with elastic registration as applied in the current study or by Rueckert et al. [13]. Registration accuracy can be estimated absolutely by comparing the discrepancy of the actual registration with that of landmarks defined by experts. To reduce further intra- and interexpert variability, we additionally applied an iterative expectation maximization method using multiple segmentations [33, 34].

6. Conclusions

Existing methods of image registration yield unreliable results when applied to register an organ, such as the liver, that has been transformed, for example, by treatment. A more sophisticated method would be useful in this case. We have tested an approach based on coregistration of organ surfaces and interpolation of internal space. The technique has been shown to work when applied to rigid organs. However, the method was developed for application to serial datasets acquired to monitor the outcome of treatment. Our data show that the method yields unsatisfactory results when used to register an organ, such as the liver, that has been transformed by treatment, for example, radiation therapy.

Obviously, taking into account treatment-related changes on the surface is not sufficient to determine internal changes

of the liver. Thus, to monitor radiation therapy of the liver, we need an elastic registration approach that uses surface information as well as information on internal organ structures in order to yield better results than 12-parameter affine registration.

Appendix

A. Standard Deviation of Image Intensity as Goodness Feature

A.1. Theory. We assume that the change in intensity is small in the region of interest (ROI) but large between the ROI and its background. Therefore, a more precise registration method should yield a smaller variance of intensity and poorer registration results when there is significantly larger variance in the image signal difference inside the ROI of the registered image. The standard deviation of the signal intensities of the reference and the coregistered image can be used as a measure.

A.2. Methods of Experimental Verification. The assumption was validated using two kidneys segmented by experts. The standard deviation of intensity between image intensities was determined after translation of the kidney image. We used five images from $P.\#1$ and four from $P.\#2$. The measurement was taken after every expanding translation with a step length of one voxel (1 mm). The greatest translation appropriated two times the maximum movement of the kidney that was estimated using surface registration between the kidneys. Each measurement was repeated 3000 times using randomly chosen translations in varying directions. For each kidney the average over all repetitions of each translation step was used. Finally, the average signal difference overall kidneys was calculated. In order to show the significance of the changes we further applied two different paired t -tests: the first one compared the changes between each step and zero translation and the second compared between neighboring steps.

A.3. Results of Experimental Verification. The dependence of the signal intensity difference on the dislocation between reference and coregistered image is demonstrated in Figure 3. The large number of repetitions yielded maximum standard error of 1.68%, represented by the error bar. A continuous increase in the standard deviation of the image difference with dislocation is demonstrated. Maximum significance between neighboring steps is $p_{N,\max} = 0.0443$; maximum significance against zero translation is $p_{\max} = 0.0029$. Thus, the reduction in standard deviation after each translation step of one voxel can be interpreted as a quality degradation of registration.

Acknowledgments

The authors would like to thank Professor Bernd Hamm and Professor Volker Budach for supporting the study.

References

- [1] C. Wybranski, M. Seidensticker, K. Mohnike et al., "In vivo assessment of dose volume and dose gradient effects on the tolerance dose of small liver volumes after single-fraction high-dose-rate ^{192}Ir irradiation," *Radiation Research*, vol. 172, no. 5, pp. 598–606, 2009.
- [2] T. Franiel, L. Lüdemann, M. Taupitz, D. Böhmer, and D. Beyersdorff, "MRI before and after external beam intensity-modulated radiotherapy of patients with prostate cancer: the feasibility of monitoring of radiation-induced tissue changes using a dynamic contrast-enhanced inversion-prepared dual-contrast gradient echo sequence," *Radiotherapy and Oncology*, vol. 93, no. 2, pp. 241–245, 2009.
- [3] J. M. Stahl, Y. Y. Chi, and W. A. Friedman, "Repeat radiosurgery for intracranial arteriovenous malformations," *Neurosurgery*, vol. 70, no. 1, pp. 150–154, 2012.
- [4] D. Prochnow, D. Beyersdorff, C. Warmuth, M. Taupitz, O. Gemeinhardt, and L. Lüdemann, "Implementation of a rapid inversion-prepared dual-contrast gradient echo sequence for quantitative dynamic contrast-enhanced magnetic resonance imaging of the human prostate," *Magnetic Resonance Imaging*, vol. 23, no. 10, pp. 983–990, 2005.
- [5] S. S. Kety, "Theory of blood-tissue exchange and its application to measurement of blood flow," *Methods in Medical Research*, vol. 8, pp. 223–227, 1960.
- [6] L. Lüdemann, B. Nafz, F. Elsner et al., "Absolute quantification of regional renal blood flow in swine by dynamic contrast-enhanced magnetic resonance imaging using a blood pool contrast agent," *Investigative Radiology*, vol. 44, no. 3, pp. 125–134, 2009.
- [7] V. Noblet, C. Heinrich, F. Heitz, and J. P. Armspach, "Retrospective evaluation of a topology preserving non-rigid registration method," *Medical Image Analysis*, vol. 10, no. 3, pp. 366–384, 2006.
- [8] V. Noblet, C. Heinrich, F. Heitz, and J. P. Armspach, "3-D deformable image registration: a topology preservation scheme based on hierarchical deformation models and interval analysis optimization," *IEEE Transactions on Image Processing*, vol. 14, no. 5, pp. 553–566, 2005.
- [9] S. Klein, M. Staring, K. Murphy, M. A. Viergever, and J. P. W. Pluim, "Elastix: a toolbox for intensity-based medical image registration," *IEEE Transactions on Medical Imaging*, vol. 29, no. 1, pp. 196–205, 2010.
- [10] K. Cao, K. Ding, J. M. Reinhardt, and G. E. Christensen, "Improving intensity-based lung CT registration accuracy utilizing vascular information," *International Journal of Biomedical Imaging*, vol. 2012, Article ID 285136, 17 pages, 2012.
- [11] X. Zhuang, K. S. Rhode, R. S. Razavi, D. J. Hawkes, and S. Ourselin, "A registration-based propagation framework for automatic whole heart segmentation of cardiac MRI," *IEEE Transactions on Medical Imaging*, vol. 29, no. 9, pp. 1612–1625, 2010.
- [12] F. Dru, P. Fillard, and T. Vercauteren, "An ITK implementation of the symmetric log-domain diffeomorphic demons algorithm," *The Insight Journal*, 2010.
- [13] D. Rueckert, L. I. Sonoda, C. Hayes, D. L. Hill, M. O. Leach, and D. J. Hawkes, "Nonrigid registration using free-form deformations: application to breast MR images," *IEEE Transactions on Medical Imaging*, vol. 18, no. 8, pp. 712–721, 1999.
- [14] M. Modat, G. R. Ridgway, Z. A. Taylor et al., "Fast free-form deformation using graphics processing units," *Computer Methods and Programs in Biomedicine*, vol. 98, no. 3, pp. 278–284, 2010.
- [15] M. Kass, A. Witkin, and D. Terzopoulos, "Snakes: active contour models," *International Journal of Computer Vision*, vol. 1, no. 4, pp. 321–331, 1988.
- [16] T. W. Sederberg and S. R. Parry, "Free-form deformation of solid geometric models," *Computer Graphics*, vol. 20, no. 4, pp. 151–160, 1986.
- [17] E. C. Hildreth, "Edge detection," Memo 858, Massachusetts Institute of Technology, Artificial Intelligence Laboratory, Cambridge, Mass, USA, 1985.
- [18] J. A. Sethian, *Level Set Methods and Fast Marching Methods: Evolving Interfaces in Computational Geometry, Fluid Mechanics, Computer Vision, and Materials Science*, vol. 3, Cambridge University Press, 2nd edition, 1999.
- [19] S. J. Osher and R. P. Fedkiw, *Level Set Methods and Dynamic Implicit Surfaces*, Springer, 1st edition, 2002.
- [20] R. Courant, K. Friedrichs, and H. Lewy, "On the partial difference equations of mathematical physics," *IBM Journal of Research and Development*, vol. 11, no. 2, pp. 215–234, 1967.
- [21] K. Levenberg, "A method for the solution of certain problems in least squares," *Quarterly of Applied Mathematics*, vol. 2, pp. 164–168, 1944.
- [22] D. W. Marquardt, "An algorithm for least-squares estimation of nonlinear parameters," *Journal of the Society for Industrial and Applied Mathematics*, vol. 11, no. 2, pp. 431–441, 1963.
- [23] J. Ahlberg, *Active contours in three dimensions [M.S. thesis]*, Linköping University, Linköping, Sweden, 1996.
- [24] P. A. Yushkevich, J. Piven, H. C. Hazlett et al., "User-guided 3D active contour segmentation of anatomical structures: significantly improved efficiency and reliability," *NeuroImage*, vol. 31, no. 3, pp. 1116–1128, 2006.
- [25] T. H. Cormen, C. E. Leiserson, R. L. Rivest, and C. Stein, *Introduction to Algorithms*, The MIT Press, 2nd edition, 2001.
- [26] J. Ricke, M. Thormann, M. Ludewig et al., "MR-guided liver tumor ablation employing open high-field 1.0T MRI for image-guided brachytherapy," *European Radiology*, vol. 20, no. 8, pp. 1985–1993, 2010.
- [27] Y. J. Zhang, "A survey on evaluation methods for image segmentation," *Pattern Recognition*, vol. 29, no. 8, pp. 1335–1346, 1996.
- [28] W. R. Crum, O. Camara, and D. L. G. Hill, "Generalized overlap measures for evaluation and validation in medical image analysis," *IEEE Transactions on Medical Imaging*, vol. 25, no. 11, pp. 1451–1461, 2006.
- [29] L. R. Dice, "Measures of the amount of ecologic association between species," *Ecology*, vol. 26, no. 3, pp. 297–302, 1945.
- [30] V. Chalana and Y. Kim, "A methodology for evaluation of boundary detection algorithms on medical images," *IEEE Transactions on Medical Imaging*, vol. 16, no. 5, pp. 642–652, 1997.
- [31] G. Gerig, M. Jomier, and M. Chakos, "Valmet: a new validation tool for assessing and improving 3D object segmentation," in *Medical Image Computing and Computer-Assisted Intervention (MICCAI '01)*, W. J. Niessen and M. A. Viergever, Eds., vol. 2208 of *Lecture Notes in Computer Science*, pp. 516–523, Springer, Berlin, Germany, 2001.
- [32] M. D. Levine and A. M. Nazif, "Dynamic measurement of computer generated image segmentations," *IEEE Transactions on Pattern Analysis and Machine Intelligence*, vol. 7, no. 2, pp. 155–164, 1985.

- [33] S. K. Warfield, K. H. Zou, M. R. Kaus, and W. M. Wells, "Simultaneous validation of image segmentation and assessment of expert quality," in *Proceedings of the International Symposium on Biomedical Imaging: Macro to Nano*, pp. 94–97, Washington, DC, USA, July 2002.
- [34] S. K. Warfield, K. H. Zou, and W. M. Wells, "Validation of image segmentation and expert quality with an expectation-maximization algorithm," in *Proceedings of the 5th International Conference on Medical Image Computing and Computer-Assisted Intervention (MICCAI '02)*, pp. 298–306, Springer, 2002.
- [35] P. Viola and W. M. Wells, "Alignment by Maximization of Mutual Information," *International Journal of Computer Vision*, vol. 24, no. 2, pp. 137–154, 1997.
- [36] J. A. Schnabel, C. Tanner, A. D. Castellano-Smith et al., "Validation of nonrigid image registration using finite-element methods: application to breast MR images," *IEEE Transactions on Medical Imaging*, vol. 22, no. 2, pp. 238–247, 2003.

Research Article

Attenuation Correction for Small Animal PET Images: A Comparison of Two Methods

Daniela D'Ambrosio,^{1,2} Federico Zagni,¹ Antonello E. Spinelli,³ and Mario Marengo¹

¹ Medical Physics Department, University Hospital S. Orsola-Malpighi, Via Massarenti 9, 40138 Bologna, Italy

² Medical Physics Department, IRCCS Fondazione Maugeri, Via Salvatore Maugeri 4, 27100 Pavia, Italy

³ Medical Physics Department, IRCCS San Raffaele, Via Olgettina 60, 20132 Milano, Italy

Correspondence should be addressed to Mario Marengo; mario.marengo@aosp.bo.it

Received 18 December 2012; Revised 9 March 2013; Accepted 10 March 2013

Academic Editor: Peng Feng

Copyright © 2013 Daniela D'Ambrosio et al. This is an open access article distributed under the Creative Commons Attribution License, which permits unrestricted use, distribution, and reproduction in any medium, provided the original work is properly cited.

In order to extract quantitative parameters from PET images, several physical effects such as photon attenuation, scatter, and partial volume must be taken into account. The main objectives of this work were the evaluation of photon attenuation in small animals and the implementation of two attenuation correction methods based on X-rays CT and segmentation of emission images. The accuracy of the first method with respect to the beam hardening effect was investigated by using Monte Carlo simulations. Mouse- and rat-sized phantoms were acquired in order to evaluate attenuation correction in terms of counts increment and recovery of uniform activity concentration. Both methods were applied to mice and rat images acquired with several radiotracers such as ¹⁸F-FDG, ¹¹C-acetate, ⁶⁸Ga-chloride, and ¹⁸F-NaF. The accuracy of the proposed methods was evaluated in heart and tumour tissues using ¹⁸F-FDG images and in liver, kidney, and spinal column tissues using ¹¹C-acetate, ⁶⁸Ga-chloride, and ¹⁸F-NaF images, respectively. *In vivo* results from animal studies show that, except for bone scans, differences between the proposed methods were about 10% in rats and 3% in mice. In conclusion, both methods provide equivalent results; however, the segmentation-based approach has several advantages being less time consuming and simple to implement.

1. Introduction

Positron emission tomography is a quantitative imaging technique, capable to provide accurate values of radiotracer concentration in each voxel of the reconstructed volume. The knowledge of radiopharmaceutical concentration is important because, combined with adequate mathematical models, it allows to evaluate several physiological parameters of interest, such as perfusion, glucose metabolic rate, and receptors density [1]. In order to obtain an accurate quantification of radiotracer concentration, several physical factors must be taken into account, such as attenuation (AC) [2], scatter [3], and partial volume correction (PVC) [4]. In this work, the attention was focused on attenuation correction for small animal PET images, which is well known to be relevant for human patients [5] but could be also significant for small animals as well. Attenuation correction has been extensively discussed in the literature for human PET and SPECT studies;

however, only few papers focus on AC for small animals [6–11].

There are several methods to obtain attenuation maps that could be employed to correct PET images for attenuation. They are mainly grouped into two categories: transmission and transmissionless methods.

The first category of methods is based on the acquisition of a transmission image of the subject. The most used approaches are based on (1) transmissive image using, for example, rotating or annular ⁶⁸Ga/⁶⁸Ge sources, (2) segmented transmissive image, and (3) X-ray CT image. Transmission scanning can be performed both in coincidence and in single mode.

A quite simple approach consists of using an annular ⁶⁸Ga/⁶⁸Ge source surrounding the object and acquiring a transmission image in coincidence mode; however, the resulting image can be very noisy. An alternative approach is to use a rotating rod source; in this case, scatter and random

coincidences decrease because only the lines of response (LORs) collinear with the rod source are accepted. The rod source is generally very active, and, thus, the detector near the source exhibits a high dead time causing an important loss of counts [13]. The same problem happens also in the case of single photon source; in order to acquire a good quality transmissive image using a fully 3D scanner, a point source with a very high radioactivity concentration must be used. This problem can be solved with use of collimated, single photon, point sources [14, 15]. However, the single mode acquisition method has also several disadvantages: (1) a significant scatter component is included in the transmissive image, and (2) an energy scaling of the attenuation map is needed because of the different photon energy of the transmissive source. For example, ^{137}Cs emits 662 keV photons. In this case, attenuation maps can be obtained segmenting transmissive images, and the known attenuation coefficients at 511 keV are assigned to each of the segmented regions [16, 17]. The last and most used category of transmission methods is based on the acquisition of CT images. Analogously to the method described before, energy scaling of the attenuation coefficients to 511 keV is needed.

Transmission methods are more accurate when estimating attenuation maps because they take into account the inhomogeneities of the object attenuation coefficients. Each of them has also several drawbacks; they are more time-consuming, as the animal has to be anesthetized for a long time and also receives larger doses of radioactivity compared to transmissionless methods. Transmissive PET images do not suffer from coregistration problems that may introduce artifacts in the attenuation map, but they can be very noisy. In order to reduce the noise in the transmissive PET images, segmentation was introduced, but other problems linked to time and dose still remained.

Transmissionless methods are carried out with manual or automatic delineation of body edges directly on emissive image assuming a uniform distribution of attenuation coefficients inside the object [18, 19], or by automatic image segmentation using a fuzzy clustering algorithm [20]. Transmissionless methods are less accurate in delineating the edges and provide a less detailed attenuation map, but they have the advantages of being less time consuming, do not increase the dose to the animal, and allow for noiseless attenuation maps. Moreover, coregistration procedure is not required, and thus the attenuation map are less sensitive to image artifacts.

In this work, two attenuation correction methods are presented: a CT-based method and a transmissionless AC method based on segmentation of PET data. We firstly estimated the magnitude of attenuation effect in small animals using mice and rat phantoms. In order to implement the X-ray based method, we calibrated the small animal CT scanner and we obtained a correspondence between CT and 511 keV attenuation coefficients. In order to evaluate the accuracy of the CT-based method with respect to beam-hardening, we performed Monte Carlo simulation for rat-sized objects. As CT scan adds either acquisition time or dose to the animal, we propose a further method based on segmentation of PET images. PET data segmentation may not provide accurate attenuation maps because, depending on the radiotracer

used, the body edges are not always well delineated. We acquired images using several radiotracers such as ^{18}F -FDG, ^{11}C -acetate, ^{68}Ga -chloride, and ^{18}F -NaF and evaluated the accuracy of the PET-based method with respect to CT-AC.

2. Methods and Materials

2.1. Photon Attenuation. As it is well known, transmission of 511 keV photons crossing matter is expressed by an exponential law formulated as follows:

$$\Phi = \Phi_0 e^{-\int_L \mu(x,y) dl}, \quad (1)$$

where Φ and Φ_0 are the transmitted and incident photon fluences, L is the path of the photon through the object, and $\mu(x, y)$ is the linear attenuation coefficient map.

The exponential term, which we refer to as P , is the probability that a photon reaches the detector. In PET, events are not detected if at least one of the two annihilation photons is absorbed by the object. In this case, the number of events for each LOR is reduced. The probability that an annihilation event is recorded is given by the product of the probability of each photon reaching the detectors, as expressed by the following equation:

$$P = P_1 P_2 = e^{-\int_{L_1(s,\phi)} \mu(x,y) dl} e^{-\int_{L_2(s,\phi)} \mu(x,y) dl} = e^{-\int_{L(s,\phi)} \mu(x,y) dl}, \quad (2)$$

where $L = L_1 + L_2$, ϕ is the projection angle, and s is the radial position. As we can see in (2), the probability depends on the total length of the path of the two annihilation photons in the object that in PET is the object thickness along the LOR. The value of L is related to the projection angle and the radial position. The equation describing the measured projections is the attenuated Radon transform, formulated as follows:

$$p(s, \phi) = \int_{L(s,\phi)} f(x, y) e^{-\int_{L(s,\phi)} \mu(x,y) dl} dr, \quad (3)$$

where $p(s, \phi)$ are the projection data at angle ϕ and bin s , $f(x, y)$ is a function representing the original activity concentration image, $\mu(x, y)$ is the attenuation coefficient map, and $L(s, \phi)$ represents the LOR.

2.2. Systems Descriptions. PET images were acquired with the eXplore Vista preclinical PET tomograph (General Electric) [21]. The scanner allows to acquire PET images using three different energy windows (100–700, 250–700, and 400–700 keV). For our purposes, all images were acquired using the 400–700 keV energy window. The scanner detector system consists of 36 detector blocks, arranged in two rings of 11.8 mm diameter. Each block is a 13×13 array of 1.45 mm square phoswich crystals: a Lutetium Yttrium Orthosilicate (LYSO) crystal of 7 mm depth optically coupled to an 8 mm depth crystal of Gadolinium Orthosilicate (GSO). This design allows to obtain depth of interaction information [22]. The transverse and axial field of view (FOV) are equal to 6.9 cm and 4.6 cm, respectively. No corrections for randoms and scatter were performed in this study. All the images were

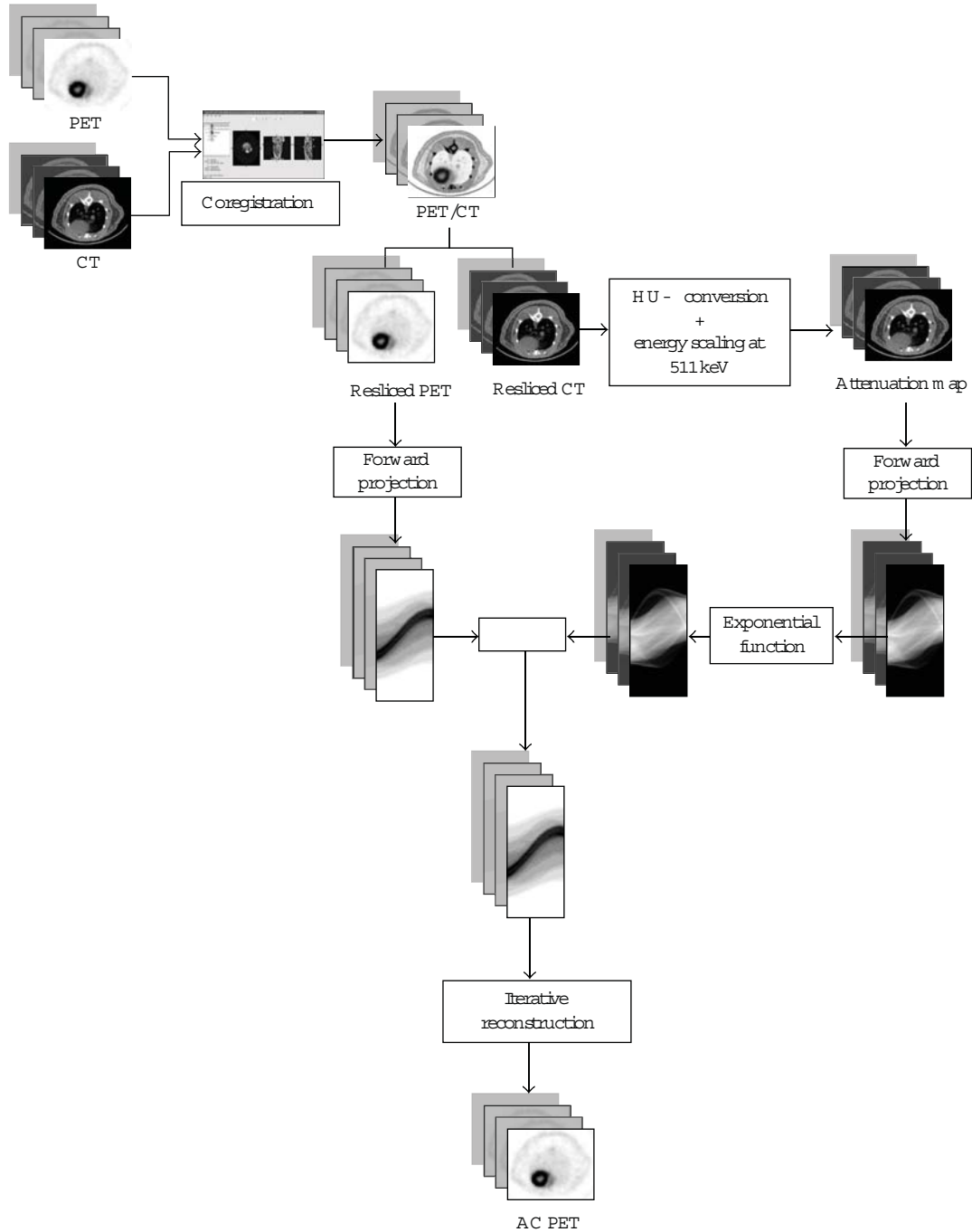


FIGURE 1: Schematic diagram of CT-AC method. CT-AC can be divided into three steps: coregistration, attenuation correction according to the attenuated Radon transform (see (3)), and iterative reconstruction. More details can be found in Section 2.3.1.

reconstructed using 2D-OSEM algorithm [23] after Fourier rebinning (FORE) [24]. CT images were acquired using the eXplore Locus small animal CT tomography (General Electric). The tube voltage was 80 kV and the current was $450 \mu\text{A}$. The system is characterized by a fixed anode with a Tungsten target source. The X-ray detector is a CCD array coupled to a Cesium Iodide (CsI) scintillation crystal. The scanner allows to acquire and to reconstruct images with different pixel binning and, thus, with different resolution

levels ($27\text{--}93 \mu\text{m}$). The transaxial FOV dimension is equal to 8 cm for acquisition at $93 \mu\text{m}$ resolution. The axial FOV is the same for all acquisition protocols, and it is equal to 4.5 cm. For our purposes, all images were acquired using a $93 \mu\text{m}$ resolution. Image reconstruction was performed with the Feldkamp cone beam algorithm [25].

2.3. Attenuation Correction Methods. All the images acquired with the eXplore Vista were attenuation-corrected using the

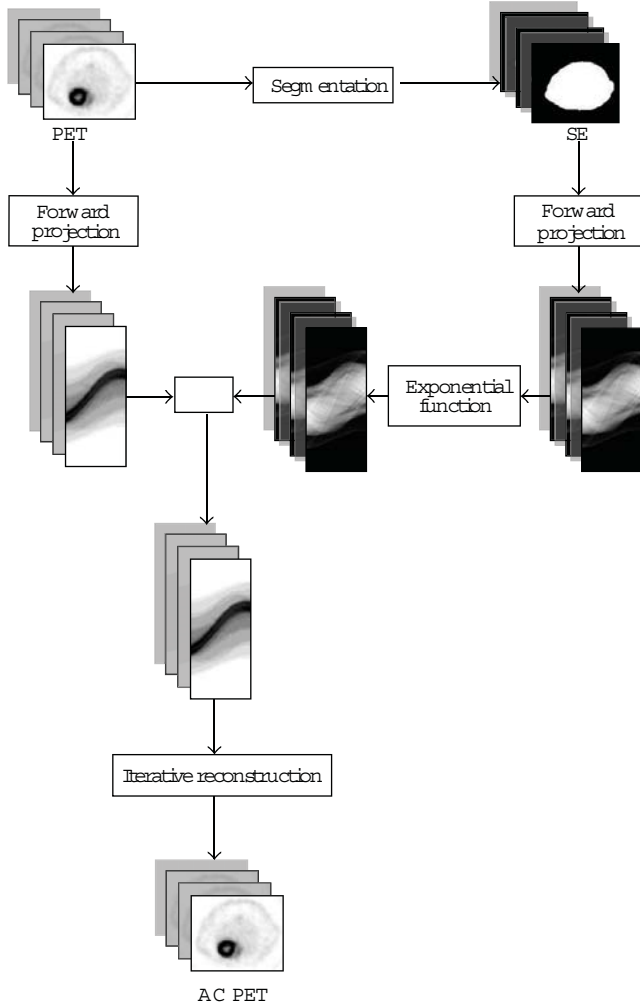


FIGURE 2: Schematic diagram of SE-AC method described in Section 2.3.2.

CT and SE methods as described later. The schematic diagrams of CT-AC and SE-AC methods are shown in Figures 1 and 2.

2.3.1. CT-AC Method. The CT AC method is based on a conversion between HU and the corresponding linear attenuation coefficients at 511 keV. CT images are useful because they provide detailed attenuation coefficients maps. The most important problem when using CT images is the beam hardening effect. In order to investigate the accuracy of the CT AC method, we used PeneloPET, a Monte Carlo code for PET simulations based on PENELOPE [27]. The geometry and composition of both rat-phantoms and eXplore Vista scanner were implemented to match those employed in the real acquisitions. We chose to simulate only the rat-phantom because the beam hardening effect is more important in this case than in mouse-sized objects. The CT-based attenuation corrected image was compared with images simulated without attenuation material. On both images, line profiles and region of interest (ROI) analysis

TABLE 1: Density and attenuation coefficient used to calibrate the CT scanner. Data were calculated by Hubbell and Seltzer and were published by the National Institute of Standards and Technology [26].

Material	Density ($\text{g} \cdot \text{cm}^{-3}$)	Attenuation coefficient at 511 keV (cm^{-1})
Air	0.001	0
Polyethylene	0.930	0.0925
Polystyrene	1.060	0.0994
Water	1.000	0.0969
Acrylic	1.190	0.1120
Polytetrafluoroethylene (Teflon)	2.250	0.1886
Aluminum	2.699	0.2280

were performed. The calibration procedure of the CT was performed by using the inserts of Mini CT QC Phantom 76–430 of Nuclear Associates. The inserts are cylinders having different values of density and linear attenuation coefficients at 511 keV. The data published by the National Institute of Standards and Technology are in Table 1 [26]. CT-AC was implemented using Matlab, and more precisely, PET and the calibrated attenuation map images were forward projected in order to perform attenuation correction according to the attenuated Radon transform (see (3)).

A CT image of each cylinder was acquired and a small (ROI) was drawn on the image in order to calculate the mean value of HU. The attenuation coefficients at 511 keV were plotted with respect to the measured HU, and a quadratic fit to the data was performed.

2.3.2. Segmentation of Emission Image AC Method. Segmentation of emission image by a global threshold was performed by means of a Matlab code, in order to obtain a 2-level image, corresponding to air and soft tissues. For PET images of phantoms, the contours are always clear, and, thus, the segmentation is quite easy to perform. In animal PET images, the detection of body edges depends on the biodistribution of the radiotracer injected. To assess applicability of the SE method, PET images with different radiotracers were acquired.

2.4. Phantom Data. In order to evaluate the effect of photon attenuation in PET images and the accuracy of the attenuation correction methods described in previous section, several phantoms studies were acquired. Two cylindrical phantoms with different diameters were filled with different concentration of [^{18}F]-fluorodeoxyglucose (^{18}F -FDG) and scanned in both PET and CT modality:

- (i) a mouse-sized phantom, filled with uniform activity concentration;
- (ii) a rat-sized phantom, filled with uniform activity concentration;
- (iii) a rat-sized phantom with a hot sphere inside (sphere to background ratio equal to 4).

A syringe of 30 mm diameter filled to 30 cc was used as mouse-sized phantom, while a cylindrical phantom with diameter of 50 mm and length of 80 mm was used as rat-sized phantom. The mouse- and rat-sized phantoms were filled with a solution of ^{18}F -FDG with activity concentrations of about 1 MBq/cc and 0.5 MBq/cc, respectively. Several zeolites soaked with a small amount of ^{18}F -FDG (about 5 MBq/cc) were fixed around the two phantoms in order to use them as fiducial marks in the coregistration procedure [28]. For each phantom, a 20-minute PET scan and a 6-minute CT acquisition were performed. In order to align PET and CT, the two images were coregistered using rigid body transformation implemented in AMIDE [29].

In order to measure the improvement obtained with AC, line profiles and ROI analysis were performed. The recovery values RV for each AC method were calculated with the following equations:

$$RV_{CT} = \frac{ROI_{AC-CT} - ROI_{NC}}{ROI_{AC-CT}}, \quad (4)$$

$$RV_{SE} = \frac{ROI_{AC-SE} - ROI_{NC}}{ROI_{AC-CT}},$$

where ROI_{NC} , ROI_{AC-CT} , and ROI_{AC-SE} are the mean values in a ROI drawn on the uncorrected image, on the AC-CT, and on the AC-SE image, respectively. In order to evaluate the shape recovery, we calculated also the flatness of the profile (i.e., the relative difference in the number of counts between the edges and the centre of a uniform phantom) with the following formula:

$$F = \frac{C_{\max} - C_{\min}}{C_{\min}}, \quad (5)$$

where C_{\max} is the maximum and C_{\min} is the minimum of the count profile. The rat-sized phantom with a hot sphere was used to simulate a PET image of a hot lesion. The recovery values RV in the sphere for each AC method were evaluated.

2.5. Animal Data. In order to test the attenuation correction methods and particularly the SE-AC on animal images, PET and CT scans of mice and rats were performed using different radiotracers, being all animals studies approved by the Ethical Committee of our institution:

- (i) 1 rat and 2 mice were injected with ^{18}F -FDG (an oncological and a cardiac study);
- (ii) 3 further rats were injected with ^{18}F -NaF, ^{11}C -acetate, and ^{68}Ga -chloride.

All animals were anesthetized with 3%–5% of sevoflurane and 1l/min of oxygen and were injected intravenously in the tail with activity of about 30 and 50 MBq, respectively. PET acquisitions of 20 minutes were performed after an uptake time depending on the radiotracer. The uptake was of about one hour for ^{18}F -FDG and ^{18}F -NaF studies, and about 30 minutes for ^{68}Ga -chloride acquisitions. The ^{11}C -acetate images were acquired immediately after the injection. A CT

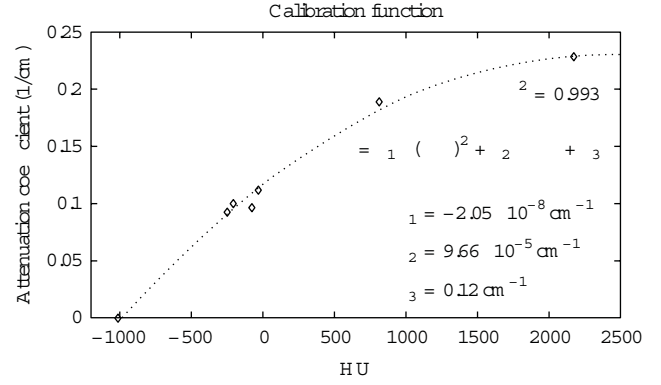


FIGURE 3: Calibration function to convert HU into attenuation coefficient at 511 keV. Attenuation coefficient at 511 keV is plotted with respect to CT numbers. This function is used to create the attenuation map to correct PET images.

scan of 6 minutes was then performed for each animal after PET acquisition. PET and CT images were coregistered in order to perform AC. The segmentation process was applied on each PET image, and the SE-AC method was tested on animals studied with different radiopharmaceuticals. In order to compare the two methods, CT-AC was performed for each image as well. We analyzed all the images performing profiles across an axial slice of a particular anatomical region related to the radiotracer used and calculating the mean value in the anatomical ROI. Thus, we calculated the recovery values according to (4) and evaluated the segmentation-based AC method on heart, spinal column, liver, and kidneys using ^{18}F -FDG, ^{18}F -NaF, ^{11}C -acetate, and ^{68}Ga -chloride, respectively.

3. Results

3.1. CT Images Calibration. In this section the results of CT images calibration are presented. The calibration function (Figure 3) is given by the following equation:

$$\mu = a_1(\text{HU})^2 + a_2\text{HU} + a_3, \quad (6)$$

where μ is the attenuation coefficient at 511 keV, HU is the CT number measured from the image, and the fit coefficients are $a_1 = -2.05 \cdot 10^{-8} \text{ cm}^{-1}$, $a_2 = 9.66 \cdot 10^{-5} \text{ cm}^{-1}$, and $a_3 = 0.12 \text{ cm}^{-1}$. The correlation coefficient r^2 was equal to 0.993.

3.2. Evaluation of CT-Based Attenuation Map by Monte Carlo Simulation. In this section, axial slices of real and simulated PET images, before and after CT-AC correction, are shown. More precisely, Figure 4 shows a transaxial slice of original PET and CT-AC images of the rat-sized phantom. Profiles traced across them are shown in Figure 6. They show a count increment of about 40%, and the flatnesses calculated according to (5) for corrected and uncorrected images are about 1% and 22%, respectively. Figure 5 shows an axial

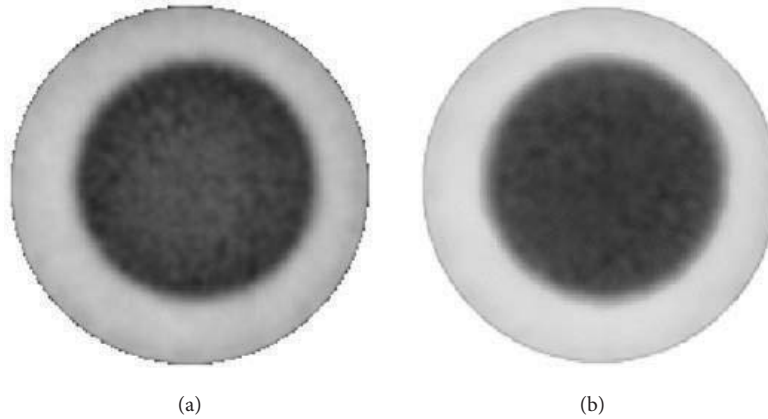


FIGURE 4: Transaxial slices of rat-phantom real PET images: original image (a) and attenuation corrected image using CT-based AC method (b). Note the uniformity in the AC image.

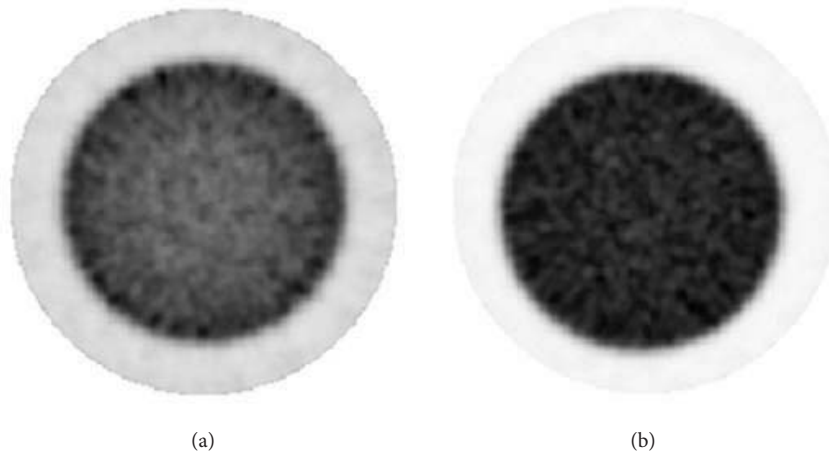


FIGURE 5: Transaxial slices of rat-phantom simulated PET images using PeneloPET. On the left side the image resulting from the simulation of uniform activity concentration with attenuation (a); on the right side the simulated image of uniform activity concentration without attenuation (b). Only in this case images were reconstructed using OSEM 3D [12].

slice of simulated PET images with and without attenuation. Profiles traced across the simulated images (see Figure 7) show an increment of counts and a shape recovery. In this case, the flatness of the profile across the uncorrected image is equal to 23%, and the counts increment without attenuation is also of the order of 40%. Then, the simulations predict the same behaviour with regard to attenuation as seen with the CT-AC procedure, thus validating the CT-AC method.

3.3. Phantom Studies. Figures 8 and 9 show profiles traced across the center of a transaxial slice of pre- and postcorrected images of the mouse-sized phantom filled with uniform activity concentration. As one can see, there is a significant improvement of image uniformity after AC. In particular, the profiles show the increment of coincidences and shape recovery. Table 2 summarized the counts measured in a ROI at the center of the slice and the flatness of the profile for the original PET, CT-AC, and SE-AC images for both phantom studies.

The values of the RV obtained from (4) show for both mouse- and rat-sized phantoms a significant count recovery. The differences between CT-based and SE-based AC RV are less than 2% and 3% for mouse and rat phantoms, respectively. Profiles traced across the images and flatness values show an improvement between pre- and postcorrected images. In rat-sized phantom, we observe the typical cupping artifact. After AC, the cupping disappears and count recovery is evident. As explained in the previous section, acquisition of a rat phantom including a hot sphere was performed. Figure 10 shows profiles across the hot sphere. The recovery of counts (calculated using (4)) in the hot sphere with respect to the original image for CT-AC, and SE-AC methods is showed in Table 2. The difference between the two methods is about 7%.

3.4. Animal Studies. In this section, results of attenuation correction of small animal images injected with several

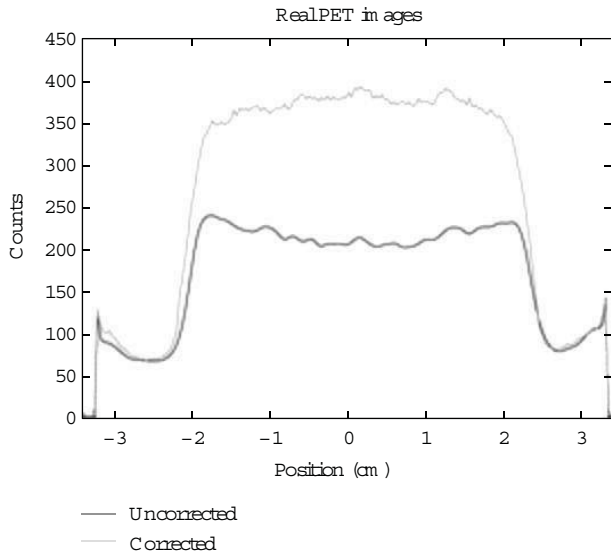


FIGURE 6: Profiles traced across the center of a transaxial slice of images reconstructed from PET acquisitions of a real rat-phantom.

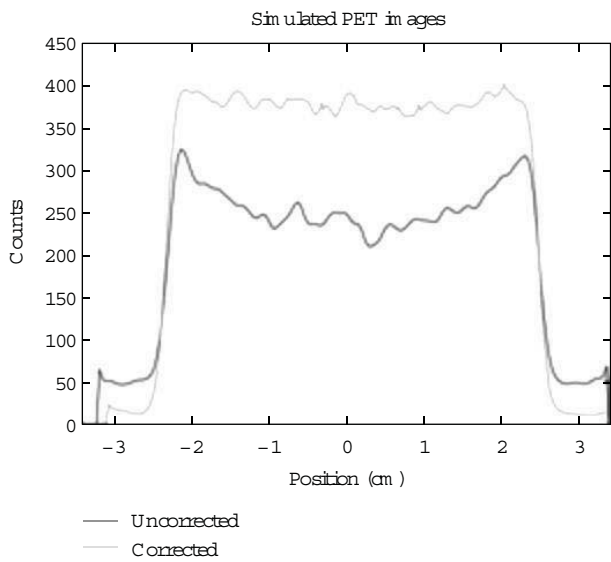


FIGURE 7: Profiles traced across the center of a transaxial slice of images reconstructed from PET acquisitions of a simulated rat-phantom.

radiotracers are presented. Figure 11 shows an example of CT image, segmented PET image, and the overlay between them.

On each graph, an axial slice of the animal image is displayed showing the position of the line profile. Moreover, for each animal study, a table summarizing the average values of specific ROI counts of uncorrected and corrected images is shown. The RV calculated from (4) is reported in each table. The thick line is traced across the original uncorrected image, and the dotted and full lines were traced across the SE-based and CT-based AC images, respectively. The position of the line profile in the PET image is shown in the right side of the plot.

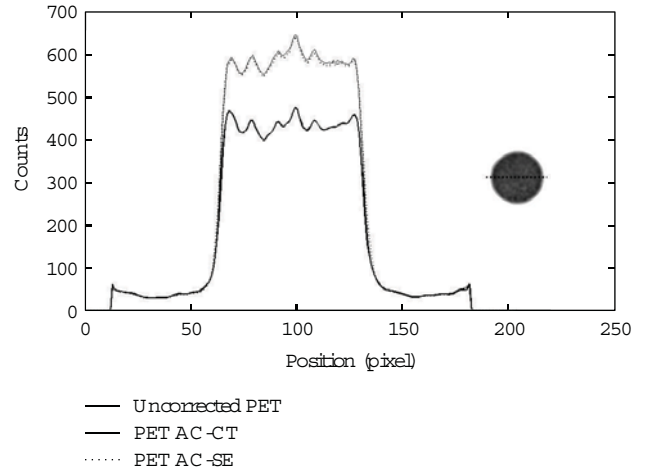


FIGURE 8: Profiles traced across the center of a cylindrical mouse-sized phantom filled with ^{18}F -FDG. The number of coincidences is plotted with respect to the position across the field of view. The thick line shows the profile across the original PET image, the dotted line shows the profile across the SE-AC image, and the full line is the profile across the image corrected with the CT-AC method.

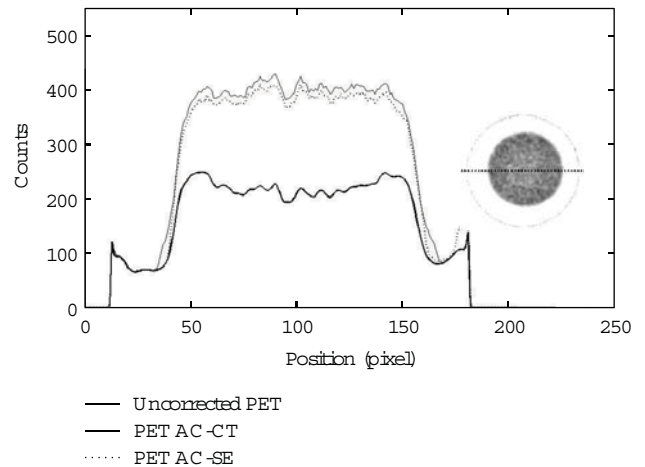


FIGURE 9: Profiles along the center of a rat-sized phantom uniformly filled with ^{18}F -FDG. The plot shows three lines; thick line is the count profile of the uncorrected PET image, and the dotted and full lines, respectively, show the profiles of the PET images corrected with the SE-AC and CT-AC method. A significant increment of counts and shape recovery for both AC images is clearly seen.

Figure 12 shows the profile across the mouse tumour. The peak on the right side of the profile is relative to the tumour. As one can see, the recovery of counts for both AC images is significant. Table 3 shows counts measured in an ROI inside the tumour. The same analysis was performed on cardiac PET image of a mouse in order to verify the performance of SE-AC method in the quantification of tracer uptake in the myocardium and in the left ventricle. Figure 13 shows the profile traced across the mouse heart. The two peaks in both AC images are well recovered, and, furthermore, they are very similar. More precisely, in Table 4, we show the average

TABLE 2: Average number of counts and recovery value measured on uniformly filled mouse and rat phantom images and in the hot sphere of a rat-sized phantom. For the uniformly filled phantoms, also the flatness is showed.

	Roi counts (cps)	RV (%)	Flatness
Mouse phantom			
Original PET image	429.68	—	3.1%
CT-AC image	623.02	31.0%	1.1%
SE-AC image	613.89	29.6%	1.2%
Rat phantom			
Original PET image	210.34	—	22.0%
CT-AC image	405.32	48.1%	1.2%
SE-AC image	396.17	45.8%	2.7%
Rat phantom with hot sphere			
Original PET image	452.79	—	—
CT-AC image	760.83	40.5%	—
SE-AC image	708.37	33.6%	—

TABLE 3: ROI counts measured in an ROI inside the tumour of a mouse obtained using ^{18}F -FDG images (the uncorrected and the two AC images) and recovery value (see (4)) calculated with the two AC methods.

	Roi counts (cps)	RV (%)
Original PET image	527.82	—
CT-AC image	716.94	26.4%
SE-AC image	726.13	27.7%

TABLE 4: ROI counts measured on the myocardium and in the left ventricle obtained using ^{18}F -FDG rat images. The RV calculated with (4) is shown for both CT-AC and SE-AC images.

	Roi counts (cps)	RV (%)
Original PET image		
Myocardium	3 463.70	—
Ventricle	1 975.00	—
CT-AC image		
Myocardium	4 478.60	22.7%
Ventricle	2 577.30	23.4%
SE-AC image		
Myocardium	4 393.40	20.8%
Ventricle	2 511.30	20.8%

value of counts in the myocardium and left ventricle for the three images and the relative recovery value for the two AC methods calculated with (4). The differences between RV obtained from the two methods are less than 3%.

In order to evaluate the effect of attenuation on cardiac rat images, the same analysis on the myocardium and in the left ventricle was performed on cardiac ^{18}F -FDG PET image of a rat. Figure 14 illustrates the profiles traced across the rat heart. In Table 5, the mean value of counts on the uncorrected and corrected images and the relative RV are shown. The differences between the SE-AC and CT-AC methods are less than 9%. As discussed in Section 2.3.2, when using ^{18}F -FDG, it is possible to see clearly the animal edges and, thus, to

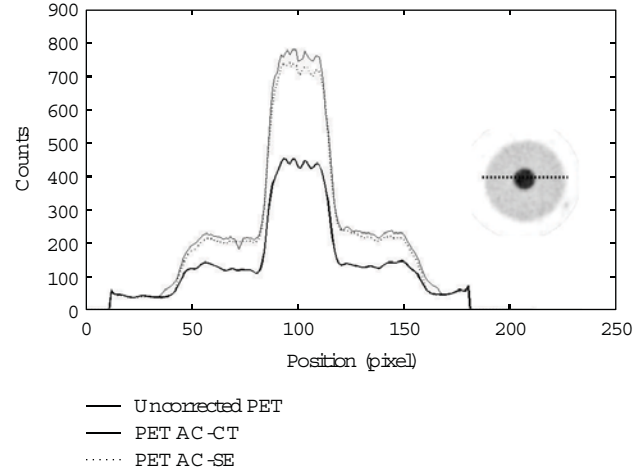


FIGURE 10: Counts measured on a line across the hot sphere using a cylindrical rat sized phantom with a hot background (sphere to background ratio is approximately equal to 4) against position in the field of view.

TABLE 5: Counts measured in an ROI inside the left ventricle and inside the myocardium of the ^{18}F -FDG rat image and of the AC ones. The recovery values calculated using (4) are shown in the last column of the table for both AC methods.

	Roi counts (cps)	RV (%)
Original PET image		
Myocardium	520.35	—
Ventricle	352.63	—
CT-AC image		
Myocardium	858.38	39.4%
Ventricle	589.99	40.2%
SE-AC image		
Myocardium	785.43	30.9%
Ventricle	537.87	31.4%

TABLE 6: Average values of coincidences calculated in an ROI inside the liver on ^{11}C -acetate rat images. The recovery values estimated with the two AC methods are shown in the last column of the table.

	Roi counts (cps)	RV (%)
Original PET image	174.92	—
CT-AC image	327.04	46.5%
SE-AC image	291.56	35.7%

perform the segmentation of the PET image to obtain the attenuation map.

In order to investigate the use of the SE-AC method with other radiopharmaceuticals, we evaluated the performance of the AC methods also on ^{11}C -acetate, ^{68}Ga -chloride, and ^{18}F -NaF images. For each of these radiopharmaceuticals, a table and line profile plots are shown. Table 6 shows the average value of counts calculated using an ROI drawn inside the rat liver on ^{11}C -acetate image and the relative RV obtained with the two AC methods. The difference between the two methods is around 11%. Figure 15 shows the profiles

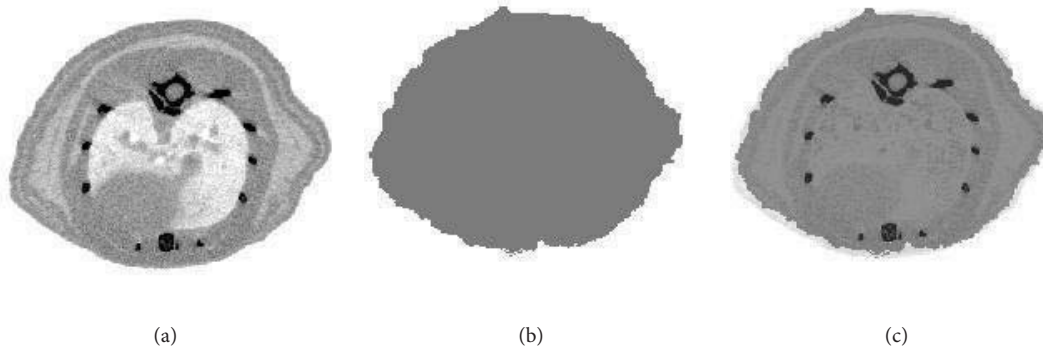


FIGURE 11: Transaxial slices of rat images: CT image (a) and segmented PET image (b). The overlay of the two previous images (c) shows how much the segmented PET image differs from the CT image.

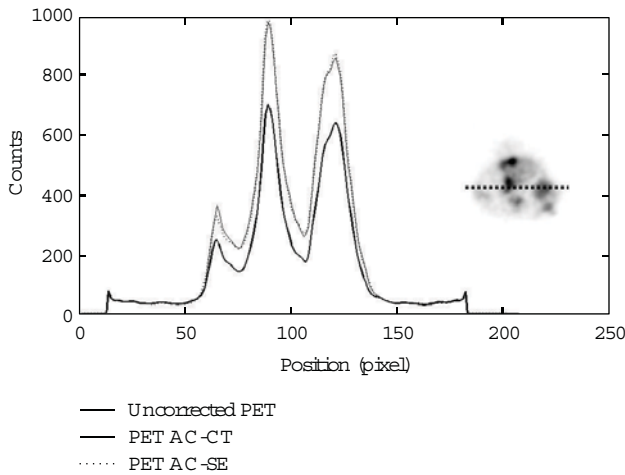


FIGURE 12: Counts profile across the mouse tumour for the uncorrected ^{18}F -FDG PET image (thick line) and for the two corrected images (full and dotted lines refer to CT-AC and SE-AC images, resp.) The peak on the right side of the profile is relative to the tumour. The image on the right shows the profile position.

TABLE 7: Average values of counts measured in an ROI inside the kidney from a ^{68}Ga -chloride rat PET image. The RV computed from both AC methods is shown in the last column of the table.

	Roi counts (cps)	RV (%)
Original PET image	245.45	—
CT-AC image	459.14	46.5%
SE-AC image	427.37	39.6%

drawn across the rat liver on ^{11}C -acetate image. The SE-AC method provides good results also for ^{11}C -acetate images.

Figure 16 and Table 7 show the results of the two AC methods for a ^{68}Ga -chloride image. Note that the profiles traced across the two AC images are very similar; the difference of RV between the two AC methods is approximately 7%. Segmentation of ^{18}F -NaF image to create the attenuation map is more difficult to obtain. The difference between the RV calculated for both CT-AC and SE-AC methods amounts to

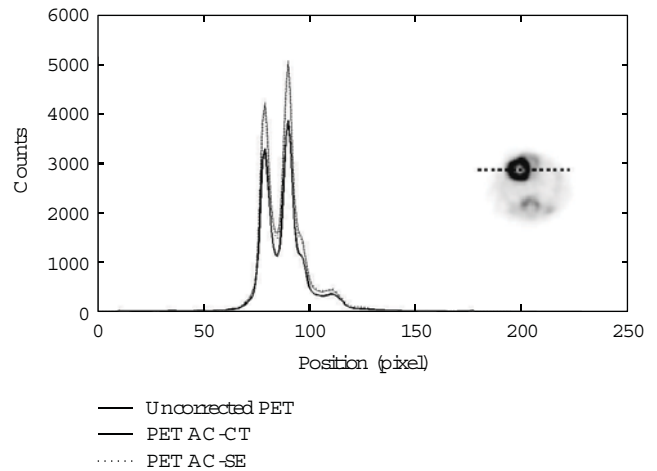


FIGURE 13: Profiles traced across mouse heart PET images acquired using ^{18}F -FDG. More precisely, thick, dotted, and full lines were traced on uncorrected PET, SE-AC, and CT-AC images.

TABLE 8: ROI average values computed from ^{18}F -PET image of a rat corresponding to the spinal column for uncorrected and AC images. In the last column of the table, the RV from both AC methods is shown.

	Roi counts (cps)	RV (%)
Original PET image	419.70	—
CT-AC image	770.14	45.5%
SE-AC image	623.67	26.5%

20%. Profiles are shown in Figure 17, and results are shown in Table 8.

4. Discussion

In order to achieve accurate estimates of radiotracer concentration, corrections for attenuation, scatter, and partial volume effects are necessary. Our main objectives were to assess the importance of attenuation in small animal PET images. On average, our results showed that the count recovery after

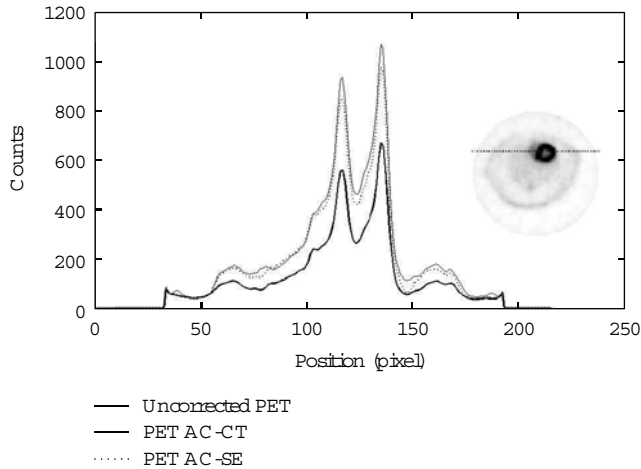


FIGURE 14: Profiles traced across the rat heart on ^{18}F -FDG PET image. The position of the profile on the image is shown on the right side of the plot. The thick line represents the counts measured across the uncorrected PET image, the dotted line is for the AC method based on PET segmentation, and the full line is the profile drawn on the CT-AC image.

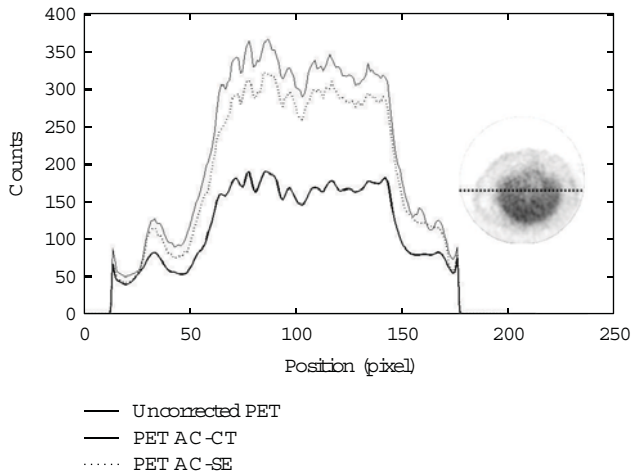


FIGURE 15: Profiles traced across the liver from ^{11}C -acetate rat PET images. The thick line corresponds to the uncorrected image, while the dotted and full lines correspond to SE and CT-based AC images.

attenuation correction with respect to uncorrected images is about 20% (40%) for mice (rats) images. Two AC methods were evaluated, namely, a CT-based and a segmented-emission-image-based AC.

Similar results were also obtained by El Ali and colleagues [30]. In their work, they evaluated attenuation correction in small animals showing an underestimation of true activity concentration of about 10%–20%. They also showed that PET-based and CT-based methods provide comparable results for attenuation compensation in PET while uniform AC method may be applied only if less accuracy is acceptable.

In our study, we acquired several phantoms, mice, and rats images. We also tested the SE-AC on images acquired

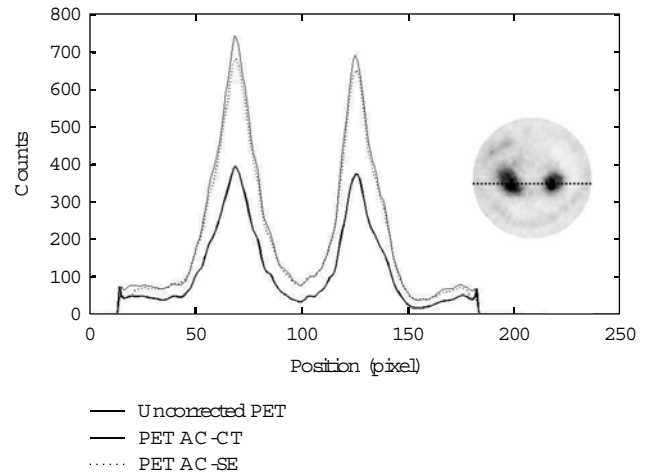


FIGURE 16: Line profiles across the kidney of the ^{68}Ga -chloride rat images. The position of the line is shown on the right side of the plot. The thick line corresponds to the uncorrected PET image. The dotted and full lines correspond to the SE-AC and CT-AC images, respectively.

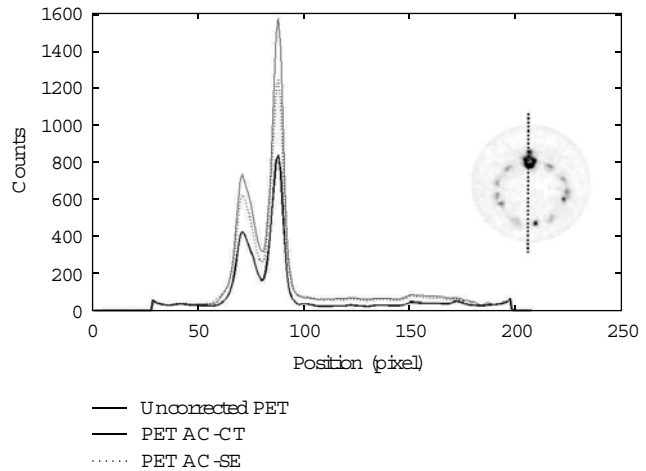


FIGURE 17: Profiles traced on ^{18}F -NaF rat images across the spinal column. The position of the line is shown on the right side of the plot. The thick line corresponds to the uncorrected PET image, and dotted and full lines correspond to SE-AC and CT-AC images, respectively.

using several radiotracers such as ^{18}F -FDG, ^{18}F -NaF, ^{11}C -acetate, and ^{68}Ga -chloride.

In order to implement the CT-AC method, we performed a calibration of GE eXplore Locus CT system to convert CT numbers to attenuation coefficients at 511 keV. Therefore, we were able to create attenuation maps at the correct energy. As the X-ray beam of the CT system employed is polyenergetic, the beam-hardening effect could lead to artifacts influencing the quality of the CT image and consequently the accuracy of the attenuation map. For this reason, we performed Monte Carlo simulation in order to evaluate the difference between CT-AC and MC simulations. The difference between

the flatness of true CT-AC PET image and AC simulated image is about 3% showing that beam hardening effects have a negligible influence in CT-AC.

In order to test both AC methods, we acquired several phantoms. A mouse-sized phantom filled with uniform activity concentration was acquired to quantify the importance of attenuation effects and to measure the shape recovery. We acquired also a rat-sized phantom uniformly filled with ^{18}F -FDG, and we observed a significant improvement in the flatness value. The differences between the SE-AC and CT-AC methods were less than 3% for the count recovery and less than 2% for the flatness value.

In order to quantify the recovery of counts after AC on the myocardium and left ventricle, we acquired both mouse and rat images using ^{18}F -FDG. Results showed that the SE-AC method leads to difference in count recovery of about 3% and 10% to the CT-AC method for mouse and rat, respectively. We evaluated also the recovery of counts in a mammary tumour in a mouse showing a difference of RV with respect to CT AC method of about 1.5%. The accuracy of the SE-AC method was also evaluated on rat images acquired with ^{11}C -acetate, ^{68}Ga -chloride, and ^{18}F -NaF. The difference between RVCT and RVSE measured in liver on ^{11}C -acetate image is approximately 11%. The ROI analysis performed on ^{68}Ga -chloride image on the kidneys leads to a difference of about 7% between CT-AC and SE-AC. ROI analysis on spinal column of ^{18}F -NaF images showed a difference in RV of about 20%. This slightly higher difference between CT-AC and SE-AC when using ^{18}F -NaF images is due to more difficulties in contour delineation during the segmentation procedure and also to the error one makes when assigning to bone tissues as seen in ^{18}F -NaF scans the attenuation coefficient of soft tissues. In vivo studies showed that the RV values obtained by using SE-AC are systematically lower than CT-AC ones, except in tumour mouse study where the RV values are quite similar for both AC methods.

5. Conclusions

The main goal of the paper was to show that SE-AC provides comparable results with respect to the more complex and time-consuming CT-AC method. We proved this for several radiotracers used in preclinical imaging such as ^{18}F -FDG, ^{11}C -acetate, ^{68}Ga -chloride, and ^{18}F -NaF. The SE-AC method has, however, some limitations and will probably fail when a very specific tracer is used. In this case, CT-AC method must be applied.

As expected, AC is more important for rat than for mouse images. For all the studies performed on animals, we observe a difference of RV between CT-AC and SE-AC method of less than 10%, except for ^{18}F -NaF images where the deviation is 20%. In all cases, RV estimated from SE-AC is smaller than the one estimated from CT-AC. Overall, we can conclude that the SE-AC method provides good quantitative estimates of count recovery, comparable to the ones obtained from CT-AC. This is important considering the advantages of the SE-AC: (1) it requires less time with respect

to the standard method based on CT images, because the CT image acquisition and, consequently, the coregistration procedure are not needed; (2) it does not add dose to the animal, and this is very important when repeated studies are needed; (3) it can be used also when a small animal CT scanner is not available.

Disclosure

The authors disclose that they have no direct financial relation with any commercial identity mentioned in the paper.

Acknowledgments

The authors would like to acknowledge the radiopharmacy staff for providing the radiotracers used in their experiments and Dr. Silvia Trespidi for the help with the animal handling. This research was partially supported by the Fondazione del Monte di Bologna and the Regione Emilia Romagna—SPINNER consortium.

References

- [1] S. Huang and M. Phelps, "Principles of tracer kinetic modeling in positron emission tomography and autoradiography," in *Emission Tomography and Autoradiography: Principles and Applications for the Brain and Heart*, pp. 287–346, Raven Press, New York, NY, USA, 1986.
- [2] H. Zaidi and B. Hasegawa, "Determination of the attenuation map in emission tomography," *Journal of Nuclear Medicine*, vol. 44, no. 2, pp. 291–315, 2003.
- [3] H. Zaidi and K. F. Koral, "Scatter modelling and compensation in emission tomography," *European Journal of Nuclear Medicine and Molecular Imaging*, vol. 31, no. 5, pp. 761–782, 2004.
- [4] M. Soret, S. L. Bacharach, and I. Buvat, "Partial-volume effect in PET tumor imaging," *Journal of Nuclear Medicine*, vol. 48, no. 6, pp. 932–945, 2007.
- [5] S. C. Huang, E. J. Hoffman, M. E. Phelps, and D. E. Kuhl, "Quantitation in positron emission computed tomography: II. Effects of inaccurate attenuation correction," *Journal of Computer Assisted Tomography*, vol. 3, no. 6, pp. 804–814, 1979.
- [6] R. Yao, J. Seidel, J. S. Liow, and M. V. Green, "Attenuation correction for the NIH ATLAS small animal PET scanner," *IEEE Transactions on Nuclear Science*, vol. 52, no. 3, pp. 664–668, 2005.
- [7] P. L. Chow, F. R. Rannou, and A. F. Chatziioannou, "Attenuation correction for small animal PET tomographs," *Physics in Medicine and Biology*, vol. 50, no. 8, pp. 1837–1850, 2005.
- [8] D. D'Ambrosio, A. E. Spinelli, S. Boschi et al., "Attenuation correction for pre-clinical PET images using a small animal CT scanner," *European Journal of Nuclear Medicine and Molecular Imaging*, vol. 34, p. S227, 2007.
- [9] J. Yu, J. Seidel, M. Pomper, and B. M. W. Tsui, "Experimental evaluation of the bilinear transformation used in the CT-based attenuation correction for small animal PET imaging," in *Proceedings of IEEE Nuclear Science Symposium and Medical Imaging Conference (NSS-MIC '07)*, vol. 6, pp. 3747–3750, November 2007.
- [10] R. Prasad, M. R. Ay, O. Ratib, and H. Zaidi, "CT-based attenuation correction on the FLEX Triumph preclinical PET/CT

- scanner,” in *Proceedings of IEEE Nuclear Science Symposium Conference Record (NSS/MIC '09)*, pp. 3357–3362, October 2009.
- [11] M. Bentourkia and O. Sarrhini, “Simultaneous attenuation and scatter corrections in small animal PET imaging,” *Computerized Medical Imaging and Graphics*, vol. 33, no. 6, pp. 477–488, 2009.
- [12] J. L. Herraiz, S. España, J. J. Vaquero, M. Desco, and J. M. Udías, “FIRST: fast iterative reconstruction software for (PET) tomography,” *Physics in Medicine and Biology*, vol. 51, no. 18, pp. 4547–4565, 2006.
- [13] G. Germano and E. J. Hoffman, “Investigation of count rate and deadtime characteristics of a high resolution PET system,” *Journal of Computer Assisted Tomography*, vol. 12, no. 5, pp. 836–846, 1988.
- [14] R. A. DeKemp and C. Nahmias, “Attenuation correction in PET using single photon transmission measurement,” *Medical Physics*, vol. 21, no. 6, pp. 771–778, 1994.
- [15] J. S. Karp, G. Muehllehner, H. Qu, and X. H. Yan, “Singles transmission in volume-imaging PET with a ^{137}Cs source,” *Physics in Medicine and Biology*, vol. 40, no. 5, pp. 929–944, 1995.
- [16] S. C. Huang, R. E. Carson, M. E. Phelps, E. J. Hoffman, H. R. Schelbert, and D. E. Kuhl, “A boundary method for attenuation correction in positron computed tomography,” *Journal of Nuclear Medicine*, vol. 22, no. 7, pp. 627–637, 1981.
- [17] E. Z. Xu, N. A. Mullani, K. L. Gould, and W. L. Anderson, “A segmented attenuation correction for PET,” *Journal of Nuclear Medicine*, vol. 32, no. 1, pp. 161–165, 1991.
- [18] A. Welch, C. Campbell, R. Clackdoyle et al., “Attenuation correction in PET using consistency information,” *IEEE Transactions on Nuclear Science*, vol. 45, pp. 3134–3141, 1998.
- [19] M. T. Madsen and J. R. Lee, “Emission based attenuation correction of PET images of the thorax,” in *Proceedings of IEEE Nuclear Science Symposium Conference Record*, vol. 2, pp. 967–997, 1999.
- [20] V. Bettinardi, E. Pagani, M. C. Gilardi et al., “An automatic classification technique for attenuation correction in positron emission tomography,” *European Journal of Nuclear Medicine*, vol. 26, no. 5, pp. 447–458, 1999.
- [21] A. E. Spinelli, D. D’Ambrosio, C. Pettinato et al., “Performance evaluation of a small animal PET scanner. Spatial resolution characterization using ^{18}F and ^{11}C ,” *Nuclear Instruments and Methods in Physics Research A*, vol. 571, no. 1-2, pp. 215–218, 2007.
- [22] M. V. Green, J. Seidel, C. A. Johnson, J. J. Vaquero, J. Pascau, and M. Desco, “Towards high performance small animal positron emission tomography,” in *Proceedings of IEEE International Symposium on Biomedical Imaging*, pp. 369–372, 2002.
- [23] H. M. Hudson and R. S. Larkin, “Accelerated image reconstruction using ordered subsets of projection data,” *IEEE Transactions on Medical Imaging*, vol. 13, no. 4, pp. 601–609, 1994.
- [24] M. Defrise, P. E. Kinahan, D. W. Townsend, C. Michel, M. Sibomana, and D. F. Newport, “Exact and approximate rebinning algorithms for 3-D pet data,” *IEEE Transactions on Medical Imaging*, vol. 16, no. 2, pp. 145–158, 1997.
- [25] I. A. Feldkamp, L. C. Davis, and J. W. Kress, “Practical cone-beam algorithm,” *Journal of the Optical Society of America A*, vol. 1, no. 6, pp. 612–619, 1984.
- [26] J. H. Hubbell and S. M. Seltzer, “Tables of X-Rays Mass Attenuation Coefficients and Mass Energy Absorption Coefficients (version 1.3),” (Gaithersburg: NIST), 2001, <http://physics.nist.gov/xaamdi>.
- [27] S. España, J. L. Herraiz, E. Vicente, J. J. Vaquero, M. Deseo, and J. M. Udías, “PenelPET, a Monte Carlo PET simulation toolkit based on PENELOPE: features and validation,” in *Proceedings of IEEE Nuclear Science Symposium Conference Record*, vol. 4, pp. 2597–2601, November 2006.
- [28] A. E. Spinelli, M. Marengo, C. Pettinato et al., “Evaluation of micro positron emission tomography and micro computed tomography image registration,” *Molecular Imaging and Biology*, vol. 8, article 103, 2006.
- [29] A. M. Loening and S. S. Gambhir, “AMIDE: a free software tool for multimodality medical image analysis,” *Molecular Imaging*, vol. 2, no. 3, pp. 131–137, 2003.
- [30] H. H. El Ali, R. P. Bodholdt, J. T. Jørgensen, R. Myschetzky, and A. Kjaer, “Importance of attenuation correction (AC) for small animal PET imaging,” *Diagnostics*, vol. 2, pp. 42–51, 2012.

Research Article

Simulation of Intra-Aneurysmal Blood Flow by Different Numerical Methods

Frank Weichert,¹ Lars Walczak,¹ Denis Fisseler,¹ Tobias Opfermann,¹ Mudassar Razaq,² Raphael Münster,² Stefan Turek,² Iris Grunwald,³ Christian Roth,⁴ Christian Veith,⁵ and Mathias Wagner⁵

¹ Department of Computer Science VII, Dortmund University of Technology, Dortmund, Germany

² Institute of Applied Mathematics, LS III, Dortmund University of Technology, Dortmund, Germany

³ Oxford Biomedical Research Centre, University of Oxford, Oxford, UK

⁴ Department of Neuroradiology, University of Saarland Medical School, Homburg Saar, Germany

⁵ Department of Pathology, University of Saarland Medical School, Homburg Saar, Germany

Correspondence should be addressed to Frank Weichert; frank.weichert@tu-dortmund.de

Received 21 December 2012; Revised 13 March 2013; Accepted 17 March 2013

Academic Editor: Wenxiang Cong

Copyright © 2013 Frank Weichert et al. This is an open access article distributed under the Creative Commons Attribution License, which permits unrestricted use, distribution, and reproduction in any medium, provided the original work is properly cited.

The occlusional performance of sole endoluminal stenting of intracranial aneurysms is controversially discussed in the literature. Simulation of blood flow has been studied to shed light on possible causal attributions. The outcome, however, largely depends on the numerical method and various free parameters. The present study is therefore conducted to find ways to define parameters and efficiently explore the huge parameter space with finite element methods (FEMs) and lattice Boltzmann methods (LBMs). The goal is to identify both the impact of different parameters on the results of computational fluid dynamics (CFD) and their advantages and disadvantages. CFD is applied to assess flow and aneurysmal vorticity in 2D and 3D models. To assess and compare initial simulation results, simplified 2D and 3D models based on key features of real geometries and medical expert knowledge were used. A result obtained from this analysis indicates that a combined use of the different numerical methods, LBM for fast exploration and FEM for a more in-depth look, may result in a better understanding of blood flow and may also lead to more accurate information about factors that influence conditions for stenting of intracranial aneurysms.

1. Introduction

The accurate incidence and prevalence of unruptured non-aortic aneurysms of 3 mm or less in diameter is controversially discussed. The likelihood of detection is increasing with improved imaging techniques [1, 2]. Among the risk factors are age, hypertension, and the habit of cigarette smoking [3]. Size and perhaps geometry of the aneurysm contribute to the risk of rupture which may be less than 5% per year [4]. A rupture of an intracranial aneurysm can cause devastating subarachnoid hemorrhage with high morbidity and mortality [5]. For the treatment of unruptured aneurysms, there is a selection of endovascular and surgery-based treatment modalities, for which the risks and rates of complication have been described elsewhere [3]. Hemorrhage as a consequence

of ruptured intracranial aneurysms can be prevented by means of minimally invasive therapy, endoluminal stenting.

In the last few years, endovascular treatment of intracranial aneurysms has become a possible minimal invasive alternative to neurosurgical therapy which was until then unequalled. The aneurysm is treated with electrolytically detachable coils, the use of which is limited for wide-necked aneurysms. It is often impossible to coil an aneurysm after stent placement, so the treatment of the aneurysm with a covered or small-cell-designed stent that would permit an immediate occlusion is preferable. Quantitative approaches however, applied to learn more about how specific design features of endovascular stents such as porosity [6], struts [7], and mesh design [8] affect intra-aneurysmal hemodynamic, have mainly provided inconsistent results [9]. In

some cases, stenting alone has been suggested to promote thrombogenic conditions such as reduced flow activity and prolonged stasi, and thereby occlude aneurysms simply by thrombosis.

But the selection of the preferred therapy is still controversially discussed. In this regard novel therapies such as flow diverters may also be considered [10]. For this reason blood flow simulations in the context of aneurysms of elastotypic and/or mixtotypic arteries have been proposed by various workgroups [11–13] and in different studies, for example, the ISAT study (International Subarachnoid Aneurysm Trial [14]). The Aneurist Project (<http://www.aneurist.org/>; as of april 1st, 2013), funded by the European Commission, is among the most renowned approaches. Their results [15, 16] state that a single simulation takes about 10 to 24 hours to complete. This does not involve testing different stent models, different placements, and varying orientations of the stent in the vessel. Such timing, however, is not helpful in a clinical setting. Computer-simulation-based therapy appears to be gaining acceptance in healthcare as several technical problems can be solved and facts be learnt without animal experimentation or by working with actual patients. The speed with which considerable quantities of simulations can be performed may reduce the number of animal experiments and identify new issues to be covered.

The present study has therefore been conducted to present a novel idea in combining the following different mathematical methods to quickly explore some of the above parameters: finite element techniques and lattice Boltzmann methods.

Finite element techniques represent the ubiquitous numerical method in structure and fluid mechanics. With its thorough theoretical background, error analysis for validation of simulation results can be achieved. Newer techniques such as lattice Boltzmann methods (LBM) provide no easy way to perform error analysis but may have advantages in different areas, for example, fast execution times. These fast execution times can be provided by using new programming paradigms for massively parallel processors such as graphics processing units (GPUs) available in most medical workstations. In order to explore giant parameter spaces, a combination of these methods may fuse the robustness of finite element results with the fast execution times of the other method.

LBM is a popular mesoscopic method in computational fluid dynamics. It has been applied to a number of interesting flow problems including multiphase and multicomponent fluid flows [17–19]. A relatively simple single-phase, single-component flow represents a good candidate for parameter exploring as it has been shown in the literature that the LBM approximates the time-dependent Navier-Stokes equations under certain circumstances [20]. The monographs [21, 22] are well-known starting points for further information; a GPU-specific discussion of LBM in the context of blood flow can be found in [23]. LBM models can be easily parallelized and therefore can be used to interactively explore different flow scenarios. The idea is that once an interesting set of boundary conditions and stent designs can be identified, highly accurate and highly detailed but much slower finite

element simulations can be substituted and provide a more in-depth look.

The paper is organized as follows. Section 2 introduces the simulation domains, the different numerical methods for simulation of blood flow and presents the concepts of finite element methods (Section 2.2) and lattice Boltzmann methods (Section 2.3). Following, Section 3 shows exemplary results that are obtainable using the presented methods for simulation and Section 4 concludes with some remarks on the current state and the further development.

2. Simulation of Blood Flow

For evaluation and comparison purposes a set of basic conditions, that all simulation models have to comply with, is defined. These conditions have to be simple enough to allow the use of simplifying simulation models for faster access to initial simulation results, yet complex enough to model most aspects required for simulation of blood flow. Consequently, our finite element and lattice Boltzmann models consist of an incompressible or weakly compressible fluid modelling and a suitable viscosity model. In addition no slip boundary conditions and a maximum inflow velocity magnitude of 50 mm/s with a parabolic shape that is suitable for a small artery with a diameter of 3 mm are applied [24].

2.1. Datasets. For the purpose of comparing the different simulation models to each other an appropriate testing environment is needed. In addition to the meshes generated directly from MRI datasets, which sometimes suffer from irregularities and which are by concept limited to one stage in the formation process of an aneurysm, a synthetic model of a so-called true arterial aneurysm (syn.: Aneurysma verum), arbitrarily assumed to be similar to the terminal-type C morphology of unruptured aneurysms [25], was designed based on available MRI data and medical expert knowledge. Additionally, two hypothetical stages of aneurysm growth for the synthetic model are included in this study. The synthetic mesh facilitates the analysis of our physical modelling by providing well-structured 2D grids (cf. Figure 1(a)), level set volumes (cf. [26, 27]) and 3D meshes (cf. Figure 1(b)) for all required simulation domains.

2.2. Finite Element Method. The solver used to perform the 2D calculations in this work is based on the ALE formulation of the Navier-Stokes equations; however to perform the 3D calculations it is modified in some important aspects. Instead of using an ALE formulation of the Navier-Stokes equations, an Eulerian approach is implemented. This approach is based on the incompressible Navier-Stokes equations, so the motion of an incompressible fluid at time t is governed by

$$\rho \left(\frac{\partial \mathbf{u}}{\partial t} + \mathbf{u} \cdot \nabla \mathbf{u} \right) - \nabla \cdot \sigma = 0, \quad \nabla \cdot \mathbf{u} = 0 \quad \forall t \in (0, T), \quad (1)$$

where σ is the stress tensor of the fluid phase:

$$\sigma = -p\mathbf{I} + \mu \left[\nabla \mathbf{u} + (\nabla \mathbf{u})^T \right]. \quad (2)$$

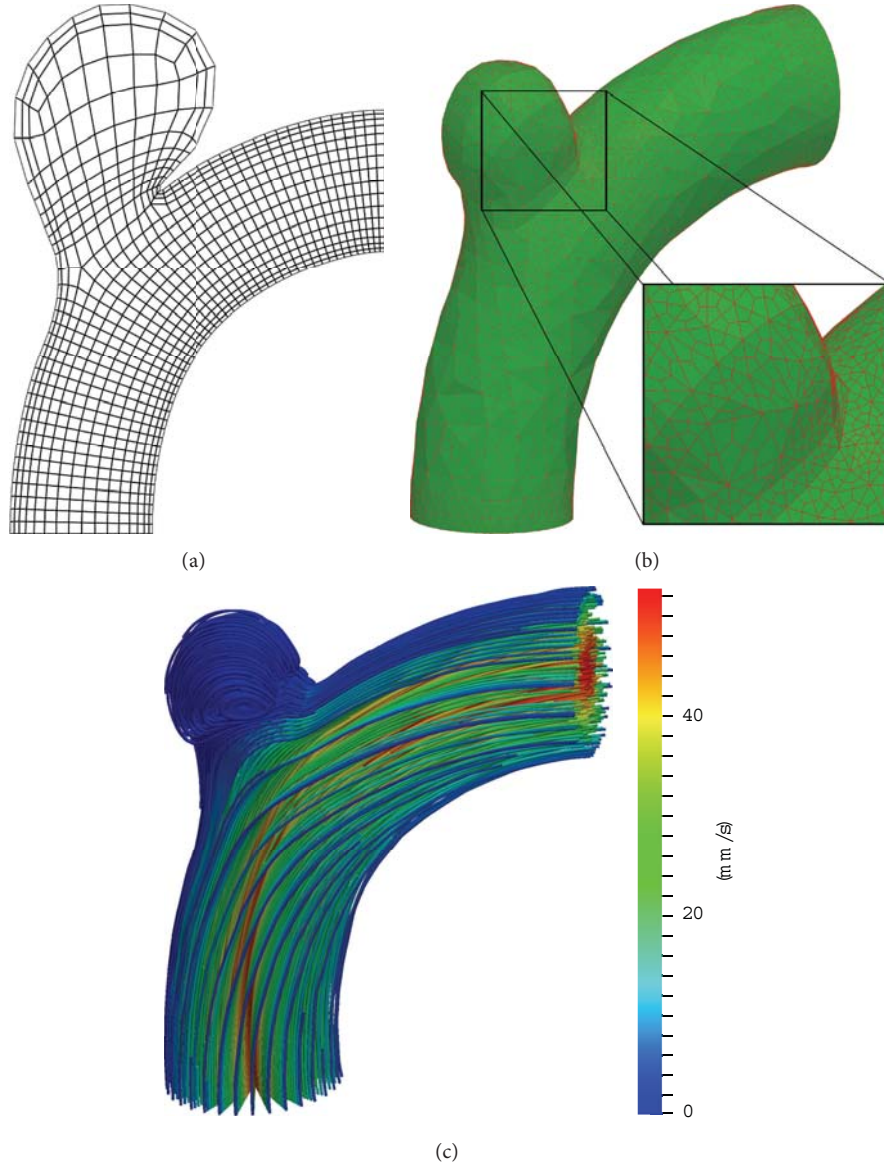


FIGURE 1: Simulation domain and border representation for (a) 2D FE mesh, (b) 3D FE mesh. (c) 3D stream line result for medium-sized aneurysm.

We denote the identity tensor by I , the fluid density by ρ , the viscosity by μ , the pressure by p , and by \mathbf{u} we refer to the fluid velocity. Space discretisation in 2D and 3D is then done by the FEM using the LBB stable conforming biquadratic, discontinuous linear Q_2/P_1 element pair. In time the equations are discretised using the Crank-Nicolson time-stepping scheme. The resulting system is then solved using a standard geometric multigrid solver in 2D [28, 29] and a parallel Newton-multigrid solver in 3D [30].

2.3. Lattice Boltzmann Method. In the last section, fluid behaviour is described by time-varying macroscopic fields. A microscopic point of view tracks the motion of each atom or molecule. The LBM takes a mesoscopic approach from statistical physics. Here, the (macroscopic) density ρ of a fluid is represented by multiple particle distribution functions

(PDF) which represent fluid particles that move in the same direction. In the LBM, the directions are discretised onto a regular three-dimensional lattice. Each direction \mathbf{e}_i linking a grid node with its neighbours corresponds to a PDF f_i . The direction \mathbf{e}_0 is the zero vector which represents particles at rest. The discretisation in three dimensions is commonly referred to as $D3Q19$ and consists of 19 directions, that is, $i = 0, \dots, 18$. In two dimensions a $D2Q9$ model with 9 discrete directions is used (details omitted, cf. [21]). The evolution of the PDFs at each lattice node with regard to collisions between fluid particles is described by (3) (see [22]). It holds

$$\begin{aligned} & f_i(\mathbf{x} + \mathbf{e}_i, t + 1) - f_i(\mathbf{x}, t) \\ &= -\frac{f_i(\mathbf{x}, t) - f_i^{\text{eq}}(\mathbf{x}, t)}{\tau}, \quad i = 0, 1, \dots, 18, \end{aligned} \quad (3)$$

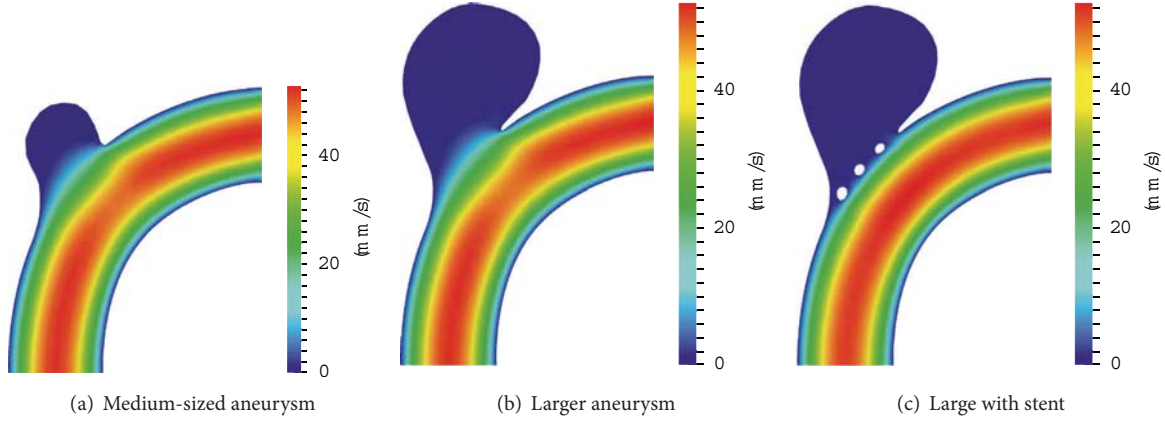


FIGURE 2: Visualization of the 2D FEM velocity field in an aneurysm bearing artery: (a), (b) nonstented case and (c) with coarse stent.

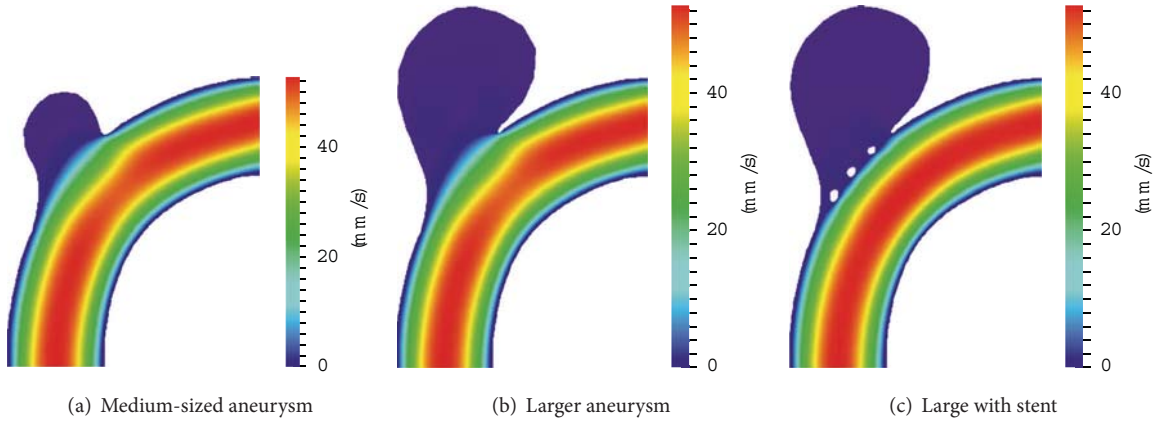


FIGURE 3: Visualization of 2D LBM velocity field in an aneurysm bearing artery: (a), (b) nonstented case and (c) with coarse stent.

in which

$$f_i^{\text{eq}} = w_i \rho \left(1 + 3 \mathbf{e}_i \cdot \mathbf{u} + \frac{9}{2} (\mathbf{e}_i \cdot \mathbf{u})^2 - \frac{3}{2} \mathbf{u} \cdot \mathbf{u} \right) \quad (4)$$

are the 19 equilibrium distribution functions and w_i are weighting factors for the $DxQy$ model. The evolution of the directional densities can be understood as a relaxation towards local equilibrium which is a function of the local density ρ , the current velocity \mathbf{u} , and the relaxation time τ which is connected to the liquid viscosity $\nu = (1/3)(\tau - 1/2)$. The equilibrium distribution functions f_i^{eq} have the property to conserve mass as can be seen from (5). The density

$$\rho(\mathbf{x}) = \sum_{i=0}^{18} f_i(\mathbf{x}) \quad (5)$$

at a lattice node is the sum of the PDFs in every direction. The current velocity

$$\mathbf{u}(\mathbf{x}) = \frac{1}{\rho} \sum_{i=0}^{18} f_i(\mathbf{x}) \cdot \mathbf{e}_i \quad (6)$$

is also computed from the PDFs.

Solid boundaries can relatively easily be incorporated by swapping opposite PDFs at solid nodes. This technique known as bounce-back is one way of simulating the no-slip condition at solid boundaries. In the simulation of blood flow using LBM this bounce-back is used at the blood vessel boundaries and the stents. The structures themselves are defined by multiple-level sets [26]. A steady blood flow through the vessel is initiated by introducing pressure or velocity boundaries at the ends of the vessel. Here, velocity Dirichlet conditions at the inflow and velocity Neumann conditions at the outflow are applied; see [31] for further details. The compressibility error depends on the Mach number. With a Mach number $M \ll 1$, the method is incompressible. It has been shown in the above literature that the lattice Boltzmann method approximates the time-dependent isothermal and incompressible Navier-Stokes equations under this circumstance. So in theory, the above finite element ansatz and the LBM should yield comparable results.

3. Results

Based on available real geometry data of blood vessels featuring an aneurysm and our synthetic aneurysm models, some basic simulations are performed to compare the simulation

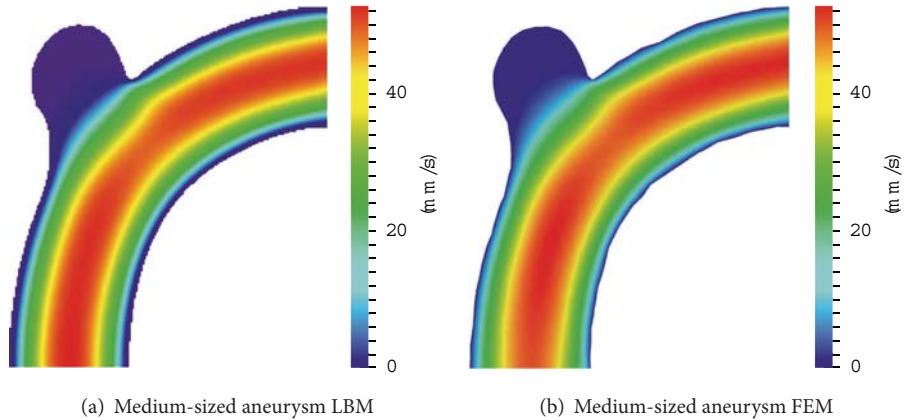


FIGURE 4: Visualization of a 2D cut through the middle of the 3D velocity field in an aneurysm-bearing artery: (a) LBM, (b) FEM.

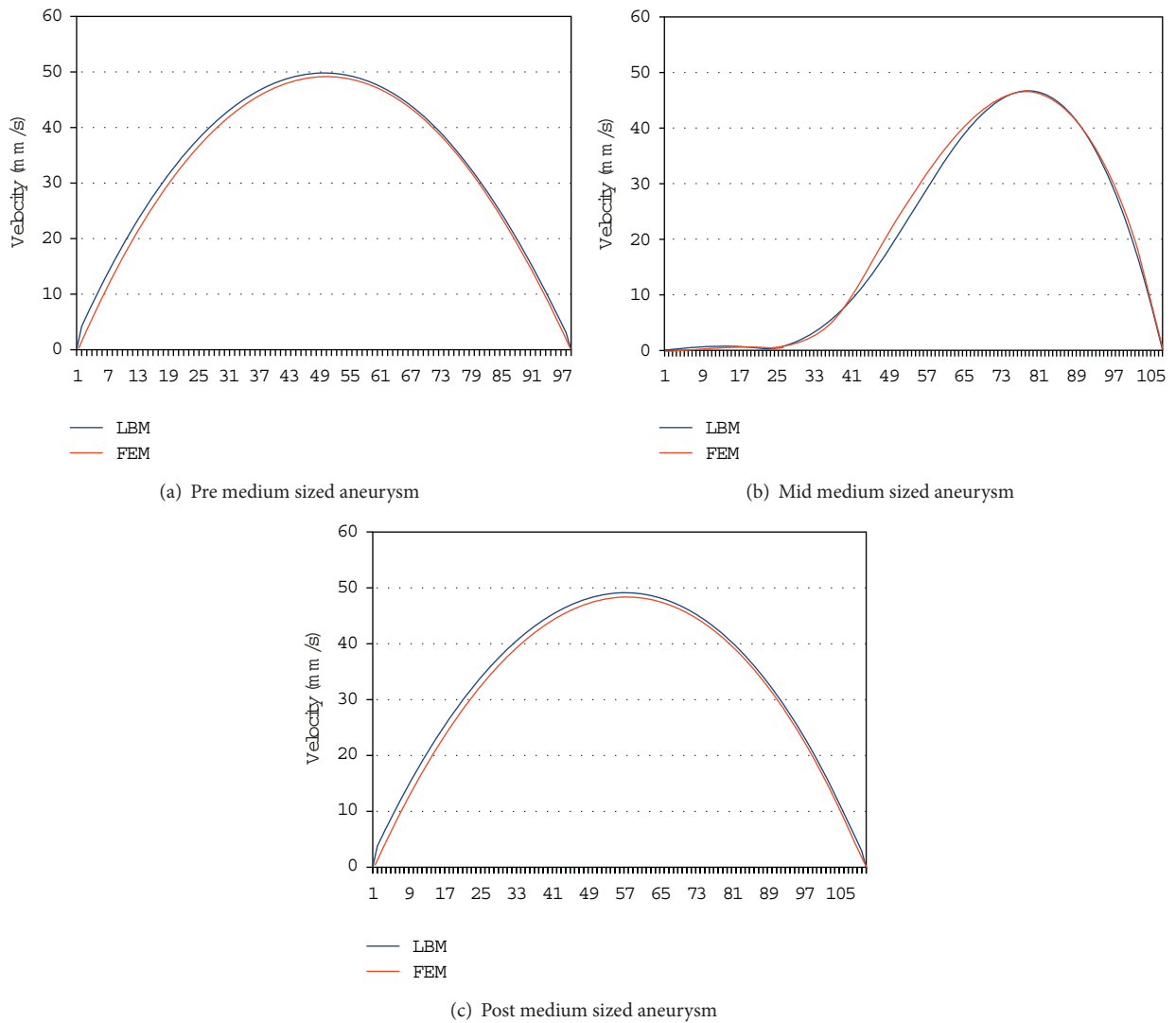


FIGURE 5: Medium-sized aneurysm: stationary stream profiles of the 2D simulations (a) in front of, (b) at and (c) after the aneurysm neck. The numbered sampling points are displayed on the x-axis. For (a), (c) the length of the cutline is 3 mm, for (b) 5 mm.

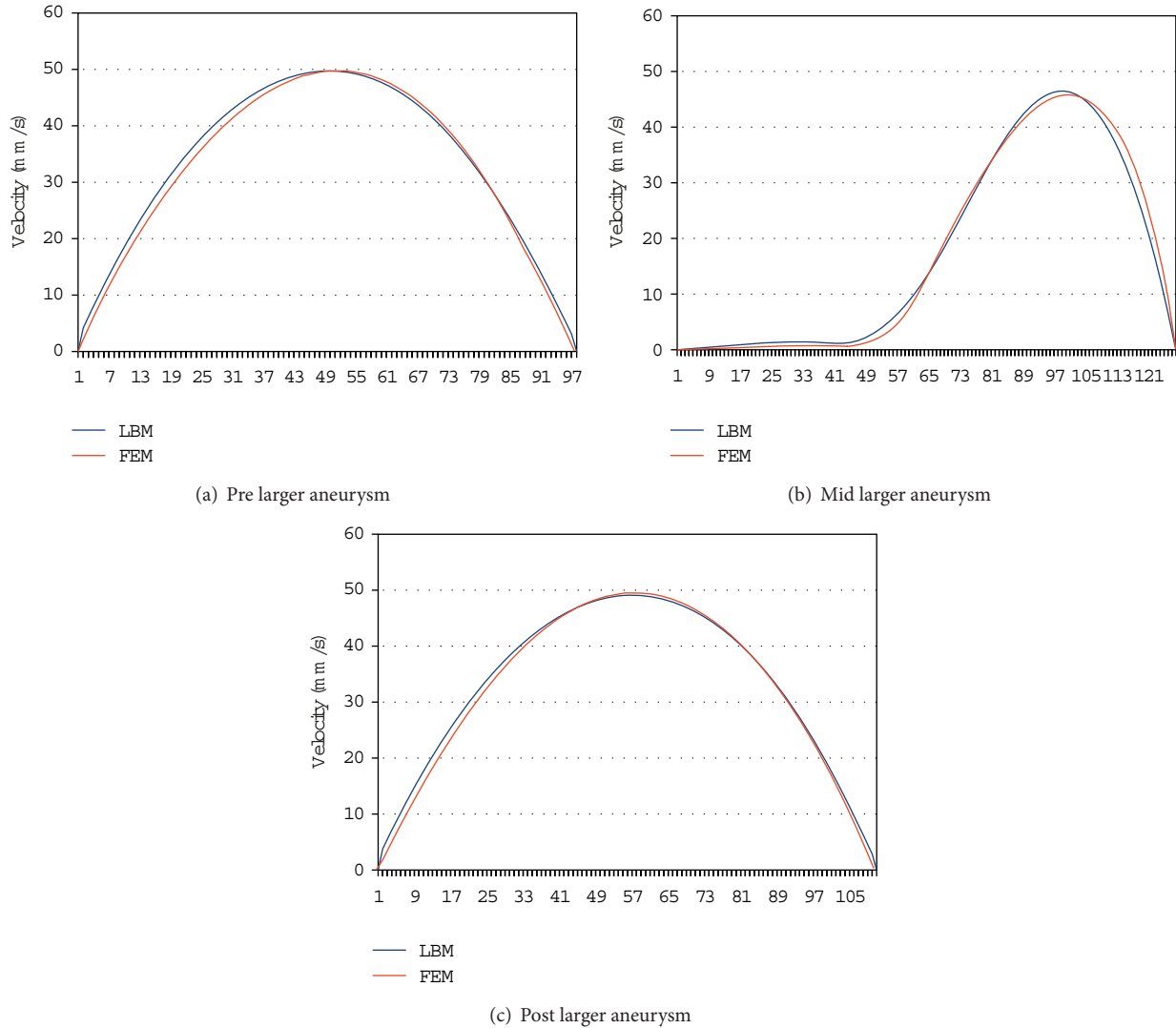


FIGURE 6: Larger aneurysm: stationary stream profiles of the 2D simulations (a) in front of, (b) at, and (c) after the aneurysm neck. The numbered sampling points are displayed on the x -axis. For (a), (c) the length of the cutline is 3 mm, for (b) 6 mm.

methods. For FEM, the 2D quad meshes consist of 4,208–4,244 elements with $\approx 81,000$ degrees of freedom and the level 1/2 3D hexahedral mesh consists of 26,177/173,600 elements with $\approx 2.1/14$ Mio unknowns. Lattice sizes for LBM are 272×384 in 2D and $188 \times 88 \times 212$ in 3D, respectively, that is, ≈ 3.44 Mio active $D3Q19$ cells with ≈ 65.2 Mio PDFs. The simulations are parameterized for a channel width of 3 mm, a parabolic velocity profile with a maximum velocity of 50 mm/s, a density of 1060 kg/m^3 , and a dynamic viscosity of 0.004 kg/ms . The resulting Reynolds number is 19.88.

To analyse aneurysm growth and its influence on the flow fields, we perform some basic tests using the two stages of our synthetic aneurysm model from Figure 1. In Figure 1(c) a streamline view of the 3D case is shown. The velocity fields obtained with the FEM and LBM models are shown color-coded in Figures 2, 3, and 4. Comparisons of three cutlines in 2D and the midline of three cut-planes in 3D (same location as in 2D) can be found in Figure 5 (2D FEM and LBM medium-sized aneurysm), Figure 6 (2D FEM and LBM larger

aneurysm), Figure 7 (2D FEM and LBM large with stent), and Figure 8 (3D FEM and LBM medium aneurysm). The cutlines/-planes are located in the vessel before the aneurysm neck (“pre”), at the aneurysm neck at a 45 degree angle to the curvature of the vessel (“mid”), and after the aneurysm neck (“post”). The results of all unstented simulation models share a (deformed) parabolic velocity profile throughout the blood vessel, a drop in velocity magnitude near the opening of the aneurysm, a widening of the parabolic profile, and a significant velocity magnitude at the aneurysm neck. The larger the aneurysm the higher the drop in magnitude in the vessel at the neck. Comparing the results inside the vessel with those inside the aneurysm, no such high velocity magnitudes do occur. On average the velocity magnitude is only ≈ 1 mm/s whereas at the aneurysm neck the velocity is ≈ 14 – 20 mm/s depending on the model used. The differences in velocity magnitude of the different numerical methods are low.

A comparison of the stented vessel with its nonstented counterpart can be found in Figures 2(c), 3(c), 6, and 7.

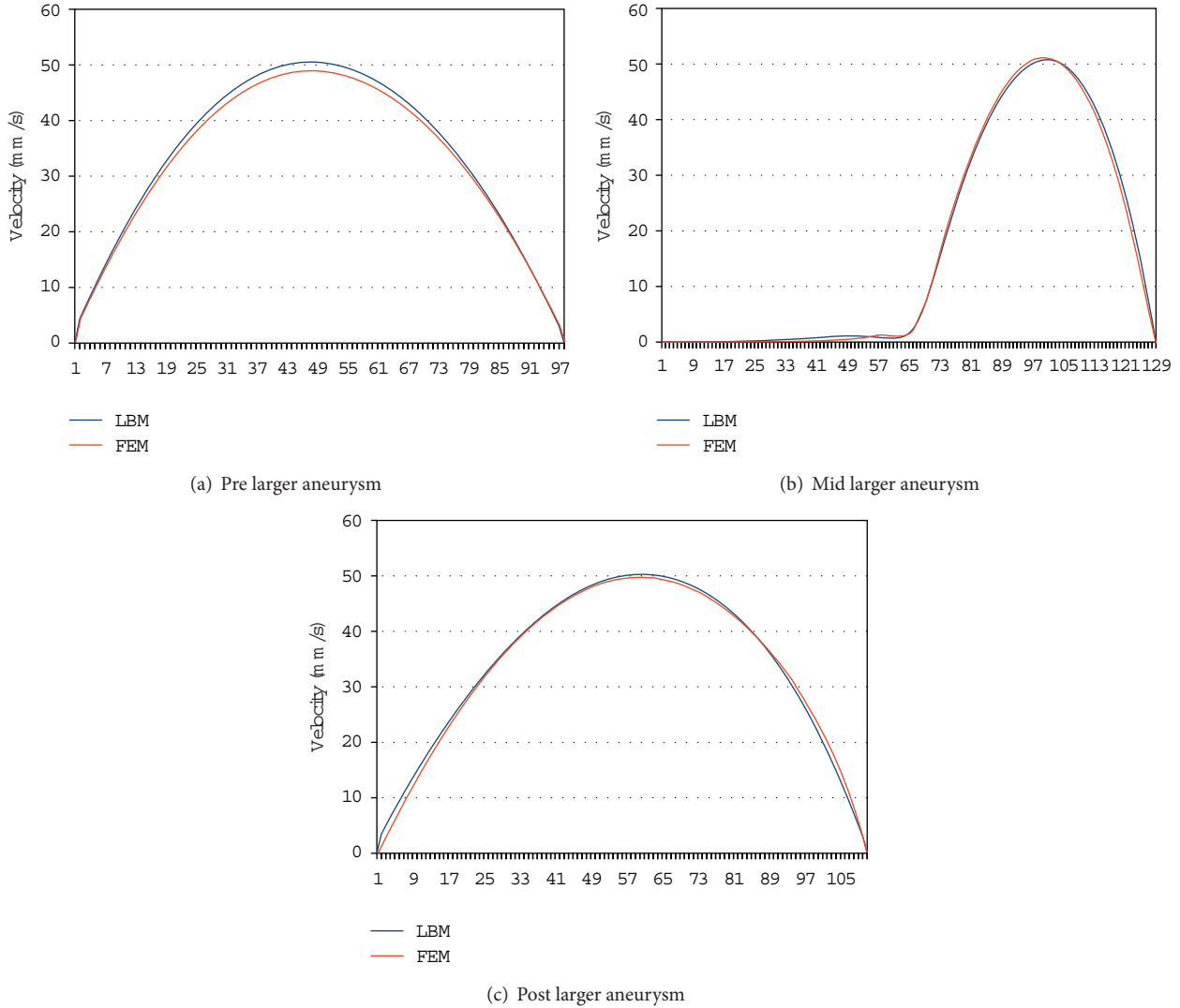


FIGURE 7: Stented larger-sized aneurysm: stationary stream profiles of the 2D simulations (a) in front of, (b) at, and (c) after the aneurysm neck. The numbered sampling points are displayed on the x -axis. For (a), (c) the length of the cutline is 3 mm, for (b) 6 mm.

It can be seen that much of the inflow at the aneurysm neck is effectively disabled by the stent. The average velocity inside the aneurysm drops from ≈ 1 mm/s in the nonstented case to ≈ 0.75 mm/s. The flow behaviour of all simulations is nearly identical. The fluid streams from the vessel into the aneurysm lumen through the first three stent gaps and leaves the aneurysm sack through the fourth gap. The velocity magnitude drops from ≈ 14 mm/s in the nonstented case to ≈ 5 mm/s in the stented case at the neck.

Regarding the initial goal of fast exploration of the parameter space running times are listed here. For 2D LBM and the shown data sets, we recorded approximately 1900 LBM iterations per second on a NVIDIA 560Ti GTX and approximately 2600 iterations per second on a NVIDIA 680GTX graphics card while 1s equals 16667 LBM time steps. In 3D and with 3.44 Mio cells, we record 71.8 and 118.3 iterations per second with the two graphics cards. With simultaneous volume visualization of the velocity field, these numbers drop to 58.2 and 88.3 iterations per second. A

simulation of a cardiac cycle with a duration of 1s equals 11667 3D LBM iterations in this parametrization. It can be simulated in under 2 min. Compared to 11 hours for 1s with 2500 time steps on 32 processors for the 3D FEM, exploration of multiple scenarios seems possible. Note that using adaptive time step sizes for FEM can reduce the execution times to 50% or less of the aforementioned value for the test case under consideration.

4. Discussion

The presented results show that the mathematical construction of patient-specific anatomy is both feasible and applicable to realistic test cases. Various practical issues have to be considered in order to establish a tailor-made aneurysm therapy based on mathematical modelling to implement personalized stenting for individual patients based on clinical and radiological findings.

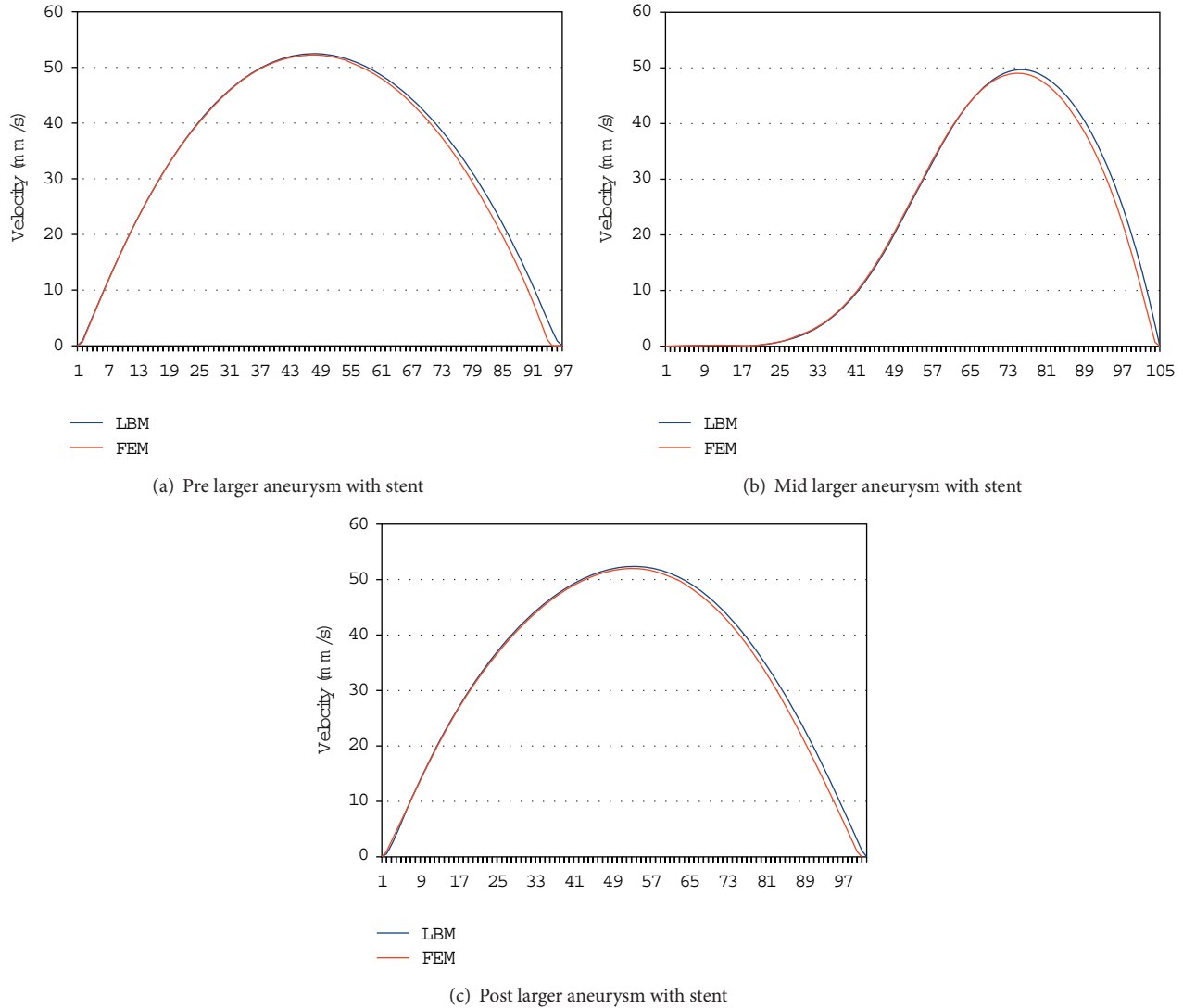


FIGURE 8: Medium-sized aneurysm: stationary stream profiles of the 3D simulations for the same plane as 2D data set: (a) in front of, (b) at, and (c) after the aneurysm neck. The numbered sampling points are displayed on the x -axis. For (a), (c) the length of the cutline is 3 mm, for (b) 5 mm.

In this comparative analysis of different methods, the FEM approach is the most expressive model at the moment. Because of its high complexity, the computation time is comparably slow and is usually a matter of hours or even days. But it is possible to resolve the fine-scale features of the flow by increasing mesh resolution or by local mesh adaptation. It seems reasonable to use an additional simulation method with very comparable results but with specific advantages for interactive parameter exploring. A comparison of both methods using the configuration described in Section 3 is provided in Table 1. Interesting flow constellations can be further analysed by the FEM after this initial exploration.

Due to the inherent parallelism of the LBM, where computation in each lattice node is only dependent on a local neighbourhood, the algorithm can be performed on highly parallel computing architectures such as graphics processors. This approach has been taken in the reference implementation which uses OpenCL (Open Computing

Language) for computation. In the test case described in this work a parallel FEM implementation on 32 cores is outperformed by a factor of 100–400 with recent NVIDIA Kepler GPU architectures and very well-comparable results. The interactive frame rates of parallel LBM simulations can provide key simulation constellations that can be investigated further with complex time-dependent nonNewtonian fluid structure interaction models. The influence of far-reaching and concentrated inflow jets on the integrity of the aneurysm sack has not been conclusively determined although some results and investigations exist [16].

On the basis of this introductory study it can be concluded that the time-dependent flow characteristics have to be analysed as well as the stationary results. Besides the above mentioned technical aspects, an optimal flow diverting stent geometry has to be found for the cardiac cycle because in the stationary case even the most basic stent is able to do its job after some time steps. Comparing the results of the

TABLE 1: Comparison of different simulation methods.

Aspect	FEM	LBM
Ansatz	Euler	Euler
Incompressibility	Yes	Yes
Time steps	Large	Implicit scheme: medium
Cost per time step	Large	Small
Boundary-fitted domain	Difficult	Fine grids
Level-set-based domain	Research topic, fictitious domain techniques	Research topic, same grid
Error analysis	Yes	Partial
Error control	Yes	No
Mesh/grid refinement	Yes	Research topic
Accuracy	High	Good
Non-Newtonian rheology	Yes	Available
Thrombosis model	Research topic	Research topic
Fluid structure interaction	Research topic	Research topic
Turbulence	Partial	Partial
Code implementation	Complicated	Good
Memory usage	Q2P1: high	D3Q19: high
Parallelisation	Complicated	Good

rather simple stent model provides no clear tendency for the influences of the inflow jets other than lower average velocities inside the aneurysm.

But these results indicate already that a multidisciplinary approach to the development of individualized aneurysm therapy is feasible and should be applied in the early development stages of novel stenting devices. Both of the approaches evaluated in the present publication encourage increasing use of numerical simulation in the development process of novel stenting devices. Especially considering that future mathematical models may allow for more features of the blood flow to be evaluated (e.g., thrombosis), such models are a part of future research activities.

In the stented case, substantial indications have been given for areas of zero velocity and without rotational behaviour in the periphery. An additional thrombosis model could be implemented to analyse thrombus growth in these regions.

The developed methods have to be refined in such a way that they provide the necessary resolution and respective pulsatory behaviour, so they are able to interact with boundary geometry and are able to model growth as well as modify other relevant parameters such as thrombosis parameters in order to automatically determine a stent geometry that is best for a specific situation. Tools for 2D/3D blood flow visualization are not only useful to showcase results of numerical computations but also to offer great help to doctors and medical professionals in the treatment of the corresponding health problems as these tools provide new information that is not accessible using traditional tools. The future research activities of this research group focus on the

analysis and development of patient-specific stent geometries or to alternatively provide a software-assisted stent geometry recommendation from a set of clinically available stents.

Acknowledgment

The authors would like to offer their sincerest gratitude to the German Research Association (DFG), funding the project as part of FOR493 and TRR30, the Jindrich Necas Center for Mathematical Modeling, project LC06052 financed by MSMT, and the Higher Education Commission (HEC) of Pakistan for their financial support of the study.

References

- [1] S. W. Joo, S. I. Lee, S. J. Noh, Y. G. Jeong, M. S. Kim, and Y. T. Jeong, "What is the significance of a large number of ruptured aneurysms smaller than 7 mm in diameter?" *Journal of Korean Neurosurgical Society*, vol. 45, no. 2, pp. 85–89, 2009.
- [2] J. Lu, J. C. Liu, L. J. Wang, P. Qi, and D. M. Wang, "Tiny intracranial aneurysms: endovascular treatment by coil embolisation or sole stent deployment," *European Journal of Radiology*, vol. 81, no. 6, pp. 1276–1281, 2012.
- [3] G. J. E. Rinkel, "Natural history, epidemiology and screening of unruptured intracranial aneurysms," *Journal of Neuroradiology*, vol. 35, no. 2, pp. 99–103, 2008.
- [4] A. Chien, J. Sayre, and F. Vintilueuella, "Comparative morphological analysis of the geometry of ruptured and unruptured aneurysms," *Neurosurgery*, vol. 69, no. 2, pp. 349–356, 2011.
- [5] A. Morita, T. Kimura, M. Shojima, T. Sameshima, and T. Nishihara, "Unruptured intracranial aneurysms: current perspectives on the origin and natural course, and quest for standards in the management strategy," *Neurologia Medico-Chirurgica*, vol. 50, no. 9, pp. 777–787, 2010.
- [6] M. Aenis, A. P. Stancampiano, A. K. Wakhloo, and B. B. Lieber, "Modeling of flow in a straight stented and nonstented side wall aneurysm model," *Journal of Biomechanical Engineering*, vol. 119, no. 2, pp. 206–212, 1997.
- [7] B. B. Lieber, V. Livescu, L. N. Hopkins, and A. K. Wakhloo, "Particle image velocimetry assessment of stent design influence on intra-aneurysmal flow," *Annals of Biomedical Engineering*, vol. 30, no. 6, pp. 768–777, 2002.
- [8] T. M. Liou, S. N. Liou, and K. L. Chu, "Intra-aneurysmal flow with helix and mesh stent placement across side-wall aneurysm pore of a straight parent vessel," *Journal of Biomechanical Engineering*, vol. 126, no. 1, pp. 36–43, 2004.
- [9] M. Kim, D. B. Taulbee, M. Tremmel, and H. Meng, "Comparison of two stents in modifying cerebral aneurysm hemodynamics," *Annals of Biomedical Engineering*, vol. 36, no. 5, pp. 726–741, 2008.
- [10] M. Kamran, J. Yarnold, I. Q. Grunwald, and J. V. Byrne, "Assessment of angiographic outcomes after flow diversion treatment of intracranial aneurysms: a new grading schema," *Neuroradiology*, vol. 53, no. 7, pp. 501–508, 2011.
- [11] A. M. Gambaruto, J. Janela, A. Moura, and A. Sequeira, "Sensitivity of hemodynamics in a patient specific cerebral aneurysm to vascular geometry and blood rheology," *Mathematical Biosciences and Engineering*, vol. 8, no. 2, pp. 409–423, 2011.
- [12] Y. Yoshimoto, "A mathematical model of the natural history of intracranial aneurysms: quantification of the benefit of

- prophylactic treatment,” *Journal of Neurosurgery*, vol. 104, no. 2, pp. 195–200, 2006.
- [13] H. S. Chang, “Simulation of the natural history of cerebral aneurysms based on data from the International Study of Unruptured Intracranial Aneurysms,” *Journal of Neurosurgery*, vol. 104, no. 2, pp. 188–194, 2006.
- [14] A. Molyneux, R. Kerr, I. Stratton et al., “International Subarachnoid Aneurysm Trial (ISAT) of neurosurgical clipping versus endovascular coiling in 2143 patients with ruptured intracranial aneurysms: a randomised trial,” *Lancet*, vol. 360, no. 9342, pp. 1267–1274, 2002.
- [15] S. Appanaboina, F. Mut, R. Löhner, C. Putman, and J. Cebal, “Simulation of intracranial aneurysm stenting: techniques and challenges,” *Computer Methods in Applied Mechanics and Engineering*, vol. 198, pp. 3567–3582, 2009.
- [16] J. R. Cebal, F. Mut, J. Weir, and C. M. Putman, “Association of hemodynamic characteristics and cerebral aneurysm rupture,” *American Journal of Neuroradiology*, vol. 32, no. 2, pp. 264–270, 2011.
- [17] T. Inamuro, T. Ogata, S. Tajima, and N. Konishi, “A lattice Boltzmann method for incompressible two-phase flows with large density differences,” *Journal of Computational Physics*, vol. 198, no. 2, pp. 628–644, 2004.
- [18] P. Yuan and L. Schaefer, “Equations of state in a lattice Boltzmann model,” *Physics of Fluids*, vol. 18, no. 4, Article ID 042101, 2006.
- [19] X. Shan and H. Chen, “Lattice Boltzmann model for simulating flows with multiple phases and components,” *Physical Review E*, vol. 47, no. 3, pp. 1815–1819, 1993.
- [20] M. Junk and W. A. Yong, “Rigorous Navier-Stokes limit of the lattice Boltzmann equation,” *Asymptotic Analysis*, vol. 35, no. 2, pp. 165–185, 2003.
- [21] S. Succi, *The Lattice Boltzmann Equation for Fluid Dynamics and Beyond*, Clarendon Press, Oxford, UK, 2001.
- [22] M. C. Sukop and D. T. Thorne, *Lattice Boltzmann Modeling: An Introduction for Geoscientists and Engineers*, Springer, Berlin, Germany, 2006.
- [23] L. Walczak, D. Fisseler, and F. Weichert, “Exploring therapy options with the interactive simulation of intra-aneurysmal blood flow on the gpu,” in *GI-Jahrestagung*, U. Goltz, M. A. Magnor, H.-J. Appelerath, H. K. Matthies, W.-T. Balke, and L. C. Wolf, Eds., vol. 208 of *LNI*, pp. 1745–1754, GI, 2012.
- [24] E.-W. Speckmann and J. Hescheler, *Physiologie*, Elsevier, 2008.
- [25] T. Ohshima, S. Miyachi, K. I. Hattori et al., “Risk of aneurysmal rupture: the importance of neck orifice positioning-assessment using computational flow simulation,” *Neurosurgery*, vol. 62, no. 4, pp. 767–773, 2008.
- [26] J. A. Sethian, *Level Set Methods and Dynamic Implicit Surfaces—Evolving Interfaces in Computational Geometry, Fluid Mechanics, Computer Vision, and Materials Science*, Cambridge Monographs on Applied and Computational Mathematics, Cambridge University Press, New York, NY, SA, 1999.
- [27] L. Walczak, F. Weichert, A. Schröder, C. Landes, H. Müller, and M. Wagner, “Evaluating the impact of shape on finite element simulations in a medical context,” in *Modelling the Physiological Human*, vol. 5903, pp. 95–109, Springer, 2009.
- [28] M. Razzaq, H. Damanik, J. Hron, A. Ouazzi, and S. Turek, “FEM multigrid techniques for fluid-structure interaction with application to hemodynamics,” *Applied Numerical Mathematics*, vol. 62, pp. 1156–1170, 2011.
- [29] M. Razzaq, *Finite element simulation techniques for incompressible fluid-structure interaction with applications to bio-engineering and optimization [Ph.D. thesis]*, TU Dortmund, 2011.
- [30] R. Münster, O. Mierka, and S. Turek, “Finite element-fictitious boundary methods (FEM-FBM) for 3D particulate flow,” *International Journal for Numerical Methods in Fluids*, vol. 69, no. 2, pp. 294–313, 2012.
- [31] Q. Zou and X. He, “On pressure and velocity flow boundary conditions for the lattice boltzmann bgk model,” *Biophysics*, vol. 9, article 16, 1995.

Research Article

Encoding Scratch and Scrape Features for Wear Modeling of Total Joint Replacements

**Karen M. Kruger,^{1,2} Nishant M. Tikekar,³ Anneliese D. Heiner,^{1,2} Thomas E. Baer,¹
John J. Lannutti,³ John J. Callaghan,^{1,2} and Thomas D. Brown^{1,2}**

¹ Orthopaedic Biomechanics Laboratory, Department of Orthopaedics and Rehabilitation, University of Iowa, 2181 Westlawn Building, Iowa City, IA 52242-1100, USA

² Department of Biomedical Engineering, University of Iowa, Iowa City, IA 52242, USA

³ Department of Materials Science and Engineering, Ohio State University, Columbus, OH 43210, USA

Correspondence should be addressed to Thomas D. Brown; tom-brown@uiowa.edu

Received 20 December 2012; Accepted 25 February 2013

Academic Editor: Kumar Durai

Copyright © 2013 Karen M. Kruger et al. This is an open access article distributed under the Creative Commons Attribution License, which permits unrestricted use, distribution, and reproduction in any medium, provided the original work is properly cited.

Damage to hard bearing surfaces of total joint replacement components typically includes both thin discrete scratches and broader areas of more diffuse scraping. Traditional surface metrology parameters such as average roughness (R_a) or peak asperity height (R_p) are not well suited to quantifying those counterface damage features in a manner allowing their incorporation into models predictive of polyethylene wear. A diffused lighting technique, which had been previously developed to visualize these microscopic damage features on a global implant level, also allows damaged regions to be automatically segmented. These global-level segmentations in turn provide a basis for performing high-resolution optical profilometry (OP) areal scans, to quantify the microscopic-level damage features. Algorithms are here reported by means of which those imaged damage features can be encoded for input into finite element (FE) wear simulations. A series of retrieved clinically failed implant femoral heads analyzed in this manner exhibited a wide range of numbers and severity of damage features. Illustrative results from corresponding polyethylene wear computations are also presented.

1. Introduction

Contemporary total hip and total knee arthroplasty (THA, TKA) procedures have excellent success rates clinically. However, in a few percent of cases, aseptic loosening due to wear-induced osteolysis remains a major impediment to implant longevity. This is especially a concern for patients with polyethylene bearings whose hard-surface counterfaces have been damaged due to scratching by 3rd bodies [1], or due to scraping from untoward events such as impingement or dislocation [2]. While it is well appreciated that damage of hard-surface counterfaces leads to elevated polyethylene wear, it is also recognized that differences in numbers, locations, and/or severities of such damage features have very different consequences in terms of wear rate elevation [3]. Unfortunately, despite the substantial morbidity of premature implant

failures from accelerated polyethylene wear caused by counterface damage, a direct dose/response relationship between hard-counterface damage and accelerated polyethylene wear has yet to be elucidated. Part of the reason for this knowledge gap is that established damage characterization techniques for hard bearing surfaces do not describe that damage in a manner appropriate for direct, deterministic quantification of polyethylene wear.

Detection of hard-surface damage features has commonly relied upon gross-level visual inspection and optical microscopy [4]. Scanning electron microscopy (SEM) provides enhanced information on the morphology of these damage features at yet higher magnification [1], but again mainly in the form of pictorial information. Quantification of surface morphology has primarily been done by means of profilometry. The majority of such work has involved stylus instruments,

where fluctuations in the vertical position are recorded as the stylus physically moves short distances horizontally across the surface of interest [4, 5]. Since stylus profilometry recordings provide height variation data only along individual sampling lines, they have limited utility for quantifying the morphology of entire surfaces. Most commonly, therefore, investigators using this technique have resorted to spot samplings of presumed representative regions. For example, Hall et al. [6] quantified damage of retrieval femoral heads on the basis of 20 line profiles (each 1.4 mm in length) per specimen, taken in what was judged to be each specimen's most heavily scratched region. Besides being limited to surface height samplings along individual traverse lines, the short sweep length capacities of most line profile instruments also have made it difficult to quantify heterogeneous topography within large areas of damage [5].

High resolution maps of surface morphology can be generated through several techniques. Scanning tunneling microscopy transduces surface topography by monitoring the tunneling current flowing between an extremely sharp conductive probe and the sample surface. Atomic force microscopy generates three-dimensional images by means of a probe attached to the tip of a cantilever moving across the surface, monitoring the minute forces of interaction between the sample surface and probe [7]. Both of these techniques are able to measure surface height changes of less than a nanometer. However, sizes of the scan areas are extremely small, typically only in the range of a few ten-thousandths of a square millimeter. This limitation, plus the slow scan times involved, make these techniques impractical for use in mapping whole implant surfaces. Ultrasonic microscopes have been developed to examine surface mechanical properties of surfaces and to detect surface cracks and texture. However, these instruments have in-plane resolutions only on the order of a few tens of μm , and they again require long scan times [8].

More recently, areal measurements of surface morphology have been facilitated by optical profilometry (OP). This technique captures surface features at subnanometer vertical resolution, using light interferometry [9]. (Laser illumination has also been used for interferometry instruments, but the coherence of laser illumination produces surface noise that is approximately twice as high as that for conventional light illumination [10].) OP's high vertical resolution is well suited to quantifying microscopic damage present on retrieval implant surfaces, with relatively high speed and high accuracy [10]. OP has been validated against stylus profilometry [11] and in turn has served as a gold standard for evaluating other imaging techniques [12]. The maximum sampling region size for OP scans is on the order of a few square millimeters. While most previous applications of OP have therefore still resorted to judgment-based spot samplings [9], OP scanning of selected substantial fractions of entire joint surfaces—while certainly tedious—is nevertheless tractable.

The measurements that are output from profilometry scans most commonly have been standard surface roughness parameters such as average roughness (R_a), peak asperity height (R_p), and maximum asperity depth (R_v). While traditional roughness parameters of this class are straightforward to evaluate and interpret, their suitability for quantifying

wear-consequential surface damage is less than ideal. For example, R_a is unable to distinguish between large groups of fine scratches versus small numbers of severe scratches. Similarly, R_p fails to differentiate between a single asperity versus multiple asperities of similar height. Also, these traditional roughness measures have normally been reported as isotropic scalar variables. Including the predominant directionality of microscopic-level damage is an important consideration, however, because physical wear tests have shown that differing angles between scratch orientation and the direction of relative surface motion can produce order-of-magnitude differences in wear rate elevation [13]. Moreover, for scrapes, the directionality of the microscratches within a given macro-level scrape is not necessarily coincident with the scrape's macro-level directionality. For example, the microscratches in scrape damage generated at an edge-loaded femoral head region during a THA dislocation event tend to be substantially askew to the macrodirection of the scrape [14].

While the microtopography of the hard-surface counterface is clearly a major influence on the rate of polyethylene wear [15], direct quantification of the damage-versus-wear relationship presently lacks physical basis. Rather, most work in this area has been empirical, usually involving simplified articulations such as those in pin-on-plate experiments [16]. At least for individual scratches, the best-correlating parameter in such work has tended to be scratch lip height, as reflected in R_p (peak asperity height). Even empirically, however, it has been difficult to identify statistically significant wear-versus-roughness relationships for the complex articulations characteristic of *in situ* function of whole implants. For example, in a study of 35 retrieval implants [6], there was only marginal correlation ($r = 0.374$, $P = 0.099$) between clinical wear factors and R_a , with corresponding R_p values having an even weaker relationship with wear ($r = 0.211$, $P = 0.225$).

In order to move beyond empirical observations, and to help underpin physics-based models of damage versus wear, it is essential to quantify the severity and directionality of individual scratches and scrapes. Novel image-based computational techniques developed for that purpose are here reported. These computational techniques for surface damage registry are applied to a series of total hip femoral heads that had been surgically retrieved following implant clinical failure. Characteristic aspects of whole-surface damage severity are reported for these retrievals. Finally, results are presented from an illustrative finite element computation of polyethylene wear acceleration associated with the damage to a specific femoral head from this series.

2. Materials and Methods

Retrieval femoral heads were first digitally photographed using a novel diffused-light illumination technique [17]. This involved positioning the implant component on an angular indexing stage, inside a translucent white tube which eliminated spurious reflections from ambient lighting and room surroundings. Globally registered 1.6 megabyte digital photos (4432 pixels/mm^2) were then taken from the polar direction and at 30 degree increments circumferentially, so as to image

the entire bearing surface. These images provided vivid visual rendition of all macroscopically apparent damage features on the entire implant bearing surface. (As noted below, images taken at this resolution have been shown to highlight scratches that are well below wear-consequential severities.) The associated (grayscale) intensity modulations provided a basis for the damage to be objectively registered for purposes of image analysis. The damage was of two principal types: scratches and scrapes. The distinction was that scratches were manifest as thin discrete individual darkened lines, whereas scrapes were manifest as broad swaths of diffuse darkening, within which individual scratch tracks could not be distinguished at the global image level.

A custom-written MATLAB routine was used to determine regions of damage apparent in the global-level images. Canny edge detection was first performed to detect regions of damage, based on grayscale discontinuity relative to (bright) undamaged regions. This edge detector distinguished edges on the basis of maximum gradients of intensity. Edges were flagged if their gradients fell above an analyst-set threshold. This threshold value was set such that it was sensitive enough to detect the fine-scale scratches, but high enough so as to avoid influence from grayscale variations associated with the necessarily nonuniform distance from the camera lens. Next, a median filter was applied to the original images, replacing each pixel's intensity with the median of pixel intensities in a surrounding square region of analyst-specified size. Median filtering in this context had the effect of "blurring away" linear damage features (i.e., scratches) whose breadths were below a specific threshold. Analyst specification of the median filter size thus provided a basis for objectively distinguishing between scratches versus scrapes, for which different computational treatments were utilized for purposes of polyethylene wear modeling (see below). Empirically, various filter sizes were applied to representative original images that contained both scratches and scrapes (Figure 1). A 20×20 filter size was judged appropriate for distinguishing between scratches and scrapes, and was therefore used for *en masse* data processing in this retrieval series.

The darkened regions remaining after the median filtering operation were then autosegmented using an analyst-set intensity threshold. These constituted the scrape features. The scrape regions thus identified were then removed from the pre-median-filtered Canny edge detection result, leaving the remaining (i.e., non-scrape) damage features to be classified as scratches (Figure 2). A Hough transform was then used to discretize these scratch damage features into straight-line scratch segments. This analysis technique used a linear transform and the parametric equation of a straight line to determine the number of points falling along any given candidate straight line. Those candidate lines whose lengths fell above an analyst-set threshold were flagged, thus discretizing curvilinear scratches into concatenations of straight-line scratch segments.

Next, OP was used to quantify the severity of each scratch or scrape. A Veeco Contour GT noncontact profiler (Bruker, Tuscon, AZ), which captured surface features by means of light interferometry, was employed for this purpose. The maximum resolution in a plane tangential to the target

surface was $0.25 \mu\text{m}^2$ per pixel, and the maximum out-of-plane resolution was $0.01 \mu\text{m}$. The instrument was capable of directly imaging individual areas of sizes up to $\sim 1 \text{ mm} \times 1 \text{ mm}$, and it could autostitch those captured individual images into composite images sized up to $\sim 5 \text{ mm} \times 5 \text{ mm}$. The instrument's internal software allowed for removal of the global (spherical) curvature that was present in the raw scans. The parameters of global spherical curvature were estimated using a least-squares-error algorithm to achieve a quadratic fit to the raw surface data. Removal of this spherical form from the raw data therefore enabled determination of local deviations from the native implant surface. The internal software also included capability to report standard surface roughness parameters (R_a , R_p , etc.).

Superimposition of analyst-selected control points allowed alignment of the OP scans with their respective global-level images (Figures 3(a)–3(c)). For each OP scan, six sets of control points were chosen from damage features that were visually distinguishable on both the global-level image and the OP scan. These control points were used to compute a 2D transformation structure, based on second order polynomials. The global image was then translated and rotated based on this 2D transformation, to associate the detected damage features with their respective locations on the OP scan.

Encoding the identified damage features involved accounting for both directionality and severity. In the case of scratches, directionality was simply the locally prevailing orientation of the scratch, and severity was based on the average scratch lip height (the dominant factor in wear elevation [18]) calculated from the OP data. To make the severity calculation, each designated scratch segment was first superimposed on its corresponding OP image(s) (Figure 3(b)). Values of surface vertical height were then queried from the OP dataset(s) along a series of equally spaced sampling lines directed perpendicular to the scratch segment. The peak surface height was identified along each of those sampling lines, and the mean of those peak heights was designated as the scratch lip height for that individual scratch segment (Figures 3(c) and 3(d)). (Convergence analysis had been performed to determine appropriate density of the sampling lines (Figure 4).)

In the case of scrapes, the directionality of interest for purposes of polyethylene wear modeling was not the macro-level direction of the scrape, but rather the direction of "micro-level" scratching within the scrape. While these two orientations were similar or nearly so for many scrapes, there were notable exceptions, such as when circumferentially oriented macroscrapes resulted from transverse sliding during egress of edge-loaded femoral heads during subluxation. To identify the direction of microscratching, a Hough transform was performed on each scrape OP dataset, which detected the micro-scratch lines within the scrape. The longest such line was designated as the scraping direction for that scrape area (Figure 5). Severity of scraping was quantified in terms of the average roughness within the segmented scrape region. This computation was made from OP data, again based on control point registration between (polygon-delineated) macrolevel scrape features and corresponding features in the OP datasets. The average roughness (R_a) value within each scrape polygon

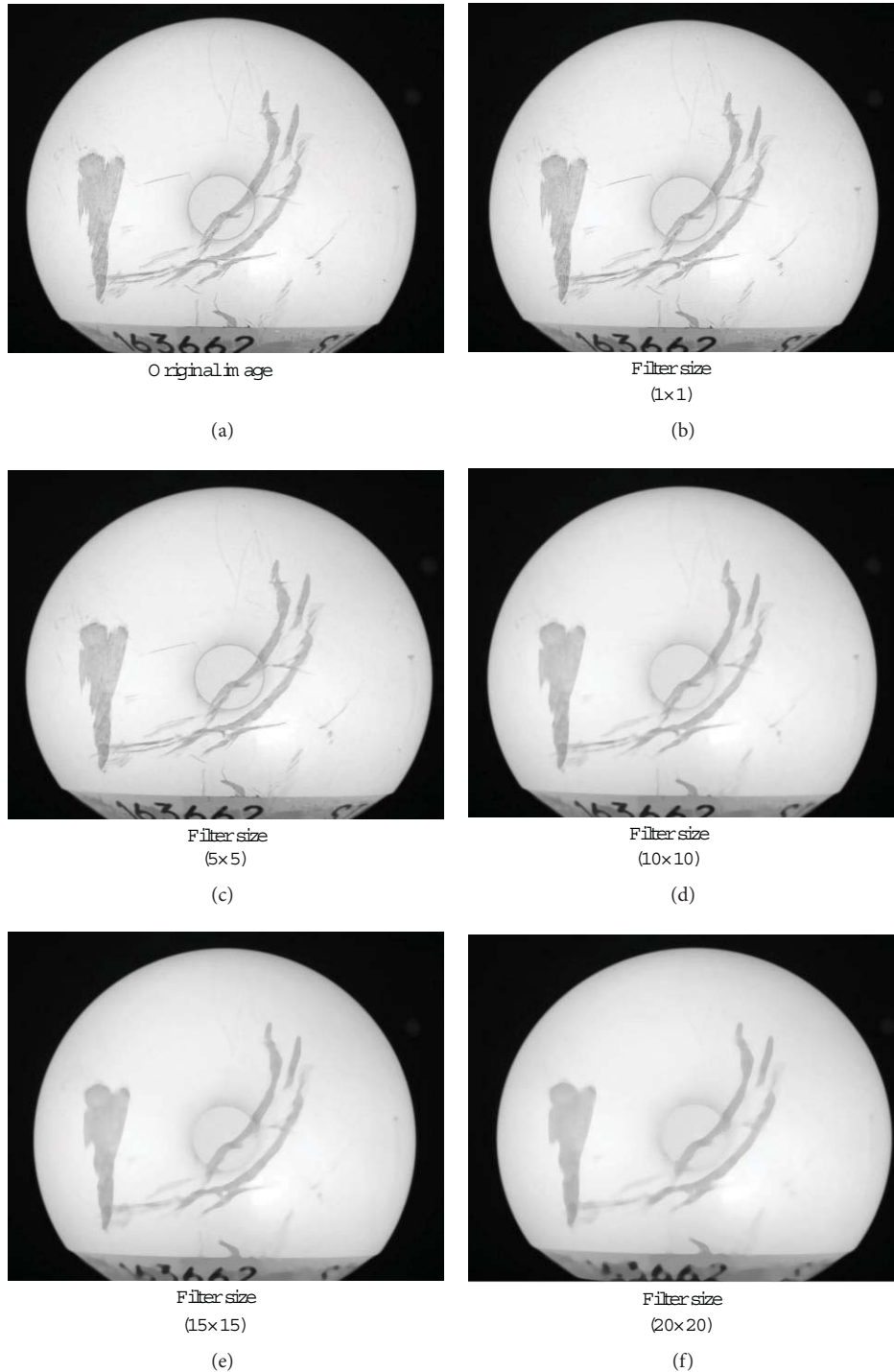


FIGURE 1: Successively stronger median filters of various sizes applied to an original image of a retrieval femoral head. The filter size indicates the neighborhood around the corresponding pixel in the input image for which the median value is calculated. This parameter allowed the analyst to control the distinction between scratch and scrape.

was simply the average of the height differences of individual pixels, relative to the mean surface height of all the pixels within the scrape polygon.

Current computational models of polyethylene wear in total joint replacements most commonly implement some form of the classic Archard wear formula [19]. This formula

estimates local wear depth as the product of (1) contact pressure, (2) sliding distance, and (3) a wear coefficient dependent on the tribological characteristics of surface contact. For computing damage-induced wear rate acceleration, the Archard wear coefficient for the baseline undamaged surface is elevated for polyethylene areas that are overpassed

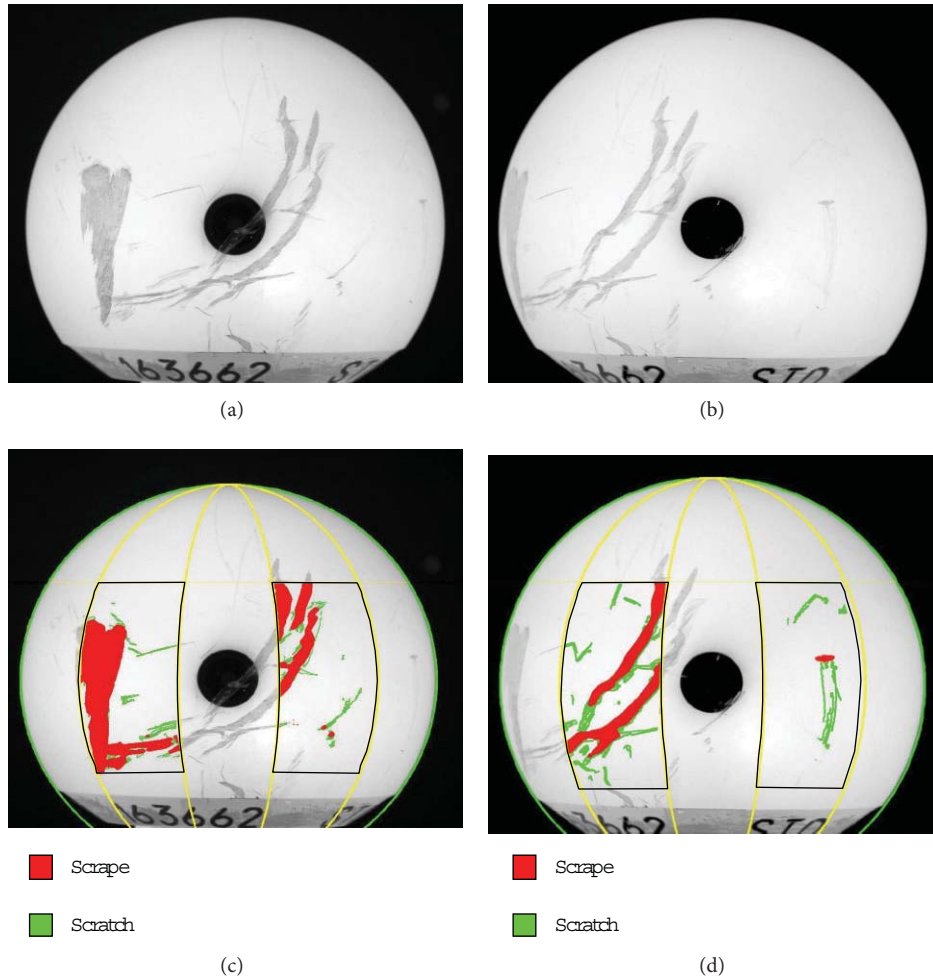


FIGURE 2: ((a), (b)) Diffused-light images of a femoral head displaying both scratch and scrape damages, captured from two orientation directions 30° apart circumferentially. (The black dot in the center of the images is from camera lens reflection. This reflection required that multiple view directions be utilized.) ((c), (d)) Image-processed results displaying identified damage regions. The sectors outlined in black indicate areas analyzed for this particular image. The top of the femoral head was captured and analyzed in companion polar images.

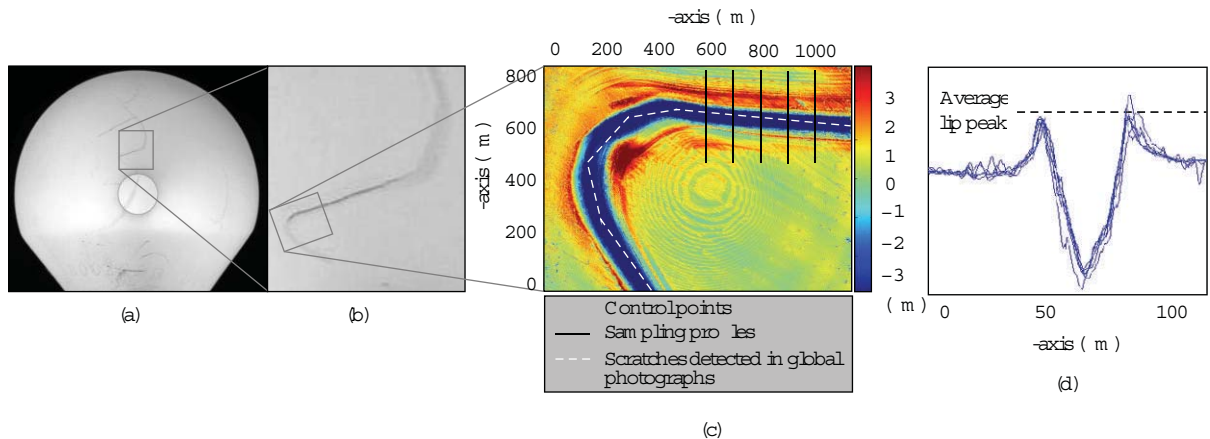


FIGURE 3: Global (a) and close-up (b) photographs of a scratched femoral head. Control points used for alignment with the OP scans are indicated by asterisks. (c) Local OP scan of selected region. (d) OP scan profiles used to calculate scratch lip height for a single scratch segment.

TABLE 1: Scratch lip heights on samples displaying scratch damage.

Femoral head	Number of scratch segments	Average scratch segment length (mm)	Scratch lip height (μm)		
			Mean \pm SD	Min	Max
1	101	0.59	1.72 ± 0.95	0.08	4.75
2	71	0.41	1.73 ± 0.46	0.56	2.48
4	172	0.91	2.31 ± 1.29	0.32	7.01
5	430	0.58	2.76 ± 1.73	0.07	9.75
6	211	1.03	1.64 ± 0.40	1.01	2.87
7	62	0.76	1.70 ± 1.13	0.62	5.38
9	190	0.87	2.39 ± 0.81	0.94	4.38

TABLE 2: Comparison of average roughness (R_a) values on samples displaying scrape damage.

Femoral head	Number of scrape regions	Average scrape area (mm^2)	R_a (μm)		
			Mean \pm SD	Min	Max
2	22	1.57	0.28 ± 0.27	0.03	1.21
3	104	1.20	0.17 ± 0.11	0.01	0.55
6	68	5.09	0.21 ± 0.08	0.05	0.39
8	71	8.03	1.12 ± 1.25	0.03	4.20
9	44	1.05	0.26 ± 0.15	0.05	0.65

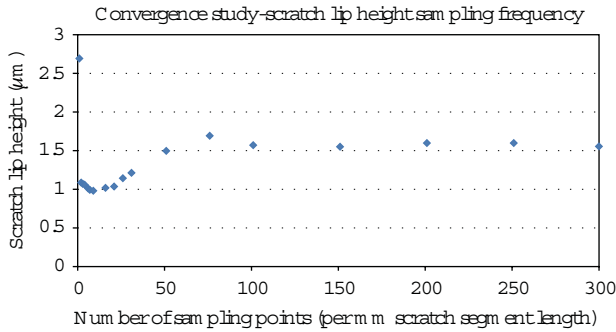


FIGURE 4: The results of a sampling convergence series, undertaken to determine appropriate sampling frequency.

by the counterface damage features. For scratches, there is an approximately exponential relationship [20] between scratch lip height (h_L) and the scaling factor (k_{inc}) for wear coefficient elevation, the specific parameters being

$$k_{\text{inc}} = 58.0985 - 58.0985 \cdot e^{-0.2237 * h_L} \quad (1)$$

when lip height is expressed in μm . For the case of scrapes, the R_a values were converted to wear coefficient scaling factors using a power law relationship [16], the specific parameters being

$$k_{\text{inc}} = 37.538 \cdot (R_a)^{1.2} \quad (2)$$

for R_a measurements in μm .

3. Results

Scratch and scrape damage was encoded for nine representative specimens from our institution's collection of femoral

head retrievals (Figure 6). The image processing routine detected scratches on seven of those specimens and scrapes on five of them. The distribution of severities of detected scratches (lip heights) and scrapes (R_a values) are reported in Tables 1 and 2, respectively. The seven specimens exhibiting scratch damage all showed large variability in the severity of individual scratches (Figure 7). The particular specimen showing the greatest amount of variability (specimen no. 5) had scratch lip heights ranging from 0.10 to 9.75 μm . In the interest of completeness, the present set of results includes scratches with lip heights as low as 0.07 μm . This may be unnecessarily exhaustive, however, since there is experimental evidence that the lip height threshold for detectable wear rate acceleration from individual scratches is substantially higher, on the order of 1 μm [18]. If desired for purposes of computational economy, wear-inconsequential scratches can be disregarded from further consideration in downstream wear modeling, simply by Boolean masking on the basis of lip height.

The computed R_a values of scraped regions also showed considerable variability (Figure 8). Series-wide, the highest scrape-average roughness value was 4.20 μm (specimen no. 8), a three-order-of-magnitude elevation relative to typical R_a values for undamaged implant surfaces [16].

These damage features can produce substantial increases in local wear rates. The presence of the most severe scratches increased the local wear coefficient by a factor of approximately 50, as shown by (1). The most severe scrapes regions produced wear coefficient increases of over 200-fold, as shown by (2).

4. Discussion

This collection of scratch lip heights and scrape R_a values, along with their associated individual directionalities,

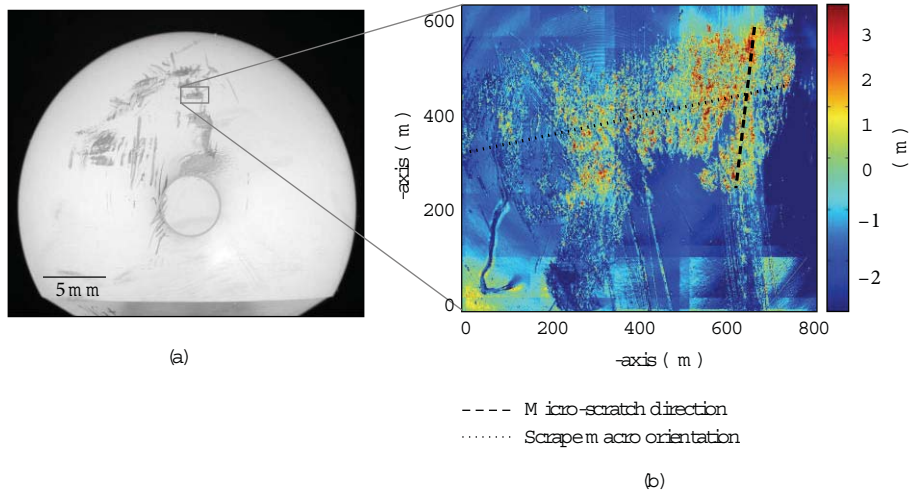


FIGURE 5: (a) Global photograph of scrape region. (b) Local OP scan, revealing scrape morphology. The dashed black line indicates the direction of microscratching, as determined by Hough transform. The dotted black line indicates the orientation of the macroscopic scrape.

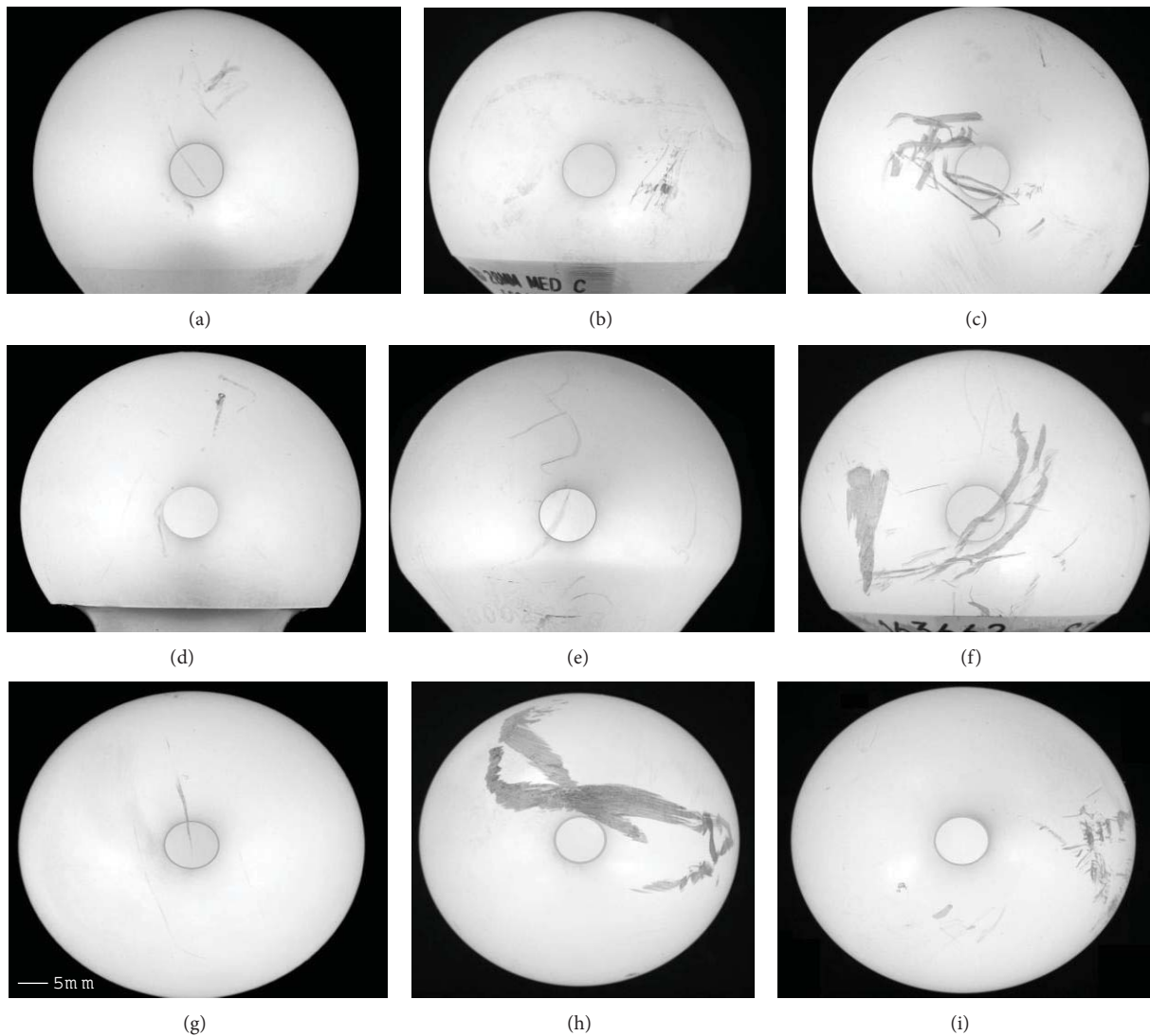
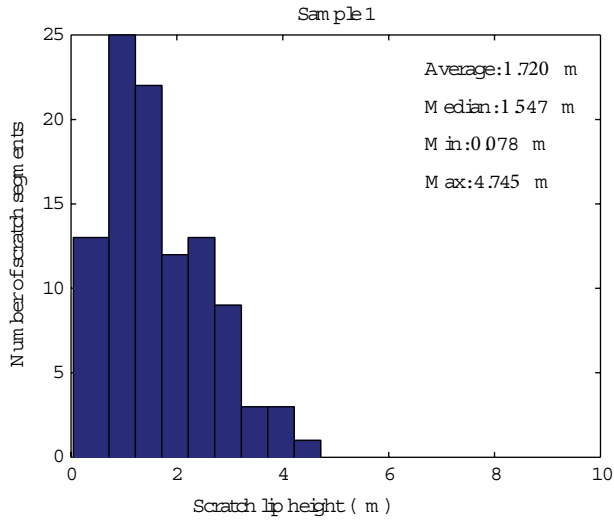
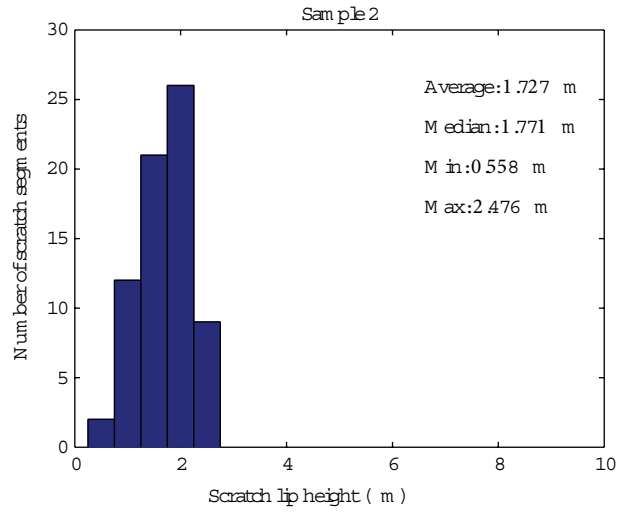


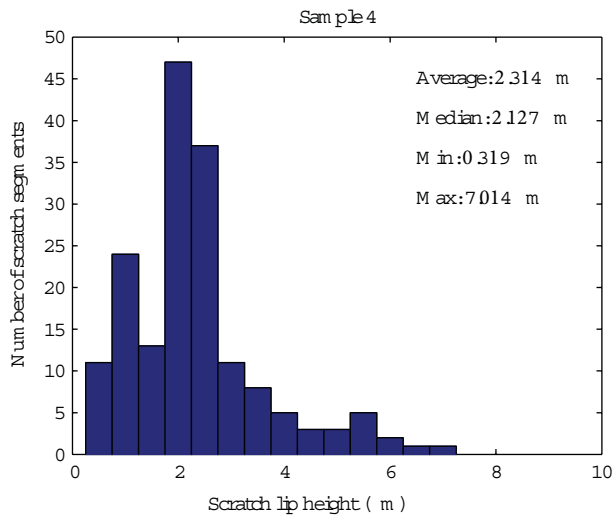
FIGURE 6: Global photographs of representative retrieval femoral heads.



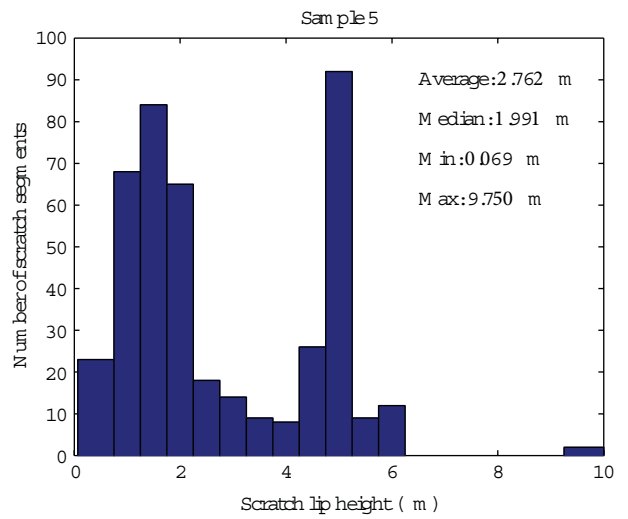
(a)



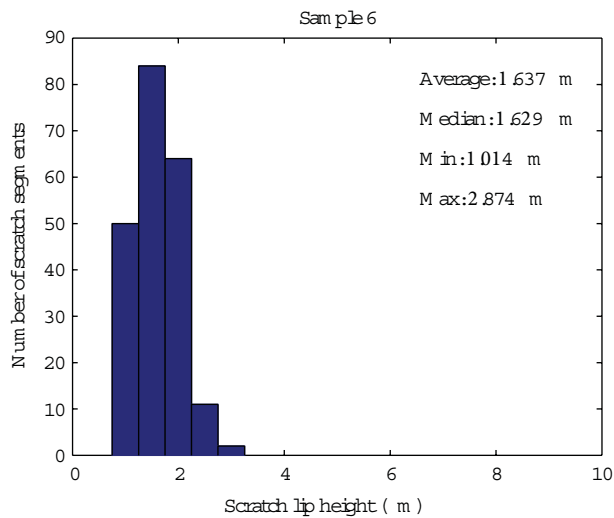
(b)



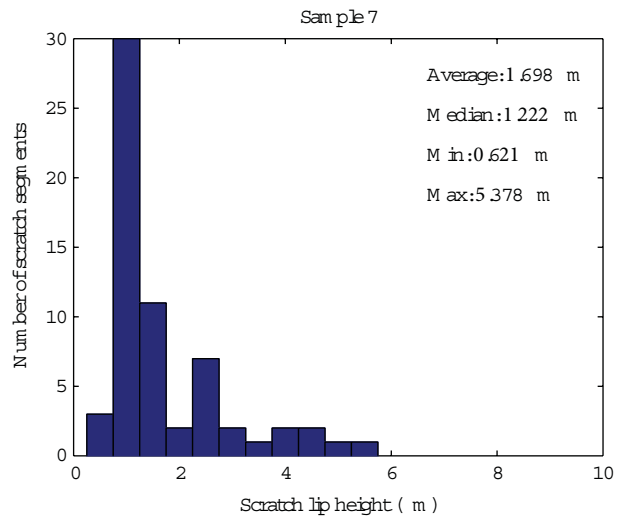
(c)



(d)



(e)



(f)

FIGURE 7: Continued.

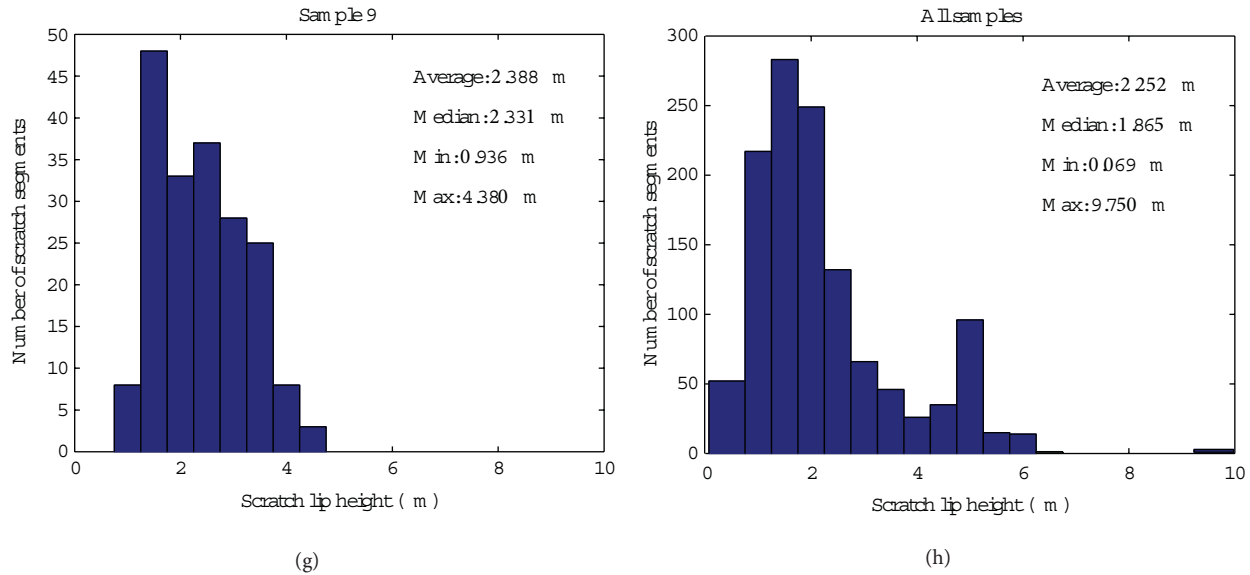


FIGURE 7: Distributions of the scratch lip height values for each femoral head that displayed scratch damage.

demonstrates a range of damage features on typical retrieval femoral heads. While the present OP data captures were similar to those for other OP applications [9, 21], the data from these computational techniques represent the first-global-implant level registry of micron-level damage features. Such datasets can be used as inputs to FE liner wear models, to allow clinically realistic simulation of femoral head damage on a case-specific basis. These data allow for damage representation on a scratch- or scrape-specific basis, and they allow for wear to be predicted due to each damage feature. This constitutes an improvement over previous methods, which have only represented damage in terms of standard surface roughness parameters and have been unable to establish strong linkage between any of these parameters and wear acceleration [6].

Illustratively, an FE wear model of one particular specimen (specimen no. 6) from this series was generated by mapping each identified damage feature’s severity, orientation, and global-level geometry onto the femoral head. Collectively, these damage features, comprised of a total of 211 scratch segments and 68 scrape regions, led to a 3.8-fold increase in polyethylene liner wear, compared to a baseline simulation of an otherwise-identical undamaged femoral head (Figure 9). Of this wear increase, 68% was due to the scratch damage and 32% was due to the scrape damage.

Wear rate increases computed using this technique have been physically validated both for isotropically roughened patches [22] and for scratches [20]. While direct physical validation has not yet been performed for directional scrapes, the only difference between FE wear simulations for directional scrapes versus for isotropically roughened patches is the incorporation of directionality into the wear factor.

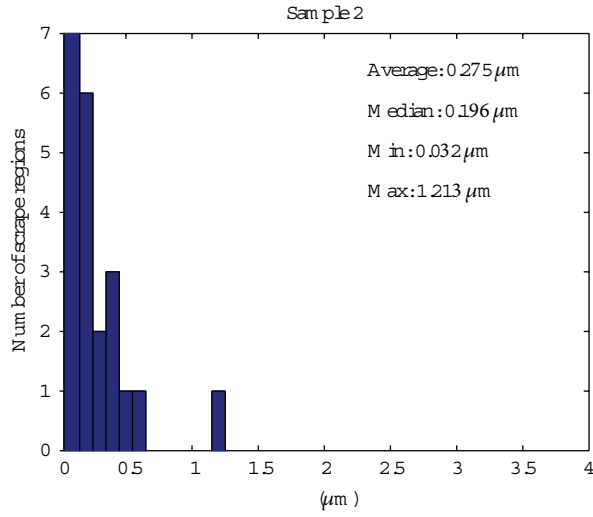
The present series was restricted to total hip femoral component retrievals. This same damage registration framework presumably could also be used to characterize hard counterfaces in other total joint replacements such as the femoral

components of total knees, which often exhibit damage features similar to those catalogued here. For example, a 2D interferometry study of TKA retrievals [23] identified both fine, closely packed scratches with lip heights on the order of $0.5\ \mu\text{m}$, and severe damage features with scratch lips approaching $4\ \mu\text{m}$.

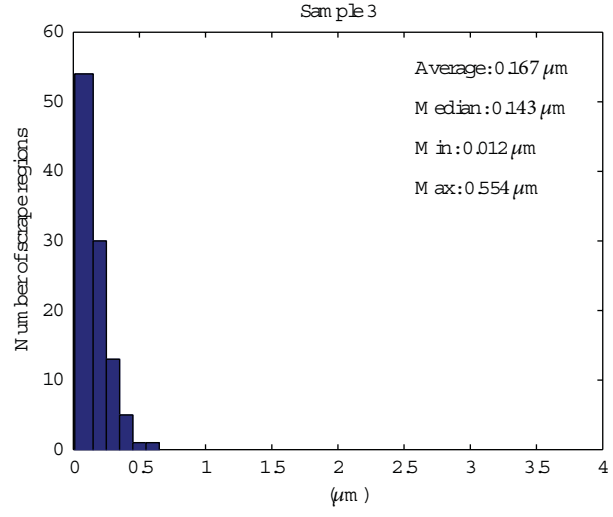
Quantification of femoral head damage through this analysis framework relies on the global diffused-light digital photographs and corresponding edge detection computations to identify damage features. While the diffused lighting technique in almost all instances provided much more vivid rendition of damage features than was apparent visually under room lighting, there were several instances where fine scratches that were visually apparent under normal room lighting were not visible in the diffused-light images. The OP scans of such “disappearing” scratches showed that these fine scratches had extremely low lips, indicative of their not being critical in terms of the end goal of determining wear rate acceleration. Further work to elucidate the relationship between diffused-light image grayscale values versus corresponding scratch lip heights may offer insight in this seemingly anomalous phenomenon.

5. Conclusion

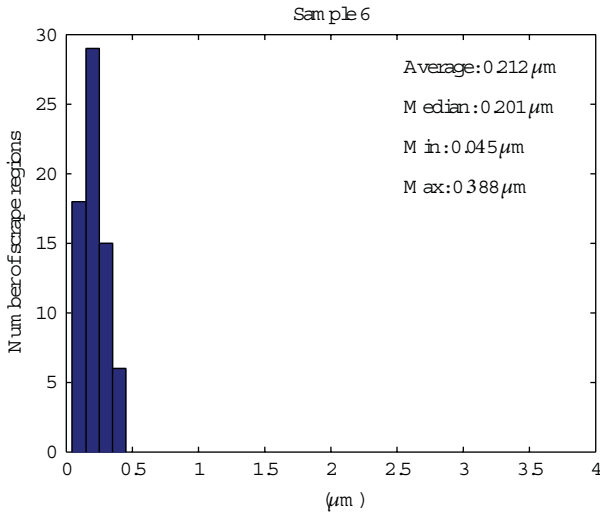
For total joint replacements with a polyethylene bearing surface, dramatically accelerated wear is often associated with accrual of scratch or scrape damage to the hard-surface counterface. Moving from qualitative to quantitative assessments of this interaction requires a basis for representing hard-surface damage in a manner conducive to performance of physics-based wear analyses. The present paper reports a multiscale experimental/computational framework for making such damage representations. Global-level and microlevel imaging are coupled to computationally register the severity



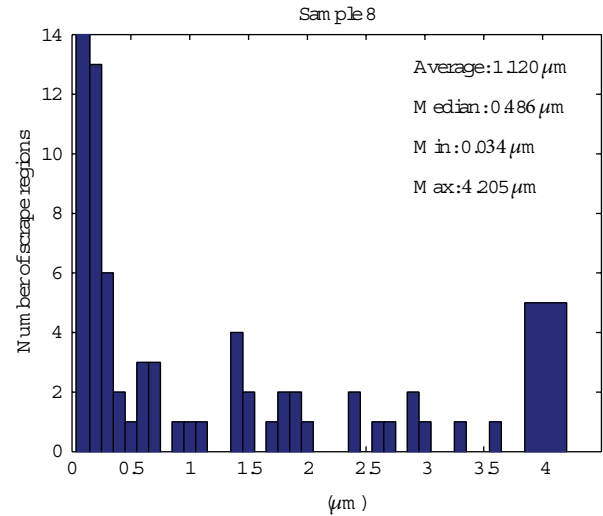
(a)



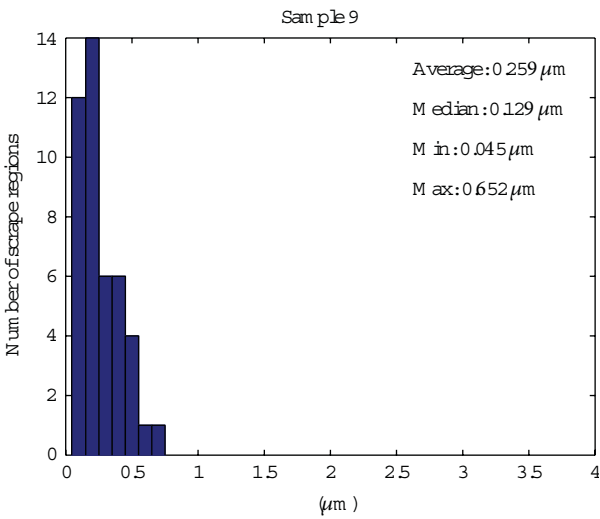
(b)



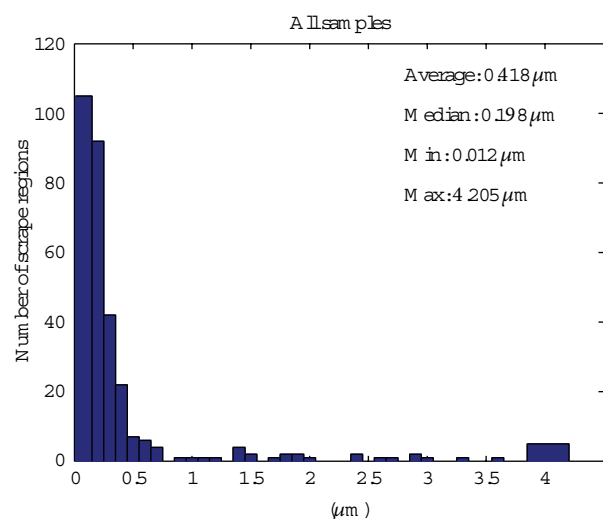
(c)



(d)



(e)



(f)

FIGURE 8: Distributions of the R_a values for each scrape region in the femoral heads that displayed scrape damage.

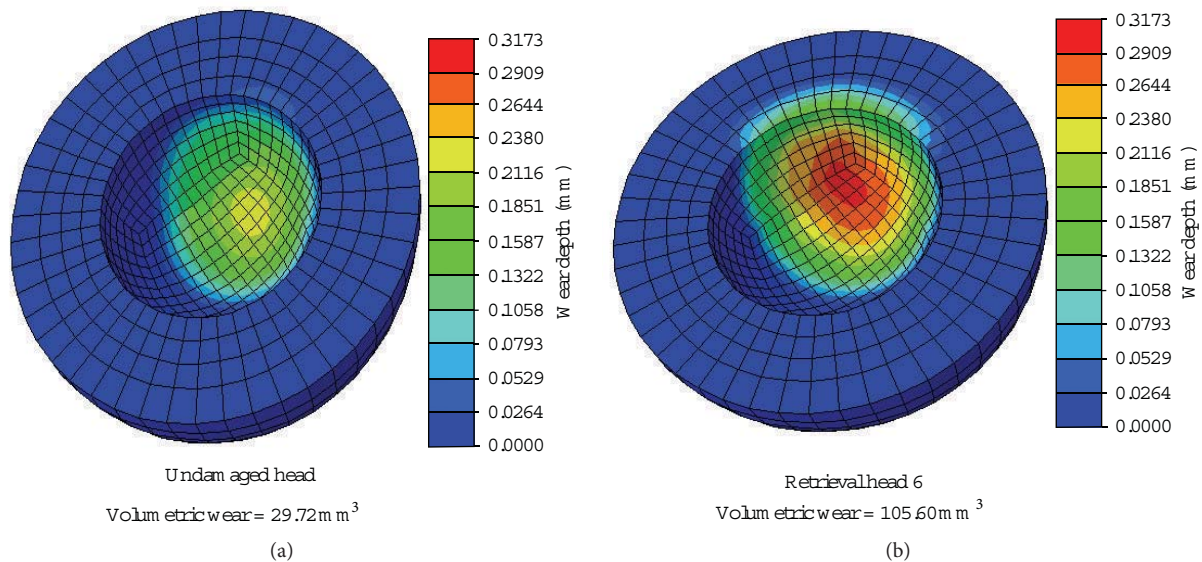


FIGURE 9: Computed wear depths (1×10^6 cycles) for an undamaged and retrieval femoral head (28 mm).

and directionality of both scratch and scrape damage present on entire implant bearing surfaces. This damage registry framework proved practical for use for typical retrieval total hip implants, thus opening the way for quantitative analyses of damage-related polyethylene wear rate acceleration on a case-specific basis.

To the authors' knowledge, the present datasets constitute the first-ever compilations of whole-surface damage features on orthopaedic total joint replacements. Besides their usage in the context of enabling wear computations, such datasets will likely prove useful in other contexts, such as for forensic assessment of specific surface damage events, and "reverse engineering" of implant designs to minimize wear-consequential counterface damage.

Acknowledgments

This research was funded by NIH Grant AR057780. Dr. Steve Liu provided invaluable assistance in coordination with the authors' institution's implant retrieval program.

References

- [1] M. Jasty, C. R. Bragdon, K. Lee, A. Hanson, and W. H. Harris, "Surface damage to cobalt-chrome femoral head prostheses," *Journal of Bone and Joint Surgery B*, vol. 76, no. 1, pp. 73–77, 1994.
- [2] J. G. Bowsher, T. K. Donaldson, P. A. Williams, and I. C. Clarke, "Surface damage after multiple dislocations of a 38-mm-diameter, metal-on-metal hip prosthesis," *Journal of Arthroplasty*, vol. 23, no. 7, pp. 1090–1096, 2008.
- [3] H. J. Lundberg, K. J. Stewart, J. J. Callaghan, and T. D. Brown, "Kinetically critical sites of femoral head roughening for wear rate acceleration in total hip arthroplasty," *Clinical Orthopaedics and Related Research*, no. 430, pp. 89–93, 2005.
- [4] D. Najjar, M. Bigerelle, H. Migaud, and A. Iost, "Identification of scratch mechanisms on a retrieved metallic femoral head," *Wear*, vol. 258, no. 1–4, pp. 240–250, 2005.
- [5] P. S. Walker, E. Salvati, and R. K. Hotzler, "The wear on removed McKee Farrar total hip prostheses," *Journal of Bone and Joint Surgery A*, vol. 56, no. 1, pp. 92–100, 1974.
- [6] R. M. Hall, P. Siney, A. Unsworth, and B. M. Wroblewski, "The effect of surface topography of retrieved femoral heads on the wear of UHMWPE sockets," *Medical Engineering and Physics*, vol. 19, no. 8, pp. 711–719, 1997.
- [7] K. Merrett, R. M. Cornelius, W. G. McClung, L. D. Unsworth, and H. Sheardown, "Surface analysis methods for characterizing polymeric biomaterials," *Journal of Biomaterials Science, Polymer Edition*, vol. 13, no. 6, pp. 593–621, 2002.
- [8] F. A. Carvalho and N. C. Santos, "Atomic force microscopy-based force spectroscopy—biological and biomedical applications," *IUBMB Life*, vol. 64, no. 6, pp. 465–472, 2012.
- [9] A. P. D. Elfick, S. L. Smith, and A. Unsworth, "Variation in the wear rate during the life of a total hip arthroplasty: a simulator and retrieval study," *Journal of Arthroplasty*, vol. 15, no. 7, pp. 901–908, 2000.
- [10] K. I. Jolic, C. R. Nagarajah, and W. Thompson, "Non-contact, optically based measurement of surface roughness of ceramics," *Measurement Science and Technology*, vol. 5, no. 6, pp. 671–684, 1994.
- [11] J. C. Wyant, C. L. Koliopoulos, B. Bhushan, and D. Basila, "Development of a three-dimensional noncontact digital optical profiler," *Journal of Tribology*, vol. 108, no. 1, pp. 1–8, 1986.
- [12] A. Kohm, J. Gaumer, V. Ravula et al., "Three-dimensional laser micrometry characterization of surface wear in total hip arthroplasty," *Journal of Biomedical Materials Research*, vol. 82, no. 2, pp. 428–439, 2007.
- [13] L. P. Glennon, T. E. Baer, J. A. Martin, W. D. Lack, and T. D. Brown, "Sliding direction dependence of polyethylene wear for metal counterface traverse of severe scratches," *Journal of Biomechanical Engineering*, vol. 130, no. 5, Article ID 051006, 2008.
- [14] A. M. Kop, C. Whitewood, and D. J. L. Johnston, "Damage of oxinium femoral heads subsequent to hip arthroplasty dislocation. Three retrieval case studies," *Journal of Arthroplasty*, vol. 22, no. 5, pp. 775–779, 2007.

- [15] J. Fisher and D. Dowson, "Tribology of total artificial joints," *Proceedings of the Institution of Mechanical Engineers H*, vol. 205, no. 2, pp. 73–79, 1991.
- [16] D. Dowson, M. M. El-Hady Diab, B. J. Gillis, and J. R. Atkinson, "Influence of counterface topography on the wear of ultra high molecular weight polyethylene under wet or dry conditions," in *Polymer Wear and Its Control: American Chemical Society*, pp. 171–187, 1985.
- [17] A. D. Heiner, K. M. Kruger, T. E. Baer, and T. D. Brown, "Enhancing damage visibility on metallic surfaces: a simple technique for photography and viewing," *Journal of Arthroplasty*. In press.
- [18] D. Dowson, S. Taheri, and N. C. Wallbridge, "The role of counterface imperfections in the wear of polyethylene," *Wear*, vol. 119, no. 3, pp. 277–293, 1987.
- [19] J. F. Archard, "Contact and rubbing of flat surfaces," *Journal of Applied Physics*, vol. 24, no. 8, pp. 981–988, 1953.
- [20] K. M. Kruger, N. M. Tikekar, A. D. Heiner et al., "A novel formulation for scratch-based wear modeling in total hip arthroplasty," *Computer Methods in Biomechanics and Biomedical Engineering*. In press.
- [21] E. W. Patten, S. A. Atwood, D. W. Van Citters, B. A. Jewett, L. A. Pruitt, and M. D. Ries, "Delamination of a highly cross-linked polyethylene liner associated with titanium deposits on the cobalt-chromium modular femoral head following dislocation," *Journal of Bone and Joint Surgery B*, vol. 92, no. 9, pp. 1306–1311, 2010.
- [22] T. D. Brown, H. J. Lundberg, D. R. Pedersen, and J. J. Callaghan, "2009 nicolas andry award: clinical biomechanics of third body acceleration of total hip wear," *Clinical Orthopaedics and Related Research*, vol. 467, no. 7, pp. 1885–1897, 2009.
- [23] C. V. Jones, I. R. Williams, D. D. Auger et al., "Quantification of third body damage to the tibial counterface in mobile bearing knees," *Proceedings of the Institution of Mechanical Engineers H*, vol. 215, no. 2, pp. 171–179, 2001.

Research Article

Acceleration of Early-Photon Fluorescence Molecular Tomography with Graphics Processing Units

Xin Wang,¹ Bin Zhang,¹ Xu Cao,¹ Fei Liu,¹ Jianwen Luo,^{1,2} and Jing Bai¹

¹ Department of Biomedical Engineering, Tsinghua University, Beijing 100084, China

² Center for Biomedical Imaging Research, Tsinghua University, Beijing 100084, China

Correspondence should be addressed to Jing Bai; deabj@tsinghua.edu.cn

Received 20 December 2012; Accepted 2 March 2013

Academic Editor: Wenxiang Cong

Copyright © 2013 Xin Wang et al. This is an open access article distributed under the Creative Commons Attribution License, which permits unrestricted use, distribution, and reproduction in any medium, provided the original work is properly cited.

Fluorescence molecular tomography (FMT) with early-photons can improve the spatial resolution and fidelity of the reconstructed results. However, its computing scale is always large which limits its applications. In this paper, we introduced an acceleration strategy for the early-photon FMT with graphics processing units (GPUs). According to the procedure, the whole solution of FMT was divided into several modules and the time consumption for each module is studied. In this strategy, two most time consuming modules (G_d and W modules) were accelerated with GPU, respectively, while the other modules remained coded in the Matlab. Several simulation studies with a heterogeneous digital mouse atlas were performed to confirm the performance of the acceleration strategy. The results confirmed the feasibility of the strategy and showed that the processing speed was improved significantly.

1. Introduction

Fluorescence molecular tomography (FMT) is a promising imaging technique for small animals that allows visualization of 3D distributions of fluorescent biomarkers *in vivo* [1, 2]. However, significant challenges remain in FMT because the high degree of light scatter in biological tissues results in an ill-posed image reconstruction problem and consequently reduces the spatial resolution [3]. Considering this point, time-gated technique is proposed, which only utilizes “early-arriving” photons that experience few scattering events so as to reduce the large amount of diffusion photons. To date, a number of groups have validated that with time-gated detection technique, the spatial resolution and fidelity of the reconstructed results can be improved [3–5].

For the reconstruction of FMT using early photons, there are several feasible algorithms, such as the filtered back-projection method, schemes based on the time-resolved diffusion equation (DE), the time-resolved telegraph equation (TE), and the second-order cumulant approximation of the radiative transport equation (RTE), [3–7]. Among them, the method based on time-resolved DE is the most popular utilized for simplicity. However, compared with continuous

wave FMT (CW-FMT), time-domain FMT (TD-FMT) will cost more time because of the time scale. Generally, solving TD-FMT will cost tens of minutes to hours and there are no efficient schemes for its acceleration at present.

Fortunately, the high-speed development of graphics processing unit (GPU) technology provides direction to the acceleration of TD-FMT solution. The highly parallel structure of GPU makes it more effective than central processing unit (CPU) for a range of algorithms on parallelizable floating point operations. However, programming on GPU had been difficult until the compute unified device architecture (CUDA) was proposed in 2006 [8]. CUDA comes with a software environment that allows developers to use C as a high-level programming language. Utilizing CUDA-enabled GPU, parallel acceleration algorithms has been studied in the field of fluorescence tomography. Fang and Boas reported a parallel Monte Carlo algorithm accelerated by GPU for modeling time-resolved photon migration in arbitrary 3D turbid media [9]. Zhang et al. implemented acceleration of adaptive finite element framework for bioluminescence tomography with CUBLAS and CULA libraries [10]. However, to date, CUDA-enabled GPU technology has not been utilized to solve TD-FMT.

In this paper, we introduced an acceleration strategy for the early-photon FMT. The time consumption of each module was studied to confirm the necessity of GPU acceleration. In the strategy, two most time consuming modules (G_d and W modules) were accelerated with CUDA language, respectively, and the other modules were coded in the Matlab. Several simulations with a heterogeneous digital mouse atlas were performed to evaluate the performance of the acceleration strategy.

The paper is organized as follows. In Section 2, the forward and inverse models based on TD-FMT are illustrated in detail. Numerical simulations with fluorescence targets embedded in a 3D mouse model are carried out. In Section 3, simulation results are shown and analyzed. Finally, we discuss the results and conclusion in Section 4.

2. Materials and Methods

2.1. Time-Domain Diffusion Equation and Finite Element Method. The radiative transfer equation (RTE) is considered as the most accurate model for describing the process of photon propagation in biological tissues. However, because RTE is computationally expensive, the diffusion approximation of RTE is commonly used. Thus, photon propagation for FMT can be modeled with the coupled time-domain DEs as follows [7]:

$$\begin{aligned} \frac{1}{c} \frac{\partial \Phi_x(r, t)}{\partial t} + \mu_a(r) \Phi_x(r, t) - \nabla \cdot [D(r) \nabla \Phi_x(r, t)] \\ = \delta(r - r_s, t) \\ \frac{1}{c} \frac{\partial \Phi_m(r, t)}{\partial t} + \mu_a(r) \Phi_m(r, t) - \nabla \cdot [D(r) \nabla \Phi_m(r, t)] \\ = \frac{\eta(r)}{\tau} [\Phi_x(r, t) * E(t)], \end{aligned} \quad (1)$$

where $\Phi_{x,m}(r, t)$ denotes the photon density for excitation and fluorescence light, respectively. $\delta(r - r_s, t)$ provides the impulse light source. μ_a is the absorption coefficient and μ'_s is the reduced scattering coefficient. $D(r)$ is the diffusion coefficient defined by $D(r) = 1/(3(\mu_a(r) + \mu'_s(r)))$. As the excitation and emission wavelength are close to each other, the optical properties are assumed to be identical at both excitation and emission wavelengths for simplification. The fluorescent targets are described by fluorescent distribution $\eta(r)$ and lifetime τ . $E(t) = \exp(-t/\tau)$ is the lifetime function. $*$ is the temporal convolution operator. c is the speed of light.

To solve these equations, Robin boundary conditions are implemented on the boundary $\partial\Omega$ of the region Ω [7]:

$$2qD(r) \frac{\partial \Phi(r)}{\partial \vec{n}} + \Phi(r) = 0, \quad (2)$$

where \vec{n} denotes the outward normal vector of the boundary. The coefficient q takes into account the refractive index mismatch between both media.

Based on the first-order Born approximation, the fluorescence signal $\Phi_m(r_{sd}, t)$ measured at a detector point r_d for

an impulsive excitation at source position r_s at time t can be written as

$$\Phi_m(r_{sd}, t) = \int_{\Omega} W(r_{sd}, r, t) \cdot \eta(r) dr^3. \quad (3)$$

The weight matrix $W(r_{sd}, r, t)$ is described as

$$W(r_{sd}, r, t) = G(r_s, r, t) * E(t) * G(r, r_d, t), \quad (4)$$

where $G(r_s, r, t)$ and $G(r, r_d, t)$ are Green's functions of excitation and emission (G_s and G_d in short). In addition, for an isotropic impulse source, G is equal to Φ .

In order to reduce the influence of heterogeneity, the normalized Born approximation [11] is employed as follows:

$$\Phi^{nB}(r_{sd}, t) = \frac{\Phi_m(r_{sd}, t)}{\Phi_x(r_{sd}, t)} = \int_{\Omega} W^{nB}(r_{sd}, r, t) \cdot \eta(r) dr^3, \quad (5)$$

where W^{nB} is the normalized Born approximation of W .

By utilizing the standard Galerkin-FEM method, the object is discretized into N mesh nodes and the time is approximated with a sequence of time points with a time interval Δt . Then, Green's functions can be derived:

$$\begin{aligned} \left(K + \frac{C}{\Delta t}\right) G_v(n, k+1) &= \frac{C}{\Delta t} G_v(n, k) + S_v(n, k) \\ G_v(n, -1) &= G_v(n, 0) = 0, \end{aligned} \quad (6)$$

where K and C are matrices of $N \times N$ with the same expression as given in [7, 12, 13]

$$\begin{aligned} K_{ij} &= \int_{\Omega} [D(r) \cdot \nabla u_i(r) \cdot \nabla u_j(r) + \mu_a(r) u_i(r) u_j(r)] d\Omega \\ &\quad + \frac{1}{2q} \int_{\partial\Omega} u_i(r) u_j(r) d(\partial\Omega) \\ C_{ij} &= \frac{1}{c} \int_{\Omega} u_i(r) u_j(r) d\Omega \end{aligned} \quad (7)$$

but $S_v(n, k)$ differs in form:

$$S_v(n, k) = \begin{cases} \int_{\Omega} \delta(n, k) u_i(r) d\Omega & v = x \\ C \frac{c\eta(n)}{\tau} G_x(n, k) * E(k) & v = m. \end{cases} \quad (8)$$

At last, (3) is converted into the following matrix-form equation:

$$\Phi^{nB} = W^{nB} \cdot \eta. \quad (9)$$

Then the unknown fluorescence distribution η at different time-gates is obtained by solving the linear equation (9) using algebraic reconstruction technique (ART) with nonnegative constraints.

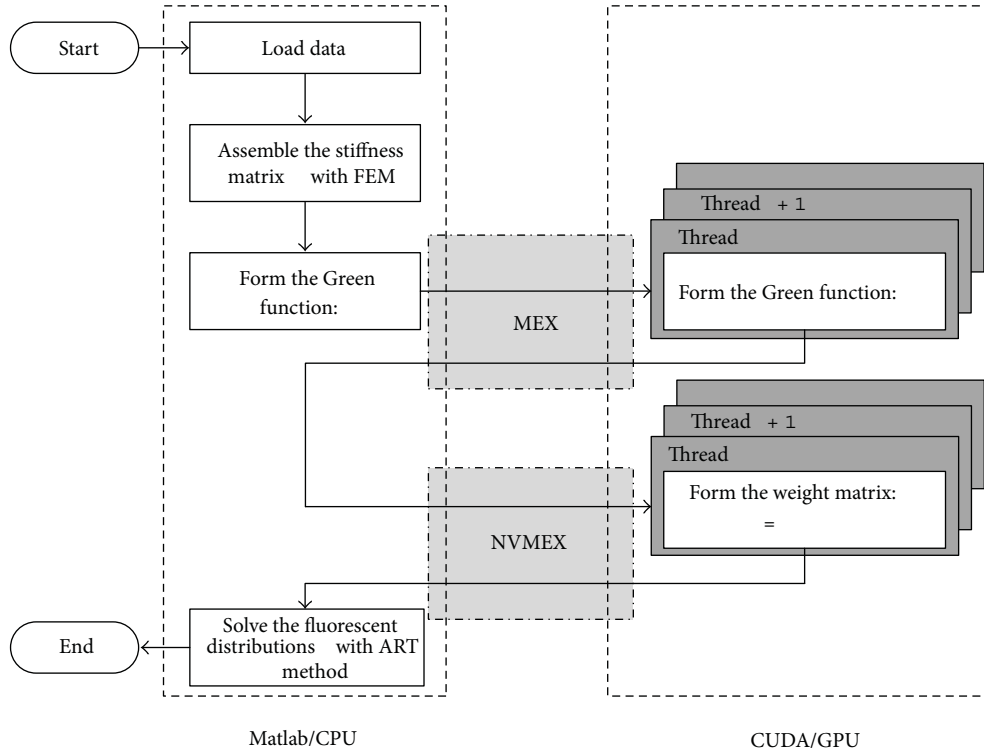


FIGURE 1: The execution flow chart of the whole acceleration strategy.

2.2. GPU Acceleration Strategy

2.2.1. The Flow Chart of the Acceleration Strategy. For the whole procedure, there is a large amount of matrix operations which are suitable for parallel accelerations by GPU. However, besides the matrix operations, there are still some other operations such as parameter configurations and mesh discretization, which are not suitable for the GPU acceleration. Therefore, the rest parts will be implemented in Matlab for programming flexibility. The execution flow chart of the whole algorithm is shown in Figure 1. The main program which contains the parts unnecessary to be accelerated is executed in Matlab. The parts of G_d and weight matrix acceleration, which need to be accelerated by GPU, are coded into subroutines so as to be called by the Matlab program. For the G_d acceleration, because CUBLAS library is used for the subroutine which can be recognized by the C compiler, “Matlab executable” (MEX) technology is available for the interface between the Matlab program and the G_d acceleration. As to the weight matrix acceleration, CUDA language is used in the subroutine and thus NVMEX technology is utilized as the interface. Details about the acceleration algorithms and the NVMEX technology are illustrated in the next subsections.

2.2.2. G_d Acceleration. In the calculation procedure, the module to solve G_d is time consuming because matrix inversion should be performed for each detector at each time node. Although the method to solve G_s is similar to that of G_d , the number of light sources is much smaller than the

number of detectors. As a result, the time consumption of G_s is very little that it is unnecessary to be accelerated. The Matrix inversion of large size is computationally complex and there are no effective methods for this problem. Fortunately, the matrices that need to be inverted for each detection point and each time node are the same. Therefore, the inversion of the matrix can be calculated in advance and thus the inversion operations can be converted into multiplication operations, which can be accelerated by GPU more effectively.

NVIDIA has provided a CUBLAS library on top of the CUDA driver for the developers to do some basic linear algebra operations. CUBLAS is an implementation of basic linear algebra subprograms (BLAS) and the “CU” stands for CUDA [10]. The multiplication operations during solving G_d can be implemented by using the CUBLAS library.

Furthermore, it can be found that G_d for each detector is irrelevant and can be parallel computing. However, for different time nodes, G_d cannot be calculated simultaneously because the calculation of the $(i + 1)$ th time node of G_d depends on the i th time node of G_d . Therefore, we can calculate G_d for all of the detectors for one time node at a time. At last, the structure of the whole G_d should be changed in order to solve the weight matrix conveniently.

2.2.3. Weight Matrix Acceleration. As mentioned in (4), to solve the weight matrix, time convolution of several matrices should be calculated. Because the number of source-detector (sd for short) pairs is large and the size of G_s or G_d for each point and each time node is large, the whole procedure of solving the weight matrix is time consuming.

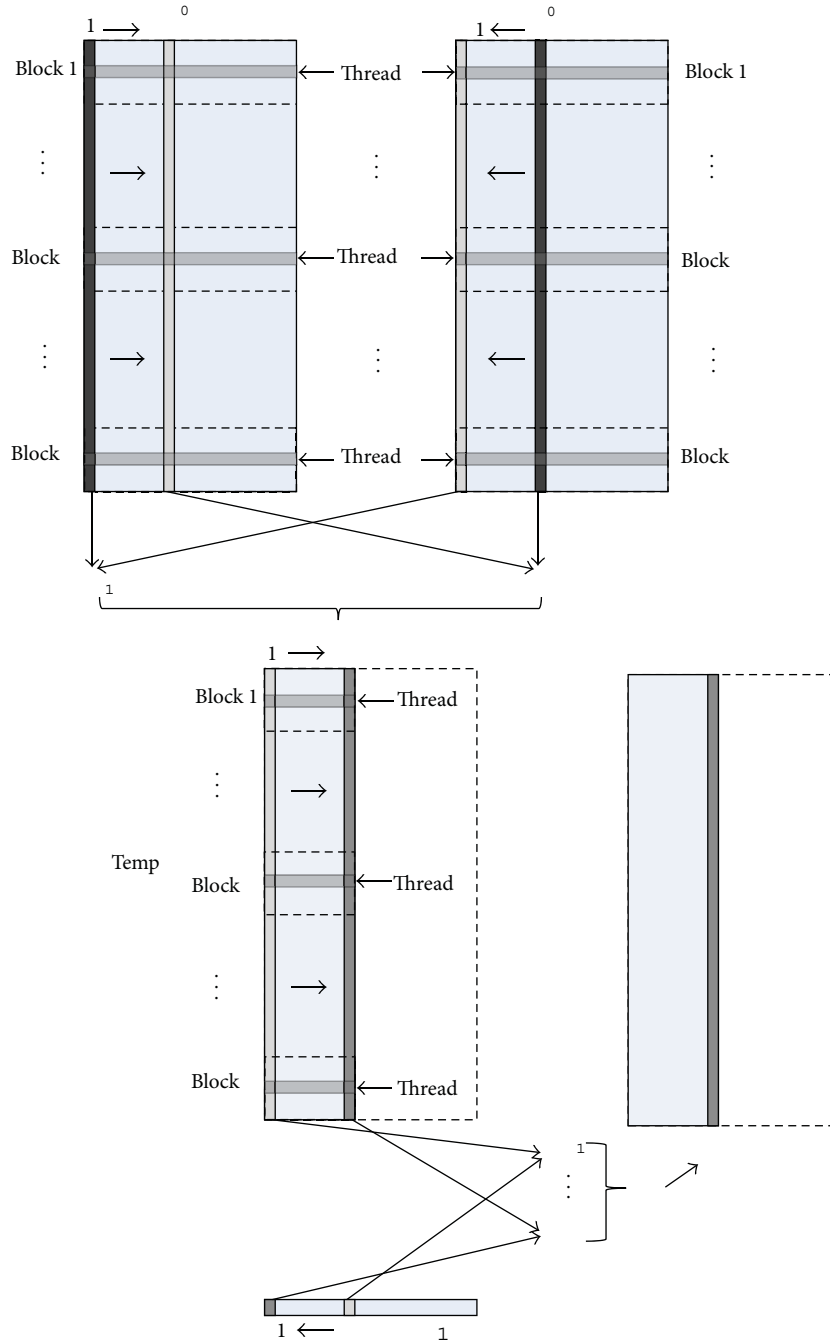


FIGURE 2: Principle of solving the weight matrix.

CUDA language is adopted for the acceleration algorithm of solving the weight matrix. Figure 2 shows the principle of the acceleration algorithm. G_{s0} and G_{d0} is Green's function for one source or detector for all the time nodes. The row stands for different mesh nodes and the column stands for different time nodes. It can be found that data of each row is irrelevant and only time convolution is calculated. Thus, data of each row can be distributed into different threads; therefore they can be implemented simultaneously. In this paper, the

number of threads contained in each block is configured 256. The total block number is configured according to the row number of the matrix. Texture memory is used to load the matrix of G_{s0} , G_{d0} , and E because it can accelerate the data visiting speed with its cache.

2.2.4. *NVMEX Technology.* As the execution efficiency of Matlab is lower than C or Fortran, the time consuming

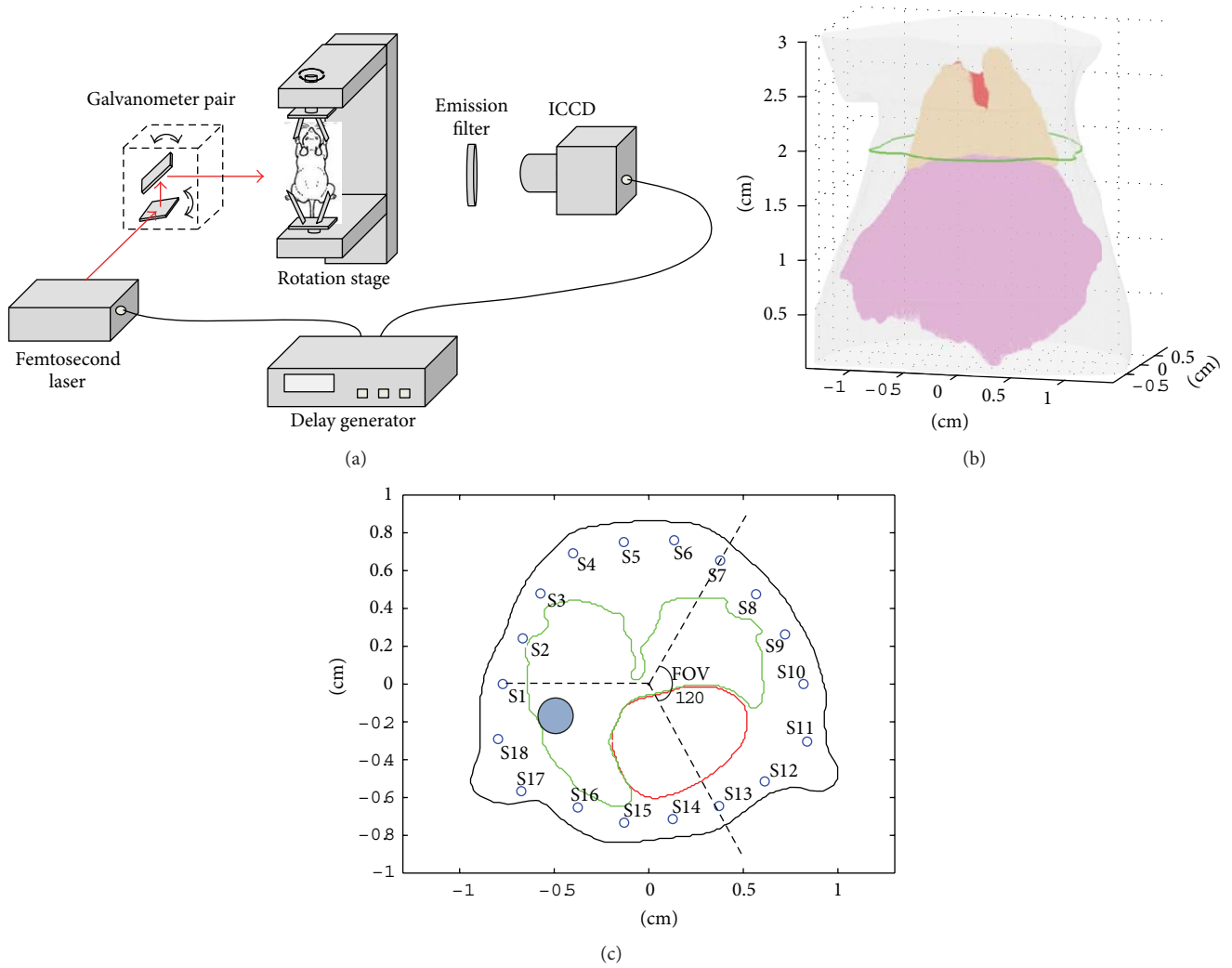


FIGURE 3: (a) Schematic of the free-space time-gated fluorescence tomography system. (b) The chest region of the digital mouse used for simulation. Different colors correspond to different tissue types (red: heart, orange: lungs, pink: liver, gray: adipose tissue). (c) Cross section of the digital mouse at the height of light source (green curve in (b)). The position of excitation lights and the field of view (FOV) with respect to source S1 are shown. The blue circle indicates the location of the fluorescent target.

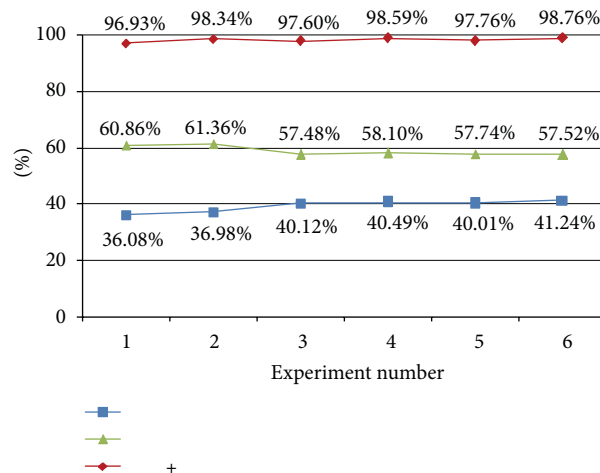


FIGURE 4: P values of the G_d (T4) module, W (T5) module and the $G_d + W$ (T4 + T5) module.

TABLE 1: Optical parameters of different tissues of the digital mouse model.

Material	Heart	Lung	Liver	Background
$\mu_a(\text{cm}^{-1})$	0.156	0.516	0.935	0.1
$\mu'_s(\text{cm}^{-1})$	9.0	21.2	6.4	10

subroutines are always programmed with C or Fortran and compiled into binary MEX-files, which can be loaded and executed by the Matlab interpreter.

However, subroutines with CUDA languages cannot be compiled into MEX-files directly because CUDA language could not be recognized by the conventional compilers based on C or Fortran. Instead, this problem can be solved by the NVMEX technology, in which “NV” stands for NVIDIA. NVMEX technology connects Matlab and CUDA language conveniently and efficiently. With NVMEX technology, the codes based on CUDA are compiled into MEX-files by the “nvcc” compiler and then called by the Matlab interpreter.

2.3. Experimental Setup. Numerical experiments are performed to validate the performance of the acceleration strategy. The synthetic measurements are generated based on a free-space, time-gated FMT system, schematically depicted in Figure 3(a). The excitation light is an ultrafast laser emitting approximately 1ps pulses. The imaged mouse is suspended on a rotation stage and the laser beam is coupled to the surface of the mouse by a pair of galvanometer-controlled mirrors. At last, the transmitted light is detected by a high-speed intensified CCD (ICCD) at the opposite side of the excitation light [7].

In this simulation study, a 3D mouse atlas is employed which provides not only the complex surface but also the anatomical information [14]. We perform the numerical simulations based on the mouse chest region, so only the mouse torso from the neck to the bottom of the liver, as shown in Figure 3(b), is selected, with a height of 3 cm.

In the simulations, the mouse is suspended on the rotation stage and the rotation axis is defined as the z -axis. The mouse is rotated over 360° with 60° increments and the data collected consisted of 6 projections. The projection number is 6 because the computational size of the whole program will enlarge as the projection number increases and the memory consumption will exceed the limit of the computer. As shown in Figure 3(c), the field of view (FOV) of the detection with respect to each excitation source is 120° . A cylindrical fluorescent target with the height of 0.2 cm and radius of 0.1 cm is located at the $(-0.31, -0.02, 1.93)$, which is indicated by the blue circle in Figure 3(c).

The simulations are performed in a heterogeneous mouse model. The absorption coefficient μ_a and the reduced scattering coefficient μ'_s shown in Table 1, which are calculated based on [15], are assigned to heart, lung, and liver to simulate photons propagation in biological tissues.

In order to evaluate the acceleration performance of the acceleration strategy, 6 simulated cases were performed. Configurations of these cases were the same except that the numbers of discretized mesh nodes and detectors were

different. The excitation and emission intensity on the surface of the mouse model were calculated by a forward simulated program in advance.

For different cases, the reconstructed fluorescent distributions at the time node of 300 ps were shown as the early-photon results. For the reconstruction, the relaxation parameter of ART was $\lambda = 0.1$ and the number of iteration steps was 100.

At last, the programs are performed on an Intel(R) Core (TM) i7-2600 CPU (3.4 GHz) platform with 16 GB memory. A NVIDIA Geforce GTX 460 graphics card with 336 cores is used for the acceleration strategy. The version number for the CUDA is 4.0. The contrasted programs are performed by Matlab 2008 and COMSOL Multiphysics 3.5 (COMSOL Inc, Stockholm, Sweden).

3. Results

3.1. The Necessity of the GPU Acceleration. For the simulated cases, the time consumption of each module by Matlab is shown in Table 2. The whole program is divided into 6 modules, among which the T4 and T5 modules are suitable for GPU-enabled acceleration. (In fact, the T3 module is also matrix operation. However, the time consumed by T3 is so short compared with the whole program that it is unnecessary to be accelerated.)

It can be found that T4 and T5 modules are time consuming compared with other modules. In order to study the time occupancy quantitatively, we define P as the time percentage of each module to the total time for each case. The P values of the G_d (T4) module, W (T5) module, and $G_d + W$ (T4 + T5) module are shown in Figure 4. It can be found that, for each case, the P value for the $G_d + W$ module is more than 95%. As a result, we can reach the conclusion that the GPU acceleration is necessary.

3.2. Speedup Performance of the Acceleration Algorithms. For the 6 simulated cases, the fluorescent target is reconstructed by the Matlab program and the GPU acceleration strategy, respectively. Time consumption of each module by the two methods is recorded. Then the speedup ratios of the G_d acceleration algorithm, the weight matrix acceleration algorithm, and the whole acceleration strategy are studied, respectively.

The time consumptions of G_d by both methods are showcased in Table 3. The speedup ratios of the G_d -accelerating algorithm for different cases are shown in Table 3. It can be found that the speedup ratios decrease as the number of mesh nodes increases. The main reason is that, in the acceleration algorithm, the G_d is calculated for all the detection points and for one time node at a time. Therefore, the structure of the G_d should be adjusted into another form in order to suit for the following weight matrix calculation. The memory need for this step is huge, and as the scale increases, the memory can exceed the physical memory of the computer which leads to more time consumption.

The time consumptions of the weight matrix by both methods and the speedup ratios are showcased in Table 4. The

TABLE 2: Time cost of each module in the Matlab program.

Experiment no.	Mesh nodes	Detectors	T1 (s)	T2 (s)	T3 (s)	T4 (s)	T5 (s)	T6 (s)
			Load data	Assemble K	Form G_s	Form G_d	Form W	Solve η
1	3074	710	0.03	5.44	1.96	128.25	216.35	3.47
2	3074	1409	0.03	4.73	1.93	250.54	415.79	4.56
3	3881	710	0.03	5.03	3.13	195.13	279.57	3.48
4	3881	1409	0.03	5.46	3.20	386.06	553.90	4.78
5	4697	710	0.03	5.87	4.09	254.56	367.33	4.29
6	4697	1409	0.03	5.60	4.03	492.57	686.95	5.10

TABLE 3: Time comparisons of forming G_d consumed by Matlab and CUDA.

Experiment no.	Mesh nodes	Detectors	Time (s) Matlab	Time (s) CUDA	Speedup ratio
1	3074	710	128.25	19.89	6.4
2	3074	1409	250.54	25.08	10.0
3	3881	710	195.13	36.00	5.4
4	3881	1409	386.06	43.91	8.8
5	4697	710	254.56	55.88	4.6
6	4697	1409	492.57	89.15	5.5

TABLE 4: Time comparisons of forming the weight matrix consumed by Matlab and CUDA.

Experiment no.	Mesh nodes	Detectors	Time (s) Matlab	Time (s) CUDA	Speedup ratio
1	3074	710	216.35	8.46	25.6
2	3074	1409	415.79	16.72	24.9
3	3881	710	279.57	9.70	28.8
4	3881	1409	553.9	19.78	28.0
5	4697	710	367.33	10.65	34.5
6	4697	1409	686.95	21.53	31.9

TABLE 5: Time comparisons of the whole strategy consumed by Matlab and CUDA.

Experiment no.	Mesh nodes	Detectors	Time (s) Matlab	Time (s) CUDA	Speedup ratio
1	3074	710	355.50	39.23	9.1
2	3074	1409	677.58	52.33	12.9
3	3881	710	486.37	57.53	8.5
4	3881	1409	953.43	76.51	12.5
5	4697	710	636.17	80.83	7.9
6	4697	1409	1194.28	125.77	9.5

speedup ratio for the weight matrix acceleration is more than 25, which is higher than that of the G_d acceleration algorithm. The reason is that the convolution operation is highly parallel, which makes it more easily for the GPU to achieve significant acceleration.

The speedup effect of the whole strategy is shown in Table 5. The final acceleration effect is a compromise of the acceleration of the computation between G_d and W .

3.3. *Accuracy of the Acceleration Strategy.* In the GPU acceleration strategy, arithmetic operations are performed with single precision, because the use of double-precision operations results in increased memory requirements and a reduction of speedup performance. However, operations with single precision may bring in some errors compared with the double-precision operations by the Matlab.

In order to study the error brought in by the single-precision operation in GPU. One simulated case with 4697 mesh nodes and 1409 detectors is selected to study the accuracy of reconstruction result (in fact, all the cases have the same conclusion and only one case is shown). Besides, 10% zero-mean, Gaussian noise was added to the synthetic data to simulate the actual case. Figure 5 shows the reconstructed results by Matlab and the GPU acceleration strategy.

Then, the max error between the results is calculated as follows:

$$\max \left| \frac{\eta_{\text{Matlab}} - \eta_{\text{GPU}}}{\eta_{\text{Matlab}}} \right| \times 100\% = 0.15\%, \quad (10)$$

where η_{Matlab} and η_{GPU} stand for the reconstructed fluorescent signals in each node by Matlab and GPU acceleration strategy, respectively. It can be found that the max error is 0.15%, which is negligible.

4. Discussions

In this paper, we introduced an acceleration strategy for the early-photon fluorescence molecular tomography with GPU. Results of several numerical simulation cases validate the feasibility of this acceleration strategy.

With the acceleration strategy, the speedup ratio is about 10 for different cases. Compared with the other GPU-enabled acceleration algorithms [9, 10], the speedup ratio is not very great. There are mainly two reasons. First, the step to solve G_d is mainly matrix inversion operations, which is less suitable for parallel acceleration compared with the operations of matrix multiplication and matrix convolution. Besides, the time consumed by the structure conversion of G_d cannot be neglected while the computational scale is large. Second, the contrasted program is executed by Matlab and the functions for matrix operations in Matlab have been optimized.

The efficiency of the whole acceleration strategy is decided by two factors: the time percentage of the parallel modules to the whole program and the speedup efficiency of each acceleration algorithm. It can be found that the speedup

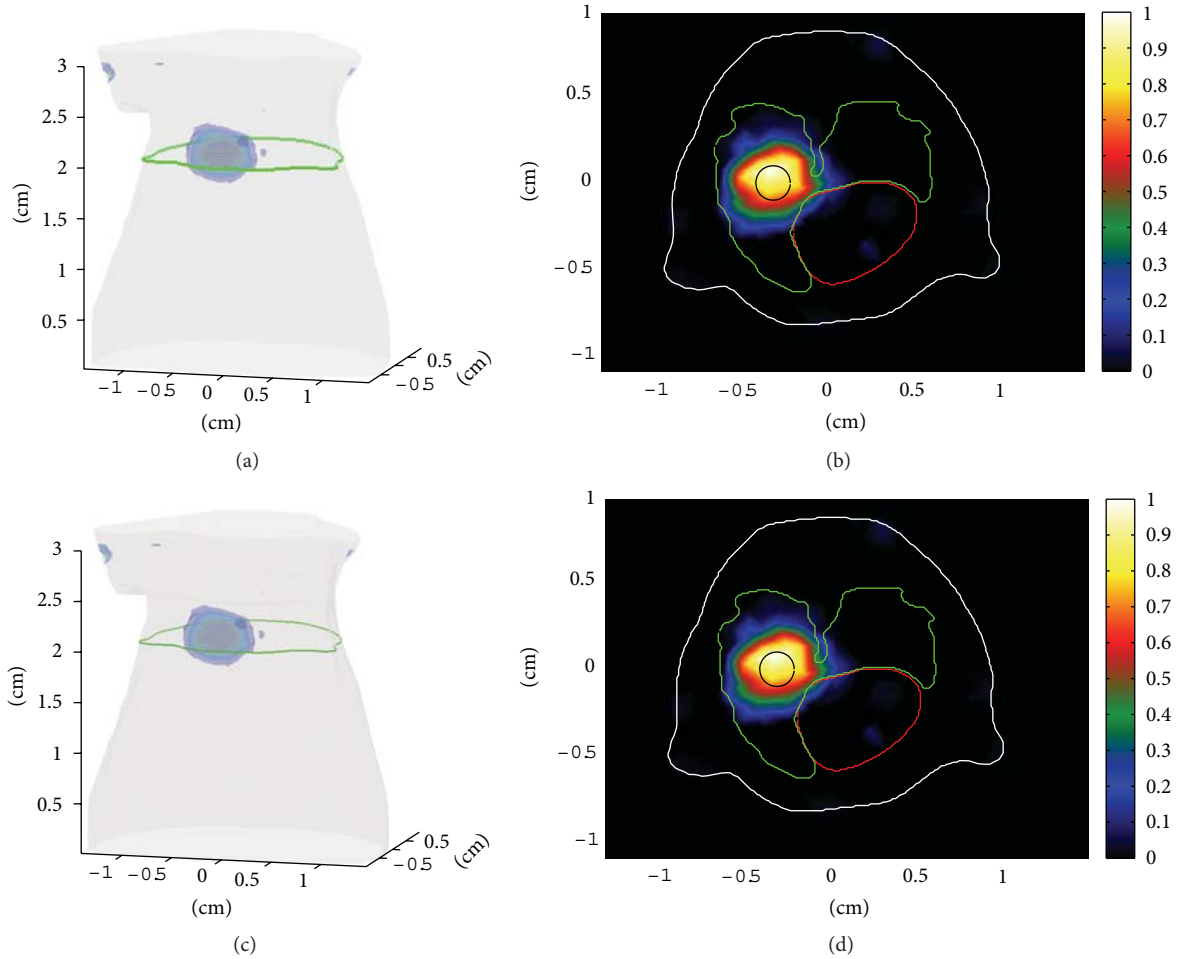


FIGURE 5: Reconstruction of the fluorescent target performed by Matlab and the GPU acceleration strategy. The first row shows the results reconstructed by Matlab while the second row shows the results reconstructed by the acceleration strategy. (a, c) The 3D views of the reconstructed results. (b, d) The cross-sections corresponding to the green curve lines in the 3D views. The black circles in (b, d) indicate the true locations of the fluorescent targets.

ratio of the weight matrix algorithm is larger than that of G_d . The cases studied in this paper are focused on different computational sizes and the projection number for each case is 6 for simplicity. If the projection number increases while the numbers of mesh nodes and detectors remain the same, the time percentage of the weight matrix module will increase. Therefore, for these cases, the final speedup ratio will be higher.

For the G_d acceleration algorithm, the speedup ratio is not very remarkable. Future work will focus on improving its performance. In fact, the stuffing matrix produced by the FEM is a sparse matrix and the sparsity is used while the matrix inversion operations are performed in Matlab. However, the sparsity has not been utilized in the GPU acceleration algorithm. It is believed that the utilization of the sparsity of matrix will further improve speedup ratio of the G_d acceleration algorithm.

We performed several cases of different parameters to test the acceleration strategy. The imaging quality is improved when the numbers of mesh nodes and detectors increase. More detectors result in better spatial resolution and finer

meshes will provide more details in the reconstructed results [16]. However, this paper is focused on the performance of the acceleration strategy for different simulation cases. The relationship between the experimental parameters and the reconstructed results is not the key point and is less considered.

In conclusion, we accelerated the early-photon fluorescence molecular tomography with GPU. Feasibility of this acceleration strategy was confirmed by several simulations. The accelerated results showed few errors while the time consumption was significantly reduced.

Acknowledgments

This work is supported by the National Basic Research Program of China (973) under Grant no. 2011CB707701, the National Natural Science Foundation of China under Grant no. 81071191, 81271617, the National Major Scientific Instrument and Equipment Development Project under Grant no. 2011YQ030114, National Science and technology support program under Grant no. 2012BAI23B00.

References

- [1] R. Weissleder and V. Ntziachristos, "Shedding light onto live molecular targets," *Nature Medicine*, vol. 9, no. 1, pp. 123–128, 2003.
- [2] V. Ntziachristos, J. Ripoll, L. V. Wang, and R. Weissleder, "Looking and listening to light: the evolution of whole-body photonic imaging," *Nature Biotechnology*, vol. 23, no. 3, pp. 313–320, 2005.
- [3] G. M. Turner, G. Zacharakis, A. Soubret, J. Ripoll, and V. Ntziachristos, "Complete-angle projection diffuse optical tomography by use of early photons," *Optics Letters*, vol. 30, no. 4, pp. 409–411, 2005.
- [4] F. Leblond, H. Dehghani, D. Kepshire, and B. W. Pogue, "Early-photon fluorescence tomography: spatial resolution improvements and noise stability considerations," *Journal of the Optical Society of America A*, vol. 26, no. 6, pp. 1444–1457, 2009.
- [5] M. Nieder and V. Ntziachristos, "Comparison of fluorescence tomographic imaging in mice with early-arriving and quasi-continuous-wave photons," *Optics Letters*, vol. 35, no. 3, pp. 369–371, 2010.
- [6] F. Gao, W. Liu, and H. Zhao, "Linear scheme for time-domain fluorescence molecular tomography," *Chinese Optics Letters*, vol. 4, no. 10, pp. 595–597, 2006.
- [7] B. Zhang, X. Cao, F. Liu et al., "Early-photon fluorescence tomography of a heterogeneous mouse model with the telegraphy equation," *Applied Optics*, vol. 50, no. 28, pp. 5397–5407, 2011.
- [8] <http://developer.nvidia.com/page/home.html>.
- [9] Q. Fang and D. A. Boas, "Monte carlo simulation of photon migration in 3D turbid media accelerated by graphics processing units," *Optics Express*, vol. 17, no. 22, pp. 20178–20190, 2009.
- [10] B. Zhang, X. Yang, F. Yang et al., "The CUBLAS and CULA based GPU acceleration of adaptive finite element framework for bioluminescence tomography," *Optics Express*, vol. 18, no. 19, pp. 20201–20213, 2010.
- [11] A. Soubret, J. Ripoll, and V. Ntziachristos, "Accuracy of fluorescent tomography in the presence of heterogeneities: study of thenormalized born ratio," *IEEE Transactions on Medical Imaging*, vol. 24, no. 10, pp. 1377–1386, 2005.
- [12] M. Schweiger, S. R. Arridge, M. Hiraoka, and D. T. Delpy, "The finite element method for the propagation of light in scattering media: boundary and source conditions," *Medical Physics*, vol. 22, no. 11 I, pp. 1779–1792, 1995.
- [13] F. Gao, H. Zhao, L. Zhang et al., "A self-normalized, full time-resolved method for fluorescence diffuse optical tomography," *Optics Express*, vol. 16, pp. 13104–13121, 2008.
- [14] B. Dogdas, D. Stout, A. F. Chatziioannou, and R. M. Leahy, "Digimouse: a 3D whole body mouse atlas from CT and cryosection data," *Physics in Medicine and Biology*, vol. 52, no. 3, article 003, pp. 577–587, 2007.
- [15] G. Alexandrakis, F. R. Rannou, and A. F. Chatziioannou, "Tomographic bioluminescence imaging by use of a combined optical-PET (OPET) system: a computer simulation feasibility study," *Physics in Medicine and Biology*, vol. 50, no. 17, pp. 4225–4241, 2005.
- [16] T. Lasser and V. Ntziachristos, "Optimization of 360° projection fluorescence molecular tomography," *Medical Image Analysis*, vol. 11, no. 4, pp. 389–399, 2007.

Research Article

Automated Detection of Healthy and Diseased Aortae from Images Obtained by Contrast-Enhanced CT Scan

Michael Gayhart and Hiroshi Arisawa

Department of Environment and Information Science, Yokohama National University, Yokohama 240-8501, Japan

Correspondence should be addressed to Michael Gayhart; michaelgayhart@gmail.com

Received 21 December 2012; Revised 30 January 2013; Accepted 30 January 2013

Academic Editor: Kumar Durai

Copyright © 2013 M. Gayhart and H. Arisawa. This is an open access article distributed under the Creative Commons Attribution License, which permits unrestricted use, distribution, and reproduction in any medium, provided the original work is properly cited.

Purpose. We developed the next stage of our computer assisted diagnosis (CAD) system to aid radiologists in evaluating CT images for aortic disease by removing innocuous images and highlighting signs of aortic disease. *Materials and Methods.* Segmented data of patient's contrast-enhanced CT scan was analyzed for aortic dissection and penetrating aortic ulcer (PAU). Aortic dissection was detected by checking for an abnormal shape of the aorta using edge oriented methods. PAU was recognized through abnormally high intensities with interest point operators. *Results.* The aortic dissection detection process had a sensitivity of 0.8218 and a specificity of 0.9907. The PAU detection process scored a sensitivity of 0.7587 and a specificity of 0.9700. *Conclusion.* The aortic dissection detection process and the PAU detection process were successful in removing innocuous images, but additional methods are necessary for improving recognition of images with aortic disease.

1. Introduction

Everyday quick and accurate decisions with inadequate information about a patient must be made by attending physicians at emergency departments. In 2007, in the United States, almost 6 million patients listed chest pains as their reason for visiting the emergency department [1]. Chest pain is a vague symptom which requires hospital admission or prolonged observation to determine the severity of a patient's condition. Negative results for inpatient cardiac evaluations cost around 6–8 billion dollars annually [2, 3]. Even with such precautions, within 6 months after a negative result, 2%–5% of these patients will have a serious cardiac event [4].

Over the past few decades, research into diagnostic radiology has provided more tools for handling symptoms of cardiac disease [5]. Due to recent improvements in multislice CT scanners, images taken in the cardiovascular region are clearer with less noise and artifacts and can be inspected with greater confidence [6, 7]. For diagnosing chest pain, several studies have demonstrated that a contrast-enhanced CT scan of thoracic cavity is an effective, accurate, and noninvasive method with a high negative predictive value for cardiac diseases [8–11]. One particular method is Triple Rule-Out

(TRO) protocol in which the coronary arteries, pulmonary arteries, thoracic aorta, and other intrathoracic structures are highlighted in the CT scan. By examining the scan for signs of serious heart conditions, for instance coronary stenosis, pulmonary embolism, and aortic dissection (AD), TRO images can be used to determine if a patient should be released or admitted for further evaluation. This method results in the cutting of cost and time involved with diagnosing a patient. In recent years, several hospitals have implemented the TRO protocol along with other protocols of CT diagnosis as a part of their procedure for managing patients with vague symptoms at emergency departments.

As these protocols become widely used in diagnosing cardiac disease, the burden of a radiologist increases considerably. These methods require the time and abilities of well-trained radiologists to be utilized effectively. The number of cardiac images per patient produced during a CT scan depends on the thickness of each slice captured and can range anywhere from the hundreds to the thousands. During the diagnosis phase, actions may become repetitive due to the large number of images and many of the images have no signs of diseases. Moreover, there are difficulties in locating candidates of potential cardiac disease due to their small size or

subtle appearance. In busy hospitals, evaluating these images may be overwhelming and this could lead to crucial misses in the diagnosis [12].

Therefore, we proposed and developed a computer aided diagnosis (CAD) system that could ease this burden of radiologists during the diagnosis of contrast-enhanced CT images of thoracic cavity. This would be accomplished by having the system perform two actions. First, identify innocuous images which would reduce the amount of time on repetitive actions by radiologists. Second, highlight areas of images with potential signs of cardiac disease which would reduce the chance of radiologists overlooking them. A successful automated diagnosis system would improve the promptness and accuracy of a radiologist's diagnosis.

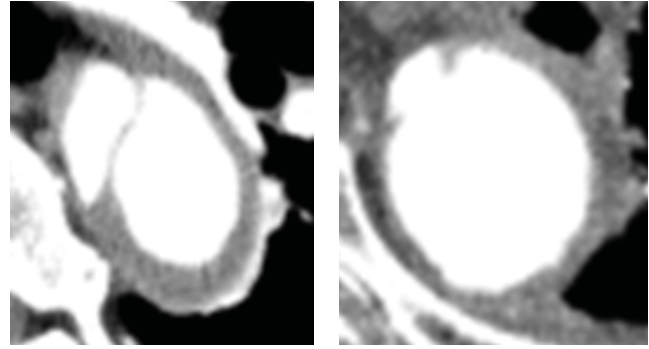
Within data of a patient's CT scan is the possibility of many kinds of cardiac diseases. To develop methods for identifying all cardiac diseases in the CAD system would be a large undertaking. Therefore, we concentrate on one branch of cardiac disease, aortic diseases, where a CAD system could assist. For instance, an aortic dissection in the ascending aorta [13, 14] requires a careful observation to diagnose CT images and could be fatal if not recognized soon. There is little literature concerning CAD systems for aortic disease. Therefore, the focal point of this paper was to develop a diagnosis process for the CAD system to detect signs of aortic diseases within images produced by contrast-enhanced cardiac image scans.

In our previous research [15], a segmentation process was developed that finds and segments the pathway of an aortic artery known as the lumen. The segmentation method took into account all of these uncertainties properly, viewed the information from the whole image while allowing adjustments for local variations, and employed morphologic operators. The process provided our system with a clear blueprint of the shape, size, and boundaries of a patient's aortic lumen.

The data from the segmentation process provides the input for the diagnostic stage. The diagnostic process currently detects two aortic diseases, aortic dissection and penetrating aortic ulcer (PAU), in contrast-enhanced CT images of the aorta. Two criteria for signs of these diseases were established for the system to be utilized in its decision making process:

- (i) for aortic dissection, if the cross-section of the aorta in an image is not circle-like;
- (ii) for PAU, if the aorta contains objects with HU values higher than normal along its wall.

In the case of an aortic dissection, blood flows into the media layer of a deteriorated section of the aortic wall and creates a new lumen. From the perspective of a CT image, the lumen is separated into two pieces and the differences in blood pressure between the two lumens cause distortions in their shapes (Figure 1(a)). The functions of the diagnostic process were designed based on edge oriented methods and should be capable of recognizing a circle-like object in an image. In the output, this process identifies aortic objects with a circle-like shape as healthy and any aortic object that does not meet that criterion as a possible candidate for aortic disease.



(a) Aortic dissection

(b) Penetrating aortic ulcer

FIGURE 1: Examples of aortic disease.

In the case of PAU, an ulceration of an atheromatous plaque erodes the intima causing a hematoma in the media of the aorta. In contrast-enhanced CT slices, a PAU appears as a contrast-filled, pouch-like protrusion of the aorta (Figure 1(b)) or as a thickened aortic wall in absence of an intimal flap or a false lumen. The Hounsfield value (HU) around the PAU can be higher than the normal lumen for two reasons. First, contrast media become temporarily trapped in these pouches and increase its concentration in this area. Second, the calcified plaque that causes PAU has a high HU value and lines the intima around the PAU. The functions for the diagnostic process were created using interest point operators to locate these objects of higher than average intensity within an aortic object. In the output every aortic object that meets this criterion is labeled as a PAU object and sign of a PAU. Otherwise, the aortic object as a whole is labeled as healthy.

To summarize, we built an automated process that determines whether an aortic object in a slice is a candidate for aortic dissection or PAU based on contrast-enhanced CT data. We report technical details of this method for this automatic identification and present preliminary results in applying the process to 9 cases of CT data.

2. Materials and Methods

2.1. Patient Selection. The patient data used in this study were obtained from Yokohama City University as a part of our laboratories joint research. Patients were undergoing an examination using the TRO protocol. They gave their permission for the use of their data in this study.

2.2. CT Technique. The basic procedure for TRO protocol used for this project, as developed at Yokohama City University, consisted of three phases: a scanogram, a precontrast scan, and a postcontrast scan.

All images were acquired with a 64-slice CT scanner. Scans were between the diaphragm and the top of the aortic arch.

The scanogram was a quick preliminary scan which determined the region where the precontrast and postcontrast scan will take place.

TABLE 1: List of case data used in evaluation.

Case number	Condition	Number of slices
1	Healthy	62
2	Aortic dissection	25
3	PAU	129
4	Normal	186
5	PAU	189
6	PAU	182
7	Normal	202
8	PAU	112
9	Aortic dissection	125

The precontrast scan was a full CT scan of the cardiac region with no injection of a contrast medium, a radioactive dye.

The postcontrast scan was a full CT scan of the cardiac region in which the patient was injected with contrast medium to illuminate key areas in the cardiac region. In this phase, the patient received 70 mL of contrast medium into the right arm to opacify the coronary arteries and the aorta and, a minute later, another 30 mL of contrast medium to opacify the pulmonary arteries. Once the contrast medium had reached a predetermined level in the blood stream, the post contrast scan began. The scan took on average about 15 seconds.

The data was stored in DICOM format, and the resolution for the images was 512×512 pixels. The diagnosis of the cases in this study is represented in Table 1.

2.3. Principles of the Segmentation Process. The CAD system for the aortic artery in this study is designed to work with the data received from a CT scan, which is composed of three inputs: (1) the DICOM data of a patient's CT scan which includes cardiac images from the top of the aortic arch to the diaphragm, (2) the range of Hounsfield unit (HU) of the contrast-enhanced aortic lumen detected during the CT scan (average range 200 HU–500 HU), and (3) the starting positions of the ascending aorta and descending aorta. The two criteria for this process are as follows: (1) a cross-section of the aortic artery is circle like in shape (Figures 2(c) and 2(d)); (2) the aortic arch creates 180-degree torus (Figures 2(a) and 2(b)). From these inputs and criteria, the segmentation process identifies objects in the CT scan which are the aorta (Figure 3) and links them together and labels them as ascending aorta, descending aorta, or aortic arch depending on their location. Afterwards, the automatic segmentation outputs image sets of the ascending aorta, the descending aorta, and the aortic arch.

2.4. Principles of the Diagnostic Process for Aortic Dissection. Utilizing the segmentation data, the CAD system initializes the diagnostic process for aortic dissection by collecting two pieces of information. First, Sobel operator provides the diagnostic process with an approximation of the gradient image of segmentation data. The gradient values represent the degree of change of intensity in the x - and y -directions at

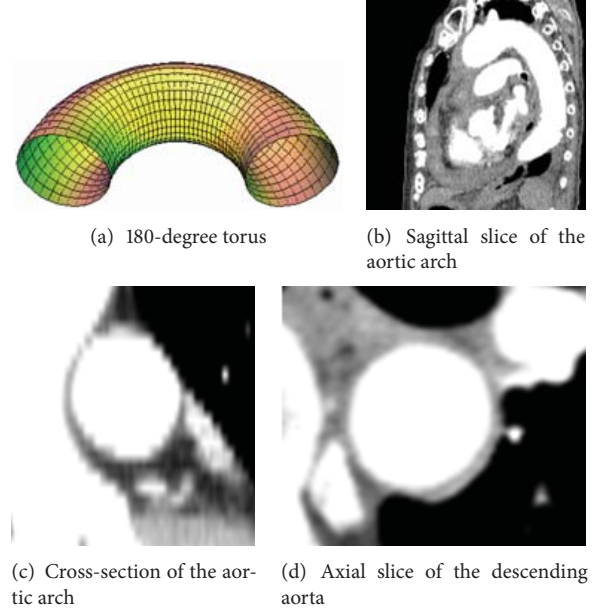


FIGURE 2: Criteria for segmentation process.

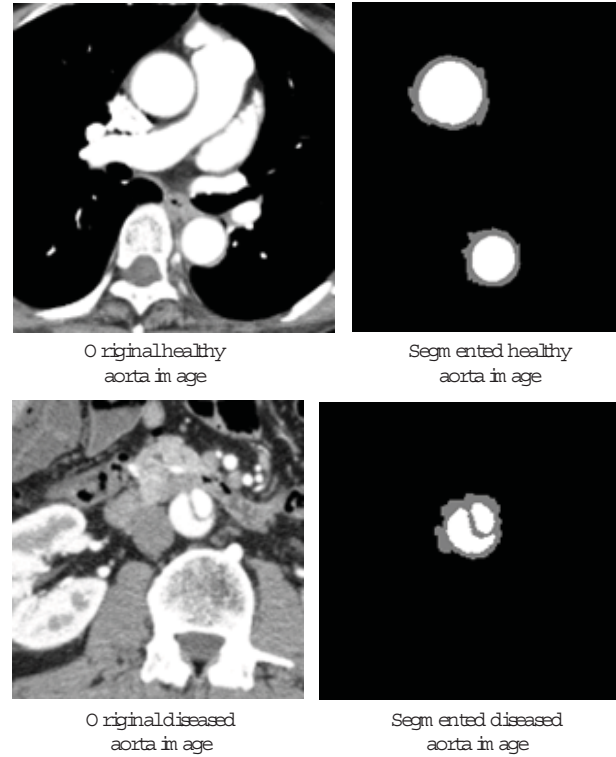


FIGURE 3: Results of segmentation.

particular pixel in an image, G_x and G_y , respectively. A pair of convolution masks (Figure 4) is applied to the HU value of each pixel to calculate G_x and G_y . Then, the gradient angle ($G\theta$) of each pixel is assessed with the following function:

$$G\theta = \tan^{-1} \frac{G_y}{G_x}. \quad (1)$$

The first part examined whether the Fast Circle Detection algorithm could correctly identify healthy and aortic dissection images in 5 cases which included 3 healthy and 2 aortic dissections. The system returned a decision of whether a slice of the aorta was healthy or a candidate for aortic dissection. The threshold for the Fast Circle Detection algorithm was set at 60% for the percentage of boundary pixels with a unique gradient pair out of the total number of boundary pixel in an object. The results were compared to the actual number of healthy aortic slices and candidate slices.

A true positive is defined as an aortic object that contains an aortic dissection and was labeled by the CAD system as a candidate for aortic dissection. A false positive is defined as an aortic object that is healthy but was labeled by the CAD system as a candidate for aortic dissection. A true negative is defined as an aortic object that is healthy and was labeled by the CAD system as healthy. A false negative is defined as an aortic object that contains an aortic dissection but was labeled by the CAD system as healthy.

The second part reviewed the process for detecting signs of PAU in the aorta with the 4 cases of PAUs. The system returned objects in a slice which were labeled as possible signs of PAU. The results were compared to the actual number of PAUs in set of test data. A true positive is defined as an aortic object that contains a PAU, and a candidate for PAU was detected by the CAD system. A false positive is defined as an aortic object that has no PAU, but a candidate for PAU was detected by the CAD system. A true negative is defined as an aortic object that has no PAU, and no candidate for PAU was detected by the CAD system. A false negative is defined as aortic object that contains a PAU, but no candidate for PAU was detected by the CAD system.

The system examined the images on a computer with Intel Core 2 Extreme CPU Q6850 3.00 GHz 2.99 GHz and 8 Gb of Ram. The total time of the process was also recorded.

3. Results

3.1. Results of the Diagnostic Process for Aortic Dissection. Of the 479 images from 5 cases, 161 slices contained the ascending aorta and 479 slices contained the descending aorta. The results are represented in Table 2.

Regarding the descending aorta, 83 were correctly identified as candidates for aortic dissection (true positive) and 0 were incorrectly identified as candidates for aortic dissection (false positive), 378 slices were correctly identified as healthy (true negative), and 18 were incorrectly identified as healthy (false negative). The false negative slices occurred when the aortic dissection only caused a change in the size of aorta but not the shape.

Concerning the ascending aorta, there was no occurrence of aortic dissection. 156 slices were correctly identified as healthy, and 5 slices were incorrectly identified as a candidate for aortic dissection. The false positive slices occurred where the ascending aorta was transitioning to the aortic arch.

3.2. Results of the Diagnostic Process for PAU. Of the 461 slices in the 4 cases with PAU, 213 slices contained the ascending aorta and 461 slices contained the descending aorta. 26 of the

TABLE 2: Results of the diagnostic process for aortic dissection.

Data type	True positive	False positive	True negative	False negative
All aorta data	83	5	534	18
Ascending data	0	5	156	0
Descending data	83	0	378	18
Sensitivity	0.8218		Specificity	0.9907

TABLE 3: Results of the diagnostic process for PAU.

Data type	True positive	False positive	True negative	False negative
All aorta data	239	10	323	76
Ascending data	48	5	116	18
Descending data	191	5	207	58
Sensitivity	0.7587		Specificity	0.9700

213 slices containing ascending aorta were removed because of an error with the segmentation process, making the final total of slices of the ascending aorta 187. The results are represented in Table 3.

In the ascending aorta, 48 slices were correctly identified with PAU (true positive), 5 slices were incorrectly identified with PAU (false positive), 116 slices were correctly identified with no PAU (true negative), and 18 slices were incorrectly identified with no PAU (false negative).

In the descending aorta, 191 slices were correctly identified with PAU, 5 slices were incorrectly identified with PAU, 207 slices were correctly identified with no PAU, and 58 slices were incorrectly identified with no PAU.

False positives occurred when the contrast media were slightly above the intensity range of the lumen, most likely due to an artifact in the CT image. False negatives generally happened when the PAU's intensity was similar to the normal lumen's intensity.

3.3. Runtimes of the CAD System. The runtimes for the CAD system to segment and perform the diagnostic process explained in this paper are represented in Table 4.

4. Conclusion

With the purpose of designing a CAD system for aortic diseases to assist radiologists, we developed two automated diagnostic processes for determining whether an aortic object in a contrast-enhanced CT image contains candidates for aortic dissection or PAU. The results of our study have brought us the following conclusions about the feasibility of this system.

The aortic dissection detection process had a sensitivity of 0.8218 and a specificity of 0.9907. This indicates that this process is capable of identifying a healthy aorta shape but not fully able to recognize all types created by an aorta dissection. The most common error occurred when the aorta dissection caused the aorta to shrink but still maintained a circle-like shape. Additional methods must be utilized by aortic dissection process to collect relevant data, such as reduction in size

TABLE 4: Runtimes of the CAD system.

Case number	Images used	Time (min:sec)
1	62	2:24
2	25	0:55
3	129	5:08
4	186	10:32
5	189	10:58
6	182	10:06
7	202	12:20
8	112	4:45
9	125	5:17

and the appearance of an intimal flap in the aortic object, to reduce the false negatives.

The PAU detection process scored a sensitivity of 0.7587 and a specificity of 0.9700. This process mostly avoided incorrect identification of PAU. This is likely due to the success of this segmentation process with removing artifacts and noise. Regarding the sensitivity, this process was able to distinguish a majority of the PAU. When it overlooked a PAU, this was because the PAU had an intensity that was similar to the lumen. A supplementary method for recognizing the shape of PAU on the boundary of an aorta should be implemented to reduce the false negatives.

This research will serve as a base for future studies of CAD system for aortic disease and expand on various methods for automated diagnosis. There were some limitations that should be addressed in the next study. The current study has examined two methods for identifying aorta dissection and PAU. More methods must be included to enhance the accuracy and precision of this CAD system. Moreover, the experimental data was relatively small. A larger set of test data is necessary for more definitive results.

In the future, concerning the aortic disease diagnosis process, more algorithms that address issues of image processing will be designed to analyze the aorta and to search for signs of aortic diseases such as aortic dissection, intramural hematoma, and penetrating atherosclerotic ulcer [13, 14]. Criteria still unaddressed for identifying aortic diseases include (1) significant changes in the size (increasing or decreasing) of aorta, (2) appearance of intimal flaps which are dark lines contained within the lumen, and (3) detection of PAU on the boundary based on shape.

In summary, the aortic dissection detection process and the PAU detection process were successful in removing innocuous images, but additional methods are necessary for improving recognition of images with aortic disease. These methods can be used for the next step in building a CAD system for detecting aortic diseases.

Acknowledgments

The authors acknowledge Professor Arisawa and Professor Inoue for their academic guidance and Dr. Yoshida and Dr. Okasaki for provision of patients' data. A part of this research is supported by no. 23300035 Study of Grant-in-Aid for

Scientific Research, Ministry of Education, Culture, Sports, Science and Technology, Japan.

References

- [1] R. Niska, F. Bhuiya, and J. Xu, "National Hospital Ambulatory Medical Care Survey: 2007 emergency department summary," *National Health Statistics Reports*, no. 26, pp. 1-31, 2010.
- [2] A. N. A. Tosteson, L. Goldman, I. S. Udvarhelyi, and T. H. Lee, "Cost-effectiveness of a coronary care unit versus an intermediate care unit for emergency department patients with chest pain," *Circulation*, vol. 94, no. 2, pp. 143-150, 1996.
- [3] A. B. Storrow and W. B. Gibler, "Chest pain centers: diagnosis of acute coronary syndromes," *Annals of Emergency Medicine*, vol. 35, no. 5, pp. 449-461, 2000.
- [4] A. F. Manini, M. A. Giondi, T. M. van der Vlugt, and D. H. Schreiber, "Adverse cardiac events in emergency department patients with chest pain six months after a negative inpatient evaluation for acute coronary syndrome," *Academic Emergency Medicine*, vol. 9, no. 9, pp. 896-902, 2002.
- [5] M. J. Lipton, L. M. Boxt, and Z. M. Hijazi, "Role of the radiologist in cardiac diagnostic imaging," *American Journal of Roentgenology*, vol. 175, no. 6, pp. 1495-1506, 2000.
- [6] P. K. Vanhoenacker, M. H. Heijenbrok-Kal, R. Van Heste et al., "Diagnostic performance of multidetector CT angiography for assessment of coronary artery disease: meta-analysis," *Radiology*, vol. 244, no. 2, pp. 419-428, 2007.
- [7] J. M. Miller, C. E. Rochitte, M. Dewey et al., "Diagnostic performance of coronary angiography by 64-row CT," *The New England Journal of Medicine*, vol. 359, no. 22, pp. 2324-2336, 2008.
- [8] K. M. Takakuwa and E. J. Halpern, "Evaluation of a "triple rule-out" coronary CT angiography protocol: use of 64-section CT in low-to-moderate risk emergency department patients suspected of having acute coronary syndrome," *Radiology*, vol. 248, no. 2, pp. 438-446, 2008.
- [9] M. Budoff, "Cardiac CT in the emergency room: Coronary calcium scoring, coronary CT angiography, and triple rule-out studies are powerful and efficient new tools in the triage of patients with chest pain," *Supplement to Applied Radiology*, pp. 48-55, 2006.
- [10] E. J. Halpern, "Triple-rule-out CT angiography for evaluation of acute chest pain and possible acute coronary syndrome," *Radiology*, vol. 252, no. 2, pp. 332-345, 2009.
- [11] E. Bouvier, D. Logeart, J. L. Sablayrolles et al., "Diagnosis of aortic valvular stenosis by multislice cardiac computed tomography," *European Heart Journal*, vol. 27, no. 24, pp. 3033-3038, 2006.
- [12] J. H. Pope, T. P. Aufderheide, R. Ruthazer et al., "Missed diagnoses of acute cardiac ischemia in the emergency department," *The New England Journal of Medicine*, vol. 342, no. 16, pp. 1163-1170, 2000.
- [13] I. A. Khan and C. K. Nair, "Clinical, diagnostic, and management perspectives of aortic dissection," *Chest*, vol. 122, no. 1, pp. 311-328, 2002.
- [14] L. F. Hiratzka, G. L. Bakris, J. A. Beckman et al., "Guidelines for the diagnosis and management of patients with thoracic aortic disease," *Circulation*, vol. 121, no. 13, pp. e266-e369, 2010.
- [15] M. Gayhart and H. Arisawa, "Automated segmentation of the aortic artery: evaluation of images obtained by contrast enhanced CT scan," *Advances in Information Technology and Applied Computing*, vol. 1, pp. 115-120, 2012.

- [16] A. Rad, K. Faez, and N. Qaragozlou, "Fast circle detection using gradient pair vectors," in *Proceedings of the 7th Digital Image Computing: Techniques and Applications*, Sydney, Australia, 2003.

Research Article

Sparse Constrained Reconstruction for Accelerating Parallel Imaging Based on Variable Splitting Method

Wenlong Xu, Xiaofang Liu, and Xia Li

Department of Biomedical Engineering, China Jiliang University, Hangzhou 310018, China

Correspondence should be addressed to Xiaofang Liu; liuxfang@cjl.u.edu.cn

Received 21 December 2012; Revised 28 February 2013; Accepted 1 March 2013

Academic Editor: Peng Feng

Copyright © 2013 Wenlong Xu et al. This is an open access article distributed under the Creative Commons Attribution License, which permits unrestricted use, distribution, and reproduction in any medium, provided the original work is properly cited.

Parallel imaging is a rapid magnetic resonance imaging technique. For the ill-conditioned problem, noise and aliasing artifacts are amplified during the reconstruction process and are serious especially for high accelerating imaging. In this paper, a sparse constrained reconstruction problem is proposed for parallel imaging, and an effective solution based on the variable splitting method is contrived. First-order and second-order norm optimization problems are first split, and then they are transferred to unconstrained minimization problem by the augmented Lagrangian method. At last, first-order norm and second-order norm optimization problems are alternatively resolved by different methods. With a discrepancy principle as the stopping criterion, analysis of simulated and actual parallel magnetic resonance image reconstruction is presented and discussed. Compared with the routine parallel imaging reconstruction methods, the results show that the noise and aliasing artifacts in the reconstructed image are evidently reduced at large acceleration factors.

1. Introduction

Parallel imaging is a robust method for accelerating the acquisition of magnetic resonance imaging (MRI) data, which exploits spatial sensitivity of an array of receiver coils to reduce the number of the required Fourier encoding steps. However, these reduced amounts of MR data lead to aliased images by the routine reconstruction method. Over the past few years, a number of parallel MRI techniques have been proposed for reconstructing MR image from these undersampled data in either k -space or image domain [1]. Sensitivity encoding (SENSE) [2] and generalized auto-calibrating partially parallel acquisitions (GRAPPA) [3] are two methods most commonly used on clinical scanners today.

As the amount of data acquired in parallel MRI is less, which depends on the acceleration factor (AF), the quality of the reconstructed image is poorer. Therefore, the AF is usually lower when parallel imaging technique is used to speed up MRI in clinic. Based on SENSE method, the image reconstruction for parallel imaging is performed by solving a linear system that explicitly depends on the sensitivity maps

of the receiver coils, and some prior information may be used to stabilize the reconstruction process. Regularization is an attractive means of restoring stability in the reconstruction mechanism, where prior information can be effectively incorporated [4]. The Tikhonov regularization is a commonly used method where a low-resolution prior image is applied in the reconstruction; that is, a quadratic minimization problem and its numerical algorithm are simple, such as the linear conjugate gradient (CG) method. However, the disadvantage of Tikhonov regularization method is that it biases the estimated reconstructed image towards the prior image [5]. More recently, total variation methods have been investigated for MR image reconstruction. The advantage of this type of regularization is that it biases the reconstructed image towards a piecewise smooth image, instead of a globally smooth image, thereby better preserving image edges [6]. With the advent of compressed sensing (CS) theory, sparsity-promoting regularization criteria have gained popularity in MRI, which is known as sparseMRI or CS-MRI [7]. The basic assumption underlying CS-MRI is that many MR images are inherently sparse in some transform domain and then can be reconstructed with high accuracy from significantly

undersampled k -space data. Certainly, the CS framework is apt for pMRI with undersampled MR data [8].

This paper investigates the problem of sparse constrained reconstruction from highly undersampled MR data for parallel MRI. Based on sparseMRI theory, we use the finite difference as the sparsity project domain, and sparsity property of anisotropic total variation (TV) of MR image is used as the prior information for stabilizing the reconstruction process. As a result, a nonlinear optimization problem is constructed for reconstructing the parallel MR image. However, as there exists both first-order norm (known as ℓ_1 -norm) and second-order norm (ℓ_2 -norm) minimization problems, the solution to the constructed optimization problem is commonly difficult. In the paper, the ℓ_1 -norm minimization problem for sparse representation of MR image and ℓ_2 -norm minimization problem, which are subject to data consistency based on SENSE method, are firstly split by variable splitting method, and then the split constrained minimization problem is converted to an unconstrained minimization problem by the augmented Lagrangian (AL) method. At last, the Lagrangian multiplier method and alternating direction method (ADM) are used to solve the split minimization problem by the different numerical algorithms. In order to evaluate the effectiveness and robustness of the proposed algorithm, the image reconstruction problem from highly undersampled parallel MR data is exploited.

2. Theory

2.1. The MR Signal Model in Parallel Imaging. As a fast imaging method, parallel imaging technique is also known as multiple coils MRI, which uses an array of RF receiver surface coils to acquire multiple sets of undersampled k -space data simultaneously. Let \vec{r} denote the two-dimension spatial coordinates (x, y) and $s_l(\vec{r})$ the demodulation information associated with the l th coil, then the MR signal associated with the l th coil is the following general forward model:

$$c_l(\vec{r}) = \int s_l(\vec{r}) f(\vec{r}) e^{-i\vec{k} \cdot \vec{r}} d\vec{r}, \quad l = 1, \dots, L. \quad (1)$$

Here, $f(\vec{r})$ denotes the object's transverse magnetization signal and forms MR image. Let y -ordinates denote the gradient encoding direction, consideration of MR signal sampled on Cartesian coordinates, and then the discrete MR signal is obtained as follows (2) in accelerating parallel imaging:

$$I_l(x, y) = \sum_{n=0}^{N_A-1} s_l(x, y + nM) f(x, y + nM), \quad (2)$$

where N_A is the number of aliased pixels; R is known as AF; $M = N_y/R$; $x = 0, \dots, N_x$; $y = 0, \dots, N_y/R$; N_x, N_y is the discrete pixels number, respectively, along the x -direction and y -direction when data are full sampled.

2.2. The Model of Image Reconstruction in Parallel Imaging. Considering of noisy samples of MR signal, the discrete model for parallel imaging is given as

$$y = FSf + \varepsilon, \quad (3)$$

where f is a $N \times 1$ column vector containing the samples of the unknown image to be reconstructed, y and ε are $ML \times 1$ column vectors corresponding to the data samples from L coils and noise, respectively. S is $NL \times N$ matrix given by $S = [s_1^H, \dots, s_L^H]$, s_l is $N \times N$ diagonal matrix corresponding to the sensitivity map of the l th coil, and $1 \leq l \leq L$, $(\cdot)^H$ represents the Hermitian-transpose. F is $ML \times NL$ matrix given by $F = I_L \otimes Fu$, Fu is $M \times N$ Fourier encoding matrix, I_L is the identity matrix of size L , and \otimes denotes the Kronecker product. In order to speed up parallel imaging, k -space MR data may be undersampled to reduce the total scan time, so $M \leq N$.

Given an estimate of the sensitivity maps S , the image reconstruction problem for parallel imaging is to find f from data y . Based on SENSE method, the MR image may be reconstructed using the least-squares estimation as

$$\hat{f} = (S^H F^H \Psi^{-1} F S)^{-1} F^H S^H \Psi^{-1} y, \quad (4)$$

where Ψ denotes the $L \times L$ receiver noise matrix, it describes the levels and correlation of noise in the receiver channels. Because of the coil configurations and the coil sensitivity error, the measurement matrix FS is commonly non-orthogonal as $S^{-1} F^{-1} FS \neq I$. The linear system as (3) is ill-posed. Using inversion matrix method as (4), noise derived from measurement data may be amplified if the small eigenvalues exist in matrix FS , which might result in the instability of reconstruction process. As noise in MRI measurements is Gaussian distribution, a natural approach is to estimate f by minimizing a regularized least-squares cost function:

$$\hat{f} = \arg \min \{ \Phi(f) = \|FSf - y\|_2 + \mu R(f) \}, \quad (5)$$

where $R(f)$ denotes the regularization term, and $\|\cdot\|_2$ is ℓ_2 -norm, which represents the data-consistent term. μ is the so-called regularization parameter to balance the regularization term and data-fidelity term.

An open problem in most regularization image reconstructions is how to best choose the regularization term. If this term is not included, then the image estimate will suffer from noise and aliasing artifacts for undersampled data. The simplest choice is the Tikhonov regularization $R(f) = \|f\|_2$ or $R(f) = \|f - f_0\|_2$, where f_0 is a prior or reference image. However, if the reference image is zero, then all pixel values in estimation f are diminished towards zero, possibly reducing contrast. Another choice is a quadratic roughness penalty function, by which it is convenient for minimization and guarantees that the cost function (5) has a unique minimization, but it has the drawback of smoothing image edges. TV regularization reconstruction may overcome the drawbacks mentioned above, but it is getting harder to be minimized and can lead to the appearance of "blocky" texture in images.

2.3. The Sparse Constrained Image Reconstruction in Parallel Imaging. Based on CS-MRI theory, MR image on finite difference domain is sparse, on which the sparse representation of MR images can be demonstrated by applying a sparsifying transform to a fully sampled image. In this paper, TV transform is used to transform the estimated MR image to finite difference domain, and then the sparse constrained minimization problem for parallel MR image reconstruction is obtained as

$$\min_f \|\nabla f\|_1 \quad \text{s.t.} \quad \|FSf - y\|_2 < \sigma, \quad (6)$$

where $\|\cdot\|_1$ denotes ℓ_1 -norm, and σ represents any error, such as noisy level derived from the data sampled process. $\|\nabla f\|_1$ is called TV norm of an image, which is defined as a function of the image gradient. $\|\nabla f\|_1$ might be computed by discrete isotropic TV or anisotropic TV as

$$\begin{aligned} \|\nabla f\|_1 &= \sum_i \sqrt{(\nabla_x f)_i^2 + (\nabla_y f)_i^2}, \\ \|\nabla f\|_1 &= \sum_i (|\nabla_x f| + |\nabla_y f|), \end{aligned} \quad (7)$$

where $\nabla_x f$ denotes the x -direction gradient of image f , and $\nabla_y f$ denotes the y -direction gradient. There are both ℓ_1 -norm term and ℓ_2 -norm term in (6). The ℓ_1 -norm term in (6) is based on the sparsity of MR image on finite difference domain, while ℓ_2 -norm term is based on the data fidelity of MR image reconstruction. Using the common numerical algorithms such as CG or Newton method, it is difficult to attain the stabilized solution to problem (6). Lustig et al. researched sparseMRI and posed the detailed computation method for sparse constrained inverse problem [8], where nonlinear CG method was applied to solve the constrained minimization problem as (6) when isotropic TV is applied to compute TV. However, the reconstructed image obtained by this method is dissatisfied according to our analysis.

According to the research product about ℓ_1 -norm minimization problem [9–11], the variable split method is adopted to split the ℓ_1 -norm term and ℓ_2 -norm term in (6) in our research. Specifically, with an auxiliary variable w , let $w = \nabla f$, then the constrained optimization problem is obtained, which denoted as P as follows:

$$P : \min_{w,f} \|w\|_1 \quad \text{s.t.} \quad w = \nabla f, \quad \|FSf - y\|_2 < \sigma. \quad (8)$$

3. The Solution to Sparse Constrained Image Reconstruction Based on Variable Splitting Method for Parallel Imaging

3.1. The Unconstrained Parallel MR Image Reconstruction Problem. In the augmented Lagrangian (AL) framework

(also known as the multiplier method [12]), an AL function can be constructed for problem (8) as

$$\begin{aligned} \min_{w,f,\gamma_1,\gamma_2} \Phi(f,w,\gamma_1,\gamma_2) &= \|w\|_1 + \gamma_1^H (FSf - y) \\ &+ \frac{\mu_1}{2} \|FSf - y\|_2 + \gamma_2^H (w - \nabla f) \\ &+ \frac{\mu_2}{2} \|w - \nabla f\|_2, \end{aligned} \quad (9)$$

where γ_1, γ_2 represent the vector of Lagrange multipliers, and μ_1, μ_2 are the regularization parameters. The solution to (9) may be in the following AL version:

$$\begin{aligned} (f^{k+1}, w^{k+1}) &\leftarrow \arg \min_{f,w} \Phi(f,w,\gamma_1^k,\gamma_2^k), \\ \gamma_1^{k+1} &\leftarrow \gamma_1^k - \lambda \mu_1 (FSf^{k+1} - y), \\ \gamma_2^{k+1} &\leftarrow \gamma_2^k - \lambda \mu_2 (w^{k+1} - \nabla f^{k+1}), \end{aligned} \quad (10)$$

where $\lambda \in (0, 2)$ guarantees convergence, as long as the subproblem is solved to an increasingly high accuracy at every iteration.

The joint minimization of Φ with respect to f and w can be computationally challenging in (10). ADM [13] is applied, which alternatively minimizes Φ with respect to one variable at a time while holding others constant. This method decouples the individual updates of f and w and simplifies the optimization task. Specifically, at the k th iteration, we perform the following individual minimizations, taking care of using updated variables for subsequent minimizations and the following algorithm:

$$\begin{aligned} w^{k+1} &\leftarrow \arg \min_w \Phi(f^k, w, \gamma_2^k, \mu_2), \\ f^{k+1} &\leftarrow \arg \min_f \Phi(f, w^{k+1}, \gamma_1^k, \mu_1, \gamma_2^k, \mu_2), \\ \gamma_1^{k+1} &\leftarrow \gamma_1^k - \lambda \mu_1 (FSf^{k+1} - y), \\ \gamma_2^{k+1} &\leftarrow \gamma_2^k - \lambda \mu_2 (w^{k+1} - \nabla f^{k+1}). \end{aligned} \quad (11)$$

3.2. The Solution to Minimization Problem with Respect to w . Holding variable f constant, we get the minimization problem with respect to w in (9) at the k th iteration as

$$w^{k+1} = \arg \min_w \left\{ \|w\|_1 + (\gamma_2^k)^H (w - \nabla f^k) + \frac{\mu_2}{2} \|w - \nabla f^k\|_2 \right\}. \quad (12)$$

Equation (12) is a ℓ_1 -norm minimization problem, the solution of which can be estimated by shrinkage rule [14] as

$$\begin{aligned} w^{k+1} &= \text{Shrink} \left\{ \nabla f^k - \frac{\gamma_2^k}{\mu_2}, \frac{1}{\mu_1 * \mu_2} \right\} \\ &\triangleq \max \left\{ \left| \nabla f^k - \frac{\gamma_2^k}{\mu_2} \right| - \frac{1}{\mu_1 * \mu_2}, 0 \right\} \cdot \text{sgn} \left(\nabla f^k - \frac{\gamma_2^k}{\mu_2} \right). \end{aligned} \quad (13)$$

3.3. *The Solution to Minimization Problem with Respect to f .* Holding variable w constant, we get the minimization problem with respect to f at the k th iteration based on (9) as

$$f^{k+1} = \arg \min_f \left\{ (\gamma_1^k)^H (FSf - y) + \frac{\mu_1}{2} \|FSf - y\|_2 + (\gamma_2^k)^H (w^k - \nabla f) + \frac{\mu_2}{2} \|w^k - \nabla f\|_2 \right\}. \quad (14)$$

Ignorant of irrelevant constant, (14) can be written as (15)

$$f^{k+1} = \arg \min_f \left\{ \frac{\mu_1}{2} \|FSf - y - \eta_1\|_2 + \frac{\mu_2}{2} \|w^k - \nabla f - \eta_2\|_2 \right\}, \quad (15)$$

where $\eta_1 = \gamma_1/\mu_1$, $\eta_2 = \gamma_2/\mu_2$. Equation (15) is a ℓ_2 -norm minimization problem, which can be solved by nonlinear conjugate gradient (NCG) descent algorithm with backtracking line search algorithm. During the iterative process, the iterative step may be calculated by inexact line search or the Barzilai and Borwein (BB) method [15].

3.4. *The Solution to Sparse Constrained Image Reconstruction for Parallel Imaging.* Combining the results in Sections 3.1, 3.2, and 3.3, we now present the algorithm for solving the unconstrained optimization problem (9) as follows.

- (1) Initialize f^0 , w^0 and regularization parameters μ_1, μ_2 .
- (2) Precompute $F^H S^H f$, and let $\eta_1^0 = \eta_2^0 = 0$, $k = 0$.
Repeat the following.
- (3) Obtain an update w^{k+1} using an appropriate technique as described in Section 3.2.
- (4) Update f^{k+1} using an appropriate technique as described in Section 3.3 by NCG method, and the inexact line search method is used to calculate the iterative step.
- (5) Update the Lagrangian multiplier γ_1 by the following function:

$$\gamma_1^{k+1} \leftarrow \gamma_1^k - \lambda \mu_1 (FSf^{k+1} - y). \quad (16)$$

- (6) Update the Lagrangian multiplier γ_2 by the following function:

$$\gamma_2^{k+1} \leftarrow \gamma_2^k - \lambda \mu_2 (w^{k+1} - \nabla f^{k+1}). \quad (17)$$

- (7) Let $k = k + 1$.

Until some stop criterion is met.

4. Experiments

4.1. *Data Simulation and Acquisition.* In all our experiments, we consider k -space MR data assigned on the Cartesian grid, and the undersampling pattern is uniformity, so Fourier

encoding matrix corresponds to an undersampling version of the DFT matrix. Two sets of parallel MR data are applied to test the proposed algorithm. One set of data is acquired from simulating parallel MRI system, and the other is actual parallel MR data.

In order to construct the simulating multichannel MRI receive system, we considered a noise-free 256×256 T1-weighted MR image obtained from the BrainWeb database [16] and then downsampled to 128×128 . The simulating system had four-channel linear phased-array coil wrapped around the whole brain circumferentially. The coil sensitivity maps were calculated using Biot-Savart's law [17]. Multichannel images were then created by multiplying T1-weighted MR image with the simulated sensitivity profiles. At last, these images were Fourier transformed to generate the multichannel k -space data whose size was $128 \times 128 \times 4$. In the research, complex Gaussian noise would be added to data set for simulating noisy parallel MR data.

The actual fully sampled brain dataset was obtained from PULSAR (a Matlab toolbox for parallel MRI) [18], which was acquired using MR systems with eight-channel head array and multichannel receiver from a healthy male volunteer with fast spoiled gradient-echo sequence, TR/TE = 300/10 ms, matrix size = 256×256 , tip angle = 15° , and FOV = 22×22 cm.

To simulate the accelerating imaging procedure for parallel MRI, k -space dataset along phased encoding direction might be uniformly decimated to produce undersampling datasets. Additionally, central 12 phase-encoding lines were preserved to be used for coil sensitivity estimation [19]. We mainly researched parallel MR image reconstruction problem when the undersampling rate (also known as AF) attained its maximum value that was the number of receive coils at theory. The size of undersampled data in simulated data analysis is $128 \times 32 \times 4$, while actual dataset is $256 \times 32 \times 8$. Meanwhile, for two sets of data, the full k -space data was acquired and then sum-of-squares (SoS) reconstruction [20] was used as a reference image.

Figure 1(a) shows the data collected from the simulating parallel MRI, which will be applied to test the proposed algorithm.

4.2. *Calibration of Sensitivity Profiles.* Calibration of the spatial sensitivity functions of coil arrays is a crucial element in parallel MRI. Accurate coil sensitivity information is required for accurate spatial encoding in parallel MRI reconstructions, and the choice of sensitivity calibration strategy is at least as important as the choice of reconstruction strategy. The most common approach has been to measure coil sensitivities directly using one or more low-resolution images acquired before or after accelerated data acquisition. However, since it is difficult to ensure that the patient and coil array will be in exactly the same positions during both calibration scans and accelerated imaging, this approach can introduce sensitivity miscalibration errors into parallel MRI reconstructions. Coil sensitivity functions vary slowly as a function of spatial position, and low-resolution in vivo images suffice to form sensitivity references. Thus, valid coil sensitivities can be

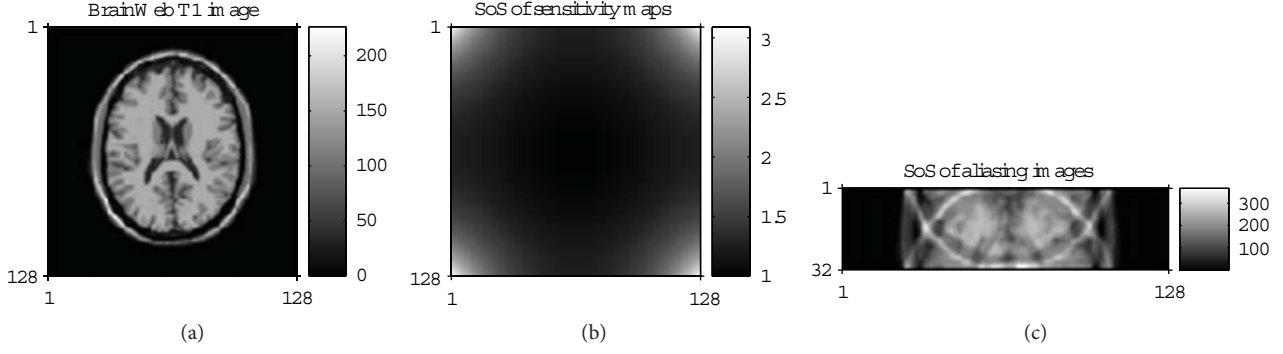


FIGURE 1: Simulated pMRI. (a) is the T1-weighted brain MR image, (b) is SoS of individual receiver coil sensitivity profiles calculated based on Biot-Savart’s law, and (c) is SoS reconstruction from undersampled data when AF is 4.

determined from the fully sampled region of the central k -space, so long as the range of spatial frequencies covered in the central region contains the spatial frequency band of the coil sensitivity functions [19]. In the paper, central 12 phase-encoding lines were Fourier transformed to produce low-resolution $f(\vec{r})$, which was used to estimate the coil sensitivity profiles. By (18), the magnetization distribution low-resolution $f(\vec{r})$ may be partly removed, and then the encoding effects of relatively pure coil sensitivities are isolated as

$$\hat{s}_1(\vec{r}) \approx \frac{[f(\vec{r}) s_1(\vec{r})]^{\text{low-resolution}}}{\sqrt{\sum_l |[f(\vec{r}) s_l(\vec{r})]^{\text{low-resolution}}|^2}}, \quad (18)$$

where the “low-resolution” superscript indicates that use of only the central k -space positions results in a low-resolution measurement of the full product of $f(\vec{r})$ and $s_l(\vec{r})$.

4.3. Data Analysis. In the study of actual parallel MRI, the standard reference image is the SoS reconstructed image of full-sampled individual coil surface images, while the T1-weighted brain image is the reference image in the simulating study. The normalized mean squared error (NMSE) between the reconstructed image and the reference image would be calculated to quantitatively analyze the quality of reconstructed image. NMSE is also known as artifact power (AP), which suggests any error as both increased image artifacts and noise. As shown in (19), a higher value of NMSE (or AP) represents the reduced image quality as

$$\text{NMSE} = \frac{\sum_{\vec{r}} (|f(\vec{r})| - |f^{\text{reference}}(\vec{r})|)^2}{\sum_{\vec{r}} |f^{\text{reference}}(\vec{r})|^2}, \quad (19)$$

where $f^{\text{reference}}$ denotes the sensitivity reference image.

To pose the effectiveness of the proposed reconstruction method as (9), the other parallel MR image reconstruction methods known as generalized encoding matrix (GEM) method [21], which is used in SENSE method, and CG method [22] are comparatively analyzed. Additionally, the

stopping criterion for the iterative algorithms used in our study is based on discrepancy principle as

$$\frac{\text{norm}(f_j - f_{j-1})}{\text{norm}(f_j)} < \text{tol}, \quad (20)$$

where description “norm” indicates Frobenius norm of matrix, “tol” denotes the convergence tolerance, and subscript “ j ” indicates the iteration number during the iterative process.

4.4. Results. We compared the proposed method to GEM method, named the basic SENSE, and to CG method, by which MR images may be reconstructed from undersampled MR data. Figure 2 shows the reconstructed images from noise-free simulating data when employing 4-fold accelerating MRI, when AF is 4. Figure 3 shows the reconstructed images from noisy 4-fold undersampled MR data, where the added noise is zero-mean Gaussian noise. In Figures 2 and 3, the three images on the top are the reconstructed images by the methods as mentioned above, and the images on the bottom are the difference profiles between the top three reconstructed images and reference image.

During the iterative process of reconstructing the images as seen in Figures 2 and 3, we let the convergence tolerance 0.0001. When the proposed algorithm (described in Section 3.4) is used to reconstruct the image in Figure 2, the penalty parameters μ_1, μ_2 are $2^{-27}, 2^{-33}$, respectively. The number of iterations is 20 for resolving the minimization problem with respect to f by the NCG method referred to in Section 3.3, and the total number of iterations for the proposed algorithm is 411, namely, the valuable k referred to in Section 3.4. At the same time, the proposed algorithm is used to reconstruct the images in Figure 3, and the penalty parameters μ_1, μ_2 are $2^{-26}, 2^{-22}$, respectively, and the number of iteration is 20 for resolving the minimization problem with respect to f by NCG method, and the total number of iterations for the algorithm proposed is 198. Tables 1 and 2 are the mean of NMSE, respectively, in Figures 2 and 3.

As shown in Figure 2, the proposed algorithm may obviously restrain the aliasing artifacts resulted from under-sampled MR data. As seen in Figure 3, noise derived from

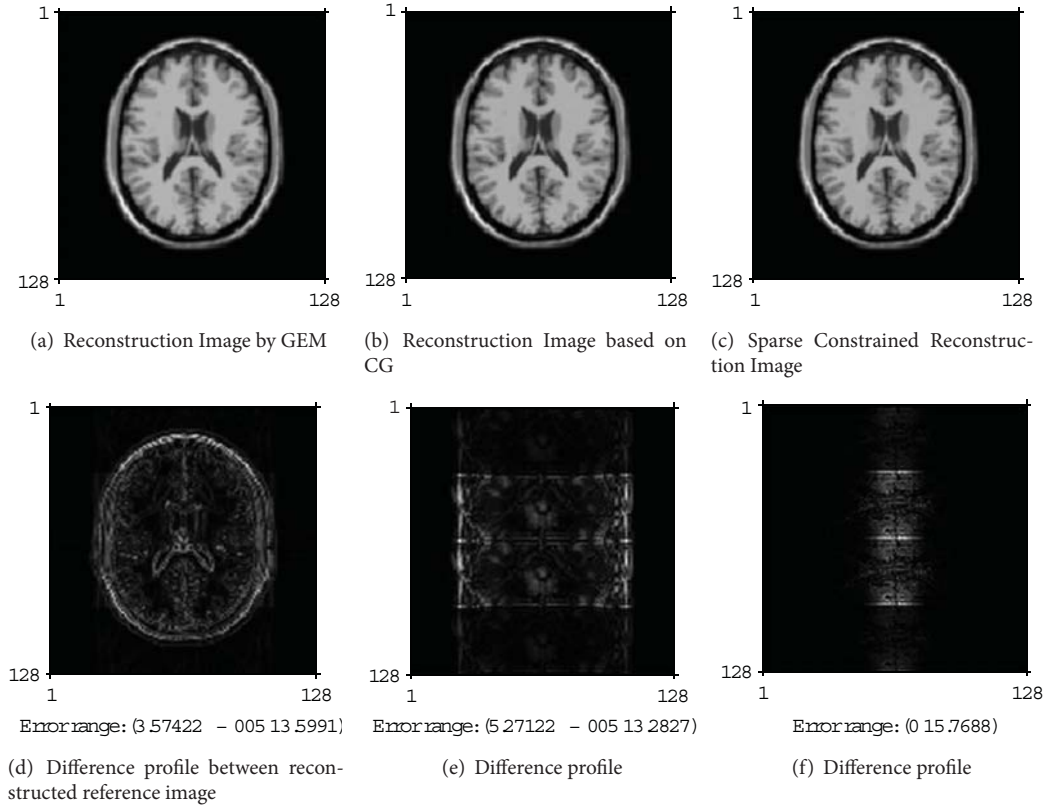


FIGURE 2: Reconstructed images from noise-free undersampling MR data for the simulated parallel MRI, where the undersampling rate is 4, which is the maximum of AF at theory. The top three images are, respectively, reconstructed by GEM method, CG method, and the proposed method as (9), which is solved by the algorithm referred to in Section 3.4. The bottom three images are the difference profiles between the above three reconstructed images and the reference image.

TABLE 1: Mean of NMSE of reconstruction image (in Figure 2).

Reconstruction method	GEM	CG	Sparse constrained reconstruction
Mean of NMSE	$4.1985e-004$	$2.8799e-004$	$2.2580e-004$

TABLE 2: Mean of NMSE of reconstruction image (in Figure 3).

Reconstruction method	GEM	CG	Sparse constrained reconstruction
Mean of NMSE	2.8860	12.5720	0.0248

measurement procedure is suppressed and result in the convergence of iterative process by our proposed algorithm.

In analysis of actual parallel MR image reconstruction, AF is set as 8, which is the maximum at theory for parallel MRI system with 8-channel coil array. Figure 4 shows the reconstructed image and the difference profiles between reconstructed images and the reference image, and the mean of NMSE is shown in Table 3.

In Figure 4, the left image on the top panel is the reference image, and the left image on the bottom is the reconstructed image by SoS method from 8-fold undersampled parallel MR data. During iterative process of reconstructing the images

TABLE 3: Mean of NMSE of reconstructions image from actual pMRI data (AF = 8, in Figure 4).

Reconstruction methods	GEM	CG	Sparse constrained reconstruction
NMSE	356.7079	343.1923	0.0095

in Figure 4, the convergence tolerance is 0.001. When the proposed algorithm is used to reconstruct the image in Figure 4, the penalty parameters μ_1, μ_2 are $2^{-20}, 2^{-11}$, respectively. The iterative number is 1 for resolving the minimization problem with respect to f by NCG method, and the total iterative number of algorithm proposed is 37.

As shown in Figures 3 and 4, the proposed algorithm can effectively reduce the aliasing artifacts and noise information.

5. Discussion

The quality of the reconstructed image for parallel imaging may be affected by the undersampling rate, noise level, the exact estimation of receiver coils sensitivity, k -space data trajectory, and reconstruction method. We only researched the image reconstruction from undersampled k -space data

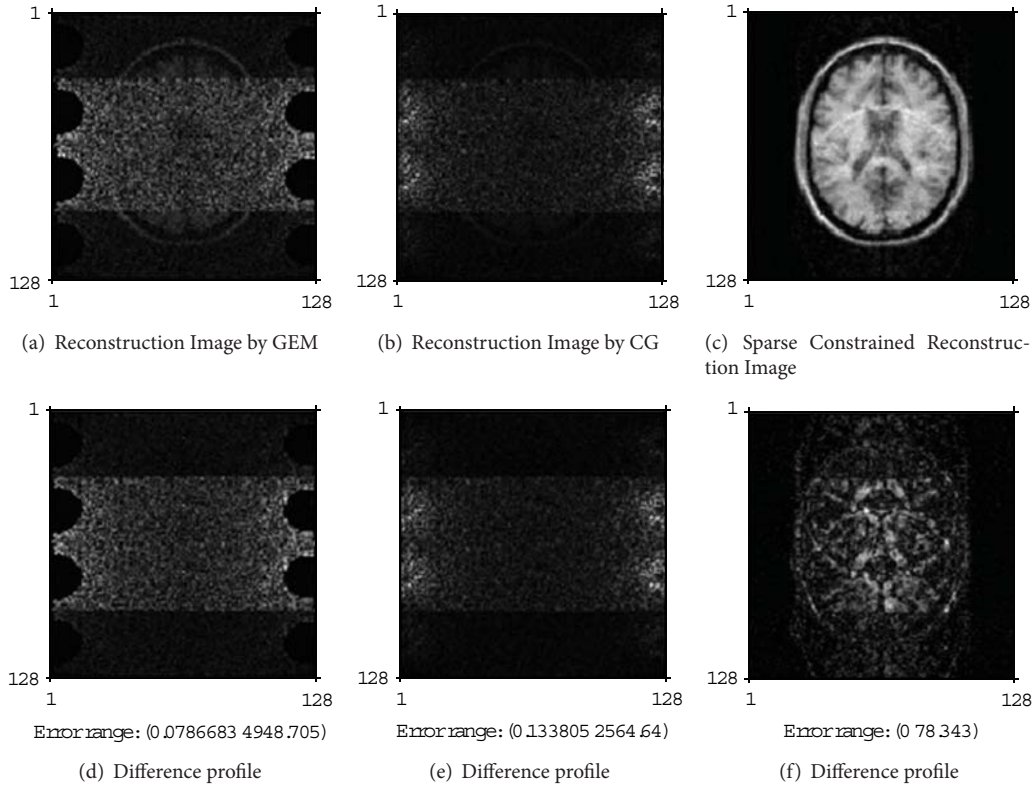


FIGURE 3: Reconstructed images from noisy undersampled MR data for the simulated parallel MRI, where the undersampling rate (named AF) is 4.

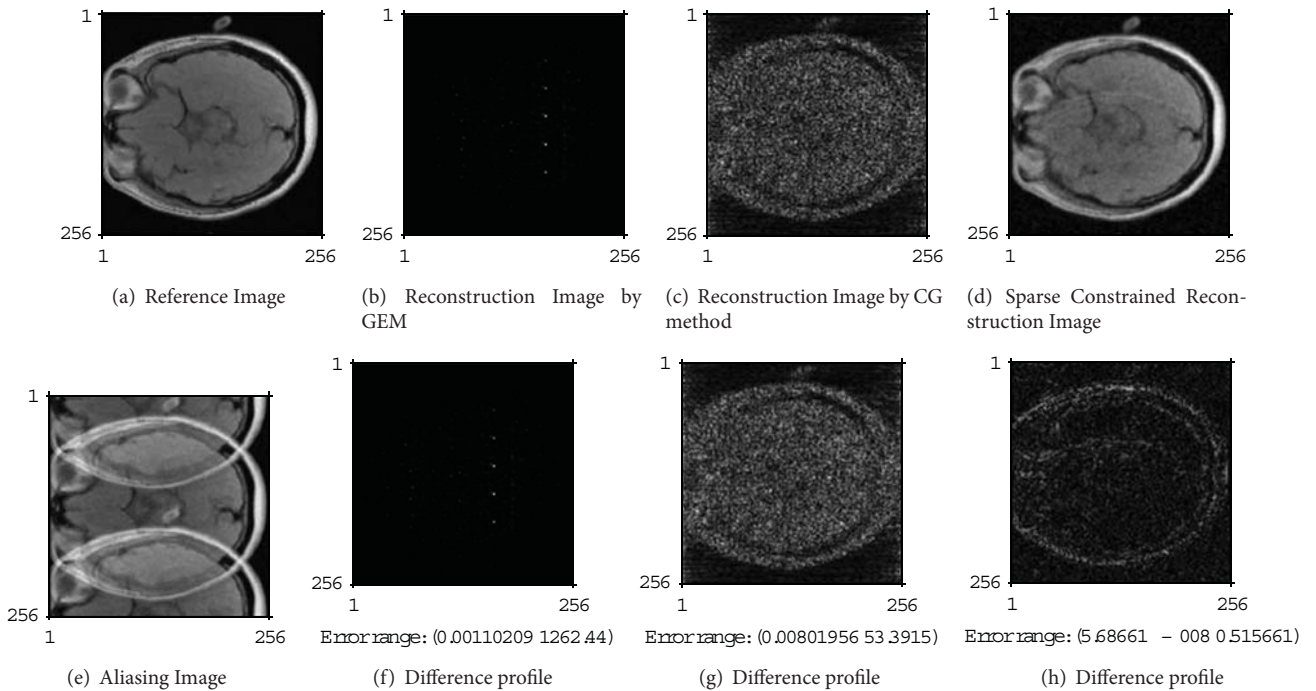


FIGURE 4: Reconstructed images from noisy undersampling MR data for in vivo parallel MRI, where the undersampling rate is 8, which is the maximum at theory. (a) is the reference image (SoS reconstruction of full-sampled coil images). (b), (c), and (d) are images reconstructed, respectively, by GEM method, CG method, and the proposed method proposed as (9). (e) is the reconstructed image by SoS method. (f), (g), and (h) are the difference profiles, respectively, between (b), (c), (d), and (a).

acquired along the Cartesian trajectory. However, the proposed algorithm is also fit to reconstruct MR image for arbitrary trajectories.

There may be two approaches to improve the quality of the reconstructed image based on SENSE method: one approach is to improve the accuracy estimation of sensitivity, another approach is to propose the effective reconstruction algorithm. However, when AF is large, only by improving the reliability of the coil sensitivity maps, the suppression of aliasing artifact and noise in the reconstructed image is indistinctive. In order to remarkably improve the quality of the reconstructed image, the constrained reconstruction is generally shown to be an effective method. The goal of our proposed method is to improve the quality of the reconstructed image, when MR data are highly undersampled in parallel imaging. As the coil sensitivity profiles are already obtained, the reconstruction problem in parallel imaging is formulated as solving a set of linear equations based on (3). These equations can be very ill conditioned depending on the coil configurations and sampling trajectories, which further deteriorate the quality of the reconstructed image, especially when high undersampling rate is used for accelerating parallel imaging procedure. Therefore, the ill-conditioned problem in parallel imaging has been partially addressed by optimizing coil geometry, optimizing sampling trajectory, or introducing regularizations. In this paper, the ill-conditioned problem is partly reformed by adding the constrained condition to stabilize the reconstruction process. As anywhere noise exits, the reconstruction method for parallel imaging should be proposed on full consideration of both noise and aliasing artifacts suppressed problem. Based on sparseMRI theory, as MR image is sparse on finite difference domain, and a sparse constrained reconstruction problem for parallel imaging is constructed in the paper. Through the methods proposed and the experiment presented, the following aspects could be taken into account.

(1) Compare the proposed reconstruction method with the other methods for parallel imaging. According to our analysis results, the GEM algorithm for usual SENSE method is usually suitable for noise-free data and the accelerating imaging procedure at low AF. CG method can effectively restrain aliasing artifacts in the reconstructed image and be fast convergence on condition of noise-free undersampled data. However, when MR image may be reconstructed from the noisy and undersampled MR data, NMSE value between the reconstructed image and reference image first rapidly decreases and then gradually increases along with CG iterative reconstruction process. As shown in Figure 3, the least mean of NMSE between the reconstructed image by CG method and the reference image was 0.0762 after 21 numbers of CG iteration, but reached the convergence condition after 975 numbers of iteration. Similarly in Figure 4, the least mean of NMSE of the reconstructed image by CG method was 0.0623, but reached the convergence condition after 1020 number of iteration, and the least mean of NMSE was shown in Table 3.

(2) Reconstruct MR image under the nonnegative constraint condition. In our proposed algorithm, the solution to

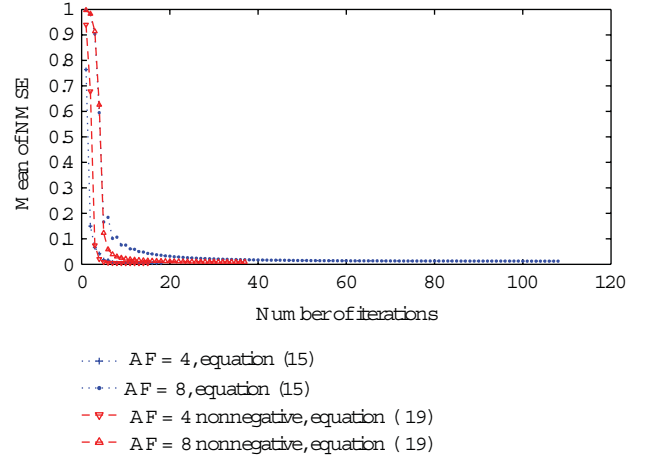


FIGURE 5: Iteration convergence process of reconstructing MR image for actual parallel MRI. The reconstruction method is the proposed algorithm described in Section 3.4, and (15) and (21) are, respectively, used for the subproblem with respect to f , where NCG descent algorithm with backtracking line search algorithm is used to solve (15) and (21).

subproblem with respect to f as (15) is a quadratic minimization problem, which may be the following subproblem on condition of nonnegative constraint:

$$\min_f \left\{ \frac{\mu_1}{2} \|FSf - y - \eta_1\|_2 + \frac{\mu_2}{2} \|w^k - \nabla f - \eta_2\|_2 \right\} \quad (21)$$

s.t. $\text{real}(f) > 0$,

where $\text{real}(\cdot)$ indicators the operator of getting the real of complex f .

Figure 5 shows the iteration process during reconstructing MR image f in analysis of actual parallel MRI, where (15) and (21) are, respectively, used in the proposed algorithm described in Section 3.4. As shown in Figure 5, when reconstructing image under the nonnegative constraint condition, the iteration process described in Section 3.4 might rapidly converge, and the mean of NMSE was reduced between the reconstructed image and the reference image.

(3) Reconstruct MR image at the different AFs for parallel imaging. Parallel MRI utilizes a radio frequency (RF) coil array to simultaneously acquire data from multiple receivers, and acceleration is achieved by a reduced phase encoding k -space trajectory. The nature of the subsampled k -space data requires the use of a reconstruction algorithm to restore aliased images into full field-of-view (FOV) images. Table 4 is the mean NMSE of reconstructed image, respectively, by GEM method, CG method and the proposed algorithm at the different AFs.

As shown in Table 4, the proposed algorithm obviously improves the quality of reconstructed images. Compared to Table 3, AF is the main reason for affecting the quality of reconstructed image, so aliasing artifacts suppression may be chiefly considered for reconstruction method.

(4) The solution to the quadratic minimization problem is as follows. The solution to subproblem with respect to f as

TABLE 4: The mean of NMSE of reconstructed image from actual pMRI data (AF = 4).

reconstruction	GEM	CG reconstruction	Sparse constrained reconstruction
NMSE (noise-free data)	0.7641	0.0024	0.0019
NMSE (noisy data)	0.6698	85.2921	0.0049

(15) is a quadratic minimization problem, which can be solved by the steepest descent method, the Newton method, or CG method. However, when resolving the subproblem with respect to f , the Newton method is inferior to the nonlinear CG method by the data analysis results.

(5) Penalty parameters and iteration convergence problem for regularization reconstruction are as follows. Convergence problem should be firstly considered for any iteration algorithm. The proposed algorithm for reconstructing MR image is an iterative solution course, and penalty parameters μ_1 , μ_2 greatly affect the iterative convergence process. As long as penalty parameters chosen are suitable, the proposed algorithm can rapidly converge. Thereby, the penalty parameters μ_1 , μ_2 are the key factors of optimization problem of sparse constrained reconstruction as shown in (9), which is a ℓ_1 -norm and ℓ_2 -norm minimization problem, named ℓ_1 - ℓ_2 optimization problem. The common L-curve method is unable to determine the penalty parameters μ_1 , μ_2 . According to the quantitative index as NMSE between the reconstructed image and the reference image, we explored the better suitable penalty parameters within a determinate range. Specifically, the ratio of μ_1 to μ_2 was fixed, and μ_1 , μ_2 increased by power of 2 in the range of 2^{-30} to 2^{10} . The penalty parameters μ_1 , μ_2 would be selected in our research, when they were used to (9) and then the least mean of NMSE between the reconstructed image and the reference image can be obtained.

6. Conclusion

In order to improve the quality of the reconstructed image for parallel imaging, a sparse constrained image reconstruction algorithm based on variable splitting method is proposed. Through the analysis of reconstructing full-FOV image from simulating and actual parallel MR data, the proposed algorithm can effectively suppress the aliasing artifacts in the reconstructed image resulted from the undersampled MR data, and also noise is obviously suppressed and the edge of image is preserved.

References

- [1] A. Deshmane, V. Gulani, M. A. Griswold, and N. Seiberlich, "Parallel MR imaging," *Journal of Magnetic Resonance Imaging*, vol. 36, no. 1, pp. 55–72, 2012.
- [2] K. P. Pruessmann, M. Weiger, M. B. Scheidegger, and P. Boesiger, "SENSE: sensitivity encoding for fast MRI," *Magnetic Resonance in Medicine*, vol. 42, no. 5, pp. 952–962, 1999.
- [3] M. A. Griswold, P. M. Jakob, R. M. Heidemann et al., "Generalized autocalibrating partially parallel acquisitions (GRAPPA)," *Magnetic Resonance in Medicine*, vol. 47, no. 6, pp. 1202–1210, 2002.
- [4] H. Omer and R. Dickinson, "Regularization in parallel MR image reconstruction," *Concepts in Magnetic Resonance A*, vol. 38, no. 2, pp. 52–60, 2011.
- [5] F. H. Lin, F. N. Wang, S. P. Ahlfors, M. S. Hämläinen, and J. W. Belliveau, "Parallel MRI reconstruction using variance partitioning regularization," *Magnetic Resonance in Medicine*, vol. 58, no. 4, pp. 735–744, 2007.
- [6] K. T. Block, M. Uecker, and J. Frahm, "Undersampled radial MRI with multiple coils. Iterative image reconstruction using a total variation constraint," *Magnetic Resonance in Medicine*, vol. 57, no. 6, pp. 1086–1098, 2007.
- [7] M. Lustig, D. Donoho, and J. M. Pauly, "Sparse MRI: The application of compressed sensing for rapid MR imaging," *Magnetic Resonance in Medicine*, vol. 58, no. 6, pp. 1182–1195, 2007.
- [8] SparseMRI V0. 2, <http://www.stanford.edu/~mlustig/SparseMRI.html>.
- [9] X. Zhang, M. Burger, X. Bresson, and S. Osher, "Bregmanized nonlocal regularization for deconvolution and sparse reconstruction," *SIAM Journal on Imaging Sciences*, vol. 3, no. 3, pp. 253–276, 2010.
- [10] W. Yin, S. Osher, J. Darbon et al., "Bregman iterative algorithms for compressed sensing and related problems," *SIAM Journal on Imaging Sciences*, vol. 1, pp. 143–168, 2008.
- [11] "L1-Related Optimization Project," <http://www.caam.rice.edu/~optimization/L1>.
- [12] M. V. Afonso, J. M. Bioucas-Dias, and M. A. T. Figueiredo, "Fast image recovery using variable splitting and constrained optimization," *IEEE Transactions on Image Processing*, vol. 19, no. 9, pp. 2345–2356, 2010.
- [13] S. Ramani and J. A. Fessler, "Parallel MR image reconstruction using augmented lagrangian methods," *IEEE Transactions on Medical Imaging*, vol. 30, no. 3, pp. 694–706, 2011.
- [14] E. T. Hale, W. Yin, and Y. Zhang, "Fixed-point continuation for ℓ_1 -minimization: methodology and convergence," *SIAM Journal on Optimization*, vol. 19, no. 3, pp. 1107–1130, 2008.
- [15] C. R. Vogel, *Computational Methods for Inverse Problems*, SIAM, Philadelphia, Pa, USA, 2002.
- [16] Brainweb, "Simulated MRI volumes for normal brain," McConnell Brain Imaging Centre, <http://www.bic.mni.mcgill.ca/brainweb/>.
- [17] M. I. Grivich and D. P. Jackson, "The magnetic field of current-carrying polygons: an application of vector field rotations," *The American Journal of Physics*, vol. 68, no. 5, pp. 469–474, 2000.
- [18] J. X. Ji, B. S. Jong, and S. D. Rane, "PULSAR: a MATLAB toolbox for parallel magnetic resonance imaging using array coils and multiple channel receivers," *Concepts in Magnetic Resonance B*, vol. 31, no. 1, pp. 24–36, 2007.
- [19] C. A. McKenzie, E. N. Yeh, M. A. Ohliger, M. D. Price, and D. K. Sodickson, "Self-calibrating parallel imaging with automatic coil sensitivity extraction," *Magnetic Resonance in Medicine*, vol. 47, no. 3, pp. 529–538, 2002.
- [20] P. B. Roemer, W. A. Edelstein, C. E. Hayes, S. P. Souza, and O. M. Mueller, "The NMR phased array," *Magnetic Resonance in Medicine*, vol. 16, no. 2, pp. 192–225, 1990.
- [21] K. P. Pruessmann, "Encoding and reconstruction in parallel MRI," *Magnetic Resonance in Medicine*, vol. 19, pp. 288–299, 2006.

- [22] K. P. Pruessmann, M. Weiger, P. Börnert, and P. Boesiger, "Advances in sensitivity encoding with arbitrary k-space trajectories," *Magnetic Resonance in Medicine*, vol. 46, no. 4, pp. 638–651, 2001.

Research Article

Improved Compressed Sensing-Based Algorithm for Sparse-View CT Image Reconstruction

Zangen Zhu,¹ Khan Wahid,¹ Paul Babyn,² David Cooper,³ Isaac Pratt,³ and Yasmin Carter³

¹ Department of Electrical and Computer Engineering, University of Saskatchewan, Saskatoon, Canada S7N 5A9

² Department of Medical Imaging, Saskatoon Health Region, Saskatoon, Canada S7N 0W8

³ College of Medicine, University of Saskatchewan, Saskatoon, Canada S7N 5E5

Correspondence should be addressed to Khan Wahid; khan.wahid@usask.ca

Received 10 January 2013; Revised 4 March 2013; Accepted 5 March 2013

Academic Editor: Wenxiang Cong

Copyright © 2013 Zangen Zhu et al. This is an open access article distributed under the Creative Commons Attribution License, which permits unrestricted use, distribution, and reproduction in any medium, provided the original work is properly cited.

In computed tomography (CT), there are many situations where reconstruction has to be performed with sparse-view data. In sparse-view CT imaging, strong streak artifacts may appear in conventionally reconstructed images due to limited sampling rate that compromises image quality. Compressed sensing (CS) algorithm has shown potential to accurately recover images from highly undersampled data. In the past few years, total-variation-(TV-) based compressed sensing algorithms have been proposed to suppress the streak artifact in CT image reconstruction. In this paper, we propose an efficient compressed sensing-based algorithm for CT image reconstruction from few-view data where we simultaneously minimize three parameters: the ℓ_1 norm, total variation, and a least squares measure. The main feature of our algorithm is the use of two sparsity transforms—discrete wavelet transform and discrete gradient transform. Experiments have been conducted using simulated phantoms and clinical data to evaluate the performance of the proposed algorithm. The results using the proposed scheme show much smaller streaking artifacts and reconstruction errors than other conventional methods.

1. Introduction

X-ray computed tomography (CT) is extensively used clinically to evaluate patients with a variety of conditions. However, by its nature, CT scans expose the patients to high X-ray radiation doses which can result in an increased lifetime risk of cancer [1, 2]. The radiation dose to the patients is proportional to the number of X-ray projections. Additionally, medical research makes extensive use of CT on the microscopic scale, known as micro-CT. Longitudinal studies on experimental animals such as rats, mice, and rabbits are also restricted in resolution and image quality by radiation dose. Currently, the defacto standard for reconstruction on the commercial CT scanners is the filtered backprojection (FBP) algorithm, which typically requires a large number (300–1000) of angular views for yielding accurate reconstruction of the image object.

Recently a number of strategies have been proposed to decrease radiation dose in CT scans. One approach to lower

the total X-ray radiation dose is to simply reduce the dose level mAs/view in data acquisition protocols. This approach typically results in an insufficient number of X-ray photons received by the detectors, increasing the noise level on the sinograms produced. The noise-contaminated sinogram data will degrade the quality of reconstructed CT images when a conventional FBP algorithm is used [3]. Another way to reduce the total radiation dose is to reduce the number of projections needed. According to the standard image reconstruction theory in image processing, when the number of the view angles does not satisfy the Shannon/Nyquist sampling theorem, aliasing artifacts will spread out in the reconstructed images. As a consequence, FBP algorithms do not produce diagnostically satisfactory images in sparse-view data collection schemes, because they are derived by assuming densely sampled projections over the scanning angular range.

Since analytical reconstruction methods, such as FBP, cause such serious streaking artifacts in the resulting reconstructed CT images, iterative algorithms have been proposed

and investigated as a means to eliminate these defects. One approach is algebraic and is based upon solving a system of linear equations. This scheme is often referred to as algebraic reconstruction technique (ART) [4, 5], and it has several variants with different iteration schemes, such as simultaneous ART (SART) [6, 7]. The ART algorithms consist of altering the grayness of each pixel intersected by the ray sum in such a way as to make the ray sum agree with the corresponding element of the measured projection. In each iteration, the current guess of the image is reprojected and checked to see how it matches with the real measurements. These algebraic methods are computationally intensive and require large amounts of memory [8]. However increases in computing power may render them more available over time. Other iterative approaches, such as statistical image reconstruction (SIR) [9], use the statistical distribution of photons resulting from the X-ray interaction process. Both the ART and SIR methods solve the reconstruction problem iteratively. Iterative algorithms have been proven to be advantageous over analytical algorithms when projection data are incomplete and noisy, for example, in the sparse-view reconstruction scenario. However, when the Shannon/Nyquist sampling requirement is violated, that is, less than 100 view angles, the linear system will become highly underdetermined and unstable, failing to maintain clinically acceptable image quality.

In the past few years, compressed sensing (CS) algorithms [10, 11] have attracted huge attention in the CT and micro-CT community. One may view CS-based algorithm as simply another iterative algorithm, but what makes the CS method distinctive from other iterative algorithms is that it exploits the sampling strategy in which the sampled data are truly helpful for an accurate reconstruction of an image object. Several compressed sensing based CT image reconstruction algorithms are proposed in the sparse-view scenario [12, 13]. In particular, the total-variation-(TV-) based methods have demonstrated their power in CT reconstruction with only a few X-ray projections with their dataset. For example, Sidky's work in [13] showed that their method can yield accurate reconstructions in ideal conditions where only 20 view angles projection data were acquired using simulated data from a jaw phantom. In such algorithms, an objective function of TV norm is minimized subject to a data fidelity posed by the acquired projection data. Minimizing the image gradient essentially suppresses those high spatial frequency parts such as streaking artifacts and noise in the reconstructed images. The major problem of this TV-based compressed sensing method is that it tries to uniformly penalize the image's gradient irrespective of the underlying image structures and thus low contrast regions are sometimes over smoothed [3]. To resolve this issue, we propose a new algorithm based on compressed sensing that jointly minimizes the wavelet transform and total variation of the object image. The 2D wavelet transform is good at capturing point singularities [14], thus preserving edges and low contrast information. This process suppresses the streaking artifacts and noise, while detailed structures are also preserved, resulting in an improved image.

2. Theory and Method

2.1. X-Ray Computed Tomography (CT) Imaging System. A parallel beam CT scanning system uses an array of equally spaced sources of X-ray beams and an array of detectors. Let $\mu(x, y)$ denote the X-ray attenuation coefficient distribution of tissue of a 2D target object and let l denote the straight line from the X-ray focal spot to the detector pixel, which is also referred to as the X-ray path. The X-ray tube emits X-ray photons which travel in a straight line through the object. The photons are attenuated by the materials in the target object. Radiation that is not absorbed by the object's internal structure reaches the detectors. According to Beer's law, the detected photon number I and the entering photon number I_0 at a given detector pixel have the following relationship [15]:

$$I = I_0 \exp\left(-\int_l \mu(x, y) dl\right), \quad (1)$$

where the line integral is performed along the X-ray path. Alternatively, one can define

$$y = \int_l \mu(x, y) dl = \ln \frac{I_0}{I}, \quad (2)$$

where y is the so-called projection data or sinogram, which is essentially the line integral in (1). Then the image reconstruction process consists of estimating the attenuation coefficients, μ , from the detected projection data y . In computer implementation, the attenuation coefficients are digitized into the so-called pixel representations [16]:

$$\mu(x, y) = \sum_{i \in S} \mu_i \omega_i(x, y), \quad (3)$$

where S denotes the index of the set of N pixel locations, i is the pixel index, and $\omega_i(x, y)$ is the basis function. Substituting (3) into the line integral equation in (2), one can obtain

$$y = \sum_{i \in S} \mu_i \int_l \omega_i(x, y) dl = \sum_{i \in S} A_{ji} \mu_i = A\mu, \quad (4)$$

where the X-ray system matrix A is given by

$$A_{ji} = \int_{l_j} \omega_i(x, y) dl, \quad (5)$$

which is the line integral of the basis function $\omega_i(x, y)$ along the j th X-ray path. The system matrix is independent of the image object; it is rather dependent on the CT scanner, including the positions of sources and detectors. Hence (4) gives a system of linear equations with μ_i .

2.2. Brief Overview of Existing Methods. In this study, our proposed algorithm will be compared with the state-of-the-art methods, including filtered backprojection (FBP) [15], algebraic reconstruction technique (ART) [4, 5], and its variants, simultaneous algebraic reconstruction technique (SART) [8]. A brief summary of these methods is given in the following.

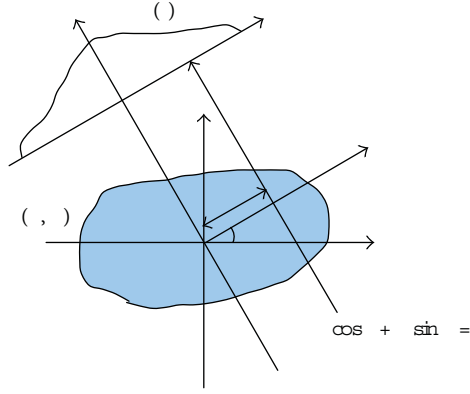


FIGURE 1: A parallel beam projection through $\mu(x, y)$ at angle θ . $P_\theta(t)$ is the measured projection.

2.2.1. *Filtered Backprojection (FBP)*. Consider the parallel beam of rays intersecting an object as shown in Figure 1. The parallel beam is inclined to the X-axis at angle θ and each ray can be characterized by its perpendicular distance, t , to the origin. Equation (2) can be rewritten as

$$P_\theta(t) = \int_{l_{\theta,t}} \mu(x, y) dl = \ln \frac{I_0}{I}. \quad (6)$$

Using a Dirac delta function, we have an alternate representation:

$$P_\theta(t) = \int_{-\infty}^{\infty} \int_{-\infty}^{\infty} \mu(x, y) \delta(x \cos \theta + y \sin \theta - t) dx dy. \quad (7)$$

FBP begins by filtering the projection data with a high pass filter, which in reality is implemented by the Ram-Lak filter or Shepp-Logan filter, then takes the integral over 0 to π with respect to θ . Since filtering in frequency domain can be done by the convolution operation in spatial domain, the formulation of filtered backprojection is

$$\mu(x, y) = \int_0^\pi d\theta \int_{-\infty}^{\infty} P_\theta(t') \varphi(t - t') dt', \quad (8)$$

where $\varphi(t)$ is the corresponding high pass filter in spatial domain.

2.2.2. *Algebraic Reconstruction Technique (ART)*. ART considers the CT imaging process as a linear system of equations as in (4):

$$y = A\mu, \quad (9)$$

where A is the system matrix (given in (5)) describing the forward projection in the CT scan. ART algorithms solve the above equations in an iterative way so that the difference between the projection data from real scan and the projection data calculated from the estimated image is backprojected onto the estimated image at current iteration step. Given that

the system matrix A is of size $m \times n$, the method involves the i th row of A in the following update of iteration:

$$x^{k+1} = x^k + \lambda_k \frac{b_i - \langle a_i, x^k \rangle}{\|a_i\|^2} a_i, \quad (10)$$

where $i = k \bmod m + 1$, a_i is the i th row of the matrix A , b_i is the i th component of the vector b , and λ_k is a relaxation parameter. In the original work in [17], Kaczmarz used a fixed $\lambda_k = \lambda = 1 \in (0, 2)$ and the k th iteration consists of a ‘‘sweep’’ through the m rows of A , that is, $i = 1, 2, \dots, m$. Kaczmarz’s method was employed in this study as comparison with the proposed algorithm.

2.2.3. *Simultaneous Algebraic Reconstruction Technique (SART)*. The reason for calling the methods ‘‘simultaneous’’ is that all the equations are used at the same time in one iteration. The general form of simultaneous iterative reconstruction technique (SIRT) is

$$x^{k+1} = x^k + \lambda_k T A^T M (b - A x^k), \quad k = 0, 1, 2, \dots, \quad (11)$$

where the matrices M and T are symmetric positive definite. Although SART was originally developed in the framework of ART [6], it can also be written and implemented in the SIRT form and takes the following matrix form [18]:

$$x^{k+1} = x^k + \lambda_k D_r^{-1} A^T D_c^{-1} (b - A x^k), \quad (12)$$

where the diagonal matrices D_r and D_c are defined in terms of the row and column sum:

$$D_r = \text{diag}(\|a_i\|_1), \quad D_c = \text{diag}(\|a^j\|_1). \quad (13)$$

ART-type methods are known to have better performance than FBP algorithms in suppressing streak artifacts and noise in sparse-view CT imaging.

3. Proposed CS-Based Algorithm

The problem of sparse-view CT image reconstruction actually leads to an underdetermined system of linear equations (equation (9)). One way to improve performance is to incorporate a priori knowledge into the iteration process. One way to do that is based on the idea of sparsity at compressed sensing [10, 11]. The essence of compressed sensing is that a signal, which in our case is the image μ , can be completely reconstructed with a high probability with far less samples than required by conventional Nyquist-Shannon sampling theorem, if the image has a sparse/compressible representation in a transform domain Φ , such that most entries of the vector $\Phi\mu$ are zero or close to zero. The entire process of compressed sensing consists of three steps [19]: encoding, sensing, and decoding. In the first step, the object image μ of size n is encoded into a smaller vector $y = A\mu$ of a size m ($m < n$) by the system matrix, as shown in Section 2.1. Then the second step is obtaining the undersampled measurements y from the imaging system, which in CT is to obtain the undersampled

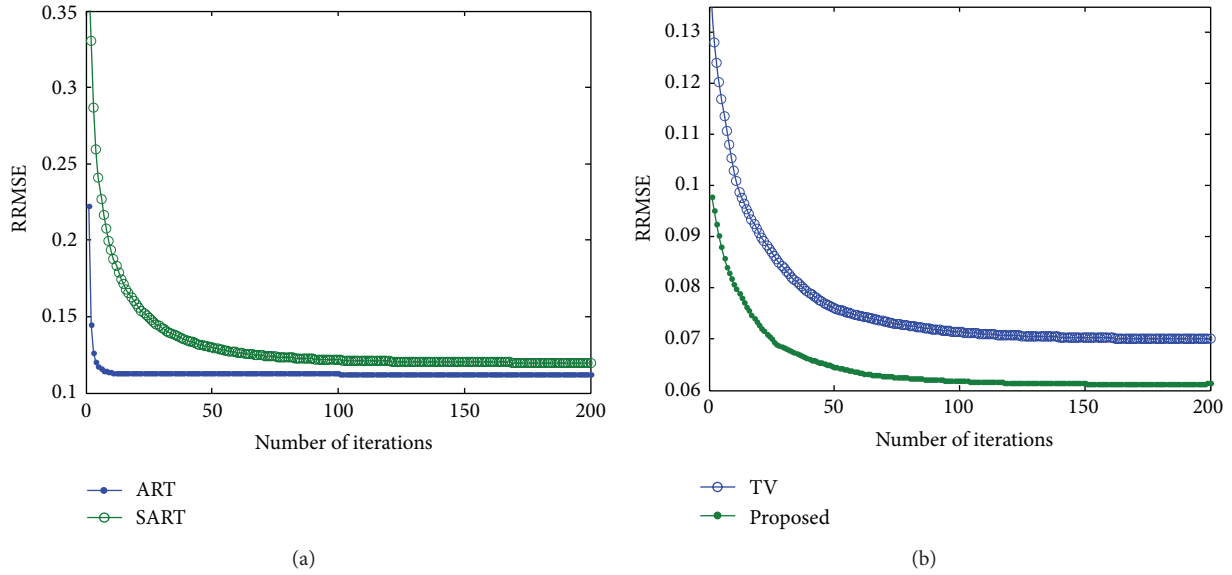


FIGURE 2: Analysis to find the optimum number of iterations for different methods: (a) ART and SART, (b) TV and the proposed scheme.

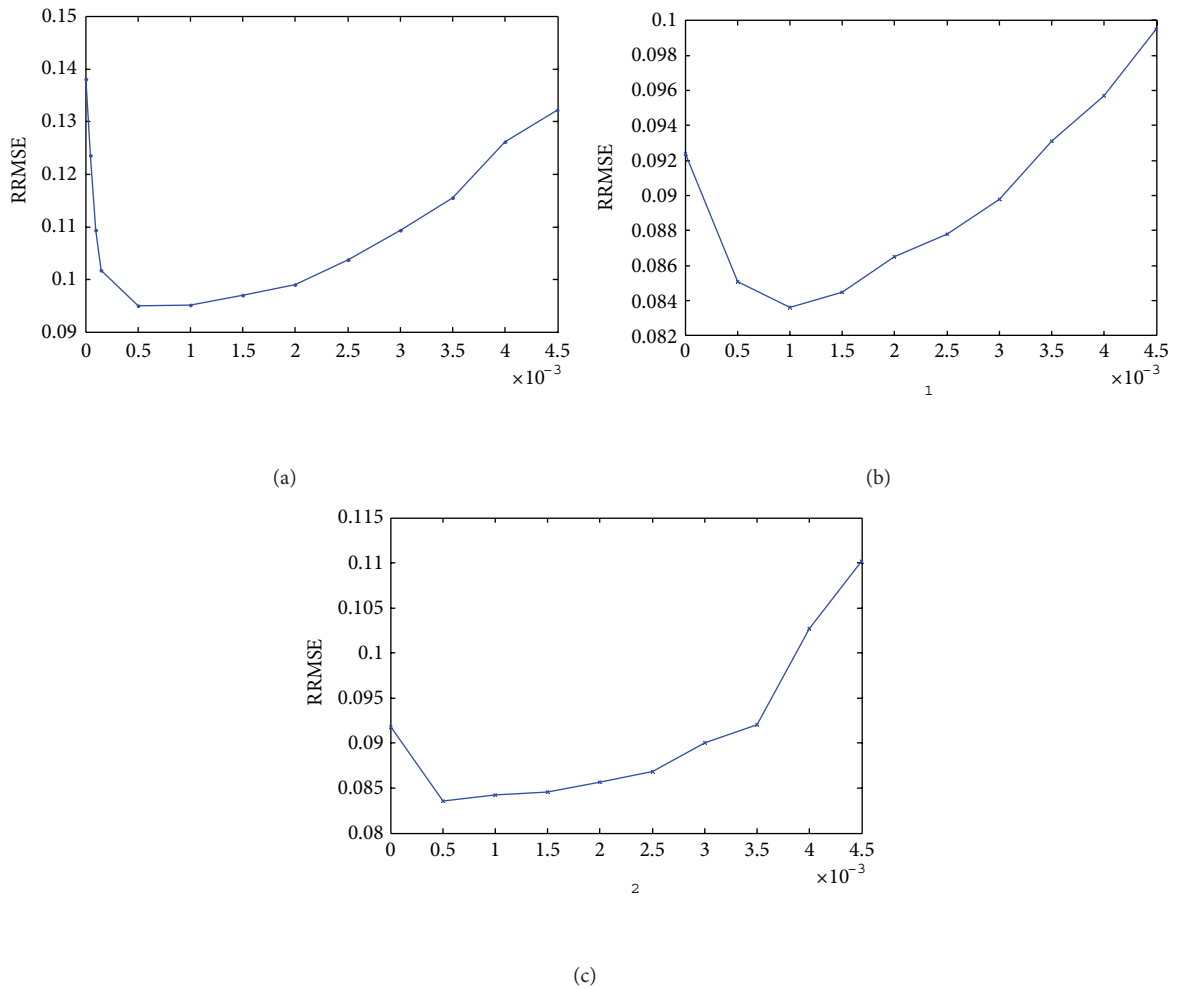


FIGURE 3: Analysis to find the optimum regularization parameters (for rat dataset): (a) λ in TV method; (b) λ_1 when $\lambda_2 = 0.0005$ for the proposed method; (c) λ_2 when $\lambda_1 = 0.001$ for the proposed method.

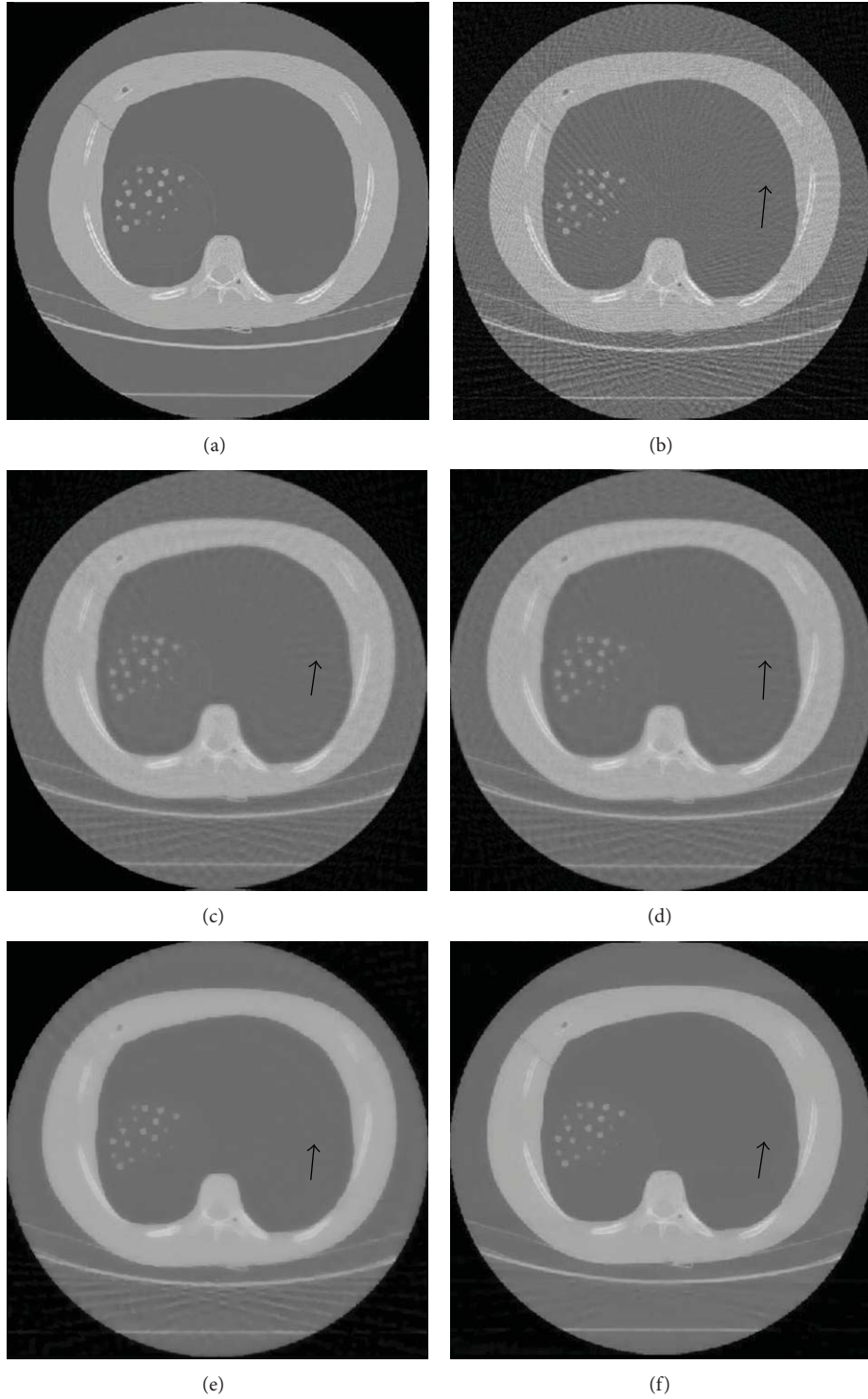


FIGURE 4: The reconstruction results of the nodule phantom using 50 projections. (a) The ground truth image, (b) the result obtained using FBP algorithm, (c) the ART algorithm, (d) the SART algorithm, (e) the TV algorithm, and (f) the proposed CS algorithm.

projection data. Incorporating the a priori knowledge into the process of image reconstruction, the third step is to solve the following constrained optimization problem:

$$\min_{\mu} \|\Phi\mu\|_1 \quad \text{subject to } \|A\mu - y\|_2 < \varepsilon, \quad (14)$$

where ε is a parameter controlling the data consistency. It has been mathematically proven that, if the image has only k entries with relatively large magnitudes, the order of $k \ln \sqrt{n}$ measurements is sufficient to accurately reconstruct μ via ℓ_1 norm minimization procedure with high probability

```

INPUTS:
y: undersampled projection data
A: system matrix associated with the measurements
Φ: wavelet transform operator
λ1, λ2: tuning constants
OPTIONAL PARAMETERS:
Tol: stopping criteria by gradient magnitude (default 10-4)
Iter: stopping criteria by number of iterations (default 100)
α, ζ: line search parameters (defaults α = 0.01, ζ = 0.6)
OUTPUTS:
μ: the numerical approximation to (18)
% Initialization
k = 0; μ0 = μFBP; g0 = ∇J(μ0); Δμ0 = -g0
% Iterations
while (||gk||2 < Tol)
{
% Backtracking line-search
t = 5; while (J(μk + tΔμk) > J(μk) + αt · Real(gk * Δμk)
and k < Iter)
{t = ζ t}
μk+1 = μk + tΔμk
gk+1 = ∇J(μk+1)
ηk = gk+1 - gk
βk+1 = max { 0, min {  $\frac{g_{k+1}^T \eta_k}{\Delta \mu_k^T \eta_k}, \frac{\|g_{k+1}\|_2^2}{\Delta \mu_k^T \eta_k}$  } }
Δμk+1 = -gk+1 + βk+1Δμk
k = k + 1}

```

ALGORITHM 1: Iterative algorithm for ℓ_1 minimization.

(Algorithm 1). A previous method called PICCS used total variation (TV) as a sparsity transform [12], where the CT image is reconstructed by minimizing the energy function with a TV regularization term:

$$\mu = \arg \min_{\mu} J(\mu) = \arg \min_{\mu} \lambda \|\mu\|_{\text{TV}} + \|A\mu - y\|_2^2, \quad (15)$$

where the regularization factor λ is introduced to leverage the cost function's emphasis on the sparseness prior and the data fidelity term. The selection of this regularization factor has been an interesting area of research in the field of regularized iterative methods [20–22]. A well-known method to find the best one is via the L curve. In our study, we chose the optimized regularization parameter for TV method for each dataset. The discussion of selection is given in Section 4. The TV term of an image in this work is defined as follows:

$$\|\mu\|_{\text{TV}} = \int |\nabla \mu| dx. \quad (16)$$

In a discrete version, (16) becomes

$$\|\mu\|_{\text{TV}} = \sum_{i,j} \sqrt{(\nabla \mu_x^2)_{i,j} + (\nabla \mu_y^2)_{i,j}}, \quad (17)$$

where $\nabla \mu_x, \nabla \mu_y$ represent the finite differences of the image along x and y directions. Despite the great success of the TV model in terms of reconstructing high-quality images, edges

with low contrast regions are sometimes oversmoothed, causing loss of low contrast information. To overcome this disadvantage, we propose a novel compressed sensing-based method by combining two sparsity transforms: TV and wavelet. Wavelet is good at preserving edges and low contrast information while TV is efficient at suppressing noise and streaking artifacts. In this way, we obtain a good balance between streaking artifacts suppression and detail preservation. Our iterative reconstruction algorithm solves the image via the following optimization problem:

$$\mu = \arg \min_{\mu} \lambda_1 \|\mu\|_{\text{TV}} + \lambda_2 \|\Phi\mu\|_1 + \|A\mu - y\|_2^2. \quad (18)$$

The two regularization factors λ_1 and λ_2 control the amount of smoothing. A large λ_1 and small λ_2 are not able to capture enough detail information. In such a circumstance, the algorithm becomes essentially the TV method. In contrast, small λ_1 and large λ_2 tend to give low weights to image gradients, making the method inefficient at suppressing noise and streaking artifacts. The process to find the optimized selections of λ_1 and λ_2 is discussed in Section 4. We exploit a fast implementation of the wavelet transform [23], which speeds up the implementation.

Since (18) poses an unconstrained convex optimization problem, we propose solving it using a nonlinear conjugate gradient descent algorithm with backtracking line search where $J(\mu)$ is the cost function as defined in (18).

The conjugate gradient requires the computation of $\nabla J(\mu)$ which is

$$\nabla J(\mu) = \lambda_1 \nabla \|\mu\|_{\text{TV}} + \lambda_2 \nabla \|\Phi\mu\|_1 + 2A^*(A\mu - y). \quad (19)$$

As the ℓ_1 norm and total variation term (16) is the sum of absolute values. The absolute value, however, is not a smooth function and as a result (19) is not well defined. In [24], Lustig et al. approximated the absolute value with a smooth function $|x| \approx \sqrt{x^*x + \xi}$, where ξ is a positive smoothing parameter. Then the gradient becomes $d|x| \approx (x/\sqrt{x^*x + \xi})$. We adopt this idea in our implementation. In particular, a smoothing factor $\xi = 10^{-15}$ is used.

4. Experimental Results

In this section, we present our experimental results. There are four sets of experiments. In the first two experiments, true CT images and simulated projections were used to study the performance of our algorithm under ideal and degraded conditions. The third and fourth experiments used real data collected using the Canadian Light Source (<http://www.lightsource.ca/>) and University of Saskatchewan facilities. In all cases, we investigated reconstructions from 20, 30, 40, 50, 60, 70, 80, 90, 100, 110, up to 120-view datasets extracted from the full dataset, respectively, representing different levels of data sampling. The study showed how the varying degree of sampling impacts the reconstruction. In each case, a uniformly spaced view angle data decimation scheme over 180° was used to obtain undersampled data.

Reconstructions were quantitatively evaluated in terms of relative root mean square error (RRMSE), streak indicator

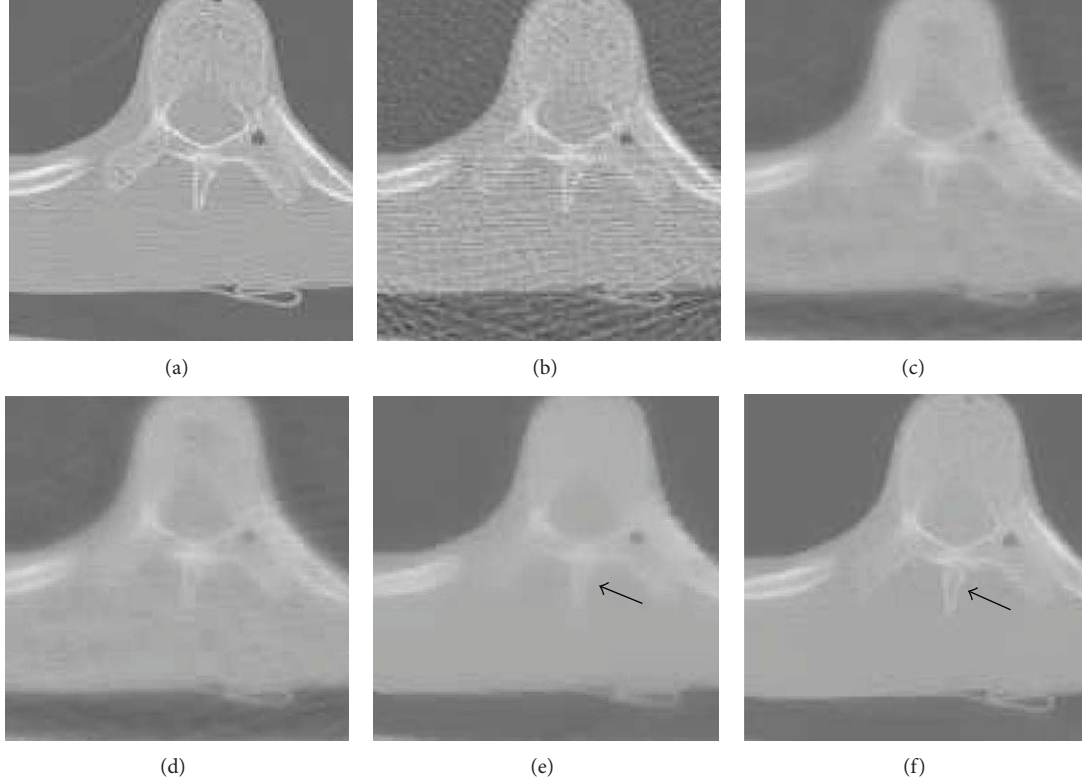


FIGURE 5: A detailed section of Figure 4: (a) ground truth, (b) FBP method, (c) ART method, (d) SART method, (e) TV method, and (f) the proposed method.

(SI), and structural similarity (SSIM) index. The relative root mean square error (RRMSE) is defined as

$$\text{RRMSE} = \frac{\|y - y_{\text{ref}}\|_2}{\|y_{\text{ref}}\|_2}, \quad (20)$$

where y is the reconstruction image by our proposed method and y_{ref} is the reference image. Since undersampling streak artifacts are an important feature in sparse-view CT image reconstruction, streaking level is also quantified by the streak indicator (SI) [25]. The streak indicator (SI) is defined as

$$\text{SI} = \text{TV}(y - y_{\text{ref}}). \quad (21)$$

The lower the value of SI is, the less the streaking artifacts are present in the reconstructed image.

The structural similarity (SSIM) index is highly effective for measuring the structural similarity between two images [26]. Suppose ρ and t are local image patches taken from the same location of two images that are being compared. The local SSIM index measures three similarities of the image patches: the similarity of luminance $l(\rho, t)$, the similarity of contrast $c(\rho, t)$, and the similarity of structures $s(\rho, t)$. Local SSIM is defined as

$$\begin{aligned} S(\rho, t) &= l(\rho, t) \cdot c(\rho, t) \cdot s(\rho, t) \\ &= \left(\frac{2\mu_\rho\mu_t + C_1}{\mu_\rho^2 + \mu_t^2 + C_1} \right) \left(\frac{2\sigma_\rho\sigma_t + C_2}{\sigma_\rho^2 + \sigma_t^2 + C_2} \right) \left(\frac{2\sigma_{\rho t} + C_3}{\sigma_\rho\sigma_t + C_3} \right), \end{aligned} \quad (22)$$

where μ_ρ and μ_t are local means, σ_ρ and σ_t are local standard deviations, and $\sigma_{\rho t}$ is cross-correlation after removing their means. C_1 , C_2 , and C_3 are stabilizers. The SSIM score of the entire image is then computed by pooling the SSIM map, for example, simply averaging the SSIM map. Although in other papers, such as in [27], a metric name universal quality index (UQI) was used, SSIM is an improved version of the algorithm. Also, the correlation coefficient (CC) defined in [27] is also similar to SSIM. Hence, SSIM is highly effective for measuring image quality. Higher SSIM value indicates higher image quality.

In order to find the optimum number of iteration, we have conducted another experiment using simulated phantom. The results are shown in Figure 2. It can be seen from Figure 2(a) that the RRMSE of ART becomes almost unchanged after 30 iterations. Hence, 30 is used as the optimum number of iterations for ART for all experiments. Similarly, the optimum number of iterations for SART, TV, and the proposed method is also estimated, and 150 is used for them. To verify the number of iterations, the experiments were repeated on noisy phantom and real data, and the results were found to be consistent with that of Figure 2.

Moreover, the reconstruction accuracy depends on the selection of optimum regularization parameters for both TV method and the proposed method. We have used a real dataset (such as rat dataset as described later in Section 4.3) using 50 projections as an example to show the methodology of determining the optimal parameters. For TV method,

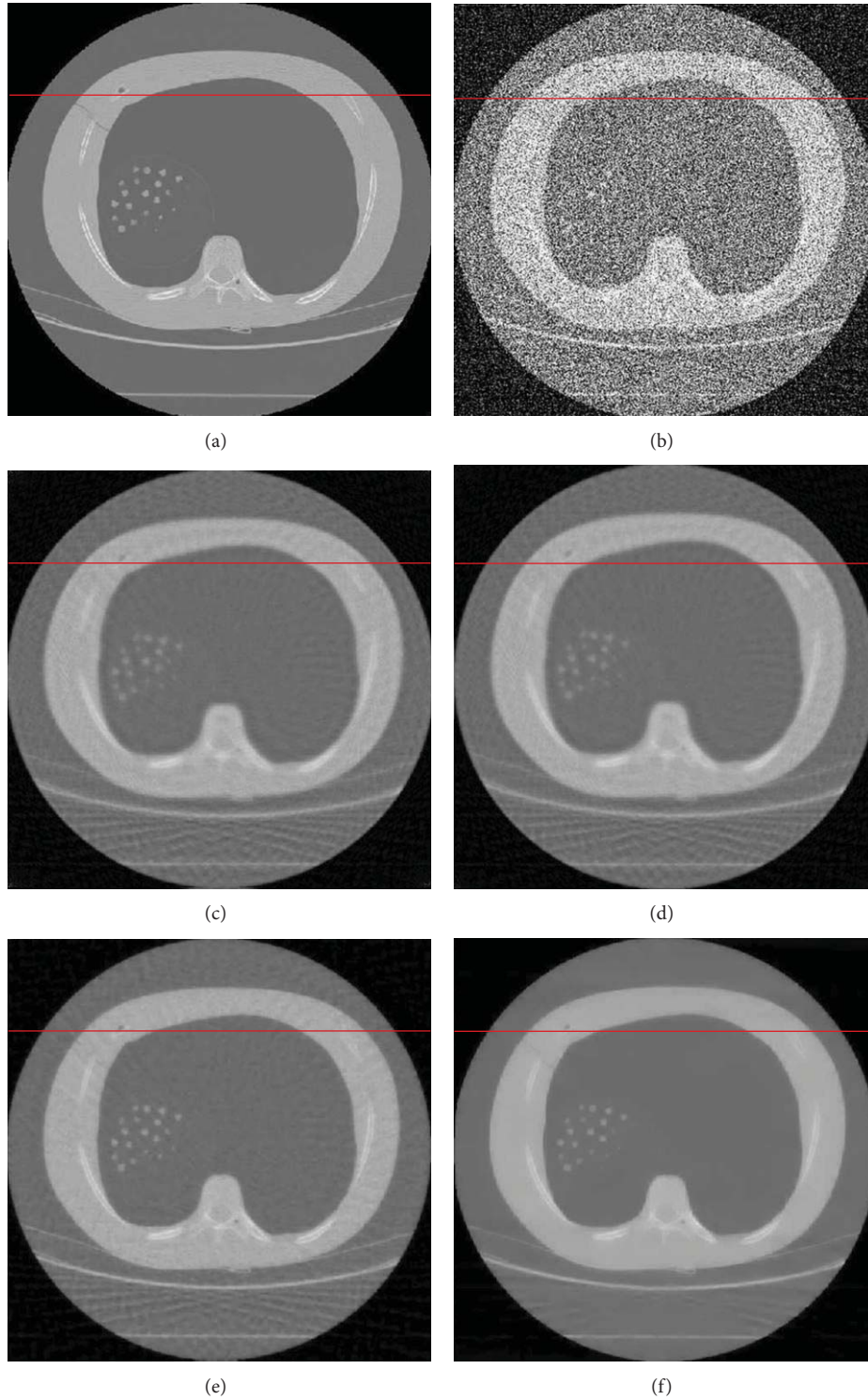


FIGURE 6: Simulated reconstruction of noisy phantom from 50 noisy projections over 180° : (a) the true image, (b) FBP, (c) ART, (d) SART, (e) TV, and (f) the proposed method.

the reconstruction error is plotted against λ (15), as shown in Figure 3(a). The lowest reconstruction error is obtained when λ is between 0.0005 and 0.001. In this study, we have selected $\lambda = 0.0005$. The optimal λ for all datasets is shown in Table 1.

For the proposed algorithm, there are two parameters. We alternately plotted the reconstruction error against one parameter keeping the other fixed. We started by setting $\lambda_2 = 0.0005$. Figure 3(b) shows that the lowest reconstruction error is obtained when λ_1 is 0.001. Then we set λ_1 to 0.001 and

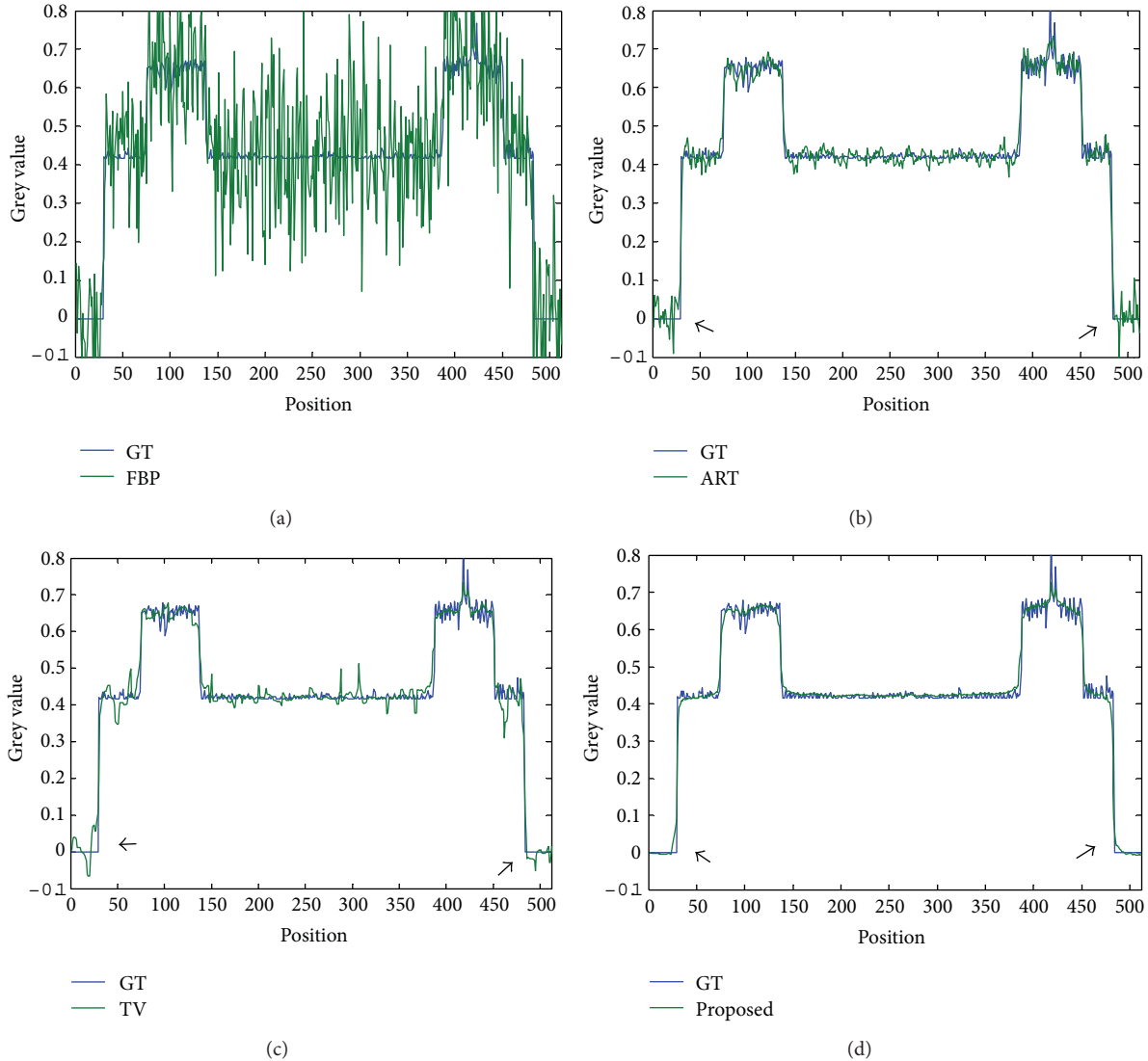


FIGURE 7: Pixel-intensity profiles of reconstructed images compared with ground truth (GT): (a) FBP, (b) ART, (c) TV, and (d) the proposed method.

TABLE 1: Optimum parameter selections for each dataset.

Data	TV algorithm	Proposed algorithm	
	λ	λ_1	λ_2
Phantom without noise	0.0005	0.0005	0.0005
Phantom with noise	0.0015	0.001	0.0006
Human bone	0.001	0.001	0.001
Rat	0.0005	0.001	0.0005

searched the optimal value for λ_2 that gives the lowest error, as shown in Figure 3(c). Thus, we used this recurring process to determine the optimum values of λ_1 and λ_2 . Similar search was conducted for all dataset. The optimal values of these parameters are shown in Table 1. The full-view FBP reconstruction image was used as the reference.

4.1. Experiment Results Using Phantom. The first experiment was performed using nodule phantom image and simulated projection without any noise purposely added. This data is provided free of charge by the National Cancer Institute (NCI) [28]. We used one typical cross-section of CT slice as a sample set. We suppose that it is the desired CT image and each pixel value presents an attenuation coefficient. The sample image was 512×512 . Simulated projections were obtained by computing the line integrals across the image with different views uniformly distributed over 180° . The reconstructed images using 50 projections are shown in Figure 4. As can be noticed from Figure 4(b), the conventional FBP algorithm is not able to reconstruct diagnostically satisfactory image with such few projections and strong streaking artifacts are present. Although streaking artifacts are reduced in ART and SART reconstructions, we can still see them in smooth regions, as indicated by black arrows in

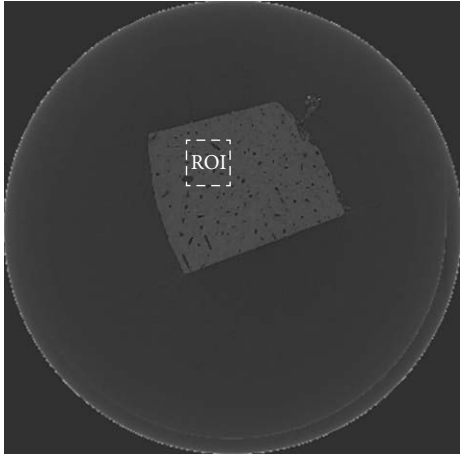


FIGURE 8: The FBP reconstruction of the complete dataset. The image has a large smooth region, so to better demonstrate the details, a region of interest (ROI) is selected.

TABLE 2: Reconstruction results using phantom image.

Reconstruction methods	RRMSE	SI	SSIM
FBP	0.1282	44.9556	0.6110
ART [17]	0.1120	25.5737	0.7681
SART [18]	0.1198	25.0023	0.7663
TV [12]	0.0715	20.0115	0.8716
Proposed method	0.0609	18.0646	0.9310

the figure. In contrast, even with fewer projections, both the TV method and the proposed algorithm can capture most of the structures, leading to visually much better results.

However, we can still see some residual streak artifacts in the TV reconstruction. The image reconstructed from our proposed method shows the least level of streaking artifacts. One possible reason for that is, in wavelet domain, the noise is uniformly spread throughout the coefficients while mostly the image information is concentrated in the few largest coefficients [29, 30]. Hence noise is of potentially small values in wavelet domain. As (18) tries to minimize the ℓ_1 norm of wavelet coefficients, small values corresponding to noise and artifacts are also suppressed, leading to better reconstruction. Besides, all TV-based methods tend to remove small structure and degrade the image resolution and image quality. But compared to TV method, the proposed method has a slight advantage in preserving edges. To see it clearly, an expanded region is shown in Figure 5. We can see from the figure that both TV method and the proposed method can further remove the streaking artifacts that are presented in ART and SART reconstructions. But the fine structures get blurred as TV method suppresses the gradient of the image. As indicated by the black arrows, the low contrast edges are better reconstructed by our proposed method. To quantify the results, we also show the RRSME, SI, and SSIM values of the reconstructed images in Table 2. Clearly, the result from our method has lower error level, less streak artifacts, and higher structural similarity.

TABLE 3: Reconstruction results using phantom image (with noise).

Methods	RRMSE	SI	SSIM
FBP	0.2908	127.4656	0.3284
ART [17]	0.1197	28.7409	0.7260
SART [18]	0.1324	28.0063	0.7344
TV [12]	0.0891	24.1023	0.7693
Proposed method	0.0687	21.2074	0.8967

4.2. *Experiment Results Using Phantom (with Noise).* The second experiment was performed using noisy simulated data. Additive Gaussian white noise e of relative magnitude $\|e\|_2/\|A\mu_{\text{true}}\|_2 = 0.05$ was purposely added to the sinograms. The results are displayed in Figure 6. To better compare the TV method and our proposed method, we also show horizontal line intensity profile going through the red line of Figure 6. The line intensity profiles are shown in Figure 7. Compared to FBP, the ART is more robust to noise and thus has greatly suppressed the streaking artifacts. SART produces similar results (not shown in Figure 7). But there are high frequency vibrations around the edges, as indicated by black arrows. The vibration is caused by limited view and added noise. The vibration is eliminated in terms of frequency and amplitude in the TV reconstruction. In contrast, the intensity profile of reconstructed image by the proposed method shows a rather smoothed curve in nonedge regions and is also much closer to the ground truth profile near the edges, demonstrating its ability to produce better edges. The results are summarized in Table 3. It was evident that our algorithm showed strong robustness against noise.

4.3. *Experiment Results Using Real Dataset.* In the third and fourth experiments, we used real data collected from the Canadian Light Source facility and from a desktop Bruker SkyScan 1172 Micro-CT system with two datasets: human femoral cortical bone and the hindpaw of a normal Wistar rat. For the human bone, micro-CT scanning was performed at the BioMedical Imaging and Therapy Bending Magnet Beamline (BMIT-BM; 05B1-1). Projections were collected with a Hamamatsu C9300 (Hamamatsu Photonics, Hamamatsu, Japan) CCD camera fitted with a beam monitor with a $10 \mu\text{m}$ thick gadolinium oxysulfide scintillator. The sample was rotated through 180° at 0.1 degree steps, generating 1800 original projections. The image size is of 3780×3780 pixels. We have selected a region of interest (ROI) from this image to further demonstrate the advantage on the reconstructed images. The FBP reconstruction using 1800 projections is shown in Figure 8. The last dataset in this study was a micro-CT scan of an adult Wistar rat hindpaw. This scan was taken at 70 kVp with the Bruker SkyScan 1172 Micro-CT in Anatomy and Cell Biology at the University of Saskatchewan. The reconstructed pixel size was $26.6 \mu\text{m}$. In total, 900 projections were acquired over a rotation through 180° at 0.2 degree steps.

The ROI reconstruction results restricted to 50 views for the human cortical bone image are shown in Figure 9. The gray tissue shown is the bone permeated with vascular canals,

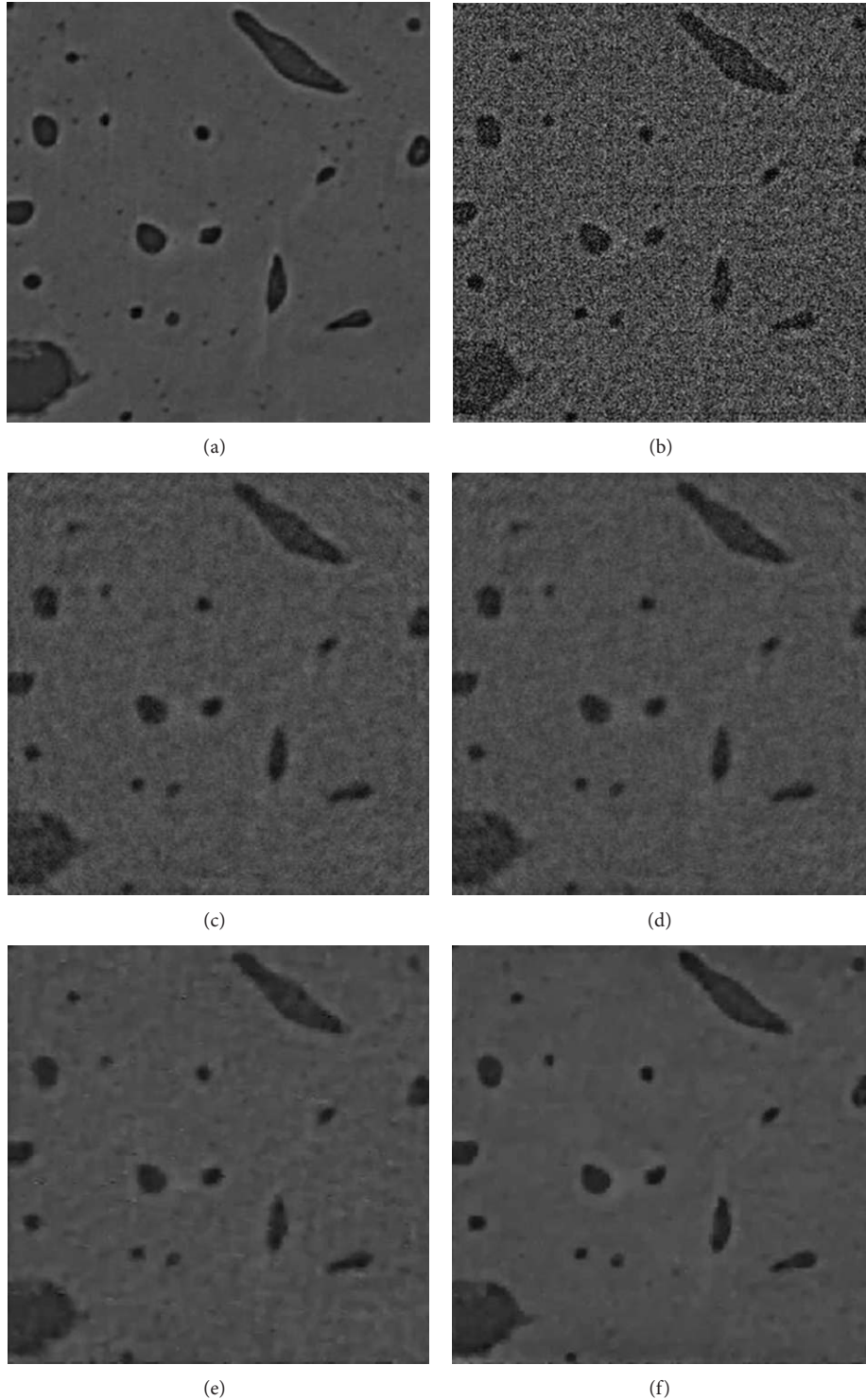


FIGURE 9: The ROI reconstructions of human bone. (a) The image reconstructed by FBP with 1800 projections, (b) the result obtained using FBP algorithm, (c) the ART algorithm, (d) the SART algorithm, (e) the TV algorithm, and (f) the proposed CS algorithm, all using 50-views.

which appear darker in the image. Surrounding these larger canals some smaller objects can be seen. These are osteocyte lacunae, spaces within the bone where cells reside. The edges of the canals and lacunae are highlighted by propagation phase contrast halos. As expected the FBP reconstruction

shows a greater amount of high spatial frequency noise over the entire area due to the limited sampling rate. The resolution is significantly diminished and many details of interest including the lacunae are lost. Image quality is lowered with strong and obvious streaking artifacts.

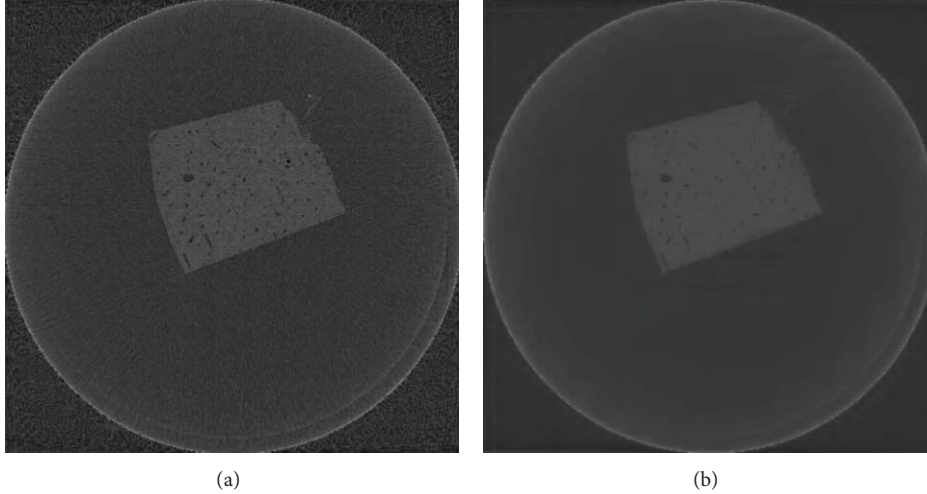


FIGURE 10: (a) The FBP reconstruction of human bone, (b) reconstruction using the proposed CS algorithm.

In the ART and SART images, the streaking artifacts and noise are reduced, but residual artifacts can be seen and the noise is still pervasive. Besides this, they suffer from edge blurring artifacts and many low contrast structures are lost. The edges of the vascular canals are no longer able to be precisely distinguished, an important feature for characterizing their shape and size. The streaking artifacts in the TV reconstruction are less conspicuous than they are in FBP, ART, and SART, but we can clearly see some relatively low frequency patchy structures present in nonedge regions. In clinical practice, these patchy structures may mimic low contrast lesions and obscure the presence of small details. By comparison, our proposed method provides reconstruction of high fidelity, as presented in Figure 9(f). It is able to remove most of the streak artifacts without visible introduction of unwanted structures. For instance, the canals in the bone are much clearer in the image reconstructed by our proposed method than that in the image reconstructed by TV method, that their edges are much cleaner.

To further quantify the reconstruction accuracy and streaking artifacts, the RRMSEs, SIs, and SSIMs values of the given ROI by these methods are shown in Table 4. From the table, we can see that the RRMSE is well below 10% for both TV and our proposed method with the latter showing superior results. This result indicates that high reconstruction accuracy can be achieved using our proposed method. As well, from the SI value and visual observation of Figure 9, one may conclude that the proposed algorithm is capable of suppressing streaking artifacts and noise, leading to an image of acceptable quality at lower number of views. To highlight the ability of our proposed method to suppress streaking artifacts, the whole reconstructions by FBP and our proposed method are also shown in Figure 10. It is clearly seen from the figure that the streaking artifacts in FBP are greatly suppressed by our proposed algorithm.

Now let us look at the adult Wistar rat hindpaw image. This image shows a transverse slice through the bones of the paw, with the bottom bone showing trabecular bone

TABLE 4: Reconstruction results using real dataset.

Reconstruction methods	RRMSE	SI	SSIM
FBP	0.5102	97.325	0.3040
ART [17]	0.1525	22.9236	0.6893
SART [18]	0.1412	20.0544	0.6955
TV [12]	0.0783	6.7528	0.7983
Proposed method	0.0557	4.1120	0.8642

and the other four bones showing cortical bone and marrow cavities. The experimental results of the rat are displayed in Figure 11. Image quality is greatly degraded by obvious streaking artifacts in FBP reconstruction due to its inability to handle incomplete data. These artifacts are not efficiently removed by either ART or SART algorithms. By comparison, images reconstructed by the TV method and proposed method appear to have higher visual image quality, indicating that TV-based methods are superior to these methods.

Although the TV method can suppress the noise and streak artifacts considerably, it is still a great challenge to reconstruct the trabecular bone, the fine structure in the bottom right-hand corner of the image as indicated by the red arrows in Figure 11(e), because of the nature of total variation regularization. By the introduction of the wavelet transform in image reconstruction procedure, our proposed method minimizes noise and streaking artifacts both in the discrete gradient domain and wavelet domains, delivering better results than previous efforts without creating unwanted smoothing effects. Our method leads to a better reconstruction with higher spatial resolution.

For a comprehensive comparison, the RRMSEs, SIs, and SSIMs of the reconstructed images are also plotted against the number of projections in Figure 12. The shape of the curves shows the effectiveness of the corresponding reconstruction method in sparse-view regime. It also indicates that RRMSEs and SIs of reconstructions by our proposed method in all

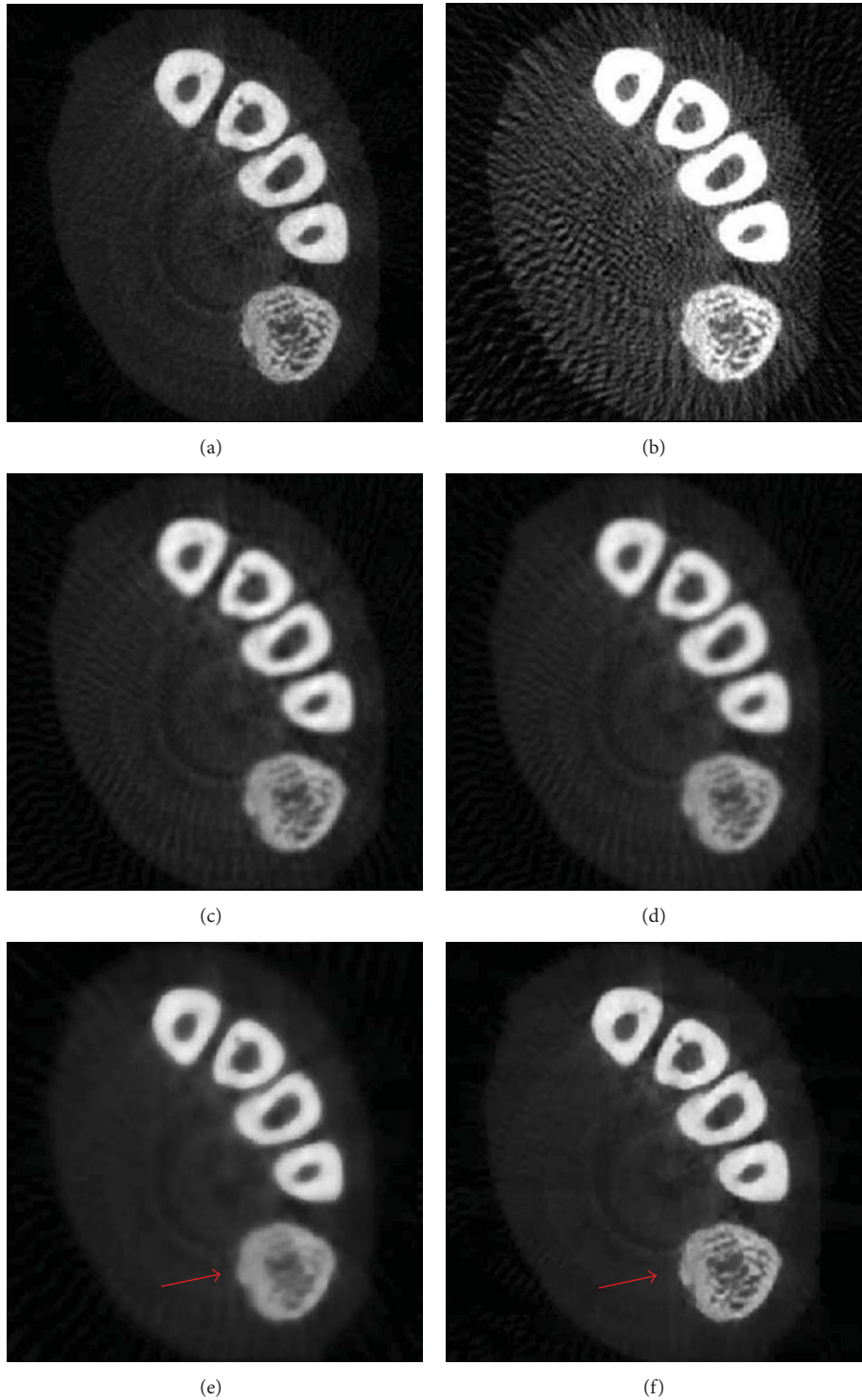


FIGURE 11: Reconstruction results of the hindpaw image of the adult rat. (a) FBP reconstruction using 900 projections, (b) FBP algorithm with 50 projections, (c) ART algorithm, (d) SART algorithm, (e) TV algorithm, and (f) the proposed CS algorithm, all using 50 views.

cases are lower than those of other methods while the SSIMs are higher than those of other methods. The results of this test confirm that our proposed method outperforms the TV method in maintaining the balance between noise suppression and spatial resolution preservation.

The convergence speed of an algorithm is a crucial factor for all iterative methods in clinical practice. To investigate the convergence speed of the proposed method, the plot of cost function value $J(\mu)$ in (18) against the number of iterations for the phantom dataset (without noise) is shown in Figure 13

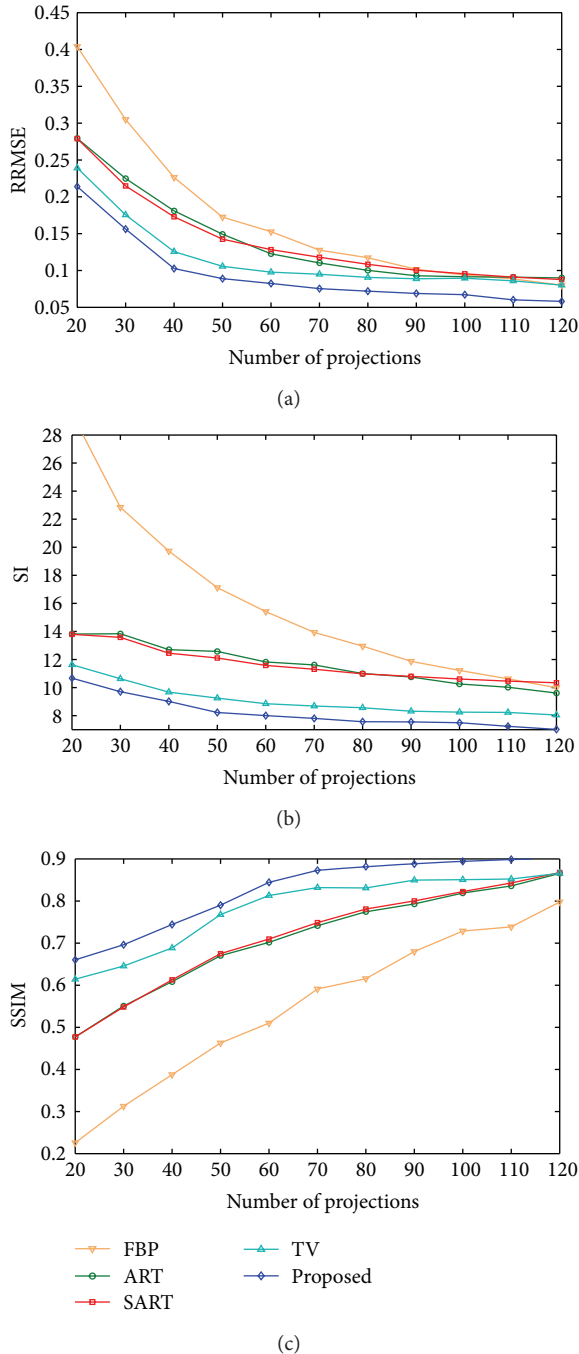


FIGURE 12: Plots of relative root mean square error (RRMSE), streak indicator (SI), and structural similarity (SSIM) for rat dataset.

with 30 views selected for demonstration. It shows that the curve decreases dramatically within 5 iterations, indicating the high convergence speed of our proposed method.

5. Conclusion

In this work, we have investigated a novel compressed sensing-based algorithm for sparse-view CT image recon-

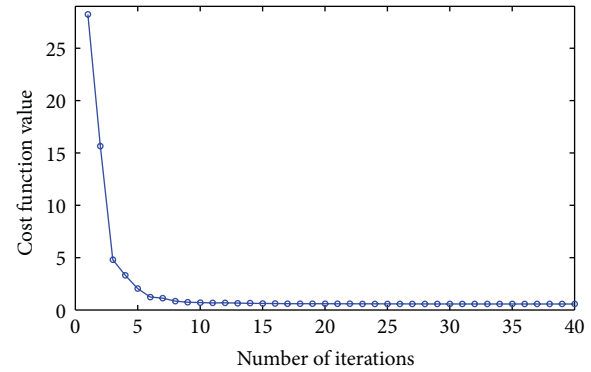


FIGURE 13: Convergence curve (cost function values versus number of iterations) for the proposed method applied to phantom dataset.

struction, in which wavelet transform is used in the reconstruction procedure. Results show that the proposed method is able to suppress streak artifacts and noise caused by incomplete and noisy projection data without visible oversmoothing of fine structure details in the images. The proposed CS-based algorithm has potential to reduce the dose in clinical computed tomography imaging techniques.

Acknowledgments

This research work was supported by Natural Sciences and Engineering Research Council of Canada (NSERC).

References

- [1] E. J. Hall and D. J. Brenner, "Cancer risks from diagnostic radiology," *British Journal of Radiology*, vol. 81, no. 965, pp. 362–378, 2008.
- [2] A. Berrington de González, M. Mahesh, K. P. Kim et al., "Projected cancer risks from computed tomographic scans performed in the United States in 2007," *Archives of Internal Medicine*, vol. 169, no. 22, pp. 2071–2077, 2009.
- [3] Z. Tian, X. Jia, K. Yuan, T. Pan, and S. B. Jiang, "Low-dose CT reconstruction via edge-preserving total variation regularization," *Physics in Medicine and Biology*, vol. 56, no. 18, pp. 5949–5967, 2011.
- [4] G. T. Herman, A. Lent, and S. W. Rowland, "ART: mathematics and applications. A report on the mathematical foundations and on the applicability to real data of the algebraic reconstruction techniques," *Journal of Theoretical Biology*, vol. 42, no. 1, pp. 1–32, 1973.
- [5] R. Gordon, R. Bender, and G. T. Herman, "Algebraic Reconstruction Techniques (ART) for three-dimensional electron microscopy and X-ray photography," *Journal of Theoretical Biology*, vol. 29, no. 3, pp. 471–481, 1970.
- [6] A. H. Andersen and A. C. Kak, "Simultaneous algebraic reconstruction technique (SART): a superior implementation of the art algorithm," *Ultrasonic Imaging*, vol. 6, no. 1, pp. 81–94, 1984.
- [7] G. Wang and M. Jiang, "Ordered-subset simultaneous algebraic reconstruction techniques (OS-SART)," *Journal of X-Ray Science and Technology*, vol. 12, no. 3, pp. 169–177, 2004.
- [8] A. Kak and M. Slaney, *Principles of Computerized Tomographic Imaging*, IEEE Press, New York, NY, USA, 1988.

- [9] I. A. Elbakri and J. A. Fessler, "Statistical image reconstruction for polyenergetic X-ray computed tomography," *IEEE Transactions on Medical Imaging*, vol. 21, no. 2, pp. 89–99, 2002.
- [10] D. L. Donoho, "Compressed sensing," *IEEE Transactions on Information Theory*, vol. 52, no. 4, pp. 1289–1306, 2006.
- [11] E. J. Candès, J. Romberg, and T. Tao, "Robust uncertainty principles: exact signal reconstruction from highly incomplete frequency information," *IEEE Transactions on Information Theory*, vol. 52, no. 2, pp. 489–509, 2006.
- [12] G. H. Chen, J. Tang, and S. Leng, "Prior image constrained compressed sensing (PICCS): a method to accurately reconstruct dynamic CT images from highly undersampled projection data sets," *Medical Physics*, vol. 35, no. 2, pp. 660–663, 2008.
- [13] E. Y. Sidky and X. C. Pan, "Image reconstruction in circular cone-beam computed tomography by constrained, total-variation minimization," *Physics in Medicine and Biology*, vol. 53, no. 17, pp. 4777–4807, 2008.
- [14] D. Donoho and X. Huo, "Combined image representation using edgelets and wavelets," in *Wavelet Applications in Signal and Image Processing VII*, vol. 3813 of *Proceedings SPIE*, pp. 468–476, Denver, Colo, USA, 1999.
- [15] H. P. Hiriyannaiah, "X-ray computed tomography for medical imaging," *IEEE Signal Processing Magazine*, vol. 14, no. 2, pp. 42–59, 1997.
- [16] J. Tang, B. Nett, and G. Chen, "Performance comparison between total variation (TV)-based compressed sensing and statistical iterative reconstruction algorithms," *Physics in Medicine and Biology*, vol. 54, no. 19, pp. 5781–5804, 2009.
- [17] S. Kaczmarz, "Angenäherte Auflösung von Systemen linearer Gleichungen," *Bulletin International de L'Académie Polonaise des Sciences et des Lettres A*, vol. 35, pp. 355–357, 1937.
- [18] P. Hansen and M. Saxild-Hansen, "AIR tools a MATLAB package of algebraic iterative reconstruction methods," *Journal of Computational and Applied Mathematics*, vol. 236, no. 8, pp. 2167–2178, 2012.
- [19] S. Ma, W. Yin, Y. Zhang, and A. Chakraborty, "An efficient algorithm for compressed MR imaging using total variation and wavelets," in *Proceedings of the 26th IEEE Conference on Computer Vision and Pattern Recognition, CVPR*, pp. 1–8, Anchorage, AK, USA, June 2008.
- [20] M. Kilmer and D. O'Leary, "Choosing regularization parameters in iterative methods for ill-posed problems," *The SIAM Journal on Matrix Analysis and Applications*, vol. 22, pp. 1204–1221, 2001.
- [21] V. Agarwal, *Total Variation Regularization and L-Curve Method For the Selection of Regularization Parameter*, vol. ECE599, 2003.
- [22] M. Belge, M. E. Kilmer, and E. L. Miller, "Efficient determination of multiple regularization parameters in a generalized L-curve framework," *Inverse Problems*, vol. 18, no. 4, pp. 1161–1183, 2002.
- [23] J. Buckheit and D. Donoho, "Wavelab architecture," Tech. Rep., Stanford University, 1995, <http://www-stat.stanford.edu/~wavelab>.
- [24] M. Lustig, D. Donoho, and J. M. Pauly, "Sparse MRI: the application of compressed sensing for rapid MR imaging," *Magnetic Resonance in Medicine*, vol. 58, no. 6, pp. 1182–1195, 2007.
- [25] S. Leng, J. Tang, J. Zambelli, B. Nett, R. Tolakanahalli, and G. H. Chen, "High temporal resolution and streak-free four-dimensional cone-beam computed tomography," *Physics in Medicine and Biology*, vol. 53, no. 20, pp. 5653–5673, 2008.
- [26] Z. Wang, A. C. Bovik, H. R. Sheikh, and E. P. Simoncelli, "Image quality assessment: from error visibility to structural similarity," *IEEE Transactions on Image Processing*, vol. 13, no. 4, pp. 600–612, 2004.
- [27] X. Li and S. Luo, "A compressed sensing-based iterative algorithm for CT reconstruction and its possible application to phase contrast imaging," *BioMedical Engineering OnLine*, vol. 10, article 73, 2011.
- [28] <http://www.via.cornell.edu/databases/crpf.html>.
- [29] U. Ruttimann, U. Michael, R. R. Robert et al., "Statistical analysis of functional MRI data in the wavelet domain," *IEEE Transactions of Medical Imaging*, vol. 17, no. 2, pp. 142–154, 1998.
- [30] K. Sidh, B. Khaira, and I. Virk, "Medical image denoising in the wavelet domain using haar and DB3 filtering," *International Refereed Journal of Engineering and Science*, vol. 1, pp. 1–8, 2012.

Research Article

Development of Image Segmentation Methods for Intracranial Aneurysms

Yuka Sen, Yi Qian, Alberto Avolio, and Michael Morgan

The Australian School of Advanced Medicine, Macquarie University, Sydney, NSW 2109, Australia

Correspondence should be addressed to Yi Qian; yi.qian@mq.edu.au

Received 17 January 2013; Accepted 8 March 2013

Academic Editor: Peng Feng

Copyright © 2013 Yuka Sen et al. This is an open access article distributed under the Creative Commons Attribution License, which permits unrestricted use, distribution, and reproduction in any medium, provided the original work is properly cited.

Though providing vital means for the visualization, diagnosis, and quantification of decision-making processes for the treatment of vascular pathologies, vascular segmentation remains a process that continues to be marred by numerous challenges. In this study, we validate eight aneurysms via the use of two existing segmentation methods; the Region Growing Threshold and Chan-Vese model. These methods were evaluated by comparison of the results obtained with a manual segmentation performed. Based upon this validation study, we propose a new Threshold-Based Level Set (TLS) method in order to overcome the existing problems. With divergent methods of segmentation, we discovered that the volumes of the aneurysm models reached a maximum difference of 24%. The local artery anatomical shapes of the aneurysms were likewise found to significantly influence the results of these simulations. In contrast, however, the volume differences calculated via use of the TLS method remained at a relatively low figure, at only around 5%, thereby revealing the existence of inherent limitations in the application of cerebrovascular segmentation. The proposed TLS method holds the potential for utilisation in automatic aneurysm segmentation without the setting of a seed point or intensity threshold. This technique will further enable the segmentation of anatomically complex cerebrovascular shapes, thereby allowing for more accurate and efficient simulations of medical imagery.

1. Introduction

Specification of intracranial aneurysm morphology and hemodynamic analysis requires segmentation of vascular geometries from three-dimensional (3D) medical images, produced via CTA or MRA. Methods for such manipulations of medical images are directly linked to the accuracy of aneurysm model construction, particularly regarding the geometry of complex shapes and volumes. In most cases, this process involves extraction of the 2D image from CTA or MRA, followed by reconstruction of the 3D aneurysm surface model. As such, several approaches exist and are currently utilized in cerebrovascular segmentation. On one hand, the fuzzy-based approach has been adapted for detecting malformed and small vessels in MRA images [1], while region growing approaches are popular in medical image segmentation due to their simplicity and computational efficiency [2]. Major problems, however, include leakage when the boundary is blurred and sensitivity to seed position. Utilization of implicit active contour methods within the level set framework seems to be widespread in medical image

segmentation [3–5] as the method does not suffer from parameterization surface problems [6] and has the capability to handle complex geometries and topological changes [7, 8]. More recently, active contour methods have also appeared in the modeling of intracranial aneurysms and cerebrovascular segmentation [9, 10]. Law and Chung proposed a method based upon multirange filters and local variances to perform the segmentation of intracranial aneurysms on Phase Contrast Magnetic Resonance Angiography data [11]. Hernandez and Frangi have developed a segmentation method for intracranial aneurysms based on Geometric Active Regions (GAR), using CTA and 3D Rotational Angiography data [12], whilst several Geodesic Active Contours (GAC) based methods have since been adapted for segmentation of brain aneurysms from CTA data [13, 14]. These methods either require sufficient training sets or they are reliant on boundary information obtained from medical imaging. Furthermore, boundary-based active contour level set methods may easily leak when the target boundary is not clearly defined. Though Firouzian et al. proposed a Geodesic Active Contours based level set method which employs region information and

intensity, it requires a user-defined seed point in order to calculate intensity threshold [15].

Despite the availability of many image segmentation methods, with varying approaches and algorithms, there is no dominant method in terms of effectiveness, across all areas [16–18]. Our previous study indicated that the volume of the aneurysm models depends strongly on the different segmentation methods. The segmentation method likewise influences the local geometric shapes of the aneurysms [19]. Validation will thus become necessary, comparing segmentation methods and adjusting the parameters of these segmentation techniques in order to assure the quality of patient-specific cerebral-vascular hemodynamic analysis. Although a number of commercial software packages for segmentation are available in the market, there is a conspicuous lack of discussion of methodology and information regarding validation processes.

In this paper, the authors propose a new Threshold-Based Level Set method for cerebral aneurysms. This method is based on the Geodesic Active Contours model [20] and Chan-Vese model (CV) [21] integrating both region and boundary information to segment cerebral aneurysms through the use of a global threshold and gradient magnitude to form the speed function. The initial threshold is calculated from the Chan-Vese model and is then iteratively updated throughout the process of segmentation. Upon reaching the aneurysm boundary, the change in the threshold value will decrease because of the contrast between aneurysm and nonaneurysm intensities and the iteration will stop. The algorithm may then be implemented in an automatic or semiautomatic manner depending on the complexity of the aneurysm shape.

The results of 3D automatic aneurysm segmentations, from the Region Growing Threshold (RGT), the Chan-Vese model (CV), and the Threshold-Based Level Set (TLS), are compared to results obtained via manual segmentation, performed by an expert radiologist over eight data sets of CTA imagery. Evaluation was based on six validation metrics: volume difference (VD), Jaccard's measure (volume overlap metric, JM), false positive ratio (rpf), false negative ratio (rfn), Hausdorff distance (maximum surface distance, HD), and mean absolute surface distance (MASD). This study will also discuss the impact of parameter adjustments on segmentation results.

2. Methods

2.1. Region Growing Threshold Connecting (RGT). The Region Growing Threshold method starts with a seed(s), selected within the area of the object to be segmented. It requires two intensity values for the pixel of the object, a low threshold T_1 , and high threshold T_2 values. Neighboring pixels whose intensity values fall within this range are accepted and included in the region. When no more neighbor pixels are found that satisfy the criterion, the segmentation is considered to have been completed. The selection criterion is described by the following equation:

$$I(X) \in [X - T_1, X + T_2], \quad (1)$$

where T_1 and T_2 represent the low and high thresholds of the region intensities, $I(X)$ represent the image, and X the position of the particular neighboring pixel being considered for inclusion in the region. Problems surrounding RGT include threshold selection and sensitivity to seed position [22].

2.2. Chan-Vese Model (CV) [21]. The Chan-Vese model is based upon the Mumford-Shah functional [23]. The associated evolution PDE in the level set framework is

$$\begin{aligned} \frac{\partial \varphi}{\partial t} = |\nabla \varphi| \left[\lambda_2 (I - \mu_{\text{out}})^2 - \lambda_1 (I - \mu_{\text{in}})^2 - \alpha \right. \\ \left. + \beta \operatorname{div} \left(\frac{\nabla \varphi}{|\nabla \varphi|} \right) \right], \end{aligned} \quad (2)$$

where μ_{in} is the mean of the target object of intensity, μ_{out} represents the mean of the background of intensity, and $\lambda_1, \lambda_2, \alpha$, and β are positive constants. The Chan-Vese model does not require a term related to the image gradient. Instead, region intensity information is utilized for the target objects of segmentation. This model has exhibited significant effectiveness in segmentation of images with blurred boundaries.

2.3. Threshold-Based Level Set (TLS). The Threshold-Based Level Set combines both the Geodesic Active Contour and the Chan-Vese model within the level set framework.

Under the level set scheme, the contour is seen to deform by the function; $\partial \Gamma(t)/\partial t + F|\nabla \varphi| = 0$, with an embedded surface $\Gamma(t)$ represented as the zero level set of φ by $\Gamma(t) = \{x, y \in R \mid \varphi(x, y, t) = 0\}$.

F represents a function for speed, which drives the $\Gamma(t)$ surface evolution in the normal direction. It is clear that F exerts a direct impact upon the quality of medical image segmentation. The associated evolution PDE in the level set framework is represented as follows:

$$\frac{\partial \varphi}{\partial t} = |\nabla \varphi| \left(\alpha (I - T) + \beta \operatorname{div} \left(g \frac{\nabla \varphi}{|\nabla \varphi|} \right) \right), \quad (3)$$

where I represents the image to be segmented, T the intensity threshold, g is the image gradient, $\kappa = \operatorname{div}(\nabla \varphi/|\nabla \varphi|)$ the curvature, α the image propagation constant, and β represents the spatial modifier constant for the curvature κ . α and β serve to weight the relative influence of each of these terms on the movement of the surface contour.

The first term of the RHS of the formula, $\alpha(I - T)$, defines the region where T is an automatically defined parameter indicating the lower boundary of the intensity level for the target object. In this work, the target aneurysm is always assumed to possess a relatively higher intensity level than its background. It can thus be seen that this first term forces the contours to enclose regions with intensity levels greater than T . When the contour lies within the aneurysm region, $(I - T) \geq 0$, it expands in the normal direction. When $(I - T) < 0$, the contour lies beyond the aneurysm region and thus shrinks with a negative speed. This process stops when the contours converge to the aneurysm boundary, with the

TABLE 1: Validation results of segmentation methods.

	Case 1	Case 2	Case 3	Case 4	Case 5	Case 6	Case 7	Case 8	Average
VD (%)									
GT	0	0	0	0	0	0	0	0	
TLS	1.55	4.69	4.48	0.46	2.92	0.12	3.55	2.27	2.51
RGT	7.65	4.47	8.86	1.37	5.52	6.09	3.21	10.90	6.01
CV	11.63	18.23	5.60	4.04	2.47	2.51	24.18	14.02	10.34
JM (%)									
GT	100	100	100	100	100	100	100	100	
TLS	91.87	89.66	88.57	93.25	91.64	92.35	91.55	93.79	91.59
RGT	90.12	88.24	87.02	93.00	91.39	90.90	94.27	89.58	90.57
CV	88.24	84.02	86.73	89.53	91.85	91.82	76.96	89.59	87.34
rfp (%)									
GT	0	0	0	0	0	0	0	0	
TLS	4.97	2.91	3.20	1.65	3.60	3.99	4.06	2.11	3.31
RGT	0.64	3.80	14.72	0.92	9.22	1.64	5.95	0.13	4.63
CV	11.84	18.02	13.26	5.38	4.60	5.54	28.75	11.62	12.38
rfn (%)									
GT	0	0	0	0	0	0	0	0	
TLS	3.57	3.25	1.51	5.21	1.40	3.97	4.73	4.23	3.48
RGT	9.26	8.40	0.17	6.15	0.18	7.61	0.12	10.30	5.27
CV	1.32	0.84	1.78	5.66	3.93	3.09	0.92	0.00	2.19
HD (pixel)									
GT	0	0	0	0	0	0	0	0	
TLS	0.51	0.65	0.68	1.17	0.79	1.89	0.65	0.79	0.89
RGT	0.77	0.64	0.89	1.41	0.55	1.86	0.49	0.76	0.92
CV	0.75	1.17	1.04	2.09	1.19	0.51	1.00	0.95	1.09
MASD (pixel)									
GT	0	0	0	0	0	0	0	0	
TLS	0.08	0.08	0.07	0.09	0.07	0.05	0.07	0.10	0.08
RGT	0.10	0.10	0.12	0.10	0.10	0.07	0.07	0.10	0.10
CV	0.06	0.06	0.07	0.11	0.08	0.05	0.07	0.10	0.08

image I reaching a threshold of T . If we isolate this first term of the RHS of (3), it becomes the selection criteria for the lower threshold in the Region Growing Threshold method. The second term in the formula would likewise become the Geodesic Active Contour term.

2.3.1. Method for Automatic Threshold Selection. The Threshold-Based Level Set requires an appropriate estimate of the threshold value from proper segmentation of the aneurysm, obtained using Chan-Vese model and the statistical data specifically, confidence interval (CI) and confidence level (CL).

2.3.2. Confidence Interval (CI) and Confidence Level (CL). The confidence level (CL) represents how often the true percentage of a population lies within the confidence interval (CI). Based on Chebyshev's inequality [24] a general relationship for symmetric distribution between CI and CL can be established. The inequality for symmetric distribution is given as

$$P(|X - \mu| \geq k\sigma) \leq \frac{1}{k^2} \quad k > 0, \quad (4)$$

where X is the random variable population, μ is the population mean, and confidence interval is represented by k times σ standard deviation. Equation (4) indicates that more than $(1 - (1/k^2) \times 100)$ percent of the population lies between k standard deviations from the population mean.

For nonsymmetric distribution, the one-tailed version of the inequality is used. This is given by

$$P(X - \mu \geq k\sigma) \leq \frac{1}{1 + k^2} \quad k > 0. \quad (5)$$

For this inequality, it follows that when $k = 1$, more than 50% of the population is located one standard deviation away from the mean.

2.3.3. Initial Threshold Selection. According to the theory of confidence interval, the lower bound threshold of the aneurysm can be defined by

$$T_i = \mu_a - k_i \sigma_a \quad i \geq 0. \quad (6)$$

The threshold T represents the difference between the mean of the intensity of the aneurysm (μ_a) and k times its standard

deviation (σ_a). The intensities of the aneurysm and its background regions are different, with the lowest intensity threshold of the aneurysm being the same as the highest intensity threshold of the background. Thus, the relationship $\mu_b + k_b\sigma_b = \mu_a - k_a\sigma_a$ would apply. The confidence levels for both the aneurysm and its background are considered to be the same; $k_b = k_a = k$, thereby allowing k to be expressed as

$$k = \frac{\mu_a - \mu_b}{\sigma_a - \sigma_b}. \quad (7)$$

We have utilized the Chan-Vese model method to perform an initial segmentation. From the results obtained, the initial k_0 was seen to be calculated via (7). The initial T_0 can likewise be found using (6).

2.4. Data Acquisition. Clinical studies were performed with the consent of the patient in relation to acquisition of aneurysm images. These protocols were approved by the local institutional review board and the regional research ethics committee, with eight data sets of patients harboring internal carotid artery aneurysms acquired by 3D CTA scans (GE Healthcare).

Cross-sectional images were acquired by a CT angiography scanner with multidetector-row capability, a table speed of 9 mm/s, and zero-degree table (and gantry tilt). Scanning was initiated from the common carotid artery and continued parallel to the orbitomeatal line to the level of the Circle of Willis, during this intravenous injection of contrast material was administered at a rate of 3.5 mls/s. Aneurysm image was 512×512 pixel field, while slices of continuous thickness were used to segment and reconstruct 3D vascular geometry. Pixels are expressed in Hounsfield Units (HU).

2.5. Experiment Setting. For quantitative evaluation, manual segmentation of eight aneurysms using open source software, 3D Slicer, was conducted by an expert radiologist. The results were utilized as a ground truth (GT) for the comparison of other methods. A region of interest (ROI), a good representation of the targeted region for segmentation, was selected depending on the aneurysm size. All the experiments were performed on cropped data sets to reduce calculation time and memory usage, with preparatory work being completed prior to the conduction of the experiments.

2.5.1. Parameter Setting

The Threshold-Based Level Set. The initial zero level set is a rectangular prism surface, constructed by the subtraction of two pixels on either side of the ROI. Thus, three parameters needed to be set: α , β from (3) and c from (8). All eight experiments utilized a fixed setting of $\alpha = 10$, $\beta = 3$, and c in the range between 0.1 and 0.01. The role of this will be analyzed in Section 4.

The Chan-Vese Model. The initial zero level set is a cuboid surface, constructed in the same manner as the TLS, with the parameters in (2) fixed for all cases; $\lambda_1 = \lambda_2 = 0.001$, $\alpha = 0$, and $\beta = 0.3$.

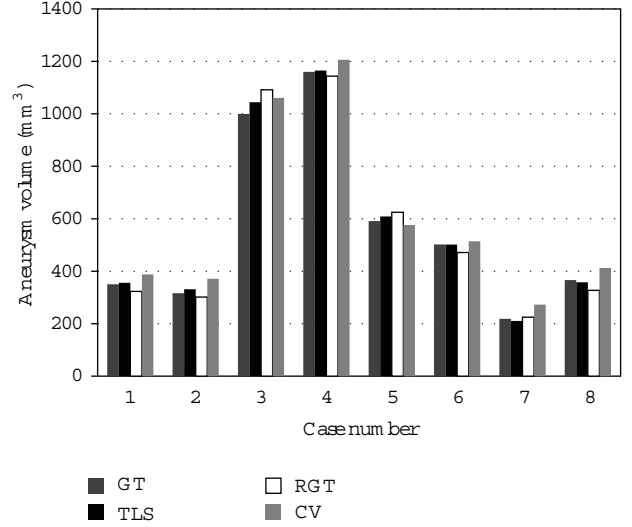


FIGURE 1: Aneurysm volume against segmentation methods.

The Region Growing Threshold. According to each case, an initial seed point is required to determine the starting loci within the specific aneurysm. For low and high intensity thresholds T_1 and T_2 in (1), T_1 was selected to utilize the threshold of the TLS result for each case, with T_2 representing the highest intensity of the aneurysm.

2.6. Evaluation

- (i) Aneurysm volume was calculated through the use of the boundary geometry, segmented using various methods. The volume difference (VD) was calculated using the equation $VD = |(V_2 - V_1)/V_1| \times 100\%$, where V_1 represents the volume of GT and V_2 represents the volume of the TLS, RGT, or CV methods.
- (ii) Jaccard's measure (JM) is a volume overlap metric, used to count the percentage of voxel intersections for the paired segmentations.

This can be seen as $JM = 2 * |S_1 \cap S_2| / |S_1 \cup S_2|$, where S_1 represents the voxels created by the GT and S_2 the voxels generated through the use of the TLS, RGT, or CV methods.

- (iii) False positive ratio (rpf) represents the percentage of the extra voxels of S_2 , located outside of S_1 . When the rpf equates to zero, no voxels in S_2 will be located outside of S_1 . Accordingly, $rpf = (|s_2| - |s_1 \cap s_2|) / |s_1|$, where S_1 represents the voxels created by the GT and S_2 represents the voxels generated by the TLS, RGT, or CV methods.
- (iv) False negative ratio (rfn) represents the percentage of the lost voxels of S_2 , which cover the internal surface of the S_1 .

This may be seen as $rfn = (|s_1| - |s_1 \cap s_2|) / |s_1|$, where S_1 represents the voxels created by the GT and S_2

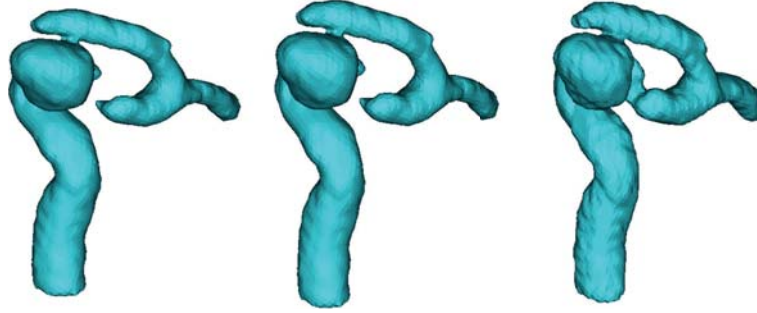


FIGURE 2: 3D geometries of segmentation results comparison, from left to right: CV, RGT, and TLS.

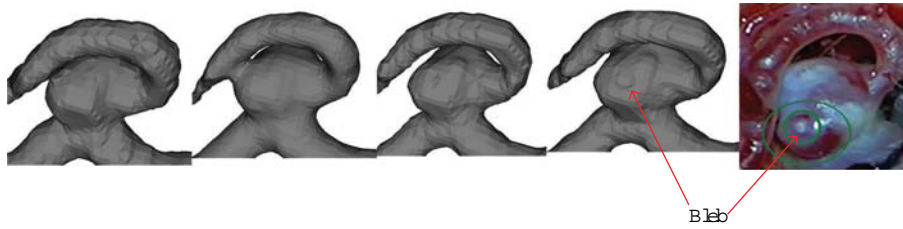


FIGURE 3: Segmentation results comparison (Case 1, aneurysm with bleb), from left to right: GT, CV, RGT, TLS, and photo from open head surgery.

represents the voxels generated by the TLS, RGT, or CV methods.

- (v) Hausdorff distance (HD) measures the maximum surface distance. This measure is extremely sensitive to outliers and may not reflect the overall degree of correlation.
- (vi) The mean absolute surface distance (MASD) indicates the average degree of difference between two surfaces and does not depend on aneurysm size [15].

3. Results

The calculated values of VD, JM, rfp, rfn, HD, and MASD for the eight cases considered are tabulated in Table 1. The average values are also shown. Figure 1 depicts the volume of the aneurysm. The minimum VD can be seen in the TLS method. The average value of VD is seen to be 2.51%. The maximum VD, however, is seen for Case 7 using the CV method. The values of JM indicate that the TLS method has the highest overlap rate in comparison to the other two methods, with an average of 91.59%. A study of rfp and rfn indicates a 3.31% overflow and 3.48% absence on average for the TLS method. The largest rfp and the smallest rfn were found to occur via the use of the CV method. These results likewise indicate that the largest volume was generated by the CV method, when compared to all other methods.

Results obtained for the surface distance metrics (HD and MASD) indicate the reliability of all segmentation methods, with the HD values for the TLS method being between 0.51 to 1.89 pixels and the maximum MASD being 0.08.

Figure 2 shows the 3D geometry of Case 4, restructured via three segmentation methods. Only TLS was effective in

fully reconstructing the parent artery and aneurysm, while the other two methods were not able to construct a portion of the artery. One reason for this is that the aneurysm size in Case 4 is larger in comparison to other cases. Another point is that the distal parent artery itself is curved to lie proximally to the aneurysm. These results likewise indicate that the TLS method may be utilized in the segmentation of aneurysms with blurred boundaries.

Figure 3 represents the segmented aneurysm surfaces of Case 1, where only TLS is able to restructure the bleb located at the top of the aneurysm. The resulting image is similar to the picture taken during open-skull surgery.

4. Discussion

4.1. TLS Boundary Detect Function. In this study, the TLS method utilizes a boundary feature map:

$$g(|\nabla I|) = \frac{1}{1 + c|\nabla I|^2}, \quad (8)$$

where g is for the detection of vascular boundaries, $|\nabla I|$ represents a gradient magnitude, and c is a constant that controls the slope of the boundary detect function, $g(|\nabla I|)$. At the region of the artery and aneurysm, the boundary intensity gradient was seen to increase significantly. Thus, a relatively low c value was sufficient for the adjustment of the decreasing speed of g , in order to ensure that the search for the boundary surface was stopped at the arterial boundary. Figure 4 shows the process of selection for the value of c in Case 1; the results indicating that both VD and JM converged to a constant and MASD ceased all fluctuation when c was taken to equate to 0.5.

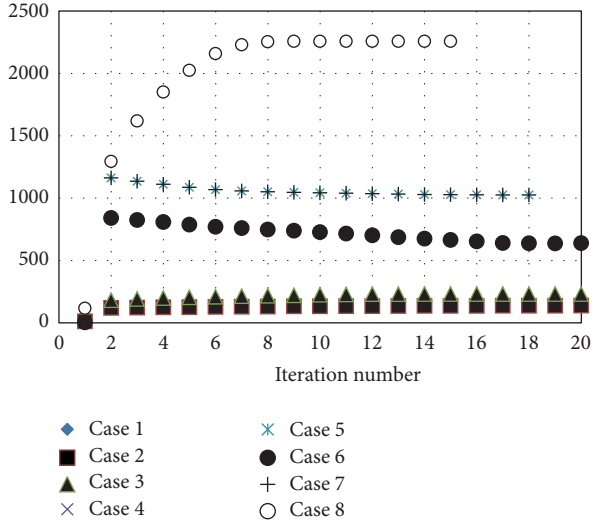


FIGURE 4: The convergence history of threshold T .

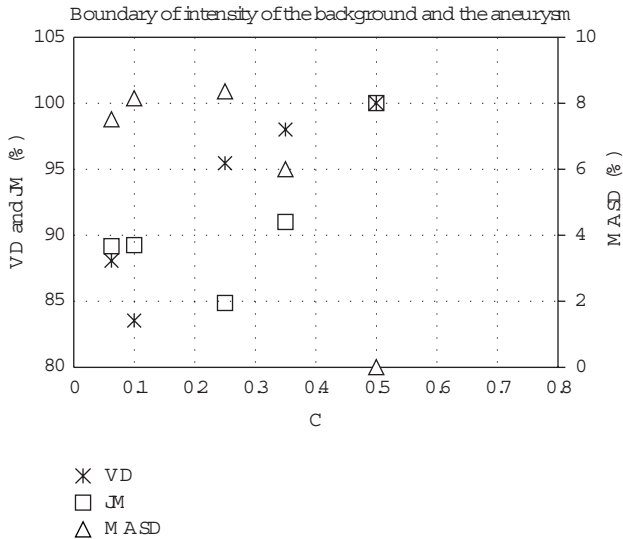


FIGURE 5: Validation of TLS boundary detect function C (Case 1).

4.2. TLS Threshold. The convergence history of threshold T is shown in Figure 5, with the T volumes exhibiting a tendency to converge after 15 iterations. The stability of the T volume against a range of value of c was likewise tested. The volume was found to be very stable for the range of c between 0.5 and 0.7. We thus suggest that the value of c is set at a volume between 0.5 and 0.7 for accurate boundary detection. As it is only TLS that does not require selection of any seeds during segmentation, it is suitable for the performance of automatic segmentations.

5. Conclusion

Various methods of segmentation generate a range of geometric models with changes in shape and volume, with the occurrence of uncertain results having the reductive

potential to negatively affect clinical treatment decisions. Through analysis of eight cerebral aneurysm models, this study indicated that limitations continue to surround current segmentation methods. The validation of the methods and analysis of errors seem vital. In this study, the TLS method was proposed to improve cerebrovascular aneurysm segmentation application. It is a technique with the ability to segment aneurysms anatomically without the setting of a seed point or intensity threshold. The method is also suitable for the segmentation of complex cerebrovascular anatomical shapes.

Acknowledgments

The authors would like to thank members of Macquarie Medical Imaging, Macquarie University Hospital, for their kind support and contributions to these cases.

References

- [1] N. D. Forkert, A. Schmidt-Richberg, J. Fiehler et al., "Fuzzy-based vascular structure enhancement in Time-of-Flight MRA images for improved segmentation," *Methods of Information in Medicine*, vol. 50, no. 1, pp. 74–83, 2011.
- [2] B. E. Chapman, J. O. Stapelton, and D. L. Parker, "Intracranial vessel segmentation from time-of-flight MRA using pre-processing of the MIP Z-buffer: accuracy of the ZBS algorithm," *Medical Image Analysis*, vol. 8, no. 2, pp. 113–126, 2004.
- [3] M. Droskey, B. Meyerz, M. Rumpfy, and K. Schaller, "An adaptive level set method for medical image segmentation," in *Proceedings of the Annual Symposium on Information Processing in Medical Imaging*, London, UK, 2001.
- [4] M. E. Leventon, W. E. L. Grimson, and O. Faugeras, "Statistical shape influence in geodesic active contours," in *Proceedings of IEEE Conference on Computer Vision and Pattern Recognition (CVPR '00)*, pp. 316–323, June 2000.
- [5] P. A. Yushkevich, J. Piven, H. C. Hazlett et al., "User-guided 3D active contour segmentation of anatomical structures: significantly improved efficiency and reliability," *NeuroImage*, vol. 31, no. 3, pp. 1116–1128, 2006.
- [6] J. A. Sethian, *Level Set Methods and Fast Marching Methods: Evolving Interfaces in Geometry, Fluid Mechanics, Computer Vision, and Materials Science*, Cambridge University, 2nd edition, 1999.
- [7] M. Kass, A. Witkin, and D. Terzopoulos, "Snakes: active contour models," *International Journal of Computer Vision*, vol. 1, no. 4, pp. 321–331, 1988.
- [8] S. Osher and J. A. Sethian, "Fronts propagating with curvature-dependent speed: algorithms based on Hamilton-Jacobi formulations," *Journal of Computational Physics*, vol. 79, no. 1, pp. 12–49, 1988.
- [9] S. Demirci, G. Lejeune, and N. Navab, "Hybrid deformable model for aneurysm segmentation," in *Proceedings of IEEE International Symposium on Biomedical Imaging: From Nano to Macro (ISBI '09)*, pp. 33–36, July 2009.
- [10] N. Wilson, K. Wang, R. W. Dutton, and C. Taylor, "A software framework for creating patient specific geometric models from medical imaging data for simulation based medical planning of vascular surgery," in *Proceedings of the 4th International Conference on Medical Image Computing and Computer-Assisted Intervention (MICCAI '01)*, pp. 449–456, 2001.

- [11] M. W. K. Law and A. C. S. Chung, "Vessel and intracranial aneurysm segmentation using multi-range filters and local variances," in *Proceedings of the International Conference on Medical Image Computing and Computer-Assisted Intervention (MICCAI '07)*, vol. 10, part 1, pp. 866–874, 2007.
- [12] M. Hernandez and A. F. Frangi, "Non-parametric geodesic active regions: method and evaluation for cerebral aneurysms segmentation in 3DRA and CTA," *Medical Image Analysis*, vol. 11, no. 3, pp. 224–241, 2007.
- [13] T. Deschamps, P. Schwartz, D. Trebotich, P. Colella, D. Saloner, and R. Malladi, "Vessel segmentation and blood flow simulation using level-sets and embedded boundary methods," *International Congress Series*, vol. 1268, pp. 75–80, 2004.
- [14] R. Manniesing, B. K. Velthuis, M. S. van Leeuwen, I. C. van der Schaaf, P. J. van Laar, and W. J. Niessen, "Level set based cerebral vasculature segmentation and diameter quantification in CT angiography," *Medical Image Analysis*, vol. 10, no. 2, pp. 200–214, 2006.
- [15] A. Firouzian, R. Manniesing, Z. H. Flach et al., "Intracranial aneurysm segmentation in 3D CT angiography: method and quantitative validation with and without prior noise filtering," *European Journal of Radiology*, vol. 79, no. 2, pp. 299–304, 2011.
- [16] T. Zuva, O. O. Olugbara, S. O. Ojo, and S. M. Ngwira, "Image segmentation, available techniques, developments and open issues," *Canadian Journal on Image Processing and Computer Vision*, vol. 2, no. 3, pp. 20–29, 2011.
- [17] H. Zhang, J. E. Fritts, and S. A. Goldman, "Image segmentation evaluation: a survey of unsupervised methods," *Computer Vision and Image Understanding*, vol. 110, no. 2, pp. 260–280, 2008.
- [18] D. Lesage, E. D. Angelini, I. Bloch, and G. Funka-Lea, "A review of 3D vessel lumen segmentation techniques: models, features and extraction schemes," *Medical Image Analysis*, vol. 13, no. 6, pp. 819–845, 2009.
- [19] Y. Sen, Y. Qian, Y. Zhang, and M. Morgan, "A comparison of medical image segmentation methods for cerebral aneurysm computational hemodynamics," in *Proceedings of the 4th International Conference on Biomedical Engineering and Informatics (BMEI '11)*, vol. 2, pp. 901–904, 2011.
- [20] V. Caselles, R. Kimmel, and G. Sapiro, "Geodesic active contours," *International Journal of Computer Vision*, vol. 22, no. 1, pp. 61–79, 1997.
- [21] T. F. Chan and L. A. Vese, "Active contours without edges," *IEEE Transactions on Image Processing*, vol. 10, no. 2, pp. 266–277, 2001.
- [22] Hu, Grossberg, and Mageras, "Survey of recent volumetric medical image segmentation techniques," in *Biomedical Engineering*, C. A. B. de Mello, Ed., InTech, 2009.
- [23] D. B. Mumford and J. Shah, "Optimal approximations by piecewise smooth functions and associated variational problems," *Communications on Pure and Applied Mathematics*, vol. 42, no. 5, pp. 577–685, 1989.
- [24] J. Russell and R. Cohn, *Chebyshev's Inequality*, Book on Demand, 2012.

Research Article

Numerical Study of Magnetoacoustic Signal Generation with Magnetic Induction Based on Inhomogeneous Conductivity Anisotropy

Xun Li,¹ Sanqing Hu,¹ Lihua Li,² and Shanan Zhu³

¹ College of Computer Science, Hangzhou Dianzi University, Hangzhou 310018, China

² College of Life Information Science and Instrument Engineering, Hangzhou Dianzi University, Hangzhou 310018, China

³ College of Electrical Engineering, Zhejiang University, Hangzhou 310027, China

Correspondence should be addressed to Xun Li; bouquet2001@gmail.com

Received 20 December 2012; Revised 18 February 2013; Accepted 18 February 2013

Academic Editor: Kumar Durai

Copyright © 2013 Xun Li et al. This is an open access article distributed under the Creative Commons Attribution License, which permits unrestricted use, distribution, and reproduction in any medium, provided the original work is properly cited.

Magnetoacoustic tomography with magnetic induction (MAT-MI) is a noninvasive imaging modality for generating electrical conductivity images of biological tissues with high spatial resolution. In this paper, we create a numerical model, including a permanent magnet, a coil, and a two-layer coaxial cylinder with anisotropic electrical conductivities, for the MAT-MI forward problem. We analyze the MAT-MI sources in two cases, on a thin conductive boundary layer and in a homogeneous medium, and then develop a feasible numerical approach to solve the MAT-MI sound source densities in the anisotropic conductive model based on finite element analysis of electromagnetic field. Using the numerical finite element method, we then investigate the magnetoacoustic effect of anisotropic conductivity under the inhomogeneous static magnetic field and inhomogeneous magnetic field, quantitatively compute the boundary source densities in the conductive model, and calculate the sound pressure. The anisotropic conductivity contributes to the distribution of the eddy current density, Lorentz force density, and acoustic signal. The proposed models and approaches provide a more realistic simulation environment for MAT-MI.

1. Introduction

Since Henderson and Webster reported an impedance camera to generate the electrical impedance image of the thorax [1], it is of increasing interests to noninvasively measure the electrical impedance of biological tissues. Several approaches, such as electrical impedance tomography (EIT) [2, 3], magnetic induction tomography (MIT) [4, 5], magnetic resonance EIT (MREIT) [6], magnetoacoustic tomography (MAT) [7, 8], and Hall effect imaging (HEI) [9], have been developed to image the electrical impedance distribution. Among these technologies, EIT, MREIT, and MAT/HEI inject electrical currents into the imaging object through the surface electrodes, so that they have to face the “shield effect” [10, 11] caused by a low-conductivity tissue layer surrounding the object and therefore have difficulties in imaging the

electrical impedance of deep biological tissue with high spatial resolution. MIT excites the deep biological tissue with time-variant magnetic field and measures the secondary magnetic field produced by the eddy current to reconstruct electrical impedance images. However, the inverse problem in MIT, as in EIT, is an ill-posed problem.

Magnetoacoustic tomography with magnetic induction (MAT-MI) is a newly proposed electrical impedance imaging modality [11]. In MAT-MI, an object is placed in an external static magnetic field \mathbf{B}_0 and a time-variant magnetic field \mathbf{B}_1 to induce the eddy currents \mathbf{J} in the object. The eddy currents are subject to Lorentz forces to induce sound vibrations in the object. The emitted sound signals are detected around the object to reconstruct the electrical impedance images of the imaging object. Through combining magnetism and sonography, MAT-MI can excite deep tissues and image the

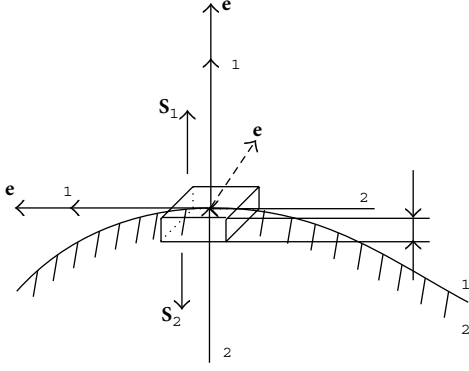


FIGURE 1: A tube on the boundary between two homogeneous conducting media.

electrical impedance with high spatial resolution. As a result of the sound measurement around the specimen, MAT-MI has a well-posed inverse problem.

Similar to MAT/HEI, MAT-MI is based on the Lorentz force-induced vibrations. The difference among them is that MAT-MI uses time-variant magnetic field, while the MAT/HEI applies current injection, and therefore the MAT/HEI sound sources are only at the boundary between regions of differing conductivity for a piecewise homogeneous isotropic conductor [7], while those of MAT-MI exist everywhere in the conductor.

It is well known that some biological materials, such as bone and skeletal muscle, are distinctly anisotropic [12]. Recently, several studies have been developed to explore the effect of electrical anisotropy, such as the influence of white matter anisotropy on EEG source localization [13], inhomogeneous anisotropic cardiac tissues [14], and the effect of conductivity anisotropy on EIT [15]. Another study has reported that the diffusion anisotropy in breast cancer is significantly different from that in normal tissue [16]. The water diffusion may have a relation with the electrical conductivity in a tissue, and the conductivity tensor can be obtained from the diffusion tensor [17]. It is obvious that breast cancers may have different anisotropic conductivity tensor from that of normal tissues.

In previous works, there are many theories and simulation models, as shown in Table 1, to study MAT-MI principles.

In the present study, we analyze the MAT-MI sound source densities in a homogeneous conducting medium and on a thin conductive boundary layer and build a magnet and a circular coil to produce inhomogeneous static magnetic field and time-variant magnetic field. We create a two-layer coaxial cylinder with different anisotropic conductivity values and solve the MAT-MI forward problem with the aid of the finite element method (FEM). By comparing anisotropic conductive model with isotropic conductive model, we investigate the magnetoacoustic effect of the conductivity anisotropy. We also discuss the difference of sound signal generation between MAT-MI and MAT/HEI.

2. Theory

According to the previous works [7, 11], MAT-MI wave equation can be described as

$$\nabla^2 p - \frac{1}{c_s^2} \frac{\partial^2 p}{\partial t^2} = \nabla \cdot (\mathbf{J} \times \mathbf{B}), \quad (1)$$

where p is the acoustic pressure, c_s is the sound speed, \mathbf{J} is the induced eddy current density, and \mathbf{B} is the magnetic flux density including the static magnetic flux density \mathbf{B}_0 and the time varying magnetic flux density \mathbf{B}_1 . The cross product of \mathbf{J} and \mathbf{B} is the Lorentz force density, and the divergence of the Lorentz force density is the sound source density. Here, we study the sound source density on three conditions including homogeneous isotropic conducting medium, a thin conductive boundary layer in the heterogeneous conducting medium, and anisotropic conducting medium.

2.1. Homogeneous Isotropic Conducting Medium. In this case, the conductivity σ is a constant in solving domain. We assume that the electrical currents producing the time-variant magnetic field are outside of the imaging object, so that the curl of \mathbf{B} is zero [7]. Then, we have [21]

$$\begin{aligned} \nabla \cdot (\mathbf{J} \times \mathbf{B}) &= (\nabla \times \mathbf{J}) \cdot \mathbf{B} - \mathbf{J} \cdot (\nabla \times \mathbf{B}) = (\nabla \times \mathbf{J}) \cdot \mathbf{B} \\ &= (\nabla \times \sigma \mathbf{E}) \cdot \mathbf{B} = -\sigma \frac{\partial \mathbf{B}}{\partial t} \cdot \mathbf{B}. \end{aligned} \quad (2)$$

Since the static magnetic field is time invariant, the sound source density is

$$\nabla \cdot (\mathbf{J} \times \mathbf{B}) = -\sigma \frac{\partial \mathbf{B}_1}{\partial t} \cdot \mathbf{B}. \quad (3)$$

2.2. A Thin Conductive Boundary Layer in a Heterogeneous Conducting Medium. When the conductivities are not homogeneous but changed abruptly, the eddy current densities and the corresponding Lorentz force densities are not continuous on both sides of the boundary layer. The source term, which is the divergence of the Lorentz force density, should be calculated in a different way. To solve the MAT-MI sources, we assume a very small tube on the boundary layer and apply the Gauss theorem on the source term to avoid the divergence on the jump discontinuity.

As shown in Figure 1, we consider a small tube on the boundary layer between two homogeneous isotropic media with conductivity values of σ_1 and σ_2 . \mathbf{e}_n is the outward normal to the tangent plane, S_1 and S_2 are the two surfaces of the tube, and the outward normal to the S_1 and S_2 is, respectively, in the same and opposite directions as \mathbf{e}_n . J_{1n} , J_{2n} and J_{1t} , J_{2t} are, respectively, the normal and tangential components of the eddy current densities, \mathbf{e}_t is in the same direction as J_{1t} and J_{2t} , and \mathbf{e}_r is orthogonal to both J_{1t} and J_{1n} . The thickness of the tube Δl is assumed to be infinitesimal.

Based on electromagnetic theory, the electromagnetic field boundary conditions are as follows [25]:

$$J_{1n} = J_{2n}, \quad E_{1t} = E_{2t}. \quad (4)$$

TABLE I: Numerical studies on MAT-MI.

	Time invariant magnetic field	Static magnetic field	Model		Sound source
			Conductivity	Structure	
Xu and He 2005 [11]	H	H	H and Iso	A sphere	Analytical solution
Li et al. 2006 [18] Li et al. 2007 [19]	H	H	Inh and Iso	A two-layer concentric sphere	Numerical solution based on magnetic vector potential and electrical scalar potential method
Brinker and Roth 2008 [20]	Inh	H	H and Ani	A uniform sheet of tissue	Analytical and numerical solutions based on magnetic vector and electrical scalar potential method
Li et al. 2009 [21]	Inh	H	Inh and Iso	Two-layer eccentric spheres; a circular coil	Numerical solution based on finite element method
Li and He 2010 [22]	Inh	H	Inh and Iso	2D conductive sample; coil group	Numerical solution based on finite element method
Li 2010 [23]	Inh	H	Inh and Iso	Human breast and tumors; a circular coil	Analytical solution for homogeneous medium and conductivity boundary; numerical solution based on finite element analysis
Zhou et al. 2011 [24]	Inh	H	Inh and Iso	Breast tumor model; a circular coil	Analytical and numerical solutions using finite element method

*H denotes homogeneous; Inh denotes inhomogeneous; Iso denotes isotropic; Ani denotes anisotropic.

Due to the magnetic field continuity across the boundary, we have

$$\mathbf{B}_1 = \mathbf{B}_2 = \mathbf{B}, \quad (5)$$

where \mathbf{B}_1 and \mathbf{B}_2 are the magnetic field on both sides of the boundary layer.

Thus, the Lorentz force density, the cross product of the eddy current density \mathbf{J} and magnetic flux density \mathbf{B} on the boundary layer, can be written in the orthogonal coordinates system $(\mathbf{e}_n, \mathbf{e}_t, \mathbf{e}_t')$ as follows:

$$\mathbf{J} \times \mathbf{B} = \begin{vmatrix} \mathbf{n} & \mathbf{t} & \mathbf{t}' \\ J_n & J_t & 0 \\ B_n & B_t & B_t' \end{vmatrix} = J_t B_t' \mathbf{n} - J_n B_t' \mathbf{t} + (J_n B_t - J_t B_n) \mathbf{t}'. \quad (6)$$

Applying the Gauss theorem, we have

$$\int_V \nabla \cdot (\mathbf{J} \times \mathbf{B}) dV = \oint_S (\mathbf{J} \times \mathbf{B}) \cdot d\mathbf{S}. \quad (7)$$

In the case of the small tube as shown in Figure 1, we have $\Delta l \rightarrow 0$ and

$$\begin{aligned} \oint_S (\mathbf{J} \times \mathbf{B}) \cdot d\mathbf{S} &= \int_{S_1} J_{1t} B_t' \mathbf{n} \cdot d\mathbf{S}_1 + \int_{S_2} J_{2t} B_t' \mathbf{n} \cdot d\mathbf{S}_2 \\ &= (\sigma_1 - \sigma_2) E_{1t} B_t' S_1, \end{aligned} \quad (8)$$

where \mathbf{e}_t' is in the same direction as $\mathbf{e}_t \times \mathbf{e}_n$.

Then, we have the sound source of the small tube on the boundary layer as follows:

$$\int_V \nabla \cdot (\mathbf{J} \times \mathbf{B}) dV = (\sigma_1 - \sigma_2) E_{1t} B_t' S_1. \quad (9)$$

From formula (9), we can compute the sound sources on the boundary layer through the outward normal to the boundary surface, the intensity, and direction of the \mathbf{E} and \mathbf{B} . Zhou et al. got the same result as formula (9) [24].

2.3. A Thin Conductive Boundary Layer in the Anisotropic Conducting Medium. Considering the MAT-MI sound source in a homogenous anisotropic conducting medium, the conductivity value σ is not a constant but a tensor. We have

$$\nabla \cdot (\mathbf{J} \times \mathbf{B}) = \nabla \cdot \left\{ \left(\begin{bmatrix} \sigma_{xx} & \sigma_{xy} & \sigma_{xz} \\ \sigma_{yx} & \sigma_{yy} & \sigma_{yz} \\ \sigma_{zx} & \sigma_{zy} & \sigma_{zz} \end{bmatrix} \begin{bmatrix} E_x \\ E_y \\ E_z \end{bmatrix} \right) \times \mathbf{B} \right\}. \quad (10)$$

We will introduce a numerical solution of this case by using finite element interpolation in Section 3.3.1.

On the boundary layer, the electromagnetic field boundary conditions are the same as described in formula (4), and we can use the same method as illustrated in Section 2.2 to analyze the MAT-MI sound source on the boundary layer in

an anisotropic heterogeneous conducting medium. Then, we have

$$\int_V \nabla \cdot (\mathbf{J} \times \mathbf{B}) dV = B_t' S_1 \left(\left(\begin{bmatrix} \sigma_{1xx} & \sigma_{1xy} & \sigma_{1xz} \\ \sigma_{1yx} & \sigma_{1yy} & \sigma_{1yz} \\ \sigma_{1zx} & \sigma_{1zy} & \sigma_{1zz} \end{bmatrix} - \begin{bmatrix} \sigma_{2xx} & \sigma_{2xy} & \sigma_{2xz} \\ \sigma_{2yx} & \sigma_{2yy} & \sigma_{2yz} \\ \sigma_{2zx} & \sigma_{2zy} & \sigma_{2zz} \end{bmatrix} \right) \begin{bmatrix} E_{1tx} \\ E_{1ty} \\ E_{1tz} \end{bmatrix} \right) \cdot \mathbf{e}_t, \quad (11)$$

where E_{1tx} , E_{1ty} , and E_{1tz} are the decomposition of the tangential component of the electric field in the Cartesian coordinate system.

2.4. Solution of the Wave Equation. Applying Green's function, we have the solution of the MAT-MI wave equation in free space [11] as follows:

$$p(\mathbf{r}, t) = -\frac{1}{4\pi} \oint_V d\mathbf{r}' \times \int_{-\infty}^{\infty} \nabla_{\mathbf{r}'} \cdot (\mathbf{J}(\mathbf{r}', t') \times \mathbf{B}(\mathbf{r}', t')) \frac{\delta(t' - t + |\mathbf{r} - \mathbf{r}'|/c_s)}{|\mathbf{r} - \mathbf{r}'|} dt', \quad (12)$$

where V is the source domain, \mathbf{r}' is a sound point source, \mathbf{r} is a point detecting the sound radiation from the sound point sources, t is the time to detect the sound signal, and δ is a Dirac Delta function. Using the previous formula, we can compute the sound pressure radiated out from the sources.

3. Simulation Study

In the previous studies, numerical simulations were conducted on solid models with isotropic conductivity [21, 23, 24] or a uniform sheet with homogeneous conductivity anisotropy [20], under homogeneous static magnetic field. In the present study, we adopt a permanent magnet to produce a more realistic and complex inhomogeneous static magnetic field and conduct numerical simulations on a conductor with inhomogeneous anisotropic conductivities. Based upon the present models, we perform the electromagnetic analysis using the finite element method software ANSYS and calculate the sound source densities in the homogeneous anisotropic medium on the conductivity boundary and the spatial distribution of the acoustic pressure. Finally, we compare the eddy currents, Lorentz forces, MAT-MI sources, and sound pressure of the anisotropic and isotropic conductive models to investigate the effect of conductivity anisotropy on the MAT-MI signal generation.

3.1. Model. The current simulation models include a two-layer conductive cylinder, a magnet, a real shape coil, and

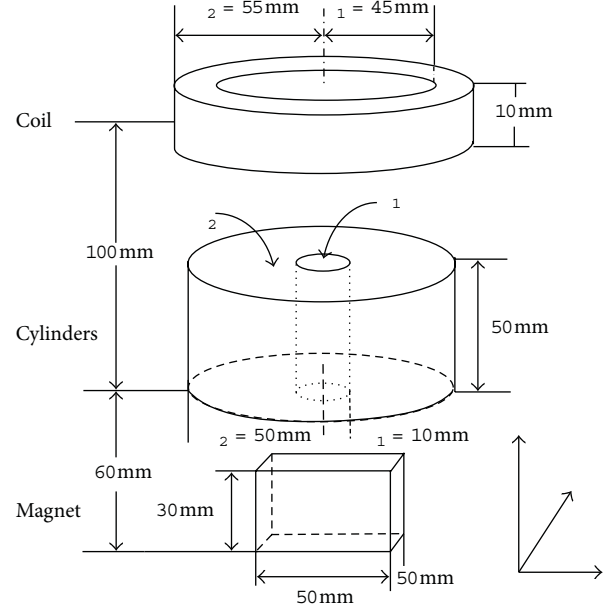


FIGURE 2: Model geometry.

the surrounding water and air media. Figure 2 shows the coaxial cylindrical model together with the coil and magnet models. In the conductive models, the radii of the inner and outer layer cylinders are, respectively, 10 and 50 mm, and the anisotropic conductivity values of the inner and outer layers are, respectively, $\sigma_1 = [\sigma_{1x} = 0.25, \sigma_{1y} = 0.125, \sigma_{1z} = 0.2]$ and $\sigma_2 = [\sigma_{2x} = 0.04, \sigma_{2y} = 0.1, \sigma_{2z} = 0.2]$ S/m. The conductivity of the two layers in the x direction σ_{1x} and σ_{2x} is the same as the isotropic conductivity values adopted in the previous work [19], and the difference between σ_{1y} and σ_{2y} is much smaller than that between σ_{1x} and σ_{2x} . This allows us to investigate the change of the eddy current density caused by the electrical anisotropy through comparing with those induced in the isotropic conductive models. The cylindrical shape of the conductor is similar to the columnar phantom employed in previous MAT-MI experiments [19, 26–28]. The width, length, and height of the permanent magnet are, respectively, 50, 50, and 30 mm. The coil has a height of 10 mm, with an inner radius and an outer radius of 45 mm and 55 mm, respectively. The water surrounding the conductive model is a cylinder with a radius of 80 mm and a height of 70 mm. The conductivity value of the water σ_w is 0.4 S/m. The coil, magnet, and water are surrounded by the cylindrical air medium with a radius of 200 mm and a height of 300 mm.

Taking the center of the underside of the two-layer coaxial cylinder as the origin, the bottom of the coil is 95 mm above, and the top of the magnet is 30 mm below the origin. The top and bottom of the water are, respectively, 60 mm above and 10 mm below the origin. The coil, two-layer coaxial cylinder, and water and air models are symmetric with respect to the z -axis, and the magnet is symmetric about the plane $x = 0$ and $y = 0$. The symmetry of the solid model allows us to explore

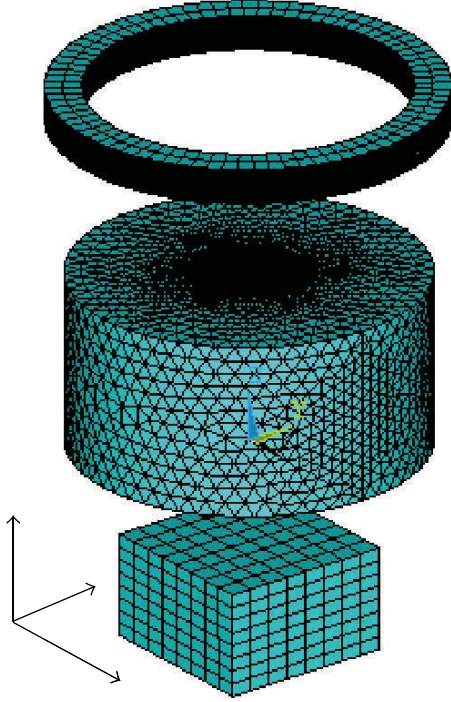


FIGURE 3: Meshed grids of the coil, permanent magnet, and two-layer coaxial cylindrical conductive models.

the effect of the electrical anisotropy specifically. The injected currents into the coil obey a quasi-step function described as

$$J(t) = \begin{cases} J_{\text{end}} & t \geq T_{\text{end}}, \\ \frac{(t - T_{\text{start}}) * J_{\text{end}}}{T_{\text{end}} - T_{\text{start}}} & T_{\text{start}} < t < T_{\text{end}}, \\ 0 & t \leq T_{\text{start}}, \end{cases} \quad (13)$$

where T_{start} and T_{end} are the time to begin and finish the electrical current injection, $T_{\text{end}} - T_{\text{start}} = 5E - 6$ s, and $J_{\text{end}} = 3E + 8$ A/m² is the magnitude of the current density at the end of the current injection. The sound speed is assumed to be homogeneous and isotropic in all the media and is set to be 1500 m/s. We create the solid models in ANSYS, meshed the coil and magnet with hexahedrons, and meshed the conductive cylinders, water, and air media with tetrahedrons. The meshed grids of the coil, magnet, and two-layer coaxial cylindrical conductive models are shown in Figure 3.

In order to evaluate the impact of the conductivity anisotropy on the magnetoacoustic signals, we adopt an isotropic conductive model sharing the same geometry with the aforementioned model. The isotropic conductivity values of the inner and outer cylinders are, respectively, 0.25 and 0.04 S/m, which are the same as those adopted in the previous isotropic conductive model [19].

3.2. Procedure

- (1) Performing the FEM electromagnetic analysis, obtaining the Lorentz force density \mathbf{F} on every node, eddy current density \mathbf{J} and magnetic flux density \mathbf{B} on

every element. And extracting the elements neighboring to the boundary layer and the corresponding nodes of the elements on the boundary layer.

- (2) Calculating the sound source density in the finite elements in the homogeneous medium and in the small tubes on the conductivity boundary.
- (3) Regarding the sound sources in the elements and tubes as point sources, assuming the sound speed in the solving domain is a constant $c_s = 1500$ m/s, and applying the discrete form of formula (12) to calculate the sound field as follows:

$$P(\mathbf{r}, t) = -\frac{1}{4\pi} \sum_{j=1}^M \frac{\nabla \cdot (\mathbf{J}_j(\mathbf{r}'_j, t - R/c_s) \times \mathbf{B}_j(\mathbf{r}'_j, t - R/c_s))}{R}, \quad (14)$$

where M is the number of the point sources, $R = |\mathbf{r} - \mathbf{r}'|$.

3.3. Sound Source

3.3.1. Source in the Homogeneous Medium. For the MAT-MI source density in the homogeneous anisotropic conducting medium, we have

$$\nabla \cdot (\mathbf{J} \times \mathbf{B}) = \nabla \cdot \mathbf{F} = \frac{\partial F_x}{\partial x} + \frac{\partial F_y}{\partial y} + \frac{\partial F_z}{\partial z}. \quad (15)$$

After performing the finite element analysis of electromagnetic field, we have the nodal solutions of the Lorentz force density. We apply the FEM interpolation to the Lorentz force density in each element to count the sound source density.

As shown in Figure 4, in a first-order tetrahedral element, $\mathbf{F}_1, \mathbf{F}_2, \mathbf{F}_3,$ and \mathbf{F}_4 are the nodal solutions of the Lorentz force density, and $\mathbf{F}(x, y, z)$ is the Lorentz force density on a point in an element. Using the finite element interpolation [29], we have

$$\mathbf{F}(x, y, z) = \mathbf{a}^e + \mathbf{b}^e x + \mathbf{c}^e y + \mathbf{d}^e z, \quad (16)$$

where $\mathbf{a}^e, \mathbf{b}^e, \mathbf{c}^e,$ and \mathbf{d}^e are vectors as $\mathbf{a}^e = [a_x^e, a_y^e, a_z^e]$ and so on. All the vectors are determined by the coordinates of the four tetrahedral vertices and the nodal solutions of the Lorentz force density \mathbf{F} . Substituting (16) into (15), we have

$$\begin{aligned} \nabla \cdot (\mathbf{J} \times \mathbf{B}) &= \nabla \cdot \mathbf{F} = b_x^e + c_y^e + d_z^e \\ &= \frac{1}{6V^e} \left(\sum_{j=1}^4 b_j^e F_{xj} + \sum_{k=1}^4 c_k^e F_{yk} + \sum_{j=1}^4 d_j^e F_{zj} \right), \end{aligned} \quad (17)$$

where $F_{xj}, F_{yj},$ and F_{zj} are the three Cartesian components of the nodal values of the Lorentz force and $b_j^e, c_j^e,$ and d_j^e are the coefficients determined from the expansion of the determinants of the elemental interpolation [29]. Through computing formula (17), we can analyze the MAT-MI sound source density in a homogeneous anisotropic conducting medium based on the solutions of the finite element analysis.

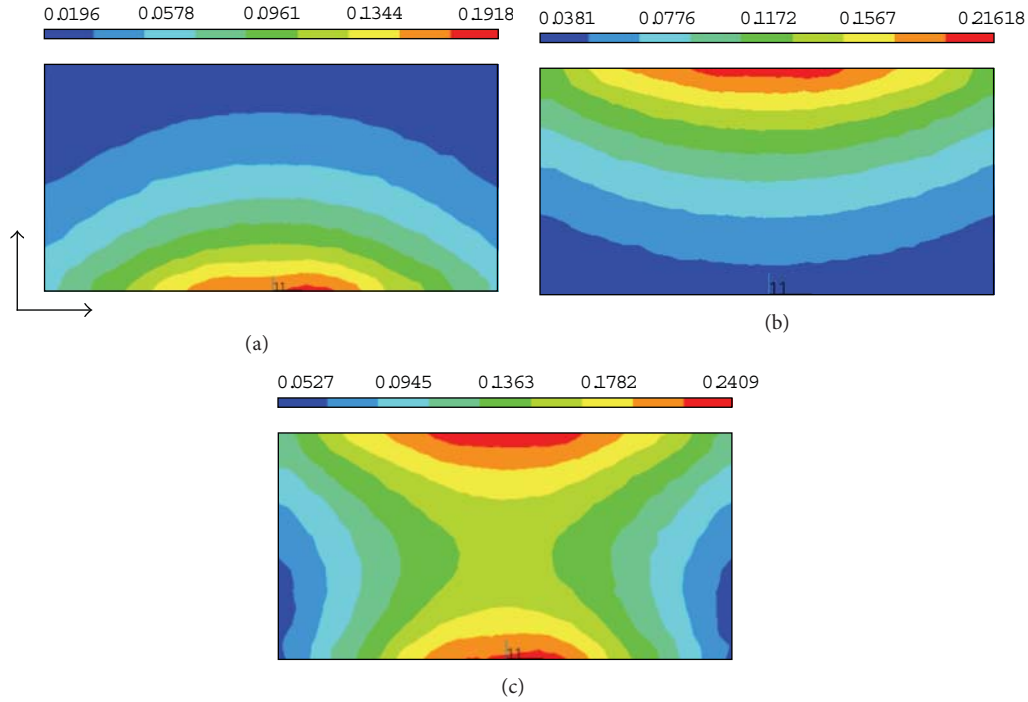


FIGURE 6: Magnetic flux density in the coaxial cylinder produced, respectively, by (a) magnet, (b) coil, and (c) both magnet and coil. The unit of magnetic flux density is Tesla (T).

from the two models. Since the geometry of the model and the magnetic field are the same, the only thing contributing to the previous differences is the conductivity of the material. In other words, the different conductive properties in the two models, which are, respectively, anisotropic and isotropic conductivities, lead to such differences.

5. Discussions

In this simulation study, we have conducted numerical simulations on the conductive models with electrical anisotropy, the real shape coil and magnet, and calculated the MAT-MI sound source densities on the conductivity boundary. The conductivity anisotropy changes the intensity of the boundary source densities through influencing the eddy current density distribution. The effect of the electrical anisotropy in MAT-MI signal generation is not negligible. Despite of the high intensity of the boundary sources, the MAT-MI acoustic signals contain the signals radiated from the sources in the homogeneous conductive media. So, we may eliminate the impact of the boundary sources as much as possible and use weak signal detection technology to extract the useful information to reconstruct the sound sources in the homogeneous medium.

Through comparing the MAT-MI sound sources and signals from the isotropic and anisotropic conductive models, we can find that the electrical anisotropy changes the source densities and the magnitude of the acoustic pressure signals.

To investigate the MAT-MI source, the present and previous works start from the divergence of the Lorentz force density ($\mathbf{J} \times \mathbf{B}$), which may cause singularity problem

on the boundary, to explore the magnetoacoustic effect of biological tissues with magnetic induction. In fact, we can further perform finite element analysis of acoustic vibrations and radiations to avoid solving the divergence on the discontinuity.

In order to study the magnetoacoustic effect of the electrical anisotropy, the present simulation conductive model is symmetric and comparatively simple. We can further create more realistic and complex breast model, including subcutaneous fat, duct system, mammographic texture, Cooper's ligaments, pectoralis muscle, skin, and abnormalities, as the breast phantom modeled for mammography [30].

Since MAT/HEI has a similar imaging principle to MAT-MI, we can further study and understand the magnetoacoustic signal generation through comparing MAT/HEI and MAT-MI. MAT injects electrical current to an object under a static magnetic field to evoke vibrations, while MAT-MI imposes time-variant magnetic field on the object under the static magnetic field to generate acoustic signals. The current injection in MAT/HEI and the magnetically induced currents in MAT-MI make a difference in the MAT/HEI and MAT-MI acoustic signals. The basic difference between MAT/HEI and MAT-MI is shown in Table 2.

In a homogeneous isotropic conducting medium, neglecting the secondary magnetic field produced by the injected currents, the curl of the current density \mathbf{J} is equal to zero in MAT [7]. Due to magnetic induction, the curl of the current density \mathbf{J} in MAT-MI is associated with the electrical conductivity σ and the partial derivative of the magnetic flux density \mathbf{B} with respect to time t [21]. So, there is no MAT/HEI source evoked in the homogeneous isotropic

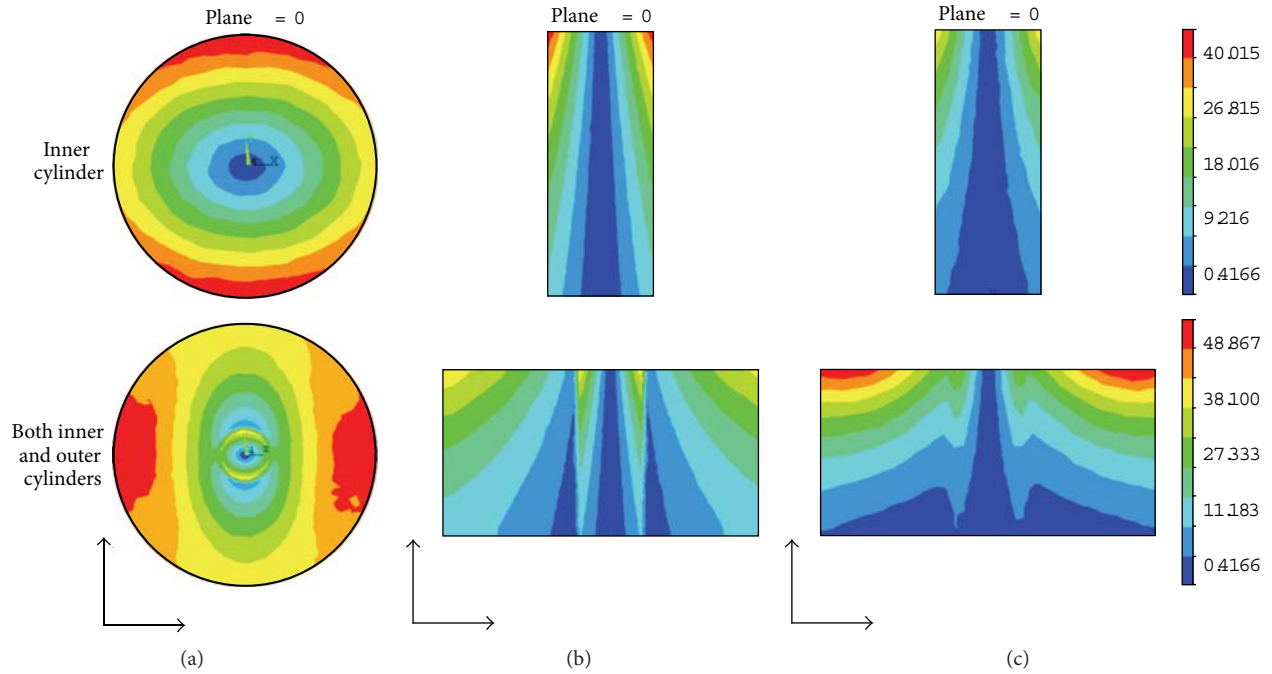


FIGURE 7: The distribution of eddy current density in the inner and outer cylinders on the planes $z = 0$, $x = 0$, and $y = 0$. The unit of eddy current density is Ampere/m² (A/m²).

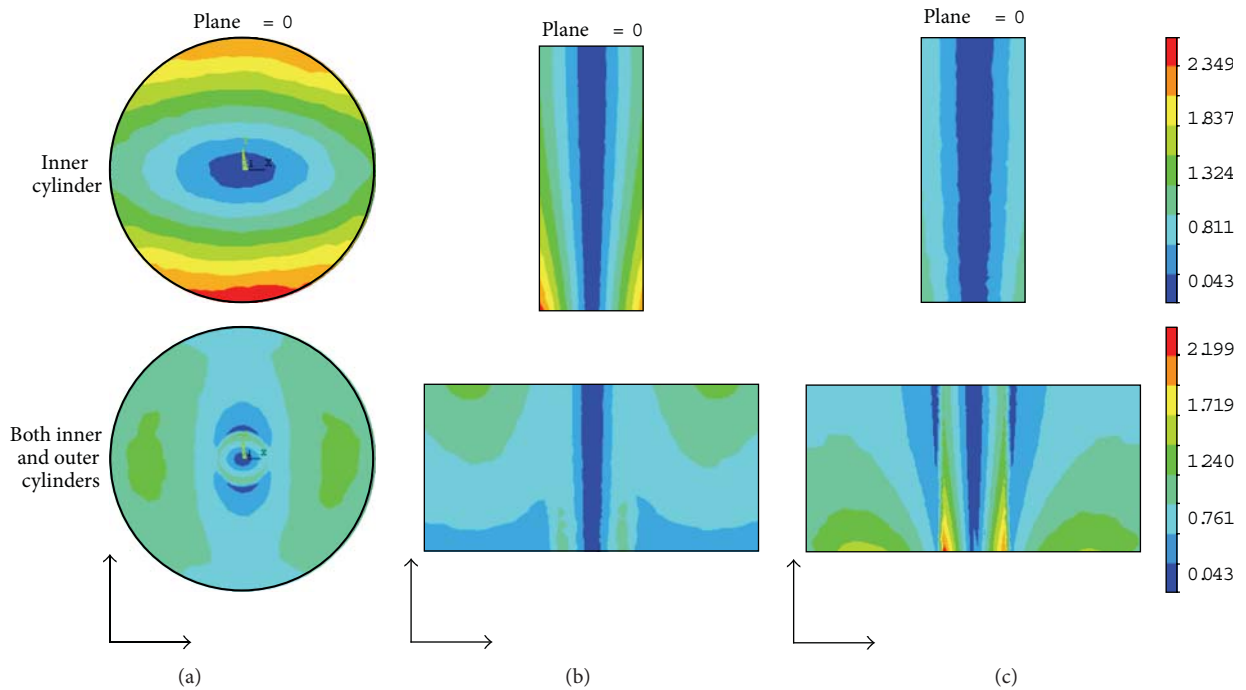


FIGURE 8: The distribution of Lorentz force density in the inner and outer cylinders on the planes $z = 0$, $x = 0$, and $y = 0$. The unit of Lorentz force density is Newton/m³ (N/m³).

conductive domain. On the contrary, MAT-MI generates the acoustic vibrations in the whole homogeneous isotropic medium.

On the conductivity boundary, both MAT/HEI and MAT-MI obey the same electromagnetic field boundary

conditions, so we can use the same approach, as described in the Section 2.2 to solve the divergence of the Lorentz force. Roth et al. studied the MAT source and put forward that the curl of the eddy current density J is nonzero only at the boundary, that there is no source on the surface

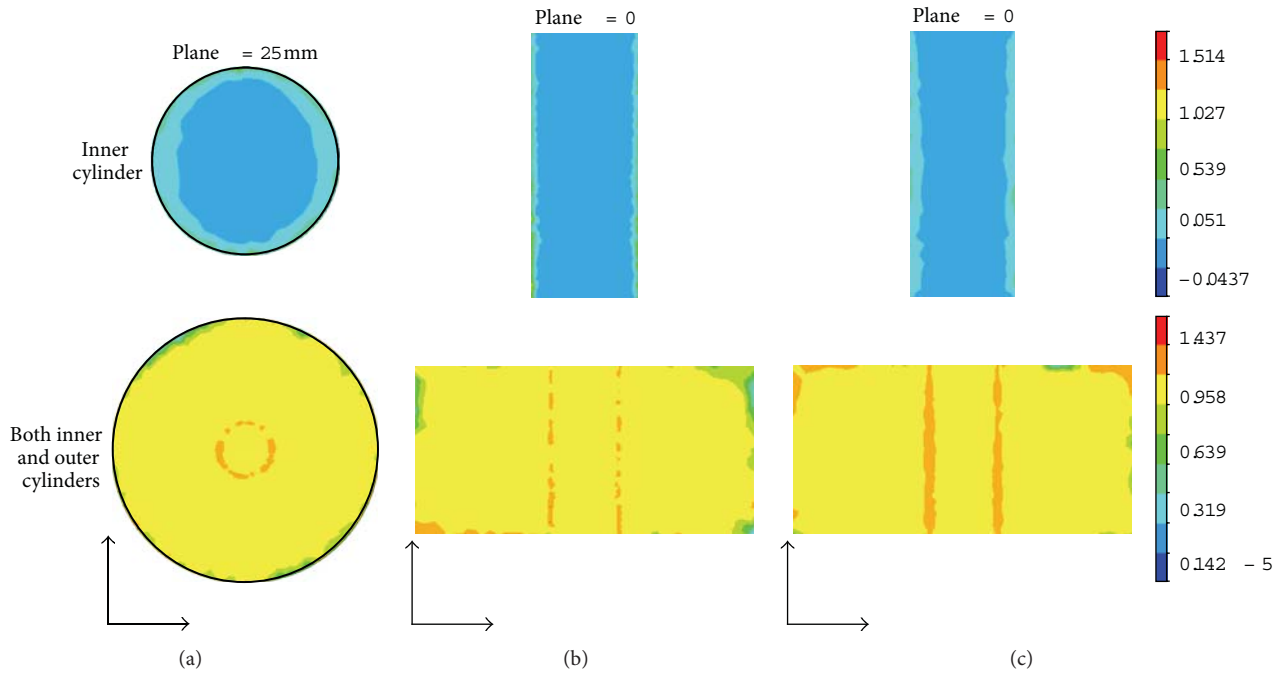


FIGURE 9: Sound source density distribution in the inner cylinder and both the inner and outer cylinders on the planes $z = 25$ mm, $x = 0$, and $y = 0$. The unit of the boundary source density is Pa/m, and that of the homogeneous source density is Pa/m².

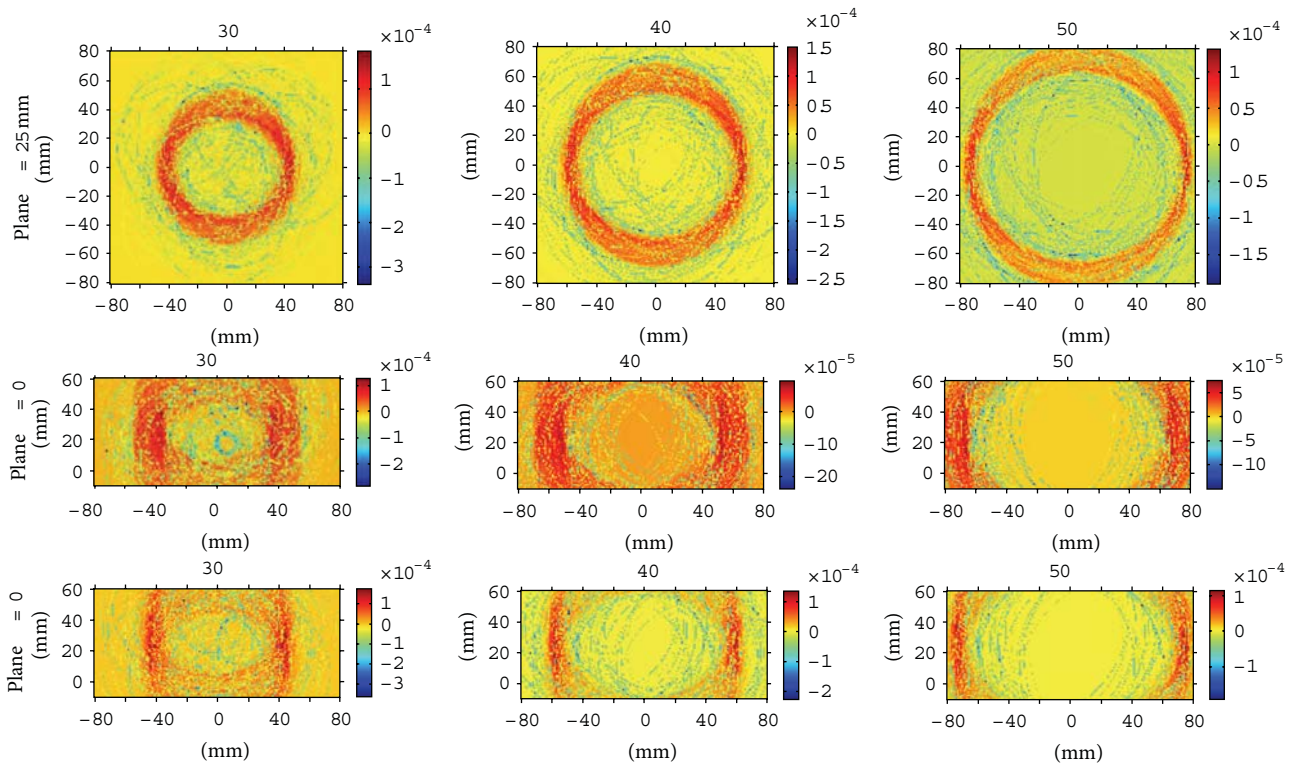


FIGURE 10: Sound pressure on the planes $z = 25$ mm, $x = 0$, and $y = 0$ at times $t = 20, 30, 40$, and 50 μs . The unit of sound pressure is Pascal (Pa).

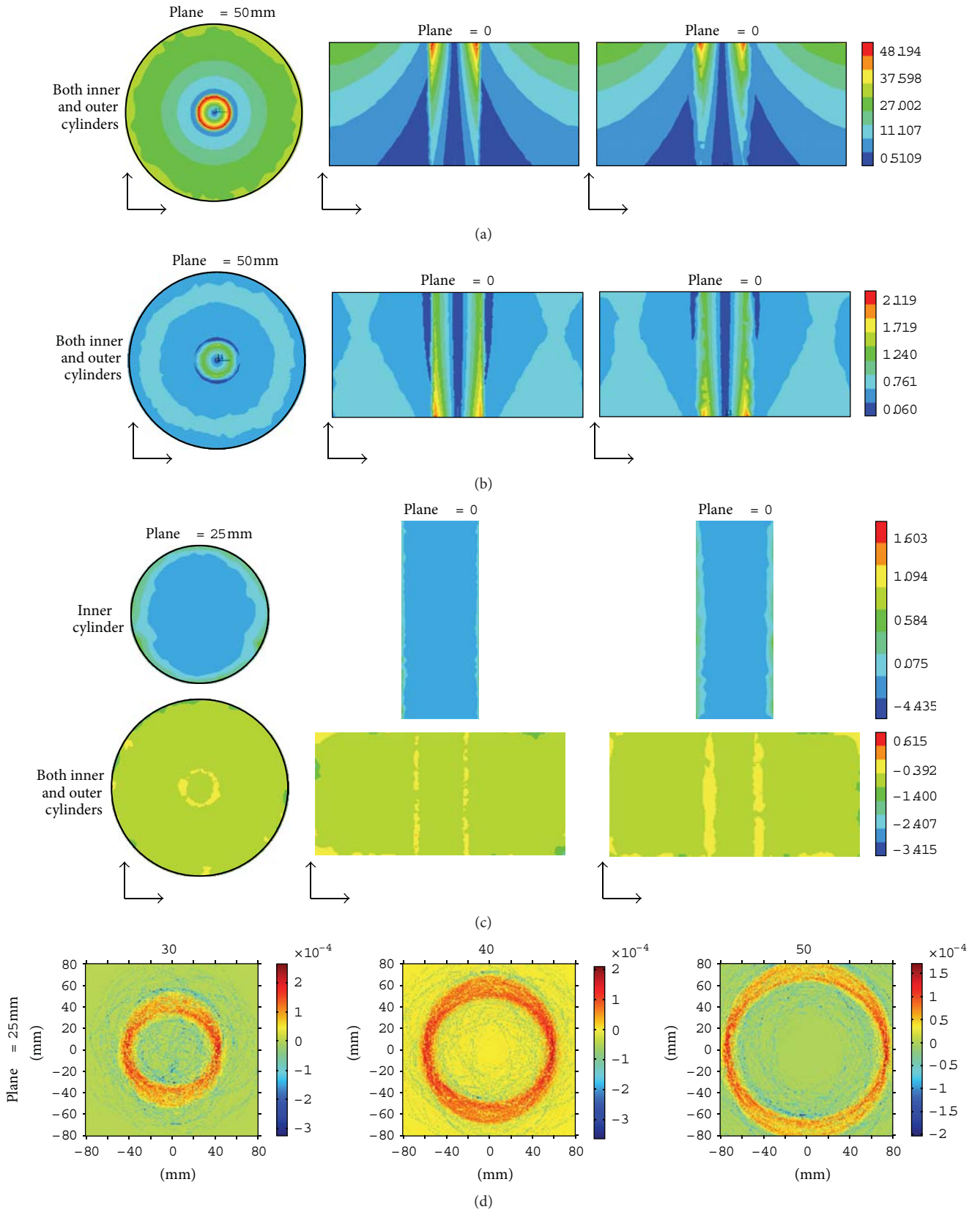


FIGURE 11: Numerical simulations on the cylindrical conductive models with isotropic conductivities. (a) Eddy current density, (b) Lorentz force density, (c) sound source density on the planes $z = 25 \text{ mm}$, $x = 0$, and $y = 0$, and (d) sound pressure on the plane $z = 25 \text{ mm}$ at time $t = 20, 30, 40$, and $50 \mu s$. The units of eddy current density, Lorentz force density, boundary source density, homogeneous source density, and sound pressure are, respectively, Ampere/m² (A/m²), Newton/m³ (N/m³), Pascal/m (Pa/m), Pascal/m² (Pa/m²), and Pascal (Pa).

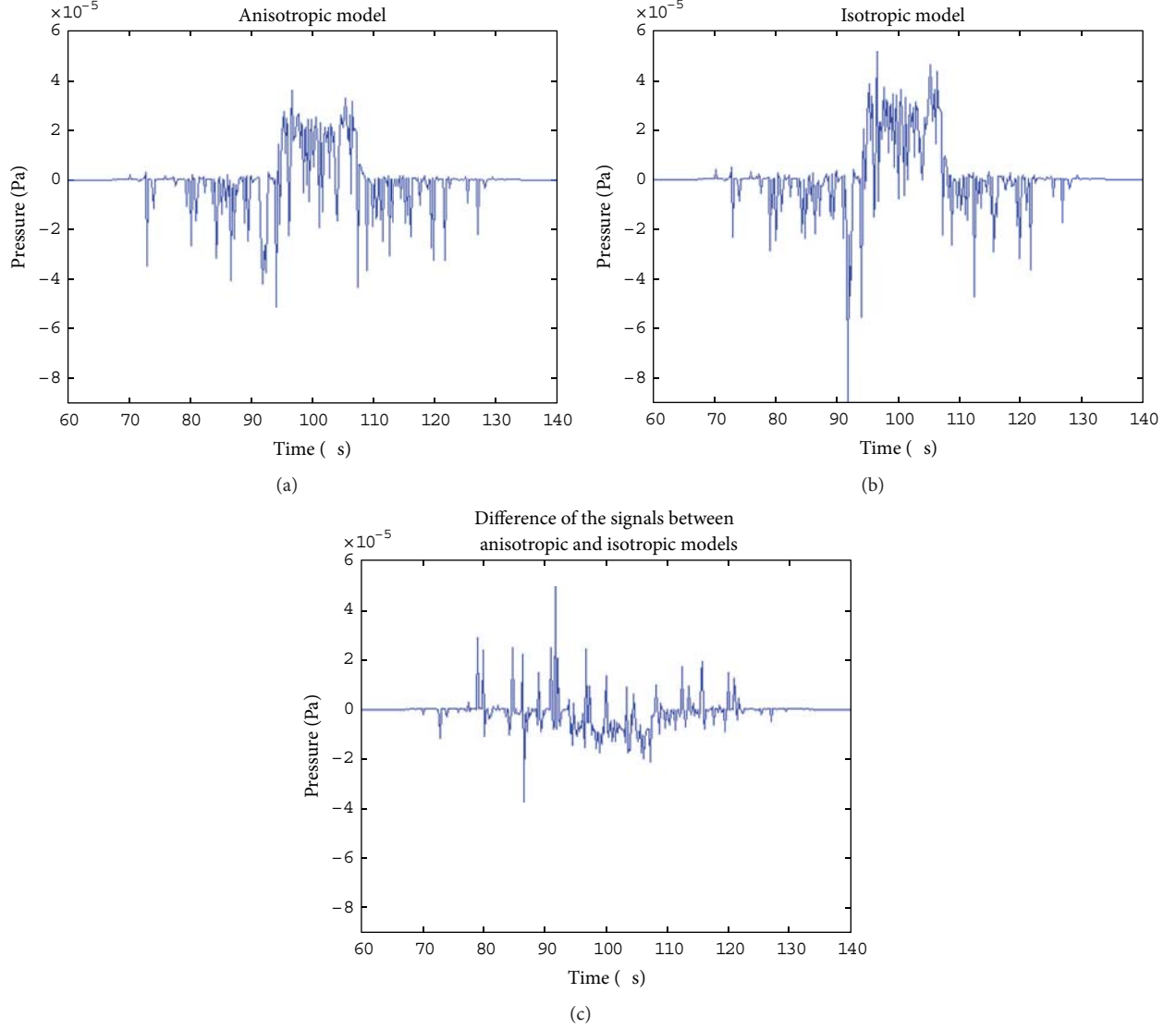


FIGURE 12: The time sequences of the acoustic signal obtained on a point whose coordinates are (0, 150, 25) mm. The unit of acoustic pressure signal is Pascal (Pa).

TABLE 2: Comparisons of MAT and MAT-MI sound generation in an inhomogeneous isotropic conductive medium.

	Boundary conditions	Sound sources	
		Homogeneous	Boundary
MAT/HEI	$E_{1t} = E_{2t}, J_{1n} = J_{2n}$	$(\nabla \times \mathbf{J}) = 0$	$\int_V \nabla \cdot (\mathbf{J} \times \mathbf{B}) dV = \mathbf{e}_{t'} \cdot ((\sigma_2 - \sigma_1) E_{1t} dS) \cdot \mathbf{B}$
MAT-MI	$B_{1n} = B_{2n}, H_{1t} = H_{2t}$	$(\nabla \times \mathbf{J}) = -\sigma \frac{\partial \mathbf{B}_1}{\partial t}$	

that is perpendicular to the applied magnetic field \mathbf{B} , and that the component of the magnetic field that is perpendicular to a surface has no contribution to the source [7]. From the formula described in Table 2, for the MAT/HEI and MAT-MI boundary source density, it is clear that the intensity of the source density is zero when the dot product of the $\mathbf{e}_{t'}$, which is a vector on the boundary surface, and \mathbf{B} is equal to zero. If we decompose \mathbf{B} into three orthogonal components B_n , B_t , and $B_{t'}$, $\mathbf{e}_{t'}$ and B_n are

perpendicular, and the corresponding dot product is zero, that is, B_n contributes nothing to the source. Obviously, formula for the MAT-MI and MAT/HEI boundary sources analyzed in this paper is well consistent with the previous conclusions, and furthermore, with the analytical expression of formula, we can solve the intensities of the MAT-MI source densities on the boundary for biological tissues or phantom with arbitrary geometry.

In summary, we have created a magnet, a coil, and a two-layer coaxial cylindrical conductive model to conduct simulations for MAT-MI forward problem under conditions of inhomogeneous static magnetic field, inhomogeneous time-variant magnetic field, and conductivity anisotropy. We have also quantitatively computed the MAT-MI boundary source densities and the source densities inside the homogeneous conducting medium. To the best of our knowledge, it is the first time that MAT-MI forward problem is solved in a conductive specimen with conductivity anisotropy together with a permanent magnet. The present models and the simulation approach based on the finite element method enable us to investigate MAT-MI signal generation in a more practical simulation environment, such as arbitrary geometric configurations of anisotropic and isotropic conductive model, inhomogeneous static magnetic field produced by a permanent magnet, and various types of time-variant magnetic field generated by a coil or coil set, and so on.

Acknowledgment

This work was supported in part by the National Natural Science Foundation of China under Grants 51107024, 61070127, 60788101, and 61102028.

References

- [1] R. P. Henderson and J. G. Webster, "An impedance camera for spatially specific measurements of the thorax," *IEEE Transactions on Biomedical Engineering*, vol. 25, no. 3, pp. 250–254, 1978.
- [2] K. Paulson, W. Lionheart, and M. Pidcock, "Optimal experiments in electrical impedance tomography," *IEEE Transactions on Medical Imaging*, vol. 12, no. 4, pp. 681–686, 1993.
- [3] P. Metherall, D. C. Barber, R. H. Smallwood, and B. H. Brown, "Three-dimensional electrical impedance tomography," *Nature*, vol. 380, no. 6574, pp. 509–512, 1996.
- [4] S. Al-Zeibak, D. Goss, G. Lyon, Z. Z. Yu, A. J. Peyton, and M. Beck, "A feasibility study of electromagnetic inductance tomography," in *Proceedings of the 9th International Conference on Electrical Bio-Impedance*, pp. 426–429, 1995.
- [5] H. Griffiths, "Magnetic induction tomography," *Measurement Science and Technology*, vol. 12, pp. 1126–1131, 2001.
- [6] O. Kwon, E. J. Woo, J. R. Yoon, and J. K. Seo, "Magnetic resonance electrical impedance tomography (MREIT): simulation study of J-substitution algorithm," *IEEE Transactions on Biomedical Engineering*, vol. 49, no. 2, pp. 160–167, 2002.
- [7] B. J. Roth, P. J. Basser, and J. P. Wikswo Jr., "A theoretical model for magneto-acoustic imaging of bioelectric currents," *IEEE Transactions on Biomedical Engineering*, vol. 41, no. 8, pp. 723–728, 1994.
- [8] B. C. Towe and M. R. Islam, "A magneto-acoustic method for the noninvasive measurement of bioelectric currents," *IEEE Transactions on Biomedical Engineering*, vol. 35, pp. 892–894, 1988.
- [9] H. Wen, J. Shah, and R. S. Balaban, "Hall effect imaging," *IEEE Transactions on Biomedical Engineering*, vol. 45, pp. 119–124, 1998.
- [10] H. Wen, "Volumetric Hall effect tomography—a feasibility study," *Ultrasonic Imaging*, vol. 21, no. 3, pp. 186–200, 1999.
- [11] Y. Xu and B. He, "Magnetoacoustic tomography with magnetic induction," *Physics in Medicine and Biology*, vol. 50, pp. 5175–5187, 2005.
- [12] K. R. Foster and H. P. Schawn, *CRC Handbook of Biological Effects of Electromagnetic Fields*, CRC, Boca Raton, Fla, USA, 1987.
- [13] D. Güllmar, J. Haueisen, M. Eiselt et al., "Influence of anisotropic conductivity on EEG source reconstruction: investigations in a rabbit model," *IEEE Transactions on Biomedical Engineering*, vol. 53, pp. 1841–1850, 2006.
- [14] H. I. Saleheen and K. T. Ng, "A new three-dimensional finite-difference bidomain formulation for inhomogeneous anisotropic cardiac tissues," *IEEE Transactions on Biomedical Engineering*, vol. 45, no. 1, pp. 15–25, 1998.
- [15] J. F. P. J. Abascal, S. R. Arridge, D. Atkinson et al., "Use of anisotropic modelling in electrical impedance tomography; description of method and preliminary assessment of utility in imaging brain function in the adult human head," *NeuroImage*, vol. 43, no. 2, pp. 258–268, 2008.
- [16] S. C. Partridge, A. Ziadloo, R. Murthy et al., "Diffusion tensor MRI: preliminary anisotropy measures and mapping of breast tumors," *Journal of Magnetic Resonance Imaging*, vol. 31, no. 2, pp. 339–347, 2010.
- [17] C. C. McIntyre, S. Mori, D. L. Sherman, N. V. Thakor, and J. L. Vitek, "Electric field and stimulating influence generated by deep brain stimulation of the subthalamic nucleus," *Clinical Neurophysiology*, vol. 115, no. 3, pp. 589–595, 2004.
- [18] X. Li, Y. Xu, and B. He, "Magnetoacoustic tomography with magnetic induction for imaging electrical impedance of biological tissue," *Journal of Applied Physics*, vol. 99, no. 6, Article ID 066112, 2006.
- [19] X. Li, Y. Xu, and B. He, "Imaging electrical impedance from acoustic measurements by means of magnetoacoustic tomography with magnetic induction (MAT-MI)," *IEEE Transactions on Biomedical Engineering*, vol. 54, pp. 323–330, 2007.
- [20] K. Brinker and B. J. Roth, "The effect of electrical anisotropy during magnetoacoustic tomography with magnetic induction," *IEEE Transactions on Biomedical Engineering*, vol. 55, no. 5, pp. 1637–1639, 2008.
- [21] X. Li, X. Li, S. Zhu, and B. He, "Solving the forward problem of magnetoacoustic tomography with magnetic induction by means of the finite element method," *Physics in Medicine and Biology*, vol. 54, no. 9, pp. 2667–2682, 2009.
- [22] X. Li and B. He, "Multi-excitation magnetoacoustic tomography with magnetic induction for bioimpedance imaging," *IEEE Transactions on Medical Imaging*, vol. 29, no. 10, pp. 1759–1767, 2010.
- [23] X. Li, "A study on forward solution of magnetoacoustic tomography with magnetic induction (MAT-MI) based on breast tumor model," *Chinese Journal of Biomedical Engineering*, vol. 29, no. 3, pp. 390–398, 2010.
- [24] L. Zhou, X. Li, S. Zhu, and B. He, "Magnetoacoustic tomography with magnetic induction (MAT-MI) for breast tumor imaging: numerical modeling and simulation," *Physics in Medicine and Biology*, vol. 56, no. 7, pp. 1967–1983, 2011.
- [25] J. R. Reitz, F. J. Milford, and R. W. Christy, *Foundations of Electromagnetic Theory*, Addison-Wesley, Reading, Mass, USA, 3rd edition, 1979.
- [26] G. Hu, X. Li, and B. He, "Imaging biological tissues with electrical conductivity contrast below 1 S m⁻¹ by means of magnetoacoustic tomography with magnetic induction," *Applied Physics Letters*, vol. 97, no. 10, Article ID 103705, 2010.

- [27] G. Hu, E. Cressman, and B. He, "Magnetoacoustic imaging of human liver tumor with magnetic induction," *Applied Physics Letters*, vol. 98, no. 2, Article ID 023703, 2011.
- [28] L. Mariappan, X. Li, and B. He, "B-scan based acoustic source reconstruction for magnetoacoustic tomography with magnetic induction (MAT-MI)," *IEEE Transactions on Biomedical Engineering*, vol. 58, no. 3, pp. 713–720, 2011.
- [29] J. Jin, *The Finite Element Method in Electromagnetics*, Wiley, New York, NY, USA, 2nd edition, 2002.
- [30] K. Bliznakova, Z. Bliznakov, V. Bravou, Z. Kolitsi, and N. Pallikarakis, "A three-dimensional breast software phantom for mammography simulation," *Physics in Medicine and Biology*, vol. 48, no. 22, pp. 3699–3719, 2003.

Research Article

In Vivo Imaging-Based Mathematical Modeling Techniques That Enhance the Understanding of Oncogene Addiction in relation to Tumor Growth

Chinyere Nwabugwu,^{1,2} Kavya Rakhra,³ Dean Felsher,³ and David Paik²

¹ Department of Electrical Engineering, Stanford University School of Medicine, Stanford, CA 94305, USA

² Department of Radiology, Stanford University School of Medicine, Stanford, CA 94305, USA

³ Department of Medicine, Stanford University School of Medicine, Stanford, CA 94305, USA

Correspondence should be addressed to David Paik; david.paik@stanford.edu

Received 21 December 2012; Accepted 15 February 2013

Academic Editor: Kumar Durai

Copyright © 2013 Chinyere Nwabugwu et al. This is an open access article distributed under the Creative Commons Attribution License, which permits unrestricted use, distribution, and reproduction in any medium, provided the original work is properly cited.

The dependence on the overexpression of a single oncogene constitutes an exploitable weakness for molecular targeted therapy. These drugs can produce dramatic tumor regression by targeting the driving oncogene, but relapse often follows. Understanding the complex interactions of the tumor's multifaceted response to oncogene inactivation is key to tumor regression. It has become clear that a collection of cellular responses lead to regression and that immune-mediated steps are vital to preventing relapse. Our integrative mathematical model includes a variety of cellular response mechanisms of tumors to oncogene inactivation. It allows for correct predictions of the time course of events following oncogene inactivation and their impact on tumor burden. A number of aspects of our mathematical model have proven to be necessary for recapitulating our experimental results. These include a number of heterogeneous tumor cell states since cells following different cellular programs have vastly different fates. Stochastic transitions between these states are necessary to capture the effect of escape from oncogene addiction (i.e., resistance). Finally, delay differential equations were used to accurately model the tumor growth kinetics that we have observed. We use this to model oncogene addiction in MYC-induced lymphoma, osteosarcoma, and hepatocellular carcinoma.

1. Introduction

Bernard Weinstein first proposed in 1997 that “oncogene addiction” is the phenomenon whereby the inactivation of a single oncogene, even if brief, may lead to sustained tumor regression, providing a weakness for a molecularly targeted therapy to exploit [1]. For example, imatinib causes dramatic tumor regression in gastrointestinal stromal tumors (GIST) [2, 3] and chronic myelogenous leukemia (CML) [3–5] by inhibiting the *Bcr-Abl* oncogene; erlotinib and gefitinib cause dramatic tumor regression in nonsmall cell lung cancer (NSCLC) [6–9], pancreatic cancer, and other tumors by inhibiting EGFR; a number of other examples of targeted therapies exist. These drugs induce dramatic tumor regression without the side effect profile of nonspecific chemotherapies.

Inactivation of the oncogene by targeted therapy produces a complex array of responses at the cellular level including apoptosis, cell cycle arrest, differentiation, senescence, and inhibition of angiogenesis. In preclinical models, the oncogene may be inactivated using conditional expression in transgenic animals (e.g., Cre/LoxP, tamoxifen, or tetracycline systems). Some of these resultant cellular programs are cell intrinsic (i.e., not involving other cells) while others are cell extrinsic, involving complex host interactions with effector cells in the immune system. While these different response mechanisms have been studied and modeled individually, there has been far less investigation into integrating the overall sequence and interactions of tumor responses into a unified mathematical model that can inform the design and optimization of therapeutic strategies. Understanding how and why some tumors relapse while others do not, as well as

how and why the specific cellular program responses depend on the tissue-specific and host immune background, is of crucial importance for designing the most effective therapies.

Previously, we have built and validated a model of tumor growth and regression kinetics in response to oncogene inactivation [10]. This model was based primarily upon microCT imaging and immunohistochemistry (IHC) and explicitly incorporated apoptosis and proliferation resulting from the stochastic balance between prosurvival and prodeath signals but included no other cellular programs. In other work, we have empirically shown the importance of cellular senescence, immune surveillance, differentiation, and angiogenesis. Here, we have created a mathematical model that now captures the tumor growth kinetics as a function of all of the aforementioned cellular programs informed primarily by bioluminescence imaging (BLI) and IHC. We are building on this to develop and calibrate a novel integrative mathematical model of the tumor responses to oncogene inactivation (cell intrinsic and cell extrinsic) that is designed to eventually predict, optimize, and validate various therapeutic strategies.

We will use the model to study the major cellular processes involved in MYC-induced lymphoma, osteosarcoma, and hepatocellular carcinoma, which involve difference combinations and sequences of these programs and to test different therapeutic strategies.

Much work has been done in characterizing tumor growth kinetics *in vivo* and in mathematically modeling the cell intrinsic mechanisms involved in the response to oncogene inactivation. *In vivo* observations of cell extrinsic mechanisms in response to oncogene inactivation have been published recently, but little if any mathematical or computational modeling has been done to complement these theories. Our work is among the first to simultaneously model all of the complex immune-mediated responses that are critical in determining the factors involved in tumor relapse thereby providing understanding of how to prevent it.

2. Materials and Methods

2.1. Biological Data. We utilize the tetracycline (Tet) system to conditionally and reversibly control the expression of the MYC oncogene in mouse models [11, 12]. Even in the absence of a putative drug, this models the effect of a targeted therapeutic that would downregulate the aberrant overexpression of MYC as a treatment for the tumor. In the Tet-Off system, doxycycline (dox) is added to the drinking water to inhibit binding of the tet-transactivating promoter (tTA) to the Tet-O promoter and thus inactivates transcription of MYC. Alternatively, in the Tet-On system, dox allows binding of reverse tTA (rtTA) and thus activates transcription of MYC [13]. MYC expression can even be titrated with a threshold on tumor regression occurring at $\leq 0.05 \mu\text{g/mL}$ of dox (in $\leq 0.2 \text{ ng/mL}$ plasma concentration) in a Tet-On system [14]. We have collected data from various conditional mouse models of MYC and concentrated on the tumor type specific responses to MYC inactivation seen in various tumor types including lymphoma (apoptosis, proliferative arrest, differentiation, senescence, antiangiogenesis, and tumor relapse)

[15–17], osteosarcoma (proliferative arrest, differentiation, and senescence) [18, 19], and hepatocellular carcinoma (apoptosis, differentiation, senescence, and dormancy) [20].

In tumor dormancy, cells can restore their neoplastic properties upon MYC reactivation. In order to improve therapy, it is important to distinguish when MYC inactivation leads to complete tumor regression characterized by permanent loss of malignant phenotype and when it simply results in a reversible state of tumor dormancy [21, 22].

MYC inactivation in MYC-induced lymphoma leads to differentiation, apoptosis, and complete tumor regression. Therefore, a permanent loss of a neoplastic phenotype occurs upon MYC inactivation. In osteogenic sarcoma, MYC inactivation induces differentiation and proliferative arrest but does not induce significant apoptosis. MYC reactivation in these apparently differentiated cells either has no consequences or leads to apoptosis. Only in very rare cells is there restoration of neoplastic properties. In hepatocellular carcinoma, MYC inactivation leads to differentiation and then eventually to gradual apoptosis of most of the tumor cells. Upon reactivation of MYC, these differentiated cells quickly become tumorigenic [23].

Senescence is the growth-arrest process by which normal cells are restrained from malignant transformation. Oncogene inactivation-induced senescence (OIS) is the irreversible cell cycle arrest of normal cells in response to inactivating an oncogene. We have recently shown cellular senescence resulting from MYC inactivation to depend on the host immune system [24]. Tumor regression upon inactivation of the MYC oncogene is associated with cellular senescence. Cellular senescence is an essential factor in bringing about sustained tumor regression upon MYC inactivation.

The *p53* gene has been shown to suppress tumor angiogenesis and regulate thrombospondin-1 (*TSP-1*), a potent antiangiogenic protein, expression [25]. The loss of *p53* upon MYC inactivation leads to a deficit of *TSP-1* and this inhibits angiogenesis thus impeding tumor regression. Restoration of *p53* leads to sustained tumor regression upon MYC inactivation. Therefore, either *p53* or *TSP-1* is required upon MYC inactivation to shut down angiogenesis and induce sustained tumor regression [26].

Tumors undergo regression initially regardless of the status of the host immune system. But in hosts that are immune compromised, tumor elimination is incomplete and the tumors eventually relapse. An intact immune system is required for oncogene inactivation-induced senescence, inhibition of angiogenesis, and chemokine expression, which lead to sustained tumor regression. CD4^+ (but not CD8^+) T-cell deficiency was enough to impede sustained tumor regression. The secretion of *TSP-1* is markedly decreased in immune compromised versus wildtype hosts. *TSP-1* expression requires host immune cells particularly CD4^+ T cells. Reconstitution of immune compromised mouse with CD8^+ T cells still showed significant minimum residual disease, whereas reconstitution with CD4^+ T cells showed no minimum residual disease, the same result found in wildtype hosts upon MYC inactivation. Hence, simply restoring CD4^+ T cells was sufficient to eliminate minimum residual disease and to lead to sustained tumor regression. CD4^+ T cells

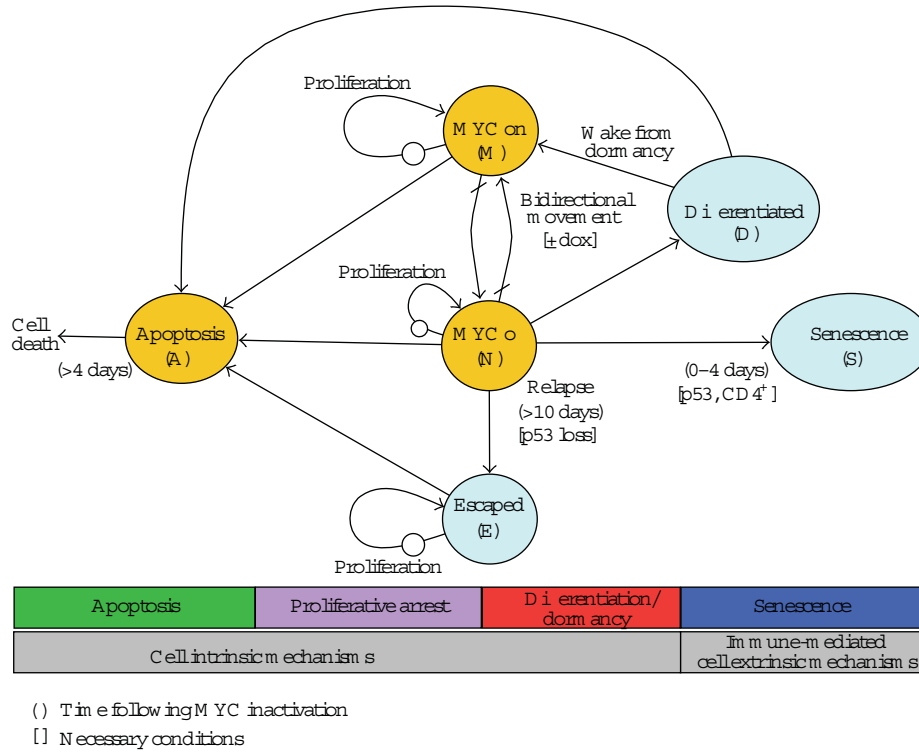


FIGURE 1: Mathematical model of cellular states. Former model shown in gold with additions shown in blue. The arrows with slashes corresponding to $\pm dox$ indicate that this is an independent variable controlled experimentally. The arrows representing proliferative loops have an implicit state during proliferation representing the mitotic phase of the cell cycle.

are the crucial host effector population necessary for tumor regression upon MYC inactivation. TSP-1 is important in immune effectors for sustained regression upon MYC inactivation, and overexpression of TSP-1 in immune compromised hosts is sufficient to increase the duration of sustained tumor regression upon MYC inactivation [27, 28].

2.2. *Mathematical Model.* Our mathematical model uses various modeling techniques that were each shown to be necessary to accurately recapitulate the experimental observations.

2.2.1. *Multiple Tumor Cell States.* We created a new mathematical model (Figure 1) of tumor growth/regression kinetics incorporating cell intrinsic mechanisms (apoptosis, proliferative arrest, differentiation/dormancy) and immune-mediated cell extrinsic mechanisms (senescence). The stochastic model consists of 6 cellular states (“MYC on,” “MYC off,” apoptosis, proliferating, differentiated, senescent) with probabilistic transitions and the ability to control the expression of transgenic MYC using the tetracycline system. In our state transition model, discrete numbers of tumor cells move from one state to another, unlike other models where single classes of cells (e.g., tumor, immune, or normal) are modeled by single homogeneous states with no transitions between them. The core of the model consists of the “MYC on” and “MYC off” states, controlled in the conditional transgenic mouse model through doxycycline (dox) in the drinking water. This is

central to the model since we are specifically investigating the effect of targeted therapeutics. “MYC off” tumor cells have been shown to be able to develop mechanisms to turn MYC back on without doxycycline through tTA, Notch, MAPK, or Wnt pathways and are represented by the “Escaped” node in the model [17]. Tumor cells may undergo proliferation or apoptosis, and “MYC off” tumor cells may alternatively undergo differentiation or oncogene inactivation-induced senescence.

The structure and topology of our mathematical model is based on *in vivo* observations from numerous studies [10, 17, 23, 24, 27]. We added an explicit transition in the model from “MYC off” to “Differentiated” to represent differentiation due to oncogene inactivation. We tested parameters over a number of values and chose values that most closely matched experimental data. Additionally, we added a transition from “Differentiated” back to “MYC on” to indicate that some tumor cells (e.g., hepatocellular carcinoma) that have differentiated to an apparently normal state may be dormant but possess the ability to regain neoplastic properties [23, 29]. The transition from “MYC off” to “Oncogene Inactivation Induced Senescence” is dependent on both p53 and CD4+ T cells and represents immune-mediated effects.

Tumor cells can exist in one of six different states; the number of cells in each state is represented as follows. M , the number of cells in which MYC is “on”; N , cells in the MYC “off” state and still under the control of the tetracycline system; A , cells which have irreversibly committed

to apoptosis; D , cells that have differentiated back into a quasinormal state, although in some tumor types they retain their neoplastic capability if MYC is reactivated; S , cells that have irreversibly committed to oncogene inactivation-induced senescence (OIIS); and E , cells that have escaped their addiction to MYC (e.g., through mutations in the tetracycline control elements or by activating expression of genes downstream of MYC). Note that due to pharmacokinetics and a number of other factors, the transitions between M and N are noninstantaneous and tetracycline dependent where the path is only open (nonzero) in one direction at a time. Note that because our current biological data uses mice that are either immunocompetent or immunodeficient (with no intermediate states and no direct measurements of immune effector cell populations), we do not explicitly model the immune cell numbers but rather have immune status dependent state transitions.

2.2.2. Stochastic Transitions between Tumor Cell States. The experimental data shows the variability in relapse kinetics, which a deterministic model cannot capture. Hence, stochasticity was added to the model. We use random sampling from a multinomial distribution (well approximated by binomial due to very low per time step probabilities) to represent a stochasticity in the number of cells transitioning from one state to another, enabling us to recapitulate the variability in tumor relapse (Figure 2).

Some parameters of the model are immune system dependent, some are MYC expression dependent, and others are tumor type dependent (Table 1).

Figure 3 shows the governing equations for each of the 6 states. We integrated the equations using Euler’s method with a time step (Δt) of 0.02 days per iteration, which was much faster than any of the kinetic parameters. Model parameters are explained in Table 1.

2.2.3. Delay Differential Equations. In biological processes, there are often “physical” delays making it vital to incorporate delays into the model in order to make the mathematical model closer to the real phenomenon. Examples of delay mathematical models in biology are population dynamics (e.g., Hutchinson’s equation), ecology (e.g., the Lotka-Volterra predator prey), and immunology (e.g., delay in immune system response). We have implemented delay differential equations (on top of our stochastic framework) for the apoptosis state. There is a delay between when a cell commits to apoptosis and when cell death actually occurs. This is important since these cells that have committed to apoptosis (in state A) are still producing BLI signals, which are being measured. There is also a delay between when a cell commences mitosis and when daughter cells are actually produced, but we chose not to explicitly include this since at this time, the comparison to biological results is not significantly affected by whether or not we explicitly model the mitotic phase.

Although our modeling philosophy has been to create the simplest possible model that could explain the salient features of our experimental data, we found multiple tumor states and stochastic transitions without explicit delays to be

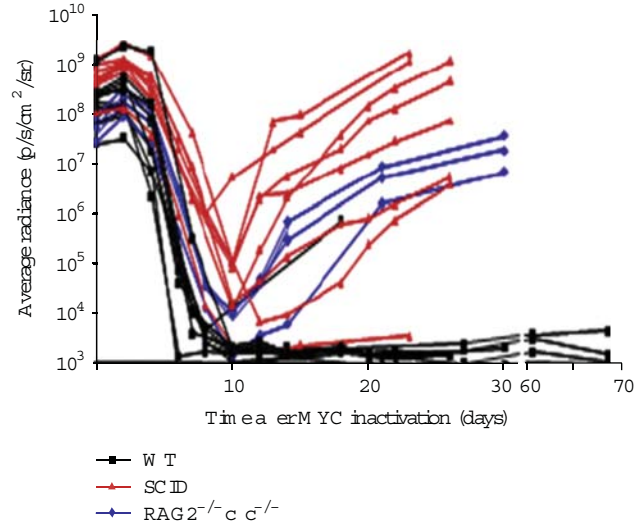


FIGURE 2: Tumor regression and relapse kinetics as measured by bioluminescence imaging. Wildtype (WT) are immunocompetent mice while SCID and $RAG2^{-/-}c\gamma c^{-/-}$ are immunodeficient mice. Excerpted from [27].

insufficient to model some of our observations from bioluminescent imaging and immunohistochemistry. In particular, we found that proliferative arrest occurs almost immediately after oncogene inactivation but apoptosis was delayed for approximately 4-5 days.

Figure 4 shows the tumor growth kinetics in the absence of delay. This captures the necessity of adding delay to accurately represent the biology.

3. Results and Discussion

By running simulations, our model recapitulates features such as the different rates and delays in the tumor kinetics measured from *in vivo* experimental data from mouse models. Several emergent behaviors of the model have come to light. Empirically, proliferative arrest immediately follows oncogene inactivation but there is a 4-5 day delay in apoptosis. This was modeled by incorporating a delay between irreversible commitment to apoptosis and actual cell death.

Furthermore, the rate of mutations leading to tumor relapse (which is captured in the term $K_{relapse}$) had almost no bearing on the kinetics of the relapse. Instead, $K_{E-prolif}$ dominates tumor relapse kinetics. We performed a basic simulation of regressing tumors followed by increasing the rate of tumor cells from “MYC off” to “Escaped” (increasing the term $K_{relapse}$) that would have otherwise gone to “Oncogene Inactivation Induced Senescence.” The rate governing mutations leading to the transition from “MYC off” to “Escaped” had little effect on deterministic simulations, which were dominated by the growth rate of the escaped cells, but a significant effect on our stochastic model. The relapse of tumors due to absence of immune-mediated senescence is demonstrated in Figure 6. This indicates that the immune system plays a significant role in sustained tumor regression.

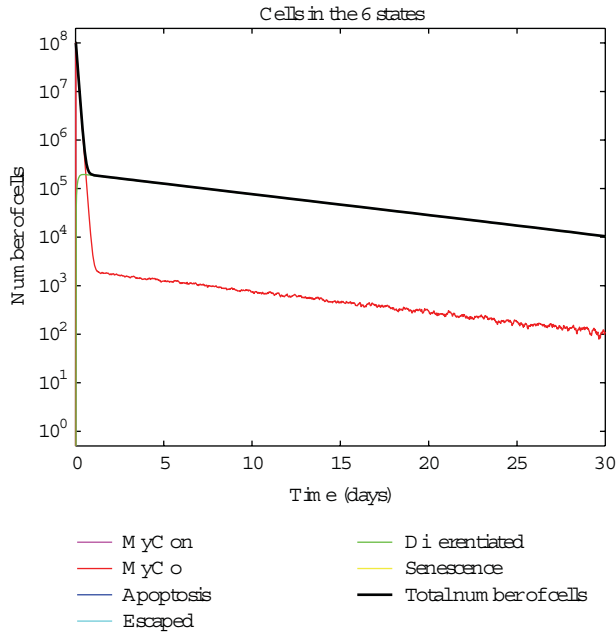


FIGURE 4: Simulated tumor growth kinetics with no delay and no escape of tumor cells from the conditional control of MYC due to an intact immune system. Note the lack of delay in the decrease of tumor cells as is observed in days 0–5.

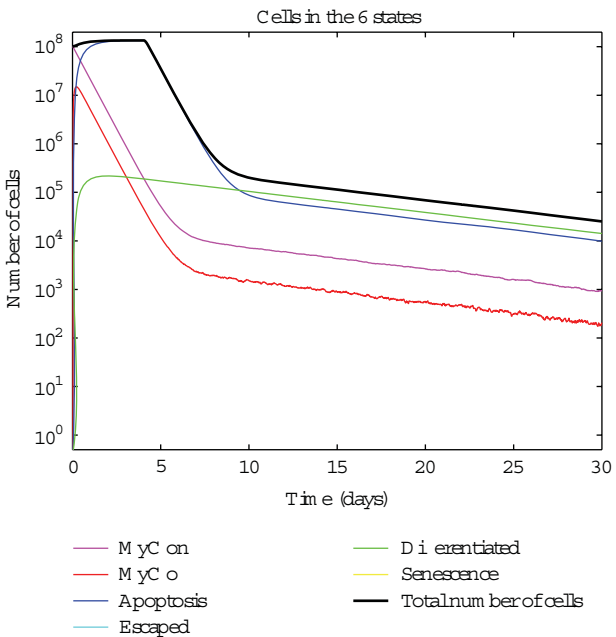


FIGURE 5: Simulated tumor growth kinetics with no escape of tumor cells from the conditional control of MYC due to an intact immune system. Note the correctly modeled delay in tumor cell death as is observed in Figure 2.

that model tumor-immune interactions similar to predator-prey dynamics.

The initial results from our new model are helping to quantitatively hypothesize about the sequence of cellular

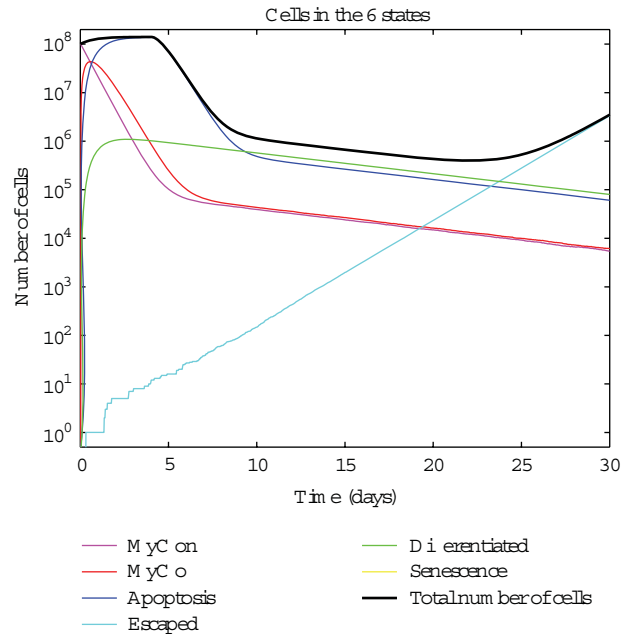


FIGURE 6: Simulated tumor growth kinetics with a low (but nonzero) rate of tumor cells escaping from conditional control of MYC due to a compromised immune system. Note the early growth kinetics of the escaped tumor cell population demonstrates stochastic variability that affects the timing of the relapse.

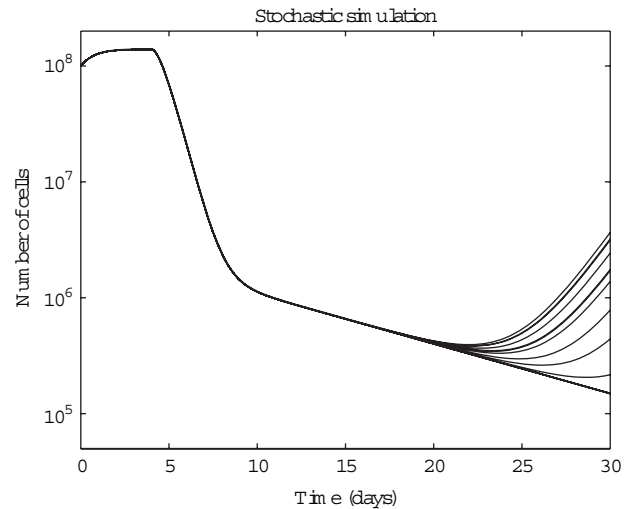


FIGURE 7: Variability in relapse kinetics captured using 20 stochastic simulations.

mechanisms involved in tumor response to oncogene inactivation such as might be encountered using targeted therapeutics, and the interactions among them. These hypotheses will be tested experimentally using the same conditional control mouse models and *in vivo* bioluminescence imaging (and immunohistochemistry). We aim to eventually use this model to help to optimize multipronged treatment regimens for patients so as to defer or even eliminate tumor relapse. Avoiding immune destruction is a crucial hallmark because it

has been shown that immune cells, CD4+ T cells in particular, are a required component for senescence, shutdown of angiogenesis and chemokine expression that result in sustained tumor regression [26, 27, 32–34].

This finding is captured in our model. If residual disease reaches a low enough level, relapse can be prevented. Large tumors have a great number of cells that can transition through an extremely low-likelihood event to the “Escaped” state. If the tumor is small enough, not enough cells remain to make it likely that any one will achieve the very low-likelihood “Escaped” state. Tumor burden is also an important factor in tumor regression mediated through the immune system. The immune system might not be able to attack and eliminate the tumor fast enough if the tumor burden is too high. Currently our model does not account for this but we are adding more sophisticated immune system components to the model in order to show this. Our model is simple in that all but one state (with explicit delay) have memoryless transitions and yet the model is able to recapitulate the complex response of tumors to oncogene inactivation. No age structuring of cells is required as with some other models [35, 36].

Our model offers more fidelity than models in the literature that just capture tumor cells in a single variable [37] because we are able to capture the various cellular states. These states have not yet been quantitatively captured over time *in vivo*. We are working on imaging methods to quantify distinct cellular processes such as apoptosis, and senescence, proliferation, which will eventually allow us to further validate our simulation results. Future work will include validating novel predictions from our model *in vivo*.

Acknowledgment

The authors gratefully acknowledge support from NIH P50 CA114747 (ICMIC@Stanford) and R01 CA180387.

References

- [1] I. B. Weinstein, M. Begemann, P. Zhou et al., “Disorders in cell circuitry associated with multistage carcinogenesis: exploitable targets for cancer prevention and therapy,” *Clinical Cancer Research*, vol. 3, no. 12, pp. 2696–2702, 1997.
- [2] G. D. Demetri, “Identification and treatment of chemoresistant inoperable or metastatic GIST: experience with the selective tyrosine kinase inhibitor imatinib mesylate (STI571),” *European Journal of Cancer*, vol. 38, pp. S52, supplement–S59, 2002.
- [3] B. J. Druker, M. Talpaz, D. J. Resta et al., “Efficacy and safety of a specific inhibitor of the BCR-ABL tyrosine kinase in chronic myeloid leukemia,” *New England Journal of Medicine*, vol. 344, no. 14, pp. 1031–1037, 2001.
- [4] H. Kantarjian, C. Sawyers, A. Hochhaus et al., “Hematologic and cytogenetic responses to imatinib mesylate in chronic myelogenous leukemia,” *New England Journal of Medicine*, vol. 346, no. 9, pp. 645–652, 2002.
- [5] E. Weisberg, P. W. Manley, W. Breitenstein et al., “Characterization of AMN107, a selective inhibitor of native and mutant Bcr-Abl,” *Cancer Cell*, vol. 7, pp. 129–141, 2005.
- [6] F. A. Shepherd, J. R. Pereira, T. Ciuleanu et al., “Erlotinib in previously treated non-small-cell lung cancer,” *New England Journal of Medicine*, vol. 353, no. 2, pp. 123–132, 2005.
- [7] M. G. Kris, R. B. Natale, R. S. Herbst et al., “Efficacy of gefitinib, an inhibitor of the epidermal growth factor receptor tyrosine kinase, in symptomatic patients with non-small cell lung cancer: a randomized trial,” *Journal of the American Medical Association*, vol. 290, no. 16, pp. 2149–2158, 2003.
- [8] G. Giaccone, “Epidermal growth factor receptor inhibitors in the treatment of non-small-cell lung cancer,” *Journal of Clinical Oncology*, vol. 23, no. 14, pp. 3235–3242, 2005.
- [9] R. S. Herbst, M. Fukuoka, and J. Baselga, “Gefitinib—a novel targeted approach to treating cancer,” *Nature Reviews Cancer*, vol. 4, no. 12, pp. 956–965, 2004.
- [10] P. T. Tran, P. K. Bendapudi, H. J. Lin et al., “Survival and death signals can predict tumor response to therapy after oncogene inactivation,” *Science Translational Medicine*, vol. 3, p. 103ra99, 2011.
- [11] M. Gossen and H. Bujard, “Tight control of gene expression in mammalian cells by tetracycline-responsive promoters,” *Proceedings of the National Academy of Sciences of the United States of America*, vol. 89, no. 12, pp. 5547–5551, 1992.
- [12] P. A. Furth, L. S. Onge, H. Boger et al., “Temporal control of gene expression in transgenic mice by a tetracycline-responsive promoter,” *Proceedings of the National Academy of Sciences of the United States of America*, vol. 91, no. 20, pp. 9302–9306, 1994.
- [13] C. Arvanitis and D. W. Felsher, “Conditional transgenic models define how MYC initiates and maintains tumorigenesis,” *Seminars in Cancer Biology*, vol. 16, no. 4, pp. 313–317, 2006.
- [14] C. M. Shachaf, A. J. Gentles, S. Elchuri et al., “Genomic and proteomic analysis reveals a threshold level of MYC required for tumor maintenance,” *Cancer Research*, vol. 68, no. 13, pp. 5132–5142, 2008.
- [15] D. W. Felsher and J. M. Bishop, “Reversible tumorigenesis by MYC in hematopoietic lineages,” *Molecular Cell*, vol. 4, no. 2, pp. 199–207, 1999.
- [16] D. Marinkovic, T. Marinkovic, B. Mahr, J. Hess, and T. Wirth, “Reversible lymphomagenesis in conditionally c-MYC expressing mice,” *International Journal of Cancer*, vol. 110, no. 3, pp. 336–342, 2004.
- [17] P. S. Choi, J. van Riggelen, and A. J. Gentles, “Lymphomas that recur after MYC suppression continue to exhibit oncogene addiction,” *Proceedings of the National Academy of Sciences of the United States of America*, vol. 108, pp. 17432–17437, 2011.
- [18] C. Arvanitis, P. K. Bendapudi, J. R. Tseng, S. S. Gambhir, and D. W. Felsher, “¹⁸F and ¹⁸F PET imaging of osteosarcoma to non-invasively monitor in situ changes in cellular proliferation and bone differentiation upon MYC inactivation,” *Cancer Biology and Therapy*, vol. 7, no. 12, pp. 1947–1951, 2008.
- [19] M. Jain, C. Arvanitis, K. Chu et al., “Sustained loss of a neoplastic phenotype by brief inactivation of MYC,” *Science*, vol. 297, no. 5578, pp. 102–104, 2002.
- [20] S. Beer, A. Zetterberg, R. A. Ihrie et al., “Developmental context determines latency of MYC-induced tumorigenesis,” *PLoS Biology*, vol. 2, no. 11, article e332, 2004.
- [21] R. B. Boxer, J. W. Jang, L. Sintasath, and L. A. Chodosh, “Lack of sustained regression of c-MYC-induced mammary adenocarcinomas following brief or prolonged MYC inactivation,” *Cancer Cell*, vol. 6, no. 6, pp. 577–586, 2004.
- [22] J. A. Aguirre-Ghisso, “Models, mechanisms and clinical evidence for cancer dormancy,” *Nature Reviews Cancer*, vol. 7, no. 11, pp. 834–846, 2007.

- [23] C. M. Shachaf and D. W. Felsher, "Tumor dormancy and MYC inactivation: pushing cancer to the brink of normalcy," *Cancer Research*, vol. 65, no. 11, pp. 4471–4474, 2005.
- [24] C. H. Wu, J. Van Riggelen, A. Yetil, A. C. Fan, P. Bachireddy, and D. W. Felsher, "Cellular senescence is an important mechanism of tumor regression upon c-Myc inactivation," *Proceedings of the National Academy of Sciences of the United States of America*, vol. 104, no. 32, pp. 13028–13033, 2007.
- [25] S. Kazerounian, K. O. Yee, and J. Lawler, "Thrombospondins: from structure to therapeutics—thrombospondins in cancer," *Cellular and Molecular Life Sciences*, vol. 65, no. 5, pp. 700–712, 2008.
- [26] S. Giuriato, S. Ryeom, A. C. Fan et al., "Sustained regression of tumors upon MYC inactivation requires p53 or thrombospondin-1 to reverse the angiogenic switch," *Proceedings of the National Academy of Sciences of the United States of America*, vol. 103, no. 44, pp. 16266–16271, 2006.
- [27] K. Rakhra, P. Bachireddy, T. Zabuawala et al., "CD4⁺ T cells contribute to the remodeling of the microenvironment required for sustained tumor regression upon oncogene inactivation," *Cancer Cell*, vol. 18, pp. 485–498, 2010.
- [28] A. Corthay, D. K. Skovseth, K. U. Lundin et al., "Primary anti-tumor immune response mediated by CD4⁺ T cells," *Immunity*, vol. 22, no. 3, pp. 371–383, 2005.
- [29] D. W. Felsher, "Tumor Dormancy: death and resurrection of cancer as seen through transgenic mouse models," *Cell Cycle*, vol. 5, no. 16, pp. 1808–1811, 2006.
- [30] K. D. Robertson and P. A. Jones, "DNA methylation: past, present and future directions," *Carcinogenesis*, vol. 21, no. 3, pp. 461–467, 2000.
- [31] R. Shanmuganathan, N. B. Basheer, L. Amirthalingam, H. Muthukumar, R. Kaliaperumal, and K. Shanmugam, "Conventional and nanotechniques for DNA methylation profiling," *Journal of Molecular Diagnostics*, vol. 15, pp. 17–26, 2013.
- [32] Z. Qin and T. Blankenstein, "CD4⁺ T cell-mediated tumor rejection involves inhibition of angiogenesis that is dependent on IFN γ receptor expression by nonhematopoietic cells," *Immunity*, vol. 12, no. 6, pp. 677–686, 2000.
- [33] N. Bercovici and A. Trautmann, "Revisiting the role of T cells in tumor regression," *Oncoimmunology*, vol. 1, pp. 346–350, 2012.
- [34] C. V. Ngo, M. Gee, N. Akhtar et al., "An in vivo function for the transforming Myc protein: elicitation of the angiogenic phenotype," *Cell Growth and Differentiation*, vol. 11, no. 4, pp. 201–210, 2000.
- [35] M. D. Johnston, C. M. Edwards, W. F. Bodmer, P. K. Maini, and S. J. Chapman, "Mathematical modeling of cell population dynamics in the colonic crypt and in colorectal cancer," *Proceedings of the National Academy of Sciences of the United States of America*, vol. 104, no. 10, pp. 4008–4013, 2007.
- [36] R. Ganguly and I. K. Puri, "Mathematical model for the cancer stem cell hypothesis," *Cell Proliferation*, vol. 39, no. 1, pp. 3–14, 2006.
- [37] R. Eftimie, J. L. Bramson, and D. J. D. Earn, "Interactions between the immune system and cancer: a brief review of non-spatial mathematical models," *Bulletin of Mathematical Biology*, vol. 73, no. 1, pp. 2–32, 2011.

Research Article

Optimization of Contrast-to-Tissue Ratio by Adaptation of Transmitted Ternary Signal in Ultrasound Pulse Inversion Imaging

Sébastien Ménigot^{1,2,3} and Jean-Marc Girault^{2,3}

¹ IUT Ville d'Avray, Université Paris Ouest Nanterre La Défense, 92 410 Ville d'Avray, France

² UMR-S930, Université François-Rabelais de Tours, 37032 Tours, France

³ U 930, Inserm, 37032 Tours, France

Correspondence should be addressed to Sébastien Ménigot; sebastien.menigot@univ-tours.fr

Received 20 December 2012; Accepted 18 February 2013

Academic Editor: Kumar Durai

Copyright © 2013 S. Ménigot and J.-M. Girault. This is an open access article distributed under the Creative Commons Attribution License, which permits unrestricted use, distribution, and reproduction in any medium, provided the original work is properly cited.

Ultrasound contrast imaging has provided more accurate medical diagnoses thanks to the development of innovating modalities like the pulse inversion imaging. However, this latter modality that improves the contrast-to-tissue ratio (CTR) is not optimal, since the frequency is manually chosen jointly with the probe. However, an optimal choice of this command is possible, but it requires precise information about the transducer and the medium which can be experimentally difficult to obtain, even inaccessible. It turns out that the optimization can become more complex by taking into account the kind of generators, since the generators of electrical signals in a conventional ultrasound scanner can be unipolar, bipolar, or tripolar. Our aim was to seek the ternary command which maximized the CTR. By combining a genetic algorithm and a closed loop, the system automatically proposed the optimal ternary command. In simulation, the gain compared with the usual ternary signal could reach about 3.9 dB. Another interesting finding was that, in contrast to what is generally accepted, the optimal command was not a fixed-frequency signal but had harmonic components.

1. Introduction

Intravenous injection of ultrasound contrast agents containing microbubbles has revolutionized medical ultrasound imaging in the past twenty years by making possible extraction of physiological and pathological information [1]. Subsequently, the contrast between the tissue perfused by the microbubbles and the nonperfused tissue, that is, contrast-to-tissue ratio (CTR), has been improved by taking into account the nonlinear behaviour of microbubbles, as in the second harmonic imaging [2], subharmonic imaging [3], superharmonic imaging [4], and attenuation correction [5].

However, the effects of the propagation of the ultrasound wave have limited these improvements since the tissue can generate nonlinearities, thereby reducing the CTR. Furthermore, since a good separation of the harmonic components requires a limited pulse bandwidth [6], the axial resolution

has been limited. To overcome this drawback, certain discrete encoding techniques such as pulse inversion imaging [7], power modulation [8], contrast pulse sequencing [9], and pulse subtraction [10] have been developed to ensure a good axial resolution while increasing the CTR. Finally, to solve the trade-off between resolution and penetration, other imaging methods such as harmonic chirp imaging [11] have extended this principle for continuous encoding.

However, whatever the imaging system used in clinical practice, the fact remains that the excitation settings are manufacturer and user dependent. From our point of view, these settings are not optimal, since they must take into account the explored medium. For adjusting these settings to any examination, it is necessary to correctly adjust this excitation. To do so, the optimal command framework in which the problem takes place is presented. Thus, the problem

can be written in such a way that the optimal command $x^*(n)$ of the ultrasound imaging system provides the best CTR:

$$x^*(n) = \underset{x(n)}{\operatorname{argmax}} (\operatorname{CTR}(x(n))), \quad (1)$$

where $x(n)$ is the signal transmitted and n is the discrete time.

Some solutions have been already proposed to solve (1) by either minimizing the tissue backscattering or maximizing the microbubble backscattering. In this context, two interesting approaches have been proposed. On the one hand, time reversal imaging only makes it possible to reduce the nonlinearities of the tissue backscattering [12]. Unfortunately, the formalism is linear and cannot take into account the microbubble nonlinearities to maximize them. On the other hand, an analytic solution has been proposed for the microbubble backscattering [13]. However, this theoretical solution requires the knowledge of all physical properties about the microbubble, the surrounding medium, and the transducer. This *a priori* information which can be accessible with difficulty, even completely inaccessible, led this analytical solution to be inapplicable in practice.

To overcome these limitations, a novel method has recently been proposed. This approach solves (1) by transcribing a shape optimization into a suboptimal parametric optimization [14]. In this latter work, the parameter to be optimized was the transmit frequency. Thus, the optimal frequency was the transmit frequency which optimized the cost-function CTR. The computation of this optimal frequency was obtained automatically by using a simple algorithm based on the gradient. Although this method is simple, it lays the groundwork of the optimal command. Unfortunately, this approach is not completely satisfactory since the initial fixed waveform may not be suitable [15]. Furthermore, this approach does not take into account the specific features of electrical signal generators in conventional ultrasound scanners. For these ultrasound scanners, transmitters are usually unipolar (voltage impulse V), bipolar (voltage $-V$ or V), or tripolar (voltage $-V$, 0 , or V) generators, because their electronic conception is easier. Recently, the nature of the generator has been taken into account in order to improve the signal-to-noise ratio [16] and microbubble detection [17] by combining a binary waveform and an advanced imaging approach. However, no input optimization process has yet been proposed to find the optimal command.

Finally, no method has been proposed to date to overcome this problem satisfactorily and optimally by taking into account the tripolar transmitter constraint. Since (i) one of the most commonly used ultrasound imaging approaches is pulse inversion imaging and (ii) a conventional transmitter is a tripolar generator, the aim of this study was to automatically determine the optimal ternary command for the ultrasound pulse inversion imaging system to provide the best CTR:

$$x^*(n) = \underset{x(n) \in \{-1, 0, 1\}, \forall n}{\operatorname{argmax}} (\operatorname{CTR}(x(n))). \quad (2)$$

We therefore modified the current system (including a tripolar ultrasound transmitter) by including feedback. To resolve the digital waveform optimization, we proposed using

a genetic algorithm through simulations. The advantage of the method was that no *a priori* information was required in order to find the optimal ternary command.

2. Closed-Loop System

The principle of pulse inversion imaging including feedback is described in Figure 1. For an individual solution at the iteration k , two ternary pulses, $x_{k,1}(n)$ and $x_{k,2}(n)$, with opposite phases were transmitted. The sum $z_k(n)$ of the two respective echoes, $y_{k,1}(n)$ and $y_{k,2}(n)$, formed a radiofrequency line l_k . By taking into account the CTR_k estimated on this radiofrequency line l_k , a new transmitted ternary signal $x_{k+1}(n)$ was proposed by the algorithm to optimize the CTR_{k+1} .

2.1. Transmitted Ternary Signal. The ternary pulse signal $x_{k,q}(n)$ was digitally computed with MATLAB (MathWorks, Natick, MA, USA):

$$x_{k,q}(n) = \begin{cases} A \cdot w_k(n) & \text{if } q = 1, \\ -A \cdot w_k(n) & \text{if } q = 2. \end{cases} \quad (3)$$

The ternary signal $w_k(n)$ was defined on a duration T , which corresponded to 100% of the fractional bandwidth of the transducer. It was thus constructed from N_s samples, where each sample could take the value -1 , 0 , or 1 .

The amplitude of the driving pressure A was then adjusted so that the power of the pulse $x_{k,p}(t)$ was constant to $P_{x_{\text{ref}}}$ for all ternary signals transmitted:

$$A = \sqrt{\frac{A_0^2 \cdot P_{x_{\text{ref}}}}{P_w}}, \quad (4)$$

where the power $P_{x_{\text{ref}}}$ was calculated for a signal x_{ref} which was the impulse response of the transducer with a driving pressure A_0 . The power P_w was the power of the signal $w_{k,p}$. The power of the transmitted wave thus remained constant by adjusting the amplitude signal A .

2.2. Cost Function. The aim was to maximize the contrast between the tissue perfused by the microbubbles and the nonperfused tissue by selecting the transmitted signal $x(n)$. Since the usual contrast estimator in ultrasound contrast imaging is the CTR, the cost function was CTR_k computed from a line $z_k(n)$:

$$z_k(n) = y_{k,1}(n) + y_{k,2}(n), \quad (5)$$

where $y_{k,p}(n)$ is the echo of the transmitted pulse $x_{k,p}(n)$. Thus, the CTR_k is defined as the ratio of the power $P_{b,k}$ backscattered by the area of the perfused medium to the power $P_{t,k}$ backscattered by the area of the nonperfused medium [18] as follows:

$$\operatorname{CTR}_k = 10 \cdot \log_{10} \left(\frac{P_{b,k}}{P_{t,k}} \right). \quad (6)$$

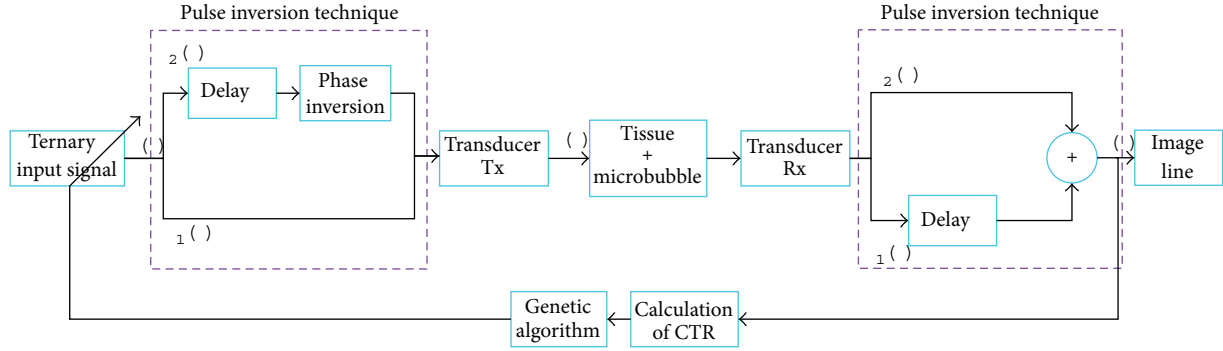


FIGURE 1: Block diagram of CTR optimization in pulse inversion imaging.

These powers were computed from the lines $z_k(n)$ of the pulse inversion image. Note that the areas were delineated manually before the optimization process, but a segmentation step could be implemented to help the delineate process.

2.3. Genetic Algorithm. The seeking of the optimal excitation $x^*(n)$ consisted in (i) transmitting ternary stochastic signals $w_k(n)$ through the medium and in (ii) selecting the optimal ternary signal which maximized the cost function. However, since this latter step required a large number of ternary stochastic signals, to reduce the computational time, we proposed using a metaheuristic. This metaheuristic based on the principle of biological reproduction [19] is a genetic algorithm. It found the optimum by setting a chromosome [20], that is, a vector composed of N_s samples of the ternary signal $w_k(n)$.

The ternary genetic algorithm was based on a binary genetic algorithm [21]. In our case, at each iteration k , a generation k with M ternary individual solutions (sample vectors) was tested, where the probability of the sample value was uniform between -1 , 0 , or 1 . As proposed in [21], the number M of individual solutions per generation was 12.

For the next generation $k + 1$, the selection operator only conserved the $M/2$ best individual solutions which maximized the CTR. These vectors became pairs and mates. The best parent was then mixed with one of the $M/2 - 1$ remaining parents by the crossover operator. The offspring was constituted of part of the first parent samples until the crossover point and part of the second parent samples from the crossover point. Note that the crossover point was randomly selected between the first and the last sample. An offspring of $M/2$ new individual solutions thus contained the ternary signal of both parents.

Finally 40% of the samples were mutated so that the optimization was robust. The best individual solution was the optimal ternary command for the generation k . Note that a small population and a high mutation rate were chosen to solve the trade-off between robustness and the computation time due to sorting of each individual solution [21].

3. Simulation Model

The simulation model was constructed on the pulse inversion imaging system (Figure 1). It was composed of different phases: transmission, 2D nonlinear propagation, nonlinear oscillations of microbubbles, and reception [14]. A pulse wave was propagated nonlinearly into an attenuating medium without microbubbles. This wave, composed of harmonic components, excited a microbubble in the vascular system. The nonlinear oscillations of this microbubble were backscattered and measured by the receiver.

3.1. Nonlinear Propagation in Tissue. A ternary signal $x_{k,1}(n)$ was generated digitally and filtered by the transfer function of a realistic transducer, centred at $f_c = 4$ MHz with a fractional bandwidth of 75% at -3 dB. The 2D nonlinear wave propagation into the medium was obtained by solving Anderson's model based on a pseudospectral derivative and a time-domain integration algorithm [22]. This solver required three grids: a grid of mean density of $928 \text{ kg} \cdot \text{m}^{-3}$, a grid of mean speed of sound of $1578 \text{ m} \cdot \text{s}^{-1}$, and a grid of B/A nonlinearity parameter of 6.7 [23]. The scatterers were generated randomly by weakly modifying the density grid of $\pm 0, 5 \text{ kg} \cdot \text{m}^{-3}$ and the speed grid of $\pm 0, 5 \text{ m} \cdot \text{s}^{-1}$. Note that an attenuation of $0.45 \text{ dB} \cdot \text{MHz}^{-1.05} \cdot \text{cm}^{-1}$ was used. Finally, the signal backscattered by tissue was recorded, and the driving pressure at 15 mm was included into the microbubble model described below.

3.2. Microbubble. The simulated ultrasound contrast agent had the properties of encapsulated microbubbles used in clinical practice with a mean diameter of $2.5 \mu\text{m}$ [24] and a resonance frequency of 2.6 MHz [25]. The acoustic response was computed for one microbubble from Marmottant's model [26] based on the Rayleigh-Plesset equation and the polytropic transformation. Finally, since the pressure was low in comparison with the transmitted pressure, the echo of the microbubble was deduced from the oscillation [27] without including nonlinear propagation. Note that in order to simulate the mean behaviour of a microbubble cloud, we hypothesized that the response of a cloud of N_b microbubbles was N_b times the response of a single microbubble with the

TABLE 1: CTR measured if the signal transmitted is (i) a ternary signal at two-thirds of the central frequency f_c of the transducer, (ii) a ternary signal at the optimal frequency f_{opt} , or (iii) the optimal ternary command.

	$2/3 f_c = 2.67 \text{ MHz}$	$f_{\text{opt}} = 1.9 \text{ MHz}$	Optimal ternary signal
CTR (dB)	18.1	21.2	22

mean properties. To simplify, the microbubble response was thus multiplied by N_b in order to simulate a mean nonlinear behaviour of a 1/2000 diluted microbubble cloud. Moreover, to be more realistic, the attenuation effects due to the high concentration of microbubbles were taken into account [28] for this dilution.

The echoes from tissue and microbubbles were added and filtered by the transfer function of the transducer to construct the first echo for the transmitted signal $x_{k,1}(n)$. The simulation process was repeated for the transmitted ternary pulse $x_{k,2}(n)$ to construct the second echo. Finally, the radiofrequency line l_k was constructed from $z_k(n)$ described by (5).

4. Results

The optimization process was applied to the previous simulation model. The driving pressure A_0 was set at 400 kPa. The duration T of the ternary signal represented 100% of the fractional bandwidth of the transducer, that is, $T = 0.3 \mu\text{s}$. According to the sampling rate required by the simulation model, there were 40 samples in $0.3 \mu\text{s}$; therefore, $N_s = 40$.

To demonstrate the efficacy of the new method, the results were compared to those of the two usual transmitted signals. To construct them, Gaussian-modulated sinusoidal pulses were digitalized to obtain a ternary signal. Their bandwidth represented 100% of the fractional bandwidth of the transducer, and their transmitted power was $P_{x_{\text{ref}}}$. Their transmit frequencies were set at (i) two-thirds of the central frequency f_c of the transducer [29] ($2/3 f_c = 2.67 \text{ MHz}$) and at (ii) the optimal frequency f_{opt} . Note that this optimal frequency f_{opt} enabled to maximize the cost function CTR as presented in [14].

Table 1 summarizes the CTR measured for the optimal ternary signal and the two usual ternary signals. By using frequency optimization, it was possible to achieve a sub-optimal solution, better than the transmitted signal at the usual transmit frequency. However, the CTR was higher with the transmitted ternary signal. This CTR value could not be achieved with the usual ternary signal digitalized from a Gaussian-modulated sinusoidal pulse, although the transmit frequency was optimized.

Figure 2 shows the best CTR as a function of generation k . As an illustration, this result was compared with the two usual ternary signals. After 239 generations, the CTR achieved an optimal value that was higher than the frequency setting cases. The gain reached 3.9 dB in comparison with the usual fixed-frequency transmitted signal and 0.8 dB in comparison with the transmitted signal at the optimal frequency f_{opt} .

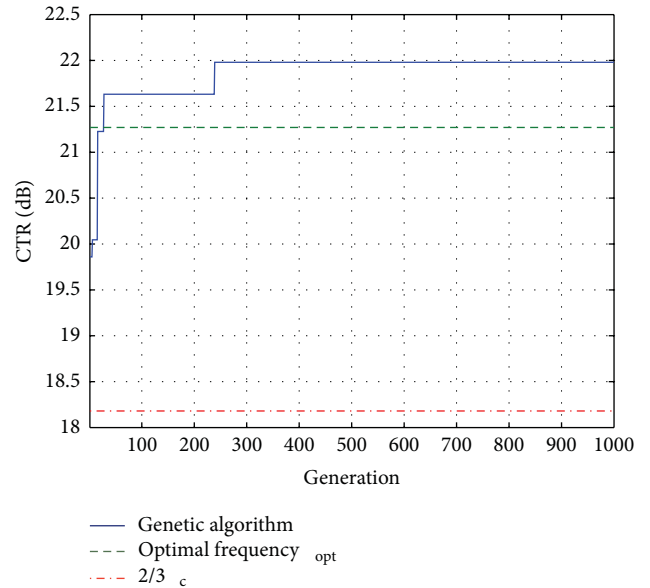


FIGURE 2: Simulation of automatic optimization of the contrast-to-tissue ratio (CTR) by a transmitted ternary signal. The optimization was compared to two ternary signals, where the transmit frequency was at the optimal frequency and at two-thirds of the central frequency of the transducer.

Figure 3(a) shows the optimal ternary command $w_{\text{opt}}(n)$. As an illustration, Figure 3(b) shows the signal $p(n)$ of the transducer output (Figure 1) transmitted to the tissue when $w(n)$ was the optimal ternary signal (Figure 3(a)), and the corresponding backscattered signal was shown in Figure 3(c). Their respective spectra were presented in Figure 3(d). Unlike a usual fixed-frequency transmitted signal, the optimal transmitted signal had nonlinear components. Note that the nonlinear components backscattered by the tissue and the microbubbles remained, because in pulse inversion imaging the linear component was suppressed.

5. Discussion and Conclusions

From results derived from Figure 2, the optimal command methods, presented in [14] and here, outperformed the nonoptimized reference method. Although these two methods are optimal command methods, they presented some significant differences. The first method [14] by imposing a waveform defined by a frequency parameter constitutes an optimal monoparametric solution, and the second method proposed here by imposing a ternary constraint on the waveform constituted an optimal multisample solution.

In this latter method, ternary sequences were automatically transmitted through a pulse inversion imaging system in order to optimize the CTR. This optimization was performed without taking into account *a priori* information about the medium or the transducer, except the fact that this method required a selection of two regions of interest (with and

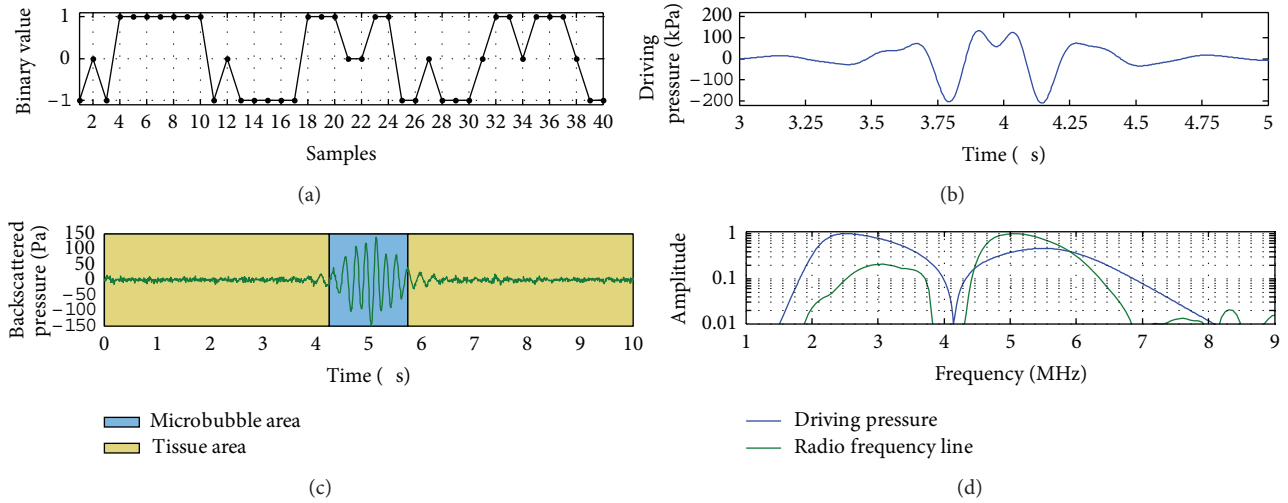


FIGURE 3: (a) Optimal transmitted ternary signal $x_1(n)$ obtained by genetic algorithm, (b) Signal $p(n)$ at the transducer output (Figure 1), when $w(n)$ was the optimal ternary signal, (c) the radiofrequency line, and (d) their spectra.

without microbubbles). The delineation of these regions of interest constituted both the strength of the method, since it enabled to define the CTR cost function and a drawback for fully perfused tissue for which no CTR computation is possible. Note that to partly overcome this problem, it can be recommended to change the organ section in a view to delineate a nonperfused area.

Nevertheless, by disregarding the latter drawback, the closed-loop system had the advantage to provide an optimal ternary command. By using this optimal ternary command, the CTR was higher than that with the usual ternary signals digitalized from Gaussian-modulated sinusoidal pulses at a fixed transmit frequency. This optimal setting proposed a filtered ternary wave composed of harmonic components transmitted to the medium being explored. While most researchers have focused on using a fixed-frequency transmitted signal, the better solution was to find a transmitted signal composed of harmonic components. These harmonic components present in the transmitted signal did not affect the CTR, because the pulse inversion properties ensured the extraction of nonlinearities generated only by the medium. This property may explain the compromise between maximizing microbubble backscattering and minimizing tissue backscattering. Furthermore, since the transducer bandwidth was not broad enough, the double frequency of the second harmonic component was not present in the backscattered signal. However, since the process reached the optimum without the presence of the double frequency of this component, the only presence of a linear interaction acting on the transmitted second harmonic component seemed to play a crucial role in the optimization process.

Finally, the last advantage which seemed to be important was that the method automatically adjusted the transmitted ternary signal for any nonlinear and attenuating medium to

be explored. The reason of this benefit was that the cost function, exclusively computed from the mean power of the output system, was independent of the microbubble size distribution. Indeed, as the backscattered mean power corresponds to an average operating on the whole spectrum, thus its value is independent of the frequency distribution, whether the spectrum had a narrow bandwidth (same microbubble size) or a large bandwidth (polydisperse microbubble size). Thus, even if the assumptions of the simulation model were simplified, the process of the CTR optimization completely ignored the nature of different underlying processes as the multiple scattering or the microbubble speckle. The method can therefore be applied to any medium to be explored.

For future integration in an ultrasound imaging system, the time to achieve optimization is crucial. Firstly, the CTR computation from regions of interest ($L \times L$ size) in the image required $2(2L + 1)^2 + 1$ operations. Secondly, the genetic algorithm required $0.4(12N_s) + 6$ random selections per generation to achieve the optimum. Taking into account the computing power available for a personal computer, the two last operations must not slow down the optimization process. However, the number of generations to achieve the optimum may be a limiting factor. Since the frame rate can reach 2000 Hz in some ultrasound scanners, this limitation should be relative. We therefore estimated that the optimization should take less than 5 seconds.

To conclude, the method reported ensured optimal CTR by selecting the appropriate transmitted ternary signal. The method could be applied to ultrasound imaging without using programmable analogue transmitters in contrast to transmit frequency optimization. Manufacturers and clinicians would not themselves need to tune the transmitted signal. This new approach could open up optimal commands for ultrasound imaging. The next step will be to implement it in an ultrasound scanner. Moreover, the future approach

should take into account the fact that the optimal transmitted signal must be composed of harmonic components.

References

- [1] P. J. A. Frinking, A. Bouakaz, J. Kirkhorn, F. J. Ten Cate, and N. De Jong, "Ultrasound contrast imaging: current and new potential methods," *Ultrasound in Medicine and Biology*, vol. 26, no. 6, pp. 965–975, 2000.
- [2] P. N. Burns, "Instrumentation for contrast echocardiography," *Echocardiography*, vol. 19, no. 3, pp. 241–258, 2002.
- [3] F. Forsberg, W. T. Shi, and B. B. Goldberg, "Subharmonic imaging of contrast agents," *Ultrasonics*, vol. 38, no. 1, pp. 93–98, 2000.
- [4] A. Bouakaz, S. Frigstad, F. J. Ten Cate, and N. de Jong, "Super harmonic imaging: a new imaging technique for improved contrast detection," *Ultrasound in Medicine and Biology*, vol. 28, no. 1, pp. 59–68, 2002.
- [5] M. X. Tang, J. M. Mari, P. N. T. Wells, and R. J. Eckersley, "Attenuation correction in ultrasound contrast agent imaging: elementary theory and preliminary experimental evaluation," *Ultrasound in Medicine and Biology*, vol. 34, no. 12, pp. 1998–2008, 2008.
- [6] M. A. Averkiou, "Tissue harmonic imaging," in *Proceedings of the IEEE Ultrasonics Symposium*, vol. 2, pp. 1563–1572, San Juan, Puerto Rico, October 2000.
- [7] D. H. Simpson, C. T. Chin, and P. N. Burns, "Pulse inversion Doppler: a new method for detecting nonlinear echoes from microbubble contrast agents," *IEEE Transactions on Ultrasonics, Ferroelectrics, and Frequency Control*, vol. 46, no. 2, pp. 372–382, 1999.
- [8] G. A. Brock-fisher, M. D. Poland, and P. G. Rafter, "Means for increasing sensitivity in non-linear ultrasound imaging systems," US Patent 5,577,505, 1996.
- [9] P. Phillips and E. Gardner, "Contrast-agent detection and quantification," *European Radiology*, vol. 14, pp. P4–P10, 2004.
- [10] J. M. G. Borsboom, A. Bouakaz, and N. De Jong, "Pulse subtraction time delay imaging method for ultrasound contrast agent detection," *IEEE Transactions on Ultrasonics, Ferroelectrics, and Frequency Control*, vol. 56, no. 6, pp. 1151–1158, 2009.
- [11] J. M. G. Borsboom, C. T. Chin, A. Bouakaz, M. Versluis, and N. De Jong, "Harmonic chirp imaging method for ultrasound contrast agent," *IEEE Transactions on Ultrasonics, Ferroelectrics, and Frequency Control*, vol. 52, no. 2, pp. 241–248, 2005.
- [12] O. Couture, J. F. Aubry, G. Montaldo, M. Tanter, and M. Fink, "Suppression of tissue harmonics for pulse-inversion contrast imaging using time reversal," *Physics in Medicine and Biology*, vol. 53, no. 19, pp. 5469–5480, 2008.
- [13] A. J. Reddy and A. J. Szeri, "Optimal pulse-inversion imaging for microsphere contrast agents," *Ultrasound in Medicine and Biology*, vol. 28, no. 4, pp. 483–494, 2002.
- [14] S. Ménigot, J.-M. Girault, I. Voicu, and A. Novell, "Optimization of contrast-to-tissue ratio by frequency adaptation in pulse inversion imaging," *IEEE Transactions on Ultrasonics, Ferroelectrics, and Frequency Control*, vol. 59, no. 11, pp. 2431–2438, 2012.
- [15] S. Ménigot and J.-M. Girault, "Analysis and modelling of the optimal command for an ultrasound pulse inversion imaging system," in *Proceedings of the 20th European Signal Processing Conference (Eusipco '12)*, pp. 1059–1063, Bucharest, Romania, August 2012.
- [16] S.-W. Huang and P.-C. Li, "Arbitrary waveform-coded excitation using bipolar square wave pulsers in medical ultrasound," *IEEE Transactions on Ultrasonics Ferroelectrics and Frequency*, vol. 53, no. 1, pp. 106–116, 2006.
- [17] R. J. Eckersley, M. X. Tang, K. Chetty, and J. V. Hajnal, "Microbubble contrast agent detection using binary coded pulses," *Ultrasound in Medicine and Biology*, vol. 33, no. 1, pp. 1787–1795, 2007.
- [18] P. Phukpattaranont and E. S. Ebbini, "Post-beamforming second-order volterra filter for pulse-echo ultrasonic imaging," *IEEE Transactions on Ultrasonics, Ferroelectrics, and Frequency Control*, vol. 50, no. 8, pp. 987–1001, 2003.
- [19] J. Dréo, A. Pérowski, P. Siarry, and E. Taillard, *Metaheuristics for Hard Optimization: Methods and Case Studies*, Springer, Heidelberg, Germany, 1st edition, 2006.
- [20] J. H. Holland, *Adaptation in Natural and Artificial System*, The University of Michigan Press, Ann Arbor, Mich, USA, 1975.
- [21] R. L. Haupt and S. E. Haupt, *Practical Genetic Algorithms*, John Wiley & Sons, Hoboken, NJ, USA, 2nd edition, 2004.
- [22] M. E. Anderson, "A 2d nonlinear wave propagation solver written in open-source matlab code," in *Proceedings of the IEEE Ultrasonics Symposium*, pp. 1351–1354, San Juan, Puerto Rico, October 2000.
- [23] T. Szabo, *Diagnostic Ultrasound Imaging: Inside Out*, Academic Press, London, UK, 2004.
- [24] C. Greis, "Technology overview: sonovue (bracco, milan)," *European Radiology*, vol. 14, pp. P11–P15, 2004.
- [25] S. M. van der Meer, M. Versluis, D. Lohse, C. T. Chin, A. Bouakaz, and N. De Jong, "The resonance frequency of sonovue: as observed by high-speed optical imaging," in *Proceedings of the IEEE Ultrasonics Symposium*, vol. 1, pp. 343–345, Montréal, Canada, August 2004.
- [26] P. Marmottant, S. van der Meer, M. Emmer et al., "A model for large amplitude oscillations of coated bubbles accounting for buckling and rupture," *Journal of the Acoustical Society of America*, vol. 118, no. 6, pp. 3499–3505, 2005.
- [27] K. E. Morgan, "Experimental and theoretical evaluation of microbubble behavior: effect of transmitted phase and bubble size," *IEEE Transactions on Ultrasonics, Ferroelectrics, and Frequency Control*, vol. 47, no. 6, pp. 1494–1509, 2000.
- [28] J. M. Gorce, M. Arditi, and M. Schneider, "Influence of bubble size distribution on the echogenicity of ultrasound contrast agents: a study of sonovue," *Investigative Radiology*, vol. 35, no. 11, pp. 661–671, 2000.
- [29] J. A. Hossack, P. Mauchamp, and L. Ratsimandresy, "A high bandwidth transducer optimized for harmonic imaging," in *Proceedings of the IEEE Ultrasonics Symposium*, vol. 2, pp. 1021–1024, San Juan, Puerto Rico, October 2000.

Research Article

Differential Diagnosis Tool for Parkinsonian Syndrome Using Multiple Structural Brain Measures

Miho Ota,¹ Yasuhiro Nakata,² Kimiteru Ito,² Kouhei Kamiya,² Masafumi Ogawa,³
Miho Murata,³ Satoko Obu,¹ Hiroshi Kunugi,¹ and Noriko Sato²

¹ Department of Mental Disorder Research, National Institute of Neuroscience, National Center of Neurology and Psychiatry, 4-1-1 Ogawa-Higashi, Kodaira, Tokyo 187-8502, Japan

² Department of Radiology, National Center of Neurology and Psychiatry Hospital, 4-1-1, Ogawa-Higashi, Kodaira, Tokyo 187-8551, Japan

³ Department of Neurology, National Center of Neurology and Psychiatry Hospital, 4-1-1 Ogawa-Higashi, Kodaira, Tokyo 187-8551, Japan

Correspondence should be addressed to Miho Ota; ota@ncnp.go.jp

Received 28 November 2012; Revised 18 February 2013; Accepted 18 February 2013

Academic Editor: Wenxiang Cong

Copyright © 2013 Miho Ota et al. This is an open access article distributed under the Creative Commons Attribution License, which permits unrestricted use, distribution, and reproduction in any medium, provided the original work is properly cited.

Clinical differentiation of parkinsonian syndromes such as the Parkinson variant of multiple system atrophy (MSA-P) and cerebellar subtype (MSA-C) from Parkinson's disease is difficult in the early stage of the disease. To identify the correlative pattern of brain changes for differentiating parkinsonian syndromes, we applied discriminant analysis techniques by magnetic resonance imaging (MRI). T1-weighted volume data and diffusion tensor images were obtained by MRI in eighteen patients with MSA-C, 12 patients with MSA-P, 21 patients with Parkinson's disease, and 21 healthy controls. They were evaluated using voxel-based morphometry and tract-based spatial statistics, respectively. Discriminant functions derived by step wise methods resulted in correct classification rates of 0.89. When differentiating these diseases with the use of three independent variables together, the correct classification rate was the same as that obtained with step wise methods. These findings support the view that each parkinsonian syndrome has structural deviations in multiple brain areas and that a combination of structural brain measures can help to distinguish parkinsonian syndromes.

1. Introduction

Multiple system atrophy (MSA) is an adult-onset, sporadic, progressive neurodegenerative disease characterized by varying severity of parkinsonian features, and cerebellar ataxia, autonomic failure, and corticospinal disorders [1–4]. According to the clinical presentation, a parkinsonian type (MSA-P) and a cerebellar type of MSA (MSA-C) are distinguished [2]. Parkinson's disease (PD) is a progressive neurodegenerative movement disorder characterized by rigidity, tremor, and bradykinesia. Its prevalence increases with age, and it affects 1% of the population over age 65 [5].

PD and MSA are both alpha-synucleinopathies [6, 7]. Pathologically, in Parkinson's disease a massive loss of dopaminergic neurons in pars compacta of substantia nigra and intraneuronal Lewy bodies are present [8]. In MSA, neuronal

loss and gliosis occur in the inferior olives, pons, transverse pontocerebellar fibers, cerebellum, substantia nigra, locus caeruleus, striatum, and the intermediolateral column of the spinal cord [9]. In MSA-P, the nigrostriatal system is the main site of pathology, but less severe degeneration can be widespread and usually includes the olivopontocerebellar system [9, 10]. In MSA-C, the olivopontocerebellar system is mainly affected along with loss of pontine neurons and transverse pontocerebellar fibres and atrophy of the middle cerebellar peduncles (MCPs) [9, 10]. Conventional magnetic resonance imaging (MRI) may also help distinguish the two forms of MSA. MSA-P shows “slit-like” marginal hyperintensity of the putamen [11]. Additionally, the “hot-cross bun” sign on T2-weighted and proton density images in the ventral pons has been reported to be related to MSA-C [12]. However, these MRI changes do not always occur

[3]. Clinical differential diagnosis between PD and MSA is difficult in the early stage of the disease. Relevant works on the other tools like SPECT [13], transcranial brain sonography [14–16] and on optical coherence tomography [17] showed the effectiveness for differentiating PD from healthy volunteer. Additionally, combined use of 123I-(S)-2-hydroxy-3-iodo-6-methoxy-N-((1-ethyl-2-pyrroldinyl)-methyl) benzamide (IBZM), 123I-N-v-fluoropropyl-2b-carbomethoxy-3b-(4-iodophenyl)nortropan (FP-CIT), and meta-123I-iodobenzylguanidine (MIBG) distinguishes Parkinsons disease from atypical parkinsonian disorder, such as PSP and MSA with the accuracy of about 90% [18]. However, 3 SPECT/scintigraphy tests only for diagnosis are not practical.

Over the last few years, a number of MRI studies have focused on the identification of diagnostic markers helpful in the differential diagnosis of parkinsonian syndromes such as MSA, PD, and progressive supranuclear palsy (PSP) [19–22]. However, no studies have discriminated among PD, MSA-P, MSA-C, and healthy subjects simultaneously. In the present study, we hypothesized that we would be able to distinguish the PD and healthy subjects from the MSA subjects by using the infratentorial brain images and MSA-P and PD from the MSA-C and healthy subjects by using supratentorial images. The characteristic distribution of regional brain changes revealed by the gray matter volume data using the optimized, voxel-based morphometry (VBM) method and by the diffusion tensor imaging data using tract-based spatial statistics (TBSS) would have diagnostic values for discriminating such diseases.

2. Materials and Methods

2.1. Subjects. From November 2006 to November 2010, 200 consecutive patients whose chief complaints were parkinsonism underwent brain MRI at our institution. We excluded the patients with cerebrovascular diseases cortical infarctions, multiple lacunar lesions, leukoaraiosis, and other lesions above Fazekas’s Grade 2 on T2-weighted images or fluid-attenuated inversion recovery (FLAIR) MRI [23], PSP, and corticobasal degeneration (CBD). Clinical diagnosis of PD and MSA was made according to the established consensus criteria [2, 24]. A probable clinical diagnosis was determined by two neurologist with more than 20 years of experience in the diagnosis of movement disorders (MO, MM). As a consequence, 18 consecutive patients with MSA-C, 12 patients with MSA-P, and 21 patients with PD were studied. Their characteristics are shown in Table 1. 24 out of 30 MSA patients were hospitalized for the detailed diagnosis, and the diagnosis of 30 MSA patients was not changed during follow-up clinical assessments (mean period = 2.2 years). As for PD, the follow-up clinical assessments were conducted (mean period = 4.7 years) after the MRI imaging, and no additional pathology was detected. 21 age- and sex-matched healthy persons who demonstrated no current or past history of psychiatric illness or contact with psychiatric services were enrolled as controls. Participants were excluded if they had a prior medical history of central nervous system disease or severe head injury. The study protocol was approved by the

TABLE 1: Characteristics of the participants.

	MSA-C	MSA-P	PD	Normal volunteers
Mean age (years)	63.6 ± 7.8	61.9 ± 7.7	62.2 ± 7.0	62.3 ± 5.6
Sex (male: female)	7:11	6:6	10:11	11:10
Duration of illness (year)	3.9 ± 2.5	3.3 ± 2.6	6.8 ± 4.1	

MSA-C: cerebellar form of multiple system atrophy; MSA-P: parkinsonism forms of multiple system atrophy; PD: Parkinson’s disease.

ethics committee of the National Center of Neurology and Psychiatry, Japan.

2.2. MRI Data Acquisition and Processing. MR studies were performed on a Magnetom Symphony 1.5 Tesla (Siemens, Erlangen, Germany). First, high-spatial-resolution, 3-dimensional (3D) T1-weighted images of the brain were obtained for morphometric study. The 3D T1-weighted images were scanned in the sagittal plane (TE/TR: 2.64/1580 ms; flip angle: 15°; effective slice thickness: 1.23 mm; slab thickness: 177 mm; matrix: 208 × 256; FOV: 256 × 315 mm²; acquisitions: 1) yielding 144 contiguous slices through the head. The raw 3D T1-weighted volume data were transferred to a workstation, and structural images were analyzed using an optimized VBM technique. Data were analyzed using Statistical Parametric Mapping 5 (SPM5) software (Wellcome Department of Imaging Neuroscience, London, UK) running on MATLAB 7.0 (Math Works, Natick, MA). Images were processed using an optimized VBM script. The details of this process are described elsewhere [25]. First, each individual 3D-T1 image was normalized with the optimized VBM method. Normalized segmented images were modulated by multiplication with Jacobian determinants of the spatial normalization function to encode the deformation field for each subject, as tissue density changes in normal space. Gray matter volume and cerebrospinal fluid (CSF) volume images were smoothed using a 12 mm full width at half maximum of an isotropic Gaussian kernel. Diffusion tensor imaging (DTI) was then performed in the axial plane (TE/TR: 106/11,200 ms; FOV: 240 × 240 mm²; matrix: 96 × 96; 75 continuous transverse slices; slice thickness 2.5 mm with no interslice gap). Diffusion was measured along 64 noncollinear directions with the use of a diffusion-weighted factor b in each direction for 1000 s/mm², and one image was acquired without use of a diffusion gradient. Recently, a novel processing technique has been published. In this technique, instead of trying to match each and every voxel in different subjects, DTI data is projected on a common pseudoanatomical skeleton and therefore does not need smoothing [26]. TBSS is available as part of the FSL 4.1 software package [27]. The TBSS script runs the nonlinear registration, aligning all fractional anisotropy (FA) images to the FMRIB58_FA template, which is supplied with FSL. The script then takes the target and affine-aligns it into a 1 × 1 × 1 mm MNI152 space. Once this is done, each subject’s FA image has the nonlinear transform to the target and then the affine transform to the MNI152 space applied, resulting in a transformation of the original FA image into

the MNI152 space. Next, TBSS creates the mean of all aligned FA images and applies thinning of the local tract structure to create a skeletonized mean FA image. In order to exclude areas of low FA and/or high intersubject variability from the statistical analysis, TBSS thresholds a mean FA skeleton with a certain FA value, typically 0.2. The resulting binary skeleton mask is a pseudoanatomical representation of the main fiber tracks and defines the set of voxels used in all subsequent processing. Finally, TBSS projects each subject's aligned FA image onto the skeleton. This results in skeletonized FA data. It is this file that feeds into the voxelwise statistics. In addition to DTI and 3D T1-weighted images, conventional axial T2-weighted images (TE/TR: 95/3500 ms; flip angle: 150°; slice thickness: 5 mm; intersection gap: 1.75 mm; matrix: 448 × 512; field of view (FOV): 210 × 240 mm²; acquisitions: 1) and fluid attenuation inversion recovery images in the axial plane (TE/TR: 101/8800 ms; flip angle: 150°; slice thickness: 3 mm; intersection gap: 1.75 mm; matrix: 448 × 512; FOV: 210 × 240 mm²; acquisition: 1) were acquired to exclude cerebrovascular disease or other diseases such as tumors, and hydrocephalus. On conventional MRI, no abnormal findings were detected in the brain of any subject.

2.3. Statistical Analysis. We first evaluated the differences between the patients and healthy subjects using analysis of variance (ANOVA). These tests were performed with the SPSS software ver. 11 (SPSS Japan, Tokyo, Japan). There were no significant differences in age among patients and controls, but there were statistically significant differences in duration of illness between the patients with MSA-P and with PD ($P = 0.012$) and with MSA-C and with PD ($P = 0.005$).

The discriminant function analyses were then conducted to assess the ability of a combination of brain anatomical variables to distinguish between patients with MSA-C, MSA-P, Parkinson's disease, and controls. The independent variables were the volume data and fractional anisotropy value derived from the normalized individual image using the region of interests (ROI) method. ROIs were put on the "single_subj_T1.nii" image regarded as the anatomically standard image in SPM5, in the fourth ventricle, cerebellum hemisphere; these were derived from the WFU_PickAtlas, extension program of SPM5 [28, 29]. We also put ROIs on the "FMRIB58-FA-skeleton_1mm.nii" image, which is the anatomically standard image in FSL, in the MCP, superior cerebellar peduncle (SCP), pons, substantia nigra, superior temporal white matter region, prefrontal white matter regions, and primary motor region where previous studies showed differences among the patients with MSA-C, MSA-P, PD, and controls (Figure 1) [20, 22, 30–37]. The value of a particular tissue was extracted using the software MarsBar [38], an extension program of SPM5.

The Box's M test confirmed the inequality of the group covariance matrices (Box- $M = 76.63$; $P < 0.001$). Discriminant functions were derived by step wise methods based on Mahalanobis' distance. The step wise selection criteria were decided by the overall multivariate F value of each variable to test differences between the patients and controls and to maximize the discriminant function between the groups. At

TABLE 2: Mean fractional anisotropy value in each region of interests and 4th ventricular and cerebellar volumes in patients with MSA-C, MSA-P, PD, and controls.

	MSA-C	MSA-P	PD	Normal
4th Vent_vol	0.31 ± 0.07	0.28 ± 0.07	0.19 ± 0.04	0.20 ± 0.04
Cerebellum_vol	0.28 ± 0.04	0.30 ± 0.03	0.33 ± 0.04	0.34 ± 0.04
MCP	0.32 ± 0.05	0.37 ± 0.05	0.41 ± 0.03	0.39 ± 0.03
SCP	0.44 ± 0.02	0.43 ± 0.02	0.45 ± 0.04	0.47 ± 0.03
Pons	0.12 ± 0.01	0.13 ± 0.01	0.14 ± 0.01	0.13 ± 0.01
SN	0.53 ± 0.04	0.54 ± 0.01	0.54 ± 0.05	0.56 ± 0.04
ST	0.21 ± 0.01	0.13 ± 0.01	0.13 ± 0.01	0.21 ± 0.02
PF	0.05 ± 0.00	0.06 ± 0.01	0.06 ± 0.00	0.05 ± 0.01
PM	0.20 ± 0.02	0.21 ± 0.02	0.22 ± 0.02	0.21 ± 0.02

4th Vent_vol: fourth ventricle volume; cerebellum_vol: cerebellum volume; MSA-C: cerebellar form of multiple system atrophy; MSA-P: parkinsonism forms of multiple system atrophy; MCP: middle cerebellar peduncle; SCP: superior cerebellar peduncle; PD: Parkinson's disease; SN: substantia nigra; ST: superior temporal region; PF: prefrontal region; PM: primary motor region.

TABLE 3: The coefficients of discriminant analysis.

		Factor 1	Factor 2	Factor 3
Stepwise method	4th Vent_vol	1.74	19.47	3.33
	SN	19.16	-9.81	38.32
	ST	-127.87	3.14	-32.07
	PF	196.3	80.22	-188.97
	(Constant)	0.66	-4.13	-5.99
Two independent variables analysis	Pons	-76.33	69.41	(-)
	ST	97.92	13.01	(-)
	(Constant)	-6.98	11.27	(-)
Three independent variables analysis	4th Vent_vol	1.14	15.82	12.23
	MCP	-24.59	-5.39	23.04
	ST	100.68	-13.21	6.19
	(Constant)	-4.01	-3.68	-13.58

4th Vent_vol: fourth ventricle volume; MCP: middle cerebellar peduncle; SN: substantia nigra; ST: superior temporal region; PM: primary motor region.

the same time, we entered the two or three independent variables together and estimated the predictive power of the discriminant function.

3. Results

We first calculated the volume and FA value from the spatially normalized images using ROIs. The mean values of these parameters are summarized in Table 2 and Figure 2. The mean FA value of the prefrontal region was too small to examine, so we did not evaluate the influence of the FA value in the prefrontal white matter region. We then conducted discriminant function analyses. The following five variables were entered in a step wise manner: fourth ventricle volume, substantia nigra, superior temporal, and prefrontal white matter region. The discriminant coefficients are shown in Table 3. The use of these variables resulted in correct

TABLE 4: Classification results.

		Predicted group membership					
		MSA-C	MSA-P	PD	Control	Total	
Stepwise method (88.9% of original grouped cases correctly classified)							
Original data	Count	MSA-C	15	0	0	3	18
		MSA-P	0	9	3	0	12
		PD	0	2	19	0	21
		Control	0	0	0	21	21
	%	MSA-C	83.3	0	0	16.7	100
		MSA-P	0	75.0	25.0	0	100
		PD	0	9.5	90.5	0	100
		Control	0.0	0	0	100.0	100
Two independent variables (84.7% of original grouped cases correctly classified)							
Original data	Count	MSA-C	15	0	0	3	18
		MSA-P	0	10	2	0	12
		PD	0	4	17	0	21
		Control	1	1	0	19	21
	%	MSA-C	83.3	0.0	0	16.7	100
		MSA-P	0	83.3	16.7	0	100
		PD	0	19.0	81.0	0	100
		Control	4.8	4.8	0.0	90.5	100
Three independent variables (88.9% of original grouped cases correctly classified)							
Original data	Count	MSA-C	14	0	0	4	18
		MSA-P	0	10	2	0	12
		PD	0	1	20	0	21
		Control	0	1	0	20	21
	%	MSA-C	77.8	0.0	0	22.2	100
		MSA-P	0	83.3	16.7	0	100
		PD	0	4.8	95.2	0	100
		Control	0.0	4.8	0.0	95.2	100

MSA-C: cerebellar form of multiple system atrophy; MSA-P: parkinsonism forms of multiple system atrophy; PD: Parkinson's disease.

classification rates of 0.89 ($\chi^2 = 294.66$; $df = 12$; $P < 0.001$; Wilks' lambda = 0.012) (Table 4).

The correct classification rates of each combination used to run the discriminant function analyses using two or three independent variables together are listed in Table 5. The highest correct classification rates were measured when we estimated the FA value of the "pons and superior temporal region" and "superior temporal region, MCP and fourth ventricle volume", respectively. Table 3 shows the discriminant coefficients, and Table 4 shows the correct classification rates derived from the analyses using two or three independent variables together, in the same way. Figure 3 shows the discriminant scores of each subject, calculated by the analysis using three independent variables together.

4. Discussion

We found that the step wise discriminant function analysis identified with fairly good accuracy the combinations of ROIs that characterized brain anatomical features distinguishing the patients with MSA-C, MSA-P, PD, and healthy subjects,

and that when discriminate analysis was conducted using the fourth ventricle volume and the FA value of MCP and superior temporal region as independent variables together, the correct classification rate was the same as that of step wise discriminant function analysis.

One study showed that patients with MSA-C and MSA-P share similar diffusion tensor imaging features in the infratentorial region [22]. Furthermore, the combination of DTI metrics can be used to distinguish between patients with MSA and with PD. However, they could not differentiate the patients with PD from healthy subjects. This may be because they were focused on the infratentorial FA value and did not investigate the focal lesions related to parkinsonism. In this study, we used the FA value of the superior temporal regions, known to be impaired in PD as an independent variable, so we could discriminate the patients with PD from healthy subjects and with MSA-C from those with MSA-P [30–32, 34, 35].

One study reported discriminating patients with MSA-P, PD, PSP, and healthy subjects [20]. They indicated that investigating the degeneration of the MCP is useful for the in vivo differential diagnosis of MSA-P and PD. These

TABLE 5: The correct classification rates of each combination of independent variables.

(a) Two independent variables

	4th Vent_vol	Cerebellum_vol	MCP	SCP	Pons	SN	ST	PM
4th Vent_vol		0.514	0.583	0.611	0.583	0.556	0.819	0.431
Cerebellum_vol			0.528	0.556	0.514	0.458	0.722	0.458
MCP				0.708	0.472	0.667	0.833	0.528
SCP					0.681	0.528	0.736	0.542
Pons						0.667	0.847	0.514
SN							0.722	0.583
ST								0.653
PM								

4th Vent_vol: fourth ventricle volume; cerebellum_vol: cerebellum volume; MCP: middle cerebellar peduncle; SCP: superior cerebellar peduncle; SN: substantia nigra; ST: superior temporal region; PM: primary motor region.

(b) Three independent variables

								Accuracy
4th Vent_vol	Cerebellum_vol	MCP						0.556
4th Vent_vol	Cerebellum_vol		SCP					0.681
4th Vent_vol	Cerebellum_vol			Pons				0.569
4th Vent_vol	Cerebellum_vol				SN			0.583
4th Vent_vol	Cerebellum_vol					ST		0.861
4th Vent_vol	Cerebellum_vol						PM	0.583
4th Vent_vol		MCP	SCP					0.708
4th Vent_vol		MCP		Pons				0.542
4th Vent_vol		MCP			SN			0.653
4th Vent_vol		MCP				ST		0.889
4th Vent_vol		MCP					PM	0.569
4th Vent_vol			SCP	Pons				0.722
4th Vent_vol			SCP		SN			0.625
4th Vent_vol			SCP			ST		0.833
4th Vent_vol			SCP				PM	0.681
4th Vent_vol				Pons	SN			0.681
4th Vent_vol				Pons		ST		0.889
4th Vent_vol				Pons			PM	0.597
4th Vent_vol					SN	ST		0.875
4th Vent_vol					SN		PM	0.611
4th Vent_vol						ST	PM	0.861
	Cerebellum_vol	MCP	SCP					0.681
	Cerebellum_vol	MCP		Pons				0.486
	Cerebellum_vol	MCP			SN			0.639
	Cerebellum_vol	MCP				ST		0.833
	Cerebellum_vol	MCP					PM	0.528
	Cerebellum_vol		SCP	Pons				0.625
	Cerebellum_vol		SCP		SN			0.583
	Cerebellum_vol		SCP			ST		0.764
	Cerebellum_vol		SCP				PM	0.583
	Cerebellum_vol			Pons	SN			0.653
	Cerebellum_vol			Pons		ST		0.833
	Cerebellum_vol			Pons			PM	0.528
	Cerebellum_vol				SN	ST		0.792
	Cerebellum_vol				SN		PM	0.583
	Cerebellum_vol					ST	PM	0.792

(b) Continued.

						Accuracy
MCP	SCP	Pons				0.681
MCP	SCP		SN			0.694
MCP	SCP			ST		0.819
MCP	SCP				PM	0.681
MCP		Pons	SN			0.694
MCP		Pons		ST		0.806
MCP		Pons			PM	0.486
MCP			SN	ST		0.833
MCP			SN		PM	0.625
MCP				ST	PM	0.819
	SCP	Pons	SN			0.667
	SCP	Pons		ST		0.819
	SCP	Pons			PM	0.681
	SCP		SN	ST		0.792
	SCP		SN		PM	0.611
	SCP			ST	PM	0.722
		Pons	SN	ST		0.819
		Pons	SN		PM	0.694
		Pons		ST	PM	0.819
			SN	ST	PM	0.764

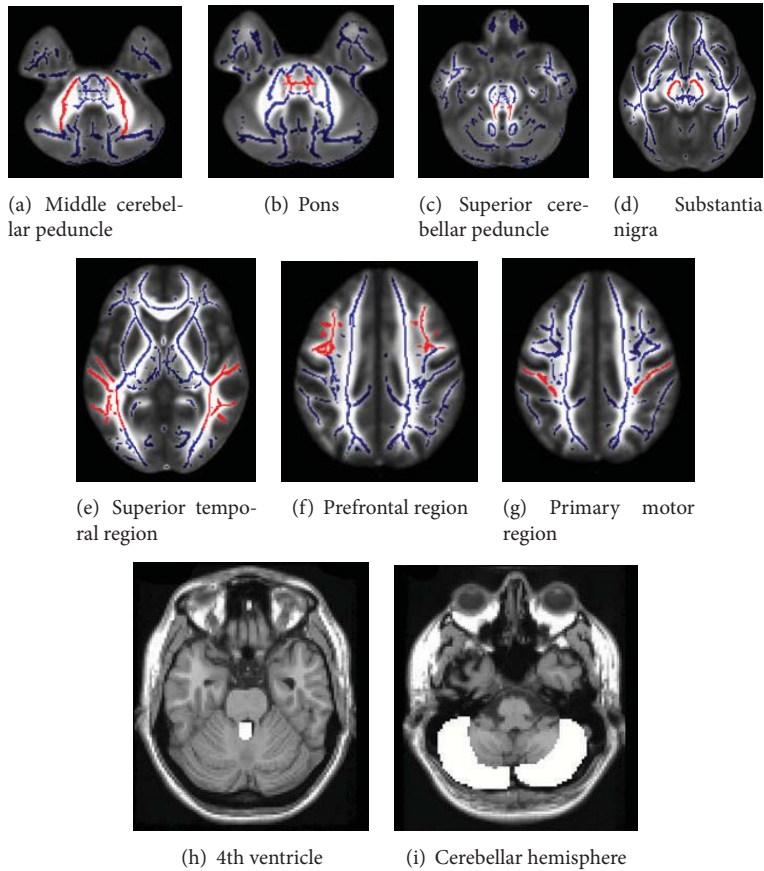


FIGURE 1: Locations of regions of interest. From (a) to (g) were put on the “FMRIB58_FA-skeleton_1 mm.nii” image, the anatomically standard image in FSL. Background fractional anisotropy image was the “MNI152_T1_1 mm.nii,” which was also the standard image in FSL. (h) and (i) were put on a “single_subj_T1.nii” image regarded as the anatomically standard image in SPM5.

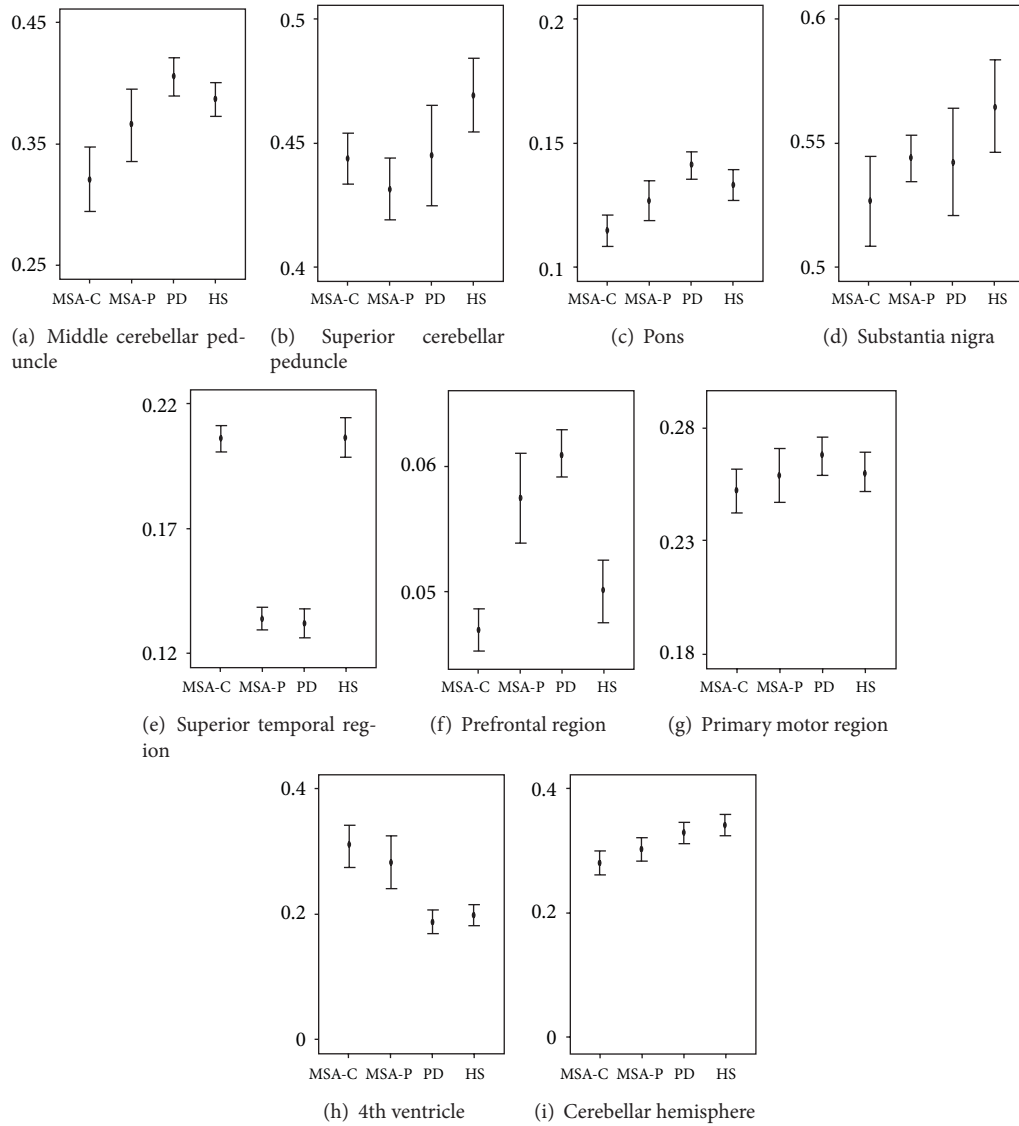


FIGURE 2: A graphic presentation of mean fractional anisotropy values in each region and mean volumes of 4th ventricular and cerebellum. MSA-C: multiple system atrophy with predominant cerebellar ataxia; MSA-P: multiple system atrophy with predominant parkinsonism; PD: Parkinson's disease; HS: healthy subjects.

results are congruent with our study. Establishing a means of differentiation using MR imaging would have potential therapeutic implications.

In this study, the participants with PD had a statistically longer duration of illness than those with MSA. It is known that MRI studies with PD show slight or no gray matter atrophy in early- to moderate-stage patients, whereas later-stage patients exhibited marked cortical atrophy [31]. We used the FA values for the independent variables to differentiate the patients with PD from others. White matter which appears normal on conventional MRI can show FA abnormalities, possibly permitting an earlier identification of the disease process which involves white matter tracts of the brain [33]. In addition, we successfully differentiated the patients with MSA-P from those with MSA-C using the same parameter.

There is significant value to distinguishing these diseases using DTI metrics.

All voxel-based analysis methods are susceptible to the effects of the spatial normalization transformation that registers images of different individuals. Regions in which this spatial transformation has relatively lower accuracy will tend to display artificially higher variability, which will adversely affect statistical significance. To date, TBSS is considered more robust and better suited for whole brain DTI data analysis. However, there are some limitations with the TBSS analysis. First, "fMRIB58_FA-skeleton_1mm.nii" did not cover the thalamus and striatum, both of which have significant relationships with parkinsonian features [39]. A previous study demonstrated signal changes of the MR image after levodopa administration in an anatomical cluster which included the

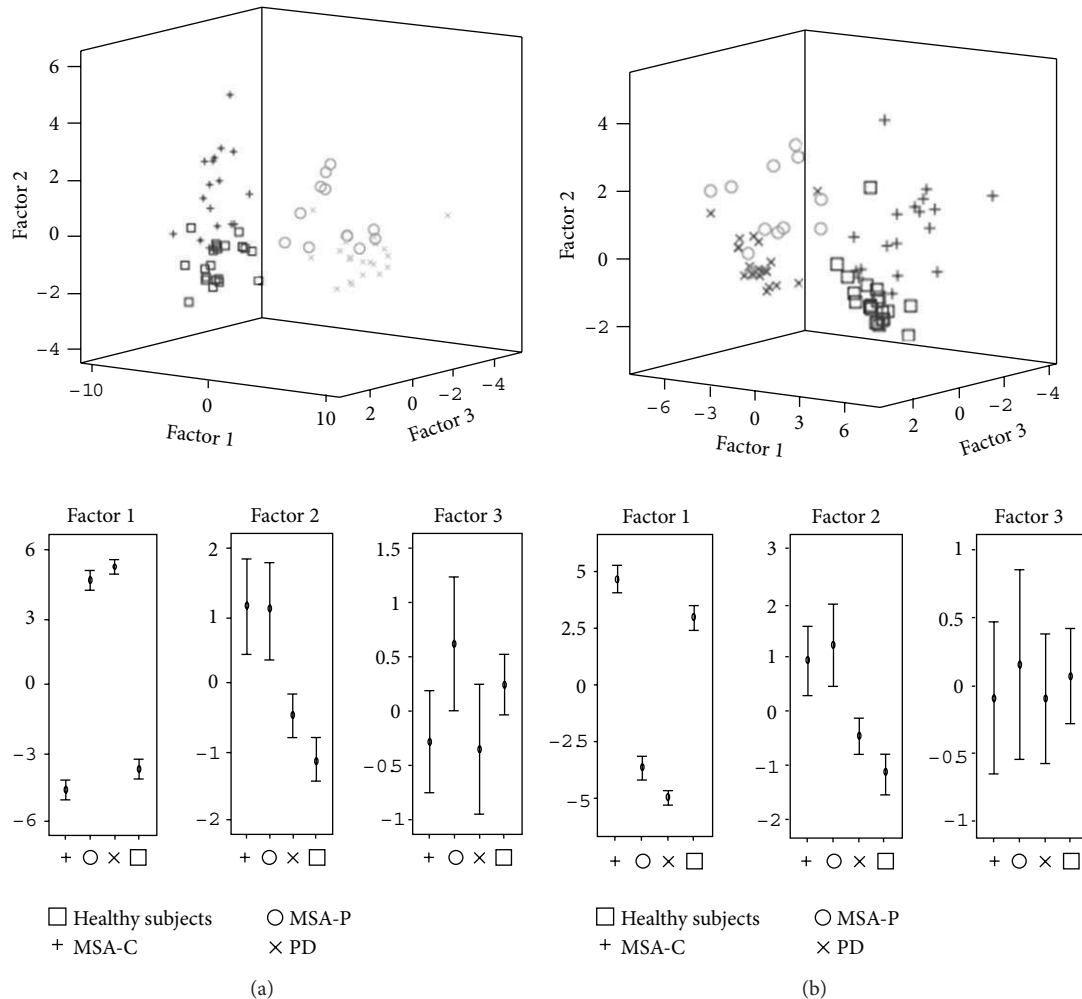


FIGURE 3: 3-dimensional scattered plots showed the discriminant scores of each subject. These were calculated (a) by the analysis using step wise method and (b) using three independent variables together. Factors 1–3 were defined in Table 3.

substantia nigra, tegmental ventral area subthalamic nucleus bilaterally, the principal origin, and first relay nuclei of projections in brain dopaminergic systems [40]. Therefore, we do not recommend using dopamine-rich regions such as the thalamus and striatum in discriminant function analysis for parkinsonian syndrome. Second, the predominant motor feature can change with time. The designation of MSA-P and MSA-C refers to the predominant feature at the time the patient is evaluated, and the predominant feature can change with time [2]. All of our MSA-C samples did not change the diagnosis to the MSA-P during follow-up clinical assessments; however, the discriminant method in this study would be fitted for the initial diagnosis. Third, our study is a small cross-sectional study, and we did not validate this discrimination method using another independent sample. MSA-P and MSA-C without cerebrovascular findings were so scarce, and we did not gather sufficient sample size. Further work with a large sample is required for the development of better discriminant capability and, if feasible, with data on another parkinsonism, PSP, would bring further clinical advantage.

5. Conclusions

Discriminant functions derived by step wise methods resulted in correct classification rates of 0.89. The present methods for automated analysis of morphometric data largely support findings from earlier studies using expert-guided ROIs or automated procedures. These findings support the view that each parkinsonian syndrome has structural deviations in multiple brain areas, and discriminant function analysis in this paper may provide objective biological information adjunct to the clinical diagnosis of parkinsonian syndromes.

References

- [1] F. Geser, G. K. Wenning, K. Seppi et al., “Progression of multiple system atrophy (MSA): a prospective natural history study by the European MSA Study Group (EMSA SG),” *Movement Disorders*, vol. 21, no. 2, pp. 179–186, 2006.
- [2] S. Gilman, G. K. Wenning, P. A. Low et al., “Second consensus statement on the diagnosis of multiple system atrophy,” *Neurology*, vol. 71, no. 9, pp. 670–676, 2008.

- [3] N. Quinn, "Multiple system atrophy—the nature of the beast," *Journal of Neurology, Neurosurgery & Psychiatry*, vol. 52, pp. 78–89, 1986.
- [4] G. K. Wenning, F. Tison, Y. B. Shlomo, S. E. Daniel, and N. P. Quinn, "Multiple system atrophy: a review of 203 pathologically proven cases," *Movement Disorders*, vol. 12, no. 2, pp. 133–147, 1997.
- [5] D. Aarsland, K. Andersen, J. P. Larsen, A. Lolk, H. Nielsen, and P. Kragh-Sørensen, "Risk of dementia in Parkinson's disease: a community-based, prospective study," *Neurology*, vol. 56, no. 6, pp. 730–736, 2001.
- [6] M. G. Spillantini, R. A. Crowther, R. Jakes, N. J. Cairns, P. L. Lantos, and M. Goedert, "Filamentous α -synuclein inclusions link multiple system atrophy with Parkinson's disease and dementia with Lewy bodies," *Neuroscience Letters*, vol. 251, no. 3, pp. 205–208, 1998.
- [7] K. Wakabayashi, M. Yoshimoto, S. Tsuji, and H. Takahashi, " α -synuclein immunoreactivity in glial cytoplasmic inclusions in multiple system atrophy," *Neuroscience Letters*, vol. 249, no. 2–3, pp. 180–182, 1998.
- [8] J. M. Fearnley and A. J. Lees, "Ageing and Parkinson's disease: substantia nigra regional selectivity," *Brain*, vol. 114, part 5, pp. 2283–2301, 1991.
- [9] G. K. Wenning, F. Tison, L. Elliott, N. P. Quinn, and S. E. Daniel, "Olivopontocerebellar pathology in multiple system atrophy," *Movement Disorders*, vol. 11, no. 2, pp. 157–162, 1996.
- [10] A. Kume, A. Takahashi, and Y. Hashizume, "Neuronal cell loss of the striatonigral system in multiple system atrophy," *Journal of the Neurological Sciences*, vol. 117, no. 1–2, pp. 33–40, 1993.
- [11] K. Bhattacharya, D. Saadia, B. Eisenkraft et al., "Brain magnetic resonance imaging in multiple-system atrophy and Parkinson disease: a diagnostic algorithm," *Archives of Neurology*, vol. 59, no. 5, pp. 835–842, 2002.
- [12] M. Savoiardo, L. Strada, F. Girotti et al., "Olivopontocerebellar atrophy: MR diagnosis and relationship to multisystem atrophy," *Radiology*, vol. 174, no. 3, pp. 693–696, 1990.
- [13] J. Spiegel, M. O. Möllers, W. H. Jost et al., "FP-CIT and MIBG scintigraphy in early Parkinson's disease," *Movement Disorders*, vol. 20, no. 5, pp. 552–561, 2005.
- [14] G. Becker, J. Seufert, U. Bogdahn, H. Reichmann, and K. Reiners, "Degeneration of substantia nigra in chronic Parkinson's disease visualized by transcranial color-coded real-time sonography," *Neurology*, vol. 45, no. 1, pp. 182–184, 1995.
- [15] K. Busse, R. Heilmann, S. Kleinschmidt et al., "Value of combined midbrain sonography, olfactory and motor function assessment in the differential diagnosis of early Parkinson's disease," *Journal of Neurology, Neurosurgery & Psychiatry*, vol. 83, no. 4, pp. 441–447, 2012.
- [16] M. Izawa Okawa and H. Miwa, "Transcranial sonography findings in Parkinson's disease," *Brain Nerve*, vol. 64, no. 4, pp. 413–422, 2012.
- [17] P. Albrecht, A. K. Müller, M. Südmeyer et al., "Optical coherence tomography in parkinsonian syndromes," *PLoS ONE*, vol. 7, Article ID e34891, 2012.
- [18] M. Südmeyer, C. Antke, T. Zizek et al., "Diagnostic accuracy of combined FP-CIT, IBZM, and MIBG scintigraphy in the differential diagnosis of degenerative parkinsonism: a multi-dimensional statistical approach," *Journal of Nuclear Medicine*, vol. 52, no. 5, pp. 733–740, 2011.
- [19] R. L. Gama, D. F. G. Távora, R. C. Bomfim, C. E. Silva, V. M. de Bruin, and P. F. de Bruin, "Morphometry MRI in the differential diagnosis of parkinsonian syndromes," *Arquivos de Neuro-Psiquiatria*, vol. 68, no. 3, pp. 333–338, 2010.
- [20] G. Nicoletti, R. Lodi, F. Condino et al., "Apparent diffusion coefficient measurements of the middle cerebellar peduncle differentiate the Parkinson variant of MSA from Parkinson's disease and progressive supranuclear palsy," *Brain*, vol. 129, no. 10, pp. 2679–2687, 2006.
- [21] A. Quattrone, G. Nicoletti, D. Messina et al., "MR imaging index for differentiation of progressive supranuclear palsy from Parkinson disease and the Parkinson variant of multiple system atrophy," *Radiology*, vol. 246, no. 1, pp. 214–221, 2008.
- [22] M. F. H. Schocke, K. Seppi, R. Esterhammer et al., "Diffusion-weighted MRI differentiates the Parkinson variant of multiple system atrophy from PD," *Neurology*, vol. 58, no. 4, pp. 575–580, 2002.
- [23] F. Fazekas, J. B. Chawluk, and A. Alavi, "MR signal abnormalities at 1.5 T in Alzheimer's dementia and normal aging," *American Journal of Roentgenology*, vol. 149, no. 2, pp. 351–356, 1987.
- [24] W. R. G. Gibb and A. J. Lees, "The relevance of the Lewy body to the pathogenesis of idiopathic Parkinson's disease," *Journal of Neurology, Neurosurgery & Psychiatry*, vol. 51, pp. 745–752, 1998.
- [25] C. D. Good, I. Johnsrude, J. Ashburner, R. N. A. Henson, K. J. Friston, and R. S. J. Frackowiak, "Cerebral asymmetry and the effects of sex and handedness on brain structure: a voxel-based morphometric analysis of 465 normal adult human brains," *NeuroImage*, vol. 14, no. 3, pp. 685–700, 2001.
- [26] S. M. Smith, M. Jenkinson, H. Johansen-Berg et al., "Tract-based spatial statistics: voxelwise analysis of multi-subject diffusion data," *NeuroImage*, vol. 31, no. 4, pp. 1487–1505, 2006.
- [27] S. M. Smith, M. Jenkinson, M. W. Woolrich et al., "Advances in functional and structural MR image analysis and implementation as FSL," *NeuroImage*, vol. 23, no. 1, pp. S208–S219, 2004.
- [28] J. A. Maldjian, P. J. Laurienti, R. A. Kraft, and J. H. Burdette, "An automated method for neuroanatomic and cytoarchitectonic atlas-based interrogation of fMRI data sets," *NeuroImage*, vol. 19, no. 3, pp. 1233–1239, 2003.
- [29] J. A. Maldjian, P. J. Laurienti, and J. H. Burdette, "Precentral gyrus discrepancy in electronic versions of the Talairach atlas," *NeuroImage*, vol. 21, no. 1, pp. 450–455, 2004.
- [30] M. K. Beyer, C. C. Janvin, J. P. Larsen, and D. Aarsland, "A magnetic resonance imaging study of patients with Parkinson's disease with mild cognitive impairment and dementia using voxel-based morphometry," *Journal of Neurology, Neurosurgery & Psychiatry*, vol. 78, no. 3, pp. 254–259, 2007.
- [31] P. Borghammer, K. Østergaard, P. Cumming et al., "A deformation-based morphometry study of patients with early-stage Parkinson's disease," *European Journal of Neurology*, vol. 17, no. 2, pp. 314–320, 2010.
- [32] A. Gerhard, N. Pavese, G. Hotton et al., "In vivo imaging of microglial activation with [¹¹C](R)-PK11195 PET in idiopathic Parkinson's disease," *Neurobiology of Disease*, vol. 21, no. 2, pp. 404–412, 2006.
- [33] N. Prakash, N. Hageman, X. Hua, A. W. Toga, S. L. Perlman, and N. Salamon, "Patterns of fractional anisotropy changes in white matter of cerebellar peduncles distinguish spinocerebellar ataxia-1 from multiple system atrophy and other ataxia syndromes," *NeuroImage*, vol. 47, supplement 2, pp. T72–T81, 2009.
- [34] B. Ramírez-Ruiz, M. J. Martí, E. Tolosa et al., "Longitudinal evaluation of cerebral morphological changes in Parkinson's disease with and without dementia," *Journal of Neurology*, vol. 252, no. 11, pp. 1345–1352, 2005.

- [35] K. Specht, M. Minnerop, M. Abele, J. Reul, U. Wüllner, and T. Klockgether, "In vivo voxel-based morphometry in multiple system atrophy of the cerebellar type," *Archives of Neurology*, vol. 60, no. 10, pp. 1431–1435, 2003.
- [36] K. Specht, M. Minnerop, J. Müller-Hübenthal, and T. Klockgether, "Voxel-based analysis of multiple-system atrophy of cerebellar type: complementary results by combining voxel-based morphometry and voxel-based relaxometry," *NeuroImage*, vol. 25, no. 1, pp. 287–293, 2005.
- [37] L. C. Tzarouchi, L. G. Astrakas, S. Konitsiotis et al., "Voxel-based morphometry and voxel-based relaxometry in parkinsonian variant of multiple system atrophy," *Journal of Neuroimaging*, vol. 20, no. 3, pp. 260–266, 2010.
- [38] M. Brett, J.-L. Anton, R. Valabregue, and J.-B. Poline, "Region of interest analysis using an SPM toolbox," in *Proceedings of the 8th International Conference on Functional Mapping of the Human Brain*, Sendai, Japan, June 2002, Available on CD-ROM in *NeuroImage*, vol. 16, no. 2, 2002.
- [39] P. Remy, M. Doder, A. Lees, N. Turjanski, and D. Brooks, "Depression in Parkinson's disease: loss of dopamine and noradrenaline innervation in the limbic system," *Brain*, vol. 128, no. 6, pp. 1314–1322, 2005.
- [40] P. Salgado-Pineda, P. Delaveau, C. Falcon, and O. Blin, "Brain T1 intensity changes after levodopa administration in healthy subjects: a voxel-based morphometry study," *British Journal of Clinical Pharmacology*, vol. 62, no. 5, pp. 546–551, 2006.

Research Article

A General Framework for Modeling Sub- and Ultraharmonics of Ultrasound Contrast Agent Signals with MISO Volterra Series

Fatima Sbeity,^{1,2} Sébastien Ménigot,^{1,2,3} Jamal Charara,⁴ and Jean-Marc Girault^{1,2}

¹ Université François Rabelais de Tours, UMR-S930, 37032 Tours, France

² INSERM U930, 37032 Tours, France

³ IUT Ville d'Avray, Université Paris Ouest Nanterre La Défense, 92410 ville d'Avray, France

⁴ Département de Physique et d'Électronique, Faculté des Sciences I, Université Libanaise, Hadath, Lebanon

Correspondence should be addressed to Jean-Marc Girault; jean-marc.girault@univ-tours.fr

Received 21 December 2012; Accepted 25 January 2013

Academic Editor: Kumar Durai

Copyright © 2013 Fatima Sbeity et al. This is an open access article distributed under the Creative Commons Attribution License, which permits unrestricted use, distribution, and reproduction in any medium, provided the original work is properly cited.

Sub- and ultraharmonics generation by ultrasound contrast agents makes possible sub- and ultraharmonics imaging to enhance the contrast of ultrasound images and overcome the limitations of harmonic imaging. In order to separate different frequency components of ultrasound contrast agents signals, nonlinear models like single-input single-output (SISO) Volterra model are used. One important limitation of this model is its incapacity to model sub- and ultraharmonic components. Many attempts are made to model sub- and ultraharmonics using Volterra model. It led to the design of multiple-input single-output (MISO) Volterra model instead of SISO Volterra model. The key idea of MISO modeling was to decompose the input signal of the nonlinear system into periodic subsignals at the subharmonic frequency. In this paper, sub- and ultraharmonics modeling with MISO Volterra model is presented in a general framework that details and explains the required conditions to optimally model sub- and ultraharmonics. A new decomposition of the input signal in periodic orthogonal basis functions is presented. Results of application of different MISO Volterra methods to model simulated ultrasound contrast agents signals show its efficiency in sub- and ultraharmonics imaging.

1. Introduction

Medical diagnostic using ultrasound imaging was greatly improved with the introduction of ultrasound contrast agents. In ultrasound imaging, contrast agents are microbubbles [1]. Historically, the important difference between the acoustic impedance of the tissue and the gas encapsulated within the microbubbles was the first step to improve the contrast of echographic images. However, the contrast was still improved by taking into account the nonlinear behavior of microbubbles. In fact, when microbubbles were insonified by a sinusoidal excitation, they respond by generating harmonic components [2]. For example, second harmonic imaging (SHI) [3] consists in transmitting a signal at frequency f_0 and receiving echoes at twice the transmitted frequency $2f_0$. However, harmonic generation during the propagation of ultrasound in the nonperfused tissue limits the contrast [4].

Many years ago, experimental studies have shown the existence of subharmonics at $f_0/2$ [5] and ultraharmonics

at $((3/2)f_0, (5/2)f_0, \dots)$ [6] in the microbubble response under specific conditions of frequency and pressure. The absence of these components in the backscattered signal by the tissue has enabled the introduction of sub- and ultraharmonics as an alternative of the harmonic imaging in order to enhance the contrast. Sub- and ultraharmonic imaging consists of transmitting a signal of frequency f_0 and extracting components at $f_0/2, (3/2)f_0, (5/2)f_0, \dots$

Many models have been developed to understand the dynamics of the microbubble [2]. Microbubble oscillation can be accurately described using models such as Rayleigh-Plesset modified equation [7–9]. However, to enable optimal separation of harmonic components, other nonlinear models like single-input single-output (SISO) Volterra model have been preferred [10]. A well known limitation of SISO Volterra model is its capacity to model exclusively harmonic components sub- and ultraharmonics are not modeled [11].

To overcome this difficulty, Boaghe and Billings [12] have proposed a multiple-input single-output (MISO) Volterra-based method. Input signals are specified by having subharmonic component at frequency f_0/N . This approach has been applied in ultrasound medical imaging [13].

However, neither Boaghe and Billings [12] nor Samakee and Phukpattaranont [13] have clearly justified the required conditions to design a MISO Volterra decomposition able to model sub- and ultraharmonics.

To answer this untreated point, we propose a more general framework which firstly gives a clear justification regarding the choice of the model and secondly can offer interesting alternatives.

This paper is organized as follows: after recalling Volterra model and presenting the general framework of MISO Volterra methods, simulations of contrast ultrasound medical imaging followed by results are presented. Finally, a discussion completed by a conclusion closes the paper.

2. SISO Volterra Model

Volterra series were introduced like Taylor series with memory [10]. Let $x(n)$ and $y(n)$ be, respectively, the input and the output signals in the discrete time domain n of the nonlinear system (see Figure 1). The output $\hat{y}(n)$ of Volterra model of order P and memory M is given in [14]. Note that, in our study focused on ultrasound imaging, a third-order Volterra model $P = 3$ is sufficient for the available transducers bandwidths. The output $\hat{y}(n)$ of SISO Volterra model of order $P = 3$ and memory M is given by

$$\begin{aligned} \hat{y}(n) = & h_0 + \sum_{k_1=0}^{M-1} h_1(k_1) x(n-k_1) \\ & + \sum_{k_1=0}^{M-1} \sum_{k_2=0}^{M-1} h_2(k_1, k_2) x(n-k_1) x(n-k_2) \\ & + \sum_{k_1=0}^{M-1} \sum_{k_2=0}^{M-1} \sum_{k_3=0}^{M-1} h_3(k_1, k_2, k_3) \\ & \times x(n-k_1) x(n-k_2) x(n-k_3), \end{aligned} \quad (1)$$

where $h_p(k_1, k_2, \dots, k_p)$ is the kernel of order p of the filter, with $p \in \{1, 2, 3\}$.

Equation (1) could be rewritten as follows

$$\mathbf{y} = \mathbf{X} \cdot \mathbf{h}, \quad (2)$$

where the output signal is:

$$\mathbf{y} = [y(M-1), y(M), \dots, y(L)]^T, \quad (3)$$

where L is the length of the signal $y(n)$, and the vector of kernels is

$$\begin{aligned} \mathbf{h} = & [h_1(0), h_1(1), \dots, h_1(M-1), h_2(0,0), \\ & h_2(0,1), \dots, h_2(M-1, M-1), \dots, \\ & h_p(0,0,0), \dots, h_3(M-1, M-1, M-1)]^T, \end{aligned} \quad (4)$$

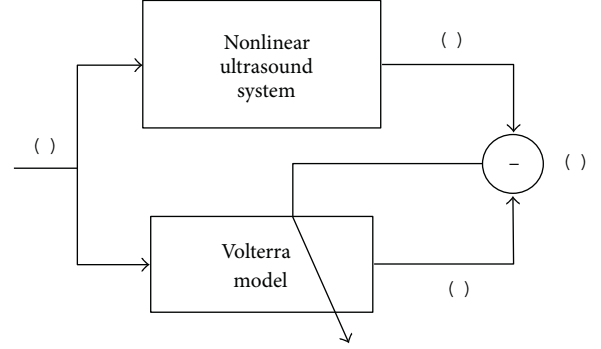


FIGURE 1: Block diagram of SISO Volterra model.

where the input matrix is

$$\mathbf{X} = [\mathbf{x}_{M-1}, \mathbf{x}_M, \dots, \mathbf{x}_L]^T, \quad (5)$$

with vector

$$\begin{aligned} \mathbf{x}_n = & [x(n), x(n-1), \dots, x(n-M+1), \\ & x^2(n), x(n)x(n-1), \dots, x^2(n-M+1), \\ & x^3(n), x(n)x(n)x(n-1), \dots, \\ & x^3(n-M+1)]^T, \end{aligned} \quad (6)$$

with $n \in \{M-1, M, \dots, L\}$.

The vector of kernels \mathbf{h} is calculated to minimize the mean square error (MSE) between $y(n)$ and $\hat{y}(n)$ according to the equation

$$\arg \min_{\mathbf{h}} (\mathbb{E} [(y(n) - \hat{y}(n))^2]), \quad (7)$$

where \mathbb{E} is the symbol of the mathematical expectation.

Vector \mathbf{h} is calculated using the least squares method

$$\mathbf{h} = (\mathbf{X}^T \mathbf{X})^{-1} \mathbf{X}^T \mathbf{y}, \quad (8)$$

if $(\mathbf{X}^T \mathbf{X})$ is invertible. Otherwise, regularization techniques can be used.

Nevertheless, as reported in [12], it is not possible to model sub- and ultraharmonics with SISO Volterra model under this formulation. This is due to the fact mentioned in [12] that SISO Volterra model can only model frequencies at integer multiples of the input frequency.

To overcome this limitation, Boaghe and Billings [12] proposed a MISO Volterra-based solution and not any more a SISO Volterra. This point is discussed in Section 3.

3. General Framework of MISO Volterra Model

According to Boaghe and Billings' claims [12], it is possible to model sub- and ultraharmonic components of the signal

$y(n)$ if the excitation signal to Volterra model has the sub-harmonic component at f_0/N . The solution proposed by Boaghe and Billings [12] to show up the sub-harmonic component at frequency f_0/N is to decompose the input signal $x(n)$ into multiple input signals $x_i(n)$, each signal having frequency components at f_0 and f_0/N . From our point of view, Boaghe and Billings' approach [12] claimed two conditions that are intrinsically coupled by the choice of the decomposition method as follows:

- (i) the input signal to Volterra model has sub-harmonic frequency component at f_0/N ;
- (ii) Volterra system is a MISO system described by

$$x(n) = \sum_{i=1}^N x_i(n). \quad (9)$$

The block diagram of MISO Volterra model is presented in Figure 2.

A third condition that is not really explained in [12], however, it is a crucial condition to carry out this modeling procedure. It is the orthogonality condition between each multiple input of MISO Volterra model. Taking into account this third condition makes it possible to generalize Boaghe and Billings' approach presented in [12] as follows:

$$x(n, f_0) = \sum_{i=1}^N x_i(n, f_0, N) = \sum_{i=1}^N \alpha_i \Psi_i(n, f_0, N), \quad (10)$$

where α_i are coefficients to be adjust and $\Psi_i(n, f_0, N)$ is the periodic orthogonal basis functions having a spectral component at f_0/N . Different bases could be proposed. In this study, two bases are presented as follows.

- (1) In [12] a first periodic basis of orthogonal functions is proposed as follows:

$$\Psi_i(n, f_0, N) = x(n, f_0) * \sum_{k=-\infty}^{+\infty} \text{Rect}_{1/f_0} \left(nT_s - \frac{kN + i - 1}{f_0} \right), \quad (11)$$

where T_s is the sampling period, $*$ represents the convolution product, and $\text{Rect}_{1/f_0}(n)$ is the rectangular function equal to 1 when $-1/2f_0 < n < 1/2f_0$ and equal to zero otherwise. Note that this approach is MISO1.

- (2) In the present work, a new periodic basis of orthogonal functions is presented as follows:

$$\begin{aligned} \Psi_i(n, f_0, N) &= x(n, f_0) + (-1)^{(i-1)} \\ &\times \left(x(n, f_0) \cos \left(nT_s w_0 \frac{N-1}{N} \right) \right. \\ &\quad \left. + \tilde{x}(n, f_0) \sin \left(nT_s w_0 \frac{N-1}{N} \right) \right), \end{aligned} \quad (12)$$

where $\tilde{x}(n) = \mathcal{H}(x(n))$ is the Hilbert transform of $x(n)$ and $w_0 = 2\pi f_0$. Note that this second is MISO2 approach.

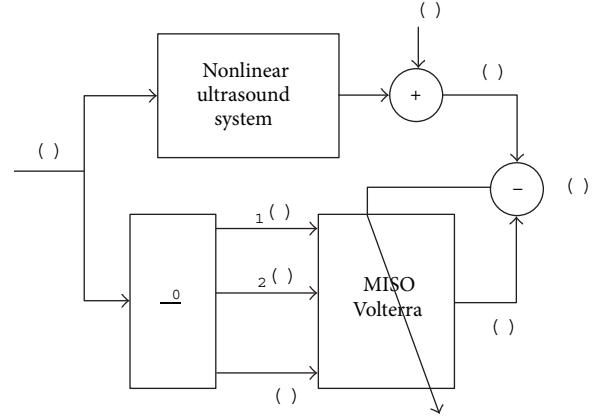


FIGURE 2: Block diagram of MISO Volterra model.

For our application in contrast medical imaging, the sub-harmonic frequency is $f_0/2$ [5–7], so $N = 2$.

As an illustration, when $x(n) = A \cos(w_0 n T_s)$ and $N = 2$, the decomposition is written:

- (1) for the first basis, as follows:

$$\begin{aligned} x(n) &= x_1(n) + x_2(n) \\ &= \alpha_1 \Psi_1(n, f_0, 2) + \alpha_2 \Psi_2(n, f_0, 2), \end{aligned} \quad (13)$$

with $\alpha_1 = \alpha_2 = 1$, and

$$\begin{aligned} \Psi_1(n, f_0, 2) &= A \cos(w_0 n T_s) * \sum_{k=-\infty}^{+\infty} \text{Rect}_{1/f_0} \left(nT_s - \frac{2k}{f_0} \right), \\ \Psi_2(n, f_0, 2) &= A \cos(w_0 n T_s) * \sum_{k=-\infty}^{+\infty} \text{Rect}_{1/f_0} \left(nT_s - \frac{2k+1}{f_0} \right), \end{aligned} \quad (14)$$

- (2) and for the second basis, as follows:

$$\begin{aligned} x(n) &= x_1(n) + x_2(n) \\ &= \alpha_1 \Psi_1(n, f_0, 2) + \alpha_2 \Psi_2(n, f_0, 2), \end{aligned} \quad (15)$$

with $\alpha_1 = \alpha_2 = 1/2$, and

$$\begin{aligned} \Psi_1 \left(n, \frac{f_0}{2} \right) &= A \cos(w_0 n T_s) * \sum_{q=1}^2 \delta \left(\frac{nT_s}{q} \right), \\ \Psi_2 \left(n, \frac{f_0}{2} \right) &= A \cos(w_0 n T_s) * \sum_{q=1}^2 (-1)^{(q-1)} \delta \left(\frac{nT_s}{q} \right), \end{aligned} \quad (16)$$

where $\delta(n)$ is the Dirac function. Finally, $\Psi_1(n, f_0/2)$ and $\Psi_2(n, f_0/2)$ can be simply rewritten as follows:

$$\begin{aligned} \Psi_1(n, f_0, 2) &= A \cos(w_0 n T_s) + A \cos \left(\frac{w_0}{2} n T_s \right), \\ \Psi_2(n, f_0, 2) &= A \cos(w_0 n T_s) - A \cos \left(\frac{w_0}{2} n T_s \right). \end{aligned} \quad (17)$$

The two signals $x_1(n)$ and $x_2(n)$ for the two previous bases are represented in Figure 3.

It is obvious to show that for the two bases, the signals $x_1(n)$ and $x_2(n)$ are orthogonal because $\sum x_1(n)x_2(n) = 0$ (From a statistical point of view, the two signals $x_1(n)$ and $x_2(n)$ are orthogonal if and only if $\mathbb{E}[x_1(n)x_2(n)] = 0$. If $x_1(n)$ and $x_2(n)$ are stationary and ergodic, then $\mathbb{E}[x_1(n)x_2(n)] = \sum(x_1(n)x_2(n))$). The algebraic area of the signal $z(n) = x_1(n)x_2(n)$, shown in Figure 3, is equal to zero.

Finally, if the components $x_i(n)$ are orthogonal to each other, then this also means that the output of Volterra model $\hat{y}(n)$ can be decomposed as follows:

$$\hat{y}(n) = \sum_{i=1}^N \hat{y}_i(n), \quad (18)$$

where the components $\hat{y}_i(n)$ are also orthogonal to each other. A proof of this propriety is given in Appendix A.

The consequence of this statement is that MISO Volterra model can be considered as N parallel SISO Volterra models as depicted in Figure 4.

4. Simulations

To validate the different proposed bases and to quantify its performances for application in contrast ultrasound medical imaging, realistic simulations are proposed. To carry out the simulations, the free simulation program BUBBLESIM developed by Hoff [7] was used to calculate the oscillations and scattered echoes for a specified contrast agent and excitation pulse. A modified version of Rayleigh-Plesset equation was chosen. The model presented by Church [15] and then modified by Hoff [7] is based on the theoretical description of microbubbles as air-filled particles with surface layers of elastic solids. In order to simulate the mean behavior of a microbubble cloud, we hypothesized that the response of a cloud of N_b microbubbles was N_b times the response of a single microbubble with the mean properties.

The incident burst to the microbubble is a sinusoidal wave of frequency $f_0 = 4$ MHz (The resonance frequency of a microbubble of $1.5 \mu\text{m}$ is about 2.25 MHz. Therefore, the emission frequency at 4 MHz is nearly the double of the resonance frequency.) To ensure the presence of sub- and ultraharmonics with moderate destruction of microbubbles, Forsberg et al. have proposed in [16] a pressure range from 1.2 MPa to 1.8 MPa. To limit the destruction of microbubbles, we set the pressure level to the lowest value at 1.2 MPa. The burst consists of 18 cycles. The sampling frequency is $f_s = 60$ MHz. The parameters of the microbubble are given in the Table 1 [13].

5. Results

In this research, the performances of different modeling methods are evaluated qualitatively and quantitatively.

5.1. Qualitative Evaluation. To evaluate qualitatively the two MISO methods, MISO1 (with the basis proposed in [12])

TABLE 1: The parameters of microbubbles [13].

Resting radius	$r_0 = 1.5 \mu\text{m}$
Shell thickness	$d_{\text{se}} = 1.5 \text{ nm}$
Shear modulus	$G_s = 10 \text{ MPa}$
Shear viscosity	$\eta = 1.49 \text{ Pa}\cdot\text{s}$

and MISO2 (with the new basis proposed in the present work) with respect to SISO Volterra method, temporal representations of $y(n)$ and $\hat{y}(n)$, and spectral representations $|Y(k)|^2$ and $|\hat{Y}(k)|^2$ of the nonlinear system backscattered by the contrast agent in nonlinear mode are presented in Figure 5.

Results presented in Figure 5 are obtained for a signal to tissue ratio $\text{SNR} = \infty$ and using Volterra model of order $P = 3$ and memory $M = 19$.

To better distinguish the different harmonic components of ultrasound signal, six cycles of $0.05 \mu\text{s}$ are presented in Figure 5(a), and a bandwidth of 13 MHz covering the 3 harmonics potentially accessible in ultrasound imaging is presented in Figure 5(b). For both types of representations, the fundamental frequency, harmonics, sub- and ultraharmonics are well apparent. In Figure 5(a) (top), only harmonic components at f_0 , $2f_0$, and $3f_0$ are modeled by SISO Volterra. This result confirms that SISO Volterra system is unable to correctly model sub- and ultraharmonics at frequencies $f_0/2$, $(3/2)f_0$, and $(5/2)f_0$. In Figure 5 (middle, bottom), all the spectral components are correctly modeled validating the two MISO approaches.

5.2. Quantitative Evaluation. To determine accurately the performances of the two methods and to know which Volterra approach provides the best performances a quantitative study is necessary. The relative mean square error (RMSE) defined as follows:

$$\text{RMSE} = \frac{\mathbb{E}[(\hat{y}(t) - y(t))^2]}{\mathbb{E}[(y(t))^2]} \quad (19)$$

is evaluated for different noise levels at the system output. The noise level, adjusted as a function of SNR, is Gaussian and white. Ten realizations are made to evaluate the fluctuations of RMSE. RMSE for $\text{SNR} = \infty, 20, 15$, and 10 dB is reported in Figure 6. A zoom in Figure 6(d) shows the fluctuations of the EQMR around a mean value.

The main result of these simulations shows that regardless the SNR values, MISO Volterra methods provide a much better RMSE than SISO Volterra method. In fact, a gap between SISO Volterra method and the two methods MISO1 and MISO2 going from 5 to 16 dB can be obtained depending on the SNR conditions. These results confirm that SISO Volterra method is not suitable for sub- and ultraharmonic modeling. A zoom on Figure 6(d) emphasizes the small fluctuations of the RMSE. This result shows the robustness of the two MISO Volterra approaches towards noise.

Note that the RMSE obtained with the two MISO Volterra approaches are similar and follows the same trend. However,

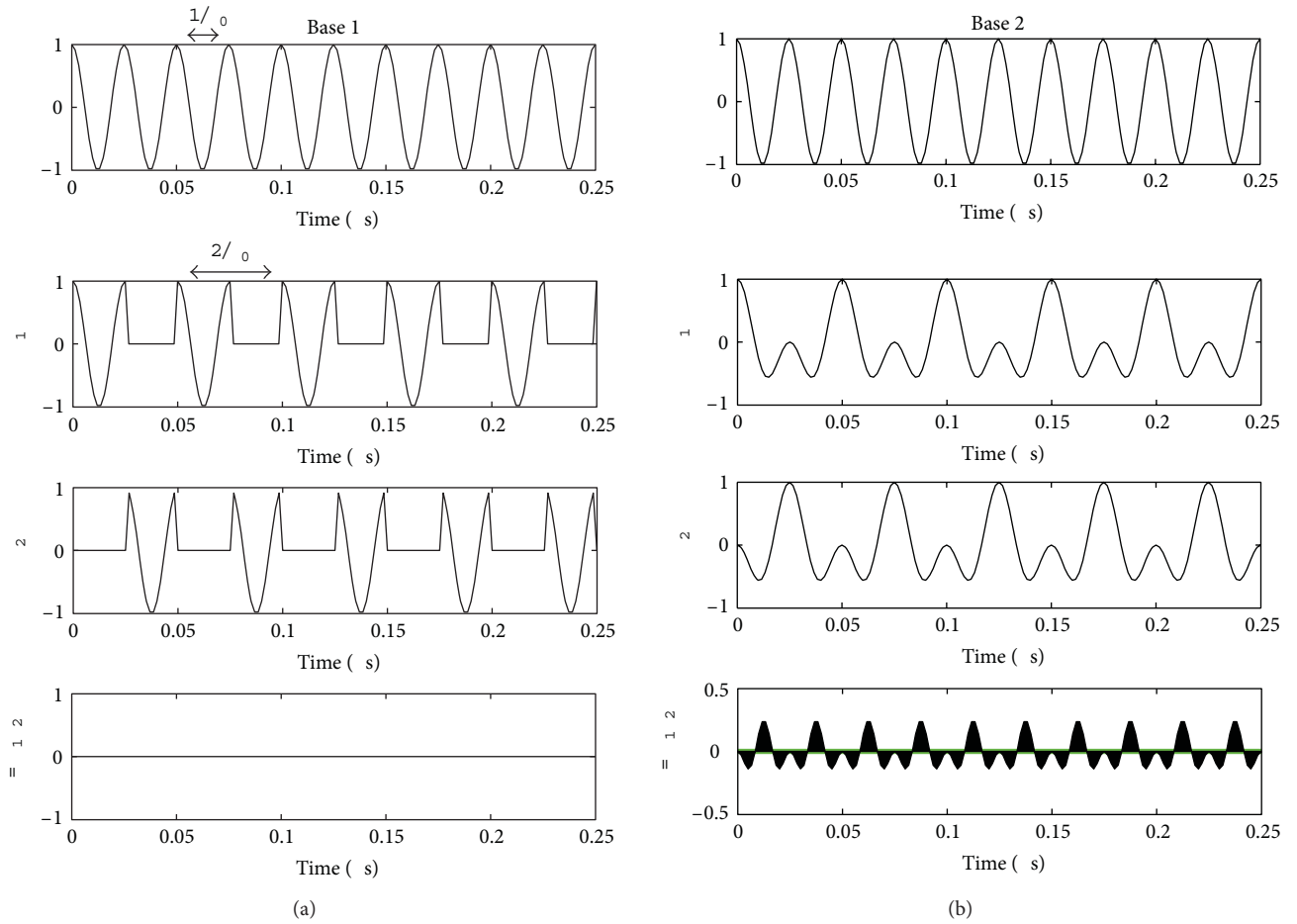


FIGURE 3: From top to bottom: input signal x , modified inputs x_1 , and x_2 , and the product $x_1 x_2$, (a) for the rectangular basis (basis 1) and (b) for the new basis (basis 2).

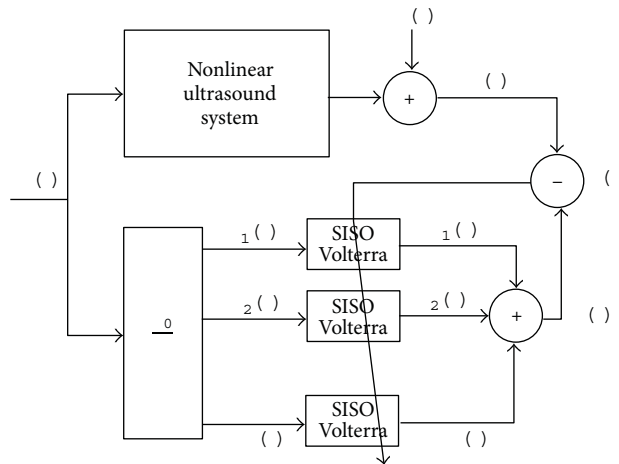


FIGURE 4: Block diagram of orthogonal MISO Volterra model.

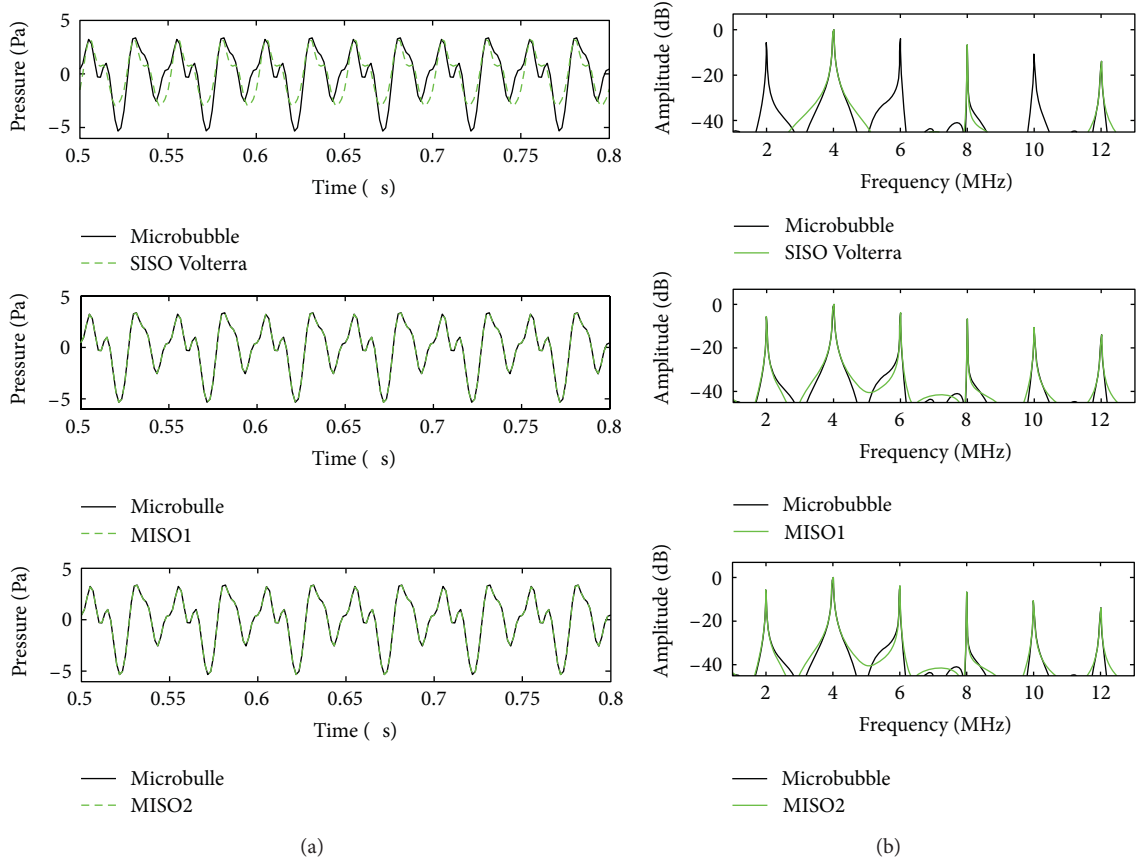


FIGURE 5: (a) Comparison between the backscattered signal by the microbubble $y(n)$ (black) and its estimation $\hat{y}(n)$ (green): (top) the modeled signal with SISO Volterra model, (middle) MISO1 method, and (bottom) MISO2 method. (b) Spectra of different signals are presented in (1). Here SNR = ∞ dB, $P = 3$, and $M = 19$.

a small advantage in favor of MISO2 method with respect to MISO1 method for memory values m smaller than 6 is noted.

Finally, the more the memory increases, the more the RMSE decreases, indicating that the different methods tend asymptotically toward the optimal solution.

6. Discussions and Conclusions

In the present research, we proposed a general framework that describes harmonic, sub-, and ultraharmonics modeling using Volterra decomposition. This framework allowed us to highlight three essential criteria instead of two, to accurately model sub- and ultraharmonics:

- (i) as suggested in [12], the basis should be periodic of period f_0/N ;
- (ii) as suggested in [12], Volterra system should be a MISO system;
- (iii) as suggested in this work, the decomposition of the input signal to Volterra model $x(n)$ must be done with an orthogonal basis.

This general framework has also justified the different steps of the decomposition thus allowing to propose new

periodic orthogonal bases more efficient. It is the same for the choice of the order of Volterra model, which was limited to three. In fact, for more or less severe constraints on the ultrasound transducers bandwidth, the order can be reduced or increased.

This more general formulation provides a methodological basis for optimal sub- and ultraharmonics contrast imaging and opens a new research axis for more efficient periodic orthogonal bases of MISO Volterra systems and also for new MISO systems based on Hammerstein models or Wiener models.

Appendix

A. Decomposition of MISO Volterra Model of 2 Inputs to 2 SISO Volterra Models

A MISO Volterra model with N inputs is equivalent to N SISO Volterra models if and only if the mean square error to be minimized between $y(n)$ and $\hat{y}(n)$ is the same in both cases. We will determine the conditions that must be satisfied by the inputs $x_1(n)$ and $x_2(n)$ of MISO Volterra when $N = 2$, to have this equivalence.

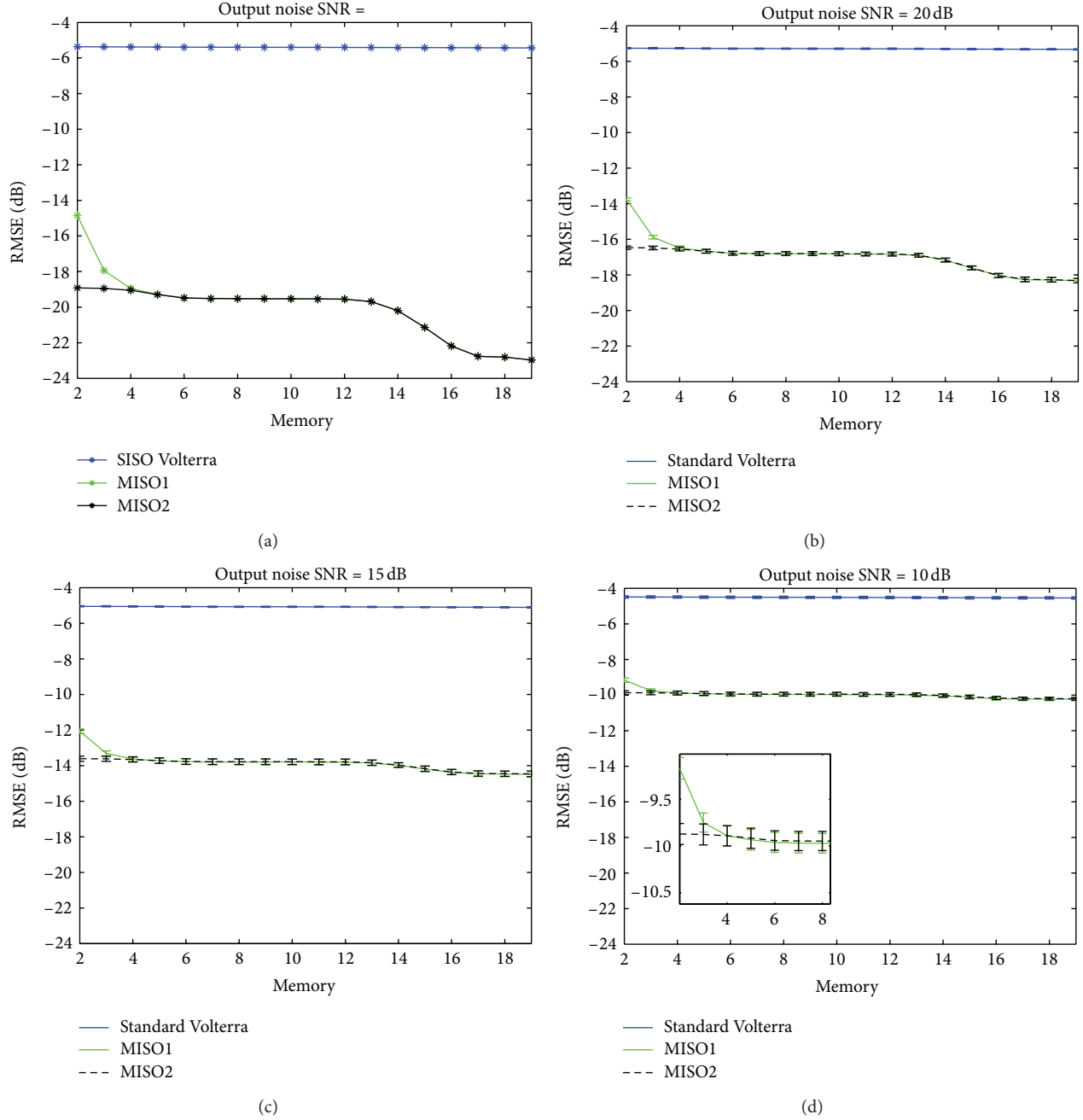


FIGURE 6: Variation of the RMSE in dB between the modeled signal with SISO Volterra (blue), MISO1 method (green), and MISO2 method (black) and the backscattered signal by the microbubble as a function of the memory of Volterra model in the presence of noisy output: (a) SNR = ∞ dB, (b) SNR = 20 dB, (c) SNR = 15 dB, and (d) SNR = 10 dB.

Volterra kernels are calculated using the least squares method by minimizing the mean square error (MSE) between $y(n)$ and the modeled signal $\hat{y}(n)$:

$$\mathbb{E} \left[(y(n) - \hat{y}(n))^2 \right]. \quad (\text{A.1})$$

For MISO Volterra model, the decomposition of $x(n)$ into $x_1(n)$ and $x_2(n)$ such that $x(n) = x_1(n) + x_2(n)$ requires that

$y(n) = y_1(n) + y_2(n)$. It follows that $\hat{y}(n) = \hat{y}_1(n) + \hat{y}_2(n)$. The error to be minimized is

$$\begin{aligned} & \mathbb{E} \left[(y(n) - \hat{y}(n))^2 \right] \\ &= \mathbb{E} \left[y(n)^2 \right] + \mathbb{E} \left[\hat{y}(n)^2 \right] - 2\mathbb{E} \left[y(n) \hat{y}(n) \right] \\ &= \mathbb{E} \left[(y_1(n) + y_2(n))^2 \right] + \mathbb{E} \left[(\hat{y}_1(n) + \hat{y}_2(n))^2 \right] \\ &\quad - 2\mathbb{E} \left[(y_1(n) + y_2(n)) (\hat{y}_1(n) + \hat{y}_2(n)) \right] \end{aligned}$$

$$\begin{aligned}
&= \mathbb{E} [y_1(n)^2] + \mathbb{E} [y_2(n)^2] + 2\mathbb{E} [y_1(n) y_2(n)] \\
&\quad + \mathbb{E} [\hat{y}_1(n)^2] + \mathbb{E} [\hat{y}_2(n)^2] + 2\mathbb{E} [\hat{y}_1(n) \hat{y}_2(n)] \\
&\quad - 2\mathbb{E} [y_1(n) \hat{y}_1(n)] - 2\mathbb{E} [y_1(n) \hat{y}_2(n)] \\
&\quad - 2\mathbb{E} [y_2(n) \hat{y}_1(n)] - 2\mathbb{E} [y_2(n) \hat{y}_2(n)].
\end{aligned} \tag{A.2}$$

For the 2 SISO Volterra models of inputs $x_1(n)$ and $x_2(n)$ and outputs $y_1(n)$ and $y_2(n)$, respectively, the error to be minimized is

$$\begin{aligned}
&\mathbb{E} [(y_1(n) - \hat{y}_1(n))^2] + \mathbb{E} [(y_2(n) - \hat{y}_2(n))^2] \\
&= \mathbb{E} [y_1(n)^2] + \mathbb{E} [\hat{y}_1(n)^2] - 2\mathbb{E} [y_1(n) \hat{y}_1(n)] \\
&\quad + \mathbb{E} [y_2(n)^2] + \mathbb{E} [\hat{y}_2(n)^2] - 2\mathbb{E} [y_2(n) \hat{y}_2(n)].
\end{aligned} \tag{A.3}$$

A MISO Volterra model could be seen as 2 SISO Volterra models if (A.2) and (A.3) are equal. This equality gives

$$\begin{aligned}
&\mathbb{E} [y_1(n) y_2(n)] + \mathbb{E} [\hat{y}_1(n) \hat{y}_2(n)] \\
&\quad - \mathbb{E} [y_1(n) \hat{y}_2(n)] - \mathbb{E} [y_2(n) \hat{y}_1(n)] = 0.
\end{aligned} \tag{A.4}$$

One possible solution is that each term of the equation is equal to zero:

$$\begin{aligned}
&\mathbb{E} [y_1(n) y_2(n)] = 0, \\
&\mathbb{E} [\hat{y}_1(n) \hat{y}_2(n)] = 0, \\
&\mathbb{E} [y_1(n) \hat{y}_2(n)] = 0, \\
&\mathbb{E} [y_2(n) \hat{y}_1(n)] = 0.
\end{aligned} \tag{A.5}$$

Therefore

$$\begin{aligned}
&y_1(n) \perp y_2(n), \\
&\hat{y}_1(n) \perp \hat{y}_2(n), \\
&y_1(n) \perp \hat{y}_2(n), \\
&y_2(n) \perp \hat{y}_1(n),
\end{aligned} \tag{A.6}$$

where \perp means orthogonal. Elsewhere, $\hat{y}_1(n)$ and $\hat{y}_2(n)$ are calculated according to (1). That implies that

$$\begin{aligned}
&\mathbb{E} [\hat{y}_1(n) \hat{y}_2(n)] \\
&= \mathbb{E} \left[\sum_{k_1=0}^{M-1} h_1(k_1) x_1(n-k_1) \sum_{k_1=0}^{M-1} h_1'(k_1) x_2(n-k_1) \right. \\
&\quad + \sum_{k_1=0}^{M-1} \sum_{k_2=0}^{M-1} h_2(k_1, k_2) x_1(n-k_1) x_1(n-k_2) \\
&\quad \times \sum_{k_1=0}^{M-1} \sum_{k_2=0}^{M-1} h_2'(k_1, k_2) x_2(n-k_1) \\
&\quad \left. \times x_2(n-k_2) + \dots \right] = 0.
\end{aligned} \tag{A.7}$$

One possible solution is that each term of the equation is equal to zero. For the first term, we get

$$\begin{aligned}
&\mathbb{E} \left[\sum_{k_1=0}^{M-1} h_1(k_1) x_1(n-k_1) \sum_{k_1=0}^{M-1} h_1'(k_1) x_2(n-k_1) \right] \\
&= \sum_{k_1=0}^{M-1} h_1(k_1) h_1'(k_1) \mathbb{E} [x_1(n-k_1) x_2(n-k_1)] \\
&= 0.
\end{aligned} \tag{A.8}$$

The last equation implies that $x_1(n) \perp x_2(n)$. For the other terms in (A.7), we obtain the same conclusion $x_1(n) \perp x_2(n)$. Therefore, $\hat{y}_1(n)$ and $\hat{y}_2(n)$ are orthogonal if $x_1(n)$ and $x_2(n)$ are also orthogonal.

Elsewhere, if $\hat{y}_1(n)$ and $\hat{y}_2(n)$ are the estimations of $y_1(n)$ and $y_2(n)$, then $\hat{y}_1(n) \approx y_1(n)$ and $\hat{y}_2(n) \approx y_2(n)$. This means that the orthogonality of $\hat{y}_1(n)$ and $\hat{y}_2(n)$ implies the orthogonality of each couple formed by the four signals presented in (A.5). This is true if and only if $x_1(n) \perp x_2(n)$.

Therefore, a MISO Volterra model with two inputs could be treated as two SISO Volterra models if the two inputs are orthogonal. This result could be generalized for MISO Volterra model with N inputs.

Acknowledgment

The authors would like to thank the Lebanese council of scientific research (CNRSL) for financing this work.

References

- [1] P. J. A. Frinking, A. Bouakaz, J. Kirkhorn, F. J. Ten Cate, and N. de Jong, "Ultrasound contrast imaging: current and new potential methods," *Ultrasound in Medicine and Biology*, vol. 26, no. 6, pp. 965–975, 2000.
- [2] T. G. Leighton, *The Acoustic Bubble*, Academic Press, London, UK, 1994.
- [3] P. N. Burns, "Instrumentation for contrast echocardiography," *Echocardiography*, vol. 19, no. 3, pp. 241–258, 2002.
- [4] M. A. Averkiou, "Tissue Harmonic Imaging," in *Proceedings of the IEEE International Ultrasonics Symposium*, vol. 2, pp. 1563–1572, October 2000.
- [5] P. M. Shankar, P. D. Krishna, and V. L. Newhouse, "Advantages of subharmonic over second harmonic backscatter for contrast-to-tissue echo enhancement," *Ultrasound in Medicine and Biology*, vol. 24, no. 3, pp. 395–399, 1998.
- [6] R. Basude and M. A. Wheatley, "Generation of ultraharmonics in surfactant based ultrasound contrast agents: use and advantages," *Ultrasonics*, vol. 39, no. 6, pp. 437–444, 2001.
- [7] L. Hoff, *Acoustic Characterization of Contrast Agents for Medical Ultrasound Imaging*, Kluwer Academic, Boston, Mass, USA, 2001.
- [8] K. E. Morgan, J. S. Allen, P. A. Dayton, J. E. Chomas, A. L. Klibaov, and K. W. Ferrara, "Experimental and theoretical evaluation of microbubble behavior: effect of transmitted phase and bubble size," *IEEE Transactions on Ultrasonics Ferroelectrics and Frequency Control*, vol. 47, no. 6, pp. 1494–1509, 2000.

- [9] P. Marmottant, S. van der Meer, M. Emmer et al., "A model for large amplitude oscillations of coated bubbles accounting for buckling and rupture," *Journal of the Acoustical Society of America*, vol. 118, no. 6, pp. 3499–3505, 2005.
- [10] V. Volterra, *Theory of Functionals and of Integral and Integro-Differential Equations*, Blackie & Son, Glasgow, UK, 1930.
- [11] M. Schetzen, *The Volterra and Wiener Theories of Nonlinear Systems*, Wiley, New York, NY, USA, 1980.
- [12] O. M. Boaghe and S. A. Billings, "Subharmonic oscillation modeling and MISO Volterra series," *IEEE Transactions on Circuits and Systems*, vol. 50, no. 7, pp. 877–884, 2003.
- [13] C. Samakee and P. Phukpattaranont, "Application of MISO Volterra Series for Modeling Subharmonic of Ultrasound Contrast Agent," *International Journal of Computer and Electrical Engineering*, vol. 4, no. 4, pp. 445–451, 2012.
- [14] V. J. Mathews and G. L. Sicuranza, *Polynomial Signal Processing*, Wiley, New York, NY, USA, 2000.
- [15] C. C. Church, "The effects of an elastic solid surface layer on the radial pulsations of gas bubbles," *Journal of the Acoustical Society of America*, vol. 97, no. 3, pp. 1510–1521, 1995.
- [16] F. Forsberg, W. T. Shi, and B. B. Goldberg, "Subharmonic imaging of contrast agents," *Ultrasonics*, vol. 38, no. 1–8, pp. 93–98, 2000.

Research Article

Ultrasound Common Carotid Artery Segmentation Based on Active Shape Model

Xin Yang,¹ Jiaoying Jin,² Mengling Xu,² Huihui Wu,² Wanji He,³
Ming Yuchi,² and Mingyue Ding^{1,2}

¹ State Key Laboratory for Multispectral Information Processing Technologies, Institute for Pattern Recognition and Artificial Intelligence (IPRAI), Huazhong University of Science and Technology (HUST), Wuhan, Hubei 430074, China

² Department of Biomedical Engineering, College of Life Science and Technology, Image Processing and Intelligence Control Key Laboratory of Education of Ministry of China, Huazhong University of Science and Technology (HUST), Wuhan, Hubei 430074, China

³ Biomedical Instrument Institute, Med-X Research Institute, Shanghai Jiaotong University, Shanghai 200030, China

Correspondence should be addressed to Mingyue Ding; myding@mail.hust.edu.cn

Received 20 December 2012; Revised 29 January 2013; Accepted 31 January 2013

Academic Editor: Peng Feng

Copyright © 2013 Xin Yang et al. This is an open access article distributed under the Creative Commons Attribution License, which permits unrestricted use, distribution, and reproduction in any medium, provided the original work is properly cited.

Carotid atherosclerosis is a major reason of stroke, a leading cause of death and disability. In this paper, a segmentation method based on Active Shape Model (ASM) is developed and evaluated to outline common carotid artery (CCA) for carotid atherosclerosis computer-aided evaluation and diagnosis. The proposed method is used to segment both media-adventitia-boundary (MAB) and lumen-intima-boundary (LIB) on transverse views slices from three-dimensional ultrasound (3D US) images. The data set consists of sixty-eight, $17 \times 2 \times 2$, 3D US volume data acquired from the left and right carotid arteries of seventeen patients (eight treated with 80 mg atorvastatin and nine with placebo), who had carotid stenosis of 60% or more, at baseline and after three months of treatment. Manually outlined boundaries by expert are adopted as the ground truth for evaluation. For the MAB and LIB segmentations, respectively, the algorithm yielded Dice Similarity Coefficient (DSC) of $94.4\% \pm 3.2\%$ and $92.8\% \pm 3.3\%$, mean absolute distances (MAD) of 0.26 ± 0.18 mm and 0.33 ± 0.21 mm, and maximum absolute distances (MAXD) of 0.75 ± 0.46 mm and 0.84 ± 0.39 mm. It took 4.3 ± 0.5 mins to segment single 3D US images, while it took 11.7 ± 1.2 mins for manual segmentation. The method would promote the translation of carotid 3D US to clinical care for the monitoring of the atherosclerotic disease progression and regression.

1. Introduction

Cardiovascular disease (CVD) is the leading cause of death globally based on the World Health Organization (WHO, 2009). The main precursors of CVD are smoking, obesity, hypertension, and a disturbed serum lipid profile [1]. The therapy evaluation and clinical data analysis are important to the cerebrovascular and cardiovascular pathologies diagnosis. Because thrombosis generation and subsequent cerebral emboli have a high risk leading to death, carotid atherosclerosis is becoming a significant issue for researches recently [2]. Measurement accuracy and geometric understanding of common carotid artery (CCA) play an important role in carotid atherosclerosis assessment and management [3], which requires precise segmentation.

Ultrasound (US) has been employed as a routine examination for inexpensive and noninvasive clinical diagnosis of atherosclerosis (the hardening of the arteries) [4, 5]. Furthermore, the three-dimensional ultrasound (3D US) [6] imaging can be used to quantitatively monitor carotid plaque progression or regression without ionizing radiation [7–10].

Among various US image segmentation methods for carotid atherosclerosis quantification [11–15], intima-media thickness (IMT) measurement is proved to work efficiently on longitudinal views of two-dimensional (2D) US images [16]. The media-adventitia boundary (MAB) and lumen-intima boundary (LIB) can be extracted simultaneously. This work focuses on the MAB and LIB segmentation on the transverse views US images and is expected to reduce diagnosticians' manual workload (Figure 1). The potential

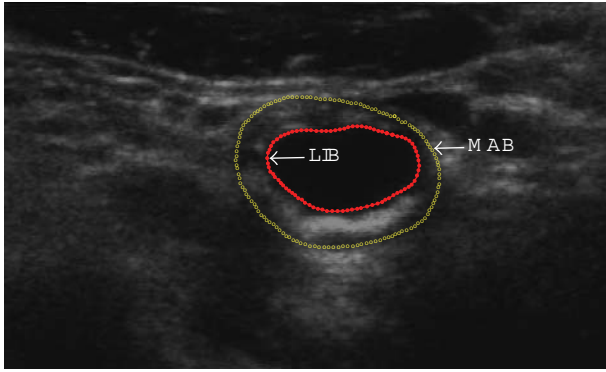


FIGURE 1: US image of a carotid artery with the expert-drawn contours delineating the LIB (red solid contour) and MAB (yellow hollow point contour).

applications mainly include patient management, genetic research, and therapy evaluation [17].

Several automatic and semiautomatic methods for the segmentation of LIB and/or MAB on 2D transverse US images have been reported [18, 19]. Mao et al. [20] proposed a deformable contour model approach for carotid LIB semiautomated segmentation. One seed point was located on the image by the user firstly. Then, the local gradient difference was obtained with local grey level ratio between the exterior and interior of the deformable contour. The method was validated by a group of seven B-mode US images. Abolmaesumi et al. [21] presented a method to fulfill real-time extraction of carotid LIB on 2D US image sequences. They modified the star algorithm by using a temporal Kalman filter to track the center of LIB and adopting a spatial Kalman filter to extract LIB contour. Digitized US video images were used for validation. Zahalka and Fenster [22] introduced a carotid LIB segmentation method on 3D US images with geometrically deformable model (GDM). Li et al. [23] also developed a GDM with automatic merge function to segment carotid contours, but only tested their method on simulated 3D US images. A scheme for detecting the normal regions in carotid artery US images was proposed by Balasundaram and Banu [24]; however, no process was taken to remove the noise in the images. Lou and Ding [25] used particle motion mechanics to segment object boundaries. The method was sensitive to noise. Fast Marching Method (FMM) [26] originally for intravascular ultrasound (IVUS) image segmentation was also adopted for vascular US image segmentation. Common carotid artery (CCA) boundary identification pipeline, a simple and effective method, was proposed according to mathematical morphology [27], but it was only tested for limited lumen boundaries segmentation. The latest segmentation method for carotid MAB and LIB in transverse US images was proposed by Ukwatta et al. [28]. They adopted an active contour based on level set method. A combination of image information from energy, geodesic energy, and anchor constraint energy was used to drive the deformable contour to the desired one. However, the global optimum of the searching parameters cannot be guaranteed. Other studies by application of regional growing

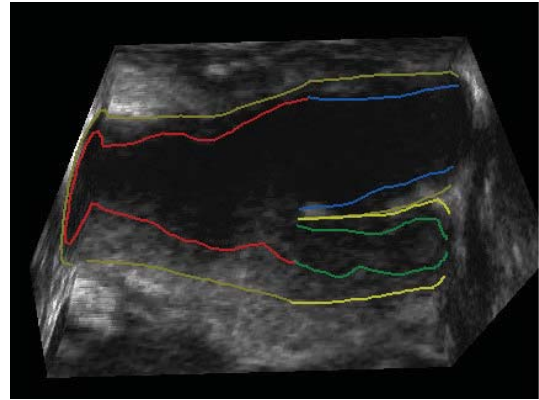


FIGURE 2: Three-dimensional ultrasound carotid artery longitudinal view in clinical trials [40]. Both baseline and follow-up 3D images, constructed from the set of 2D frames, were examined simultaneously to visually match the bifurcation (BF) points in both images by an operator blinded to time point and treatment. Each 3D US image was manually segmented starting from the bifurcation point extending into around 10–15 mm of common carotid artery (CCA) and about 10 mm into internal carotid artery (ICA) at 1 mm interval perpendicular to the artery axis; refer to Figure 3. This study was only carried out on the CCA, since the focus was on stroke risk.

[29], diffusion-based filters [30], edge detection combined with morphology methods [31], and Hough transforms [32], were also reported.

Our purpose is therefore to develop and validate a new segmentation approach, which would be used to delineate the lumen-intima boundary (LIB) and media-adventitia boundary (MAB) of the common carotid artery (CCA) from 3D US images. The key innovation of this work is applying the Active Shape Model (ASM) segmentation to two separate time points, which used baseline data for training and follow-up data for segmentation. And the technology enables the accurate, inexpensive, and noninvasive method for progression and regression monitoring of atherosclerosis and drug therapy evaluation.

The following of this paper is organized as follows. In Section 2, the proposed method is explained in details. The results are shown in Section 3. Sections 4 and 5 will contain the discussion and conclusion.

2. Methods

The proposed algorithm is validated by comparing the LIB and MAB segmentation results with the manual ones from the expert. The typical US images used in this paper are shown in Figures 1 and 2. Figure 1 shows a transverse view of a CCA with manually annotated MAB and LIB boundaries superimposed. Figure 2 shows the surface of the manual segmented inner and outer walls, including CCA, internal carotid artery (ICA), external carotid artery (ECA), and carotid sinus (bifurcation (BF)).

The atheromatous plaque has been well described in terms of its progression, and the clinical characterization of the atherosclerotic lesion has also been well documented

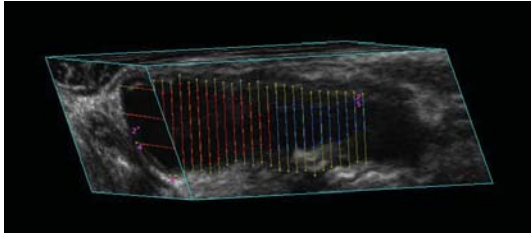


FIGURE 3: Sagittal cross-section of a common carotid artery (CCA) in 3D US image. The contours on the image show the manual delineations done by the physician. The inner boundary is lumen-intima boundary (LIB), and the outer boundary is the media-adventitia boundary (MAB). The segmentations were performed on parallel images with interslice distance (ISD) 1 mm.

[33]. Furthermore, it is true that plaques (a) extend into the internal carotid artery and (b) that rupture of these plaques will lead to stroke which has been well documented. However, the vulnerable plaque in terms of its concepts is still a novel area [34]. “Vulnerable plaque” is a term that has been derived from a subgroup known as stenotic plaques. They are prone to both rupture and erosion, sometimes causing acute coronary syndromes and sudden cardiac death. Rupture prone plaques have been shown in postmortem evaluation to have specific characteristics [35]. Depending on the severity level of the plaque, dietary change, drug treatment, or eventually surgical treatment such as carotid endarterectomy (CEA) may be introduced to prevent major heart attacks or strokes.

As will be described in the following sections, the assessment of plaque vulnerability and risk of potential rupture is very difficult noninvasively [36, 37]. And the three-dimensional (3D) US vessel wall volume (VWV) measurement is a 3D measurement of the vessel wall thickness plus plaque within the carotid arteries. 3D US VWV measurements are sensitive to changes in both intima-media thickness and plaque and thus provide alternative and complementary information to IMT [38, 39]. The MAB and LIB segmentation on cross-section is a vital step for both qualitative and quantitative evaluation. In most cases, the CCA can be used to reflect and evaluate the carotid atherosclerosis severity much more comprehensively and accurately than ICA and ECA; this may be due to the significant amount of plaque present proximal to the BF of the carotid artery. Therefore, the proposed segmentation method was only carried out on the CCA, since the focus was on the essential part of stroke risk.

In this study, we only segmented a portion of the common carotid artery (CCA). However, in the future, we will investigate the segmentation of the internal and external carotid arteries (ICA, ECA) as well. The proposed algorithm segments each transverse slice independently and is a first step toward reducing the operator interaction for carotid segmentation. As for a future work, we will investigate the use of both slice-by-slice propagation and direct 3D segmentation to reduce the operator interaction further by utilizing the image information along the out of plane direction as well.

2.1. Image Acquisition. The mechanical 3D US system utilized in this study was described previously in [40]. The images were acquired by driving a linear ultrasound transducer (L12-5, Philips, Bothell, WA, USA, 8.5 MHz central frequency) with a motorized linear device along the neck of the subject at a uniform speed of 3 mm/s for about 4 cm without cardiac gating [6].

The 2D ultrasound frames were captured by the US machine (ATL HDI 5000, Philips, Bothell, WA, USA) and reconstructed to 3D images with 3D Quantify (a multiplanar visualization software) [41]. The voxel size was approximately $0.1 \times 0.1 \times 0.15 \text{ mm}^3$.

The 3D Quantify generates 2D images of the artery by slicing through the 3D image orthogonally to the medial axis, in the inferior direction from the bifurcation (BF), with an interslice distance (ISD) of 1 mm (Figure 3).

2.2. Study Subjects. Seventeen patients with carotid stenosis over 60% were enrolled in this study [6]. The presence of stenosis was verified using carotid Doppler US flow velocities. 8 subjects, 4 males and 4 females with mean age \pm SD (65 ± 6.6 years), were supplied with 80 mg atorvastatin daily for 3 months. The remaining 9 subjects, 4 males and 5 females with mean age \pm SD (68 ± 8.4 years), were assigned to the placebo. Baseline and follow-up (3 months later) 3D US images were acquired for each subject, for both left and right carotid arteries. All subjects, in this study, were recruited from the Premature Atherosclerosis Clinic and the Stroke Prevention Clinic at University Hospital (London Health Sciences Center, London, Canada) and the Stroke Prevention and Atherosclerosis Research Center (Robarts Research Institute, London, ON, Canada).

A written informed consent of the study protocol approved by the University of Western Ontario Standing Board of Human Research Ethics was provided to all subjects.

2.3. Manual Segmentation. Manual segmentation of CCA boundaries is labor intensive and time consuming [42]. There are several studies on semiautomated segmentation methods for delineating carotid walls with 2D US images [21].

The manual segmentation method used in our work was proposed by Egger et al. [18]. Prior to contouring, the expert first located the BF and defined an approximate medial axis of the carotid artery by choosing two end points of the axis. The multiplanar 3D viewing software then presented 2D images of the artery by slicing through the 3D image orthogonally to the medial axis, in the inferior direction from the BF, with an ISD of 1 mm. The expert then performed contouring of arteries on each of these images. Figure 1 showed a transverse view of a common carotid artery with manually annotated boundaries overlaid. An expert outlined the vessel boundaries for five times within one-day intervals. The image sequences were randomized, and the operators were blinded to the image order during each repetition to reduce memory bias [28].

2.4. Preprocessing. Several preprocessing steps were applied prior to LIB and MAB segmentation. Firstly, contrast limited adaptive histogram equalization (CLAHE) [43] was applied

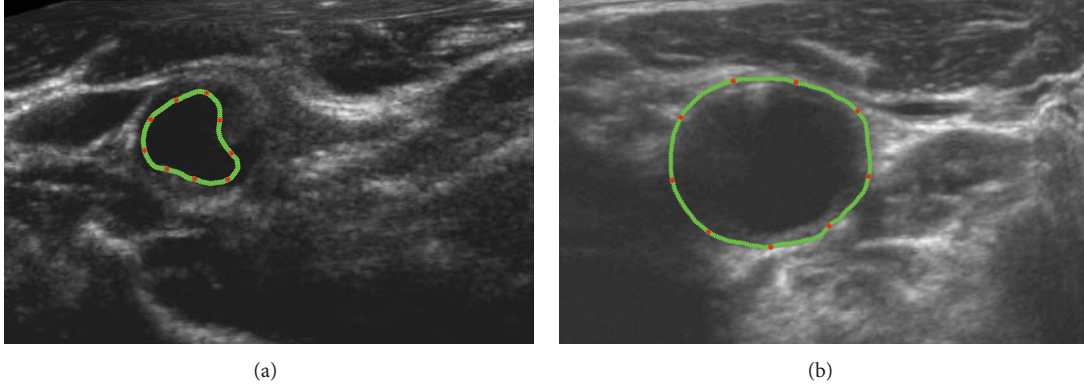


FIGURE 4: Nine equally spaced landmark points (red points) along the manual contour (green points) were averagely picked for ASM training ((a): LIB; (b): MAB; refer to Figure 1). Three hundred and forty images were labelled by senior physicians. Some of the points may locate on weak edges.

to enhance the local contrast of the US image. CLAHE partitioned the images into contextual regions and applied histogram equalization by fitting a Rayleigh distribution to each region [44]. Next, Speckle Reducing Anisotropic Diffusion Method (SRAD) was used for US speckle noise reduction [45]. The SRAD was used to enhance the edges by inhibiting diffusion across edges and allowing diffusion on either side of the edges.

2.5. Active Shape Model (ASM). Active Shape Model (ASM) is one of the statistical shape models (SSMs) developed by Cootes et al. in 1995 [46]. The shape of an object is usually represented by a set of n points in ASM. By analysing the variations in shape, a statistical model is built which can mimic the variation [47]. The ASM algorithm seeks to match a set of model points to an image, constrained by the statistical model of shape which learns the valid ranges of shape variation from the training set of labelled images [48]. The general working steps of ASM are as follows: (a) look in the image around each point for a better position for that point (to locate a better position for each point one can look for strong edges, or an expected match to a statistical model at the point); (b) compute the changes in the pose and shape parameters based on (a); (c) update the model parameters to improve the match between a shape model and image instance to ensure the model only deforms into shapes consistent with the training set.

The technique is widely used to analyse images of faces, mechanical assemblies, and medical images in 2D applications. Given a rough starting approximation (X^0), the ASM matches the CCA model points to a new image using an iterative technique. An ASM is defined by (1):

$$X = \bar{X} + P \cdot b, \quad (1)$$

where \bar{X} represents the mean shape of the training set, P is a matrix of the first few principal components of the shape, created by using Principal Component Analysis (PCA), and b is shape parameters for the model, along with parameters defining the global pose (the position, orientation, and scale)

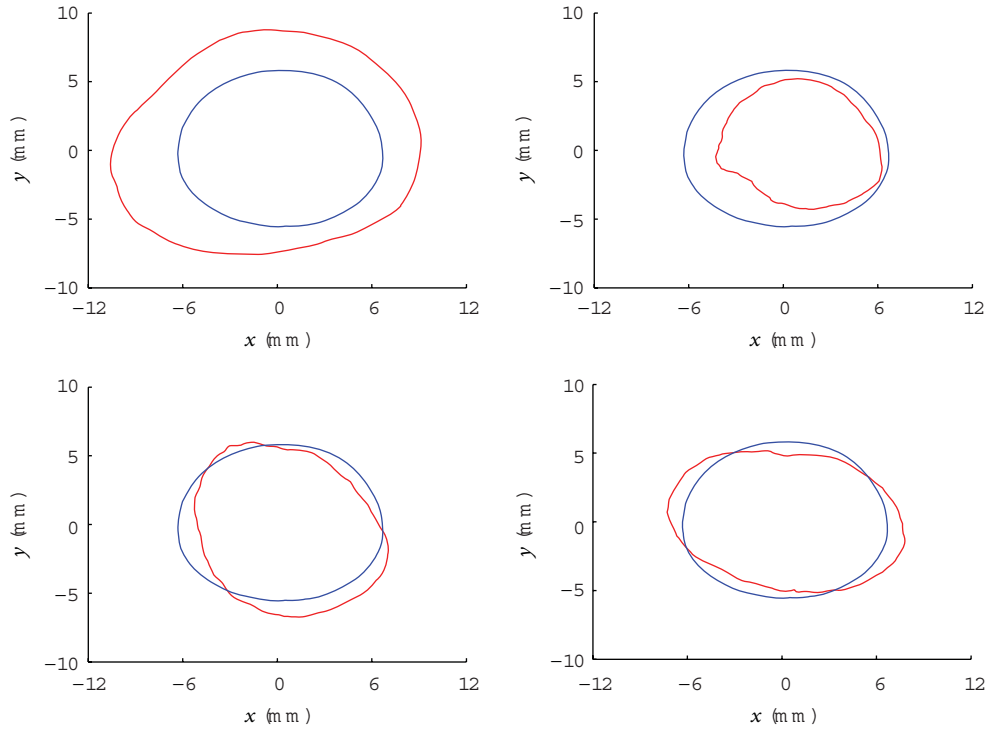
[48], whose standard deviation from the mean shape ranges between -3 and $+3$. Therefore, X is defined by the variable b . Given a set of landmark points X^i for iteration i , the goal is to find the landmark points \hat{X}^i closest to the object border. The shape is then updated by (2):

$$b = P^T \cdot (\hat{X}^i - X^i), \quad (2)$$

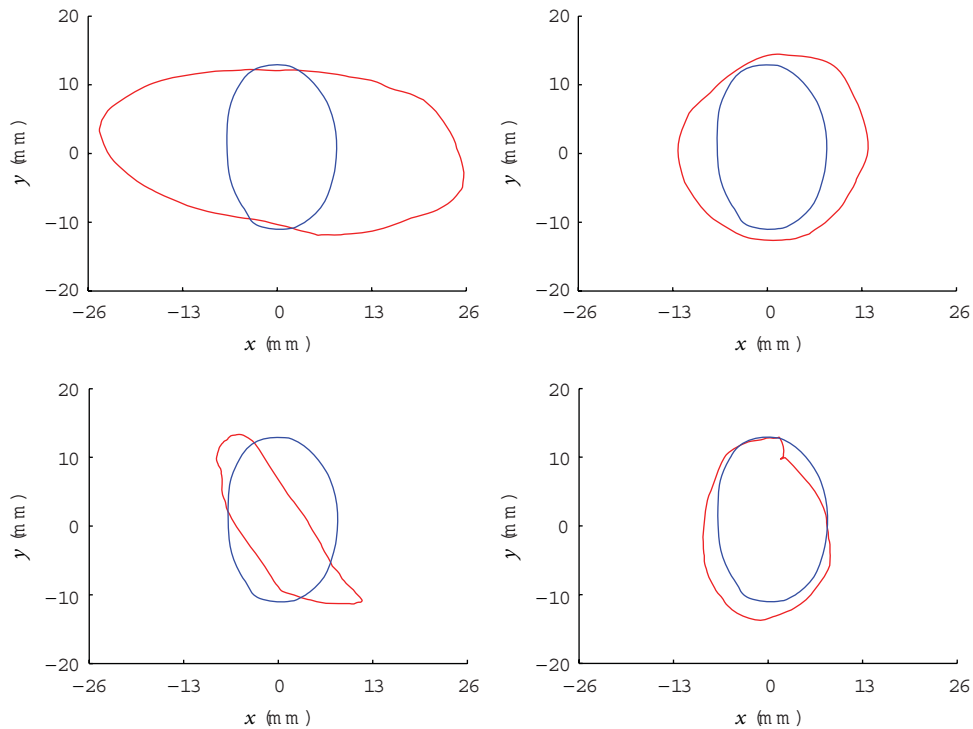
where each element of b can only be within ± 3 standard deviations of the mean shape. The final ASM segmentation is denoted as X^{Final} . The training set of the ASM to determine \bar{X} and P is performed by manual delineation of the artery boundaries followed by manual alignment of 9 equally spaced landmark points (red points) along the contour (green points) on both LIB and MAB as shown in Figure 4.

It should be noted that once the ASM is trained with the training set, it can be used for the new CCA image segmentations without significant manual intervention. Six hundred and eighty 2D CCA images in total, extracted from the 3D US data (10 two-dimensional images per each of 17 patients of two sides at 2 time points), have had their arterial walls manually segmented previously as the golden standard. Three hundred and forty ($10 \times 17 \times 2$) 2D CCA baseline images data and manual boundaries results were used for ASM learning as shown in Figure 5, while another three hundred and forty treatment images data were used for ASM segmentation and evaluation. And a demonstration of MAB segmentation progress is shown in Figure 6.

CVD morbidity and mortality rates are higher in atherosclerosis patients than in the general population [49], leading to a reduced lifespan, lower quality of life, and increased medical expenditures. Cross-sectional studies have shown that underlying these higher CVD rates is a greater burden of atherosclerosis in both the coronary [50] and carotid [51] vasculature of patients. Therefore, imaging technique needs to be considered to monitor substantial plaque progression or regression of atherosclerosis [52], even though the progression or regression of the disease may be significant or not between the two time points [6].



(a) Modelling LIB shape and its variations of training set: the fixed blue-solid contours are the mean lumen shapes, while the red-solid contours are deformed lumen shapes of the first four eigenvectors



(b) Modelling MAB shape and its variations of training set: the fixed blue-solid contours are the mean adventitia shapes, while the red-solid contours are deformed adventitia shapes of the first four eigenvectors

FIGURE 5: Mean shapes in each panel are the fixed (in blue); the first four eigenvectors-corresponded deformed shapes are diverse (in red), because of the variety shapes of the LIB (a) and MAB (b) of training set. The units of both x - and y -axes of every subpicture are (mm). The training results are generated from three hundred and forty 2D CCA baseline images data. The blue contour is the average shape of baseline images data (training set), while the red one is the deformed shapes. The average shape contour would be superposed on follow-up images data (test set) as the initialization contour for ASM segmentation (refer to movie 1 in Supplementary Material available online at <http://dx.doi.org/10.1155/2013/345968>).

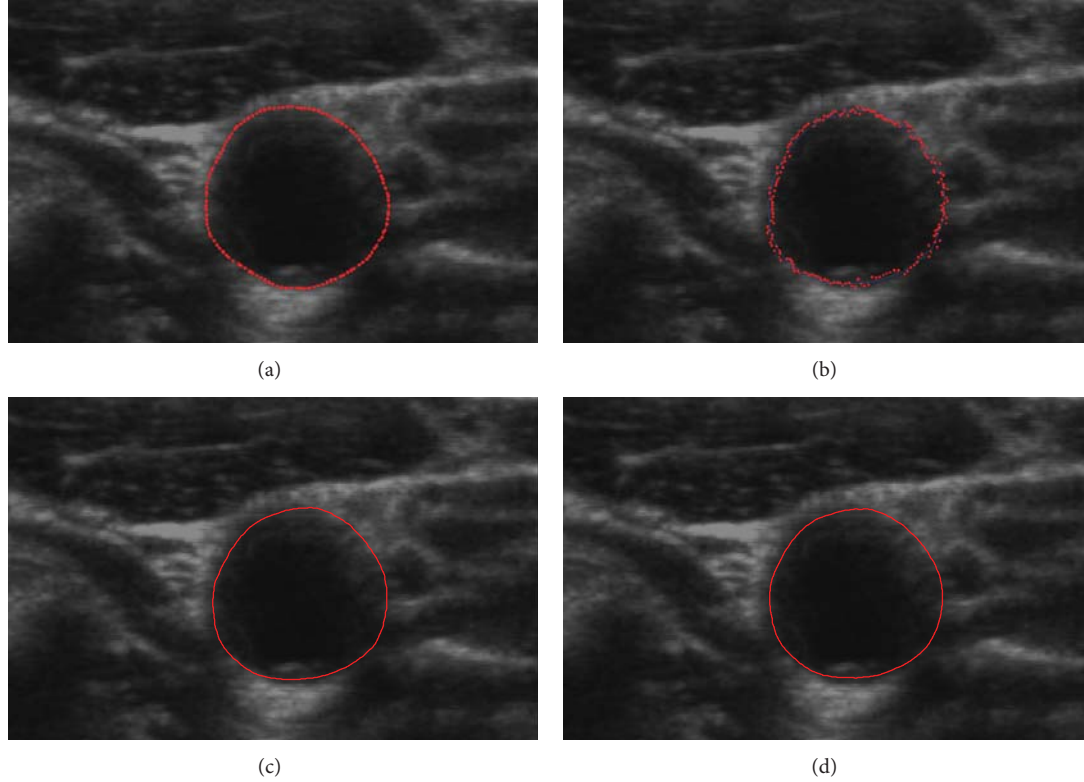


FIGURE 6: Adventitia results comparison after the three-month therapy: (a) original image with the manual segmentation result as a golden standard; (b) ASM segmentation process (refer to movie II in Supplementary Material available online at <http://dx.doi.org/10.1155/2013/345968>); (c) segmentation result of the proposed method; (d) segmentation result of the training set without the example data.

The main findings in the study [53] is that dietary interventions can induce a significant regression of carotid atherosclerosis, which could be detectable by B-mode and 3-dimensional ultrasound (3D US). What is more, based on the research of [40], the change is also significant during three-month statin treatment (atorvastatin) [54].

Since carotid anatomy varies considerably within individuals between left and right carotid arteries even in two different time points, which affects the development of plaque, and the low correlation coefficient between the left and right sides, each carotid artery can be considered an independent object [55]. Thus, the data sets used in this study could be considered as different objects, which were lowly correlated ones with statistical significance significant change.

Also, the authors would use completely different slices from various scans of diverse patients in future work as totally uncorrelated individual data to thoroughly separate the test and training data sets. And a preliminary test results showed that there was no obvious subjective differences, from which the training set is within (Figure 6(c)) and without (Figure 6(d)) the example baseline data.

Furthermore, external or internal carotid arteries (ECA, ICA) stenosis is less frequent and clinically less important than CCA stenosis, and the segmented contours of CCA could be used for drug treatment evaluation between baseline time and follow-up time.

2.6. Evaluation Metrics. The Dice Similarity Coefficient (DSC) was used as a region-based measure to compare segmentation results on slice-by-slice basis. The DSC quantifies the overlapping areas of two segmentation methods by the following equation (3):

$$DSC = 2 \frac{|R_M \cap R_P|}{|R_M| + |R_P|}, \quad (3)$$

where R_M and R_P denote the region of the manual and proposed method boundaries, respectively.

The mean absolute distance (MAD) and maximum absolute distance (MAXD) were used as boundary distance-based metrics. The averages of MAD (see (4)) and MAXD (see (5)) were computed using all vessels in the testing images to obtain an overall estimate of boundary disagreement. And the computational time is also estimated:

$$MAD_{M,T} = \frac{1}{K} \sum_{i=1}^K |d(m_i, T)|, \quad (4)$$

$$MAXD_{M,T} = \max_{i \in [1, K]} \{|d(m_i, T)|\}, \quad (5)$$

where $d(m_i, T)$ is the distance between the vertex m_i of the manual drawn contour and its corresponding vertex on ASM contour T , and K is the number of vertices.

3. Results

Figure 6 shows the MAB segmentation progress after follow-up treatment. Figure 7 shows the segmentation results of 18 slices with the proposed approach and manually contours for 3 subjects with a moderate level of plaque.

3.1. Validation. The validation of our segmentation algorithm will require comparison with manual segmentation results. The accuracy, variability, and reproducibility of the proposed algorithm were evaluated by comparing with the physician-drawn contours. Three to five experts delineated the CCA boundaries on 340 2D slices. The method of Chalana and Kim [56] was used to compute the mean boundary from the repeated manual and algorithm-generated segmentations. The ordering of the images was randomized to reduce learning effects.

DSC, MAD, and MAXD were computed from 3D US images to obtain overall estimates of each metric for the image set. Table 1 shows the overall evaluation results of the proposed algorithm for 340 transverse 2D US slices extracted from 17 subjects after treatment.

The proposed method yielded a DSC of $94.4\% \pm 3.2\%$ and $92.8\% \pm 3.3\%$ for the MAB and LIB, respectively. The method gave submillimeter error values for the MAD of 0.26 ± 0.18 mm and 0.33 ± 0.21 mm and MAXD of 0.75 ± 0.46 mm and 0.84 ± 0.39 mm for the MAB and LIB, respectively. Our approach took 4.3 ± 0.5 mins comparing to 11.7 ± 1.2 mins of operator processing time for manual segmentation to initialize/delineate a single 3D image [44].

4. Discussion

ASM performs exceptionally well when compared to other deformable models, especially when segmenting objects that do not have a clear, continuous boundary like the CCA. It can capture expert prior knowledge in the training examples annotation and compare resulting shapes easily simultaneously, since they have a strict point correspondence between landmark points. Therefore, ASM has been extensively explored and still under investigation as well in methodological aspects as in concrete applications.

The ASM algorithm is an iterative approach. It would be applied to the training set of CCA arteries to locate the other arteries. Assuming there is not a big difference between the frames, the shape for one frame can be used as the starting point for the search in the next, and it will require a few iterations to lock on. This approach is particularly useful for cases where the objects have a well-defined shape with a representative and available set of examples [57]. In medical image segmentation, because of the complexity of human anatomy and the volatility of the appearance, traditional approaches cannot obtain desired results. It requires a flexible framework which can combine the properties of the image itself with its prior knowledge.

In this paper, we introduced the ASM segmentation method to delineate the LIB and MAB boundaries of the CCA on transverse view sliced from 3D US images. The proposed method was evaluated by comparing the resulting

boundaries and expert manually outlined boundaries which act as a surrogate for ground truth. The algorithm yielded a higher DSC for the MAB than for the LIB, and the algorithm gave similar MAD and MAXD errors for both vascular walls. It was obvious that the adventitia value is better than lumen, which implies that we got the better MAB segmentation result. The observations may result from (a) weak image edges, particularly on boundary segmentation that are parallel to the US beam direction and are not hard for ASM learning and segmentation; (b) different components between the two layers caused the different performance. Inside lumen is liquid blood, while the outside adventitia is complex connective tissue from the view of CCA physiology; (c) the initialized average contours from baseline training data have differences with the test data.

Most previous studies of the relationship between hemodynamic factors and plaque stability have used in vitro models. It is difficult to determine how accurate these models represent conditions in vivo.

By studying carotid bifurcation angiograms, Schulz and Rothwell [58] found the relationship between vessel anatomy and plaque stability in vivo. And they have shown that carotid anatomy varies considerably between individuals and can be very asymmetrical within individuals, which is not similar to faces or hands at all. Although it is possible that the variation in arterial anatomy might influence training and test results, there have been no previous studies of the association between arterial anatomy and ASM algorithm stability in either the coronary or carotid circulations of atherosclerosis.

Ideally, a study of the association between carotid anatomy and statistical model would require a large community-based cohort imaged with double-blinded randomly selected. Unfortunately, given the relatively low prevalence of moderate or severe carotid disease in the community (only dozens of cases) is not possible. And training and testing in this study may be performed within a round-robin (leave-one-case-out) protocol later.

The ASM approach has been demonstrated in 2D data. Our future work will extend it to 3D application. More 3D data needed to be collected. In addition, the definitions of surfaces and 3D topology are more complex than those required for 2D arteries boundaries. However, 3D models which represent shape deformation can be successfully used to locate structures in 3D data sets.

5. Conclusion

The main purpose of this work was to develop and evaluate a new segmentation algorithm for outlining both MAB and LIB of CCA on 2D transverse views sliced from 3D US images. From a quantitative evaluation of the results, we concluded that the proposed method could accurately segment the CCA and also the saved time on average was substantial.

We have used the point distribution model to represent an object as a set of labelled points, giving their mean positions and a small set of modes of variation. Applying limits to the parameters of the model enforces global shape constraints. The constraints ensure that the properties of the testing one

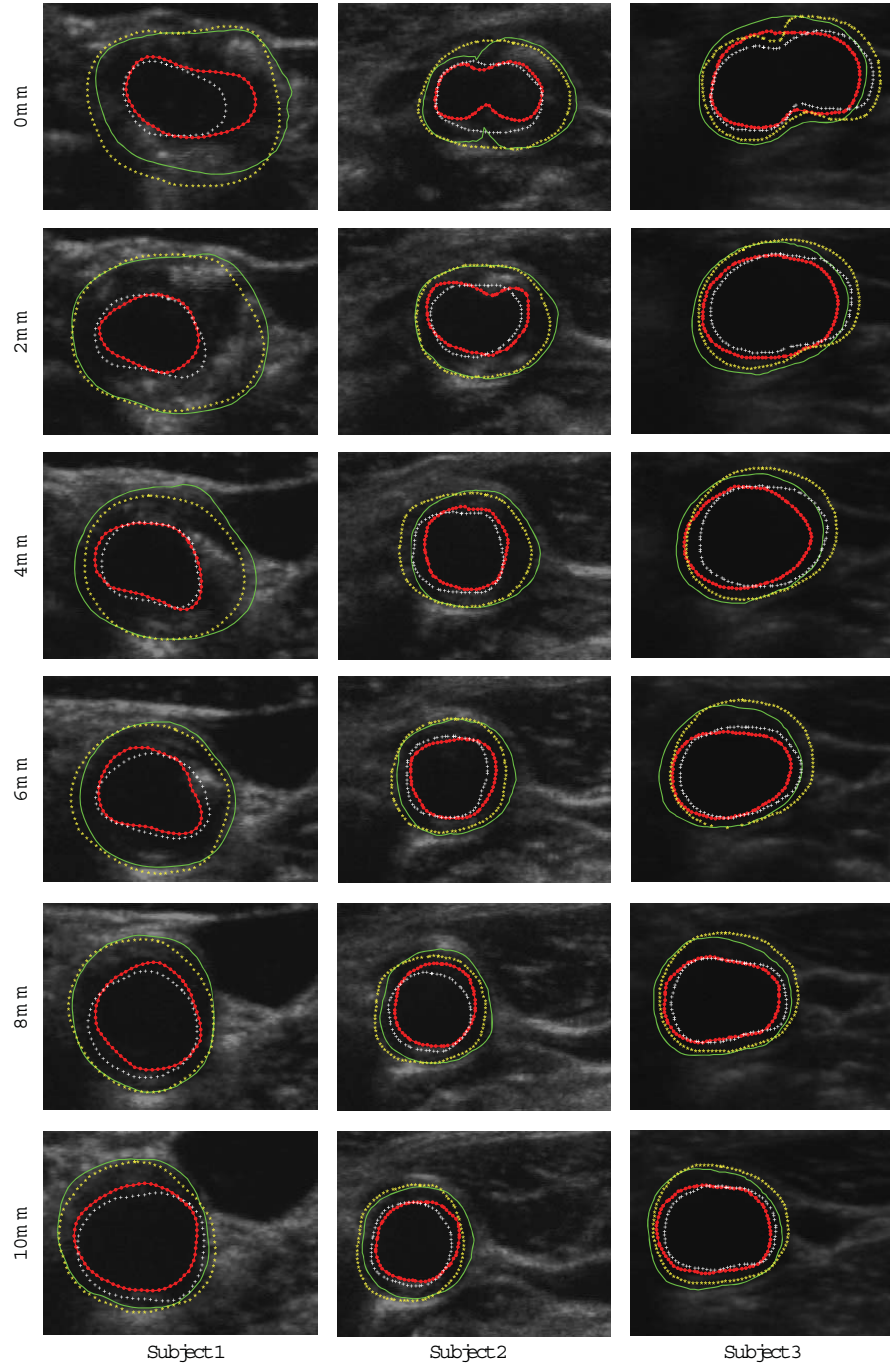


FIGURE 7: In order to subjectively and objectively evaluate the performance between the proposed approach and manually method, both inner and outer contours are synchronized overlapped together. Green-solid-line outer contour and red-dotted-line inner contour represent manual MAB and LIB, respectively; while yellow-starred outer contour and white-plus-signed inner contour represent algorithm-generated MAB and LIB, respectively. Each column represents the images of individual patient. For each row from the top to the bottom, there are images at different distance of 0, 2, 4, 6, 8 and 10 mm from the slice to the bifurcation (BF).

are similar to those of the training set. Given a set of shape parameters, ASM can match the generated model to a new similar image rapidly.

Preliminary experimental results showed that the segmented areas could accurately define the locations of CCA contours. This method could save the physicians' time. Our

work provides an easy-handle technique to simplify the job of labeling the contours in CCA manually. Therefore, it would be helpful to promote the translation of 3D carotid US to clinical care for the fast, safety, and economical monitoring of the atherosclerotic disease progression and regression during therapy.

TABLE 1: Overall performance results of the proposed algorithm. Validation results of segmentation for 340 transverse slices of both left and right sides from seventeen subjects (eight with 80 mg atorvastatin and nine with placebo, resp.,) after three-month treatment.

Metric	DC (%)	MAD (mm)	MAXD (mm)
Media-adventitia boundary (MAB)	94.4 ± 3.2	0.26 ± 0.18	0.75 ± 0.46
Lumen-intima boundary (LIB)	92.8 ± 3.3	0.33 ± 0.21	0.84 ± 0.39

In this method, the segmentations of the MAB and LIB can be used as a fundamental step in the analysis of carotid plaque composition for the early identification of vulnerable plaques and treatment evaluation to prevent a possible stroke [40]. The proposed approach has another merit, as clinical trials will be carried out temporal continuity on the same patients by serially imaging them. Thus, manual segmentation of the first time point followed by the authors, more automated method would save analysis time.

Future work would be focused on (a) ICA and ECA segmentation, (b) directly artery segmentation, and (c) thoroughly reducing the potential correlation between training and test sets for reasonable double-blinded test.

Acknowledgments

This work is supported by the National 973 Project (Grant no. 2011CB933103), the National Natural Science Foundation of China (NSFC) (Grant no. 30911120497/H0215, 61001141), the Project of the National 12th-Five Year Research Program of China (Grant no. 2012BA113B02), and the Research Fund for the Doctoral Program of Higher Education of China (Grant no. 20090142120091). The authors would like to thank Dr. Aaron Fenster, Mr. Eranga Ukwatta, and Dr. Wu Qiu, from Robarts Research Institute, London, ON, Canada, for the collaborative work on project named as “Analysis of Carotid Atherosclerosis Using 3D US Imaging.” The authors also would like to thank Dr. Xuming Zhang, Dr. Wenguang Hou, Miss Yanping Jia and Mr. Xidian Wang, from Huazhong University of Science and Technology (HUST), for their assistance with data collection, insightful comments, and revision feedback.

References

- [1] I. F. Groeneveld, K. I. Proper, A. J. van der Beek, and W. van Mechelen, “Sustained body weight reduction by an individual-based lifestyle intervention for workers in the construction industry at risk for cardiovascular disease: results of a randomized controlled trial,” *Preventive Medicine*, vol. 51, no. 3-4, pp. 240–246, 2010.
- [2] C. Warlow, “MRC European Carotid Surgery Trial: interim results for symptomatic patients with severe (70–99%) or with mild (0–29%) carotid stenosis,” *The Lancet*, vol. 337, no. 8752, pp. 1235–1243, 1991.
- [3] A. Fenster, G. Parraga, A. Landry, B. Chiu, M. Egger, and J. D. Spence, “3DUS imaging of the carotid arteries,” in *Advances in Diagnostic and Therapeutic Ultrasound Imaging*, pp. 67–92, Artech House, 1st edition, 2008.
- [4] A. J. Lusis, “Atherosclerosis,” *Nature*, vol. 407, no. 6801, pp. 233–241, 2000.
- [5] P. N. T. Wells, “Current status and future technical advances of ultrasonic imaging,” *IEEE Engineering in Medicine and Biology Magazine*, vol. 19, no. 5, pp. 14–20, 2000.
- [6] C. D. Ainsworth, C. C. Blake, A. Tamayo, V. Beletsky, A. Fenster, and J. D. Spence, “3D ultrasound measurement of change in carotid plaque volume: a tool for rapid evaluation of new therapies,” *Stroke*, vol. 36, no. 9, pp. 1904–1909, 2005.
- [7] T. S. Hatsukami, B. D. Thackray, J. F. Primozich et al., “Echolucent regions in carotid plaque: preliminary analysis comparing three-dimensional histologic reconstructions to sonographic findings,” *Ultrasound in Medicine and Biology*, vol. 20, no. 8, pp. 743–749, 1994.
- [8] U. Schminke, L. Motsch, B. Griewing, M. Gaull, and C. Kessler, “Three-dimensional power-mode ultrasound for quantification of the progression of carotid artery atherosclerosis,” *Journal of Neurology*, vol. 247, no. 2, pp. 106–111, 2000.
- [9] W. Steinke and M. Hennerici, “Three-dimensional ultrasound imaging of carotid artery plaques,” *Journal of Cardiovascular Technology*, vol. 8, no. 1, pp. 15–22, 1989.
- [10] A. Troyer, D. Saloner, X. M. Pan, P. Velez, and J. H. Rapp, “Major carotid plaque surface irregularities correlate with neurologic symptoms,” *Journal of Vascular Surgery*, vol. 35, no. 4, pp. 741–747, 2002.
- [11] F. Destrempes, J. Meunier, M. F. Giroux, G. Soulez, and G. Cloutier, “Segmentation in ultrasonic B-mode images of carotid arteries using mixture of Nakagami distributions and stochastic optimization,” *IEEE Transactions on Medical Imaging*, vol. 28, pp. 215–229, 2009.
- [12] Q. Liang, I. Wendelhag, J. Wikstrand, and T. Gustavsson, “A multiscale dynamic programming procedure for boundary detection in ultrasonic artery images,” *IEEE Transactions on Medical Imaging*, vol. 19, no. 2, pp. 127–142, 2000.
- [13] C. P. Loizou, C. S. Pattichis, M. Pantziaris, T. Tyllis, and A. Nicolaides, “Snakes based segmentation of the common carotid artery intima media,” *Medical and Biological Engineering and Computing*, vol. 45, no. 1, pp. 35–49, 2007.
- [14] F. Molinari, K. M. Meiburger, G. Zeng, A. Nicolaides, and J. S. Suri, “CAUDLES-EF: carotid automated ultrasound double line extraction system using edge flow,” *Journal of Digital Imaging*, vol. 24, no. 6, pp. 1059–1077, 2012.
- [15] R. Rocha, A. Campilho, J. Silva, E. Azevedo, and R. Santos, “Segmentation of ultrasound images of the carotid using RANSAC and cubic splines,” *Computer Methods and Programs in Biomedicine*, vol. 101, no. 1, pp. 94–106, 2011.
- [16] M. L. Bots, A. W. Hoes, P. J. Koudstaal, A. Hofman, and D. E. Grobbee, “Common carotid intima-media thickness and risk of stroke and myocardial infarction: the Rotterdam Study,” *Circulation*, vol. 96, no. 5, pp. 1432–1437, 1997.
- [17] J. D. Spence, “Technology insight: ultrasound measurement of carotid plaque—patient management, genetic research, and therapy evaluation,” *Nature Clinical Practice Neurology*, vol. 2, no. 11, pp. 611–619, 2006.
- [18] M. Egger, J. D. Spence, A. Fenster, and G. Parraga, “Validation of 3D ultrasound vessel wall volume: an imaging phenotype

- of carotid atherosclerosis," *Ultrasound in Medicine and Biology*, vol. 33, no. 6, pp. 905–914, 2007.
- [19] A. Krasinski, B. Chiu, J. D. Spence, A. Fenster, and G. Parraga, "Three-dimensional ultrasound quantification of intensive statin treatment of carotid atherosclerosis," *Ultrasound in Medicine and Biology*, vol. 35, no. 11, pp. 1763–1772, 2009.
- [20] F. Mao, J. Gill, D. Downey, and A. Fenster, "Segmentation of carotid artery in ultrasound images: method development and evaluation technique," *Medical Physics*, vol. 27, no. 8, pp. 1961–1970, 2000.
- [21] P. Abolmaesumi, M. Sirouspour, and S. Salcudean, "Real-time extraction of carotid artery contours from ultrasound images," in *Proceedings of the 13th IEEE Symposium on Computer-Based Medical Systems (CBMS '00)*, pp. 181–186, June 2000.
- [22] A. Zahalka and A. Fenster, "An automated segmentation method for three-dimensional carotid ultrasound images," *Physics in Medicine and Biology*, vol. 46, no. 4, pp. 1321–1342, 2001.
- [23] X. Li, Z. Wang, H. Lu, and Z. Liang, "Automated segmentation method for the 3D ultrasound carotid image based on geometrically deformable model with automatic merge function," in *Medical Imaging*, vol. 4684 of *Proceedings of the SPIE*, pp. 1458–1463, 2002.
- [24] J. K. Balasundaram and R. S. D. W. Banu, "A non-invasive study of alterations of the carotid artery with age using ultrasound images," *Medical and Biological Engineering and Computing*, vol. 44, no. 9, pp. 767–772, 2006.
- [25] L. Lou and M. Ding, "Principle and approach of boundary extraction based on particle motion in quantum mechanics," *Optical Engineering*, vol. 46, no. 2, Article ID 027005, 2007.
- [26] M. R. Cardinal, G. Soulez, J. Tardif, J. Meunier, and G. Cloutier, "Fast-marching segmentation of three-dimensional intravascular ultrasound images: a pre- and post-intervention study," *Medical Physics*, vol. 37, no. 7, pp. 3633–3647, 2010.
- [27] X. Yang, M. Ding, L. Lou, M. Yuchi, W. Qiu, and Y. Sun, "Common carotid artery lumen segmentation in b-mode ultrasound transverse view images," *International Journal of Image, Graphics and Signal Processing*, vol. 3, no. 5, pp. 15–21, 2011.
- [28] E. Ukwatta, J. Awad, A. D. Ward et al., "Three-dimensional ultrasound of carotid atherosclerosis: semiautomated segmentation using a level set-based method," *Medical Physics*, vol. 38, no. 5, pp. 2479–2493, 2011.
- [29] A. Abdel-Dayem and M. El-Sakka, "Carotid artery ultrasound image segmentation using Fuzzy region growing," in *Image Analysis and Recognition*, M. Kamel and A. Campilho, Eds., vol. 3656, pp. 869–878, Springer, Berlin, Germany, 2005.
- [30] A. Abdel-Dayem and M. El-Sakka, "Diffusion-based detection of carotid artery lumen from ultrasound images," in *Image Analysis and Recognition*, M. Kamel and A. Campilho, Eds., vol. 5627, pp. 782–791, Springer, Berlin, Germany, 2009.
- [31] A. K. Hamou and M. R. El-Sakka, "A novel segmentation technique for carotid ultrasound images," in *Proceedings of the IEEE International Conference on Acoustics, Speech, and Signal Processing (ICASSP'04)*, pp. III521–III524, May 2004.
- [32] S. Golemati, J. Stoitsis, E. G. Sifakis, T. Balkizas, and K. S. Nikita, "Using the Hough transform to segment ultrasound images of longitudinal and transverse sections of the carotid artery," *Ultrasound in Medicine and Biology*, vol. 33, no. 12, pp. 1918–1932, 2007.
- [33] C. Schwartz, A. Valente, E. A. Sprague, J. Kelley, and R. Nerem, "The pathogenesis of atherosclerosis: an overview," *Clinical Cardiology*, vol. 14, no. 2, pp. 1–16, 1991.
- [34] A. V. Finn, M. Nakano, J. Narula, F. D. Kolodgie, and R. Virmani, "Concept of vulnerable/unstable plaque," *Arteriosclerosis, Thrombosis, and Vascular Biology*, vol. 30, no. 7, pp. 1282–1292, 2010.
- [35] J. Layland, A. Wilson, I. Lim, and R. Whitbourn, "Virtual histology: a window to the heart of atherosclerosis," *Heart Lung and Circulation*, vol. 20, no. 10, pp. 615–621, 2011.
- [36] F. Tavora, N. Cresswell, L. Li, D. Fowler, and A. Burke, "Frequency of acute plaque ruptures and thin cap atheromas at sites of maximal stenosis," *Arquivos Brasileiros de Cardiologia*, vol. 94, no. 2, pp. 143–159, 2010.
- [37] I. M. Graf, J. Su, D. Yeager, J. Amirian, R. Smalling, and S. Emelianov, "Methodical study on plaque characterization using integrated vascular ultrasound, strain and spectroscopic photoacoustic imaging," in *Photons Plus Ultrasound: Imaging and Sensing*, vol. 7899 of *Proceedings of the SPIE*, San Francisco, Calif, USA.
- [38] G. Parraga, A. A. House, A. Krasinski, J. D. Spence, and A. Fenster, "Volumetric evaluation of carotid atherosclerosis using 3-dimensional ultrasonic imaging," in *Ultrasound and Carotid Bifurcation Atherosclerosis*, pp. 263–277, Springer, New York, NY, USA, 1st edition, 2012.
- [39] D. N. Buchanan, T. Lindenmaier, S. McKay et al., "The relationship of carotid three-dimensional ultrasound vessel wall volume with age and sex: comparison to carotid intima-media thickness," *Ultrasound in Medicine & Biology*, vol. 38, no. 7, pp. 1145–1153, 2012.
- [40] J. Awad, A. Krasinski, G. Parraga, and A. Fenster, "Texture analysis of carotid artery atherosclerosis from three-dimensional ultrasound images," *Medical Physics*, vol. 37, no. 4, pp. 1382–1391, 2010.
- [41] A. Fenster, D. B. Downey, and H. N. Cardinal, "Three-dimensional ultrasound imaging," *Physics in Medicine and Biology*, vol. 46, no. 5, pp. R67–R99, 2001.
- [42] B. Chiu, M. Egger, J. D. Spence, G. Parraga, and A. Fenster, "Quantification of carotid vessel wall and plaque thickness change using 3D ultrasound images," *Medical Physics*, vol. 35, no. 8, pp. 3691–3700, 2008.
- [43] S. M. Pizer, E. P. Amburn, J. D. Austin et al., "Adaptive histogram equalization and its variations," *Computer Vision, Graphics, and Image Processing*, vol. 39, no. 3, pp. 355–368, 1987.
- [44] E. Ukwatta, J. Awad, A. Ward et al., "Segmentation of the lumen and media-adventitia boundaries of the common carotid artery from 3D ultrasound images," in *Medical Imaging: Computer-Aided Diagnosis*, vol. 7963 of *Proceedings of the SPIE*, Lake Buena Vista, Fla, USA, February 2011.
- [45] Y. Yu and S. T. Acton, "Speckle reducing anisotropic diffusion," *IEEE Transactions on Image Processing*, vol. 11, no. 11, pp. 1260–1270, 2002.
- [46] T. F. Cootes, C. J. Taylor, D. H. Cooper, and J. Graham, "Active shape models-their training and application," *Computer Vision and Image Understanding*, vol. 61, pp. 38–59, 1995.
- [47] T. F. Cootes and C. J. Taylor, "Statistical models of appearance for computer vision," *World Wide Web Publication*, 2001.
- [48] T. F. Cootes, G. Edwards, and C. J. Taylor, "Comparing active shape models with active appearance models," in *Proceedings of the British Machine Vision Conference*, pp. 173–183, 1999.
- [49] N. N. Mehta, R. S. Azfar, D. B. Shin, A. L. Neimann, A. B. Troxel, and J. M. Gelfand, "Patients with severe psoriasis are at increased risk of cardiovascular mortality: cohort study using the general practice research database," *European Heart Journal*, vol. 31, no. 8, pp. 1000–1006, 2010.

- [50] J. T. Giles, M. Szklo, W. Post et al., "Coronary arterial calcification in rheumatoid arthritis: comparison with the Multi-Ethnic Study of Atherosclerosis," *Arthritis Research and Therapy*, vol. 11, no. 2, article R36, 2009.
- [51] H. Kobayashi, J. T. Giles, J. F. Polak et al., "Increased prevalence of carotid artery atherosclerosis in rheumatoid arthritis is artery-specific," *Journal of Rheumatology*, vol. 37, no. 4, pp. 730–739, 2010.
- [52] S. J. Nicholls and P. Lundman, "Monitoring regression and progression of atherosclerosis," in *Cardiovascular Imaging for Clinical Practice*, S. Nicholls and S. Worthley, Eds., pp. 237–373, Jones & Bartlett Learning, 1st edition, 2010.
- [53] I. Shai, J. D. Spence, D. Schwarzfuchs et al., "Dietary intervention to reverse carotid atherosclerosis," *Circulation*, vol. 121, no. 10, pp. 1200–1208, 2010.
- [54] X. Yang, R. Wang, L. Li, A. Fenster, and M. Ding, "Classification of atorvastatin effect based on shape and texture features in ultrasound images," in *Medical Imaging*, vol. 8669 of *Proceedings of the SPIE*, Lake Buena Vista, Fla, USA, February 2013.
- [55] U. G. R. Schulz and P. M. Rothwell, "Major variation in carotid bifurcation anatomy: a possible risk factor for plaque development?" *Stroke*, vol. 32, no. 11, pp. 2522–2529, 2001.
- [56] V. Chalana and Y. Kim, "A methodology for evaluation of boundary detection algorithms on medical images," *IEEE Transactions on Medical Imaging*, vol. 16, no. 5, pp. 642–652, 1997.
- [57] B. Van Ginneken, A. F. Frangi, J. J. Staal, B. M. Romeny, and M. A. Viergever, "Active shape model segmentation with optimal features," *IEEE Transactions on Medical Imaging*, vol. 21, pp. 924–933, 2002.
- [58] U. G. R. Schulz and P. M. Rothwell, "Association between arterial bifurcation anatomy and angiographic plaque ulceration among 4,627 carotid stenoses," *Cerebrovascular Diseases*, vol. 15, no. 4, pp. 244–251, 2003.

Research Article

Group Factor Analysis for Alzheimer's Disease

Wei-Chen Cheng, Philip E. Cheng, and Michelle Liou

Institute of Statistical Science, Academia Sinica, Taipei 11529, Taiwan

Correspondence should be addressed to Wei-Chen Cheng; wcheng@stat.sinica.edu.tw

Received 21 December 2012; Accepted 18 January 2013

Academic Editor: Kumar Durai

Copyright © 2013 Wei-Chen Cheng et al. This is an open access article distributed under the Creative Commons Attribution License, which permits unrestricted use, distribution, and reproduction in any medium, provided the original work is properly cited.

For any neuroimaging study in an institute, brain images are normally acquired from healthy controls and patients using a single track of protocol. Traditionally, the factor analysis procedure analyzes image data for healthy controls and patients either together or separately. The former unifies the factor pattern across subjects and the latter deals with measurement errors individually. This paper proposes a group factor analysis model for neuroimaging applications by assigning separate factor patterns to control and patient groups. The clinical diagnosis information is used for categorizing subjects into groups in the analysis procedure. The proposed method allows different groups of subjects to share a common covariance matrix of measurement errors. The empirical results show that the proposed method provides more reasonable factor scores and patterns and is more suitable for medical research based on image data as compared with the conventional factor analysis model.

1. Introduction

Modern medical imaging techniques are capable of measuring human brain in vivo [1]. For instance, magnetic resonance (MR) imaging measures nuclei of atoms, and positron emission tomography detects the positron-emitting radionuclides to construct three-dimensional images. The imaging procedures are designed and settled before medical or cognitive experiments. Once the protocol is established, the laboratory and the hospital begin to recruit a variety of subjects of interest into experimental sessions. Errors resulting from individual scans are actually generated from common sources, such as the scanner, protocol, and software. Initial classification of subjects into groups can be realized by using clinical diagnosis, which may be uncertain to some extent, provided by physicians along with subjects' anamnesis.

Conventional factor analysis [2] models reduce high-dimensional data into a few latent variables and assume that data \mathbf{x} were generated by a set of unobserved independent unit-variance Gaussian source \mathbf{f} plus uncorrelated zero-mean Gaussian random noise \mathbf{u} , $\mathbf{x} = L\mathbf{f} + \mathbf{u}$, where L is the factor loading matrix. The sample covariance of \mathbf{x} can be

expressed as $LL^T + \Psi$, where Ψ is a diagonal covariance matrix of random noises. The goal of factor analysis is to find L and Ψ that maximally fit the sample covariance [3–5]. The EM algorithm was proposed to estimate the matrices [6]. Factor analysis is commonly applied to the dataset as a whole or to different groups of data separately, which may result in factor patterns hard to interpret and limit the potential use of the method in a wider range of medical applications. In this study, we propose a mixture factor analysis model (MFAM) to assign a common covariance matrix of noises or measurement errors to different groups of subjects but to allow individual groups having their own latent structures. In the empirical application, we analyzed an Alzheimer's disease (AD) dataset by first extracting the volumetric information from MR anatomical images for both healthy controls and the patients suffering either AD or mild cognitive impairment, followed by applying the proposed MFAM to the volumetric data.

2. Material and Method

2.1. The Model. Let M be the number of subject groups. To find multiple sets of factor loadings, $\{L_j; j = 1, \dots, M\}$, with

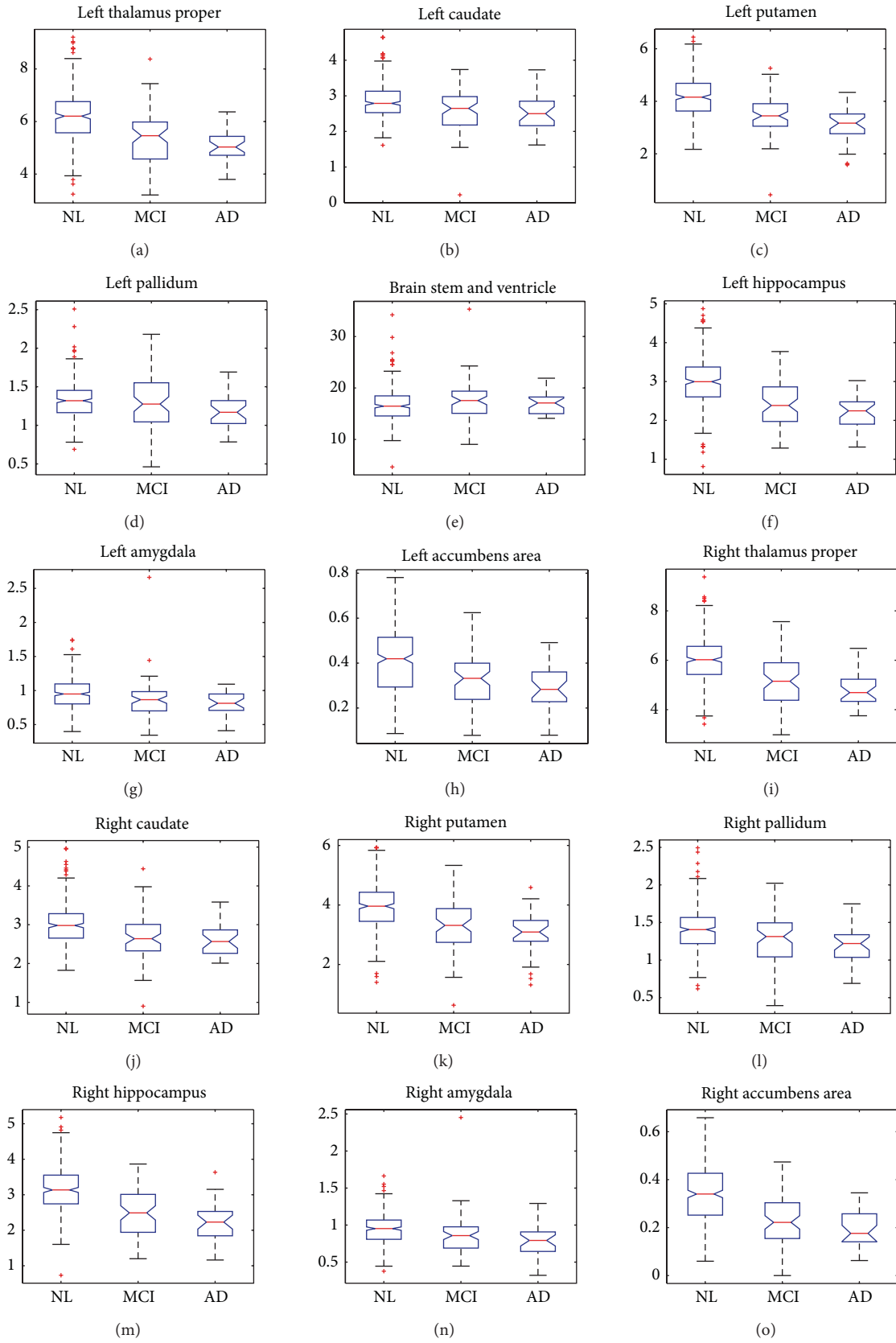


FIGURE 1: The plots of means and standard deviations for the three groups in different subcortical structures.

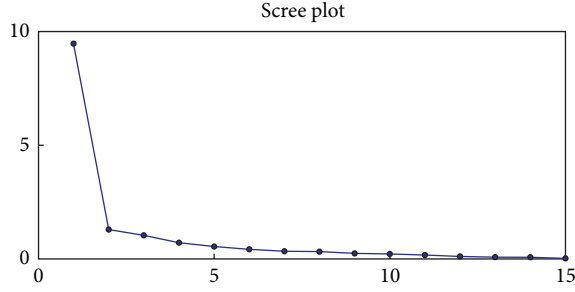


FIGURE 2: The scree plot for the ordered eigenvalues.

the \mathbf{f} scores distributed as Gaussian within each group, the data vector can be decomposed into a linear combination of factor loadings for each group [7, 8], that is, $L_j \in R^{D \times K}$,

$$\mathbf{x} = \sum_j \pi_j (\boldsymbol{\mu}_j + L_j \times \mathbf{f} | w_j) + \mathbf{u}, \quad (1)$$

where \mathbf{x} is D -dimensional and each factor scores $\mathbf{f} | w_j$ has K variables, that is, $\mathbf{f} \in R^K$. The parameter π is associated with the proportion of subjects in the j th group, $\pi_j = p(w_j)$. The indicator variable w is one, $w_j = 1$, when the data belongs to j th group, otherwise w is set to zero, $w_j = 0$. The formula (1) using π introduces the main difference from previous mixture models of factor analysis. The data vector \mathbf{x} need not be centered and the mean of the j th group data is $\boldsymbol{\mu}_j$. The covariance matrix of residuals \mathbf{u} is a diagonal matrix $\Psi = \text{diag}[\Psi_1, \Psi_2, \dots, \Psi_D]$. The data distribution can be expressed as

$$P(\mathbf{x}) = \sum_{j=1}^M \int P(\mathbf{x} | \mathbf{f}, w_j) P(\mathbf{f} | w_j) p(w_j) d\mathbf{f}. \quad (2)$$

In this work, capitalized P denotes the probability function of a vector or a matrix and lowercase p denotes the probability function of a scalar. The factor scores are assumed to be distributed as Gaussian

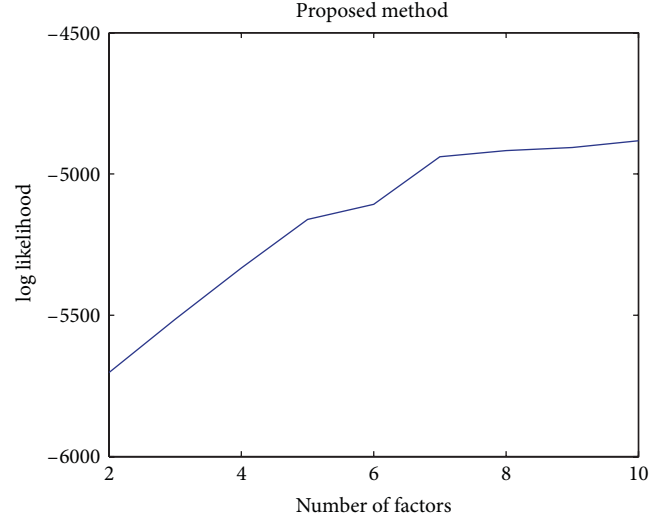
$$P(\mathbf{f} | w_j) = N(0, I), \quad \forall j. \quad (3)$$

The notation I is the identity matrix of order D . The distribution of data \mathbf{x} in each group is given by

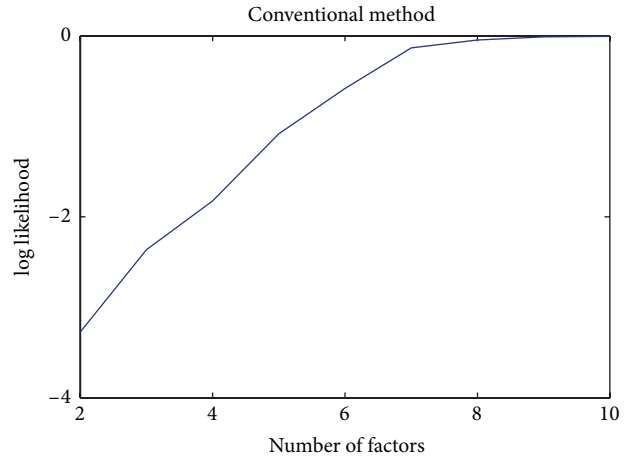
$$P(\mathbf{x} | \mathbf{f}, w_j) = N(\boldsymbol{\mu}_j + L_j \mathbf{f}_j, \Psi). \quad (4)$$

Based on the MFAM (2), the likelihood function Q is as follows:

$$Q = E \left[\prod_{i=1}^N \prod_{j=1}^M \left\{ (2\pi)^{-D/2} |\Psi|^{-1/2} \exp \left[-(\mathbf{x}_i - \boldsymbol{\mu}_j - L_j \mathbf{f}_i)^T \Psi^{-1} \right. \right. \right. \\ \left. \left. \left. \times (\mathbf{x}_i - \boldsymbol{\mu}_j - L_j \mathbf{f}_i) \right] \right\}^{w_j} \right], \quad (5)$$



(a)



(b)

FIGURE 3: The two curves record the approximate value of log likelihood for two methods.

where E denotes the expectation. The N is the number of data vectors (subjects) with subscript i for the i th subject. We need to compute the expectation of the variables,

$$E(w_j \mathbf{f}_i | \mathbf{x}_i) = E(w_j | \mathbf{x}_i) E(\mathbf{f}_i | w_j, \mathbf{x}_i). \quad (6)$$

To estimate Q in (5), the posterior probability of the j th group is calculated as

$$P(w_j | \mathbf{x}) = \frac{P(\mathbf{x} | w_j) P(w_j)}{P(\mathbf{x})} \\ = \frac{\pi_j N(\mathbf{x} - \boldsymbol{\mu}_j, L_j L_j^T + \Psi)}{\sum_u \pi_u N(\mathbf{x} - \boldsymbol{\mu}_u, L_u L_u^T + \Psi)}, \quad (7)$$

where the probability of \mathbf{x} given w_j is

$$P(\mathbf{x} | w_j) = N(\mathbf{x} - \boldsymbol{\mu}_j, L_j L_j^T + \Psi). \quad (8)$$

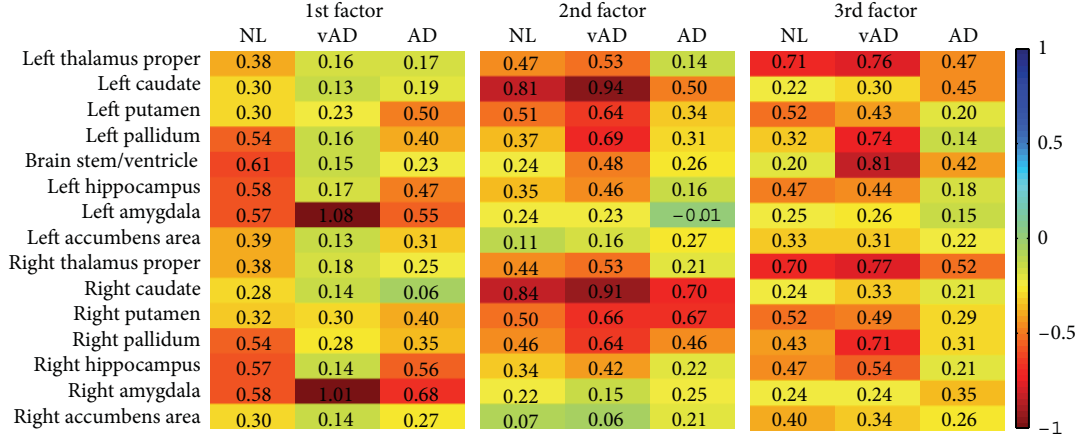


FIGURE 4: The factor loading matrices for the three groups.

The parameters π in (7) is the prior probability derived from the clinical diagnosis. Therefore, the expectation of w_j given \mathbf{x}_i in (6) is proportional to the numerator in (7),

$$h_{ij} = E[w_j | \mathbf{x}_i] \propto \pi_j N(\mathbf{x}_i - \boldsymbol{\mu}_j, L_j L_j^T + \Psi). \quad (9)$$

To calculate (6), we consider that the posterior probability of \mathbf{f} given \mathbf{x} is

$$\begin{aligned} P(\mathbf{f} | \mathbf{x}) &= \frac{P(\mathbf{x} | \mathbf{f}) P(\mathbf{f})}{P(\mathbf{x})} \\ &\propto \exp\left(-[\mathbf{f}^T (L^T \Psi^{-1} L + I) \mathbf{f} - 2\mathbf{f}^T L^T \Psi^{-1} \mathbf{x}]\right). \end{aligned} \quad (10)$$

After some arithmetic calculation, $P(\mathbf{f} | \mathbf{x})$ can be expressed as

$$P(\mathbf{f} | \mathbf{x}) \sim N(R^{-1} L^T \Psi^{-1} \mathbf{x}, R), \quad (11)$$

where $R = (L^T \Psi^{-1} L + I)$. Hence, the expectation of \mathbf{f} given \mathbf{x} is

$$E[\mathbf{f} | \mathbf{x}] = R^{-1} L^T \Psi^{-1} \mathbf{x}. \quad (12)$$

From above, $E(\mathbf{f}_i | w_j, \mathbf{x}_i)$ in (6) is calculated as

$$E(\mathbf{f}_i | w_j, \mathbf{x}_i) = R_j^{-1} L_j^T \Psi^{-1} (\mathbf{x}_i - \boldsymbol{\mu}_j), \quad (13)$$

where $R_j = (L_j^T \Psi^{-1} L_j + I)$, according to (12).

There is no constraint on those factor loadings L_j . The estimation of L_j is simply the maximum of Q . A convenient way to express Q in (5) is achieved by setting $\tilde{\mathbf{f}}_i = [\mathbf{f}_i^T \ 1]^T$

and $\tilde{L}_j = [L_j \ \boldsymbol{\mu}_j]$. The expected log likelihood function can be expressed as

$$\begin{aligned} E[\log Q] &= E \left[\log \prod_{i=1}^N \prod_{j=1}^M \left\{ (2\pi)^{-D/2} |\Psi|^{-1/2} \exp \left[-\frac{1}{2} (\mathbf{x}_i - \tilde{L}_j \tilde{\mathbf{f}}_i)^T \Psi^{-1} \right. \right. \right. \\ &\quad \left. \left. \left. \times (\mathbf{x}_i - \tilde{L}_j \tilde{\mathbf{f}}_i) \right] \right\}^{w_j} \right] \\ &= -\frac{D \times N}{2} \times \log(2\pi) - \frac{N}{2} \log |\Psi| \\ &\quad - \sum_{i,j} \frac{1}{2} h_{ij} \mathbf{x}_i^T \Psi^{-1} \mathbf{x}_i - h_{ij} \mathbf{x}_i^T \Psi^{-1} \tilde{L}_j E[\tilde{\mathbf{f}}_i | \mathbf{x}_i, w_j] \\ &\quad + \frac{1}{2} h_{ij} \times \text{trace} \left[\tilde{L}_j^T \Psi^{-1} \tilde{L}_j E[\tilde{\mathbf{f}}_i \tilde{\mathbf{f}}_i^T | \mathbf{x}_i, w_j] \right]. \end{aligned} \quad (14)$$

To maximize Q with respect to \tilde{L}_j , we equate the derivative of (14) to zero,

$$\begin{aligned} \frac{\partial \log E[Q]}{\partial \tilde{L}_j} &= -\sum_i h_{ij} \Psi^{-1} \mathbf{x}_i E[\tilde{\mathbf{f}}_i | \mathbf{x}_i, w_j]^T \\ &\quad + h_{ij} \Psi^{-1} \tilde{L}_j E[\tilde{\mathbf{f}}_i \tilde{\mathbf{f}}_i^T | \mathbf{x}_i, w_j]^T = 0 \\ \implies \tilde{L}_j &= \left(\sum_i h_{ij} \mathbf{x}_i E[\tilde{\mathbf{f}}_i | \mathbf{x}_i, w_j]^T \right) \\ &\quad \times \left(\sum_s h_{sj} E[\tilde{\mathbf{f}}_s \tilde{\mathbf{f}}_s^T | \mathbf{x}_s, w_j]^T \right)^{-1}, \end{aligned} \quad (15)$$

where

$$E[\tilde{\mathbf{f}}_i | w_j, \mathbf{x}_i] = \left[E[\mathbf{f}_i | w_j, \mathbf{x}_i]^T \ 1 \right]^T. \quad (16)$$

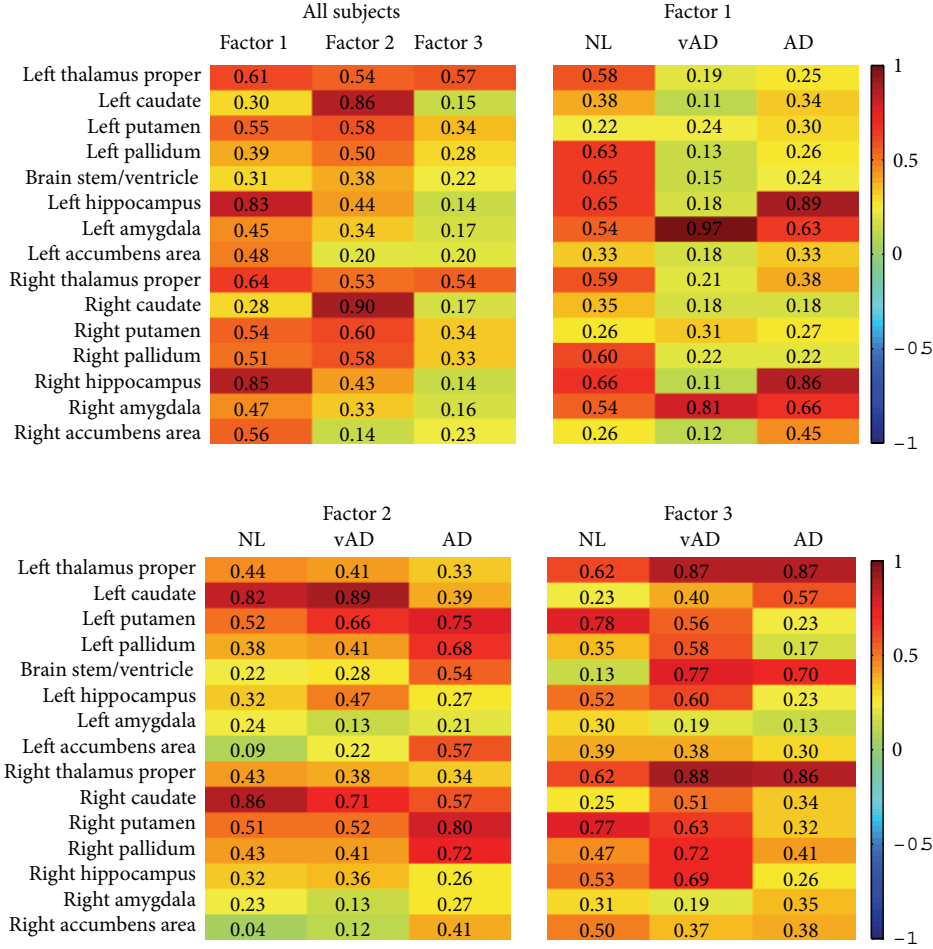


FIGURE 5: The result of maximum likelihood method and rotated by varimax with Kaiser normalization. The results of healthy controls are not unique and unstable.

All the variables are estimated by the EM algorithm. In the E-step, the algorithm computes the expectation of the factor scores in (6) and the second moment of the scores,

$$E[w_j \mathbf{f} \mathbf{f}^T | \mathbf{x}] = E[w_j | \mathbf{x}] E[\mathbf{f} \mathbf{f}^T | w_j, \mathbf{x}], \quad (17)$$

by

$$E[w_j \mathbf{f}_i \mathbf{f}_i^T | \mathbf{x}_i] = h_{ij} \text{Cov}(\mathbf{f}_i | w_j, \mathbf{x}_i) + h_{ij} E[\mathbf{f}_i | w_j, \mathbf{x}_i] E[\mathbf{f}_i | w_j, \mathbf{x}_i]^T. \quad (18)$$

The covariance matrix of residual, Ψ , can be estimated by its inverse matrix,

$$\begin{aligned} \frac{\partial Q}{\partial \Psi^{-1}} &= \frac{-N}{2} \Psi^{-1} - \frac{1}{2} \sum_{i,j} h_{ij} \mathbf{x}_i \mathbf{x}_i^T + h_{ij} \mathbf{x}_i E[\tilde{\mathbf{f}}_i | \mathbf{x}_i, w_j]^T \tilde{L}_j^T \\ &\quad - \frac{1}{2} h_{ij} \tilde{L}_j E[\tilde{\mathbf{f}}_i \tilde{\mathbf{f}}_i^T | \mathbf{x}_i, w_j]^T \tilde{L}_j^T = 0. \end{aligned} \quad (19)$$

Substituting (15) for \tilde{L}_j and making constraints on the diagonal of Ψ , we obtain

$$\Psi = \frac{1}{N} \text{diag} \left(\sum_{i,j} h_{ij} (\mathbf{x}_i - \tilde{L}_j E[\tilde{\mathbf{f}}_i | \mathbf{x}_i, w_j]) \mathbf{x}_i^T \right). \quad (20)$$

The prior probability $p(w_j)$ should be proportional to the clinical diagnosis such that the estimation of the factor loadings and the factor scores can capture the latent factors of different disease groups. The proposed model also carries the same indeterminacy problem associated with factor patterns; that is there exist numerous orthogonal transformations to rotate the matrix of factor loadings without changing the maximum of Q [9]. Considering H be any $K \times K$ orthogonal matrix, $HH^T = H^T H = I$. Equation (1) can be written

$$\begin{aligned} \mathbf{x} &= \sum_j \pi_j (\boldsymbol{\mu}_j + L_j \times (HH^T) \times \mathbf{f} | w_j) + \mathbf{u} \\ &= \sum_j \pi_j (\boldsymbol{\mu}_j + L_j^* \times \mathbf{f}^* | w_j) + \mathbf{u}, \end{aligned} \quad (21)$$

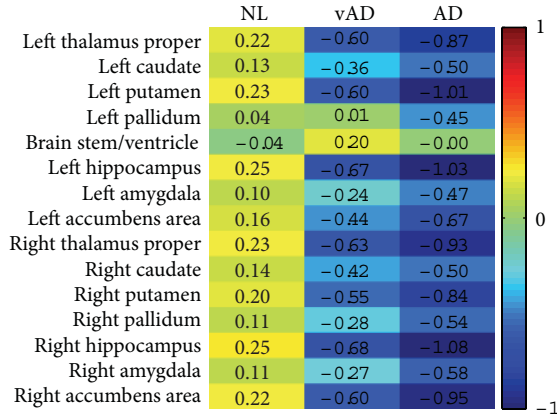


FIGURE 6: The cluster means of the three groups.

where $L_j^* = L_j H$ and $\mathbf{f}^* | w_j = H^T \times \mathbf{f} | w_j$. The assumption, $\mathbf{f}^* | w_j \sim N(0, I)$, is kept. The covariance of \mathbf{x} is $L_j^*(L_j^*)^T + \Psi = L_j H H^T L_j^T + \Psi = L_j L_j^T + \Psi$, which remains the same. Therefore, there are infinite equivalent solutions to satisfy the maximum of (5). Imposing reasonable constraints to identify a set of model parameters can make the factor loadings scientifically interpretable. A widely used approach for a simple factor structure is realized by setting some factor loadings to hypothetical values such as zeros.

The permutation and changing the sign of columns in the factor loading matrix with factor scores does not affect the model at all and the algorithm will yield the same solution. In order to realize consistent, interpretable, and comparable results, we suggest to recursively test all combinations to find the one of them that has the highest similarity among M factor loading matrices so that we can find a coherent interpretation for different groups of subjects. Each pair of factor loading and factor scores can be multiplied by either +1 or -1. The M sets of loadings has $(2^K)^M$ combinations. The possible permutation of the M set of loadings is the factorial of K . The complexity of the recurrence is therefore $2^{KM} \times (K!)^M$. The problem can be formulated as a bipartite matching and the Hungarian algorithm can find the match in a lower complexity.

2.2. Data Description. The T1-weighted MR images of 416 subjects were downloaded from the Open Access Series of Imaging Studies [10], which is publically available for analysis. All the T1-weighted images were acquired on a 1.5-T Siemens Vision scanner. Among all 416 subjects, there are 316 normal subjects (average age: 45.09 ± 23.90), 70 subjects who have been clinically diagnosed with very mild AD (average age: 76.21 ± 7.19), and 30 are with moderate AD (average age: 78.03 ± 6.91). The proportions of each type of subject are $\boldsymbol{\pi} = [75.96\%, 16.83\%, 7.21\%]^T$. Multiple intrasession acquisitions provide extremely high signal-to-noise ratio, making the data amenable to our analysis. The available images were provided skull stripped, gain field corrected, and registered to the atlas space of Talairach and Tournoux [11] with a 12-parameter rigid affine transform. The resolution of the images

TABLE 1: The ANOVA results for the three groups in different subcortical structures.

Structure	p -value
Left thalamus proper	2.0183×10^{-15}
Left caudate	1.3736×10^{-5}
Left putamen	6.9145×10^{-18}
Left pallidum	0.0351
Brain stem and ventricle	0.1707
Left hippocampus	1.5656×10^{-20}
Left amygdala	9.1999×10^{-4}
Left accumbens area	1.0958×10^{-8}
Right thalamus proper	2.6864×10^{-17}
Right caudate	1.6556×10^{-6}
Right putamen	1.6447×10^{-13}
Right pallidum	8.8771×10^{-5}
Right hippocampus	3.5498×10^{-22}
Right amygdala	6.5971×10^{-5}
Right accumbens area	8.7323×10^{-17}

is $176 \times 208 \times 176$. The number of voxels, which is more than six million, is much larger than the number of subjects. We extracted the clinically and psychologically interested regions instead of processing whole voxels in the image. The subcortical structures are extracted by the segmentation method [12] which uses manually labeled image data as priori information for a Bayesian framework that utilizes the principles of the active shape and appearance models. The size of a subcortical region was calculated by multiplying the voxel size and the number of voxels in the region. Fifteen subcortical regions were successfully extracted.

According to a demographic study by the National Institute on Aging and Alzheimer's Association based on the data collected in the Chicago Health and Aging Project, the prevalence of dementia among individuals aged 71 and older was 13.9%, and AD (Alzheimers disease) was 9.7% [13]. The study was based on a sample of 856 individuals. The $\boldsymbol{\pi}$ was estimated to be $[76.4\%, 13.9\%, 9.7\%]^T$ which is close to the statistics in our empirical data. The data vector of each subject had fifteen dimensions, each corresponding to the volume size of a subcortical structure divided by the estimated total intracranial volume. The average size of all of the intracranial volume is 1480.5 cm^3 . The intracranial volume is estimated by the linear registration from a manually measured intracranial volume of a standard brain to the individual brain [14]. The analysis of variance (ANOVA) of the data for each structure were calculated and shown in Table 1 and Figure 1. The smaller p value indicates high probability of inequality of the structure size among the three groups.

We subtracted the mean from the data and used the remainder for analysis. Using the covariance matrix of the data to estimate the factor scores would cause that a few structures dominate the factor loadings; therefore, we divided each dimension by its standard deviation to compel each of them to have unit variance. After the algorithm converged, we used varimax rotation [15], which transforms the loadings

TABLE 2: The normality test of factor score by Kolmogorov-Smirnov test.

p value	Proposed method			Traditional method		
	Factor 1	Factor 2	Factor 3	Factor 1	Factor 2	Factor 3
NL	0.20	0.12	0.53	0.51	0.19	0.82
vAD	0.00	0.55	0.29	0.54	0.44	0.30
AD	0.02	0.14	0.14	0.81	0.89	0.83

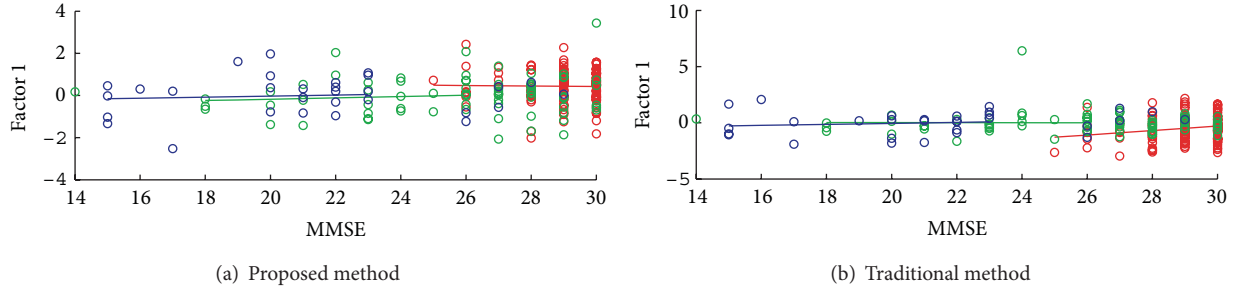


FIGURE 7: Correlations of factor scores with the MMSE scores. The red color denotes healthy subjects; the green color denotes very mild AD patients; the blue color denotes the moderate AD patients. The regression lines of the three groups by the (a) proposed method and (b) conventional method are also plotted in the figures.

into the space that maximizes the variance, to rotate the factor loadings. Given data, the expectation of its type was set to

$$[h_{i1}, h_{i2}, h_{i3}] = \begin{cases} [1, 0, 0] & \text{if subject } i \text{ belongs to NL} \\ [0, 1, 0] & \text{if subject } i \text{ belongs to vAD} \\ [0, 0, 1] & \text{if subject } i \text{ belongs to AD.} \end{cases} \quad (22)$$

3. Results

Figure 3 shows the trend of the likelihood climbs as adding the number of factors in the analysis. In the scree plot in Figure 2, three eigenvalues of the covariance matrix of the whole dataset are greater than one and the cumulative percentage of variance from the largest three eigenvalues reaches 78%. Thus we set $K = 3$ in this analysis.

The factor loadings for the three groups are shown in Figure 4, in which the vertical axis marks the fifteen regions. The vAD denotes the group of very mild AD. The log likelihood in (5) after the algorithm converges is -5475.814 . The loading of structures has symmetric property and usually the right and left structures have similar loadings. Using the factor loadings to estimate π and the expected group information given x by (9), we obtain the adjusted and turned proportions as $[82.89\%, 7.97\%, 9.14\%]^T$. This may suggest the underlying variation among different groups of subject and need further investigation. Note that the reestimated proportion h_{ij} is not binary anymore.

We show the results of conventional factor analysis in Figure 5 as a comparison. The program run on the mild AD patients in the dataset cannot achieve reproducible results; therefore, the quantity of mild AD's results in Figure 5 varies from time to time. The analysis for the AD group cannot converge, however the factor loadings are reproducible. The distance of whole factor loading matrices among the three

groups for conventional factor analysis is 5.28 while the proposed method is 4.54. The correlation of the three-factor loading matrix estimated by conventional factor analysis methods is $[C_{12}, C_{13}, C_{23}] = [0.3879, 0.1698, 0.3633]$. The correlation by proposed method is $[0.5388, 0.5564, 0.4986]$. Table 2 lists the p values for all factors by the Kolmogorov-Smirnov test [16] on the factor scores against a Gaussian distribution. The test examines the difference between input distributions and a Gaussian distribution. The smaller the p values, the more strongly the test rejects the Gaussian assumption. The algorithm tries to search for loads with normally distributed factor score, hence large p indicates the factor fit well to Gaussian distribution.

The means (centers) of the clusters are shown in Figure 6. The means are near the origin and include negative value because the data are standardized by the subtraction of the overall mean of the data in the preprocess stage. The yellow color in the first column indicates that healthy controls have larger sizes in subcortical structures, and the second and the third columns indicate that the patients have smaller sizes in different subcortical regions in general. The AD patient has very small thalamus, putamen, and hippocampus. The hippocampus is related to memory and learning. The putamen is a structure involved in the regulation of voluntary movement. The abnormal pallidum in Figure 4 can cause movement disorders. Figure 7 shows the associations of first factor scores with the score of minimal state examination (MMSE) by both methods.

4. Conclusions

The proposed method finds closer and more correlated factor loadings than the conventional method because it considers the same error matrix for different groups of data. The result of conventional factor analysis having higher normality

for AD patients than normal subjects is less convincing. Conventional factor analysis that decomposes the observed data together intermixes the latent factors. Taking the data apart will misseparate the noise. This work proposed using a mixture model of factor analysis method for neurodegenerative disease research by showing highly correlated factor loading across different groups of subjects and together with proper normality of the factor scores.

Acknowledgment

This work was supported by National Science Council under project NSC101-2811-M-001-082.

References

- [1] W. C. Cheng, P. E. Cheng, and M. Liou, "Modeling local distortion in shape for brain MR images," in *Proceedings of the 17th Annual Meeting of the Organization for Human Brain Mapping*, 2011.
- [2] C. Spearman, "General intelligence, objectively determined and measured," *American Journal of Psychology*, vol. 15, no. 1, pp. 201–293, 1904.
- [3] D. N. Lawley, "The estimation of factor loadings by the method of maximum likelihood," *Proceedings of the Royal Society of Edinburgh*, vol. 60, pp. 64–82, 2014.
- [4] K. Jöreskog, "Some contributions to maximum likelihood factor analysis," *Psychometrika*, vol. 32, pp. 443–482, 1967.
- [5] K. Jöreskog and D. N. Lawley, "New methods in maximum likelihood factor analysis," *Mathematical and Statistical Psychology*, vol. 21, pp. 85–96, 1968.
- [6] D. B. Rubin and D. T. Thayer, "EM algorithms for ML factor analysis," *Psychometrika*, vol. 47, no. 1, pp. 69–76, 1982.
- [7] Z. Ghahramani and G. E. Hinton, "The EM algorithm for mixtures of factor analyzers," Tech. Rep. CRG-TR-96-1, Department of Computer Science, University of Toronto, 1996.
- [8] C. Y. Liou and W. C. Cheng, "Manifold construction by local neighborhood preservation," *Lecture Notes in Computer Science*, vol. 4985, no. 2, pp. 683–692, 2008.
- [9] R. I. Jennrich and P. F. Sampson, "Rotation for simple loadings," *Psychometrika*, vol. 31, no. 3, pp. 313–323, 1966.
- [10] D. S. Marcus, T. H. Wang, J. Parker, J. G. Csernansky, J. C. Morris, and R. L. Buckner, "Open Access Series of Imaging Studies (OASIS): cross-sectional MRI data in young, middle aged, nondemented, and demented older adults," *Journal of Cognitive Neuroscience*, vol. 19, no. 9, pp. 1498–1507, 2007.
- [11] J. Talairach and P. Tournoux, *Co-Planar Stereotaxic Atlas of the Human Brain: 3-Dimensional Proportional System—An Approach to Cerebral Imaging*, Thieme Medical Publishers, New York, NY, USA, 1988.
- [12] B. Patenaude, S. M. Smith, D. N. Kennedy, and M. Jenkinson, "A Bayesian model of shape and appearance for subcortical brain segmentation," *NeuroImage*, vol. 56, no. 3, pp. 907–922, 2011.
- [13] B. L. Plassman, K. M. Langa, G. G. Fisher et al., "Prevalence of dementia in the United States: the aging, demographics, and memory study," *Neuroepidemiology*, vol. 29, no. 1-2, pp. 125–132, 2007.
- [14] R. L. Buckner, D. Head, J. Parker et al., "A unified approach for morphometric and functional data analysis in young, old, and demented adults using automated atlas-based head size normalization: reliability and validation against manual measurement of total intracranial volume," *NeuroImage*, vol. 23, no. 2, pp. 724–738, 2004.
- [15] H. F. Kaiser, "The varimax criterion for analytic rotation in factor analysis," *Psychometrika*, vol. 23, no. 3, pp. 187–200, 1958.
- [16] F. J. Massey, "The kolmogorov-smirnov test for goodness of fit," *Journal of the American Statistical Association*, vol. 46, no. 253, pp. 68–78, 1951.

Research Article

A Semiautomatic Segmentation Algorithm for Extracting the Complete Structure of Acini from Synchrotron Micro-CT Images

Luosha Xiao,¹ Toshihiro Sera,² Kenichiro Koshiyama,¹ and Shigeo Wada¹

¹ Department of Mechanical Science and Bioengineering, Graduate School of Engineering Science, Osaka University, 1-3 Machikaneyama, Toyonaka, Osaka 560-8531, Japan

² The Center for Advanced Medical Engineering and Informatics, Osaka University, 1-3 Machikaneyama, Toyonaka, Osaka 560-8531, Japan

Correspondence should be addressed to Shigeo Wada; shigeo@me.es.osaka-u.ac.jp

Received 4 January 2013; Accepted 21 January 2013

Academic Editor: Peng Feng

Copyright © 2013 Luosha Xiao et al. This is an open access article distributed under the Creative Commons Attribution License, which permits unrestricted use, distribution, and reproduction in any medium, provided the original work is properly cited.

Pulmonary acinus is the largest airway unit provided with alveoli where blood/gas exchange takes place. Understanding the complete structure of acinus is necessary to measure the pathway of gas exchange and to simulate various mechanical phenomena in the lungs. The usual manual segmentation of a complete acinus structure from their experimentally obtained images is difficult and extremely time-consuming, which hampers the statistical analysis. In this study, we develop a semiautomatic segmentation algorithm for extracting the complete structure of acinus from synchrotron micro-CT images of the closed chest of mouse lungs. The algorithm uses a combination of conventional binary image processing techniques based on the multiscale and hierarchical nature of lung structures. Specifically, larger structures are removed, while smaller structures are isolated from the image by repeatedly applying erosion and dilation operators in order, adjusting the parameter referencing to previously obtained morphometric data. A cluster of isolated acini belonging to the same terminal bronchiole is obtained without floating voxels. The extracted acinar models above 98% agree well with those extracted manually. The run time is drastically shortened compared with manual methods. These findings suggest that our method may be useful for taking samples used in the statistical analysis of acinus.

1. Introduction

The mammalian respiratory system can be separated into two functional zones: conducting and respiratory. The conducting zone, as an airway tree, comprises abundant branching tubes originating from the trachea, dividing dichotomously into the bronchi and bronchioles, and ending in the terminal bronchioles. Between the conducting zone and the respiratory zone, there is an intermediary region called the transitional bronchiole. Functionally, the acinus is defined as the largest airway unit, which is provided with alveoli, the smallest air-filled structures in the lung where blood/gas exchange takes place. The most precise definition is that the pulmonary acinus comprises the branched complex of alveolated airways that are connected to the same first order respiratory or transitional bronchiole [1]. Exploring the depth of the lung, for example, microstructure of the acinus, is significant

for the characterization of the respiratory system at both the structural and functional level, in particular, from the viewpoint of biomechanics.

The microstructure of the lung is harder to reconstruct and visualize relative to that of the conducting airways. Common X-ray CT images lack resolution for imaging microscale subjects, so the technique is unavailable to visualize fine structures of the lung [2]. Previously, silicone rubber cast models (3D) [3] and serial histological section reconstruction (2D-3D) [4, 5] have been used to visualize the structure of the lung parenchyma. These approaches can provide the morphological information of pulmonary acinus. However, both approaches have limitations when they are used to reconstruct the 3D structure of fine lung parenchyma for biomechanical simulation. Recently, advances in micro-CT [6, 7] and synchrotron micro-CT imaging [8–11] have made it possible to visualize the *in situ* lung anatomical structure

in 3D with micrometer resolution. Because synchrotron radiation gives a much higher flux with a collimated X-ray beam compared with laboratory microfocus X-ray sources, the contrast of a synchrotron image is higher than that of a conventional X-ray source. Even though the required image resolution was available, the identification (segmentation) of the acinus structure in synchrotron micro-CT images was still hard to achieve because of the complexity of the porous structure and the razor-thin membrane wall.

A reconstruction method of a certain region of the lung parenchyma has been published [10], but it is not an entire functional structure. A complete structure of the acinus is necessary to measure the pathway of gas exchange and to simulate gas diffusion, tissue deformation, and air particle deposition [12–14]. Commonly, segmentation of the acinus structure is performed manually by an expert but is very tedious and time-consuming. In such situations, it is impractical to carry out the statistical analysis for investigating pulmonary morphology and function. Therefore, a segmentation technique for rapidly extracting the entire acinus structure is desired.

Here, we propose a semi-automatic segmentation algorithm for extracting pulmonary microstructures from three-dimensional synchrotron micro-CT images. Improvements of basic dilation, region growing, and erosion techniques are used to achieve extraction of various scales of airway structures, such as terminal bronchioles and acini. A cluster of acini structures belonging to a terminal bronchiole can also be obtained completely without isolated alveoli.

This paper is organized as follows. The specimen and micro-CT image preparation are given in Section 2. In Section 3, preprocessing and extraction of terminal bronchioles and acini are explained in detail. Section 4 describes our experimental results and includes a discussion.

2. Specimen and Micro-CT Images

The preparation of images has been previously described in detail elsewhere [9], and thus are only recapitulated briefly here. Intact, healthy mouse lungs (A/J, 9 weeks) were visualized using the synchrotron refraction-enhanced CT system at SPring-8 (<http://www.spring8.or.jp/>) [15]. Images were obtained when lung pressure was kept at 0 cmH₂O. The resolution was $4000 \times 4000 \times 1343$ voxels, with cubic voxels of $2.8 \mu\text{m}^3$. Figure 1 shows a representative CT image.

3. Segmentation Algorithm

The entire process of extracting the acinus structure from 3D synchrotron micro-CT images is shown in Figure 2. We start by preprocessing raw micro-CT data to transform grayscale images to binary and to reduce the effects of image noise on the segmentation after binarizing. Based on the hierarchical anatomical structure of the lung, with scales decreasing from bronchioles to the alveoli, the separation of connected acini was divided into two stages in terms of dimension. For clarity and simplicity, we describe this algorithm in a 2D illustration as shown in Figure 2.

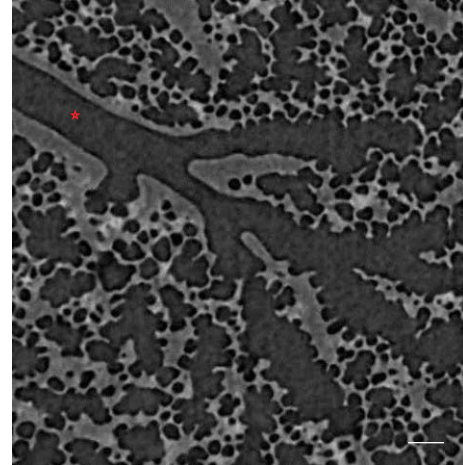


FIGURE 1: Representative synchrotron micro-CT image of the parenchyma of a mouse lung. The star marks a terminal bronchiole that is the terminal branch of conducting airways. Bar = $100 \mu\text{m}$.

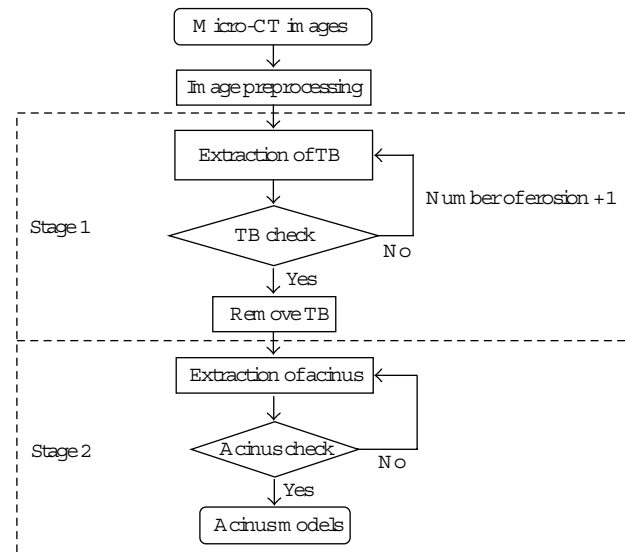


FIGURE 2: Flowchart of the semi-automatic segmentation algorithm of the pulmonary acinus. TB means terminal bronchiole.

3.1. Preprocessing: Binarization and Noise Reduction. In preprocessing, binarization and noise reduction were performed. The original micro-CT images contain too much information of lung structure to process; thus, we cropped the 3D images as $1000 \times 1000 \times 1000$ cubes including sufficient lower lung information. As CT images are susceptible to impulse noise, and to reduce the influence of such image noise, we start by preprocessing the image data set by a simple denoising operation (medium filter) before the segmentation algorithm.

As each pixel (voxel in 3D case) must represent either air space or tissue in the lung microstructure image, all gray values were binarized into either lung tissue or air space. The selection of the threshold value for binarization can greatly influence the computational complexity of the

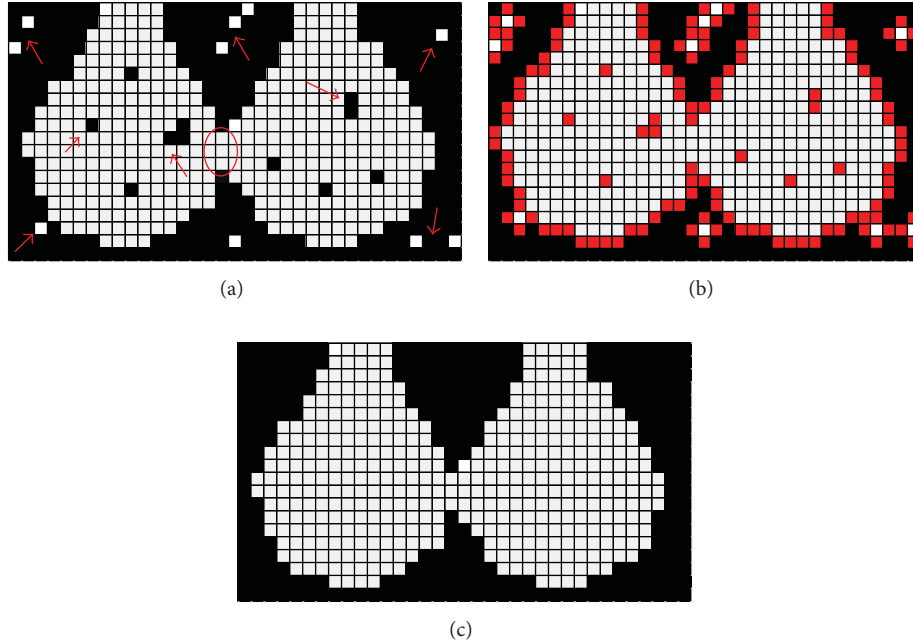


FIGURE 3: Two-dimensional illustration for preprocessing. (a) Binarization with a reasonable threshold value. (b) Elimination of the noise inside the airspace. (c) Recovery of the airspace to the original location and elimination of the outside noise.

algorithm. We used the value at the nadir of the saddle-like CT brightness histogram as an objective selection criterion for the gray scale threshold separating airspace from tissue. If the value of nadir causes irreparable noisy influence, a slight adjustment in fuzzy region can be approved reasonably. The dark gray corresponding to CT values greater than the threshold separating the two peaks was set to white (air space), and CT values less than this threshold were set to black (tissue).

Let us assume that two neighboring alveoli were binarized by a reasonable threshold value as in the example shown in Figure 3(a). As indicated in the figure, two types of binarized noises exist. Type I (shown in Figure 3(a) by arrows) is the imaging noise inside or outside the alveolar space, which can distort the image of the anatomic structure of pulmonary acinus, and type II (indicated in Figure 3(a) by an oval) is the image artifacts between different alveoli caused by the razor-thin wall of tissue between them. To avoid the effects of binarized noise (only type I) and to maintain the real structure of acini air space, we also need to preprocess the binarized images.

Internal noise influences the subsequent steps of preprocessing. Depending on the mean noise size, we first dilated the air space (white) by a reasonable number to fill up the internal noisy holes (Figure 3(b)). This process was performed by 6-connected erosion operator for tissue using a 3×3 square structuring element (in 3D, a $3 \times 3 \times 3$ cube structuring element). Then, to eliminate the redundant voxels caused by dilation, a reasonable number of 26-connected dilation operators for tissue (several times larger than the number of erosion operator) were performed (Figure 3(c)). After this, external binarized noise is eliminated. Detailed

procedures of the dilation and erosion operators are given in the Appendix.

3.2. Separation of Connected Acini. After reducing the type I noise from binary images, the fundamental structure of several clusters of connected acini was revealed. To some extent, type II binarized noise exists between two alveoli that belong to different acini. Thus, intact structure of a lung acinus cannot be extracted by only the region growing method [16] from a seed point in the target acinus.

By definition, the terminal bronchiole is the previous generation of acinus structure, and the scale of it is large enough to avoid binarized noise caused by image artifacts. Thus, by deleting the terminal bronchiole from the working space, the acini belonging to it can be isolated from the entrances. However, from the entrance of each acinus, the single-seed region growing still faults to extract acinus as type II binarized noise. The problem regarding separation of connected acini translates into the elimination of type II noise between alveoli belonging to different acini.

3.2.1. Extraction of Terminal Bronchioles. Using binarized 3D synchrotron micro-CT slices, the acinus was segmented starting at the terminal bronchiole. First, the extraction of the terminal bronchioles was performed by carrying out the 6-connected erosion operator using a 3×3 square structuring element (in 3D, a $3 \times 3 \times 3$ cube structuring element) with a reasonable number to eliminate the connection between a terminal bronchiole and its subsequent acini. The number of erosion for extracting terminal bronchioles is based on the average path length from a pulmonary model of mouse lungs [17–19] and the resolution of a synchrotron micro-CT

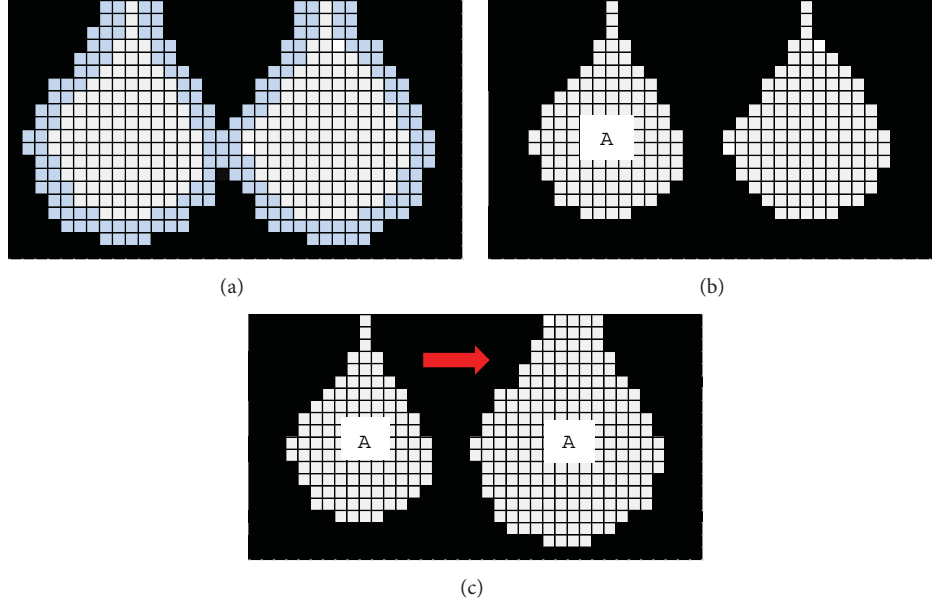


FIGURE 4: Two-dimensional illustration for the extraction of acinus. (a) Two neighbouring alveoli before erosion. (Blue shows preeroded region.) (b) Two neighbouring alveoli after erosion. (c) Dilation of the acinus to the original location.

TABLE 1: Diameter of the small airways and equivalent number of erosion for elimination.

Airway name	Diameter (μm)*	Erosion number for eliminating airway
Terminal bronchiole	160	29 times
Transitional and respiratory bronchiole	100	18 times
Alveolar duct	90	15 times
Alveolus	58	11 times

*Taken from previous morphometric data published by Oldham and Robinson [17] on *in situ* lung casts of BALB/c mice. The lung pressure is the same as in this study.

image. In addition, considering the nuances of airway size in different mouse stains, these parameters were adjusted slightly to increase robustness. Therefore, the equivalent erosion number was calculated as the quotient of these two parameters rounded to the nearest integer. Details of the data set are given in Table 1.

Second, to select a seed point in the remaining terminal bronchiole region, we performed single-seed region growing. The region-growing operator starts from a certain seed point inside the eroded terminal bronchiole to be segmented. The pixels neighboring this seed point were evaluated by a 3×3 square structuring element (in 3D, a $3 \times 3 \times 3$ cube structuring element) to determine if they should also be considered as part of the terminal bronchiole. If so, they were added to the seed region, and the process continued as long as new pixels were added to the region.

Finally, the 26-connected dilation operator using a 3×3 square structuring element (in 3D, a $3 \times 3 \times 3$ cube structuring element), which uses the same number for erosion, was

carried out to recover the terminal bronchiole to the original location. Detailed procedures of the dilation and erosion operators are given in the Appendix.

3.2.2. Extraction of Acini. After deleting terminal bronchioles from the working space, all acini belonging to it can remain with isolated entrance. Because of the type II noise between alveoli belonging to different acini, an acinus still cannot be extracted directly. We continue to use the two neighboring alveoli samples as shown in Figure 3(c) and assume that they belong to two different acini.

First, a 6-connected erosion operator using a 3×3 square structuring element (in 3D, a $3 \times 3 \times 3$ cube structuring element) should be performed for acinus air space. The illustration before and after erosion is shown in Figures 4(a) and 4(b). Since the dimension of acinus is very fine and the diameter of an alveolar mouth opening is usually less than the diameter of a mature alveolus, the number of erosion for extracting an acinus has a threshold. The ratio of an alveolar mouth opening to a mature alveolar diameter was assumed to be the criterion for evaluating the number of erosion for extracting the acinus structure. The threshold of the number of erosion N was defined as

$$N = \left\lceil \frac{\text{Diameter of alveolar mouth opening}}{\text{Voxel size} \times 2} \right\rceil. \quad (1)$$

In this study, $N = 4$, where the ratio is 40% [20] and the mature alveolar diameter is $58 \mu\text{m}$ [19].

After erosion, the target acinus was isolated from the other connected acini. A single-seed region growing operator using a 3×3 square structuring element (in 3D, a $3 \times 3 \times 3$ cube structuring element) was performed to select the target acinus (assuming A in Figure 4(b)).

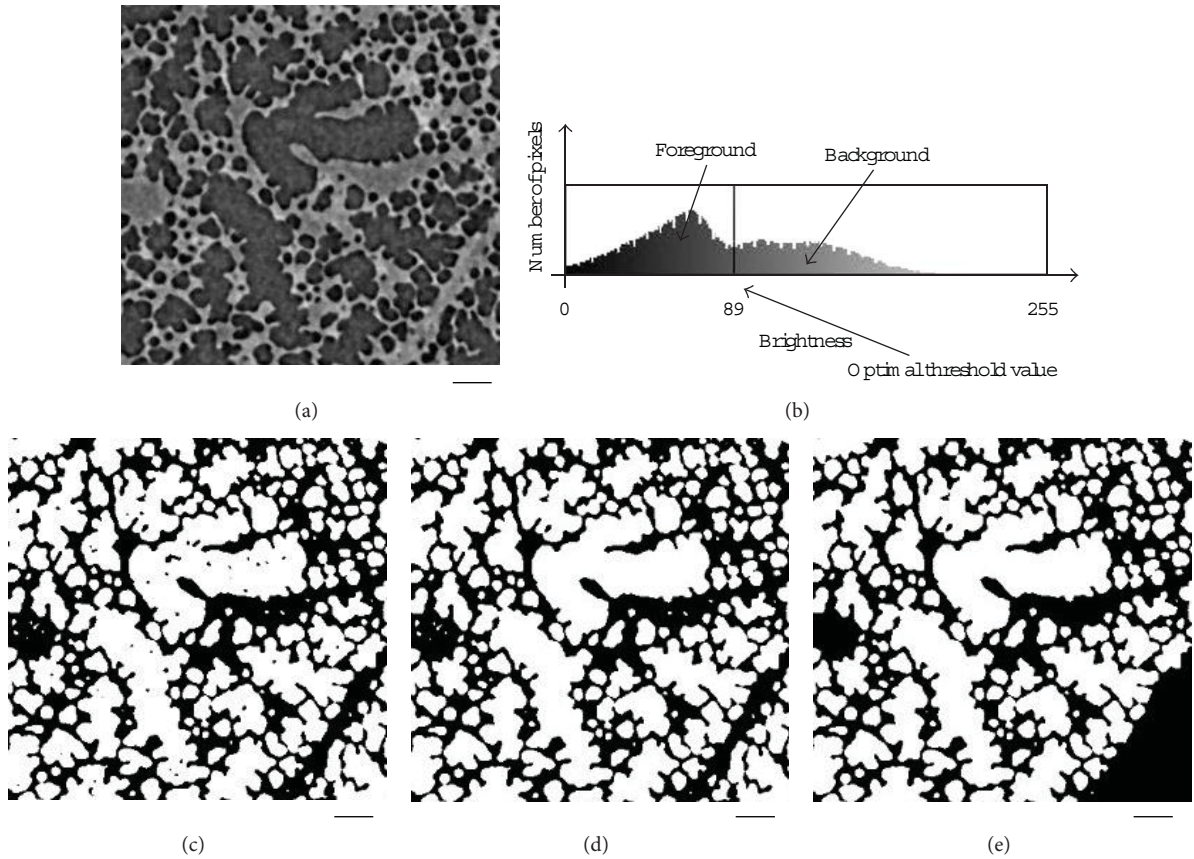


FIGURE 5: Original slice from a mouse lung synchrotron micro-CT image, binarization threshold value and noise reduction results. Bar = 100 μm .

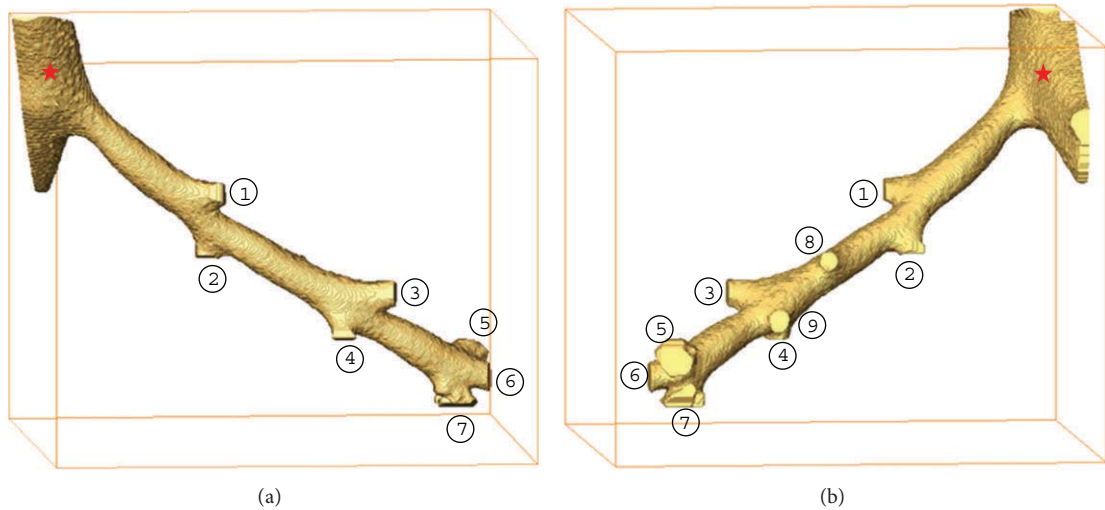


FIGURE 6: (a) 3D reconstruction of the extracted terminal bronchiole without following acini. (b) Back view of the same reconstruction data. Stars mark part of a previous generation of its associated terminal bronchiole. Entire branches are marked by serial numbers. The dimensions of the bounding boxes (a) and (b) are $1.26 \times 1.06 \times 1.26 \text{ mm}^3$.

Finally, a 26-connected dilation operator using a 3×3 square structuring element (in 3D, a $3 \times 3 \times 3$ cube structuring element), which uses the same number as erosion, was carried out to recover the target acinus to the original location (Figure 4(c)). The detailed procedures of the dilation erosion operator are given in the Appendix.

3.3. Validation

3.3.1. *Completeness.* The incompleteness of the extracted acinus is caused when type II noise existing between alveoli belonging to different acini is larger than the alveolar mouth opening, that is, $N > 4$. If this phenomenon occurred, except

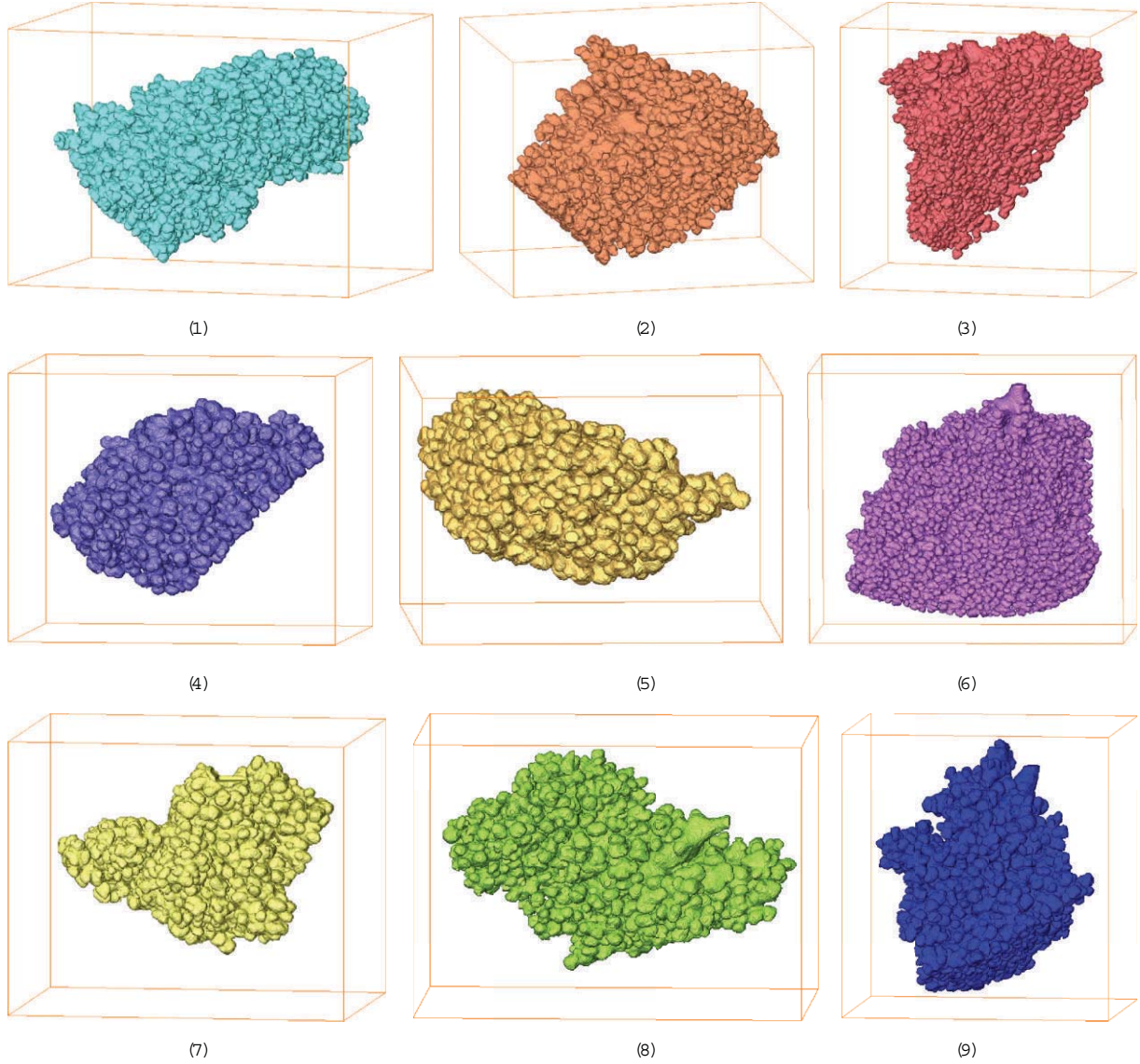


FIGURE 7: 3D reconstruction of all 9 extracted acini. The dimensions of the bounding boxes (mm^3): (1) $1.23 \times 1.20 \times 1.68$; (2) $0.98 \times 1.06 \times 1.37$; (3) $1.37 \times 0.95 \times 1.34$; (4) $0.81 \times 0.87 \times 1.06$; (5) $0.56 \times 0.84 \times 0.81$; (6) $1.46 \times 1.68 \times 0.98$; (7) $0.81 \times 0.84 \times 1.04$; (8) $0.81 \times 0.78 \times 1.15$; and (9) $0.76 \times 0.95 \times 1.01$.

in the extracted acinus region, the omissive parts of alveolus and the other acini remained in the working space. To obtain the omissive parts, the other acini regions were eliminated by single-seed region growing using a 3×3 square structuring element (in 3D, a $3 \times 3 \times 3$ cube structuring element). Combining the extracted acinus structure and the omissive parts, a complete acinus can be restored.

3.3.2. Comparison of Manual and Semi-Automatic Methods. To evaluate the accuracy of our semi-automatic segmentation algorithm, we segmented several of the same acini by our semi-automatic method and manual method. The quantitative comparison α was defined as match ratio

$$\alpha = \frac{n_{\text{match}}}{n_{\text{match}} + n_{\text{error}}} \times 100, \quad (2)$$

where n_{match} is the number of matched voxels that are segmented by both methods, and n_{error} is the number of error voxels that are different between the two methods.

4. Results and Discussion

4.1. Original Micro-CT Image Preprocessing. Based on the synchrotron micro-CT images, binarization and noise reduction were performed to preprocess and maintain the real acinus structure. Figure 5 shows an example for preprocessing the original synchrotron micro-CT slice. Here, Figure 5(a) shows the original slice from a mouse lung synchrotron micro-CT image, and Figure 5(b) shows the pixel intensity histogram for binarizing the original image with an optimal threshold value. Meanwhile, the binary image, the binary image with inside noise eliminated (in air space), and the

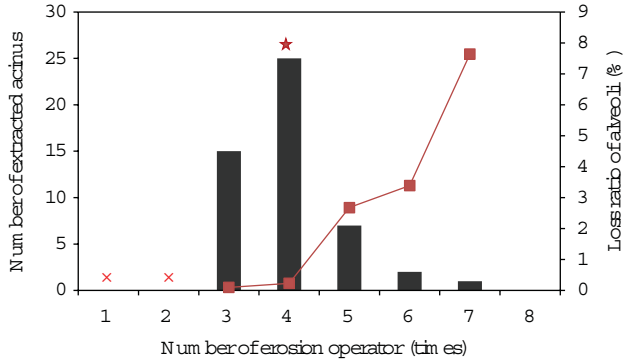


FIGURE 8: Total number of samples is 50. \times marks the number of erosion operations that are not suitable for extracting an acinar model, and the red star marks the ideal number of erosion operations. Columns show the number of extracted acini (left Y axis) and the line shows the loss ratio of alveoli (right Y axis).

binary image with all noise eliminated are shown in Figures 5(c), 5(d), and 5(e), respectively. Based on the binarization and noise reduction of preprocessing, the images became clear, and all pixels only represent either air space (white) or tissue (black).

It is worth pointing out that the acinus belonging to other terminal bronchioles means that such acinus was considered noise and needed to be eliminated. The black region remained in the lower right corner of Figure 5(e), which shows the elimination of acinus as noise.

4.2. 3D Reconstruction of ROI. Using the preprocessed binary images, the acinus was segmented starting from the deletion of terminal bronchioles. A representative terminal bronchiole without the subsequent acini was segmented as shown in Figure 6. According to the branch point of acini belonging to this terminal bronchiole, 9 clusters of acini were detected and positioned for further segmenting.

Using our semi-automatic segmentation algorithm, acinus structures were segmented quickly. The extracted acini are shown in Figure 7. All these models, except number 5, were deemed complete depending on the threshold N . The branches of the terminal bronchiole correspond to the entrances of each acinus.

To verify the threshold of completeness criterion, a mass of experiments were carried out via trial and error. We extracted 50 intact acinus samples to create a database. The distribution of the number of erosion for acinus is shown in Figure 8. The red star marks the ideal value of the number of erosion as the high ratio of extraction and low ratio of loss of alveolar fine texture, which agrees well with the threshold N . When the number of erosion is less than or equal to 2, type II noise between neighbouring alveoli belonging to different acini is too large to eliminate. Therefore, the initial number of erosion for all segmentation process is set as 3.

As indicated in Figure 8, when the number of erosion is larger than 4, the loss ratio of alveoli increases from 0.23 to 7.64. Even though the percentage is not very large, the

TABLE 2: Quantitative comparison of the four pairs of acinus models in Figure 11.

Sample No.	n_{match}	n_{error}	α
(a)	1648004	7537	99.5
(b)	2418765	46274	98.1
(c)	11718520	9990	99.9
(d)	4234352	714	99.9

omission of alveolar structure influences the morphometry such as an investigation of an airway branch to the terminal alveolus.

The adjustment of an incomplete acinus was shown by 3D reconstruction of the number 5 acinus in Figure 9. This incomplete acinus was extracted by five erosion operations, which is larger than the threshold of completeness check. The omission of alveoli fine texture after segmentation and the recovered result are shown in Figures 9(a) and 9(b).

Here, we successfully segmented and repaired nine clusters of acini belonging to the same terminal bronchiole. All the acini fill the space in the lung where they localized as shown in Figure 10.

4.3. Comparison of Manual and Semiautomatic Results. Both qualitative and quantitative comparisons for the manual and semi-automatic methods were performed. Four acinus models were extracted manually by commercial software (Amira 5.4.1), and the same regions were also extracted by our semiautomatic algorithm. Figure 10 shows the 3D reconstruction of these four acini models. Intuitively, the results of the segmentation by the two methods were basically the same except for the entrance.

As indicated in the (b) and (c) group in Figure 11, the sharpness of the acinar entrance is significantly different. The manual method has difficulty processing an acinus that has a direction of entrance perpendicular to the direction of the 3D image slice. The processing time of an acinus model running manually was about 1 wk; otherwise, the running time of the semiautomatic algorithm was about 2 hr.

Table 2 shows the quantitative comparison α , and overall values are above 98%.

5. Conclusion

We have described a semi-automatic segmentation algorithm for extracting lung microstructure acinus from synchrotron micro-CT images. The algorithm uses a combination of binary image processing operators: erosion, region growing, and dilation based on the multiscale structure of the lung. A cluster of extracted lung acini structures belonging to the same terminal bronchiole is possible to fill in the space in the lung where it is localized. The extracted acini models with α values above 98% agree well with those extracted manually. The run time is drastically shortened compared with the manual method.

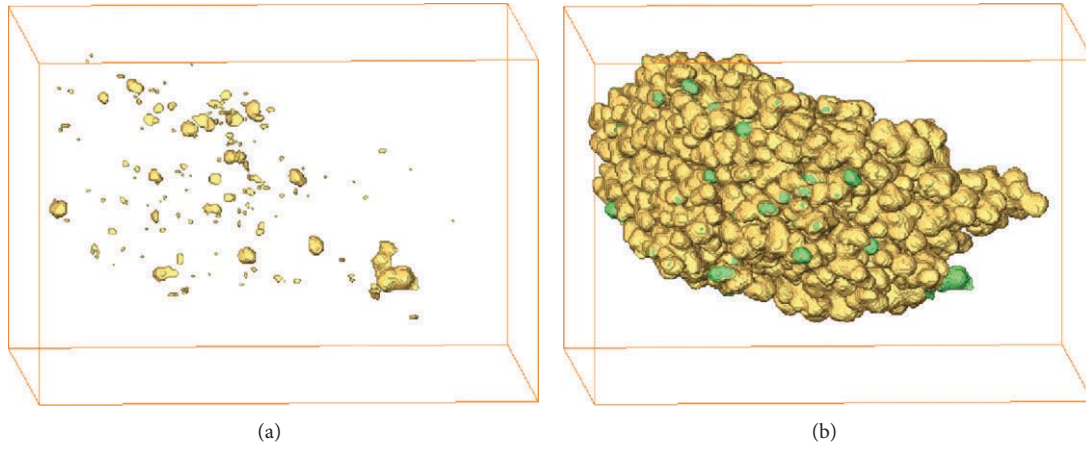


FIGURE 9: 3D reconstruction of the adjustment for an incomplete acinus. (a) Omission of alveoli fine texture. (b) Repaired complete acinus.

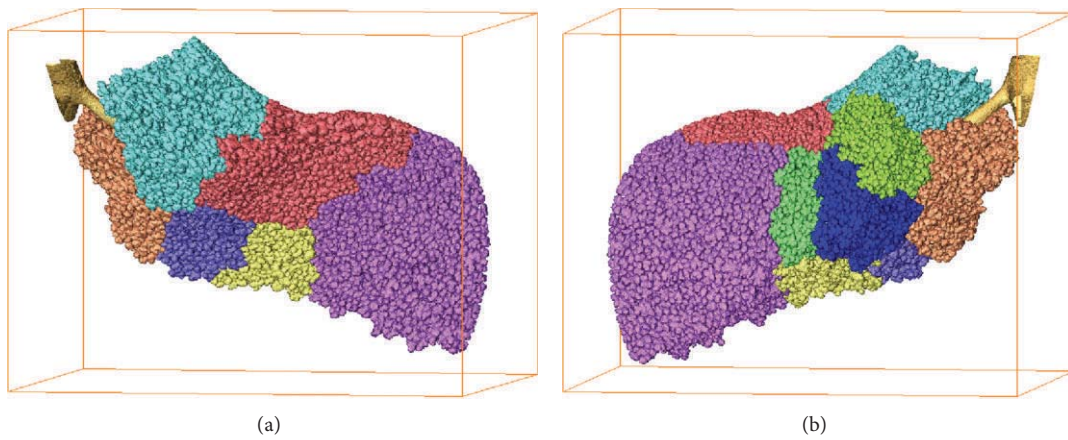


FIGURE 10: (a) 3D reconstruction of the extracted terminal bronchiole acini. (b) Back view of the same reconstruction data. The dimensions of bounding boxes (a) and (b) are $2.80 \times 2.18 \times 2.21 \text{ mm}^3$.

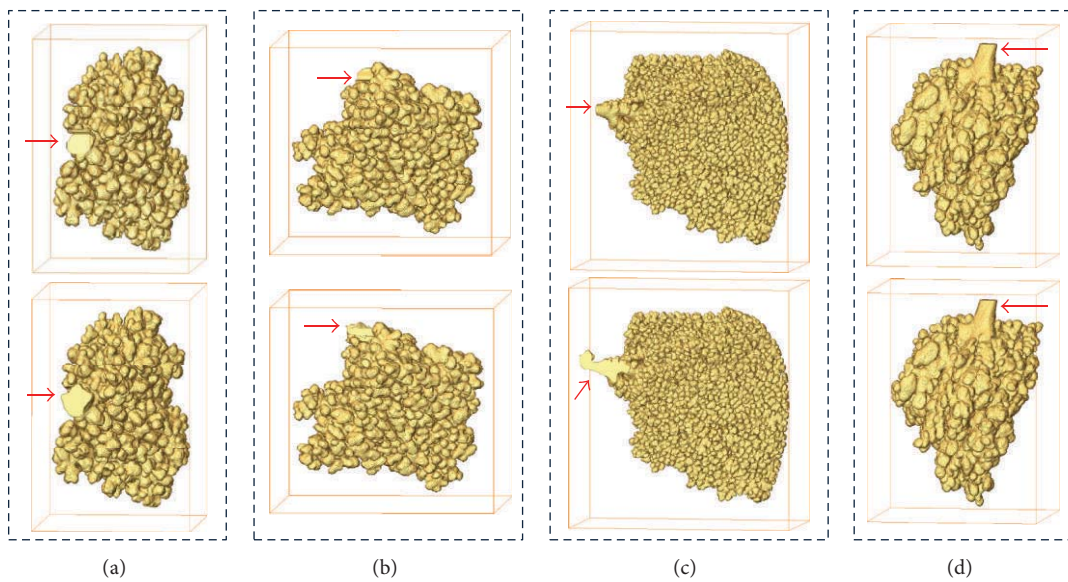


FIGURE 11: Four intact reconstructed acini. In each group, the upper acinus was extracted by our semi-automatic method, and the lower acinus was extracted by the manual method.

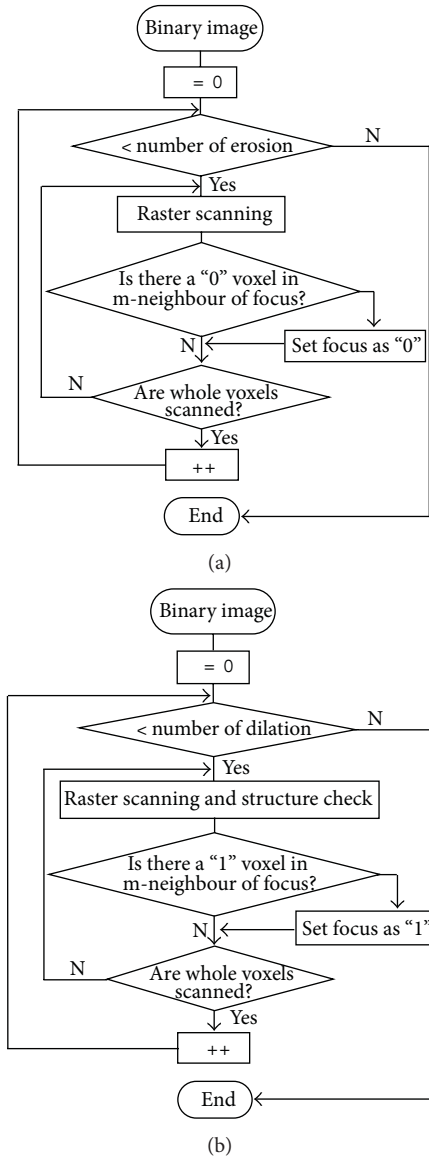


FIGURE 12: Flowchart of the modified erosion (a) and dilation (b) operator (for air space).

Appendix

Detailed Procedure of Image Processing Operator

Figure 12 shows the flowchart of erosion (a) and modified dilation (b) operator (for air space) used in our algorithm. The erosion operator is the basic effect of the operator, which is to erode away the boundaries of regions of foreground voxels. The dilation operator is another basic effect of the operator which is to gradually enlarge the boundaries of regions of foreground voxels. In particular, the dilation operator was modified on the basis of an acinus structure.

For air space, “1” means foreground and “0” means background, otherwise for tissue, “0” means foreground and “1” means background; m is the number of connectedness.

Acknowledgments

This work is supported in part by JSPS Grants-in-Aid for Scientific Research (no. 24240073) and the MEXT project, “Creating Hybrid Organs of the Future” at Osaka University.

References

- [1] E. R. Weibel, B. Sapoval, and M. Filoche, “Design of peripheral airways for efficient gas exchange,” *Respiratory Physiology and Neurobiology*, vol. 148, no. 1-2, pp. 3–21, 2005.
- [2] D. Aykac, E. A. Huffman, G. McLennan, and J. M. Reinhardt, “Segmentation and analysis of the human airway tree from three-dimensional X-ray CT images,” *IEEE Transactions on Medical Imaging*, vol. 22, no. 8, pp. 940–950, 2003.
- [3] B. Haefeli-Bleuer and E. R. Weibel, “Morphometry of the human pulmonary acinus,” *Anatomical Record*, vol. 220, no. 4, pp. 401–414, 1988.
- [4] H. S. Bal and N. G. Ghoshal, “Morphology of the terminal bronchiolar region of common laboratory mammals,” *Laboratory Animals*, vol. 22, no. 1, pp. 76–82, 1988.
- [5] R. R. Mercer and J. D. Crapo, “Three-dimensional reconstruction of the rat acinus,” *Journal of Applied Physiology*, vol. 63, no. 2, pp. 785–794, 1987.
- [6] H. D. Litzlbauer, C. Neuhaeuser, A. Moell et al., “Three-dimensional imaging and morphometric analysis of alveolar tissue from microfocal X-ray-computed tomography,” *American Journal of Physiology*, vol. 291, no. 3, pp. L535–L545, 2006.
- [7] H. Parameswaran, E. Bartolák-Suki, H. Hamakawa, A. Majumdar, P. G. Allen, and B. Suki, “Three-dimensional measurement of alveolar airspace volumes in normal and emphysematous lungs using micro-CT,” *Journal of Applied Physiology*, vol. 107, no. 2, pp. 583–592, 2009.
- [8] T. Sera, K. Uesugi, and N. Yagi, “Localized morphometric deformations of small airways and alveoli in intact mouse lungs under quasi-static inflation,” *Respiratory Physiology and Neurobiology*, vol. 147, no. 1, pp. 51–63, 2005.
- [9] T. Sera, H. Yokota, G. Tanaka, K. Uesugi, N. Yagi, and R. Schroter, “The relationship between alveoli and alveolar ducts in lung inflation,” in *Proceedings of the 6th World Congress on Biomechanics*, 2010.
- [10] A. Tsuda, N. Filipovic, D. Haberthür et al., “Finite element 3D reconstruction of the pulmonary acinus imaged by synchrotron X-ray tomography,” *Journal of Applied Physiology*, vol. 105, no. 3, pp. 964–976, 2008.
- [11] H. D. Litzlbauer, K. Korbelt, T. L. Kline et al., “Synchrotron-based micro-CT imaging of the human lung acinus,” *Anatomical Record*, vol. 293, no. 9, pp. 1607–1614, 2010.
- [12] T. Sera, K. Uesugi, and N. Yagi, “Localized morphometric deformations of small airways and alveoli in intact mouse lungs under quasi-static inflation,” *Respiratory Physiology and Neurobiology*, vol. 147, no. 1, pp. 51–63, 2005.
- [13] R. C. Schroter and M. F. Sudlow, “Flow patterns in models of the human bronchial airways,” *Respiration Physiology*, vol. 7, no. 3, pp. 341–355, 1969.
- [14] A. Tsuda, F. S. Henry, and J. P. Butler, “Gas and aerosol mixing in the acinus,” *Respiratory Physiology and Neurobiology*, vol. 163, no. 1-3, pp. 139–149, 2008.
- [15] S. Goto, K. Takeshita, Y. Suzuki et al., “Construction and commissioning of a 215-m-long beamline at SPring-8,” *Nuclear Instruments and Methods in Physics Research A*, vol. 467-468, pp. 682–685, 2001.

- [16] J. Toriwaki and S. Murakami, *Introduction to 3D Image Processing*, Tokyo Denki University Press, Tokyo, Japan, 2010.
- [17] M. J. Oldham and R. J. Robinson, "Predicted tracheobronchial and pulmonary deposition in a murine asthma model," *Anatomical Record*, vol. 290, no. 10, pp. 1309–1314, 2007.
- [18] M. J. Oldham and R. F. Phalen, "Dosimetry implications of upper tracheobronchial airway anatomy in two mouse varieties," *The Anatomical Record*, vol. 268, no. 1, pp. 59–65, 2002.
- [19] R. R. Mercer, M. L. Russell, and J. D. Crapo, "Alveolar septal structure in different species," *Journal of Applied Physiology*, vol. 77, no. 3, pp. 1060–1066, 1994.
- [20] R. R. Mercer, J. M. Laco, and J. D. Crapo, "Three-dimensional reconstruction of alveoli in the rat lung for pressure-volume relationships," *Journal of Applied Physiology*, vol. 62, no. 4, pp. 1480–1487, 1987.

Research Article

Piecewise-Constant-Model-Based Interior Tomography Applied to Dentin Tubules

Peng He,^{1,2} Biao Wei,¹ Steve Wang,³ Stuart R. Stock,⁴ Hengyong Yu,^{2,5} and Ge Wang^{2,5}

¹The Key Laboratory of Optoelectronic Technology and Systems of the Education Ministry of China, Chongqing University, Chongqing 400044, China

²Biomedical Imaging Division, VT-WFU School of Biomedical Engineering and Sciences, Virginia Tech, Blacksburg, VA 24061, USA

³Argonne National Laboratory, 9700 South Cass Avenue, Argonne, IL 60439, USA

⁴Department of Molecular Pharmacology and Biological Chemistry, Feinberg School of Medicine, Northwestern University, 303 East Chicago Avenue, Chicago, IL 60611-3008, USA

⁵Biomedical Imaging Division, VT-WFU School of Biomedical Engineering and Sciences, Wake Forest University Health Sciences, Winston-Salem, NC 27157, USA

Correspondence should be addressed to Biao Wei; weibiao@cqu.edu.cn and Ge Wang; ge-wang@ieee.org

Received 28 November 2012; Accepted 16 January 2013

Academic Editor: Kumar Durai

Copyright © 2013 Peng He et al. This is an open access article distributed under the Creative Commons Attribution License, which permits unrestricted use, distribution, and reproduction in any medium, provided the original work is properly cited.

Dentin is a hierarchically structured biomineralized composite material, and dentin's tubules are difficult to study in situ. Nano-CT provides the requisite resolution, but the field of view typically contains only a few tubules. Using a plate-like specimen allows reconstruction of a volume containing specific tubules from a number of truncated projections typically collected over an angular range of about 140° , which is practically accessible. Classical computed tomography (CT) theory cannot exactly reconstruct an object only from truncated projections, needless to say a limited angular range. Recently, interior tomography was developed to reconstruct a region-of-interest (ROI) from truncated data in a theoretically exact fashion via the total variation (TV) minimization under the condition that the ROI is piecewise constant. In this paper, we employ a TV minimization interior tomography algorithm to reconstruct interior microstructures in dentin from truncated projections over a limited angular range. Compared to the filtered backprojection (FBP) reconstruction, our reconstruction method reduces noise and suppresses artifacts. Volume rendering confirms the merits of our method in terms of preserving the interior microstructure of the dentin specimen.

1. Introduction

Teeth are important and interesting biomineralized tissues with remarkable mechanical properties through their hierarchy of structures [1]. Enamel, a hard, resistant material almost totally composed of carbonated apatite (cAp), covers the outer, exposed portion of the tooth. The tooth's interior (and the majority of its volume) consists of dentin, a tough composite of carbonated apatite (cAp) and collagen. Prominent features within dentin are the tubules that extend from near the junction with enamel to the pulp cavity in the tooth's interior. Tubule diameters are typically $1\text{--}2\ \mu\text{m}$, and tubule spacing is $\sim 5\text{--}10\ \mu\text{m}$. Smaller channels called canaliculi run from the tubules into the surrounding dentin, and their diameters are in the range of $100\text{--}300\ \text{nm}$ [2].

Dentin tubules and their surroundings remain of interest not just to microanatomists but also to those studying the efficacy of prostheses' attachment. The small dimensions of dentin tubules make them difficult to evaluate and have motivated major research efforts. Up to date, tubules and their surroundings have been characterized with microradiography [3], scanning electron microscopy (SEM) [4], transmission electron microscopy (TEM) [5], secondary ion mass spectroscopy (SIMS) [6] position-resolved X-ray diffractometry [7], micro-CT [8, 9] and nano-CT [10, 11]. With the exception of the CT techniques, these techniques provide essentially 2D views of intrinsically 3D tubules.

Of particular interest, nano-CT provides the requisite 3D spatial resolution for studying dentin's tubules and canaliculi.

However, exact nano-CT reconstruction typically requires that the specimen remains within the field-of-view (FOV) during a 180° scan. Suitable cross sections, say $25\ \mu\text{m}$ across, can be machined from thin wafers of dentin using focused ion beams, but this process is quite slow and would limit the number of tubules that could be examined. Local or region-of-interest (ROI) tomography is quite valuable for reconstructing samples larger than the FOV but requires reasonable X-ray transmissivity for all projection directions and would be subject to the throughput limitations. Plate-like samples $25\text{--}50\ \mu\text{m}$ thick and millimeters in lateral extent would contain hundreds of tubules extending significant lengths, but any attempts at nano-CT reconstruction would suffer from significant data truncation and angular limitation, significantly degrading image quality. If plate-like dentin samples could be used for nano-CT, dozens of tubules would be imaged without extraordinary sample preparation efforts. Such datasets would greatly improve understanding of tubule morphology and its variability within a tooth. Accordingly, we performed synchrotron nano-CT on a thin dentin plate and reconstructed its microstructure using an interior tomography method.

In classic CT theory, an interior ROI cannot be reconstructed exactly from truncated projections. As a result, features outside the ROI may seriously disturb the features inside the ROI, often hiding or distorting vital information. A recent progress demonstrated that the interior problem can be exactly and stably solved if a subregion in the ROI is known [12–15], which is referred to as interior tomography. However, it can be difficult to obtain precise prior knowledge of a subregion in many cases. A further progress in interior tomography was inspired by compressive sensing (CS) theory. The main idea of CS theory is that an image can be reconstructed from a rather limited amount of data as long as an underlying image can be sparsely represented in an appropriate domain and determined from these data [16–18]. Inspired by CS theory, it was found that an interior ROI can be exactly and stably reconstructed via the total variation (TV) minimization if the ROI is piecewise constant [19, 20].

For dentin image reconstruction, we employed an ordered-subset simultaneous algebraic reconstruction technique (OS-SART) to reconstruct the dentin slice images [21–24]. After analyzing the characteristics of the dentin slices, we found that the dentin slice can be divided into two types of regions: the pores and the dentin between the pores. The attenuation coefficient inside the pores differs from that of the dentin, but both are approximately constant. Therefore, the sample images can be sparsified by a discrete gradient transform (DGT), and the total variation (TV) minimization can be used to reconstruct high-quality dentin images from truncated projections even if the angular range of a scan is limited, as we observed in this project.

This paper is organized as follows. Section 2 describes a specimen and data acquisition, characteristics of the data, and our interior tomography algorithm. Section 3 compares the reconstructions by interior tomography and filtered backprojection (FBP) methods. Section 4 discusses relevant issues and concludes the paper.

2. Materials and Methods

2.1. Sample Preparation. A thin wafer of bovine dentin was cut from a molar using a diamond wafering saw (Isomet 1000, Buehler, Lake Bluff, IL) to a thickness of about $150\ \mu\text{m}$. The wafer was thinned to $\sim 25\text{--}50\ \mu\text{m}$ by polishing with 1000 grit SiC paper between two glass microscope slides. Its lateral dimensions were greater than 2 mm.

2.2. Nano-CT. Compared to medical and micro-CT, nano-CT uses an X-ray lens to bring spatial resolution into the nanometer domain. To date, better than 20 nm has been achieved for routine use with multi-keV hard X-ray radiation which is able to penetrate hundreds of microns of dental tissue [25].

The dentin specimen was imaged by the transmission X-ray microscope at Sector 32-ID of the Advanced Photon Source, Argonne National Laboratory, USA. The synchrotron nano-CT system can be viewed as in a typical parallel-beam geometry and employs monochromatic 8 keV X-radiation. The X-ray detector contained 2048×2048 pixels with 12.5 nm pixel size and 25×25 micron FOV. The angular scanning range for nano-CT was $\pm 70^\circ$ with a 0.25° steps, producing 561 projections. The voxel size in the reconstruction was 12.5 nm. Due to the small FOV of the nano-CT system, the X-ray beam could not cover the specimen completely, and all of the projections were truncated. Figure 1 shows a truncated projection of the specimen in which several tubules can be clearly seen running from upper left to lower right. Figure 2 is an extracted sinogram for one image slice along the marked line in Figure 1. Preliminary reconstructions revealed that the specimen consisted of two types of material, pores (tubules and canaliculi) and the dentin between the pores. The specimen is, therefore, approximately piecewise constant.

2.3. Reconstruction Algorithm. The conventional CT approach cannot exactly reconstruct an internal ROI only from truncated projections through the ROI because this interior problem does not have a unique solution in an unconstrained setting. Interestingly, recent results show that the interior problem is solvable if appropriate yet practical prior information is available. In particular, if the attenuation coefficient distribution on a small sub-region in an ROI is known, or the attenuation coefficient distribution over the ROI is piecewise constant, the interior problem has a unique solution. Theoretically, a function can be well approximated by piecewise constant functions, so the present dentin specimen is modeled as being piecewise constant. In this project, the piecewise-constant-model-based interior tomography algorithm was used to reconstruct dentin images from truncated projections over a limited angular range. The interior tomography algorithm is robust against noise by minimizing the image TV. Specifically, we employed the ordered-subset simultaneous algebraic reconstruction technique (OS-SART) for interior reconstruction of the dentin specimen.

The imaging process can be modeled as a linear system in terms of the popular pixel basis functions: $Af = b$, where $b = (b^1, \dots, b^M) \in R^M$ represents the truncated projection

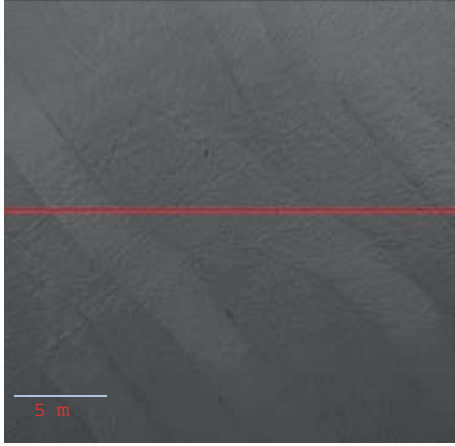


FIGURE 1: One truncated projection of the dentin specimen.

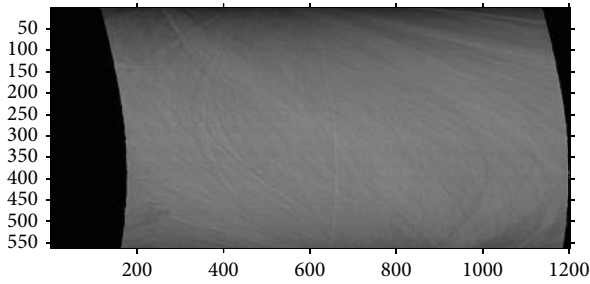


FIGURE 2: Sinogram consisting of 561 truncated projections for the slice marked by the red line in Figure 1.

data with M being the total projection number, $f = (f_1, \dots, f_N) \in R^N$ denotes an object to be reconstructed with N being the total pixel number, and $A = (a_{ij})$ is the system measurement matrix with $i = 1, \dots, M$, $j = 1, \dots, N$. The major algorithmic steps are described as follows.

While the ART method is the first iterative algorithm used for CT reconstruction [26], the SART is a major refinement to the ART [27]. In recent years, some advanced techniques were developed to accelerate the iterative reconstruction, among which the ordered-subset (OS) scheme is very attractive. As a result, the SART algorithm can be accelerated by the OS scheme. This combination is called OS-SART [23, 24]. To formulate an OS version of the SART technique, we assume that the index set $B = \{1, \dots, M\}$ can be partitioned into T non-empty disjoint subsets $B_t = \{i_1^t, \dots, i_{M(t)}^t\}$ such that

$$B = \{1, \dots, M\} = \bigcup_{1 \leq t \leq T} B_t. \quad (1)$$

Then, a possible version of the OS-SART formulation can be expressed as

$$f_j^{(n+1)} = f_j^{(n)} + \sum_{i \in B_{[n]}} \frac{a_{ij}}{a_{+j}} \frac{b_i - A^i f^{(n)}}{a_{i+}}, \quad (2)$$

where $a_{i+} \equiv \sum_{j=1}^N a_{ij} \neq 0$, $a_{+j} \equiv \sum_{i=1}^M a_{ij} \neq 0$.

The above OS-SART reconstruction method can be empowered by the CS technique to improve the image quality

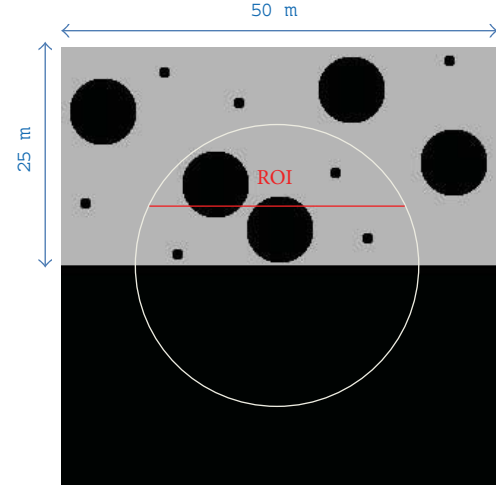


FIGURE 3: Dentin phantom. The circular region indicates a ROI, with the line labeled "X" for subsequent profiling.

under less favorable measurement conditions. As mentioned earlier, the discrete gradient transform (DGT) is a valid sparse transform for dental images. Hence, a dentin image can be reconstructed from truncated projections data via the ℓ_1 -norm minimization of the DGT, which is the TV minimization [19, 28]. Mathematically, it can be modeled as

$$\min_f \|\nabla f\|_1, \quad \text{subject to } Af = b, \quad f > 0, \quad (3)$$

where $\|\nabla f\|_1$ denotes TV of f , and

$$\|\nabla f\|_1 = \sum_{i,j} d_{i,j}, \quad d_{i,j} = \sqrt{(f_{i,j} - f_{i+1,j})^2 + (f_{i,j} - f_{i,j+1})^2}, \quad (4)$$

where $f_{i,j}$ is a pixel value of the discrete 2D image and $d_{i,j}$ is a discrete gradient.

Equation (3) can be implemented in two loops. The outer loop implements OS-SART to reduce data discrepancy, and the inner loop minimizes the image TV. In the inner loop, we use the gradient descent method:

$$f^{(m+1)} = f^{(m)} - \lambda \omega v, \quad (5)$$

where λ is a gradient descent control coefficient, $v = (\partial \|\nabla f\|_1 / \partial f_{i,j})|_{f_{i,j}=f_{i,j}^{[n,m]}}$ is a gradient direction with $f_{i,j} = f_{i,j}^{[n,m]}$, $\omega = \max(|f^{(m)}|) / \max(|v|)$ is a scaling coefficient of the gradient descent and n and m are the outer and inner loop iteration indices, respectively.

The whole iteration process can be summarized in the following steps.

Step 1. Input measured data b and an initial image $f = 0$.

Step 2. Update the current image using OS-SART by (2).

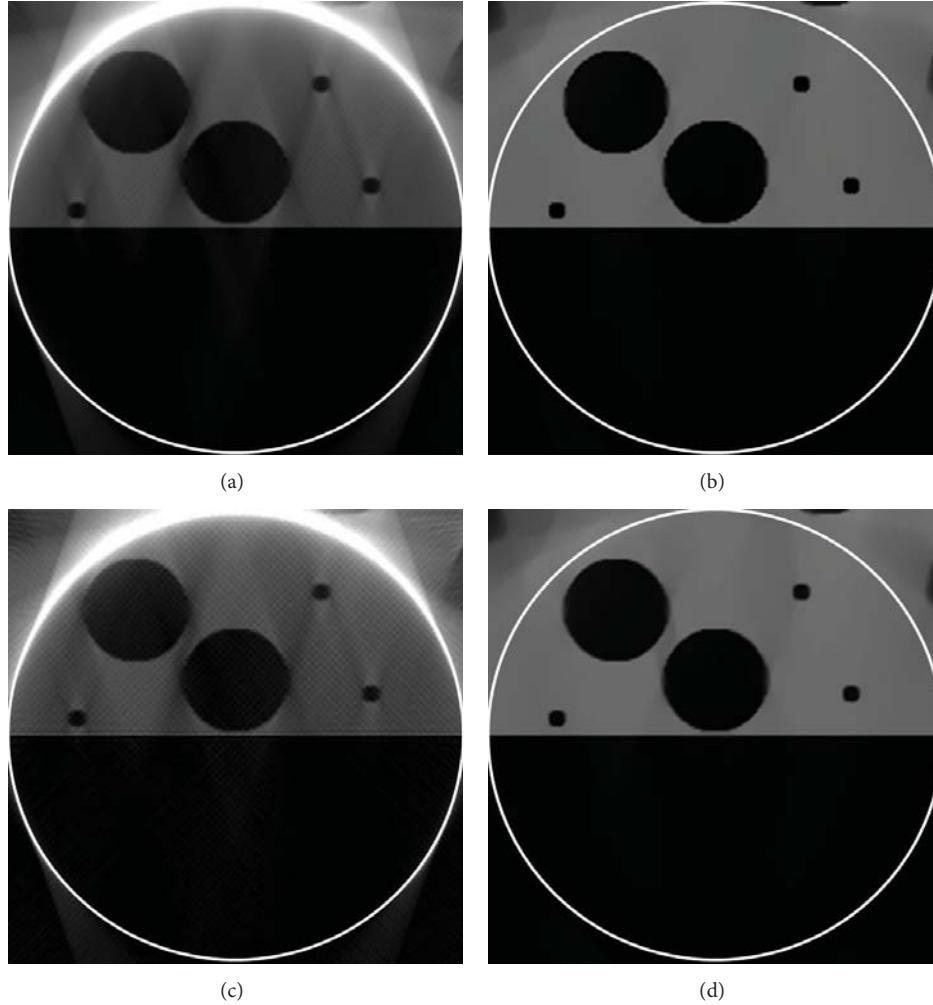


FIGURE 4: Reconstruction results. (a) The reconstructed ROI using FBP from 561 projections, (b) the reconstructed ROI using interior tomography from 561 projections, (c) the reconstructed ROI using FBP from 141 projections, and (d) the reconstructed ROI using interior tomography from 141 projections. The display window is $[0, 585] \text{ cm}^{-1}$.

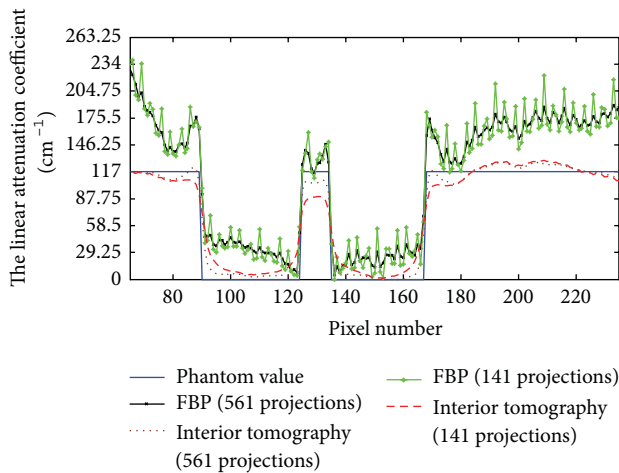


FIGURE 5: Profiles corresponding to the line “X” in Figure 3.

Step 3. Minimize the TV of the current image using the gradient descent method by (5).

Step 4. Go to Step 2 until a stopping criterion is met.

In our implementation, the gradient descent control coefficient was $\lambda = 0.2$, the TV iteration number was $m = 30$, and the OS-SART iteration number was $n = 20$.

3. Results and Analysis

3.1. Numerical Simulation. To evaluate the performance of interior tomography for studying the dentin specimen, we designed a dentin phantom as shown in Figure 3. This phantom has two distinct sizes of pores representing tubules and canaliculi. The dentin phantom was made $25 \mu\text{m} \times 50 \mu\text{m}$ in size and discretized into a 150×300 matrix (the pixel size: $0.17 \mu\text{m} \times 0.17 \mu\text{m}$). The tubules and canaliculi outside a pre-specified ROI represent structures that might affect the interior reconstruction. Because the dentin composition is similar to cortical bone, we used cortical bone to mimic dentin attenuation characteristics in the simulation. The linear attenuation coefficient of cortical bone was estimated as 117 cm^{-1}

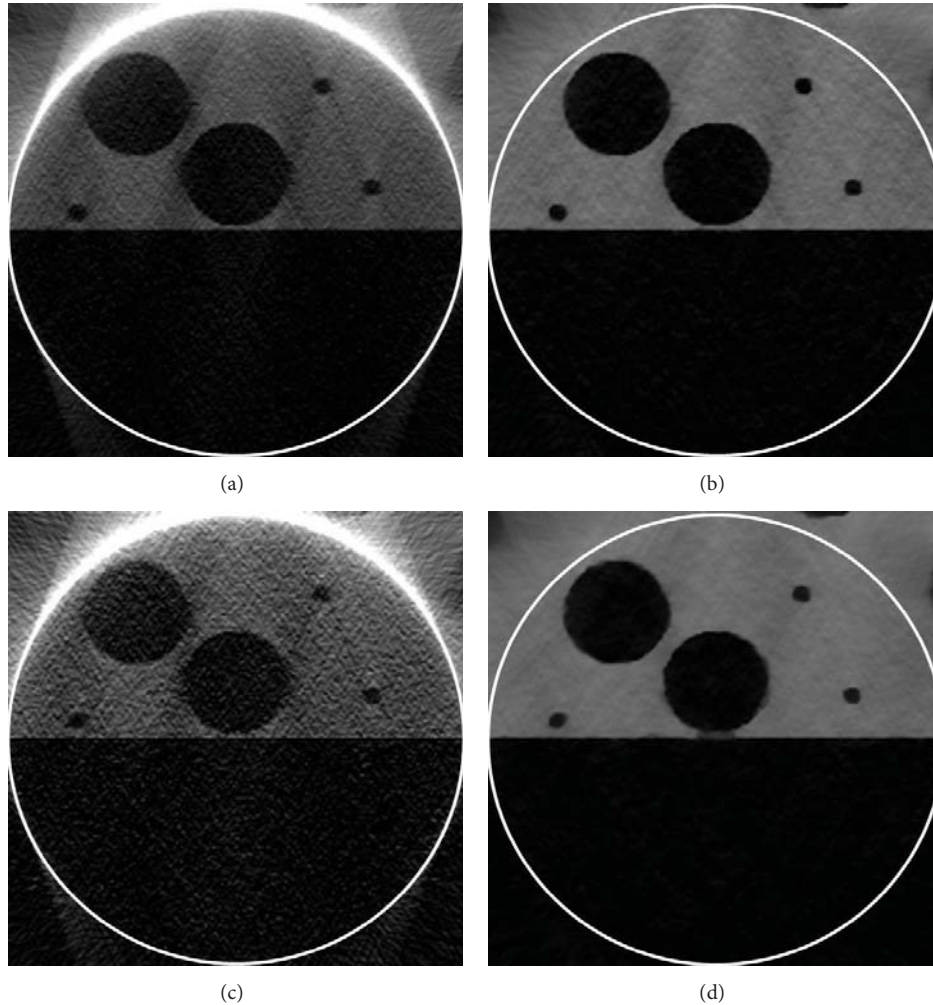


FIGURE 6: Reconstruction results from the data with 1% Gaussian noise. (a) The reconstructed ROI using FBP from 561 projections, (b) the reconstructed ROI using interior tomography from 561 projections, (c) the reconstructed ROI using FBP from 141 projections, and (d) the reconstructed ROI using interior tomography from 141 projections. The display window is $[0, 585] \text{ cm}^{-1}$.

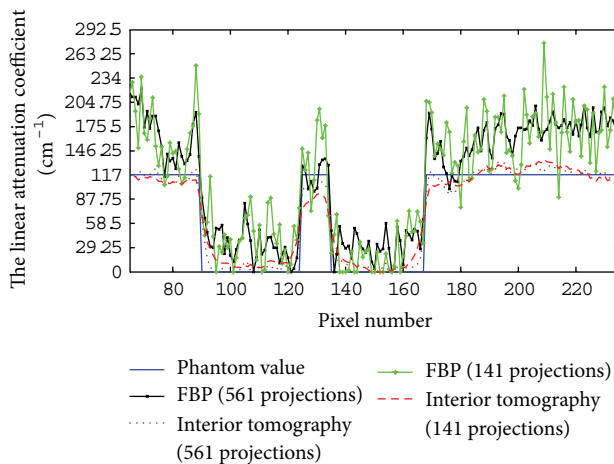


FIGURE 7: Profiles corresponding to the line “X” in Figure 3.

for an X-ray energy 8 keV according to the X-ray Attenuation Databases reported by the National Institute of Standards and

Technology (NIST). The scanning range was -70° to $+70^\circ$ (0° is for the normal to the plate-like specimen) with either a 0.25° or 1° angular increment and captured two groups of truncated projection data (a total of 561 or 141 projections, resp.). We then used FBP and CS-based interior tomography methods, respectively, to reconstruct the ROI from the two datasets for comparison.

The reconstructed results are in Figure 4. It can be seen in Figure 4 that there were some streak and shadow artifacts in the reconstructed images using FBP from truncated projections, and the interior tomography method could suppress these artifacts effectively. Figure 5 shows the profiles along the line “X” in Figure 4.

To test the stability of interior tomography against data noise, we repeated the reconstructions from projections contaminated with 1% Gaussian noise level. The reconstructed results from the data with 1% Gaussian noise are in Figure 6. It can be seen that there were strong noises in the images reconstructed using FBP from noise projections, and interior tomography could suppress these noises well. Figure 7 shows

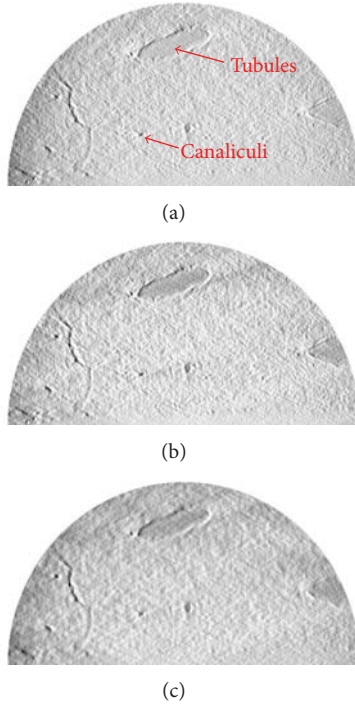


FIGURE 8: ROI reconstruction of the dentin specimen. (a) The reconstruction using FBP from 561 projections, (b) The reconstruction using interior tomography from 561 projections, and (c) the reconstruction of interior tomography from 141 projections. The display window is consistent.

TABLE 1: RMSE values for the reconstructed ROI images.

Reconstruction protocol	Noise-free data	Data with 1% noise
FBP (561 projections)	117.00	122.85
FBP (141 projections)	140.40	152.10
Interior tomography (561 projections)	9.65	10.59
Interior tomography (141 projections)	11.81	12.75

representative profiles corresponding to Figure 6, along the line “X” in Figure 3.

Then, we used the root mean square error (RMSE) to quantify the reconstructed results, which is expressed as

$$\text{RMSE} = \sqrt{\frac{\sum_{i,j \in \text{ROI}} (\mu_{i,j} - \hat{\mu}_{i,j})^2}{N_{\text{ROI}}}}, \quad (6)$$

where $\hat{\mu}_{i,j}$ is the reconstructed pixel value, $\mu_{i,j}$ is the true value of the phantom, and N_{ROI} is the number of the pixels in the ROI. The RMSE values are in Table 1.

3.2. Experimental Study. Supported by our encouraging numerical results, we applied the interior tomography method to study the dentin specimen. Figure 8 compares the reconstructions of the dentin specimen with FBP and interior tomography. The interior tomographic reconstructions were performed from 561 and 141 projections, respectively. Similar

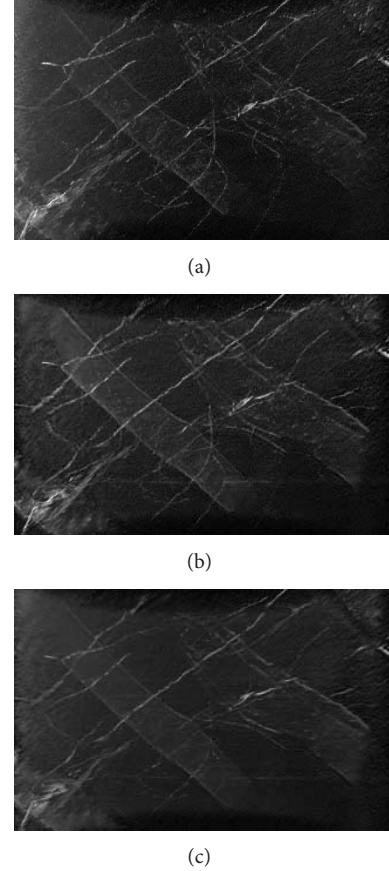


FIGURE 9: Reconstructed dentin structures. (a) The volume rendering based on the FBP reconstruction from 561 projections, (b) the volume rendering based on the interior tomographic reconstruction from 561 projections, and (c) the volume rendering based on the interior tomographic reconstruction from 141 projections. The 3D visualization display window is consistent.

to simulation analysis, there were some noise and artifacts in the reconstructed results from actual data. In theory, the pixel values in canaliculi and tubules regions should be similar and smaller than that of dentin. From the FBP reconstruction (Figure 8(a)), the gray values of the tubule region can be found, which may be imperfect due to data noise (higher brightness). Quantitatively, the slices reconstructed using interior tomography produced less noises and artifacts than the FBP image, and interior tomography has better stability than FBP.

To analyze the internal microstructures, two volumes of 600 high-resolution dentin slices were reconstructed using interior tomography from 561 projections and 141 projections, respectively. As a benchmark, a volume of the same 600 high-resolution dentin slices was also reconstructed using FBP from the 561 projections. All of these image volumes were rendered, as shown in Figure 9. Figure 9(a) shows the 3D result using FBP from truncated projections. In the interior tomographic reconstructions from truncated projections, noises and artifacts were significantly suppressed, producing 3D visualization with a better signal-to-noise ratio, even with only 141 projections, as shown in Figures 9(b) and 9(c).

4. Discussions and Conclusion

For high-resolution image reconstructions, the FBP algorithm is very efficient and accurate. With truncated datasets, however, the FBP method is subject to more noises and artifacts than those reconstructed by the iterative approach. In the piecewise-constant-model-based interior tomography framework, we have employed several techniques to increase convergence rate while improving image quality. First, an OS version of the Landweber scheme has been used. Second, the code has been optimized, combining the merits of C++ and multicore techniques. Third, a high-performance computer has been utilized to run our code program. Particularly, we have simultaneously reconstructed 8 slices using 8 central processing units (CPU).

The CS theory indicates that an image can be often accurately reconstructed from a rather limited amount of data when it can be sparsely represented in an appropriate domain. The internal feature of the dentin specimen is complex, and porosity is characteristic. We consider a dentin object approximately piecewise constant. Then, a dentin image is sparsified by a discrete gradient transform. Because the dentin projections are intrinsically truncated, it is inevitable that there are some artifacts in the image reconstructed using the FBP method. On the other hand, interior tomography is shown to be promising in meeting the challenge. In particular, the ability to generate a volume rendering with a high signal-to-noise ratio from a very limited number of truncated projections is quite feasible using interior tomography.

For real data study, our purpose is to reconstruct a high-quality dentin image. For 2D image reconstruction, there were some shadows (lower brightness) in the canaliculi and tubules regions reconstructed by the CS-based interior tomography method, which could reflect the attenuation characteristics of dentin interior structure. However, for 3D image reconstruction, the CS-based interior tomography method could suppress image artifacts and noises for the reconstructed images from truncated projections. Moreover, the CS-based interior tomography minimizes the TV of a reconstructed image by the steepest gradient descent method to generate a better looking 3D perspective view, which might oversmooth fine details if the number of views is too small. In the future studies we will analyze more dentin specimens to evaluate the performance of interior tomography and use the dictionary learning technique to capture more information.

In conclusion, we have developed a piecewise-constant-model-based interior tomography method to deal with truncated projections collected over a limited angular range, and investigated the feasibility and potential of the interior tomographic application in dentin characterization. It has been demonstrated that the CS-based interior tomography method is advantageous for the dentin reconstruction from incomplete nano-CT data. Further improvements are underway to facilitate dental research.

Acknowledgments

This work was partially supported by the US NIH/NIBIB Grant EB011785, US NICDR Grant DE001374, and the

National Natural Science Foundation of China Grant 61171157. The use of the Advanced Photon Source was supported by the US Department of Energy, Office of Science, Office of Basic Energy Sciences, under Contract no. DE-AC02-06CH11357.

References

- [1] A. Nanci, *Ten Cate's Oral Histology—Development, Structure, and Function*, Mosby, St. Louis, Mo, USA, 7th edition, 2008.
- [2] I. A. Mjör and I. Nordahl, “The density and branching of dentinal tubules in human teeth,” *Archives of Oral Biology*, vol. 41, no. 5, pp. 401–412, 1996.
- [3] S. Takuma and S. Eda, “Structure and development of the peritubular matrix in dentin,” *Journal of Dental Research*, vol. 45, pp. 683–692, 1966.
- [4] S. J. Jones and A. Boyde, “Ultrastructure of dentin and dentinogenesis,” in *Dentin and Dentinogenesis*, A. Linde, Ed., vol. 1, pp. 81–134, CRC Press, Boca Raton, Fla, USA, 1984.
- [5] S. Weiner, A. Veis, E. Beniash et al., “Peritubular dentin formation: crystal organization and the macromolecular constituents in human teeth,” *Journal of Structural Biology*, vol. 126, no. 1, pp. 27–41, 1999.
- [6] B. A. Gotliv, J. S. Robach, and A. Veis, “The composition and structure of bovine peritubular dentin: mapping by time of flight secondary ion mass spectroscopy,” *Journal of Structural Biology*, vol. 156, no. 2, pp. 320–333, 2006.
- [7] S. R. Stock, A. Veis, A. Telser, and Z. Cai, “Near tubule and intertubular bovine dentin mapped at the 250 nm level,” *Journal of Structural Biology*, vol. 176, pp. 203–211, 2011.
- [8] G. R. Davis and F. S. L. Wong, “X-ray microtomography of bones and teeth,” *Physiological Measurement*, vol. 17, no. 3, pp. 121–146, 1996.
- [9] S. R. Stock, A. E. M. Vieira, A. C. B. Delbem, M. L. Cannon, X. Xiao, and F. D. Carlo, “Synchrotron microComputed tomography of the mature bovine dentinoenamel junction,” *Journal of Structural Biology*, vol. 161, no. 2, pp. 162–171, 2008.
- [10] S. Zabler, H. Rieseemeier, P. Fratzl, and P. Zaslansky, “Fresnel-propagated imaging for the study of human tooth dentin by partially coherent x-ray tomography,” *Optics Express*, vol. 14, no. 19, pp. 8584–8597, 2006.
- [11] C. R. Parkinson and A. Sasov, “High-resolution non-destructive 3D interrogation of dentin using X-ray nanotomography,” *Dental Materials*, vol. 24, no. 6, pp. 773–777, 2008.
- [12] Y. Ye, H. Yu, Y. Wei, and G. Wang, “A general local reconstruction approach based on a truncated hilbert transform,” *International Journal of Biomedical Imaging*, vol. 2007, Article ID 63634, 8 pages, 2007.
- [13] H. Kudo, M. Courdurier, F. Noo, and M. Defrise, “Tiny a priori knowledge solves the interior problem in computed tomography,” *Physics in Medicine and Biology*, vol. 53, no. 9, pp. 2207–2231, 2008.
- [14] M. Courdurier, F. Noo, M. Defrise, and H. Kudo, “Solving the interior problem of computed tomography using a priori knowledge,” *Inverse Problems*, vol. 24, no. 6, Article ID 065001, 2008.
- [15] Q. Xu, X. Mou, G. Wang, J. Sieren, E. A. Hoffman, and H. Yu, “Statistical interior tomography,” *IEEE Transactions on Medical Imaging*, vol. 30, no. 5, Article ID 5688240, pp. 1116–1128, 2011.
- [16] E. J. Candès, J. Romberg, and T. Tao, “Robust uncertainty principles: exact signal reconstruction from highly incomplete frequency information,” *IEEE Transactions on Information Theory*, vol. 52, no. 2, pp. 489–509, 2006.

- [17] D. L. Donoho, "Compressed sensing," *IEEE Transactions on Information Theory*, vol. 52, no. 4, pp. 1289–1306, 2006.
- [18] G. H. Chen, J. Tang, and S. Leng, "Prior image constrained compressed sensing (PICCS): a method to accurately reconstruct dynamic CT images from highly undersampled projection data sets," *Medical Physics*, vol. 35, no. 2, pp. 660–663, 2008.
- [19] H. Yu and G. Wang, "Compressed sensing based interior tomography," *Physics in Medicine and Biology*, vol. 54, no. 9, pp. 2791–2805, 2009.
- [20] J. Yang, H. Yu, M. Jiang, and G. Wang, "High-order total variation minimization for interior tomography," *Inverse Problems*, vol. 26, no. 3, Article ID 035013, 2010.
- [21] H. M. Hudson and R. S. Larkin, "Accelerated image reconstruction using ordered subsets of projection data," *IEEE Transactions on Medical Imaging*, vol. 13, pp. 601–609, 1994.
- [22] C. L. Byrne, "Accelerating the EMML algorithm and related iterative algorithms by rescaled block-iterative methods," *IEEE Transactions on Image Processing*, vol. 7, no. 1, pp. 100–109, 1998.
- [23] M. Jiang and G. Wang, "Convergence studies on iterative algorithms for image reconstruction," *IEEE Transactions on Medical Imaging*, vol. 22, no. 5, pp. 569–579, 2003.
- [24] G. Wang and M. Jiang, "Ordered-subset simultaneous algebraic reconstruction techniques (OS-SART)," *Journal of X-Ray Science and Technology*, vol. 12, no. 3, pp. 169–177, 2004.
- [25] J. Vila-Comamala, Y. Pan, J. Lombardo et al., "Zone-doubled Fresnel zone plates for high-resolution hard X-ray full-field transmission microscopy," *Journal of Synchrotron Radiation*, vol. 19, no. 5, pp. 705–709, 2012.
- [26] R. Gordon, R. Bender, and G. T. Herman, "Algebraic Reconstruction Techniques (ART) for three-dimensional electron microscopy and X-ray photography," *Journal of Theoretical Biology*, vol. 29, no. 3, pp. 471–482, 1970.
- [27] A. H. Andersen and A. C. Kak, "Simultaneous algebraic reconstruction technique (SART): a superior implementation of the art algorithm," *Ultrasonic Imaging*, vol. 6, no. 1, pp. 81–94, 1984.
- [28] H. Yu and G. Wang, "A soft-threshold filtering approach for reconstruction from a limited number of projections," *Physics in medicine and biology*, vol. 55, no. 13, pp. 3905–3916, 2010.

Research Article

A Fusion Algorithm for GFP Image and Phase Contrast Image of Arabidopsis Cell Based on SFL-Contourlet Transform

Peng Feng, Jing Wang, Biao Wei, and Deling Mi

Key Laboratory of Optoelectronics Technology & System, Ministry of Education, Chongqing University, Chongqing 400044, China

Correspondence should be addressed to Peng Feng; coe-fp@cqu.edu.cn

Received 13 December 2012; Accepted 26 December 2012

Academic Editor: Wenxiang Cong

Copyright © 2013 Peng Feng et al. This is an open access article distributed under the Creative Commons Attribution License, which permits unrestricted use, distribution, and reproduction in any medium, provided the original work is properly cited.

A hybrid multiscale and multilevel image fusion algorithm for green fluorescent protein (GFP) image and phase contrast image of Arabidopsis cell is proposed in this paper. Combining intensity-hue-saturation (IHS) transform and sharp frequency localization Contourlet transform (SFL-CT), this algorithm uses different fusion strategies for different detailed subbands, which include neighborhood consistency measurement (NCM) that can adaptively find balance between color background and gray structure. Also two kinds of neighborhood classes based on empirical model are taken into consideration. Visual information fidelity (VIF) as an objective criterion is introduced to evaluate the fusion image. The experimental results of 117 groups of Arabidopsis cell image from John Innes Center show that the new algorithm cannot only make the details of original images well preserved but also improve the visibility of the fusion image, which shows the superiority of the novel method to traditional ones.

1. Introduction

The purpose of image fusion is to integrate complementary and redundant information from multiple images of the same scene to create a single composite that contains all the important features of the original images [1]. The resulting fused image will thus be more suitable for human and machine perception or for further image processing tasks in many fields, such as remote sensing, disease diagnosis, and biomedical research. In molecular biology, the fluorescence imaging and the phase contrast imaging are two common imaging systems [2]. Green fluorescent protein (GFP) imaging can provide the function information related to the molecular distribution in biological living cells; phase contrast imaging provides the structural information with high resolution by transforming the phase difference which is hardly observed into amplitude difference. The combination of GFP image and phase contrast image is valuable for function analyses of protein and accurate localization of subcellular structure. Figure 1 shows one group of registered GFP image and phase contrast image for Arabidopsis cell; it is obvious that there is a big difference between the GFP image and the phase contrast image. Due to low similarity between the

originals, various fusion methods that had been widely used in remote image fusion [3–5], such as Wavelet/Contourlet-based ARSIS fusion method [6], will result in spectral and color distortion, dark and nonuniform background, and poor ability of detailed preservation. Recently, Li and Wang have proposed SWT-based (stationary wavelet transform) [7] and NSCT-based (nonsubsampling Contourlet transform) [8] fusion algorithms which utilize the translation invariance of two kinds of transform to reduce the artifacts of fused image, but complicated procedure, high time-consumption, and low robustness hinder its fusion capability. In order to overcome these disadvantages, we bring sharp frequency localization Contourlet transform (SFL-CT) [9] into the fusion of GFP image and phase contrast image, in the manner of SFL-CT's merit of excellent edge expression ability, multiscale, directional characteristics, and anisotropy. We propose a new hybrid multiscale, and multilevel image fusion method combining intensity-hue-saturation (IHS) transform and SFL-CT. Different fusion strategies are utilized for the coefficients of different subbands in order to keep the localization information in GFP image and detailed information of high resolution in phase contrast image. The research conducts a fusion test of 117 groups of Arabidopsis cell images from

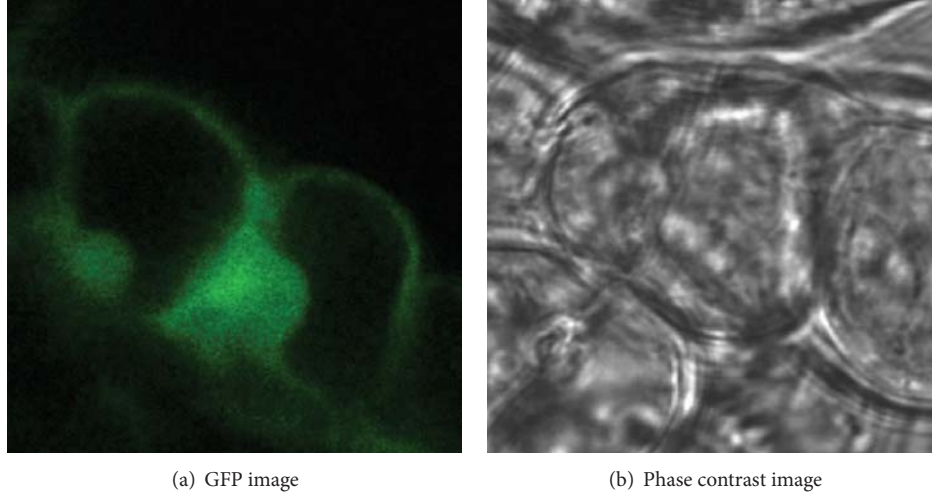


FIGURE 1: Arabidopsis cell images.

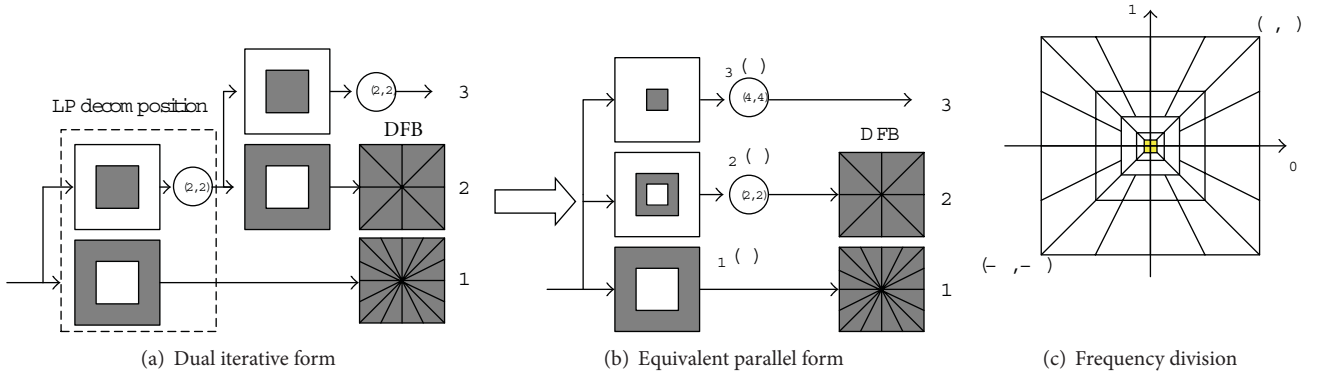


FIGURE 2: Block diagram of Contourlet transform with 2 levels of multiscale decomposition.

the GFP database of John Innes Center [10]. Visual information fidelity (VIF) [11] is also introduced to quantify the similarity inside and outside the fluorescent area between the fused image and original ones.

The outline of this paper is as follows. In Section 2, the SFL-CT and IHS transforms are introduced in detail. Section 3 concretely describes our proposed fusion algorithm based on the neighborhood consistency measurement. Experimental results and performance analysis are presented and discussed in Section 4. Section 5 gives the conclusion of this paper.

2. SFL-Contourlet Transform and IHS Transform

2.1. Traditional Contourlet Transform. In 2005, Do and Vetterli [12] proposed the Contourlet transform as a directional multiresolution image representation that can efficiently capture and represent smooth object boundaries in natural images. The Contourlet transform is constructed as a combination of the Laplacian pyramid transform (LPT) [13] and the directional filter banks (DFB) [14], where the LPT

iteratively decomposes a 2D image into low-pass and high-pass subbands, and the DFB are applied to the high-pass subbands to further decompose the frequency spectrum into directional subbands.

The block diagram of the Contourlet transform with two levels of multiscale decomposition is shown in Figure 2(a), followed by angular decomposition. Note that the Laplacian pyramid shown in the diagram is a simplified version of its actual implementation. Nevertheless, this simplification serves our explanation purposes satisfactorily. By using the multirate identities, we can rewrite the filter bank into its equivalent parallel form, as shown in Figure 2(b), where $H_i^B(\omega)$, $i = 1, 2, 3$, is the equivalent filter of LPT for each decomposition level [15]. Obviously, using ideal filters, the Contourlet transform will decompose the 2D frequency spectrum into trapezoid-shaped regions as shown in Figure 2(c).

Due to the periodicity of 2D frequency spectrums for discrete signals and intrinsic paradox between critical sample and perfect reconstruction of DFB, it means that we cannot get perfect reconstruction and frequency domain localization simultaneously by a critically sampled filter bank with

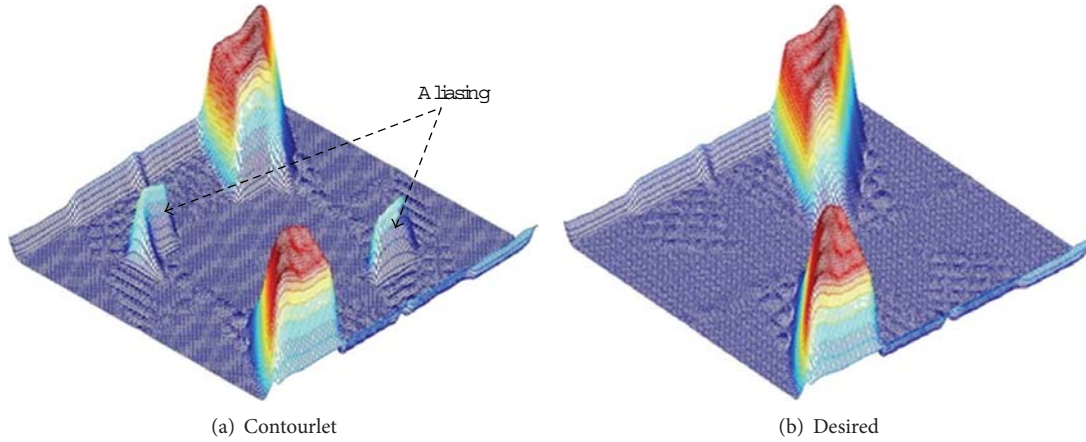


FIGURE 3: Frequency support of one channel for Contourlet transform and desired scheme.

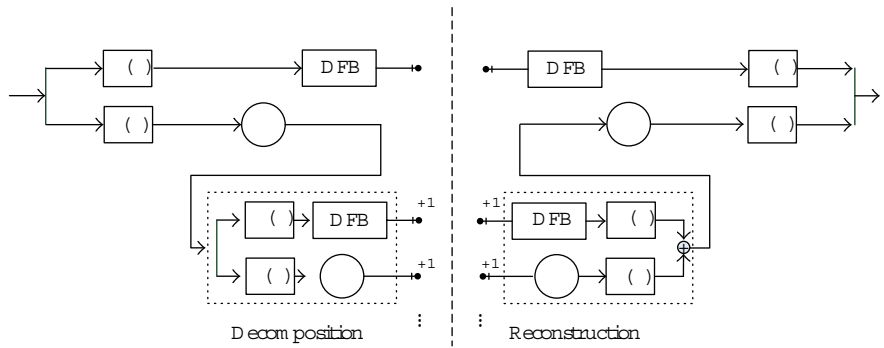


FIGURE 4: Block diagram of SFL-CT.

the frequency partitioning of the DFB. When the DFB is combined with a multiscale decomposition as in the Contourlet transform, the aliasing problem becomes a serious issue. For instance, Figure 3(a) shows the frequency support of an equivalent directional filter of the second channel in Figure 2(b). We can see that Contourlets are not localized in the frequency domain, with substantial amount of aliasing components outside of the desired trapezoid-shaped support as shown in Figure 3(b).

2.2. Sharp Frequency Localization Contourlet Transform. In order to overcome the aliasing disadvantage of Contourlet transform, Lu proposed a new construction scheme which employed a new pyramidal structure for the multiscale decomposition as the replacement of LPT [15]. This new construction is named as sharp frequency localization Contourlet transform (SFL-CT) [9], and its block diagram is shown in Figure 4.

In the diagram, $H(\omega)$ represents the high-pass filter, and $L(\omega)$ represents low-pass filter in the multiscale decomposition, with $\omega = (\omega_0, \omega_1)$. The DFB which is the same as in Contourlet transform (CT) is attached to the high-pass channel at the finest scale and bandpass channel at all coarser scales. The low-pass filter $L(\omega)$ in each levels is downsampled by matrix M , with M normally being set as diagonal matrix

(2,2). To have more levels of decomposition, we can iteratively insert at point a_{n+1} a copy of the diagram contents enclosed by the dashed rectangle. As an important difference from the LPT shown in Figure 2, the new multiscale pyramid can employ a different set of low-pass and high-pass filters for the first level and all other levels, and this is a crucial step in reducing the frequency-domain aliasing of traditional Contourlet transform. We leave the detailed explanation for this issue as well as the specification of the filters $H(\omega)$ and $L(\omega)$ to [9].

Figure 5 shows one Contourlet basis image and its corresponding SFL-Contourlet part in the frequency and spatial domains. As we can see from Figure 5(a), the original Contourlet transform suffers from the frequency nonlocalization problem. In sharp contrast, SFL-Contourlet produces basis image that is well localized in the frequency domain, as shown in Figure 5(b). The improvement in the frequency localization is also reflected in the spatial domain. As shown in Figures 5(c) and 5(d), the spatial regularity of SFL-Contourlet is obviously superior to the one of Contourlet.

2.3. IHS Transform. The intensity-hue-saturation (IHS) transform substitutes the gray image for the intensity component of the color image and thus handles the fusion

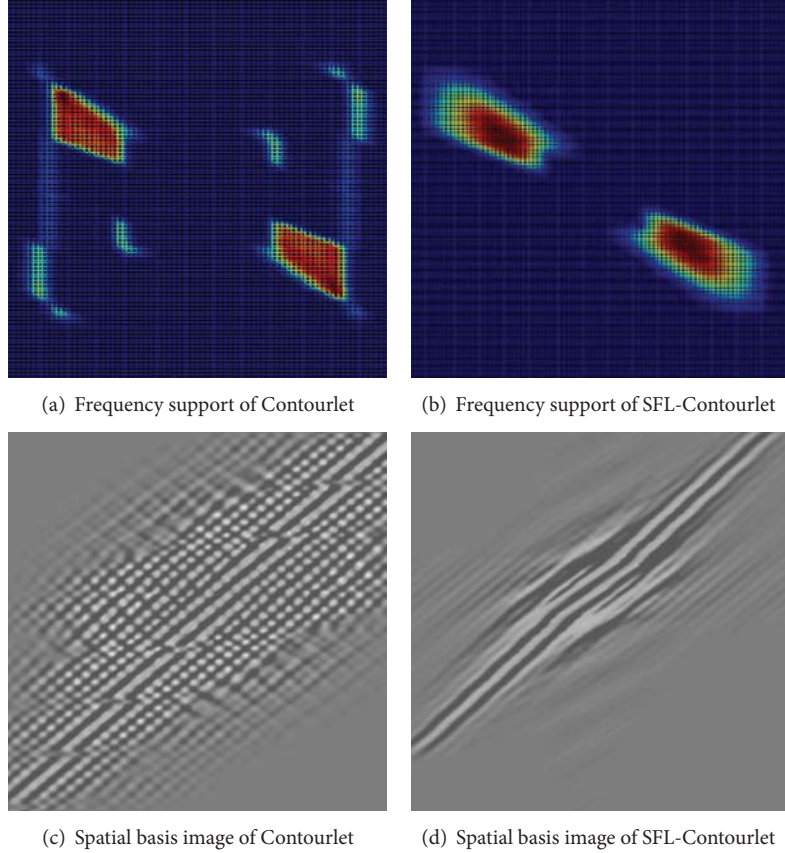


FIGURE 5: Comparison of basis image.

of the gray and color images [1] and defines three color attribute based on the human visual mechanism, that is, intensity (I), hue (H), and saturation (S). I stands for the information of the source image, H stands for the spectrum and color attributes, and S stands for the purity relative to the grayscale of some color. In IHS space, H component and S component are closely tied to the way that people feel about color, while I component almost has nothing to do with the color component of the image.

There are various algorithms that can transform image from RGB to IHS space, common transformation model including sphere transformation, cylinder transformation, triangle transform, and single six cones [16]. We use triangle transform here. The formula of the forward and inverse transforms are as follows.

From RGB to IHS space (forward transform),

$$\begin{aligned}
 I &= \frac{R+G+B}{3}, \\
 S &= 1 - \frac{3}{R+G+B} [\min(R, G, B)], \\
 H &= \begin{cases} 0 & B \leq G \\ 2\pi - \alpha & B > G, \end{cases} \quad (1)
 \end{aligned}$$

where

$$\alpha = \arccos \left\{ \frac{(1/2) [(R-G) + (R-B)]}{[(R-G)^2 + (R-B)(G-B)]^{1/2}} \right\}. \quad (2)$$

The reverse transform

$$\begin{aligned}
 &\text{for } 0 \leq H < \frac{2\pi}{3}, \quad \begin{cases} B = I(1-S) \\ R = I \times \left[1 + \frac{S \cos(H)}{\cos(\pi/3 - H)} \right] \\ G = 3I - (R+B), \end{cases} \\
 &\text{for } \frac{2\pi}{3} \leq H < \frac{4\pi}{3}, \quad \begin{cases} B = I(1-S) \\ R = I \times \left[1 + \frac{S \cos(H - 2\pi/3)}{\cos(\pi/3 - H)} \right] \\ G = 3I - (R+B), \end{cases} \\
 &\text{for } \frac{4\pi}{3} \leq H < 2\pi, \quad \begin{cases} B = I(1-S) \\ R = I \times \left[1 + \frac{S \cos(H - 4\pi/3)}{\cos(\pi - H)} \right] \\ G = 3I - (R+B). \end{cases} \quad (3)
 \end{aligned}$$

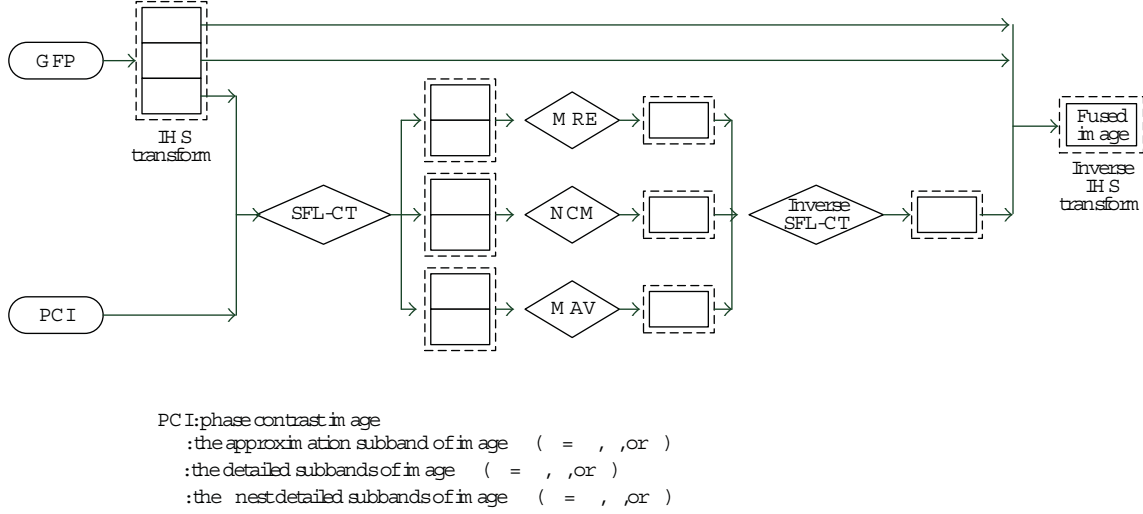


FIGURE 6: Schematic diagram of the proposed image fusion algorithm, where subscripts A , B , and F mean GFP image, phase contrast image, and the fused image, respectively.

3. The Proposed Fusion Rule

From Figure 1(a), we can see that the background of the GFP image is partially dark; in order to avoid the influence of low contrast after fusion, the intensity component of the original GFP image is extracted by IHS transform which not only keeps most of the information from the original one, but also entirely improves the brightness of the fused image. In this way, we can explore a hybrid multiscale and multilevel fusion algorithm for biological cell image. We use SFL-CT to decompose the intensity components of GFP image and phase contrast image; different fusion schemes are used for different subband coefficients in order to keep a balance between the localization information in GFP image and detailed information of high frequency in phase contrast image. To get the protein distribution information of GFP image, the approximation (coarsest) subband coefficients of fused image are obtained with maximum region energy rule (MRE) [17]. To get structural information of the phase contrast image, coefficients of the finest detailed subband of fused image are based on maximum absolute value rule (MAV) [17]. To balance structural information and color molecular distribution information from the originals, a locally adaptive coefficient fusion rule named neighborhood consistency measurement (NCM) is adopted on coefficients of other detailed subbands. The schematic diagram is shown in Figure 6.

3.1. Maximum Region Energy (MRE) Rule. When GFP image and phase contrast image are decomposed by the SFL-CT, the coefficients of the coarsest subband represent the approximation component of the input images. Considering approximate information of fused image is constructed by the two kinds of approximation subband coefficients; maximum region energy rule (MRE) is a good choice for the fused approximation subband coefficients.

MRE rule is defined as follows:

$$c_j^F(m, n) = \begin{cases} c_j^A(m, n), & \text{if } E_j^A(m, n) > E_j^B(m, n) \\ c_j^B(m, n), & \text{if } E_j^A(m, n) \leq E_j^B(m, n), \end{cases} \quad (4)$$

where the regional energy E is defined as

$$E_j^X(m, n) = \sum_{(x,y) \in \Omega(m,n)} [c_j^X(x, y) - \mu_j^X(m, n)]^2, \quad (5)$$

$X = A, B \text{ or } F$,

where $E_j^A(m, n)$, $E_j^B(m, n)$, and $E_j^F(m, n)$ denote regional energy of original image A , B , and fused image F in the coarsest scale J and location (m, n) . $\Omega(m, n)$ represents a square region with 3×3 size whose center is located at position (m, n) . $c_j^X(m, n)$ denotes the coefficient of the images $X = A, B$, or F within the region $\Omega(m, n)$ in the coarsest subband J and location (m, n) . $\mu_j^X(m, n)$ means the average value of coefficients within $\Omega(m, n)$.

3.2. Maximum Absolute Value (MAV) Rule. After decomposing the input images using SFL-CT, the image details are contained in the directional subbands in SFL-CT domain. The directional subband coefficients with larger absolute values, especially for subband coefficients at the finest scale, generally correspond to pixels with sharper brightness in the image and thus to the salient features such as edges, lines, and regions boundaries. Therefore, we can use the maximum absolute value (MAV) scheme to make a decision on the selection of coefficients at the finest detailed subbands.

MAV fusion rule is defined as follows:

$$d_{j,l}^F(m, n) = \begin{cases} d_{j,l}^A, & \text{if } \text{abs}[d_{j,l}^A(m, n)] > \text{abs}[d_{j,l}^B(m, n)] \\ d_{j,l}^B, & \text{if } \text{abs}[d_{j,l}^A(m, n)] < \text{abs}[d_{j,l}^B(m, n)], \end{cases} \quad (6)$$

where $d_{j,l}^A(m,n)$, $d_{j,l}^B(m,n)$, and $d_{j,l}^F(m,n)$ denote the coefficients of the images A , B , and the fused image F in the j th scale, l th directional subband, and location (m,n) . $\text{abs}[\cdot]$ denotes absolute operator.

3.3. Neighborhood Consistency Measurement (NCM). Let $N_{j,l}^X(m,n)$ denote a region centered at coefficient $d_{j,l}^X(m,n)$ in j th level and l th directional subband of image X , and the energy of this region is defined as $\rho_{j,l}^X(m,n)$. Then,

$$\rho_{j,l}^X(m,n) = \sum_{(k,p) \in N_{j,l}^X(m,n)} [d_{j,l}^X(k,p)]^2, \quad X = A, B \text{ or } F. \quad (7)$$

The NCM is defined as a threshold for directional coefficients based on one region mentioned above. Let $\Psi_{j,l}(m,n)$ denote NCM as follows:

$$\Psi_{j,l}(m,n) = \frac{2 \times \left\{ \sum_{(k,p) \in N_{j,l}^A(m,n)} [d_{j,l}^A(k,p)] \times [d_{j,l}^B(k,p)] \right\}}{\rho_{j,l}^A(m,n) + \rho_{j,l}^B(m,n)}. \quad (8)$$

It is not hard to see that the NCM is smaller than 1. In fact, NCM indicates whether the neighborhood is homogenous. Bigger NCM means being more homogenous.

Taking the number of directions in each detailed subband into consideration, we classify neighborhood into two classes: Nhd I and Nhd II which are shown in Figures 7(a) and 7(b). Nhd I is mainly used in horizontal and vertical subbands, and Nhd II is in other subbands. For instance, if the direction number is 8 or 16, we can use empirical distribution model as Figure 8.

We define a threshold T which is normally $0.5 < T < 1$.

If $\Psi_{j,l}(m,n) < T$, then

$$d_{j,l}^F(m,n) = \begin{cases} d_{j,l}^A, & \text{if } \rho_{j,l}^A(m,n) \geq \rho_{j,l}^B(m,n) \\ d_{j,l}^B, & \text{if } \rho_{j,l}^A(m,n) < \rho_{j,l}^B(m,n). \end{cases} \quad (9)$$

If $\Psi_{j,l}(m,n) \geq T$, then

$$\begin{aligned} d_{j,l}^F(m,n) &= \Psi_{j,l}(m,n) \times \max [d_{j,l}^A(m,n), d_{j,l}^B(m,n)] \\ &\quad + [1 - \Psi_{j,l}(m,n)] \\ &\quad \times \min [d_{j,l}^A(m,n), d_{j,l}^B(m,n)]. \end{aligned} \quad (10)$$

3.4. Fusion Procedure. The fusion process, accompanied with the proposed fusion rule, is carried out as in the following steps.

- (1) Define the register original images: GFP image as image A , phase contrast image as image B , and fused image as image F .
- (2) Make IHS transform for image A , and calculate the corresponding intensity components I_A , hue component H_A , and saturation component S_A .

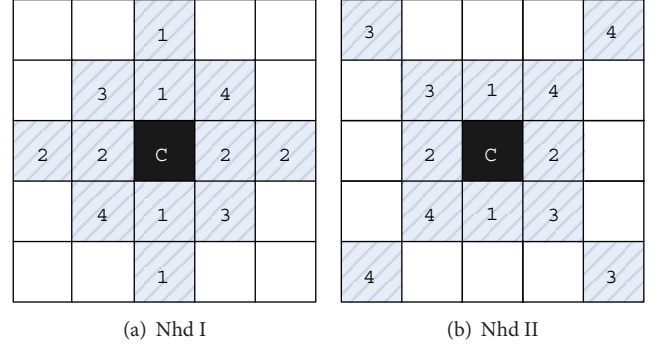


FIGURE 7: Neighborhood coefficients of SFL-CT.

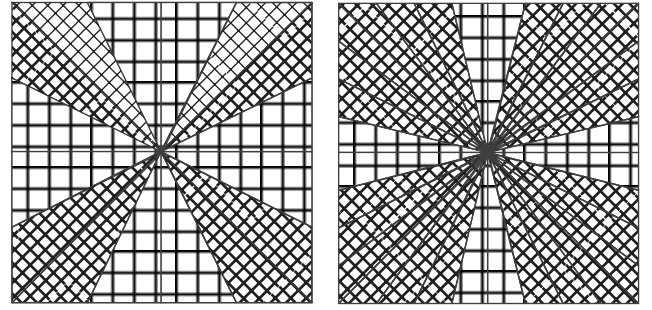


FIGURE 8: Empirical distribution model for neighborhood selection.

- (3) Decompose I_A and image B by SFL-CT, and get two approximation subbands $\{\varphi_A, \varphi_B\}$, a series of the finest detailed subbands $\{\theta_A, \theta_B\}$, and other detailed subbands $\{\varepsilon_A, \varepsilon_B\}$.
- (4) Combine transform coefficients according to the selection rule: coefficients of approximation subbands are based on MRE rule; coefficients of the finest detailed subbands are based on MAV rule; coefficients of other detailed subbands are based on NCM. We can get the approximation subband φ_F , detailed subbands ε_F , and θ_F of the fused image F .
- (5) Reconstruct the intensity of the fused image I_F with φ_F , ε_F , and θ_F by the inverse SFL-CT.
- (6) Reconstruct the fused image F with the hue H_A and saturation S_A , together with the I_F by the inverse IHS transform.

4. Experimental Results and Discussion

4.1. Dataset. All images used in this experiment come from the GFP database of John Innes Center [10]. The original size of images is 358×358 pixels. We resize and crop them into 256×256 pixels in order to facilitate processing. The experiment contains 117 sets of GFP images (24-bit true color)

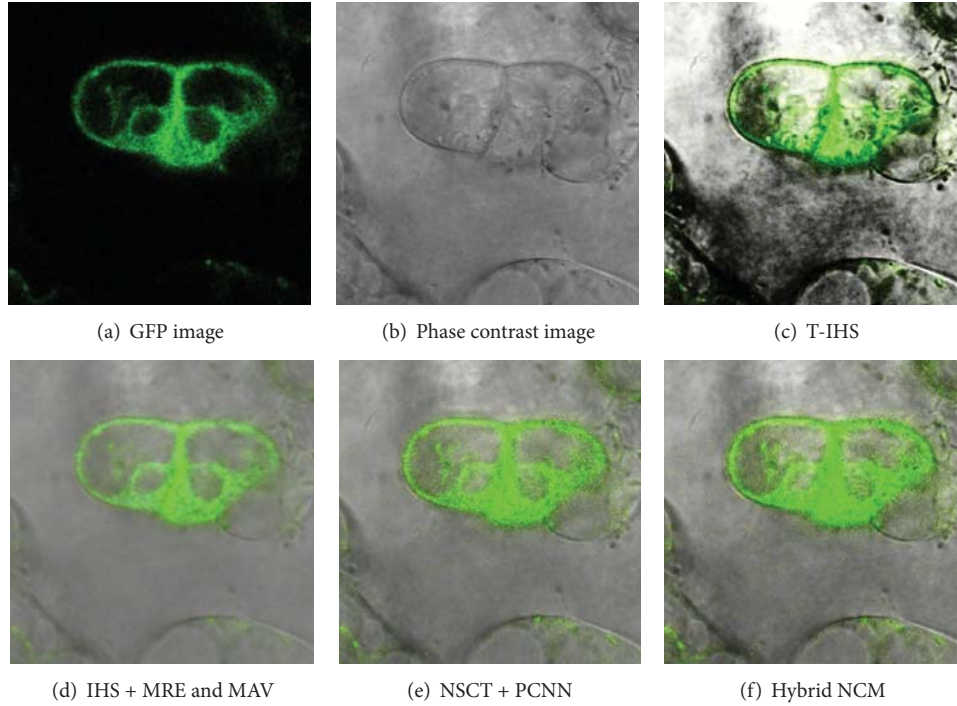


FIGURE 9: Fused images using different methods.

and their corresponding phase contrast images (8-bit grey scale) of the Arabidopsis. The former reveal the distribution of the labeled protein, and the latter present cell structures information.

4.2. Parameters Selection. For the proposed method, the practical windows (Ω) in NCM rule are usually chosen to be of size 3×3 , 5×5 , or 7×7 . We have investigated these practical windows and found that size 5×5 provides good results considering fusion clarity and time consumption. Apart from the sizes of the practical windows, the frequency parameters of SFL-CT are also needed to choose for improving the fusion performance. A larger number of experimental results demonstrate that the passband frequency ω_p and stopband frequency ω_s which should be $4\pi/21$ and $10\pi/21$, respectively, can not only provide pleasing fusion performance in most cases, but also keep good balance between fusion result and computation complexity.

4.3. Results Comparison. We compare the proposed fusion rule with the traditional methods or rules. They include traditional IHS fusion method (T-IHS) [18], MRE and MAV fusion method based on IHS space (IHS + MRE and MAV) [1], and PCNN-based fusion method [19] in which all the images are decomposed by the nonsubsampled Contourlet transform (NSCT + PCNN), and our method (Hybrid NCM). Among them, MAV stands for the maximum absolute value rules; MRE stands for maximum region energy rules; MRE and MAV represents MRE rule for approximation subband and MAV rule for detailed subbands. The parameters of the

above method are set as follows. For the rule of the fusion of MRE, neighborhood window is of size 3×3 pixels. SFL-CT makes a decomposition for 4 layers; the numbers of directions of each layer are (4, 8, 16, and 16); the filter for DFB is “pkva” filter; the set of NSCT + PCNN fusion algorithm is just the same as that in [20].

The fusion results, shown in Figure 9, which are obtained by four different methods demonstrate visual difference. It is obvious to see that the fused image using T-IHS method is unsatisfactory. The foreground and background are significantly nonuniform, especially along the cell outlines as there exist fuzzy blacks, so it is difficult to distinguish the inner information. However, the brilliance shown in Figures 9(d)–9(f) is largely improved, and the details of the images are also clearer. All in all, the location information of the cell structure in the phase contrast image and the distribution information of the protein are largely retained. Nevertheless, it is not easy to objectively judge the quality of the above three methods. For better judging these fusion results, the quantitative parameter that is visual information fidelity (VIF) [11] is taken into consideration. In the recent studies, large-scale subjective experiments assess VIF, a novel image similarity criterion, and prove it to be a good substitution for the subjective assessment. We know that there are two kinds of traditional evaluations that are subjective evaluation and objective evaluation. The former depends on the perception of human eye vision; different people would have different perception. The latter method has a little link with subjective factor, but it does not well measure the difference between the fusion image and the original image. As for the characteristic, that is, the little similarity between GFP fluorescence image

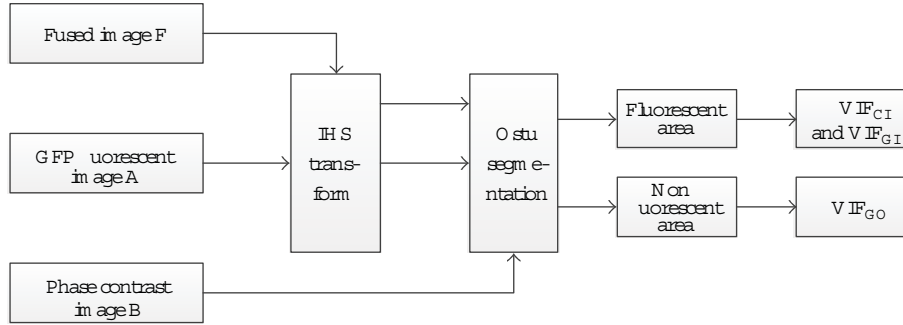


FIGURE 10: VIF algorithm flow chart.

and phase image, the VIF method, which is the combination of human visual system (HVS) and image characteristic statistics, is introduced into this paper to measure the quality of fusion image. This method can tell us the similarity between different regions of fusion image and the original image in quantitative aspect. The VIF value (the range is 0~1) is closer to 1; then it indicates that the fusion image has more similarity to the original image. A number of experimental results have proved that the VIF method and the human subjective evaluation have a better similarity for image quality than the traditional methods such as root mean square error (RMSE), correlation coefficients (CCs), and mutual information (MI).

Considering the difference in function orientation of the two kinds of images, especially the corresponding relationship between the fluorescence area in GFP images and the protein distribution in cells, the fluorescence area is firstly extracted from the original two images, then the VIF between fused image and phase contrast image is calculate, and thirdly the VIF between fused image and fluorescence image is calculated too. Fused image should keep high similarity with both phase contrast image and fluorescence image in fluorescence area. However, in the other area, only the similarity between it and the phase contrast image is considered. Therefore, this paper first segments both fused image and source image into fluorescence area and nonfluorescence area with Otsu method [20] and calculates VIF between fused image and source image in fluorescence area and nonfluorescence area, respectively. The calculation procedure is shown in Figure 10. Table 1 displays the calculation result of VIF of the fused image in Figure 9.

In the table, superscript fl refers to the fluorescent area while nfl refers to nonfluorescence area, A represents GFP fluorescence image, and B represents phase contrast image. VIF^{A-fl} refers to the similarity between fused image and GFP fluorescence image in fluorescence area, and VIF^{B-fl} refers to the similarity between fused image and phase contrast image in fluorescence area, while VIF^{B-nfl} refers to the similarity between fused image and phase contrast image in nonfluorescence area.

From Table 1, VIF^{B-fl} and VIF^{B-nfl} of the other three fusion methods are almost the same except T-HIS; the similar results indicate that all the detailed information of fused image comes from the phase contrast image no

TABLE 1: VIF computing result.

Fusion methods	VIF^{A-fl}	VIF^{B-fl}	VIF^{B-nfl}
T-IHS	0.4368	0.2759	0.4975
IHS + MRE and MAV	0.3119	0.8318	0.8318
NSCT + PCNN	0.3188	0.8992	0.8992
Hybrid NCM	0.3112	0.9299	0.9299

matter in fluorescent area or nonfluorescent area. Compared with other three methods, the proposed one we use in this experiment gets the highest VIF^{B-nfl} ; it does coincide with the observed results that the black background of the GFP image gets repressed. With luminance improved, the structural information will be well embedded in the fused image, which contributes the increase of VIF^{B-nfl} . The method we use can still get higher VIF^{A-fl} and VIF^{B-fl} , which indicates that the function information in GFP image and phase contrast image is well preserved in fluorescent area, and also the highest VIF^{B-fl} explains that SFL-CT can capture the structural information of the phase contrast image effectively.

VIF distribution histogram of 117 groups of Arabidopsis cell fusion image is shown in Figure 11; the red squared line represents the VIF^{A-fl} , and the blue dotted line represents the VIF^{B-fl} . It is obvious that VIF^{B-fl} is higher than VIF^{A-fl} , which does coincide with the objective of using SFL-CT to outstand the inner structural information of the phase contrast image. With the increasing VIF within fluorescent area, the VIF in nonfluorescent area also tends to improve; this indicates the following: if the intensity in fluorescent area is strengthening, VIF will increase with the function information fully reflected; and once the brightness increases, the high resolution structural information of the image can be fully shown, and the corresponding VIF^{B-fl} will increase; the phase image is affected by the intensity whereas low in fluorescence area, structural information cannot be reflected very well which reduces VIF's numerical similarity.

5. Conclusions

This paper proposes a hybrid multiscale and multilevel image fusion method based on IHS transform and SFL-CT

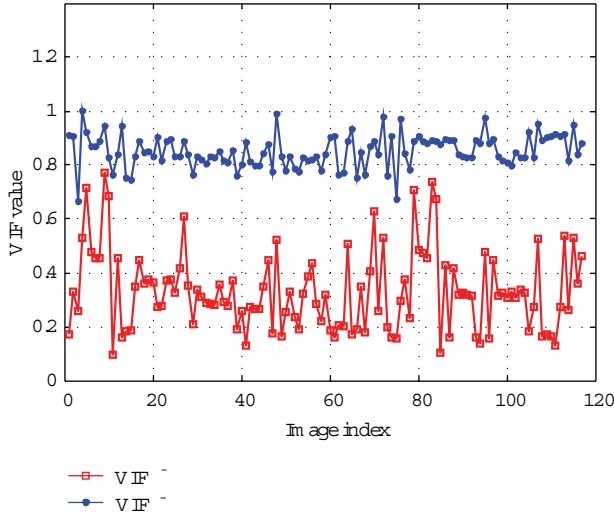


FIGURE 11: 117 groups of VIF distribution histogram of Arabidopsis cell fusion image.

to balance the gray structural information and molecular distribution information for the fusion of GFP image and phase contrast image. In manner of SFL-CT's advantage of directional and excellent detailed expression ability, we use SFL-CT to decompose the intensity components of both GFP image and phase contrast image, and different fusion rules are utilized for coefficients of different subbands in order to keep the localization information in GFP image and detailed high-resolution information in phase contrast image. Visual information fidelity (VIF) is introduced to assess the fusion result objectively which quantifies the similarity inside and outside the fluorescent area between the fused image and original images. The experiment fusion results of 117 groups of Arabidopsis cell images from John Innes Center demonstrate that the new algorithm can both make the details of original images well preserved and improve the visibility of the fusion image and also show the superiority of the novel method to traditional methods. Although the results of the proposed method and NSCT + PCNN look similar, the former is much better in line with the image of fused image similarity degree which means that this algorithm has made full use of the advantages of SFL-CT to keep the structural information of the phase contrast image effectively. The complexity of the algorithm is obviously lower than the latter and more advantageous to the actual application.

It is also needed to point out that from the experiment we find that VIF^{B-fl} is no longer equal with VIF^{B-fl} when we try to improve the intensity of the fluorescent image to make a new fusion image reconstruction; this is partially due to the nonlinear relationship between similarity and intensity within fluorescent area and nonfluorescence area of the fused image. Otsu segmentation method can also cause certain disturbance to the calculation of VIF. One evaluation method cannot be perfect for different kinds of images, and a suitable fusion and evaluation method for biological cells is still a further problem to be solved.

Acknowledgment

This paper is partially supported by the Fundamental Research Funds for the Central Universities (no. CDJZR11120006).

References

- [1] O. Ukimura, *Image Fusion*, InTech Press, Rijeka, Croatia, 2011.
- [2] S. Li, B. Yang, and J. Hu, "Performance comparison of different multi-resolution transforms for image fusion," *Information Fusion*, vol. 12, no. 2, pp. 74–84, 2011.
- [3] D. S. Huang, M. H. Yang, X. H. Yao, and J. Yin, "A method to fuse SAR and multi-spectral images based on contourlet and HIS transformation," *Journal of Astronautics*, vol. 32, no. 1, pp. 187–192, 2011.
- [4] B. Khaleghi, A. Khamis, and F. O. Karray, "Multisensor data fusion: a review of the state-of-the-art," *Information Fusion*, vol. 14, no. 1, pp. 28–44, 2013.
- [5] X. J. Long, Z. W. He, Y. S. Liu et al., "Multi-method study of TM and SAR image fusion and effectiveness quantification evaluation," *Science of Surveying and Mapping*, vol. 35, no. 5, pp. 24–27, 2010.
- [6] T. Ranchin, B. Aiazzi, L. Alparone, S. Baronti, and L. Wald, "Image fusion—the ARSIS concept and some successful implementation schemes," *ISPRS Journal of Photogrammetry & Remote Sensing*, vol. 58, no. 1-2, pp. 4–18, 2003.
- [7] T. J. Li and Y. Y. Wang, "Fusion of GFP fluorescent and phase contrast images using stationary wavelet transform based variable-transparency method," *Optics and Precision Engineering*, vol. 17, no. 11, pp. 2871–2879, 2009.
- [8] T. Li and Y. Wang, "Biological image fusion using a NSCT based variable-weight method," *Information Fusion*, vol. 12, no. 2, pp. 85–92, 2011.
- [9] Y. Lu and M. N. Do, "A new contourlet transform with sharp frequency localization," in *Proceedings of IEEE International Conference on Image Processing (ICIP '06)*, pp. 1629–1632, Atlanta, Ga, USA, October 2006.
- [10] Information on website, <http://data.jic.bbsrc.ac.uk/cgi-bin/gfp/>.
- [11] H. R. Sheikh and A. C. Bovik, "Image information and visual quality," *IEEE Transactions on Image Processing*, vol. 15, no. 2, pp. 430–444, 2006.
- [12] M. N. Do and M. Vetterli, "The contourlet transform: an efficient directional multiresolution image representation," *IEEE Transactions on Image Processing*, vol. 14, no. 12, pp. 2091–2106, 2005.
- [13] P. Feng, Y. Pan, B. Wei, W. Jin, and D. Mi, "Enhancing retinal image by the Contourlet transform," *Pattern Recognition Letters*, vol. 28, no. 4, pp. 516–522, 2007.
- [14] R. H. Bamberger and M. J. T. Smith, "A filter bank for the directional decomposition of images: theory and design," *IEEE Transactions on Signal Processing*, vol. 40, no. 4, pp. 882–893, 1992.
- [15] P. Feng, *Study on some key problems of non-aliasing Contourlet transform for high-resolution images processing [Dissertation]*, Chongqing University, 2007.
- [16] J. R. Harris, R. Murray, and T. Hirose, "IHS transform for the integration of radar imagery with other remotely sensed data," *Photogrammetric Engineering & Remote Sensing*, vol. 56, no. 12, pp. 1631–1641, 1990.

- [17] X. X. Chen, *Image and Video Retrieving and Image Fusion*, Mechanical Industry Press, Beijing, China, 2012.
- [18] T. M. Tu, S. C. Su, H. C. Shyu, and P. S. Huang, "A new look at IHS-like image fusion methods," *Information Fusion*, vol. 2, no. 3, pp. 177–186, 2001.
- [19] X. B. Qu, J. W. Yan, H. Z. Xiao, and Z. Q. Zhu, "Image fusion algorithm based on spatial frequency-motivated pulse coupled neural networks in nonsubsamped contourlet transform domain," *Acta Automatica Sinica*, vol. 34, no. 12, pp. 1508–1514, 2008.
- [20] N. Otsu, "A threshold selection method from gray-level histograms," *IEEE Transactions on Systems, Man and Cybernetics*, vol. 9, no. 1, pp. 62–66, 1979.

Research Article

Nonrigid Medical Image Registration Based on Mesh Deformation Constraints

XiangBo Lin,¹ Su Ruan,² TianShuang Qiu,¹ and DongMei Guo³

¹ Faculty of Electronic Information and Electrical Engineering, Dalian University of Technology, Dalian 116024, China

² Laboratory of Computer Science, Information Processing and Systems, University of Rouen, 76183 Rouen, France

³ Department of Radiology, Second Affiliated Hospital of Dalian Medical University, Dalian 116027, China

Correspondence should be addressed to XiangBo Lin; linxbo@dlut.edu.cn

Received 1 December 2012; Accepted 4 January 2013

Academic Editor: Peng Feng

Copyright © 2013 XiangBo Lin et al. This is an open access article distributed under the Creative Commons Attribution License, which permits unrestricted use, distribution, and reproduction in any medium, provided the original work is properly cited.

Regularizing the deformation field is an important aspect in nonrigid medical image registration. By covering the template image with a triangular mesh, this paper proposes a new regularization constraint in terms of connections between mesh vertices. The connection relationship is preserved by the spring analogy method. The method is evaluated by registering cerebral magnetic resonance imaging (MRI) image data obtained from different individuals. Experimental results show that the proposed method has good deformation ability and topology-preserving ability, providing a new way to the nonrigid medical image registration.

1. Introduction

Deformable registration is an important tool in medical imaging with many applications, such as atlas-based image segmentation and labeling, statistical analysis of normal and pathological variations in anatomy, and the study of the growth and development of normal and abnormal anatomical structures. It has been an active research topic for many years, and plenty of achievements have been published [1, 2]. The basic task of image registration is to find a spatial transformation which maps each point of one image onto its corresponding point of another image. The problem of image registration is often considered as a minimization problem, because it looks for increasing some similarity metric between the two images to be registered by moving points with a reasonable deformation field. Common choices of image similarity metric include sum of squared differences (SSD), normalized/cross-correlation (NCC/CC), normalized/mutual information (NMI/MI), or other divergence-based or information-theoretic measures [3]. However, it is not sufficient to rely only on similarity metric, because the solution does not ensure any spatial correlation between the adjacent points. Such high dimensional transformations involved in nonrigid registration make the problem ill-posed. Therefore, additional regularizing constraints are required to

enable a reasonable estimation of the displacement field. In general, given the target image B and the template image A , the common form of deformable registration problem is

$$\mathbf{T}^* = \arg \min_{\mathbf{T} \in \Gamma} E(\mathbf{T}) = \arg \min_{\mathbf{T} \in \Gamma} E_{\text{sim}}(B, A \circ \mathbf{T}) + E_{\text{reg}}(\mathbf{T}). \quad (1)$$

The first term $E_{\text{sim}}(B, A \circ \mathbf{T})$ in (1) measures the similarity between the deformed template image and the target image. The second term $E_{\text{reg}}(\mathbf{T})$, the regularization constraint, ensures the minimization problem is to be well-posed. The set Γ is the space of admissible transformations. The optimal transformation $\mathbf{T}^* \in \Gamma$ is obtained by minimizing the overall cost function, where Γ is the space of admissible transformations.

The regularization constraint plays crucial role in non-rigid registration problem. Different constraints have been proposed in the literature. References [4, 5] introduced inverse consistency as regularization constraint, which can be explained that the composition of the optimal forward transformation and the backward transformation between the template image and the target image is the identity. Smooth deformation field is also a commonly used constraint [6, 7] against noise. Reference [8] used an incompressibility constraint ensured by limiting the Jacobian determinant of a

transformation should be unity. Diffeomorphic transformation is studied much in recent years [9–11], that means continuous, differentiable, and reversible transformation. If the transformation is diffeomorphic, the deformed image should be topologically preserved. Miller et al. [12] proposed the group of diffeomorphic mappings for fluid flow registration. The optimal solution is obtained by regularizing the velocity field to avoid singular solution in numerical implementation. LDDMM [13] aims at finding smooth diffeomorphic mapping for large deformation by searching the smallest geodesic distance.

Direct topology-preserving constraint is another important regularization for nonlinear image registration. The main intuition behind topology preservation in a deformation field is the desire to maintain connectivity between neighboring morphological structures. One way to ensure the topology unchanged during deformation is to keep the Jacobian determinant of the transformation always positive. The other way is to identify a credible deformation space according to the registration model and then to find the optimal transformation in the credible deformation space. Reference [14] derived elegant linear constraints that provide necessary and sufficient conditions to ensure that the Jacobian determinant values of such transformations are positive everywhere. Reference [15] extended the work of [14] to 3D B-splines deformations. They adopted an interval analysis to find the maximum reasonable step along optimal searching path to ensure positive Jacobian determinant. Reference [16] considered enforcing topology preservation as a hard constraint at several intermediate steps of a deformable registration procedure or after the registration was done. Reference [17] used a large-scale constrained optimization method to solve the registration problem. By adding conditions involving the gradient of the Jacobian determinant, this method encouraged the topology preserving to be achieved everywhere.

Over the past years, more and more studies have investigated the nonrigid image registration problem with proper regularization energies. Nevertheless, the existing research is far from being mature. There are still different drawbacks. Some methods need to track the discrete Jacobian determinant or its gradient, which significantly increases computational cost. Some deformable registration models are built in continuous domain. Although topology preservation holds for the continuous transformation, it is no longer guaranteed when the practical solution is obtained on the discrete image grid. Here, we propose a new regularization scheme for nonrigid image registration to hold topology preservation. The details are organized as follows. Section 2 illustrates the entire scheme of the proposed nonrigid registration algorithm. Section 3 provides the experimental results and evaluations of the registration algorithm. The conclusion is drawn in Section 4.

2. Methods

The nonrigid image registration model proposed here focuses on maintaining the unchanged topology of the deformed image. A desirable property of intersubject medical image

warping is the preservation of the topology of anatomical structures. From medical perspective, some normal homology tissue or structure for any individual, such as internal brain structures, should have the same topology. A topology-preserving transformation guarantees the unchanged connectivity inside a structure and the relationships between the neighboring structures in the deformed image. There is no tearing, no folding, and no appearance or disappearance of structures. To achieve such performance, we propose to cover the deformable template image with a triangular mesh. The triangular mesh is generated according to the position rather than the value of control points. Then the topological relations are controlled by limiting the mesh deformation. The advantage is that the algorithm will get a better deformation quality even if no explicit Jacobian determinant constraint is used. The entire procedure of NR-MDC is showed in Figure 1. The registration procedure employs iterative style: extraction rough displacement field by measurements of similarity without considering spatial relations between points and optimization the displacement field by measurements of regularization energy. A multiresolution strategy propagating solutions from coarser to finer scales is used here to speed up the convergence of the algorithm and to avoid local optima.

2.1. Similarity Measures. Different features can be used to establish a similarity metric between the deformed template image and the target image to guide the deformed image towards the target image [3]. Here we use SSD as the similarity metric because it is simple and easy to deal with. The SSD forms the basis of the intensity-based image registration algorithms, and the optimal solution can be obtained by classical optimization algorithms [18]. It can be written as

$$E_{\text{sim}}(B, A \circ \mathbf{T}) = \sum_{\mathbf{p} \in \Omega} (B(\mathbf{p}) - A \circ \mathbf{T}(\mathbf{p}))^2, \quad (2)$$

where \mathbf{p} is pixel position, $\mathbf{p} = (x, y)$, and Ω is the image domain. Optical flow field theory [19] is usually adopted to find the displacement field. To better understand the method, we will describe its basic principle roughly. Suppose an object evolving over time, and $I(\mathbf{p}(t), t)$ is the images of this object. Based on intensity conservation assumption, the image function satisfies

$$I(\mathbf{p}(t), t) = \text{const}. \quad (3)$$

By differentiating (3) with respect to t ,

$$\frac{\partial I}{\partial x} \frac{\partial x}{\partial t} + \frac{\partial I}{\partial y} \frac{\partial y}{\partial t} = -\frac{\partial I}{\partial t}. \quad (4)$$

Consider image $A \circ \mathbf{T}$ and B being two samples of $I(\mathbf{p}(t), t)$ and let the sampling time to be unit time, then

$$\mathbf{v}(\mathbf{p}) \cdot \nabla B(\mathbf{p}) = A \circ \mathbf{T}(\mathbf{p}) - B(\mathbf{p}), \quad (5)$$

where $\mathbf{v}(\mathbf{p}) = (\partial x / \partial t, \partial y / \partial t)$ is the object moving velocity. By approximation, the velocity can be expressed as

$$\mathbf{v}(\mathbf{p}) = \frac{(A \circ \mathbf{T}(\mathbf{p}) - B(\mathbf{p})) \nabla B(\mathbf{p})}{\|\nabla B(\mathbf{p})\|^2}. \quad (6)$$

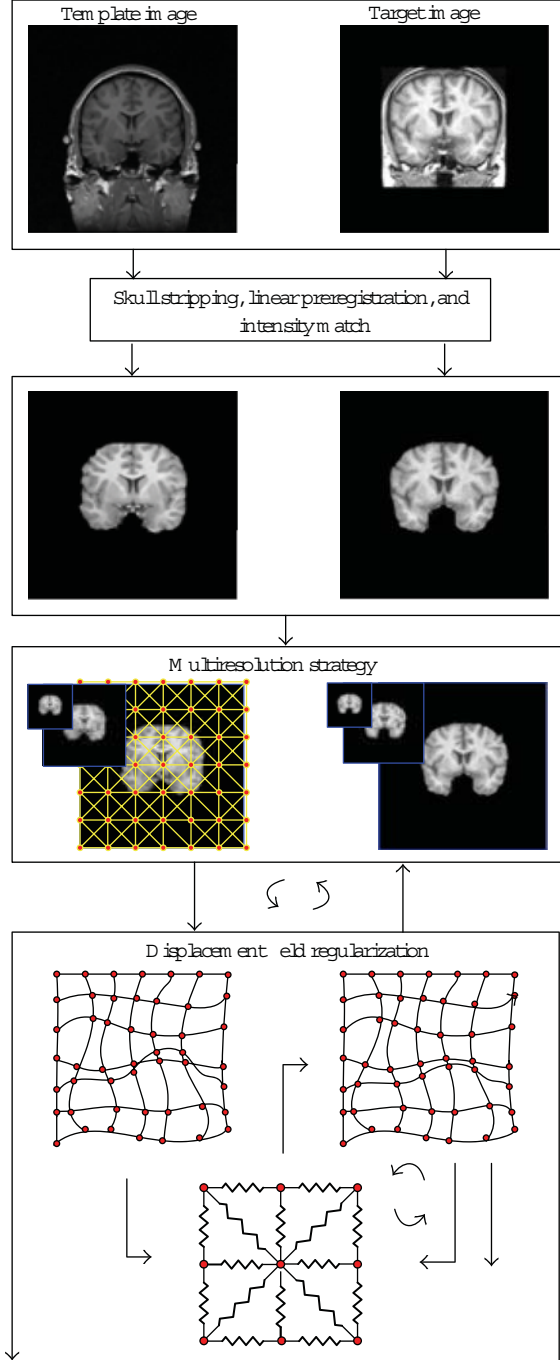


FIGURE 1: The framework of the NR-MDC algorithm.

Generally, the displacement of the point \mathbf{p} is $\mathbf{u}(\mathbf{p}) = -\mathbf{v}(\mathbf{p})$. To avoid unstable solution for small values of $\nabla B(\mathbf{p})$, (6) can be renormalized to

$$\mathbf{v}(\mathbf{p}) = \frac{(A \circ \mathbf{T}(\mathbf{p}) - B(\mathbf{p})) \nabla B(\mathbf{p})}{\|\nabla B(\mathbf{p})\|^2 + (A \circ \mathbf{T}(\mathbf{p}) - B(\mathbf{p}))^2}. \quad (7)$$

SSD metric is based on the implicit assumption that the intensities of two corresponding points in images A and B are equal. However this condition is seldom fulfilled in real-world medical image registration, because there are many

factors that may affect observed intensity of a tissue over the imaged field, such as the different scanner or scanning parameters, normal aging, different subjects, and so on. In view of such situation, intensity normalization is necessary. In addition, small motion assumption should be satisfied in optical flow field theory. To reduce the difference between the template image and the target image as much as possible, it is better to do spatial normalization using rigid or affine transformation before using (7) to complete the registration.

2.2. Regularization. The deformation field obtained from similarity measures does not consider any spatial relations among neighboring points. The points' interdependencies should be guaranteed by certain regularization constraints. Here we focus on topology preservation constraints. It is one basic topology property that the connection relationship between points and edges is unchanged in topology transformation. As is analyzed in [20], three main behaviors, fold, cross, and tear, will cause topological changes during deformation. To eliminate the unfavorable defects, an extra topology correction procedure was done in [20] by tracking the Jacobian determinant of the deformation field. Thus computational cost will increase inevitably.

The basic motivation of our work is to establish a topology preservation transformation in discrete domain directly and to avoid calculating the Jacobian determinant from time to time. To do that, we assume to cover the deformable image with a suitable mesh. The central idea of the proposed method is to deform the template image in terms of the similarity metric, while controlling the deformation range according to the intrinsic topologies of the triangular mesh. That means for each pixel in image level there is a corresponding mesh node to control its motion. The crucial problem is to control mesh deformation perfectly.

Research about mesh deformation was done in computational fluid dynamics [21, 22]. The common applications in engineering include deformable aircraft, airfoil pneumatic elastic vibration, bionic flow, and so on. To satisfy the topology preservation transformation requirements, we adopt segment spring analogy dynamic mesh technology [23], which is initially used to deform a mesh around a pitching airfoil. Its basic idea is to replace each mesh edge by a spring. Thus the vertex motion will be controlled by all the springs connected to this vertex.

Suppose the mesh edge between two adjacent vertices, i and j , to be a line spring. Initially, the mesh is in static equilibrium state with the spring equilibrium length equals to the edge length. Given an external force along the spring, the spring length will change. According to Hook's Law, the force at vertex i will be

$$\mathbf{F}_{ij} = k_{ij} (\mathbf{u}_j - \mathbf{u}_i), \quad (8)$$

where k_{ij} is the spring stiffness between i and j and \mathbf{u}_j is the displacement of vertex j . Influenced by all the neighboring vertices, the composition of forces at vertex i is

$$\mathbf{F}_i = \sum_{j \in n_v} \mathbf{F}_{ij} = \sum_{j \in n_v} k_{ij} (\mathbf{u}_j - \mathbf{u}_i), \quad (9)$$

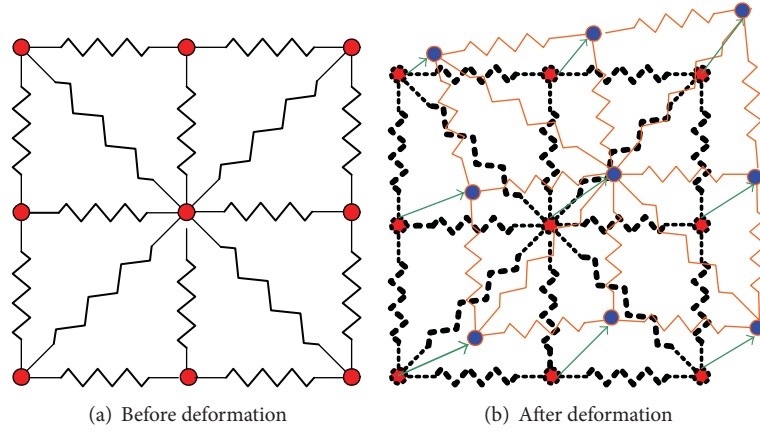


FIGURE 2: The interpretation of the spring analogy.

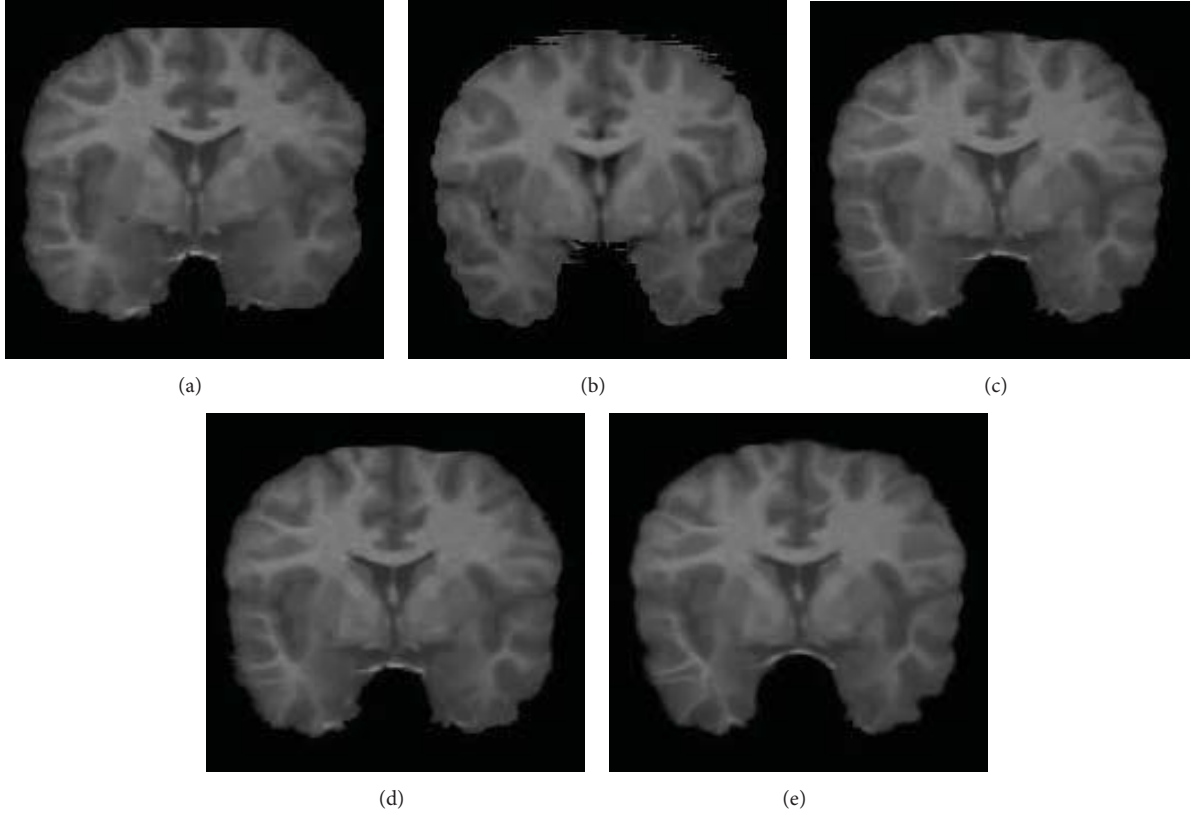


FIGURE 3: Brain MRI images registration results using NR-MDC algorithm. (a) Template image, (b) target image, (c) result without additional regularization, (d) result without updating the template image, and (e) result with 3 times updating the template image.

where n_v is the vertex set whose element connects to vertex i directly. For the mesh to be in equilibrium state again, the force at each vertex should be zero. That is

$$\sum_{j \in n_v} k_{ij} (\mathbf{u}_j - \mathbf{u}_i) = \mathbf{0}. \quad (10)$$

Regrouping (10) yields

$$\mathbf{u}_i = \frac{1}{\sum_{j \in n_v} k_{ij}} \sum_{j \in n_v} k_{ij} \mathbf{u}_j. \quad (11)$$

In an iterative style, (11) can be rewritten as

$$\mathbf{u}_i^{n+1} = \frac{1}{\sum_{j \in n_v} k_{ij}} \sum_{j \in n_v} k_{ij} \mathbf{u}_j^n, \quad (12)$$

where n denotes the iterative number. Then the new position of vertex i is

$$\mathbf{x}_i^{n+1} = \mathbf{x}_i^n + \mathbf{u}_i^{n+1}. \quad (13)$$

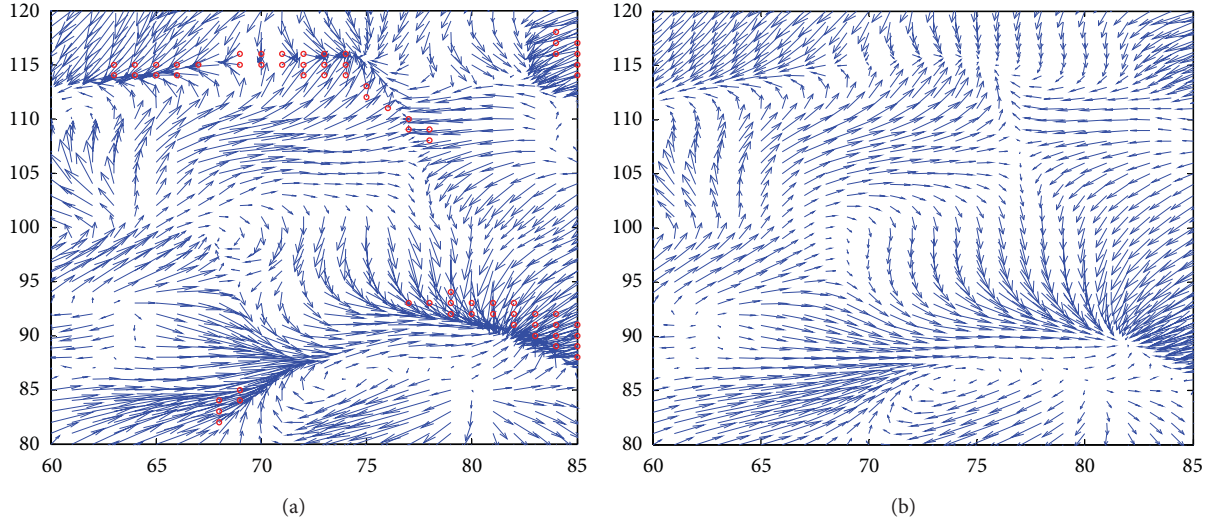


FIGURE 4: The deformation field using NR-MDC algorithm (a) without additional regularization and (b) with additional regularization.

The interpretation of the segment spring analogy deformation behavior is showed in Figure 2. The green arrow represents the vertex displacement vector from previous position (red dot) to next position (blue dot).

As can be seen from (12), the displacement vector of vertex i is calculated as a weighted result of the neighboring vertices' displacement. The weighting value is determined by the spring stiffness. There are different ways to choose the spring stiffness. For simplicity, the spring stiffness proposed by Batina [23] is used here, which is inversely proportional to the edge length. Consider,

$$k_{ij} = \frac{1}{|\mathbf{x}_j - \mathbf{x}_i|}. \quad (14)$$

As is analyzed in [24], this spring stiffness diminishes the probability of vertex collision during the mesh deformation. This means that the factors causing topological changes during deformation (fold, cross, and tear) will also be reduced.

Introducing segment spring analogy into nonrigid medical image registration as a regularization constraint, the expression can be written as

$$E_{\text{reg}} = \sum_{\mathbf{p} \in \Omega} \left| \sum_{j \in n_v} k_{ij} (\mathbf{u}_j - \mathbf{u}_i(\mathbf{p})) \right|, \quad (15)$$

where index i represents vertex i , whose position is \mathbf{p} .

Therefore the problem is described as

$$\mathbf{T}^* = \arg \min_{\mathbf{T} \in \Gamma} \sum_{\mathbf{p} \in \Omega} (B(\mathbf{p}) - A \circ \mathbf{T}(\mathbf{p}))^2 + \sum_{\mathbf{p} \in \Omega} \left| \sum_{j \in n_v} k_{ij} (\mathbf{u}_j - \mathbf{u}_i(\mathbf{p})) \right|, \quad (16)$$

$$\mathbf{T} = \mathbf{x} + \mathbf{u}. \quad (17)$$

2.3. Implementation. The registration energy function (16) is the sum of two measures. The first term is the sum of scalar, while the second term is the sum of vector. One can minimize this function with respect to \mathbf{u} simultaneously. However, it is not a trivial work. Fortunately, alternating minimization can be used to approximate the optimal solutions [7, 25]. First, the rough displacement field \mathbf{u} is found by minimizing the similarity metric term. Then the optimized displacement field $\tilde{\mathbf{u}}$ is found by minimizing the regularization term. This strategy enables the partial minimizations quite fast. In addition, to avoid falling into local minima and to reduce the computational cost, multiresolution framework is adopted. The image is downsampled into several different scales. The registration starts from the coarsest scale to the finest scale. Accordingly, the resulting deformation transfers from the coarsest scale to the finest scale by upsampling. Here the resampling factor is set to be 2, and the image dimensions of the coarsest scale should not be too small. The primary algorithm implementation procedure is summarized as follows.

Algorithm Implementation

- (1) Given the template image A and the target image B , perform preprocess procedure, which includes
 - (i) skull stripping using the BrainSuite software [26];
 - (ii) linear spatial normalization using FSL software [27];
 - (iii) intensity normalization using histogram match.
- (2) Decompose the images into different scales. For each position at the coarsest scale, set the initial displacement field $\mathbf{u}^n = 0$, $n = 0$:
 - (a) compute the transient displacement field \mathbf{u} using (7);

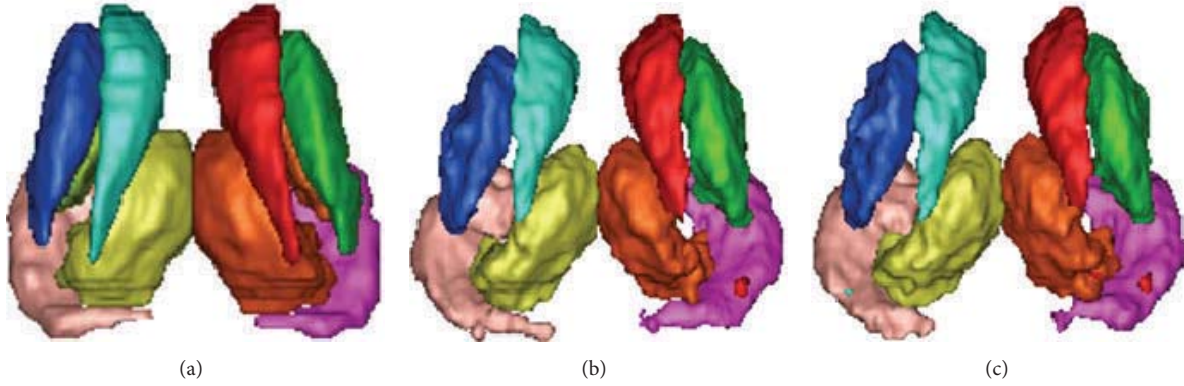


FIGURE 5: Typical 3D views for the segmented structures: (a) “ground truth” segmentation, (b) NR-MDC segmentation, and (c) DD segmentation.

TABLE 1: Comparison of the topology preservation ability between NR-MDC algorithm and DD algorithm.

Algorithm	Strategy	CC	N_j	Time (minutes)
NR-MDC	S1	0.971	0.5%	14.8
	S2	0.966	0%	15.3
	S3	0.984	0%	41.7
DD		0.972	0.03%	54.1
[20]		0.979	0%	84.6

- (b) get the rough displacement field $\mathbf{u}^{n+1} = \mathbf{u}^n + \mathbf{u}$;
 - (c) get the regularized displacement field $\tilde{\mathbf{u}}^{n+1}$ using (12);
 - (d) repeat step (a)–(c) until convergence;
 - (e) transfer to the next finer scale, and repeat step (a)–(d) until the finest scale is processed.
- (3) If there exists a negative Jacobian determinant value of the final deformation field, do 3–5 iterations using (12) to optimize the displacement field.
 - (4) If the similarity between the deformed template image and the target image does not reach the established criteria, update the template image using the obtained transformation and repeat steps (2)–(3).

3. Results

The proposed nonrigid registration approach is evaluated on real individual’s MRI images and compared with Diffeomorphic Demons algorithm (DD) [28]. The reference image used in the experiment is the one offered by the Surgical Planning Laboratory of Harvard Medical School [29]. It consists of $256 \times 256 \times 160$ voxels with a spatial resolution of $0.9375 \text{ mm} \times 0.9375 \text{ mm} \times 1.5 \text{ mm}$. The test images are real brain MRI images of fifteen normal subjects provided by the Center for Morphometric Analysis at Massachusetts General Hospital and available from Internet Brain Segmentation Repository (IBSR) [30].

3.1. Evaluation of the Topology Preservation Ability. During the registration, both a criterion based on the cross-correlation (noted as CC_t) and the iteration number constitute the iteration stopping criteria. If the cross-correlation between the deformed reference image and the target image equals or exceeds CC_t or the iteration number of reregistration using the deformed image as the new reference image reaches the upper limit (here it is three, while within a scale, the iteration number is set to be ten), the algorithm will stop. CC_t is defined as

$$CC_t = \frac{(1 - CC_0)}{\alpha} + CC_0, \quad (18)$$

where CC_0 is the initial cross-correlation between the reference image and the target image. The value of 1.2 is suitable for parameter α in the experiment.

Figures 3 and 4 show some typical registration results. Figure 3 gives a visual inspection of the registration result using NR-MDC algorithm. Obviously, the deformed template image with updating scheme (Figure 3(e)) is more similar to the target image (Figure 3(b)) than the other two results (Figures 3(c) and 3(d)). Figure 4 compares the local deformation field before and after regularization, where the red circles (Figure 4(a)) mark out the locations with negative Jacobian determinant. It can be seen that after several iterations, the regularized deformation field becomes realistic.

Table 1 compares the NR-MDC algorithm, Diffeomorphic Demons algorithm and method in [20]. In Table 1, the criterion CC (cross-correlation factor) depicts the similarity degree between the deformed template image and the target image. $CC = 1$ means the maximum similarity. The criterion N_j depicts the number of points with a negative Jacobian determinant of the deformation field when compared to the total point. S1 represents the registration result without additional regularization. S2 represents the registration result without updating the template image. S3 represents the registration result with regularization and updating steps. Since the vertex motion has high-freedom degree and each vertex is closely related to its surrounding vertices, immediate deformation regularization is inadequate. There still exists a small amount of points with changed topologies.

TABLE 2: Comparison of averaged KI value between our NR-MDC algorithm and DD algorithm.

	L-Caudate	R-Caudate	L-Putamen	R-Putamen	L-Thalamus	R-Thalamus	L-Hippocampus	R-Hippocampus
NR-MDC	0.728	0.778	0.749	0.755	0.746	0.779	0.729	0.691
DD	0.710	0.762	0.732	0.741	0.722	0.754	0.711	0.682

Thus in most cases, additional regularization is necessary. Fortunately, less iteration is required to achieve acceptable deformations. In addition, the need for template image updating and the updating number depend on both the initial difference between the template image and the target image after global linear registration and the expected similarity. Proper updating will improve the similarity. The DD algorithm is carried out in a multiresolution manner. The main parameters are three scales; regularization with a Gaussian convolution kernel, whose standard deviation is set to be one; the maximum template image updating number is three. It can be seen from Table 1 that the average CC value is 0.984 for NR-MDC algorithm using S3 strategy, and the deformation field is topologically preserved. While for the DD algorithm, the average CC value is about 0.97, and there are still a small amount of points with negative Jacobian determinants. Since an additional Jacobian determinant tracking procedure was carried out in the method of [20], the algorithm running time is relatively long.

3.2. Evaluation of the Brain Internal Structures Segmentation Ability. To further evaluate the reasonability of the obtained deformation field, the brain internal structures segmentation experiment is carried out. The segmented structures are left and right caudate (L-Caudate, R-Caudate), putamen (L-Putamen, R-Putamen), thalamus (L-Thalamus, R-Thalamus), and hippocampus (L-Hippocampus, R-Hippocampus). As is known, these brain subcortical structures have relatively small sizes, complex shapes. Moreover, there is only small spacing between different structures, while their intensities in MRI images are very similar. All these negative factors make the fully automatically accurate segmentation a challenging task.

To validate the results quantitatively, a kappa statistic-based similarity index, Dice coefficient, is adopted in this paper. The similarity index measures the overlap ratio between the segmented structure and the ground truth, which is defined as

$$KI = \frac{2 \times TP}{2 \times TP + FN + FP}. \quad (19)$$

The definitions of the parameters are as follows:

TP = $G \cap E$: the number of true positive;

FP = $\bar{G} \cap E$: the number of false positive;

FN = $G \cap \bar{E}$: the number of false negative;

where G is the ground truth segmentation of a given structure, E is the estimated segmentation of the same structure, and \bar{O} denotes the complement of a set O . Perfect spatial correspondence between the two segmentations will result in $KI = 1$, whereas no correspondence will result in $KI = 0$.

The results are presented in Table 2, where the KI values are the mean values of all the volumes. The results indicate that the proposed NR-MDC algorithm gives better segmentations than the DD algorithm.

Typical 3D views for the segmented structures are presented in Figure 5.

4. Conclusions

In this paper, a new nonrigid medical image registration method, named NR-MDC, is proposed. A new deformable source, a triangular mesh, is added to cover the template image. This mesh is independent of the image intensities. It reflects the points' intrinsic spatial relations and is used to regularize the basic deformation field computed from the image intensity information. The proposed cost function is optimized in an alternative minimization way. The deformation field is first computed by optimizing a SSD metric and then is regularized by using spring analogy method. This approach enforces a valid topology of the deformed mesh, which means a valid image deformation. To evaluate the performance of NR-MDC algorithm, intersubject brain MRI image registration experiments are done. And a comparative experiment is also done between the proposed method and the state-of-the-art DD algorithm. The results verify NR-MDC method's excellent deformation ability, as well as its good topology-preserving ability.

Acknowledgment

This work was supported by National Science Foundation of China (no. 61101230).

References

- [1] A. Gholipour, N. Kehtarnavaz, R. Briggs, M. Devous, and K. Gopinath, "Brain functional localization: a survey of image registration techniques," *IEEE Transactions on Medical Imaging*, vol. 26, no. 4, pp. 427–451, 2007.
- [2] M. Holden, "A review of geometric transformations for nonrigid body registration," *IEEE Transactions on Medical Imaging*, vol. 27, no. 1, pp. 111–128, 2008.
- [3] A. Klein, J. Andersson, B. A. Ardekani et al., "Evaluation of 14 nonlinear deformation algorithms applied to human brain MRI registration," *NeuroImage*, vol. 46, no. 3, pp. 786–802, 2009.
- [4] G. E. Christensen and H. J. Johnson, "Consistent image registration," *IEEE Transactions on Medical Imaging*, vol. 20, no. 7, pp. 568–582, 2001.
- [5] H. J. Johnson and G. E. Christensen, "Consistent landmark and intensity-based image registration," *IEEE Transactions on Medical Imaging*, vol. 21, no. 5, pp. 450–461, 2002.

- [6] D. Rueckert, L. I. Sonoda, C. Hayes, D. L. G. Hill, M. O. Leach, and D. J. Hawkes, "Nonrigid registration using free-form deformations: application to breast MR images," *IEEE Transactions on Medical Imaging*, vol. 18, no. 8, pp. 712–721, 1999.
- [7] J. P. Thirion, "Image matching as a diffusion process: an analogy with Maxwell's demons," *Medical Image Analysis*, vol. 2, no. 3, pp. 243–260, 1998.
- [8] T. Rohlfing Jr., C. R. Maurer, D. A. Bluemke, and M. A. Jacobs, "Volume-preserving nonrigid registration of MR breast images using free-form deformation with an incompressibility constraint," *IEEE Transactions on Medical Imaging*, vol. 22, no. 6, pp. 730–741, 2003.
- [9] P. Dupuis, U. Grenander, and M. I. Miller, "Variational problems on flows of diffeomorphisms for image matching," *Quarterly of Applied Mathematics*, vol. 56, no. 3, pp. 587–600, 1998.
- [10] J. Ashburner, "A fast diffeomorphic image registration algorithm," *NeuroImage*, vol. 38, no. 1, pp. 95–113, 2007.
- [11] T. Vercauteren, X. Pennec, A. Perchant, and N. Ayache, "Diffeomorphic demons: efficient non-parametric image registration," *NeuroImage*, vol. 45, no. 1, pp. S61–72, 2009.
- [12] M. I. Miller, A. Trounev, and L. Younes, "On the metrics and Euler-Lagrange equations of computational anatomy," *Annual Review of Biomedical Engineering*, vol. 4, pp. 375–405, 2002.
- [13] M. F. Beg, M. I. Miller, A. Trounev, and L. Younes, "Computing large deformation metric mappings via geodesic flows of diffeomorphisms," *International Journal of Computer Vision*, vol. 61, no. 2, pp. 139–157, 2005.
- [14] O. Musse, F. Heitz, and J. P. Armspach, "Topology preserving deformable image matching using constrained hierarchical parametric models," *IEEE Transactions on Image Processing*, vol. 10, no. 7, pp. 1081–1093, 2001.
- [15] V. Noblet, C. Heinrich, F. Heitz, and J. P. Armspach, "3-D deformable image registration: a topology preservation scheme based on hierarchical deformation models and interval analysis optimization," *IEEE Transactions on Image Processing*, vol. 14, no. 5, pp. 553–566, 2005.
- [16] B. Karaçalı and C. Davatzikos, "Estimating topology preserving and smooth displacement fields," *IEEE Transactions on Medical Imaging*, vol. 23, pp. 868–880, 2004.
- [17] M. Sdika, "A fast nonrigid image registration with constraints on the Jacobian using large scale constrained optimization," *IEEE transactions on medical imaging*, vol. 27, no. 2, pp. 271–281, 2008.
- [18] X. Pennec, P. Cachier, and N. Ayache, "Understanding the "Demon's algorithm": 3D non-rigid registration by gradient descent," in *2nd International Conference on Medical Image Computing and Computer-Assisted Intervention (MICCAI '99)*, pp. 19597–22605, Cambridge, UK, September 1999.
- [19] J. K. Aggarwal and N. Nandhakumar, "On the computation of motion from sequences of images—a review," *Proceedings of the IEEE*, vol. 76, no. 8, pp. 917–935, 1988.
- [20] X. Lin, T. Qiu, F. Morain-Nicolier, and S. Ruan, "A topology preserving non-rigid registration algorithm with integration shape knowledge to segment brain subcortical structures from MRI images," *Pattern Recognition*, vol. 43, no. 7, pp. 2418–2427, 2010.
- [21] D. R. Mcdaniel and S. A. Morton, "Efficient mesh deformation for computational stability and control analyses on unstructured viscous meshes," in *Proceedings of the 47th AIAA Aerospace Sciences Meeting including the New Horizons Forum and Aerospace Exposition*, AIAA Paper 2009-1363, Orlando, Fla, USA, January 2009.
- [22] X. Zhou, S. X. Li, S. L. Sun, J. F. Liu, and B. Chen, "Advances in the research on unstructured mesh deformation," *Advances in Mechanics*, vol. 41, pp. 547–561, 2011.
- [23] J. T. Batina, "Unsteady Euler airfoil solutions using unstructured dynamic meshes," *AIAA journal*, vol. 28, no. 8, pp. 1381–1388, 1990.
- [24] F. J. Blom, "Considerations on the spring analogy," *International Journal for Numerical Methods in Fluids*, vol. 32, pp. 647–668, 2000.
- [25] P. Cachier, E. Bardinnet, D. Dormont, X. Pennec, and N. Ayache, "Iconic feature based nonrigid registration: the PASHA algorithm," *Computer Vision and Image Understanding*, vol. 89, no. 2-3, pp. 272–298, 2003.
- [26] D. W. Shattuck and R. M. Leahy, "Brainsuite: an automated cortical surface identification tool," *Medical Image Analysis*, vol. 6, no. 2, pp. 129–142, 2002.
- [27] S. M. Smith, M. Jenkinson, M. W. Woolrich et al., "Advances in functional and structural MR image analysis and implementation as FSL," *NeuroImage*, vol. 23, no. 1, pp. S208–S219, 2004.
- [28] T. Vercauteren, X. Pennec, A. Perchant, and N. Ayache, "Diffeomorphic demons: efficient non-parametric image registration," *NeuroImage*, vol. 45, supplement 1, pp. S61–S72, 2009.
- [29] R. Kikinis, M. E. Shenton, D. V. Losifescu et al., "A digital brain atlas for surgical planning, model-driven segmentation, and teaching," *IEEE Transactions on Visualization and Computer Graphics*, vol. 2, no. 3, pp. 232–241, 1996.
- [30] "Internet brain segmentation repository," M. G. H. Technical Report, Center for Morphometric Analysis IBSR, 2000, <http://www.cma.mgh.harvard.edu/ibsr/>.

Research Article

A 3D Visualization Method for Bladder Filling Examination Based on EIT

Wei He, Peng Ran, Zheng Xu, Bing Li, and Song-nong Li

State Key Laboratory of Power Transmission Equipment & System Security and New Technology, Chongqing University, Chongqing 400030, China

Correspondence should be addressed to Peng Ran, p.ran@cqu.edu.cn

Received 20 September 2012; Revised 23 November 2012; Accepted 30 November 2012

Academic Editor: Peng Feng

Copyright © 2012 Wei He et al. This is an open access article distributed under the Creative Commons Attribution License, which permits unrestricted use, distribution, and reproduction in any medium, provided the original work is properly cited.

As the researches of electric impedance tomography (EIT) applications in medical examinations deepen, we attempt to produce the visualization of 3D images of human bladder. In this paper, a planar electrode array system will be introduced as the measuring platform and a series of feasible methods are proposed to evaluate the simulated volume of bladder to avoid overfilling. The combined regularization algorithm enhances the spatial resolution and presents distinguishable sketch of disturbances from the background, which provides us with reliable data from inverse problem to carry on to the three-dimensional reconstruction. By detecting the edge elements and tracking down the lost information, we extract quantitative morphological features of the object from the noises and background. Preliminary measurements were conducted and the results showed that the proposed algorithm overcomes the defects of holes, protrusions, and debris in reconstruction. In addition, the targets' location in space and roughly volume could be calculated according to the grid of finite element of the model, and this feature was never achievable for the previous 2D imaging.

1. Introduction

Bladder filling causes the desire to urinate when the bladder contains a certain volume of urine. But for unconsciousness elders, some handicapped with spinal cord injury or patients with urological disease, this sense will not occur. Urinary incontinence or lack of bladder control is an embarrassing problem, in case that many patients need professional nursing. And the work of nursing may be greatly reduced if the urination is detected and alarmed in time. In clinical, the traditional method to solve this problem is draining urine out by a catheter inserted in the bladder. But the intubation is invasive and not suitable for most patients, because it may cause secondary infection of the urinary tract. A way for measure in real time is the ultrasound imaging. Researchers have developed ultrasound bladder volume measurement devices to evaluate bladder volume. However, these devices are inconvenient for continuous monitoring, moreover, the ultrasonic images are greatly influenced by the human intraperitoneal gas [1, 2].

Several investigators over the last 20 years have verified that the electrical properties of human tissues and body fluids are significantly different and have demonstrated that measurement of these properties has obvious clinical potential [3]. Electric impedance tomography distills biomedicine information without trauma and generates real-time image, which examination is not necessary straight line to avoid the intra-peritoneal gas affection. Consequently, this technology is applied to measure and visualize impedance changes in bladder.

As we know, the filling bladder is located just a little beneath the lower abdomen. On account of different physiological and structural characteristics of patient's abdomen, traditional closed EIT system is difficult to meet in different shape and location of focus detection [4]. Therefore, we chose planar array EIT system due to its convenience in operation [5]. In order to solve the problem of lack in effective precondition in the past researches of 3D volume estimation, we propose a system of 64 electrodes rectangular array with adaptable combination mode of injection and

measurement [6]. This system has features of adjustable multifrequency, high accuracy, and being portable and flexible in application, which is quite suitable for long-term clinical monitoring via appropriate upgrade.

Another reason that restricts the 3D EIT development is the lacking of proper algorithms. The previous algorithms applied in EIT included Filtered Back-projection [7], Spectral Expansion method [8], Newton's one-step error reconstruction [9], Genetic Algorithms [10], and Weighted Minimum Norm method [11], most of which are confronted with the severely ill-posed problem and the great amount of calculation. Through the analysis of the respective advantage and disadvantage of Tikhonov [12] and NOSER regularizations [9], we developed the combined regularization algorithm of expectable spatial resolution for 3D EIT, which ensures more uniform impedance estimation and deeper investigation depth.

Since the boundary of the targets or structures are usually contained in the cell of the three-dimensional image, the detection and reconstruction of the edge surfaces from the reconstructed electrical impedance are among the important research issues in three-dimensional image analysis [13]. The isosurface is a common approximation of the boundary surface within biomedical images. However, a fixed values isosurface is not suitable in approximating the boundary surface in EIT inverse problems due to large errors of the results [14]. To adapt the local difference of the complex boundary surface, we have improved the work of the literatures [15]. The formation of new method, by which, constructs the adaptively approximating to the boundary surface of the targets with different surface patches in different local regions. Consequently, the approximation accuracy has been considerably improved.

2. Materials and Methods

2.1. System Description. On account of different physiological and structural characteristics of patient's waist, the open EIT system in Figure 1(a), by simply placing the measuring probe onto the targets, could make the measurement and avoid the trouble of routine electrode pasting. The measuring probe is an 8×8 electrode array with a back electrode as the signal ground is placed on the patient's back to make the current evenly distributed into the body for deeper detection. The measurement and reconstruction field are the area between the electrode array and the back electrode.

As in examination, a sinusoidal current is injected from the 64 electrodes in turn and outflows from the back electrode in Figure 1(b). The measurements are taken from the rest 63 electrodes. In each examination, we will obtain $64 \times 63 = 4032$ independent measurements from excitation, which greatly increased the amount of available data comparing with most current reported methods, as the 32 electrodes are in round for chest examination (maximum $32 * 31 = 992$ measurements) [16] and the fixed voltage source with $16 * 16$ measuring points for breast cancer detection [17].

This system has features of constant current source, good antijamming capability, low output impedance, and deep

detection area, which is supplied by medical power and communicates with notebook via USB as in Figure 1(c). While used for long-term monitoring, the device can be replaced with lithium battery powered, Bluetooth communication and belt-contact electrode array, which enables the application for inpatients or even patients at home.

2.2. EIT Inverse Problems. The inverse problem is the process of calculating the internal conductivity distribution based on the boundary voltage. EIT image reconstruction is a nonlinear ill-posed problem, and it is only to deduce the impedances in the measurement filed by approximation. In principle, small enough perturbations in conductivity can be reconstructed accurately enough by considering just the linear problem. In EIT, starting from a known and usually homogeneous distribution x_p , a set of measurement V_p is gathered. In sequence, a perturbation δx occurs causing a new $x \neq x_p$ and consequently a $V \neq V_p$. Calculating the Jacobian matrix (J) in which a computing method is introduced in [18] based on x_p , the discrete form of the linear forward problem used in difference imaging becomes

$$J\delta x = \delta V \Leftrightarrow J(x_p - x) = V_p - V. \quad (1)$$

In (1) only V is physically collected from the boundary of the volume as V_p is obtained by forward calculations:

$$J(x_p - x) = F(x_p) - V, \quad (2)$$

in which $F(x_p)$ denotes the vector of simulated measurements derived from forward computations based on a model x_p .

The Least squares method (LS) could be used to solve (2):

$$\min_{x_p-x} \|J(x_p - x) - [F(x_p) - V]\|_2. \quad (3)$$

For the linear least squares problem, the Jacobian matrix J is very ill-conditioned and singular. This problem is remedied by regularizing the matrix J and solving a new problem that is well conditioned. A general version of Tikhonov regularization method is used:

$$\min \left\{ \|J(x_p - x) - [F(x_p) - V]\|_2^2 + \lambda \|L(x_p - x)\|_2^2 \right\}, \quad (4)$$

where λ is Tikhonov regularization parameter, and L is a matrix that defines a norm on the solution through which the "size" is measured. Often, L represents the first or second derivative operator. If L is the identity matrix, then the Tikhonov problem is said to be in standard form. So we can get the solution from (2)~(4):

$$\delta x = x_p - x = (J^T J + \lambda I)^{-1} J^T \times [F(x_p) - V]. \quad (5)$$

It has the effect of damping any large oscillations. A scaled identity matrix adding to the Jacobian matrix J makes the solution stable. But the condition number which indicates the sensitivity of the uncertainty is still large and the

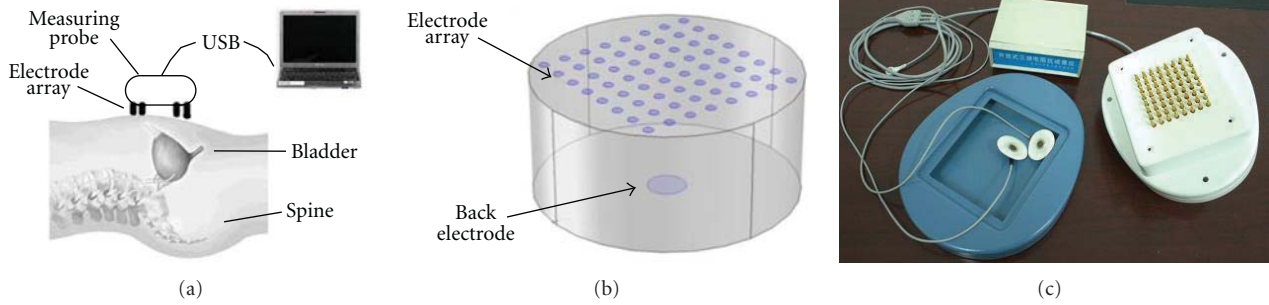


FIGURE 1: (a) System measurement, (b) Electrodes arrangement, and (c) Experimental Prototype.

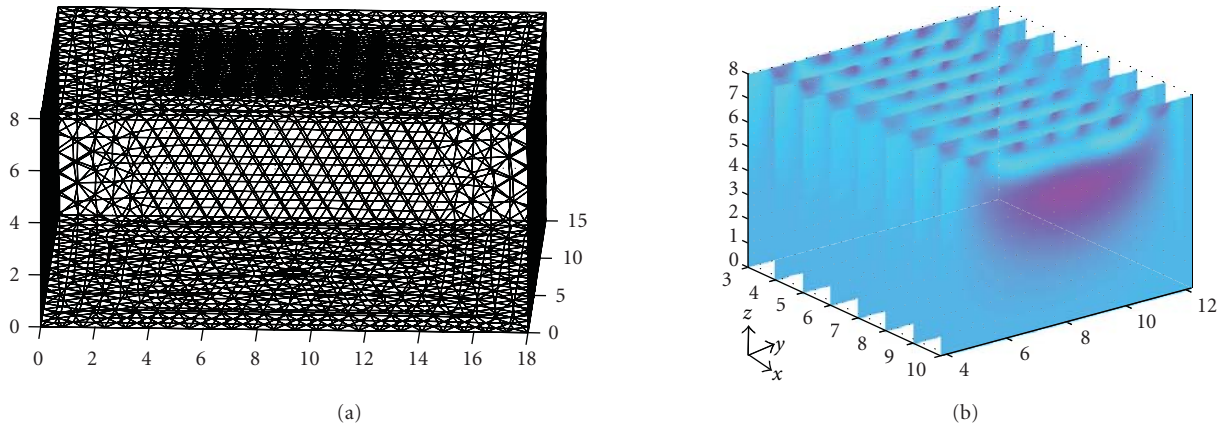


FIGURE 2: (a) Tetrahedral finite elements, (b) Electrical impedance slices by solving the inverse problem.

solution has the side effect of the smoothing caused by that identity matrix [9].

To reduce the condition number and side effect, we combined Tikhonov regularization with NOSER type regularization. In NOSER regularization, the regularization matrix is a simple diagonal weighting for $J^T J$ corresponding to the first and second difference operators. The equation is

$$\delta x = (J^T J + \varepsilon \times \text{diag}(J^T J))^{-1} J^T \times [F(x_p) - V], \quad (6)$$

where $0 < \varepsilon < 1$ is the NOSER regularization parameter and $\text{diag}(J^T J)$ denotes the diagonal matrix and also represents an approximation for the missing part of the second derivative of the mapping [19].

NOSER regularization works well in 2D field, but cannot correct the error caused by the noise in 3D model which is a very ill-posed problem. Tikhonov regularization could correct the error caused by weak noises and also has the side effect of the smoothing caused by that identity. If these two methods are combined, the condition number would be reduced (in Table 1), consequently, a better image will be obtained. The equation with combined regularization method can be written as

$$\delta x = (J^T J + \lambda I + \varepsilon \times \text{diag}(J^T J))^{-1} J^T \times [F(x_p) - V]. \quad (7)$$

As comparison and experiments between reconstructed results of different algorithms, including parameters choosing and discussions, have been made in previous work [20],

the combined regularization was proved to be effective in eliminating errors and demonstrate better spatial resolution such as target's location and size.

2.3. Finite Element Mesh and Impedance Calculation. To calculate the discrete impedance within three-dimensional space, we first have to conduct tetrahedral finite element meshing in the whole measurement space as in Figure 2(a). As in the followed experiment, for example, the cuboid phantom was meshed into 79 307 finite elements with 14 876 nodes in space. Then, the Jacobian matrix could be obtained via complete electrode model by calculating the voltage of each node with analytical method [21]. The combined regularization matrix could be then deduced from Jacobian by choosing the proper parameters λ and ε . Finally, spatial distribution of the electrical impedance in the model could be approximated from the boundary conditions which were the voltage measurements from the electrodes. Although the accuracy of discrete impedance calculated from the combined regularization had been improved and large, there was still disturbance around the electrodes, as we could see from Figure 2(b). Another problem was that the electrical impedance changes gradually, in case that we were not able to draw the actual boundary of the anomaly buried in the background. Therefore, we had to develop a feasible and reliable way to eliminate the noise, sketch out the boundary

TABLE 1: Typical condition number of Jacobian matrix and regularization algorithms.

	Jacobian matrix	Tikhonov regularization	NOSER regularization	Combined regularization
Condition number	1.536×10^{16}	1.109×10^{11}	3.854×10^9	9.294×10^8

of objects, and reconstruct images with boundary surface detection in 3D field.

2.4. Boundary Detection. In many cases, the gray-level-based decent isosurface of boundary surfaces can well separate voxels belonging to an object from voxels belonging to the background and therefore can be applied in the segmentation of 3D images [22]. However, the impedance approximations obtained from inverse problems are usually of high level noises which are not applicable for direct isosurface calculation. As the boundaries of the target object are usually across intensity values which have great differences from the background, they are actually steplike edge surfaces, defined as surface where great change of intensity value occurs. A volumetric image can be considered as the discrete sampling of the underlying three-dimensional continuous function at the grid points of the three-dimensional regular grid.

The boundary surface within the volumetric image can be considered as the implicitly defined continuous surface contained in the continuous sampling region of the volumetric image. Recall that, in a volumetric image, different structures usually correspond to different image intensities. Thus, the impedance intensities on either side of the boundary surface of the structure within a volumetric image have sharp changes. Such a boundary surface belongs to a steplike edge surface and therefore it is a continuous zero-crossing surface with a high gradient value. Mathematically, the boundaries within 3D image could be presented as follows [23]:

$$\begin{aligned} \nabla^2 f(x, y, z) &= 0, \\ \|\nabla f(x, y, z)\| &\geq T, \end{aligned} \quad (8)$$

where T is a predetermined gradient threshold, $\nabla^2 f(x, y, z)$ represents the Laplacian function of $f(x, y, z)$, and $\|\nabla f(x, y, z)\|$ represents the gradient magnitude function of $f(x, y, z)$. T can be selected by other methods that are used to select the gradient threshold in the edge detection of a 2D image [24].

Since the boundary surface of the volumetric image is determined, the subsequent processing can be performed to reduce the noises and improve the reconstruction quality, which will be further elaborated in the following sections.

2.5. Edge Elements Detection. The electrical impedance is sampled from tetrahedron grid as described above, and all such tetrahedrons form a continuous space occupied by 3D image. Steplike edge surfaces in the volume pass through, or are included in, some tetrahedrons. All tetrahedron elements are divided into two categories: those that are passed through by a steplike edge and the rest which are not. We first detect the edge elements and then compute the steplike edges in each edge element. For each edge element, since steplike edge

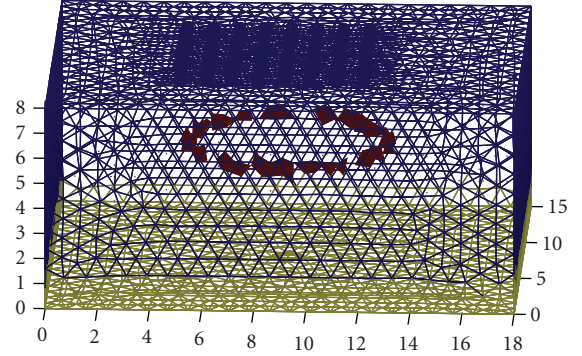


FIGURE 3: Extracted edge elements from tetrahedron slice.

passes through it, at least three of its edges are intersected by steplike edges. Without loss of generality, we assume that the edge linking vertexes of one tetrahedron are $P_1(i, j, k)$ and $P_2(i-1, j, k)$. In terms of the literature [23], if the one side of the tetrahedron intersects with the edge surfaces, the two endpoints in the side of the section, respectively, having a high value of the gradient, and their Laplacian values, are of different signs.

In the edge elements, each edge intersected has the following characterizations:

- (1) both vertices have high gradient values: $\|\nabla f(P_1)\| + \|\nabla f(P_2)\| \geq 2T$,
- (2) two vertices are a pair of zero-crossing points: $\|\nabla^2 f(P_1)\| \cdot \|\nabla^2 f(P_2)\| < 0$.

Accordingly, by tagging the edge surfaces intersection as well as determining whether three edges of the tetrahedron are intersected by the edge surfaces, we will find out the edge elements and locate the edge surface from the three-dimensional images.

2.6. Extraction and Reconstruction. Among the detected edge elements, there are true elements which contain the edge surfaces, besides pseudo-edge elements which caused by the noise and object details. The pseudo-edge elements, usually just a small collection of interlinked tetrahedron, and the tetrahedrons which include the edge surfaces, are typically a relatively large collection according to the characteristics in bladder filling process. Therefore, judging by whether the edge elements are coplanar, we can extract the larger connected set by removing the small ones.

All the tetrahedron elements in the model are divided into slices in horizontal, each slice contains incomplete seed elements representing the edge surfaces (in Figure 3), from which the edge surface of the object can be tracked. If the edge surface intersects with one face of an edge element, the adjacent tetrahedron of mutual face of that one is inevitable

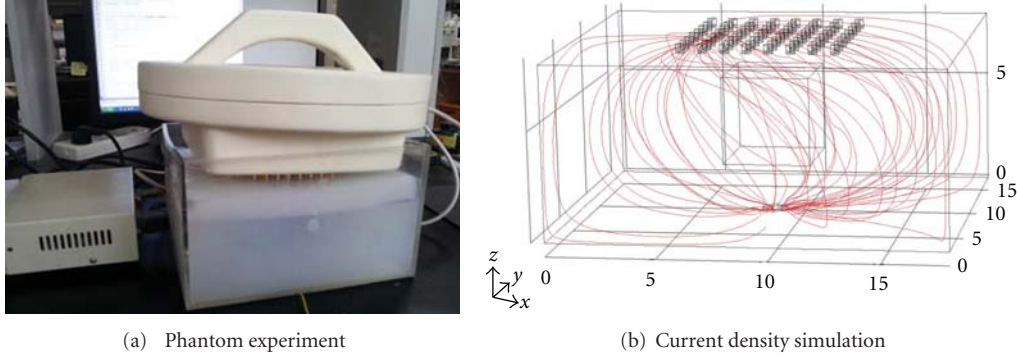


FIGURE 4

an edge element as well. This definition originated in the region growing method, the algorithm using 3D region growing method [25]. By checking the adjacent elements which meet the coplanar criteria, the seed grows in the original area, until the target area does not grow any longer. In virtue of this property, we can track and recombine the most similar edge elements to the objects, by which are not detected yet, starting from the determined seed elements.

Each edge element contains a piece of edge surface which is in fact the isosurface of zero value of the Laplacian function in three-dimensional image. By computing the zero-crossing surface of the Laplacian in each edge element, eventually, a triangulated model of steplike edges is obtained. From each edge element, the surface patch could be extracted by using the Marching Cubes and its improved algorithm as the polygonal approximation. This algorithm guarantees that the surface patches extracted from the adjacent edge elements can be spliced together and constitute a polygonal surface model [26].

3. Results and Discussion

3.1. Experiment Platform. The process of imaging reconstruction was illustrated and verified by applying the algorithm on a dataset obtained from an experimental feasibility trial. The cuboid phantom was made of polycarbonate, with 18 cm long, 15 cm wide and 10 cm high as in Figure 4(a). The 8×8 electrodes array, of each electrode diameter 4 mm and gap of 8 mm between each, was placed on the upper surface and the back electrode as the ground was placed on the center of lower surface. The current density simulation model was represented in Figure 4(b), and from which we could configure that the current density in the middle area below the electrode array was larger which indicated higher sensitivity.

The experiment was carried out by using agar of 0.1 S/m (at 200 kHz) as the background with a different size of cuboid hole in the middle of background as the inclusion (detailed in Section 3.2). The hole was filled with saline solution dropped of India ink, which conductivity measures as 0.892 S/m by the Mettler-Toledo hand-held portable liquid conductivity measurement instrument SG7, then it was covered with 1.5 cm thick of 0.1 S/m agar same as the background. So the

saline solution was wrapped in agar to simulate the urine in the bladder.

As the conductivity of saline varies with the frequency, a relatively sharp change in order to distinguish it from the agar happens at the frequency around 200 kHz [27]. Furthermore, there is also a strict regulation to limit the injection current into the body, which is less than 10 mA of frequency at 100 kHz or higher frequency [28]. Accordingly, we set the current waveform frequency 200 kHz with the amplitude of 10 mA. The injection-and-measurement strategy was that of Section 2.1 described.

3.2. Preliminary Data Analysis. A completely full bladder of human is capable of holding approximately 1 liter of fluid. However, the urge to urinate ordinarily occurs when the bladder contains about 200 mL of urine, which value should be smaller considering of the age and body figure [29]. So we chose different volume of saline solution to simulate the urine in the experiment, as in Figures 5(a)–5(d) in red. They were, respectively, 0 mL in Figure 5(a), $4 \text{ cm} \times 4 \text{ cm} \times 4 \text{ cm}$ that was 64 mL in Figure 5(b), $5 \text{ cm} \times 5 \text{ cm} \times 5 \text{ cm}$ that was 125 mL in Figure 5(c), and $8 \text{ cm} \times 8 \text{ cm} \times 5 \text{ cm}$ that was 320 mL in Figure 5(d). As long as these volumes are able to be estimated, we are able to predict the right moment to micturate or whether the volume reaches the critical value.

Figures 5(e)–5(h) illustrate the 2D image projection from direct acquisition data without any algorithm applied. That means the color of image reflects the voltage which corresponds to the impedance from the measurement electrodes. We can figure out that the results are with perturbations at the corners due to the edge effect of container in Figures 5(e) and 5(f). As the volume increases in Figures 5(g) and 5(h), the blue area indicating the lower impedance increases, but obviously, the shapes are irregular without any depth information. As a result, it is ambiguous for diagnose which inspirit us to improve the results by utilizing more optimized methods and algorithms.

3.3. Three-Dimensional Reconstruction and Discussion. The 3D representations of the reconstructed perturbation from the experiments were shown above. Figure 6(a) was the reconstructed image from $4 \text{ cm} \times 4 \text{ cm} \times 4 \text{ cm}$ saline solution, Figures 6(b) and 6(c) are the corresponding lateral and

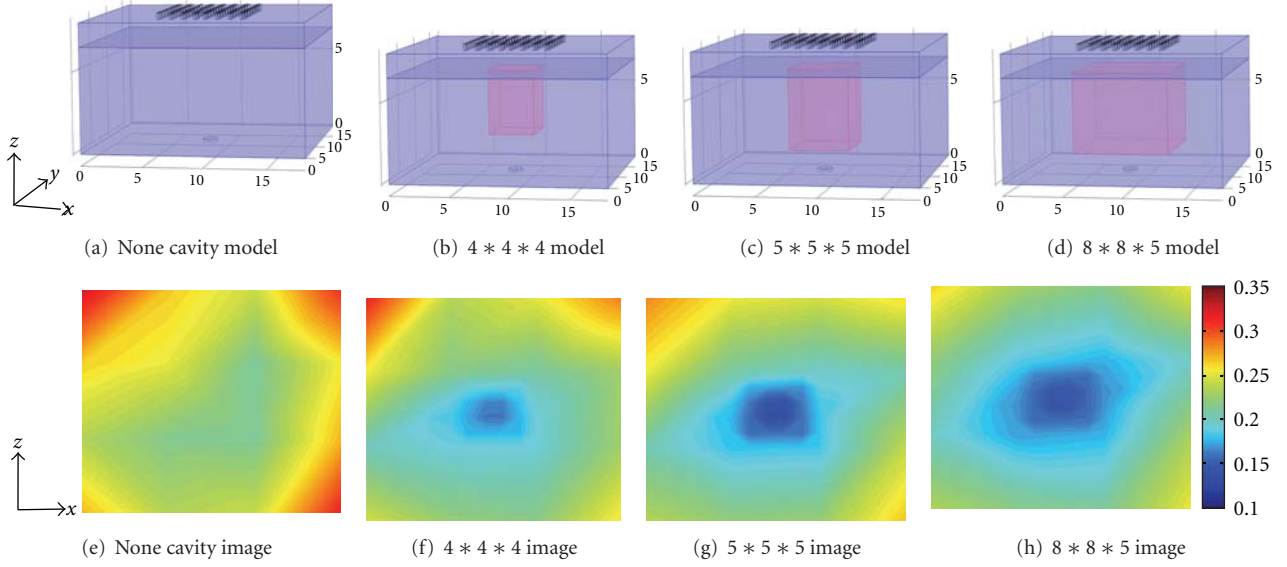


FIGURE 5: Experiment models and the corresponding 2D images.

top views. From those of which we could figure out that the reconstructed target's location was basically identical, whereas the shape of target transferred from cubic to round-like. It was by reason of the regularization-based algorithms applied the least squares method, which is different from back-projection [7] and genetic algorithms [10], and approached the perturbation generally, in case that the sharp changes were smoothed and some object details were as well omitted. Reconstructions from other two volumes in Figures 6(d)–6(i) reflected the similar characteristic. In addition, we could point out that while the volume increased, the distortion was getting more serious, because of the sensor array was getting comparatively smaller in contrast of the volume. As a result, the sensitivity of the algorithm decreased and the image deteriorated because of incomprehensive boundary conditions.

To estimate the object volume precisely, the tank model was gridded by the interval of 1 mm in x, y, z coordinates. We could judge the entire space being divided into $180 \times 150 \times 80 = 2,160,000$ cubes. Each cube volume of 1×10^{-3} mL, and each node from the cubes could be surrounded in the edge surface or not. Here, we defined the cube which has at least 4 noncoplanar vertices in the edge surface considered to be a valid one. As in our experiment, the number of included cubes in Figure 6(a) was 62,783, the number of Figure 6(d) was 115,429, and Figure 6(g) was 307,725. The corresponding estimated volumes were approximately 62.8 mL, 115.4 mL and 308.7 mL. Comparing with the origin volume with estimation, Figure 7(a) reveals that the estimation of model 4*4*4 is almost identical to that of actual volume, even though their shapes are inconsistent. Whereas the 5*5*5 and 8*8*5 models' estimation are lower than that of real ones, the volumetric errors are less than 10% which was still at acceptable level.

The position of an anomaly is defined to be located as the centre of mass of HA set in reconstruction images as

$$\text{position} = \frac{\sum_m \sigma_m \cdot p_m}{\sum_m \sigma_m}. \quad (9)$$

Here, p_m is the position vector (x_m, y_m, z_m) within the domain. Position error is a figure of merit defined as the proportional difference in position of the centre of mass of the reconstructed image HA set and the centre of mass of the generating anomaly. The smaller PE indicating the reconstructed image is more approximate to the center of the target object.

As we consider the conductivity of saline solution to be homogeneous, the centre of origin should be at the center of the cuboids. In terms of position error in Figure 7(b), the configurations show that relative position errors are various at different axes. Although the result indicates nonlinearity in different models, the error percentages are generally between $-8\% \sim 8\%$. We could also figure out that, the errors on z -axis in green is comparatively greater than that of x - and y -axis which exceed of 10%. It is because of the higher sensitivity as the object closer to the electrode array, this is resulting from both the current density distribution and the finite elements at the top are smaller than the bottom in our algorithm. Moreover, we realize that, as the size of target increase especially for the model 8*8*5, the target is getting closer to the edge of the electrode array, namely, the position errors increase.

By utilizing the combined regularization algorithm and integrating with edge elements filtering and rearrangement, 3D images were able to display for qualitative image evaluation. The differences between the objectives and background from reconstructions were significant. By and large, the target's locations were easy to be distinguished, nevertheless the reconstructed object did not directly correspond with the

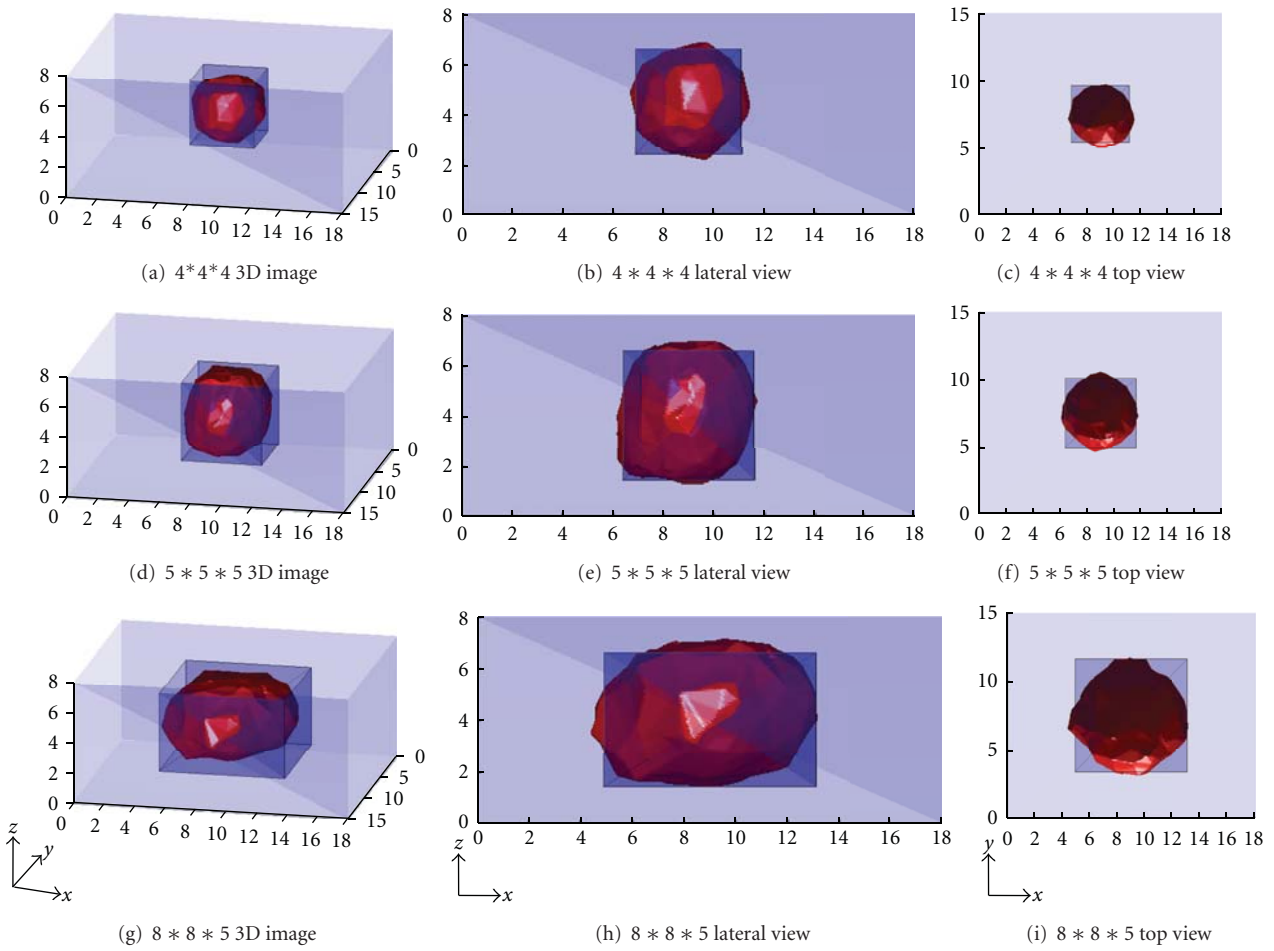


FIGURE 6: 3D reconstructions from different volumes of saline solution.

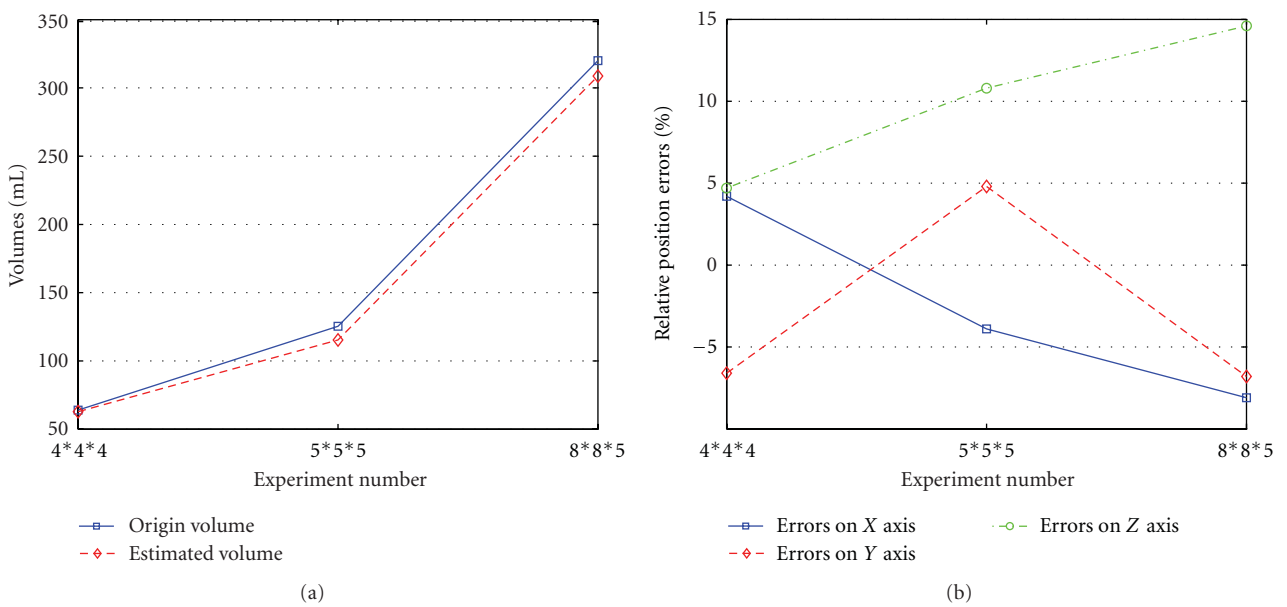


FIGURE 7: (a) Volume comparison of models and (b) Relative position errors.

exact shape of the original. This experiment demonstrated that it was possible to obtain and localize reliable 3D images of conductivity changes, employing 65 channels, the result presented to be superior to that of traditional methods and of considerably highly approximation to the target.

4. Conclusions

This paper addresses the issue of presenting a method for EIT 3D reconstruction and targets identification, by which aim to predict the urine volume in bladder. The performance of the proposed algorithms has been investigated and demonstrated by mathematical exposition. The approximation problem of boundary surface within 3D images is also described, it is applied not only to reduce the system noise which leads to holes, protrusions, and debris in reconstruction, but also deliver us readily to identify and calculate visual images. The reconstruction images provide more information as well, including depth and volume, and contrast from the background.

Overall, EIT image reconstruction is a nonlinear and ill-posed inverse problem of spatially variant estimation. Uncertainties caused by these properties prevent EIT images from having high resolution. These preliminary results indicate that sufficient finite element modeling of the impedance distribution in the abdomen, proper inverse problem, and tracking algorithms choosing enable this technology to be applicable for routine measurement of bladder volume.

This approach is convenient to apply with image reconstructions that are spatially variant, which promises to deliver a joint distribution and material identification and estimates in a single measurement process. It yields an alternative method for reporting the bladder filling so that instead of reporting in terms of pressure and ultrasound images, we may be able to present clinicians medical visualization and extract certain boundary surface structure.

Acknowledgment

This work was supported by the Fundamental Research Funds for the Central Universities of China (no. CDJZR 10150021).

References

- [1] E. J. W. Merks, N. Born, N. N. De Jong, and A. F. W. Steen, "Quantitative bladder volume assessment on the basis of nonlinear wave propagation," in *proceedings of the IEEE International Ultrasonics Symposium (IUS '08)*, pp. 1158–1162, November 2008.
- [2] R. Tanaka and T. Abe, "Measurement of the bladder volume with a limited number of ultrasonic transducers," in *Proceedings of the IEEE International Ultrasonics Symposium (ISU '10)*, pp. 1783–1786, 2010.
- [3] R. H. Smallwood, A. Keshtkar, B. A. Wilkinson, J. A. Lee, and F. C. Hamdy, "Electrical impedance spectroscopy (EIS) in the urinary bladder: the effect of inflammation and edema on identification of malignancy," *IEEE Transactions on Medical Imaging*, vol. 21, no. 6, pp. 708–710, 2002.
- [4] D. Holder, "Electrical tomography for industrial applications electrical impedance tomography: methods, history and applications," *Medical Physics and Biomedical Engineering*, pp. 295–347, 2004.
- [5] X. J. Zhang, M. Y. Chen, W. He, and C. H. He, "Modeling and simulation of open electrical impedance tomography," *International Journal of Applied Electromagnetics and Mechanics*, vol. 33, no. 1-2, pp. 713–720, 2010.
- [6] D. R. Stephenson, R. Mann, and T. A. York, "The sensitivity of reconstructed images and process engineering metrics to key choices in practical electrical impedance tomography," *Measurement Science and Technology*, vol. 19, no. 9, Article ID 094013, 2008.
- [7] M. Wang, J. Zhao, S. Zhang, and G. Wang, "Electrical impedance tomography based on filter back projection improved by means method," in *Proceedings of the 3rd International Conference on BioMedical Engineering and Informatics (BMEI '10)*, pp. 218–221, October 2010.
- [8] S. Meeson, A. L. T. Killingback, and B. H. Blott, "The dependence of EIT images on the assumed initial conductivity distribution: a study of pelvic imaging," *Physics in Medicine and Biology*, vol. 40, no. 4, pp. 643–657, 1995.
- [9] M. Cheney, D. Isaacson, J. C. Newell, S. Simske, and J. C. Goble, "NOSER: an algorithm for solving the inverse conductivity problem," *Image Systems & Technology*, vol. 2, pp. 66–75, 1990.
- [10] R. Olmi, M. Bini, and S. Priori, "A genetic algorithm approach to image reconstruction in electrical impedance tomography," *IEEE Transactions on Evolutionary Computation*, vol. 4, no. 1, pp. 83–88, 2000.
- [11] M. T. Clay and T. C. Ferree, "Weighted regularization in electrical impedance tomography with applications to acute cerebral stroke," *IEEE Transactions on Medical Imaging*, vol. 21, no. 6, pp. 629–638, 2002.
- [12] P. Jiang, L. Peng, and D. Xiao, "Tikhonov regularization based on second order derivative matrix for electrical capacitance tomography image reconstruction," *Journal of Chemical Industry and Engineering*, vol. 59, no. 2, pp. 405–409, 2008.
- [13] J. S. Suri, K. Liu, S. Singh et al., "Shape recovery algorithms using level sets in 2DP 3D medical imagery : a state of the art review," *IEEE Transactions on Information Technology in Biomedicine*, vol. 6, no. 1, pp. 8–28, 2002.
- [14] C. Pudney, M. Robins, B. Robbins, and P. Kovsi, "Surface detection in 3D confocal microscope images via local energy and ridge tracing," *Journal of Computer-Assisted Microscopy*, vol. 8, no. 1, pp. 5–20, 1996.
- [15] M. Brejl and M. Sonka, "Directional 3D edge detection in anisotropic data: detector design and performance assessment," *Computer Vision and Image Understanding*, vol. 77, no. 2, pp. 84–110, 2000.
- [16] J. Solà, A. Adler, A. Santos, G. Tusman, F. S. Sipmann, and S. H. Bohm, "Non-invasive monitoring of central blood pressure by electrical impedance tomography: first experimental evidence," *Medical and Biological Engineering and Computing*, vol. 49, no. 4, pp. 409–415, 2011.
- [17] A. Michel, L. M. Oras et al., "The T-SCANTM technology: electrical impedance as a diagnostic tool for breast cancer detection," *Physiological Measurement*, vol. 22, no. 1, pp. 1–8, 2001.
- [18] N. Polydorides, *Image Reconstruction Algorithms for Soft-Field Tomography*, University of Manchester Institute of Science and Technology, 2002.
- [19] J. L. Mueller, D. Isaacson, and J. C. Newell, "A reconstruction algorithm for electrical impedance tomography data collected

- on rectangular electrode arrays," *IEEE Transactions on Biomedical Engineering*, vol. 46, no. 11, pp. 1379–1386, 1999.
- [20] W. He, B. Li, Z. Xu, H. Luo, and P. Ran, "A combined regularization algorithm for electrical impedance tomography system using rectangular electrodes array," *Biomedical Engineering*, vol. 24, no. 4, pp. 313–322, 2012.
- [21] E. Somersalo, M. Cheney, and D. Isaacson, "Existence and uniqueness for electrode models for electric current computed tomography," *SIAM Journal on Applied Mathematics*, vol. 52, no. 4, pp. 1023–1040, 1992.
- [22] J. O. Lachaud and A. Montanvert, "Continuous analogs of digital boundaries: a topological approach to iso-surfaces," *Graphical Models*, vol. 62, no. 3, pp. 129–164, 2000.
- [23] A. H. Pheng, L. Wang, T. W. Tien, S. L. Kwong, and J. C. Y. Cheng, "Edge surfaces extraction from 3D images," in *The International Society for Optical Engineering*, vol. 4322 of *Proceedings of SPIE*, no. 1, pp. 407–416, 2001.
- [24] A. Rosenfeld and A. Kak, *Digital Picture Processing*, vol. 1, Academic Press, 1982.
- [25] D. Stroppiana, G. Bordogna, P. Carrara, M. Boschetti, L. Boschetti, and P. A. Brivio, "A method for extracting burned areas from Landsat TM/ETM+ images by soft aggregation of multiple spectral indices and a region growing algorithm," *ISPRS Journal of Photogrammetry and Remote Sensing*, vol. 69, pp. 88–102, 2012.
- [26] G. M. Nielson, L. Y. Zhang, K. Lee, and A. Huang, "Spherical parameterization of marching cubes isosurfaces based upon nearest neighbor coordinates," *Journal of Computer Science and Technology*, vol. 24, no. 1, pp. 30–38, 2009.
- [27] S. Gabriel, R. W. Lau, and C. Gabriel, "The dielectric properties of biological tissues: II. Measurements in the frequency range 10 Hz to 20 GHz," *Physics in Medicine and Biology*, vol. 41, no. 11, pp. 2251–2269, 1996.
- [28] "For limiting exposure to time varying electric, magnetic and electromagnetic fields (up to 300 GHz)," *Health Physics*, vol. 74, no. 4, pp. 494–522, 1998.
- [29] *Magill's Medical Guide*, vol. 3, Salem, Englewood Cliffs, NJ, USA, 1998.

Research Article

Two-Dimensional Matrix Algorithm Using Detrended Fluctuation Analysis to Distinguish Burkitt and Diffuse Large B-Cell Lymphoma

Rong-Guan Yeh,¹ Chung-Wu Lin,² Maysam F. Abbod,³ and Jiann-Shing Shieh^{1,4}

¹ Department of Mechanical Engineering, Yuan Ze University, 135 Yuan-Tung Road, Chungli 32003, Taiwan

² Department of Pathology, National Taiwan University Hospital, Taipei 100, Taiwan

³ School of Engineering and Design, Brunel University, London UB8 3PH, UK

⁴ Center for Dynamical Biomarkers and Translational Medicine, National Central University, Chungli 32001, Taiwan

Correspondence should be addressed to Jiann-Shing Shieh, jsshieh@saturn.yzu.edu.tw

Received 19 September 2012; Accepted 19 November 2012

Academic Editor: Wenxiang Cong

Copyright © 2012 Rong-Guan Yeh et al. This is an open access article distributed under the Creative Commons Attribution License, which permits unrestricted use, distribution, and reproduction in any medium, provided the original work is properly cited.

A detrended fluctuation analysis (DFA) method is applied to image analysis. The 2-dimensional (2D) DFA algorithms is proposed for recharacterizing images of lymph sections. Due to Burkitt lymphoma (BL) and diffuse large B-cell lymphoma (DLBCL), there is a significant different 5-year survival rates after multiagent chemotherapy. Therefore, distinguishing the difference between BL and DLBCL is very important. In this study, eighteen BL images were classified as group A, which have one to five cytogenetic changes. Ten BL images were classified as group B, which have more than five cytogenetic changes. Both groups A and B BLs are aggressive lymphomas, which grow very fast and require more intensive chemotherapy. Finally, ten DLBCL images were classified as group C. The short-term correlation exponent α_1 values of DFA of groups A, B, and C were 0.370 ± 0.033 , 0.382 ± 0.022 , and 0.435 ± 0.053 , respectively. It was found that α_1 value of BL image was significantly lower ($P < 0.05$) than DLBCL. However, there is no difference between the groups A and B BLs. Hence, it can be concluded that α_1 value based on DFA statistics concept can clearly distinguish BL and DLBCL image.

1. Introduction

Natural phenomena almost are random, nonlinear, non-stationary, disordered, and uncertain systems. It is difficult to follow the traditional Newtonian rules to be completely forecast or control. Therefore, opening up fractal methods to investigate complex, rough, fragment shape, and noninteger dimension naturally objects (trees, coastlines, clouds, and mountains, etc.) is necessity. In the 1960s, the mathematician Mandelbrot had been indicated the fractal objects whose complex geometry cannot be characterized by an integral dimension [1]. This phenomenon is often expressed by spatial or time-domain statistical scaling laws and is mainly characterized by the power-law behavior of real-world physical systems. It represents fractal applies to objects in space or fluctuations in time that possess a form

of self-similarity [2]. The object has self-similarity means; the variant of object expressed same qualitatively, irrespective reduction or magnification of the object. Self-similarity is one way to calculate fractal dimension. For example, one can subdivide a line segment into m self-similar intervals, each with the same length, and each of which can be magnified by a factor of n to yield the original segment [3]. Due to the fractal geometry having an approximately copy of the whole, the fractal dimension is consistent over a wide range of scales, which is known as scale invariance [4]. This property provided a useful measurement of complexity object.

DFA method was developed from a modified root mean square analysis of a random walk to exclude the local trend induced by characteristic time scales from the fluctuations of the multicomponent systems and get a long-range correlation [5–7]. It was originally a method to

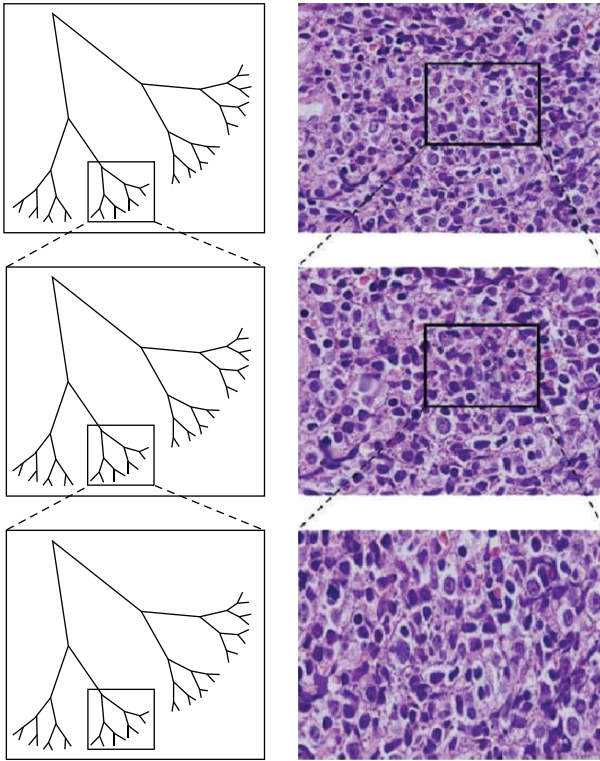


FIGURE 1: Fake tree (left hand side) and real lymphoma cell (right hand side) showed the self-similarity characteristics of pattern repeated in different zoom scales.

measure scale invariant behavior developed by Peng et al. [6] that evaluated trends of all sizes in the presence or absence of fractal correlation properties of time series data [8, 9]. This method has been applied to heart rate dynamics such as autonomic nervous system [10], congestive heart failure [8], dilated cardiomyopathy [11], ventricular fibrillation [12], and other physiological nonstationary time series systems (DNA sequences [13], neuron spiking [14, 15], human gait analysis [16], electroencephalogram (EEG) in sleep [17–20], stock returns [21], periodic trends [22], estimating dependence [23], etc.). Experience has shown that monodimensional detrended fluctuation analysis (DFA) used in the scaling analysis of fractal time series is accurate and easy to implement regardless in long-term and short-term time scale series [24, 25]. In recent years, there are some modified DFA method researches that are proposed such as generalized the monodimensional DFA and multifractal detrended fluctuation analysis (MF-DFA) to higher-dimensional versions and derived multifractal detrended cross-correlation analysis method to investigate the multifractal behaviors in the power-law cross correlations between two time series or higher-dimensional quantities recorded [26–28]. The multifractal detrended cross-correlation analysis based on DFA (MF-X-DFA) [27] is actually a multifractal generalization of the detrended cross-correlation analysis (DCCA) [29], which has other variants such as the multifractal detrended cross-correlation analysis based on DMA (MF-X-DMA) [30]. Those study results validated well for distinguishing fractal/multifractal properties of synthetic surfaces (including

fractional Brownian and multifractal surfaces), one/two-dimensional cross correlation of two financial time series, and linear/nonlinear correlation analysis of traffic time series (to find the cross correlation of traffic flow and volume data).

Although there are many varieties of malignant lymphomas, one of them is aggressive B-cell lymphoma. Diffuse large B-cell lymphoma (DLBCL) is the largest category of aggressive B-cell lymphomas. Less than 50% of patients can be cured by combination chemotherapy [31]. DLBCL has two important subgroups, which are germinal center B-cell-like (GCB) and activated B-cell-like (ABC) lymphoma. In medicine, cDNA microarrays method can successfully use to distinguish GCB and ABC DLBCL. The advantage of distinguish GCB and ABC DLBCL subgroups has significantly different 5-year survival rates after multiagent chemotherapy (GCB over 60%) [32, 33]. A similar situation exists between Burkitt lymphoma (BL) and DLBCL. Both lymphomas were all classified as aggressive B-cell non-Hodgkin's lymphoma in the World Health Organization [34]. Therefore, how to distinguish the difference between BL and DLBCL is a challenge, as the two diseases require different treatment and have different cure rate. Existing diagnosis and classification between BL and DLBCL evaluated their morphologic, immunophenotypic, and cytogenetic features and clinical outcomes [35, 36]. Recently, the Cui et al. study [37] had successful applied nonmedical methods (i.e., statistical and engineering methods, linguistic analysis, and ensembled artificial neural networks) to classify two types of GCB and ABC DLBCL. Because fractal temporal process may generate fluctuations on different area scales that are statistically self-similarity [38], therefore, the same concept of fractal temporal process and the statistically self-similarity of cell image are used as shown in Figure 1 because the lymphoma cells exist big and small cells at the same time which can easily display statistical self-similarity characteristics. In this paper, a nonmedical method/two-dimensional (2D) algorithms of DFA has been proposed based on the original design method concepts. The proposed method was used to recharacterize the images of lymph sections. It is anticipated that 2D DFA could be helpful to distinguish BL and DLBCL section images.

2. Material and Methods

2.1. Material. A total of 38 lymph section images cataloged into 3 lymphoma groups were used in the classification as shown in Table 1. Eighteen BL images were classified as group A, which have one to five cytogenetic changes. Ten BL images were classified as group B, which have more than five cytogenetic changes. Both group A and B BLs are high grade aggressive lymphomas, which grow very fast and require more intensive chemotherapy. Finally, ten DLBCL images were grouped as C. Some images of healthy cell, BL and DLBCL (4080×3072 pixels), are shown in Figure 2.

2.2. Two-Dimensional Analysis Algorithm of DFA. The algorithm of monodimensional DFA method described in [6] quantifies fractal-like correlation properties by calculating

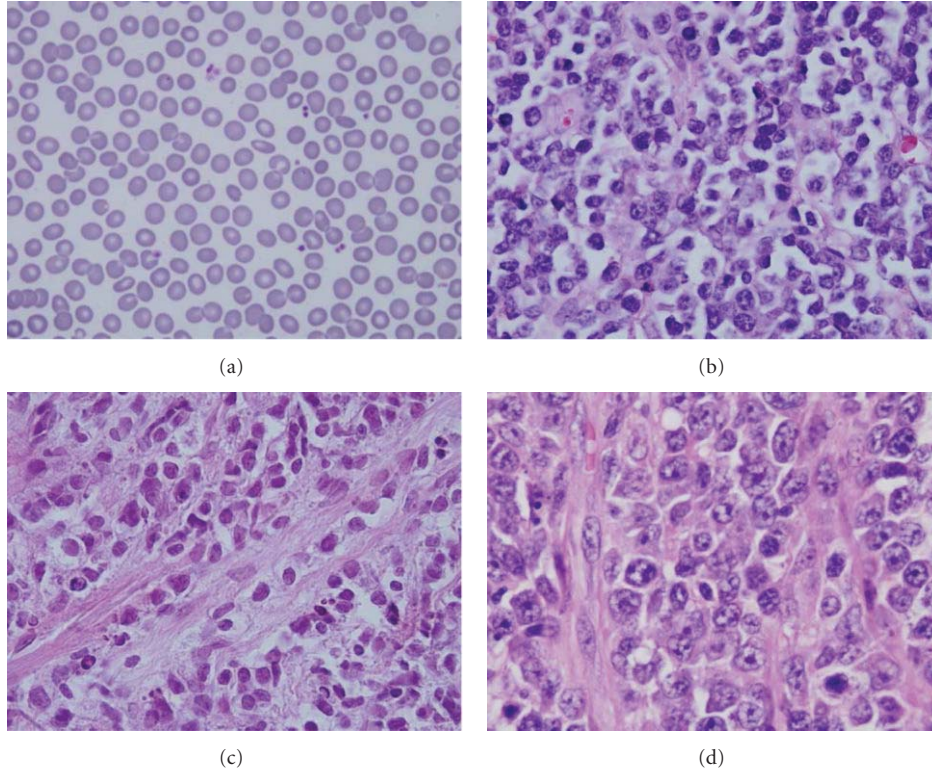


FIGURE 2: Healthy cell images, BL and DLBCL. (a) Healthy cell image, (b) BL image (one to five cytogenetic changes), (c) BL image (more than five cytogenetic changes), and (d) DLBCL image, which image is 4080×3072 pixels.

TABLE 1: The groups of Burkitt lymphoma (BL) and diffuse large B cell lymphoma (DLBCL) section images and case number.

Groups		Case number
A	Burkitt lymphoma (BL)	One to five cytogenetic changes
B		More than five cytogenetic changes
C	Diffuse large B cell lymphoma (DLBCL)	10

the scaling property of the root-mean-square fluctuation of the integrated and detrended time series data. To illustrate the DFA algorithm, a time series signal (with N samples) is used and analyzed as in the following equations:

$$y(k) = \sum_{i=1}^k [B(i) - \bar{B}], \quad (1)$$

where $B(i)$ is the i th sample of a signal; \bar{B} is the average of overall signal; and $y(k)$ is the value of the k th sample of the integrated time series. Then, the fluctuation of integrated and detrended time series for a given window with scale of n is calculated by

$$F(n) = \sqrt{\frac{1}{N} \sum_{k=1}^N [y(k) - y_n(k)]^2}, \quad (2)$$

where $F(n)$ is the fluctuation of an integrated time series for a given window with scale of n , and $y_n(k)$ is the k th point on the trend derived using a predetermined window with scale of n . A straight line of $\log(F(n))$ versus $\log(n)$ plot indicates

the presence of power law (fractal) correlation between scales and the fluctuations of the detrended time series. The slope of log-log plot is defined the DFA scaling exponent α . For the α exponent, Peng et al. indicate it as an indicator that describes the “roughness” of the original time series: the larger the value of α , the smoother the time series [6].

As the application of DFA in image analysis, two-dimensional algorithm of DFA should be refined in both integration and detrending processes. Considering the integration in both dimensions, the formula of integration should be as the following steps.

Step 1. The color image should be gray-scale processing at first. Consider a self-similar surface, which is denoted by a two-dimensional array $B(i, j)$, where $i = 1, 2, \dots, M$ and $j = 1, 2, \dots, N$. Content of $B(i, j)$ is the pixel value of surface image. Like monodimensional DFA method, the first integrated equation is as follows:

$$y(m, n) = \sum_{i=1}^m [B(i, n) - \bar{B}_{nc}] + \sum_{j=1}^n [B(m, j) - \bar{B}_{mr}] \quad (3)$$

for $1 \leq m \leq M$, $1 \leq n \leq N$, where $y(m, n)$ is the value of the pixel (m, n) on the integrated image, $B(i, n)$ is the i th pixel on the n th column, \bar{B}_{nc} is the average of the n th column, $B(m, j)$ is the j th pixel on the m th row, and \bar{B}_{mr} is the average of the m th row.

Step 2. The surface is partitioned into $M_s \times N_s$ disjoint square segments of the same size $s \times s$, where $M_s = \lceil M/s \rceil$, $N_s = \lceil N/s \rceil$, and $4 \leq s \leq \min(M/4, N/4)$. $y(m, n)$ can be denoted by $y_{k,l}$, segments such that $y_{k,l}(o, p) = y(k_1 + o, l_1 + p)$ for $1 \leq o, p \leq s$, $1 \leq k \leq M_s$, and $1 \leq l \leq N_s$, where $k_1 = (k-1)s$ and $l_1 = (l-1)s$.

Step 3. Use least square method to calculate the trend of matrix $y_{k,l}(s, s)$ expressed as $\hat{y}_{k,l}(s, s)$. The trend matrix $\hat{y}_{k,l}(s, s)$ is the mathematical model of linear regression. The trend decomposes into row and column, two directions.

Step 4. The mean squared error (MSE) represents the fluctuation of an integrated and detrended segment image with scale of $s \times s$ as

$$E_{k,l} = \frac{1}{s^2} \sum_{o=1}^s \sum_{p=1}^s [y_{k,l}(o, p) - \hat{y}_{k,l}(s, s)]^2 \quad (4)$$

for $E_{k,l}$ value expected to be minimized.

Step 5. The overall detrended fluctuation is calculated by averaging overall the segments, that is

$$F^2(s) = \frac{1}{M_s N_s} \sum_{k=1}^{M_s} \sum_{l=1}^{N_s} E_{k,l}. \quad (5)$$

Substituting (4) into (5) to get (6)

$$F^2(s) = \frac{1}{M_s N_s} \sum_{k=1}^{M_s} \sum_{l=1}^{N_s} \left\{ \frac{1}{s^2} \sum_{o=1}^s \sum_{p=1}^s [y_{k,l}(o, p) - \hat{y}_{k,l}(s, s)]^2 \right\}. \quad (6)$$

Then

$$F(s) = \sqrt{\frac{1}{M_s N_s} \sum_{k=1}^{M_s} \sum_{l=1}^{N_s} \left\{ \frac{1}{s^2} \sum_{o=1}^s \sum_{p=1}^s [y_{k,l}(o, p) - \hat{y}_{k,l}(s, s)]^2 \right\}}. \quad (7)$$

Moreover, the least square plans with size of $s \times s$ were used to fit the s th segment of local trends in images. Then, the s th trend can be removed from the integrated image to derive the s th fluctuation. DFA scaling exponent is defined as the power-law correlation between the using scales and the derived fluctuations. Finally, the DFA scaling exponent α by the straight line of $\log(F(s))$ versus $\log(s)$ plot is obtained.

2.3. Statistical Analysis. Values were expressed as means \pm SD. Data were analyzed by one-way analysis of variance (ANOVA) (SigmaStat statistical software, Jandel Scientific, San Rafael, CA). The Tukey test was conducted for multiple

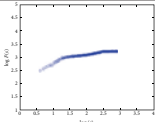
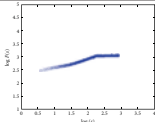
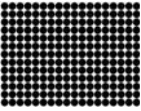
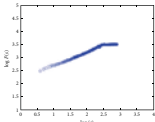
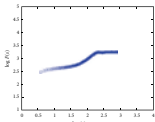
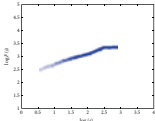
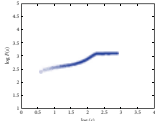
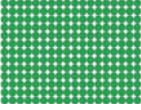
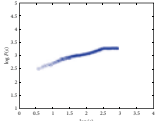
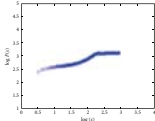
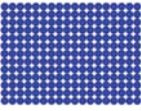
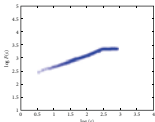
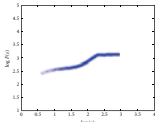
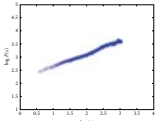
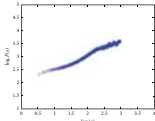
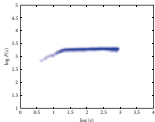
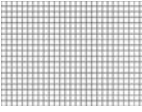
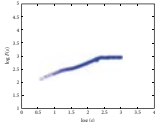
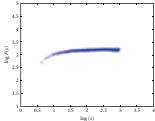
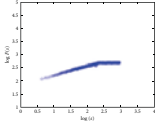
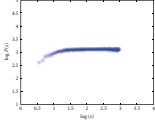
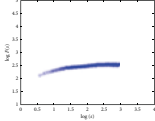
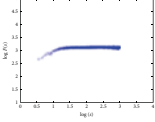
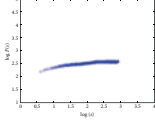
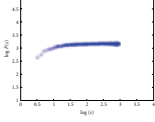
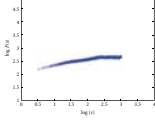
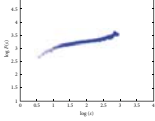
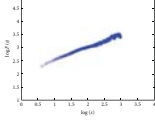
comparisons when the null hypothesis was not applicable for the same group. It was also used for all pairwise comparisons of the mean responses to the different treatment groups. Differences were considered significant at a value of $P < 0.05$.

3. Results and Discussion

3.1. Simulation. 24 images (4080×3072 pixels, same as lymph section images scale) were used to check the proposed two-dimensional analysis DFA method for image analysis. Different shape, color, and size images are used. Some images of simulation are shown in Figure 3. The image shape has circle and square, two types, which color has white, black, red, green, blue, and mix color, six modes, and size has large and small, two categories. The scaling exponent α can be estimated by a linear fit on the log-log plot of $F(s)$ versus s . The monodimensional DFA method has three types α value. It represents the correlation properties of the statistically self-similarity. Reflecting on two-dimensional DFA method, the global scaling exponent α value was calculated within the range of s between $s = 4$ and $s = \min(M/4, N/4)$, the short-term correlation exponent α_1 was calculated within the range between $s = 4$ and $s = 11$ [7, 39, 40], and the long-term correlation exponent α_2 was calculated within the range of s between $s = 12$ and $s = \min(M/4, N/4)$. Plotted $\log F(s)$ versus $\log s$ picture by the DFA analysis method of red small circle image was shown in Figure 4. End of the plotted curve is displayed nearly the horizon line. This trend is similar as other 23 simulation images. Because this curve trend, not displaying the line slope style, is unable to calculate the α and α_2 values, we selected α_1 to calculate total 24 simulation images and compared between the different shape, color, and size as shown in Table 2. The results show that different shapes, colors, and size images have different α_1 values. The 24 simulation images show three cases. First case is similar shape with same color which is all the large size α_1 value bigger than the small size. The small size shape means the numbers are more, and the shape area and length have larger values and complexity which are the same α exponent roughness concept of monodimensional DFA method from Peng et al. [6]. It is found that complex images have lower value of α_1 . Second case is similar size (i.e., the square diagonal length equal circle diameter) and color situation where the square shape α_1 value is greater than or equal (only white large image) the circle shape α_1 value. This observation corresponds the larger area image (i.e., circle area) and has lower α_1 value as initially observed. Third case is similar shape and size situation where α_1 values of different colors almost have no significant differences. This means the image color influence is very low when using 2D DFA method to analysis image characteristic. Therefore, when clinical images are influenced by light, the resulting images which are different in colors and cause a change in the characteristic value can be reduced. In summary, the index of the α_1 value has distinctive capability and consistency in image analysis.

3.2. Healthy Cell, BL and DLBCL Lymphoma Image Calculated Results. Figure 5 shows a healthy cell image plotted using

TABLE 2: The DFA α_1 value of 24 simulation images.

Image	DFA plot	α_1 value	Image	DFA plot	α_1 value
		0.65			0.29
		0.47			0.29
		0.43			0.33
		0.47			0.32
		0.43			0.33
		0.48			0.36
		0.65			0.47
		0.73			0.38
		0.73			0.36
		0.63			0.36
		0.75			0.35
		0.72			0.61

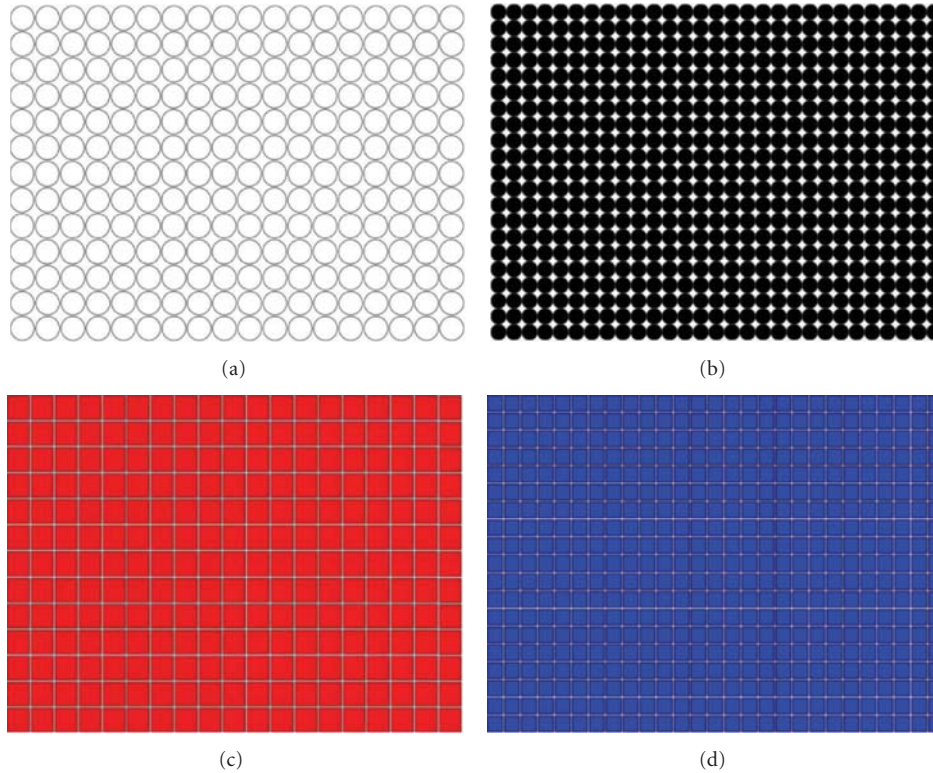


FIGURE 3: Simulation images. (a) White large circle, (b) black small circle, (c) red large square, and (d) blue small square, which image is 4080×3072 pixels. The shape of image has circle and square, two types. Every type's color has white, black, red, green, blue, and mix color, six modes, and size has large and small, two categories.

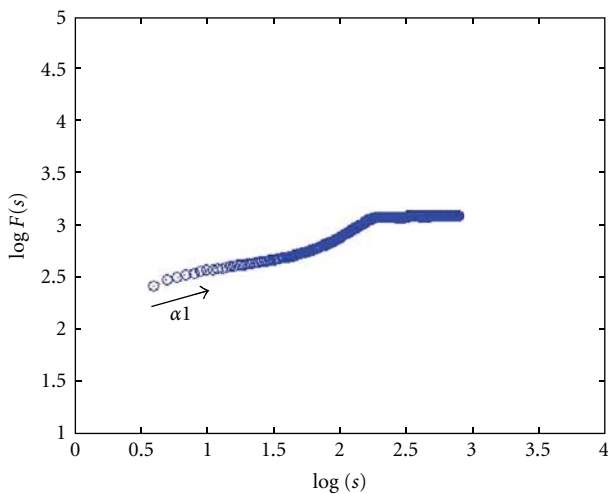


FIGURE 4: Red small circle image plot of $\log(F(s))$ versus $\log(s)$ using DFA analysis method.

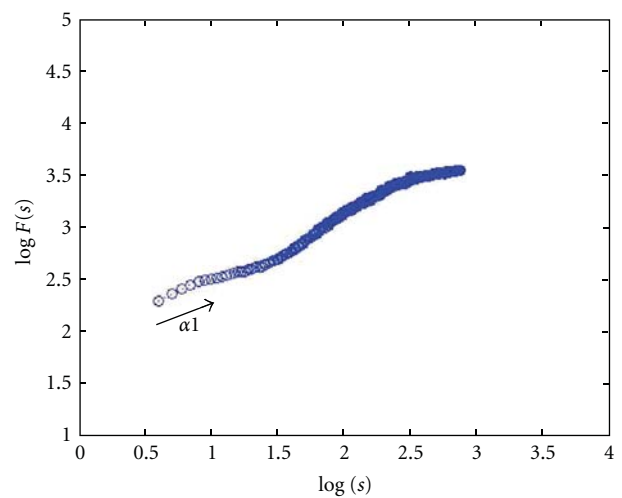


FIGURE 5: Healthy cell image plot of $\log(F(s))$ versus $\log(s)$ using DFA analysis method.

$\log(F(s))$ versus $\log(s)$ picture based on the DFA analysis method. Figure 6 shows a BL image of group B. All the simulation images show that the lymphoma images have similar curve trend. Therefore the DFA method was used to calculate α_1 value for a healthy cell image for a total of 38 lymphoma images classified into three groups. The α_1

value for healthy cell of Figure 2(a) is 0.50 which is due to the clarity of healthy cell images. The mean values of the short-term correlation exponent α_1 of groups A, B, and C are 0.370 ± 0.033 , 0.382 ± 0.022 , and 0.435 ± 0.053 , respectively, as shown in Table 3. It is observed that the healthy cell α_1 value was different from lymphoma cells. Furthermore, the

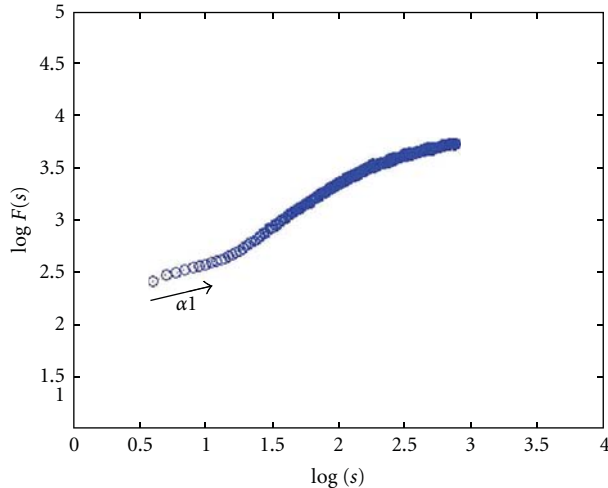


FIGURE 6: BL image (more than five cytogenetic changes) plot of $\log(F(s))$ versus $\log(s)$ using DFA analysis method.

α_1 value of BL image (both BLs) was significantly lower ($P < 0.05$) than DLBCL image (including groups A and C, groups B and C) and has no difference between both BLs (groups A and B). Hence, it could be concluded that α_1 values based on DFA statistics concept could clearly distinguish pathologic states between BL and DLBCL images.

4. Conclusions

DFA method was utilized to measure the scale invariant behavior that evaluates trends in the presence or absence of fractal correlation properties of time series data [8, 9]. In this study, 2D DFA method was derived and used to explore the trend of fractal images where the α_1 value can be easily identified.

In this paper, the DFA method has been applied to image analysis. The two-dimensional matrix algorithm of DFA, both integration and detrending processes, was used for time series data field. The DFA method has been used to investigate the characteristic of different type of simulated and lymphoma image. The lymphoma images test results show that the short-term correlation exponent α_1 value of DFA obtained from BL and DLBCL have statistical significant difference. This result is very encouraging, which α_1 value could be an index, to help the doctor for distinguishing between BL and DLBCL.

However, the authors had been testing the matrix performance of a two-dimensional image as in equation (1) of [26]. The 2D DFA results calculation of the matrix performance are very time consuming. For example, one image (4080×3072 pixels) takes over three days. This is disadvantageous for the real-time requirements. Therefore, the 1D DFA concept is being used to solve the aforementioned image's problem. We assume the lymphoma cell shape, color, and size were influenced by the row and column cells before it. By this way, the verification results of calculation time were great reduced for the 2D DFA, about 3 hours for one image.

TABLE 3: The DFA α_1 value of Burkitt and DLBCL images.

Classification	Group A	Group B	Group C	P value
α_1 value	0.370 ± 0.033^a	0.382 ± 0.022^b	0.435 ± 0.053	<0.001

Values are expressed as mean \pm standard deviation.

$P < 0.05$ was considered statistically significant difference using the ANOVA method.

^a $P < 0.05$ for group A versus group C comparison using the Tukey test.

^b $P < 0.05$ for group B versus group C comparison using the Tukey test.

Fortunately, statistical analysis of calculation results can distinguish between BL and DLBCL lymphoma. However, groups A and B in BL still cannot be classified in this study. Therefore, further investigations are needed to improve the sensitivity and specificity of classification. Results of this study can be compared to 2D DFA algorithm in [26] or 2D-DMA algorithm in [41, 42] to investigate how widely this method can be applied in clinical analysis.

Acknowledgments

The authors wish to thank the National Science Council (NSC) of Taiwan (Grant no. NSC 99-2622-E-155-007-CC2) for supporting this research. This research was also supported by the Center for Dynamical Biomarkers and Translational Medicine, National Central University, Taiwan, which is also sponsored by National Science Council (NSC100-2911-I-008-001).

References

- [1] B. Mandelbrot, "The variation of certain speculative prices," *The Journal of Business*, vol. 36, no. 4, pp. 394–419, 1963.
- [2] R. Lopes and N. Betrouni, "Fractal and multifractal analysis: a review," *Medical Image Analysis*, vol. 13, no. 4, pp. 634–649, 2009.
- [3] W. Klonowski, "Signal and image analysis using chaos theory and fractal geometry," *Machine Graphics and Vision Journal*, vol. 9, pp. 403–432, 2000.
- [4] O. Zmeřkal, M. Veselý, M. Nežádal, and M. Buchniček, "Fractal Analysis of Image Structures," *Harmonic and Fractal Image Analysis*, pp. 3–5, 2001.
- [5] C. K. Peng, S. V. Buldyrev, S. Havlin, M. Simons, H. E. Stanley, and A. L. Goldberger, "Mosaic organization of DNA nucleotides," *Physical Review E*, vol. 49, no. 2, pp. 1685–1689, 1994.
- [6] C. K. Peng, S. Havlin, H. E. Stanley, and A. L. Goldberger, "Quantification of scaling exponents and crossover phenomena in nonstationary heartbeat time series," *Chaos*, vol. 5, no. 1, pp. 82–87, 1995.
- [7] R. G. Yeh, J. S. Shieh, G. Y. Chen, and C. D. Kuo, "Detrended fluctuation analysis of short-term heart rate variability in late pregnant women," *Autonomic Neuroscience*, vol. 150, no. 1–2, pp. 122–126, 2009.
- [8] H. E. Stanley, L. A. N. Amaral, A. L. Goldberger, S. Havlin, P. C. Ivanov, and C. K. Peng, "Statistical physics and physiology: monofractal and multifractal approaches," *Physica A*, vol. 270, no. 1, pp. 309–324, 1999.
- [9] R. G. Yeh, G. Y. Chen, J. S. Shieh, and C. D. Kuo, "Parameter investigation of detrended fluctuation analysis for short-term human heart rate variability," *Journal of Medical and Biological Engineering*, vol. 30, no. 5, pp. 277–282, 2010.

- [10] T. Nakamura, H. Horio, S. Miyashita, Y. Chiba, and S. Sato, "Identification of development and autonomic nerve activity from heart rate variability in preterm infants," *BioSystems*, vol. 79, no. 1–3, pp. 117–124, 2005.
- [11] N. G. Mahon, A. E. Hedman, M. Padula et al., "Fractal correlation properties of R-R interval dynamics in asymptomatic relatives of patients with dilated cardiomyopathy," *European Journal of Heart Failure*, vol. 4, no. 2, pp. 151–158, 2002.
- [12] T. H. Mäkikallio, J. Koistinen, L. Jordaens et al., "Heart rate dynamics before spontaneous onset of ventricular fibrillation in patients with healed myocardial infarcts," *American Journal of Cardiology*, vol. 83, no. 6, pp. 880–884, 1999.
- [13] C. K. Peng, S. V. Buldyrev, A. L. Goldberger et al., "Long-range correlations in nucleotide sequences," *Nature*, vol. 356, no. 6365, pp. 168–170, 1992.
- [14] S. Bahar, J. W. Kantelhardt, A. Neiman et al., "Long-range temporal anti-correlations in paddlefish electroreceptors," *Europhysics Letters*, vol. 56, no. 3, pp. 454–460, 2001.
- [15] S. Blesić, S. Milošević, D. Stratimirović, and M. Ljubišavljević, "Detrended fluctuation analysis of time series of a firing fusimotor neuron," *Physica A*, vol. 268, no. 3–4, pp. 275–282, 1999.
- [16] J. M. Hausdorff, S. L. Mitchell, R. Firtion et al., "Altered fractal dynamics of gait: reduced stride-interval correlations with aging and Huntington's disease," *Journal of Applied Physiology*, vol. 82, no. 1, pp. 262–269, 1997.
- [17] J. M. Lee, D. J. Kim, I. Y. Kim, K. S. Park, and S. I. Kim, "Detrended fluctuation analysis of EEG in sleep apnea using MIT/BIH polysomnography data," *Computers in Biology and Medicine*, vol. 32, no. 1, pp. 37–47, 2002.
- [18] J. M. Lee, D. J. Kim, I. Y. Kim, K. Suk Park, and S. I. Kim, "Nonlinear-analysis of human sleep EEG using detrended fluctuation analysis," *Medical Engineering and Physics*, vol. 26, no. 9, pp. 773–776, 2004.
- [19] M. Staudacher, S. Telsler, A. Amann, H. Hinterhuber, and M. Ritsch-Marte, "A new method for change-point detection developed for on-line analysis of the heart beat variability during sleep," *Physica A*, vol. 349, no. 3–4, pp. 582–596, 2005.
- [20] C. J. Stam, T. Montez, B. F. Jones et al., "Disturbed fluctuations of resting state EEG synchronization in Alzheimer's disease," *Clinical Neurophysiology*, vol. 116, no. 3, pp. 708–715, 2005.
- [21] P. Grau-Carles, "Long-range power-law correlations in stock returns," *Physica A*, vol. 299, no. 3–4, pp. 521–527, 2001.
- [22] R. Nagarajan and R. G. Kavasseri, "Minimizing the effect of periodic and quasi-periodic trends in detrended fluctuation analysis," *Chaos, Solitons and Fractals*, vol. 26, no. 3, pp. 777–784, 2005.
- [23] R. Weron, "Estimating long-range dependence: finite sample properties and confidence intervals," *Physica A*, vol. 312, no. 1–2, pp. 285–299, 2002.
- [24] R. G. Yeh, J. S. Shieh, Y. Y. Han, Y. J. Wang, and S. C. Tseng, "Detrended fluctuation analyses of short-term heart rate variability in surgical intensive care units," *Biomedical Engineering*, vol. 18, no. 2, pp. 67–72, 2006.
- [25] R. G. Yeh, Y. Y. Han, J. S. Shieh, Y. J. Wang, S. C. Tseng, and Y. C. Fu, "Nonrandomness index applied for heart rate variability in surgical intensive care units using frequency and rank order statistics," *Biomedical Engineering*, vol. 19, pp. 303–311, 2007.
- [26] G. F. Gu and W. X. Zhou, "Detrended fluctuation analysis for fractals and multifractals in higher dimensions," *Physical Review E*, vol. 74, no. 6, Article ID 061104, 2006.
- [27] W. X. Zhou, "Multifractal detrended cross-correlation analysis for two nonstationary signals," *Physical Review E*, vol. 77, no. 6, Article ID 066211, 2008.
- [28] K. Dong and P. Shang, "Statistical properties of detrended cross-correlation analysis," *Journal of Beijing Jiaotong University*, vol. 34, no. 6, pp. 64–67, 2010.
- [29] B. Podobnik and H. E. Stanley, "Detrended cross-correlation analysis: a new method for analyzing two nonstationary time series," *Physical Review Letters*, vol. 100, no. 8, Article ID 084102, 2008.
- [30] Z. Q. Jiang and W. X. Zhou, "Multifractal detrending moving-average cross-correlation analysis," *Physical Review E*, vol. 84, no. 1, Article ID 016106, 2011.
- [31] T. Ando, M. Suguro, T. Hanai, T. Kobayashi, H. Honda, and M. Seto, "Fuzzy neural network applied to gene expression profiling for predicting the prognosis of diffuse large B-cell Lymphoma," *Japanese Journal of Cancer Research*, vol. 93, no. 11, pp. 1207–1212, 2002.
- [32] G. Wright, B. Tan, A. Rosenwald, E. H. Hurt, A. Wiestner, and L. M. Staudt, "A gene expression-based method to diagnose clinically distinct subgroups of diffuse large B cell lymphoma," *Proceedings of the National Academy of Sciences of the United States of America*, vol. 100, no. 17, pp. 9991–9996, 2003.
- [33] C. P. Hans, D. D. Weisenburger, T. C. Greiner et al., "Confirmation of the molecular classification of diffuse large B-cell lymphoma by immunohistochemistry using a tissue microarray," *Blood*, vol. 103, no. 1, pp. 275–282, 2004.
- [34] C. Bellan, L. Stefano, D. F. Giulia, E. A. Rogena, and L. Lorenzo, "Burkitt lymphoma versus diffuse large B-cell lymphoma: a practical approach," *Hematological Oncology*, vol. 28, no. 2, pp. 53–56, 2010.
- [35] N. Nakamura, H. Nakamine, J. I. Tamaru et al., "The distinction between Burkitt lymphoma and diffuse large B-cell lymphoma with c-myc rearrangement," *Modern Pathology*, vol. 15, no. 7, pp. 771–776, 2002.
- [36] X. F. Zhao, A. Hassan, A. Perry, Y. Ning, S. A. Stass, and L. P. Dehner, "C-MYC rearrangements are frequent in aggressive mature B-cell lymphoma with atypical morphology," *International Journal of Clinical and Experimental Pathology*, vol. 1, no. 1, pp. 65–74, 2008.
- [37] X. Cui, C. W. Lin, M. F. Abbod, Q. Liu, and J. S. Shieh, "Diffuse large B-cell lymphoma classification using linguistic analysis and ensembled artificial neural networks," *Journal of the Taiwan Institute of Chemical Engineers*, vol. 43, no. 1, pp. 15–23, 2012.
- [38] A. L. Goldberger, L. A. N. Amaral, J. M. Hausdorff, P. C. Ivanov, C. K. Peng, and H. E. Stanley, "Fractal dynamics in physiology: alterations with disease and aging," *Proceedings of the National Academy of Sciences of the United States of America*, vol. 99, no. 1, pp. 2466–2472, 2002.
- [39] T. H. Mäkikallio, T. Seppänen, K. E. J. Airaksinen et al., "Dynamic analysis of heart rate may predict subsequent ventricular tachycardia after myocardial infarction," *American Journal of Cardiology*, vol. 80, no. 6, pp. 779–783, 1997.
- [40] T. H. Mäkikallio, T. Ristimäe, K. E. J. Airaksinen, C. K. Peng, A. L. Goldberger, and H. V. Huikuri, "Heart rate dynamics in patients with stable angina pectoris and utility of fractal and complexity measures," *American Journal of Cardiology*, vol. 81, no. 1, pp. 27–31, 1998.
- [41] A. Carbone, "Algorithm to estimate the Hurst exponent of high-dimensional fractals," *Physical Review E*, vol. 76, no. 5, Article ID 056703, 2007.
- [42] G. F. Gu and W. X. Zhou, "Detrending moving average algorithm for multifractals," *Physical Review E*, vol. 82, no. 1, Article ID 011136, 2010.

Research Article

Wavelet-Based Color Pathological Image Watermark through Dynamically Adjusting the Embedding Intensity

Guoyan Liu,¹ Hongjun Liu,² and Abdurahman Kadir³

¹Department of Dermatology, Affiliated Hospital of Weifang Medical University, Weifang 261031, China

²Department of Information Engineering, Weifang Vocational College, Weifang 261041, China

³School of Computer Science and Engineering, Xinjiang University of Finance and Economics, Urumqi 830012, China

Correspondence should be addressed to Hongjun Liu, smithliu@126.com

Received 24 September 2012; Revised 20 October 2012; Accepted 22 October 2012

Academic Editor: Kumar Durai

Copyright © 2012 Guoyan Liu et al. This is an open access article distributed under the Creative Commons Attribution License, which permits unrestricted use, distribution, and reproduction in any medium, provided the original work is properly cited.

This paper proposes a new dynamic and robust blind watermarking scheme for color pathological image based on discrete wavelet transform (DWT). The binary watermark image is preprocessed before embedding; firstly it is scrambled by Arnold cat map and then encrypted by pseudorandom sequence generated by robust chaotic map. The host image is divided into $n \times n$ blocks, and the encrypted watermark is embedded into the higher frequency domain of blue component. The mean and variance of the subbands are calculated, to dynamically modify the wavelet coefficient of a block according to the embedded 0 or 1, so as to generate the detection threshold. We research the relationship between embedding intensity and threshold and give the effective range of the threshold to extract the watermark. Experimental results show that the scheme can resist against common distortions, especially getting advantage over JPEG compression, additive noise, brightening, rotation, and cropping.

1. Introduction

For content owners and distributors, there emerged a necessary concern in regard to the content authentication of pathological images as well as copyright protection. A latent solution to this issue is bestowed by digital watermarking. In general, image watermarking can be divided into two categories, according to the processing domain of cover images where the watermark is embedded: (1) the spatial domain method, which directly modifies the intensity value of the image and these algorithms are simple and speedy but not robust; (2) the frequency domain method, which is to modify the frequency coefficients.

In recent years, chaos is employed to encrypt the image, for it has sensitive dependence on initial conditions and can be employed to generate pseudorandom sequences, so the algorithm has large key space. Shyamsunder and Kaliyaperumal [1] proposed an image encryption scheme, which incorporates the concept of modular arithmetic and chaos theory. A necessary random matrix is generated for image encryption, and the look-up table is used to find

the element by modular inverse of the random matrix for decryption. Rawat and Raman [2] proposed a chaos-based watermarking scheme for image authentication and tamper detection. Their scheme can detect any modification made to the image and can also indicate the specific locations that have been modified. To improve the security of the proposed scheme, two chaotic maps are employed. Li et al. [3] used logistic system and Chebyshev maps to construct a hybrid chaotic mapping system, the aim is to set risk transfer, process and improve risk management efficiency in projects management. That is a good case for applying chaos in enterprise management.

The DWT approach remains one of the most effective ways for image watermarking. Lin et al. [4] proposed a blind watermarking algorithm based on maximum wavelet coefficient quantization; the blocks are randomly selected from different subbands, by adding different energies to the maximum wavelet coefficient to embed the watermark. The wavelet functions will analyze image features such as edges and borders through good space-frequency localization. They are used in several fields: image compression, signal

denoising, image smoothing, and texture analysis. The main advantages of embedding watermarks in the DWT can be found in [5, 6].

The most important issue in DWT-based image watermarking is how to choose the effective coefficients to be embedded and extracted. Liu [7] estimates the noise detection threshold of each wavelet coefficient in luminance and chrominance components of color image. The thresholds are derived into a locally dynamic fashion based on the wavelet decomposition, through which the perceptually significant coefficients are selected for embedding watermark. Al-Otum and Samara [8] proposed a watermark scheme based on the wavelet trees, which exploits the significant features and relations between the color pixel components in the wavelet domain. The watermark is embedded by spreading it that the interpixel robust relations carry the watermark bit sign with sufficient energy. Zhang et al. [9] proposed an adaptive block-based for embedding binary watermark into grayscale image. In these articles, the watermark bits are only shuffled by pseudorandom sequence, they are not scrambled to uniformly, and randomly distributed in the host image, which will lead to be attacked easily. The threshold is a fixed experimental value, and the authors did not explain how to get the threshold.

Hornig et al. [10] proposed a blind watermarking algorithm based on the significant difference of wavelet coefficient quantization. The maximum wavelet coefficients are quantized that their significant difference between watermark bit 0 and 1 exhibits a large energy difference, which can be used for watermark extraction. An adaptive threshold is designed to extract the watermark.

In this paper, we propose a dynamic blind watermarking scheme for color pathological image based on DWT; the watermark is scrambled firstly by Arnold cat map and XOR with pseudorandom sequence generated by Chebyshev map. The host image is divided into $n \times n$ blocks, and each bit of the encrypted watermark is embedded into the detail wavelet sub-band, that is, the higher-frequency domain of blue component. We modify the wavelet coefficient dynamically according to the mean and variance of the subbands to embed "0" or "1." In addition, we research the relationship between the embedding intensity and the threshold and deduce the range of the threshold, by which to extract the watermark correctly.

2. Watermarking Algorithm

2.1. Preprocessing the Watermark Image. The watermark used for embedding is a binary logo image, which is very small in size compared to the host image. The watermark needs to be very small so that it is spatially localized and becomes robust against the intentional and unintentional attacks.

For a binary logo image, in order to uniformly and randomly spread the bits over the host image, it is needed to be preprocessed, or the watermarked image cannot resist against even the simplest attack: cropping. The watermark can be preprocessed in numerous ways, such as randomly select the embedding position, generate pseudorandom sequences

to shuffle these bits [11], or the original watermark itself is dynamically generated from a pseudorandom Gaussian sequence [12, 13].

Here we take two measures to preprocess the watermark bits. Firstly, in order to make the watermarked image be more robust to resist against cropping attack, the two-dimensional Arnold cat map [14] is employed to scramble these binary bits. Suppose the watermark is an $n \times n$ binary image W ; after scrambling, we get the binary image W_A ; the aim is to uniformly spread the watermark bits in the host image. By this means, the watermarked image can be more robust against cropping than the method in [7]. The iteration times t is served as one of the keys. The Arnold cat map can be described as follows:

$$\begin{bmatrix} x_{n+1} \\ y_{n+1} \end{bmatrix} = \begin{bmatrix} 1 & 1 \\ 1 & 2 \end{bmatrix} \begin{bmatrix} x_n \\ y_n \end{bmatrix} \bmod n. \quad (1)$$

Secondly, watermarks generated from low-pass chaotic signals have superior performance over other signal types [13]. In order to eliminate the statistical significance and make the numbers of 0 and 1 approximately equal, a pseudorandom sequence $S_n \in \{0, 1\}$ will be generated by the Chebyshev map.

The expression of Chebyshev map is as follows:

$$z_{i+1} = \cos(w(\arccos z_i)), \quad -1 \leq z_i \leq 1, \quad (2)$$

where w is the degree of Chebyshev map. Its corresponding invariant density is as follows:

$$\rho(z) = \frac{1}{(\pi\sqrt{1-z^2})}. \quad (3)$$

Chebyshev map has important properties of excellent cryptosystem [14, 15]. While $w \geq 2$, the Lyapunov exponent of the Chebyshev map is positive, which predicates that Chebyshev map is chaotic, as shown in Figure 1.

Different sequences can be generated with different initial values; we get the sequence $S_n \in \{0, 1\}$ by

$$S_n = \begin{cases} 0, & z_n \in [-1, 0), \\ 1, & z_n \in [0, 1]. \end{cases} \quad (4)$$

Finally, we can get the binary image W_{AX} by the XOR operation:

$$W_{AX} = W_A \oplus S_n, \quad (5)$$

which is a binary sequence to be embedded into the host image.

The preprocessing process, including the original image W , the scrambled image W_A , and the image W_{AX} , is shown in Figure 2.

2.2. Analysis of Wavelet Coefficients. The host image I of size $w \times h$ is transformed into wavelet coefficients using the L -level discrete wavelet transform (DWT). With L -level decomposition, we can get $3 \times l + 1$ subbands, as shown in Figure 3. The lowest band (approximation band) LL_l is

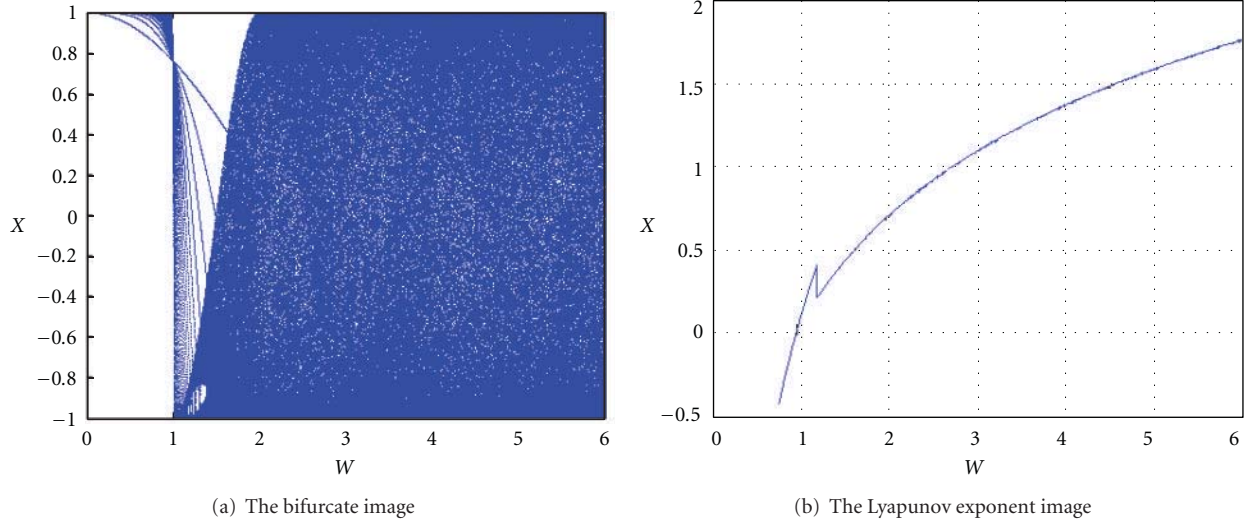


FIGURE 1: The bifurcate and Lyapunov exponent figures of Chebyshev map.

the basic band of the decomposed wavelet, which includes most of the energy from the original image; it has a crucial effect on quality; therefore, LL_l frequency band is unsuitable to be modified.

Only embedding the watermark into HH_l , HH_{l-1}, \dots , HH_1 subbands is also unsuitable, for they have the highest wavelet coefficients; the subbands can easily be eliminated and modified by lossy compression or other processing [14].

According to these characteristics, we design to adaptively adjusting, the high-frequency coefficient of the subbands HL_l , LH_l , and HH_l , to embed the watermark bits.

Generally, watermark embedding is realized by modifying some special values of pixels or transforming domain coefficients [16]. When the watermarked image receives some attacks, though the quality is still high, the pixel value or coefficient may be seriously eliminated, which will lead to the watermark detecting failed [17, 18]. Here we take advantage of the statistic characteristic, such as mean and variance of the LH_l , HL_l , and HH_l subbands, to modify the whole coefficients of them to dynamically embed the watermark and implement the compromise between quality and robustness.

2.3. Watermark Embedding. After preprocessing the binary watermark image W to get W_{AX} , we reshape W_{AX} to binary sequence wm ; its length is still $n \times n$. According to Human Visual System (HVS) [19], small changes to the blue component of color image are the most difficult to detect by human eyes; then we select the blue component to embed.

Here we improve the method in [9] to embed pre-processed watermark into the blue component of color image. Suppose the host color image is I . Firstly, we divide the blue component of I into a set of nonoverlapping $n \times n$ subblocks $b_j \in B$, $j = 1, 2, \dots, n^2$. Then a l -level DWT decomposition of each sub-block of image I is performed

using Haar wavelet, and then compute the mean E_j of each wavelet block S_D by

$$E_j = \frac{1}{M} \left(\sum_{(x,y) \in S_D} c_j^{(l,s)}(x,y) \right), \quad (6)$$

where $c_j^{(l,s)}(x,y)$ is the wavelet coefficient of the j th sub-block, l is the level of wavelet decomposition, s refers to the three subbands of LH_l , HL_l and HH_l . (x,y) is the coordinate for wavelet coefficient in the wavelet blocks, and M is the total number of wavelet coefficient in S_D .

For example, here we set $l = 2$, for the j th sub-block $b(j) \in B$; we use the $dwt2()$ function in Matlab to perform a single-level two-dimensional wavelet decomposition. Finally, $c_j^{(2,s)}(x,y)$ can be gotten by (9)

$$\left[LL_{j1}, LH_{j1}, HL_{j1}, HH_{j1} \right] = dwt2(b(j), 'haar'), \quad (7)$$

$$\left[LL_{j2}, LH_{j2}, HL_{j2}, HH_{j2} \right] = dwt2(LL_{j1}, 'haar'), \quad (8)$$

$$c_j^{(2,s)}(x,y) = \left[LH_{j2}, HL_{j2}, HH_{j2} \right]. \quad (9)$$

The purpose of E_j is to keep the average of $c_j^{(l,s)}(x,y) - \lambda E_j$ in (10) and (11) close to zero.

If $wm(j) = 1$, we modify the whole wavelet coefficients in S_D by

$$c_j'^{(l,s)}(x,y) = c_j^{(l,s)}(x,y) - \lambda E_j. \quad (10)$$

If $wm(j) = 0$, we modify the whole wavelet coefficients in S_D by

$$c_j'^{(l,s)}(x,y) = c_j^{(l,s)}(x,y) - \lambda E_j + P. \quad (11)$$

Here $c_j'^{(l,s)}(x,y)$ is the modified wavelet coefficient; the distribution of wavelet coefficient is modulated by $wm(j)$.

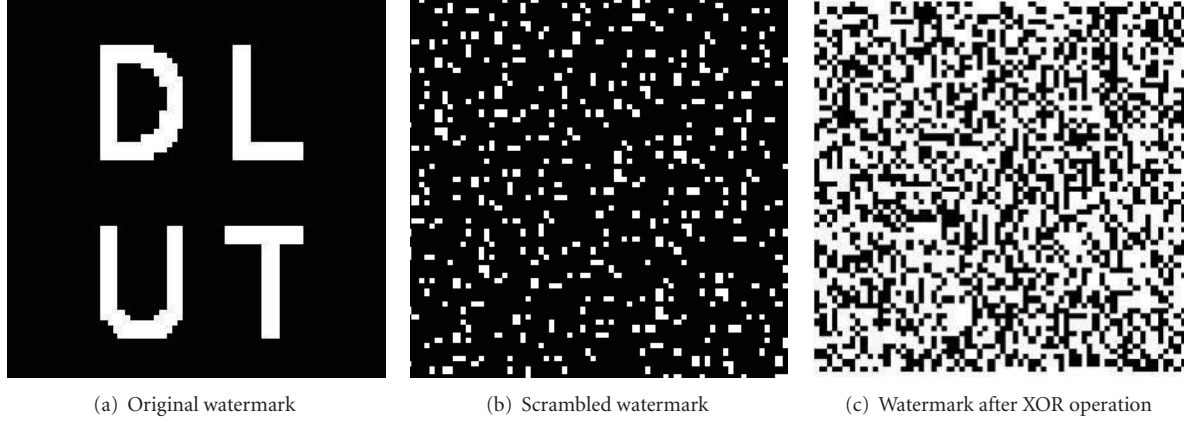


FIGURE 2: The preprocessing process of the original watermark.

LL3	LH3	LH2	LH1
HL3	HH3		
HL2		HH2	
HL1		HH1	

FIGURE 3: Wavelet subbands of 3-level.

s refers to the three detail subbands of LH_i , HL_i , and HH_i . That is to say, embedding “0” means that the coefficient mean of wavelet block S_D is P , and embedding “1” means 0. λ refers to the magnification of E_j ; here we set $\lambda = 1.5$ to ensure the range of threshold Th larger enough to extract the watermark.

Because the variance is bigger in the textures and edges than that in the smooth region, we use the variance of the coefficient as the modulation coefficient P to control the dynamically embedding intensity [19]. Raising embedding intensity within the definition can enhance the robustness [15]. So P can be defined by

$$P = A + T(j). \quad (12)$$

$T(j)$ is defined as

$$T(j) = \left(\sqrt{\left(\sum_{(x,y) \in S_D} (c_j^{(l,a)}(x,y) - c_j^{(l,b)}(x,y)) - \lambda E_j \right)^2} \right)^\beta. \quad (13)$$

We can find that $T(j)$ is the local variance of the j th wavelet sub-block except the approximate sub-band LL_i , and β is a constant. In (12), A is the intensity coefficient, which ensures to embed some watermark in the smooth region while $T(j)$ is approximately 0. So (11) can be fully expressed by (14).

$$c_j'^{(l,s)}(x,y) = c_j^{(l,s)}(x,y) - \lambda E_j + A + \left(\sqrt{\left(\sum_{(x,y) \in S_D} (c_j^{(l,a)}(x,y) - c_j^{(l,b)}(x,y)) - \lambda E_j \right)^2} \right)^\beta. \quad (14)$$

Using (10) and (14) we embed watermark by modify the wavelet coefficients. Finally, the IDWT is applied to each block, to get the watermarked image I_w .

2.4. Watermark Extraction. The watermark can be extracted correctly from the watermarked image, without the original host image or the watermark image, so the scheme belongs to blind watermark algorithm. The transformed coefficients are compared with the threshold Th of the coefficients, those coefficients above the threshold are retained, and all the others are discarded [20].

The extracting process is as follows, which is mirroring the embedding process.

Step 1. We divide the blue component of the watermarked color image I into a set of nonoverlapping $n \times n$ subblocks.

Step 2. To extract the embedded bit from a sub-block, the L -level DWT decomposition of each block is firstly obtained. Then we compute $\text{Sum}(j)$, the coefficients sum of the wavelet block S_D using

$$\text{Sum}(j) = \sum_{(x,y) \in S_D} c_j'^{(l,s)}(x,y). \quad (15)$$

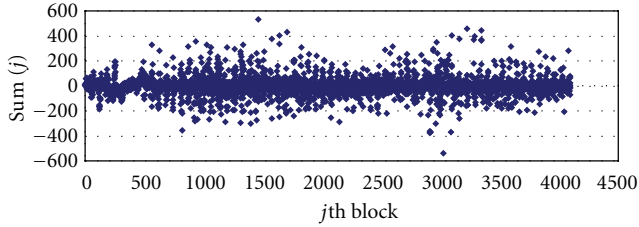


FIGURE 4: Distribution: $\text{Sum}(j)$ of the wavelet blocks S_D before embedding.

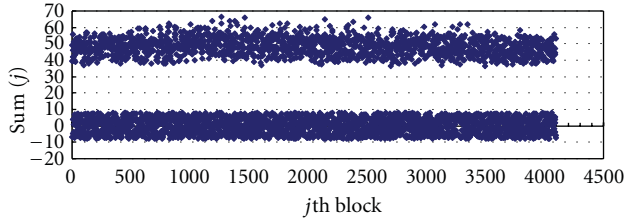


FIGURE 5: Distribution: $\text{Sum}(j)$ of S_D after embedding ($\beta = 0.218$).

For all the wavelet blocks of $j = 1, 2, \dots, n^2$,

$$\begin{aligned} \text{Sum}(j) &\in [r1, r2], & \text{if } S_D \text{ carries bit "1"}, \\ \text{Sum}(j) &\in [r3, r4], & \text{if } S_D \text{ carries bit "0"}, \end{aligned} \quad (16)$$

where $r1 < r2 < r3 < r4$, then we can get the range of $\text{Th} \in (r2, r3)$.

Step 3. $\text{Sum}(j)$ is compared with the threshold Th , to decide whether the coefficient carries a bit "1" or "0" using

$$wm(j) = \begin{cases} 1 & \text{Sum}(j) < \text{Th}, \\ 0 & \text{Sum}(j) \geq \text{Th}, \end{cases} \quad (17)$$

where $wm(j)$ is the extracted bit.

Step 4. Finally, the extracted watermark bits are recovered into a binary image according to the inverse process.

During the embedding and extracting processes, the iteration times t of Arnold transform, the initial value of Chebyshev map, the size $n \times n$ of each block, the values of A , λ , and β , the threshold Th , and the type of wavelet are all served as keys, which can guarantee the security of the watermarked image; it is impossible to extract the watermark without these keys.

3. Experimental Result Analysis

3.1. Get the Effective Range of the Threshold in Experiment.

The threshold is a critical factor, which can ensure to extract the watermark correctly from watermarked image under some attacks, and some papers only provide a fixed value [3, 7, 8]. The proposed scheme provides an exact range of the threshold by testing dozens of images, and it keeps constant even if the watermarked image has been attacked in some degree.

Figure 4 is Image1 distribution of $\text{Sum}(j)$ before embedding; we can find that most of the coefficients in the detail

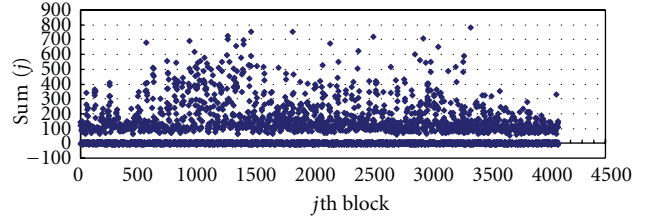


FIGURE 6: Distribution: $\text{Sum}(j)$ of S_D after embedding ($\beta = 0.818$).

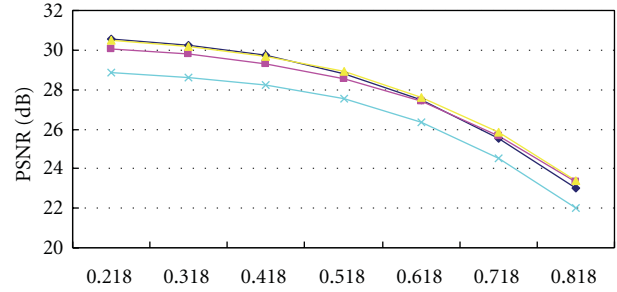


FIGURE 7: The relationship between β and PSNR (dB).

subbands after DWT are close to zero, and the mean of each detail sub-band is approximately zero.

Figures 5 and 6 are the Image1 distribution of $\text{Sum}(j)$ after embedding with $\beta = 0.218$ and $\beta = 0.818$; from them we can find that when $\beta = 0.218$, the distribution of $\text{Sum}(j)$ is relatively concentrated, but when $\beta = 0.818$, the values of $\text{Sum}(j)$ distribute in larger range. The distribution of other images, such as Image3 and Airplane, is similar to Image1 when we set $\beta = 0.218$.

Experiment results demonstrate that when we set $\beta \in [0.218, 0.818]$, the threshold $\text{Th} \in (10, 35)$, which is consistent with the result of (16), the range of Th watermark can ensure the watermark to be extracted clearly from the watermarked images.

3.2. The Relationship between β and PSNR. The quality of watermarked image is based on the PSNR [12]. From Figure 7 we can find that the PSNRs decrease smoothly with the increase of $\beta \in [0.218, 0.818]$, which can increase the embedding intensity P . What's more, Figure 7 shows that the PSNR values of Image1, Image2, and Image3 are similar, and they are greater than that of Image4, for they have richer edges and borders than Image4, as shown in Figure 8.

4. Experimental Results and Key Space

4.1. Experimental Result. Here we made a 64×64 binary image as the watermark. Some standard color images with the size of $512 \times 512 \times 24$ bits, including Image1, Airplane, and Image3, are being tested. The size of the sub-block is set to 8×8 , $\lambda = 1.5$, $l = 2$, when $A \in [4, 22]$, $\beta \in [0.218, 0.818]$, and $\text{Th} \in (10, 35)$; the results of watermarked images are satisfactory, as shown in Figure 9.

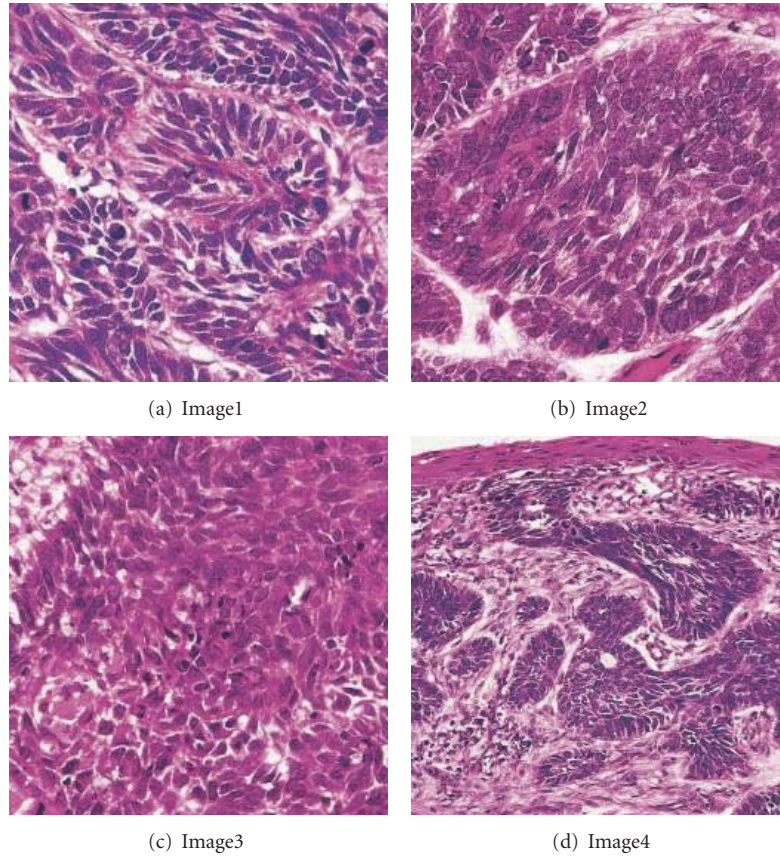


FIGURE 8: Sample images.

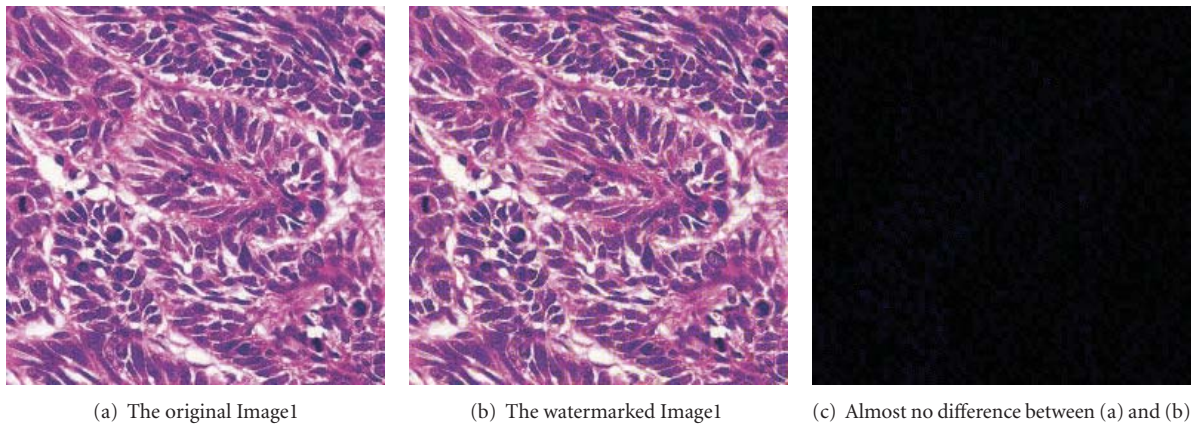


FIGURE 9: The original and the watermarked Image1, and the difference between them.

4.2. Key Space Analysis. The high sensitivity to initial conditions is inherent to any chaotic system. To provide an secure algorithm, the key space should be large enough to make any brute force attack ineffective. Our scheme has some of the following secret keys: (1) for the Arnold cat map, the initial values of x_0 and y_0 , the iteration times t ; (2) Chebyshev maps, the initial value z_0 , and the parameter w .

For the Arnold cat map, $x_0, y_0 \in [1, n]$ and $t \in [1, 256]$, here $n = 64$. For the Chebyshev maps, when the tiny

change in the initial value $\Delta z_0 = 10^{-16}$, the scrambled watermark image is completely different. A large number of experimental results indicate that the key spaces for initial values are $S_{z_0} = 10^{16}$. Similarly, the variation of the parameter w in the chaotic region is between 2 and 6 with a step of 10^{-16} , so $S_w \approx 4 \times 10^{16}$.

Finally, the total key space is $S = S_{x_0} \times S_{y_0} \times S_t \times S_{z_0} \times S_w \approx 4.19 \times 10^{38}$, which is larger than 2^{100} , so even the scrambled watermark is extracted; it's difficult to recover it.

TABLE 1: Noise attacking results for Image1.

Density	$d = 0.001$	$d = 0.005$	$d = 0.01$	$d = 0.02$	$d = 0.05$
Salt and pepper					
NC	0.9585	0.8520	0.7462	0.6488	0.5309
Mean and variance	$m = 0, v = 0.0005$	$m = 0, v = 0.001$	$m = 0, v = 0.002$	$m = 0, v = 0.005$	$m = 0, v = 0.01$
Gaussian					
NC	0.8503	0.7124	0.6258	0.5615	0.5137

TABLE 2: Compression results with different ratios.

$A = 20, \beta = 0.128$	0.80	0.65	0.50	0.25	0.10
Image1					
NC	0.8071	0.7325	0.7143	0.5497	0.4449
Image2					
NC	0.7765	0.6970	0.6603	0.5368	0.4186
Image3					
NC	0.6363	0.5789	0.5621	0.5100	0.5037

5. Attack Test Results

The attacks to the whole watermarked image can modify the red, green, and blue components simultaneously. The modifications in the red or green component are easier to be observed, that is only because of the Human Visual System. There is no evidence to show that the modification in the blue component can be more robust than the other components.

The peak signal-to-noise ratio (PSNR) is used to evaluate the quality between an attacked image and the original image. For the sake of completeness, we list the PSNR formula as follows:

PSNR =

$$10 \times \log_{10} \frac{255 \times 255}{1/(I_h \times I_w) \sum_{x=0}^{I_h-1} \sum_{y=0}^{I_w-1} [f(x, y) - g(x, y)]^2} \text{dB}, \quad (18)$$

where I_h and I_w are the height and width of the image, respectively. $f(x, y)$ and $g(x, y)$ are the values located at coordinates (x, y) of the original image and the attacked image, respectively.

After extracting the watermark, the normalized correlation coefficient (NC) is computed using the original watermark and the extracted watermark to judge the existence of the watermark and to measure the correctness of an extracted watermark. It can be defined as

$$\text{NC} = \frac{1}{W_h \times W_w} \sum_{i=0}^{W_h-1} \sum_{j=0}^{W_w-1} W(i, j) \times W'(i, j), \quad (19)$$

where W_h and W_w are the height and width of the watermark, respectively. $W(i, j)$ and $W'(i, j)$ are the watermark bits located at coordinates (i, j) of the original watermark and the extracted watermark.

5.1. Attack of Noise. Noise attack is a common attack during the transmission of the watermarked image on the network

TABLE 3: Extracting results for Image1 and Image2 after being cropped.

Cropping	5%	10%	25%	50%	75%
Image1 Watermark extracted					
NC	0.9128	0.8245	0.6617	0.4701	0.3470
Image2 Watermark extracted					
NC	0.8911	0.8245	0.6320	0.4622	0.3332

TABLE 4: Randomly select the cropping position and the extracting result.

$A = 20, \beta = 0.128$	Randomly cropped	Quadrately cropped	Ambiently cropped
Cropped watermarked image			
Extracted watermark before reverse transformation			
Extracted watermark after reverse transformation			

TABLE 5: Extracting results from the image with enhanced and decreased brightness.

Enhanced brightness	10%	30%	50%
Extracted watermark			
Decreased brightness	-10%	-30%	-50%
Extracted watermark			

set to 0.05, the NC is 0.5309, and the extracted watermark can still be distinguishable. Similarly, for the watermarked image attacked by Gaussian white noise, when the mean value is set to zero, more noise points appear in the extracted watermark with the increase of variance; when variance is set to 0.01, the extracted watermark can still be distinguishable.

5.2. Attack of JPEG Compression. JPEG lossy compression is the most common image compression technique. The watermarked image Image1 is compressed using JPEG with different value of β , horizontal resampling by 2:1, and compression ratios, 0.80, 0.65, 0.50, 0.25, and 0.10 respectively. The results obtained are summarized in Table 2; the distinguishable watermark can still be extracted even the ratio is set to 0.10, so the algorithm is very robust against compression.

[21]. In the experiment, we add salt and pepper noise and Gaussian white noise to Image1 image, as shown in Table 1.

For the watermarked image with salt and pepper noise, with the increase of noise density, more and more noise points appear in the extracted watermark, when the density is

5.3. Attack of Cropping. The algorithm is also very robust against the cropping operation. In order to resist true cropping, that is, only a portion of the image is kept and the remaining part is thrown away, the width and height of the host image, along with the other keys, are sent to the

TABLE 6: Compare the proposed method with the algorithms in [4, 11, 18].

Attacks	NC			
	Reference [4] (PSNR = 42.02 dB)	Reference [11] (PSNR = 44.73 dB)	Reference [18] (PSNR = 42.98 dB)	Our algorithm (PSNR = 31.14 dB)
Median filter (3×3)	0.90	0.88	0.93	1
JPEG (ratio = 0.80)	0.99	NA	1	0.9997
JPEG (ratio = 0.50)	0.96	0.95	0.96	0.9976
JPEG (ratio = 0.10)	0.34	0.33	0.32	0.9987
Rotation (degree: 0.25°)	0.59	0.61	0.65	0.9897
Rotation (degree: -0.25°)	0.60	0.65	0.72	0.9900
Cropping 1/4	0.66	0.60	0.67	0.8561
Scaling 256×256	0.88	0.71	0.85	0.9999

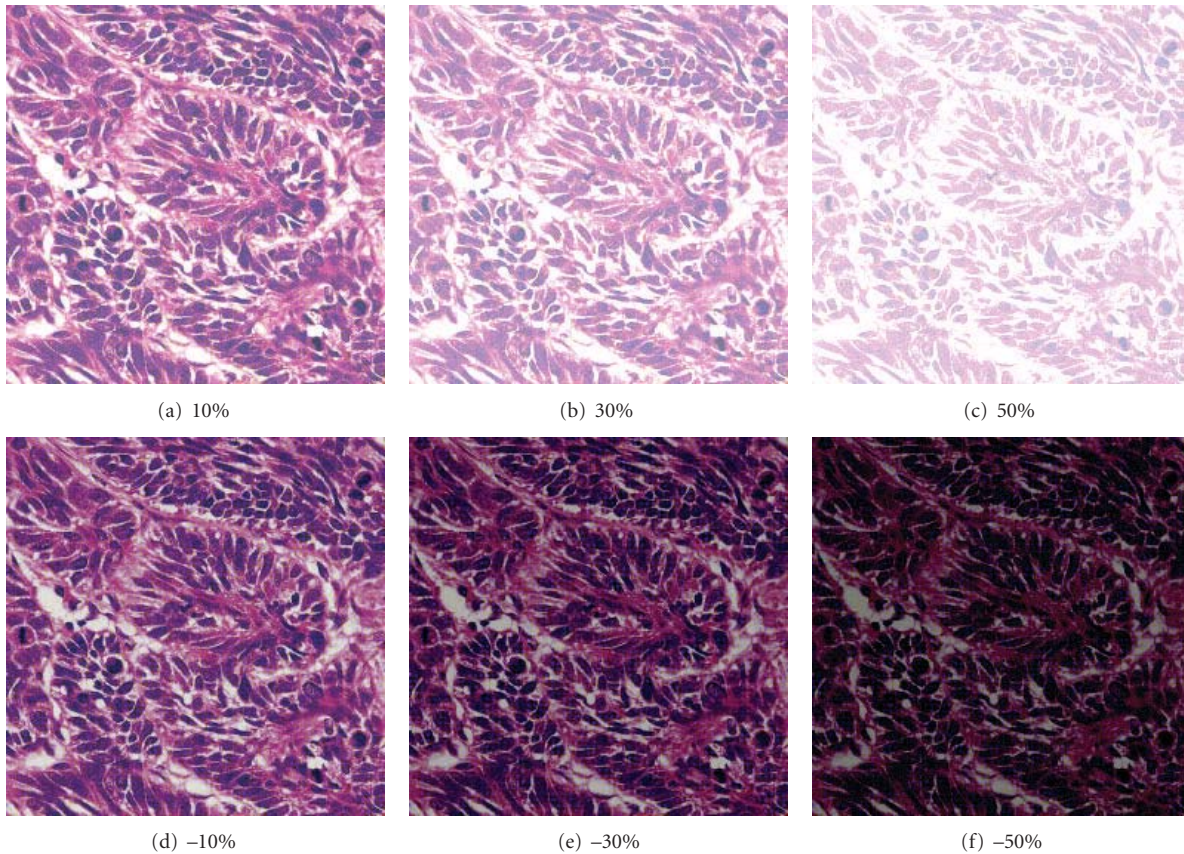


FIGURE 10: Image1: enhance and decrease the brightness.

detector. If the detector receives a portion of the image, he can recover it to the original size by zero padding, to extract the watermark.

After randomly selecting the position and crop 5%, 10%, 25%, 50%, and 75% of the watermarked image, respectively, then extract the watermark, as shown in Table 3. When 50% of the whole image is cropped, we can still extract the distinguishable watermark. That is to say, the algorithm has high robustness against cropping.

After cropping the randomly selected position, and filling the cropped region with zero, the extracted watermark before and after the reverse transformation is shown in Table 4;

from it we can find that the randomly cropping has no effect on the extracted watermark.

Without the preprocessing to scramble the watermark, the four letters "DLUT" on the original watermark may be unexpectedly cropped; that is, the extracted watermark may be fragmentary, so scrambling the watermark by Arnold cat map in Section 2.1 can help to make the bits randomly distributed, which contributes to the robustness.

5.4. *Attack of Brightness.* We increase and decrease the brightness by 10%, 30%, and 50%, respectively, as shown in

Figure 10. The extracted watermarks demonstrate that increasing the brightness has less effect on the watermark than decreasing the brightness, as shown in Table 5. So the algorithm has high robustness against the attack of brightness.

5.5. *Comparison.* Finally, we use Image1 with $\beta = 0.218$ to compare our algorithm with the algorithms proposed in [4, 11, 18]. The results show that our algorithm gets advantages over the others in the attacks of median filter, compression, rotation, and cropping, as shown in Table 6.

6. Conclusion

We propose a dynamic block-based blind watermark algorithm based on a 2-level DWT, using Haar filter to embed a preprocessing binary image into the blue component of the color pathological image. By analyzing the coefficients' characteristic after wavelet decomposition, we select the detail subbands to embed watermark. During the embedding procedure, the statistic characteristics of the mean and variance are applied to dynamically adjust the embedding intensity, so as to generate the effective range of threshold to extract the watermark. Experiment results demonstrate that the quality of the watermarked image, which is based on the PSNR, decreases smoothly with the increase of the embedding intensity, and the algorithm is robust against common distortions, especially, getting advantages over noise, compression, cropping, rotation, and brightening.

Acknowledgments

The research is supported by the Science and Technology Development Plan of Weifang (no. 20121346) and the Minority Nationality Technology Talent Cultivation Plan of Xinjiang (no. 201123116).

References

- [1] S. Shyamsunder and G. Kaliyaperumal, "Image encryption and decryption using chaotic maps and modular arithmetic," *American Journal of Signal Processing*, vol. 1, no. 1, pp. 24–33, 2011.
- [2] S. Rawat and B. Raman, "A chaotic system based fragile watermarking scheme for image tamper detection," *International Journal of Electronics and Communications*, vol. 65, no. 10, pp. 840–847, 2011.
- [3] C. B. Li, P. Li, and G. S. Lu, "Enterprise projects set risk element transmission chaotic genetic model," *Research Journal of Applied Sciences, Engineering and Technology*, vol. 4, no. 17, pp. 3162–3167, 2012.
- [4] W. H. Lin, Y. R. Wang, S. J. Horng, T. W. Kao, and Y. Pan, "A blind watermarking method using maximum wavelet coefficient quantization," *Expert Systems with Applications*, vol. 36, no. 9, pp. 11509–11516, 2009.
- [5] S. Agreste and G. Andaloro, "A new approach to pre-processing digital image for wavelet-based watermark," *Journal of Computational and Applied Mathematics*, vol. 221, no. 2, pp. 274–283, 2008.
- [6] S. Agreste, G. Andaloro, D. Prestipino, and L. Puccio, "An image adaptive, wavelet-based watermarking of digital images," *Journal of Computational and Applied Mathematics*, vol. 210, no. 1–2, pp. 13–21, 2007.
- [7] K. C. Liu, "Wavelet-based watermarking for color images through visual masking," *International Journal of Electronics and Communications*, vol. 64, no. 2, pp. 112–124, 2010.
- [8] H. M. Al-Otum and N. A. Samara, "A robust blind color image watermarking based on wavelet-tree bit host difference selection," *Signal Processing*, vol. 90, no. 8, pp. 2498–2512, 2010.
- [9] G. Zhang, S. Wang, and Q. Wen, "An adaptive block-based blind watermarking algorithm," in *Proceedings of the 7th International Conference on Signal Processing Proceedings (ICSP '04)*, vol. 3, pp. 2294–2297, September 2004.
- [10] S. J. Horng, T. W. Kao, P. Fan, C. L. Lee, and Y. Pan, "An efficient watermarking method based on significant difference of wavelet coefficient quantization," *IEEE Transactions on Multimedia*, vol. 10, no. 5, pp. 746–757, 2008.
- [11] W. H. Lin, Y. R. Wang, and S. J. Horng, "A wavelet-tree-based watermarking method using distance vector of binary cluster," *Expert Systems with Applications*, vol. 36, no. 6, pp. 9869–9878, 2009.
- [12] W. Lu, W. Sun, and H. Lu, "Robust watermarking based on DWT and nonnegative matrix factorization," *Computers and Electrical Engineering*, vol. 35, no. 1, pp. 183–188, 2009.
- [13] H. A. Al-Otum and A. O. Al-Taba'a, "Adaptive color image watermarking based on a modified improved pixel-wise masking technique," *Computers and Electrical Engineering*, vol. 35, no. 5, pp. 673–695, 2009.
- [14] X. Wu and Z. H. Guan, "A novel digital watermark algorithm based on chaotic maps," *Physics Letters A*, vol. 365, no. 5–6, pp. 403–406, 2007.
- [15] A. Mooney, J. G. Keating, and I. Pitas, "A comparative study of chaotic and white noise signals in digital watermarking," *Chaos, Solitons and Fractals*, vol. 35, no. 5, pp. 913–921, 2008.
- [16] J. M. Amigó, L. Kocarev, and J. Szczepanski, "Theory and practice of chaotic cryptography," *Physics Letters A*, vol. 366, no. 3, pp. 211–216, 2007.
- [17] D. Tsolis, S. Nikolopoulos, L. Drossos, S. Sioutas, and T. Papatheodorou, "Applying robust multibit watermarks to digital images," *Journal of Computational and Applied Mathematics*, vol. 227, no. 1, pp. 213–220, 2009.
- [18] R. S. Run, S. J. Horng, W. H. Lin, T. W. Kao, P. Fan, and M. K. Khan, "An efficient wavelet-tree-based watermarking method," *Expert Systems with Applications*, vol. 38, no. 9, pp. 14357–14366, 2011.
- [19] H. Chen and P. K. Varshney, "A human perception inspired quality metric for image fusion based on regional information," *Information Fusion*, vol. 8, no. 2, pp. 193–207, 2007.
- [20] G. Bhatnagar and B. Raman, "A new robust reference watermarking scheme based on DWT-SVD," *Computer Standards and Interfaces*, vol. 31, no. 5, pp. 1002–1013, 2009.
- [21] A. Mooney, J. G. Keating, and D. M. Heffernan, "Performance analysis of chaotic and white watermarks in the presence of common watermark attacks," *Chaos, Solitons and Fractals*, vol. 42, no. 1, pp. 560–570, 2009.

Research Article

Modified Global and Modified Linear Contrast Stretching Algorithms: New Colour Contrast Enhancement Techniques for Microscopic Analysis of Malaria Slide Images

Aimi Salihah Abdul-Nasir,¹ Mohd Yusoff Mashor,¹ and Zeehaida Mohamed²

¹Electronic & Biomedical Intelligent Systems (EBItS) Research Group, School of Mechatronic Engineering, Universiti Malaysia Perlis, Campus Pauh Putra, Perlis, 02600 Pauh, Malaysia

²Department of Medical Microbiology & Parasitology, School of Medical Sciences, Health Campus, Universiti Sains Malaysia, 16150 Kubang Kerian, Kelantan, Malaysia

Correspondence should be addressed to Aimi Salihah Abdul-Nasir, aimi_salihah@yahoo.com

Received 14 July 2012; Accepted 14 August 2012

Academic Editor: Kumar Durai

Copyright © 2012 Aimi Salihah Abdul-Nasir et al. This is an open access article distributed under the Creative Commons Attribution License, which permits unrestricted use, distribution, and reproduction in any medium, provided the original work is properly cited.

Malaria is one of the serious global health problem, causing widespread sufferings and deaths in various parts of the world. With the large number of cases diagnosed over the year, early detection and accurate diagnosis which facilitates prompt treatment is an essential requirement to control malaria. For centuries now, manual microscopic examination of blood slide remains the gold standard for malaria diagnosis. However, low contrast of the malaria and variable smears quality are some factors that may influence the accuracy of interpretation by microbiologists. In order to reduce this problem, this paper aims to investigate the performance of the proposed contrast enhancement techniques namely, modified global and modified linear contrast stretching as well as the conventional global and linear contrast stretching that have been applied on malaria images of *P. vivax* species. The results show that the proposed modified global and modified linear contrast stretching techniques have successfully increased the contrast of the parasites and the infected red blood cells compared to the conventional global and linear contrast stretching. Hence, the resultant images would become useful to microbiologists for identification of various stages and species of malaria.

1. Introduction

Malaria is a widely prevalent disease, affecting millions of people in the world. Research has shown that malaria is caused by a protozoan parasite of the genus *Plasmodium*. *Plasmodium* is a small, single-cell organism which originated from a species of mosquito named *Anopheles* [1]. Malaria is passed on by the female *Anopheles* mosquito biting a person who has malaria parasites in their blood. If the disease is not treated, it can lead to serious problems such as anemia, retinal damage, and convulsions [2]. Malaria infection ends in one of two ways either the patient dies or the parasites are defeated by immune system or medications. Up to this date, five species of genus *Plasmodium* that can cause human infection have been discovered namely, *P. falciparum*, *P. vivax*, *P. ovale*, *P. malariae*, and *P. knowlesi* [3]. In 2009, it is

estimated that 3.3 billion people which is half of the world population are at risk of malaria, with approximately 225 million cases and 781,000 of deaths [4]. The vast majority of cases occur in children under the age of 5 and also pregnant women. In Malaysia, a total of 7,010 malaria cases were diagnosed among Malaysians in 2009 [4].

Diagnosis of malaria must be prompt, as a few hours of delay in treatment involves a matter of life and death. Currently, there are several new methods have been employed for diagnosis of malaria. These include the use of fluorescent microscopy, rapid antigen detection method, and polymerase chain reaction (PCR) technique [5]. Despite these advances, the most economic and reliable diagnosis which is based on microscopic examination of blood slide remains the gold standard for laboratory confirmation of malaria [5, 6]. The procedure is performed manually by

expert microbiologists through visual identification under light microscope [6]. The percentage of parasitaemia as well as the species and life-cycle stages of the detected parasite must be determined in order to provide the best treatment. The scheme that requires the examination of both thick and thin blood smears for the presence of plasmodia is believed to be the most sensitive and specific one [7]. Besides these numerous advantages, there are also some limitations associated with the identification of malaria based on light microscopy, such as time consumption and labour intensity. In addition, the accuracy of the final diagnosis varies depending on the skill and experience of the experts [7, 8]. In comparison to the expert microscopy, standard laboratory microscopy has a sensitivity of approximately 90%, a figure which drops dramatically in the field [7]. In Malaysia, there are more than 1.5 million slides examined each year in a population at risk of approximately 1 million [3]. Due to human error and time consumption, better and more efficient method is needed.

The contrast of the malaria image is one of the factors that may influence the accuracy of interpretation by microbiologists. The malaria slide images that have been captured through the microscope may have their own weaknesses such as blurred or low contrast due to the magnification or underexposure of the light built in the system of the image analyzer. In addition, variable smears quality and the conditions of the slide are highly influenced by the time and storage. Due to the low quality of the image, it will be hard to visualize and analyze the morphological features between the different plasmodia species on the screen, hence increasing the false diagnosis rate. Thus, contrast enhancement technique at the preprocessing stage is developed to adjust the quality of image for better human visual perception [9]. The resulting enhanced medical image will provide clearer and cleaner images for better and easier disease screening process by the doctor.

Various approaches of contrast enhancement techniques have been developed for enhancing the image contrast. Despite of histogram equalization, contrast stretching is one of the popular contrast enhancement technique that has been applied in X-ray [10] and various medical images such as leukaemia [11], retinal fundus [12], and computed tomography (CT) brain images [13]. There are several contrast enhancement techniques that have been developed for malaria image. Tek [14] proposed a new colour normalization method that has been applied on peripheral thin-film blood images. This method has been developed in order to maintain the colour constancy of the images that have been captured from various sources. The normalization has been applied separately to the foreground and background regions. A rough estimation of the foreground-background regions is done by mathematical morphology and followed by a refined segmentation using histograms of these regions. Then, an illumination-independent response is calculated using the background region. The normalization is completed by transforming the foreground region according to the grey values determined by a reference set. The proposed method has been tested on various images and has been found successful.

Another example for the application of contrast enhancement technique is the use of dark stretching technique for enhancing and segmenting the *P. falciparum* based on thick blood smear images [15]. By applying the dark stretching technique, the darkest region of the image which is referred to the parasite will be stretched, while the bright region will be compressed. Thus, the appearance of the parasites will become clearer due to the stretching process in dark stretching technique. Due to the requirement for enhancing the malaria image, the current study investigates the performance of contrast enhancement techniques namely, global and linear contrast stretching as well as the proposed modified global and modified linear contrast stretching that have been applied to enhance the malaria slide images. The proposed contrast enhancement technique is expected to improve the performance of microscopy by improving the quality and clarity especially on degrading or low contrast malaria image as well as easing the image segmentation process in the later part of the diagnostic system.

2. Morphological Features of Malaria

Generally in malaria diagnosis, the process is performed by searching for the parasites in blood slide through a microscope. The visual aspect of the parasites and the red blood cells (RBCs) can be distinguished based on colour due to the used of chemical named Giemsa stain [1]. Then, specific morphological features will be observed in order to identify the stages and species of malaria. During the life-cycle in peripheral blood, the five malaria species may be observable in the four different life-cycle stages which are morphologically distinguishable between the ring, trophozoite, schizont, and gametocyte [1]. In this study, the four contrast enhancement techniques have been applied on four life-cycle stages of *P. vivax* images. The malaria images for the four life-cycle stages of *P. vivax* are shown in Figure 1.

Here, The variations of malaria parasite morphology that are generally being observed are as follows [1, 16];

- (a) size: the size of the parasite and the infected RBC (red circle);
- (b) form: the configuration of the nucleus and cytoplasm of the parasite which occur during the growth of the parasite;
- (c) colour: the fraction of the stain taken up by the various elements of the parasite;
- (d) pigment: the presence or absence of malarial pigment.

3. Methodology

In this study, the proposed work comprises of three main steps. These include image acquisition, image enhancement, and measurement of image quality for the four contrast enhancement techniques

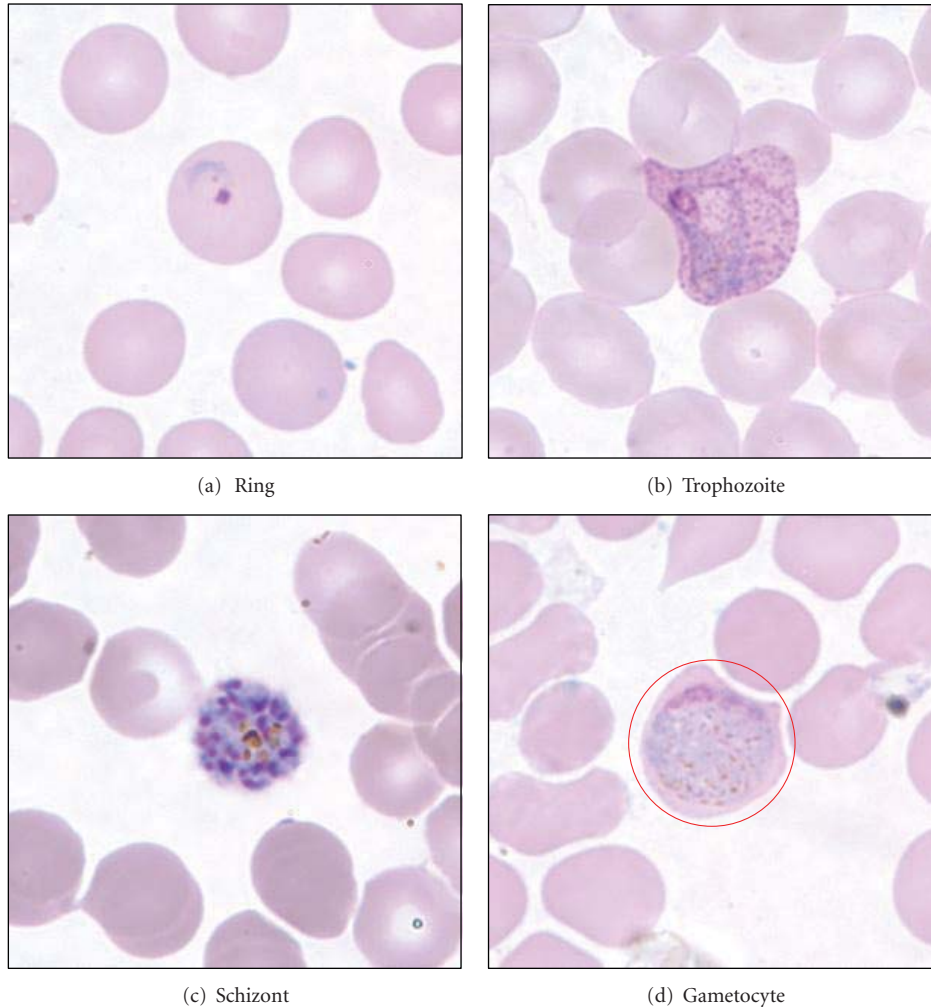


FIGURE 1: The malaria images for the four life-cycle stages of *P. vivax* [16].

3.1. Image Acquisition. Image acquisition is the first stage of vision system and image processing area. In this study, 150 malaria images which consist of the ring, trophozoite, schizont, and gametocyte stages have been captured from eight different slides of thin blood smear from *P. vivax* samples. The malaria slides are prepared by the Medical Microbiology & Parasitology Department, Hospital University Science Malaysia (HUSM). The slides are examined under 100x oil immersion objective using Leica DLMA microscope. The images are then captured using Infinity-2 camera at a resolution setting of 800×600 pixels and saved in bitmap (*.bmp) format. The captured images are studied under the supervision of microbiologists in order to recognize and differentiate between the four life-cycle stages of *P. vivax* species.

3.2. Contrast Enhancement Techniques. The malaria slide images captured through the microscope may have their own weaknesses such as blurred or low contrast. Thus, contrast enhancement technique plays an important role in

enhancing the quality and contrast of malaria images. In general, an image can be enhanced by spreading the range of colour values to make use of all possible values. This method is called contrast stretching. It changes the distribution and range of the digital numbers assigned to each pixel in an image. Here, there are four types of contrast stretching methods that have been applied on malaria images namely global, linear, modified global, and modified linear contrast stretching techniques.

3.2.1. Global and Linear Contrast Stretching. Global contrast stretching (GCS) technique remedies problems that manifest themselves in a global fashion such as excessive or poor lighting conditions in the source environment [17]. This technique enhances the image from the luminance information of an entire image. Image with a high global contrast will cause a global feeling of a detailed and variation-rich image. On the other hand, image with a lower global contrast contain less information, less details and appears to be more uniform [18].

The formula for global contrast stretching is governed by the following equation [19]:

$$\text{out}_{\text{RGB}}(x, y) = 255 * \left[\frac{(\text{in}_{\text{RGB}}(x, y) - \text{min}_{\text{RGB}})}{\text{max}_{\text{RGB}} - \text{min}_{\text{RGB}}} \right], \quad (1)$$

where $\text{in}_{\text{RGB}}(x, y)$ is The original RGB value of the pixel, $\text{out}_{\text{RGB}}(x, y)$ is the new RGB value of the pixel, min_{RGB} is minimum value between the RGB components, and max_{RGB} is maximum value between the RGB components

Based on (1), (x, y) is the image pixel location. min_{RGB} and max_{RGB} are the minimum and maximum values between the RGBs (red, green, and blue) of the original image. The GCS technique will consider all ranges of RGB colours at once to determine the minimum and maximum values between the RGB components. The combination between the RGB components will give only one value for each minimum and maximum parameter which will later be used for the contrast stretching process. However, the process for selecting these minimum and maximum values is different for the linear contrast stretching (LCS) technique.

For LCS technique, the stretching process for each of the RGB components is carried out separately. Here, the amount of stretching that will be applied in a neighborhood will be controlled by the original contrast in that neighborhood. The formula for linear contrast stretching is governed by (2) [20]:

$$\text{out}_{\text{RGB}}(x, y) = 255 * \left[\frac{(\text{in}_{\text{RGB}}(x, y) - \text{min})}{\text{max} - \text{min}} \right], \quad (2)$$

where $\text{in}_{\text{RGB}}(x, y)$ is the original RGB value of the pixel, $\text{out}_{\text{RGB}}(x, y)$ is the new RGB value of the pixel, min is minimum value for each RGB components, and max is maximum value for each RGB component

Based on (2), the LCS technique will consider each range of RGB components in the image. Thus, the range of each colour component will be used during the contrast stretching process to represent each range of colour. This will give each colour component a set of minimum and maximum values. By applying this technique, each RGB component will be distributed linearly over the whole histogram so that the dynamic range of the histogram (0–255) is fulfilled [9].

3.2.2. Modified Global and Modified Linear Contrast Stretching. The enhancement of malaria images depends directly on the minimum and maximum values that will be used during the contrast stretching process. Here, new contrast enhancement techniques namely, modified global contrast stretching (MGCS) and modified linear contrast stretching (MLCS) have been proposed. Both techniques include a step to determine the new minimum and maximum values, which are beyond the original minimum and maximum values for each of the RGB components in the image. The modified global and modified linear contrast stretching techniques are similar to the minimum-maximum global and linear contrast stretching, except that these techniques use specified minimum and maximum values that lie in a certain percentage of pixels from the total number of pixels in the image.

In order to obtain the new minimum and maximum values for each of the RGB components in the image for both MGCS and MLCS techniques, several parameters are required during the calculation process. These include the value for minimum percentage, min_p , maximum percentage, max_p , number of pixels in each pixel level, T_{pix} , total number of pixels that lie in a specified minimum percentage, T_{min} , and total number of pixels that lie in a specified maximum percentage, T_{max} . The procedures to develop the proposed MGCS and MLCS techniques are as follows.

- (1) Select the desired values for min_p and max_p .
- (2) Initialize $T_{\text{min}} = 0$ and $T_{\text{max}} = 0$. Set the value of $k = 0$, where k is the current pixel level.
- (3) Calculate the histogram for the red component.
- (4) Obtain the number of pixels, $T_{\text{pix}}[k]$ at k . If $T_{\text{pix}}[k] \geq 1$, set $T_{\text{min}} = T_{\text{min}} + T_{\text{pix}}[k]$.
- (5) Check the following condition:

$$\frac{T_{\text{min}}}{\text{Total number of pixels in the image}} * 100 \geq \text{min}_p. \quad (3)$$

- (6) If T_{min} satisfies (3), set the new minimum value, N_{min} for the red component in the image to the k value that satisfies this condition; else set $k = k + 1$.
- (7) Repeat steps 4 to 6 for the next pixel levels until N_{min} is obtained based on the k value that satisfies (3).
- (8) Set the value of $k = 255$.
- (9) Obtain $T_{\text{pix}}[k]$ at k . If $T_{\text{pix}}[k] \geq 1$, set $T_{\text{max}} = T_{\text{max}} + T_{\text{pix}}[k]$.
- (10) Check the following condition:

$$\frac{T_{\text{max}}}{\text{Total number of pixels in the image}} * 100 \geq \text{max}_p. \quad (4)$$

- (11) If T_{max} satisfies (4), set the new maximum value, N_{max} for the red component in the image to the k value that satisfies this condition; else set $k = k - 1$.
- (12) Repeat steps 9 to 11 for the next pixel levels until N_{max} is obtained based on the k value that satisfies (4).
- (13) Repeat steps 2 to 12 in order to calculate the N_{min} and N_{max} for the green and blue components.
- (14) Determine the new minimum value between the RGB components, $N_{\text{min}_{\text{RGB}}}$ and the new maximum value between the RGB components, $N_{\text{max}_{\text{RGB}}}$ based on the N_{min} and N_{max} that have been obtained for each of the RGB components.
- (15) For MGCS algorithm, substitute min_{RGB} and max_{RGB} in (1) with the $N_{\text{min}_{\text{RGB}}}$ and $N_{\text{max}_{\text{RGB}}}$ that have been obtained based on step 14.
- (16) For MLCS algorithm, substitute min and max in (2) with the N_{min} and N_{max} that have been obtained for each of the RGB components.
- (17) End.

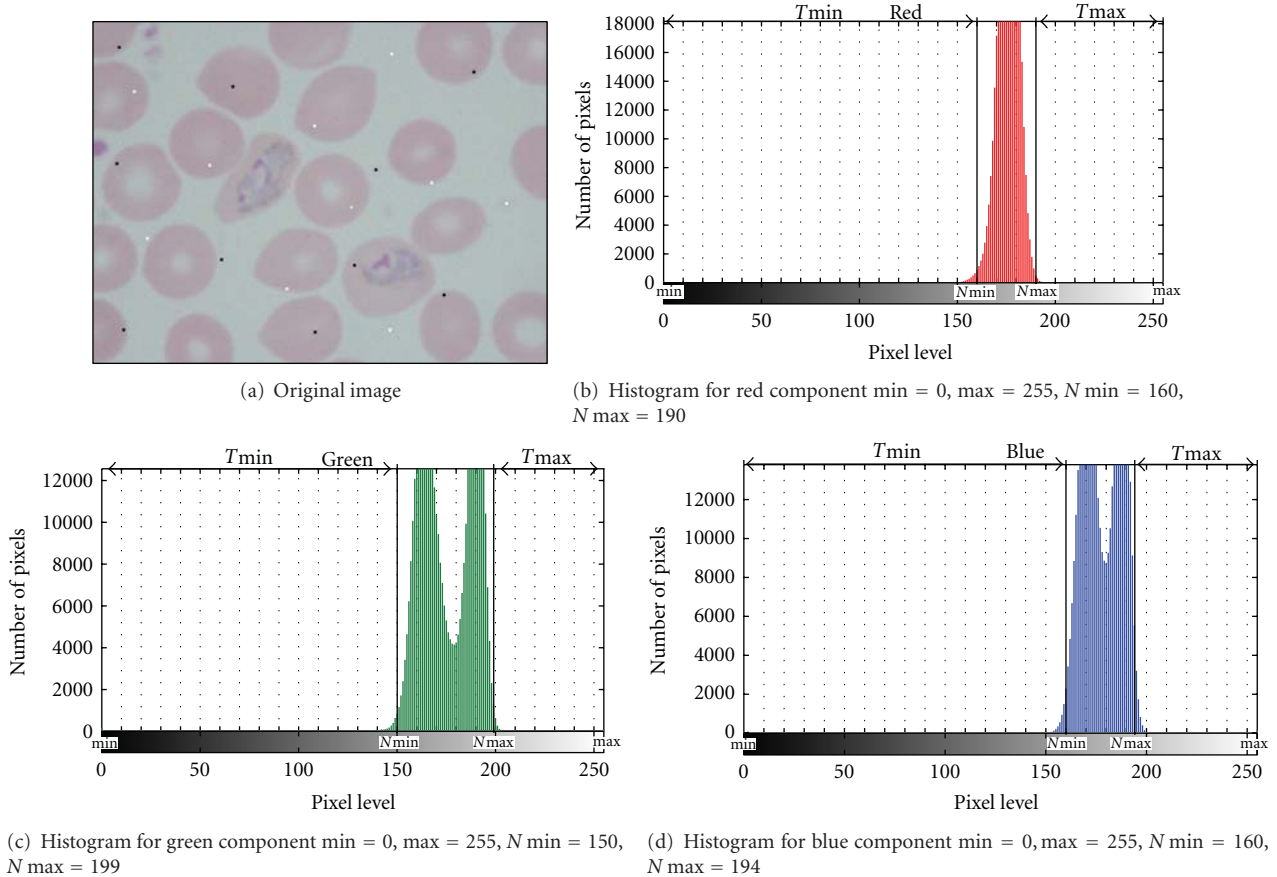


FIGURE 2: An example for determining the minimum and maximum values for each of the RGB components based on the proposed MGCS and MLCS techniques.

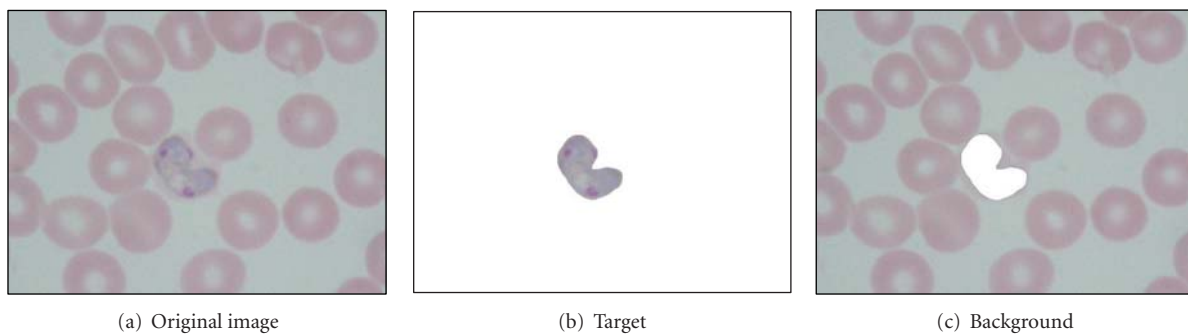


FIGURE 3: Original malaria image and its segmented parasite and background regions after performing the manual segmentation.

Figure 2 shows an example for determining the minimum and maximum values for each of the RGB components based on the proposed MGCS and MLCS techniques. Here, Figure 2(a) shows the original image of trophozoite stage with the addition of salt-and-pepper noise. Meanwhile, the histograms for the red, green, and blue components of the original image are shown in Figures 2(b), 2(c) and 2(d), respectively. By referring to Figure 2, it is found that all the minimum and maximum values for each of the RGB components are 0 and 255, respectively. Thus, these values are not suitable to be applied for the contrast stretching

process. By applying the MGCS and MLCS techniques with min_p and max_p of 1%, the minimum and maximum values for each of the RGB components have been changed, and the N_{min} and N_{max} values can be referred to in Figure 2.

3.3. Quantitative Measure of Contrast Enhancement Techniques. Image quality measure has become crucial for most image processing applications. In general, the measurement of image quality can be divided into two primary ways which are qualitative and quantitative measures. In malaria

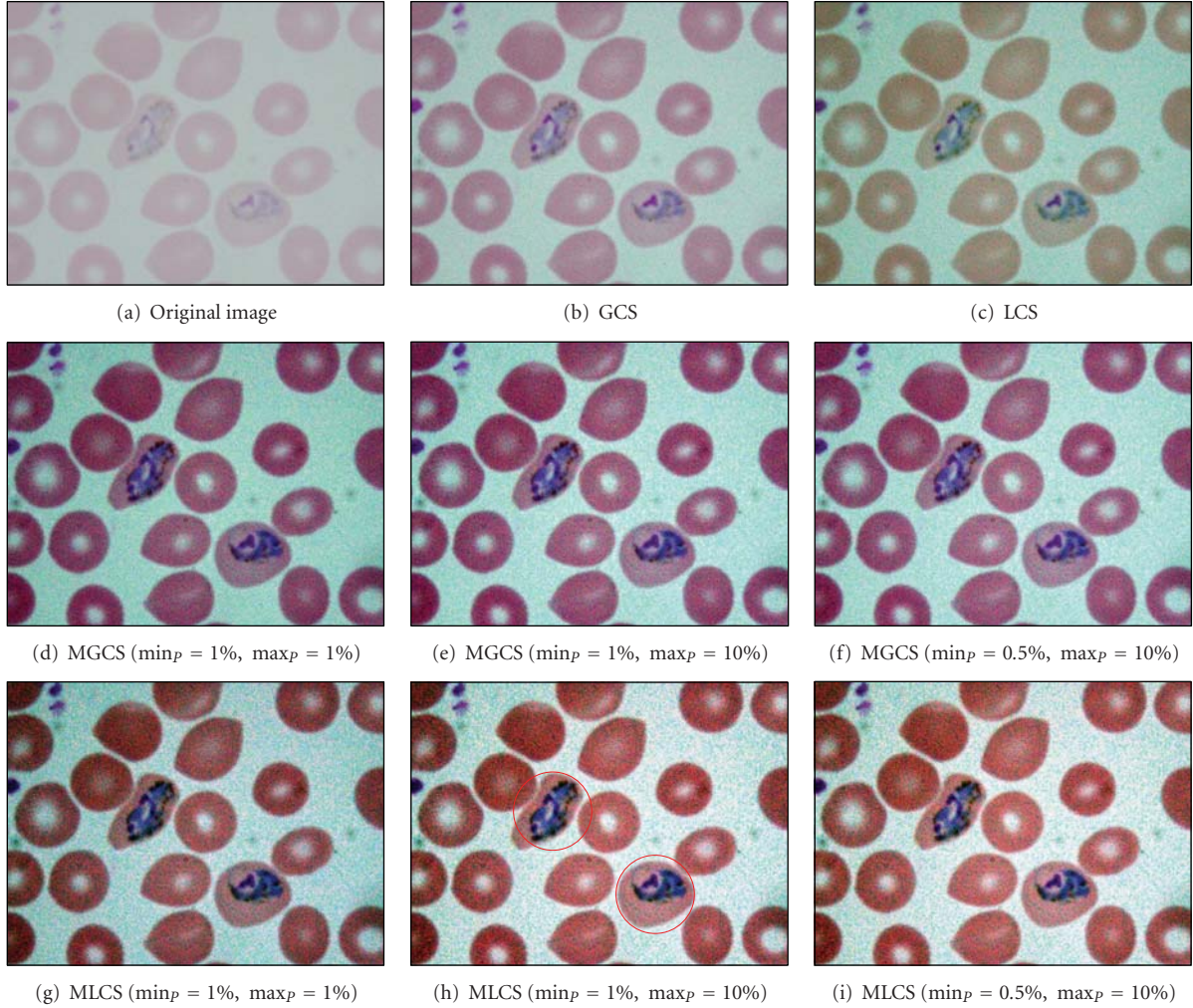


FIGURE 4: Results of contrast enhancement techniques for the blurred trophozoite image.

image, the level of contrast improvement provided by the proposed contrast enhancement techniques is judged by the fact that it should increase the contrast between the target and background regions so that the target is visible against the background as well as keeping the colour structure of the original image. Here, the target is referred to the parasite. Figure 3 shows the original malaria image and its segmented parasite and background regions after performing the manual segmentation.

Generally, it is hard to state the level of enhancement by only depending on human visual interpretation. Thus, a quantitative measure of contrast enhancement is required in order to quantify the degree of contrast between these two regions. Based on this argument, a quantitative measure namely, distribution separation measure (DSM) which is based on the probability density function (PDF) of the target and the background regions, before and after enhancement, has been used for the quantitative analysis [21, 22]. By using DSM, a measure of separation between these two PDFs would be an indicator of the performance of the proposed contrast enhancement techniques on malaria images. The

procedures to apply the quantitative measure of contrast enhancement techniques on malaria images are as follows.

- (1) Apply the four contrast enhancement techniques which are GCS, LCS, MGCS, and MLCS on malaria images.
- (2) Apply manual segmentation on both original and enhanced malaria images in order to obtain the target, T (parasite), and background, B , regions as shown in Figure 3.
- (3) Calculate the best decision boundary for the original image between the target and background regions based on the following equation [21]:

$$D1 = \frac{(\mu_B^O \sigma_T^O) + (\mu_T^O \sigma_B^O)}{(\sigma_T^O + \sigma_B^O)}, \quad (5)$$

where μ_T^O , σ_T^O , μ_B^O , and σ_B^O are the mean and standard deviation for each of the RGB components comprising the parasite and background regions for the original image, respectively.

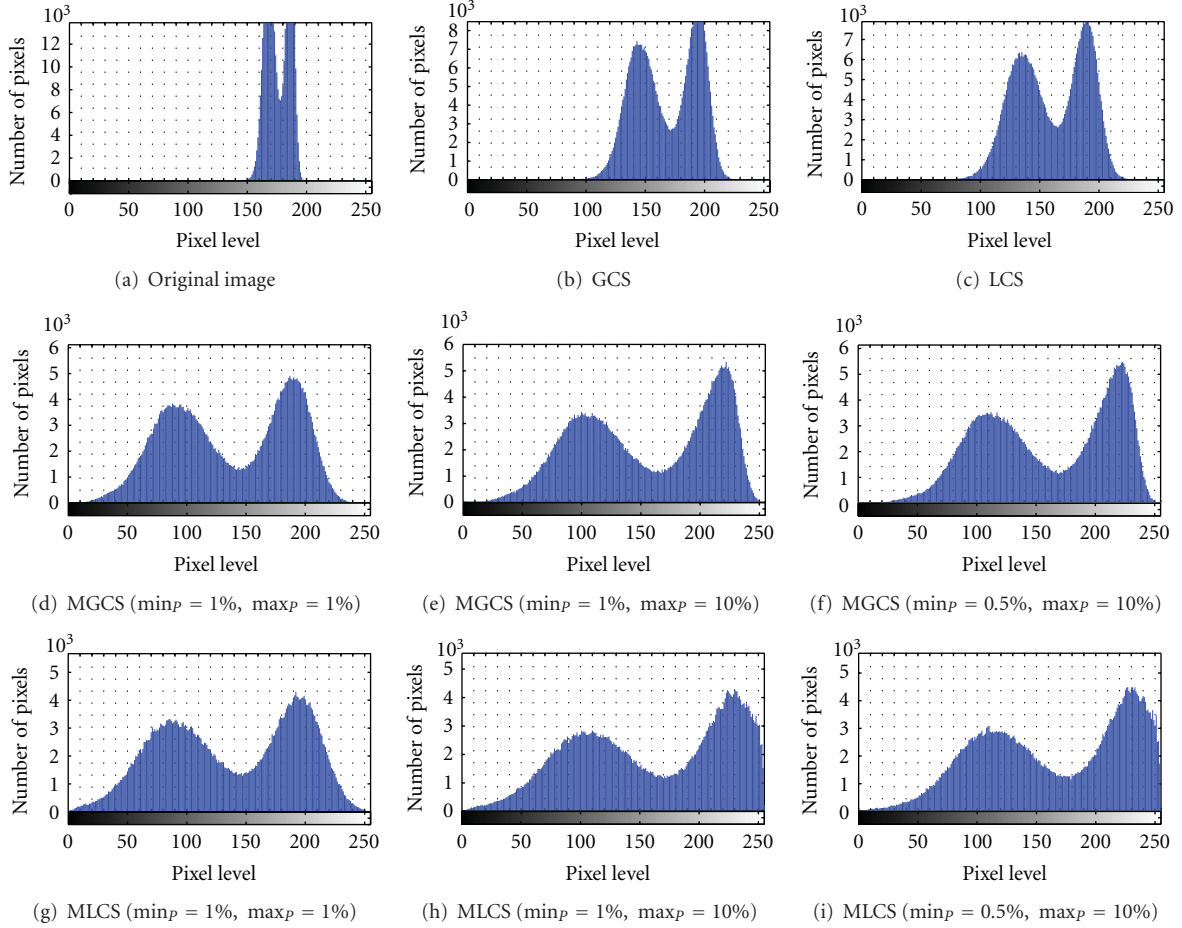


FIGURE 5: Intensity histograms for Blurred Trophozoite image after applying contrast enhancement techniques.

- (4) Calculate the best decision boundary for the enhanced image between the target and background regions based on the following equation [21]:

$$D2 = \frac{(\mu_B^E \sigma_T^E) + (\mu_T^E \sigma_B^E)}{(\sigma_T^E + \sigma_B^E)}, \quad (6)$$

where μ_T^E , σ_T^E , μ_B^E , and σ_B^E are the mean and standard deviation for each of the RGB components comprising the parasite and background regions for the enhanced image, respectively.

- (5) Calculate the value of DSM based on the following equation [21]:

$$DSM = \left(\left| D2 - \mu_B^E \right| + \left| D2 - \mu_T^E \right| \right) - \left(\left| D1 - \mu_B^O \right| + \left| D1 - \mu_T^O \right| \right). \quad (7)$$

A good enhancement technique must provide a DSM value greater than 0. The higher the DSM, the better separation between the distributions. Hence, the better is the enhancement technique. If the value of DSM is less than 0, there is no enhancement in the image [21].

4. Results and Discussions

In this study, the four contrast enhancement techniques namely, global, linear, modified global, and modified linear contrast stretching have been applied on 150 malaria images which consist of the ring, trophozoite, schizont, and gametocyte stages of *P. vivax* species. In order to access the significance of the enhancement technique on malaria image, the comparison between the original image and enhanced image is needed. For each enhancement technique, the qualities of images are initially evaluated based on human visual interpretation and then further analyzed by using a quantitative measure namely, distribution separation measure.

4.1. Qualitative Analysis. Exposure of a microscope as well as variable smears quality and the conditions of the slides are some factors that may influence the quality of the captured images. In order to assess the proposed work, the captured images with normal, blurred, and underexposure conditions have been processed using the proposed procedure.

Figure 4(a) shows the original blurred image of trophozoite stage named as blurred trophozoite image. Based on this malaria image, the morphologies of the parasites are

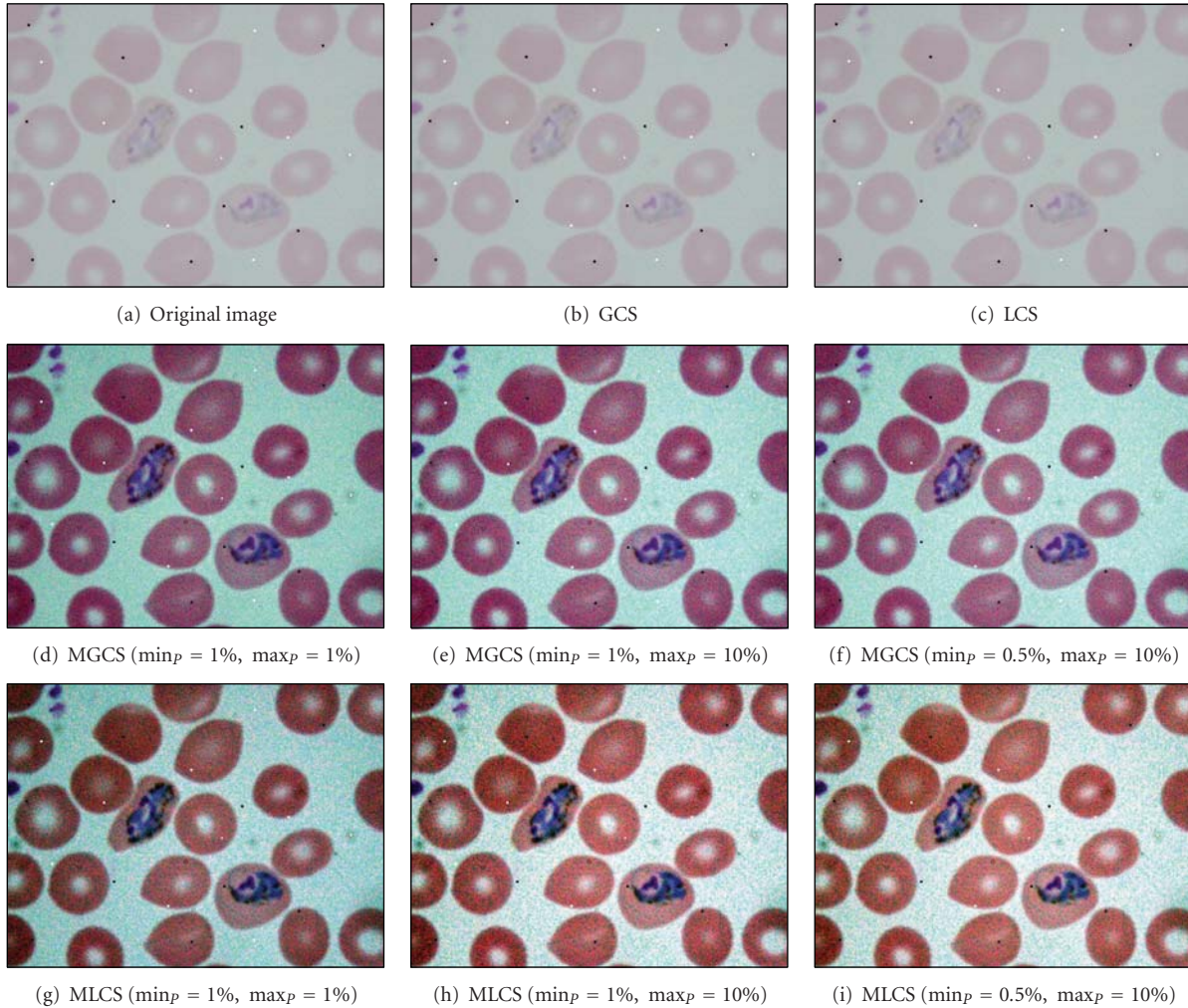


FIGURE 6: Results of contrast enhancement techniques for the blurred trophozoite image with 0.1% density of salt-and-pepper noise.

hardly be seen due to the blurred and low image contrast. The results of applying the four contrast enhancement techniques on blurred trophozoite image are shown in Figures 4(b)–4(i), while their corresponding intensity histograms are shown in Figures 5(b)–5(i).

The result of applying the GCS technique is shown in Figure 4(b). Generally, this technique has produced an image which does not much differ in terms of changes in RGB colour from the original image. Based on the resultant image, there is a slight increase of contrast in malaria image. The GCS technique has very limited dynamic adjustment range. Thus, the resultant image has become slightly brighter compared to the original image. The result of applying the LCS technique on malaria image is shown in Figure 4(c). Based on the resultant image, there is also a slight increase of contrast in malaria image. The application of LCS technique will result in obtaining different colour structures between the RGB components inside the image. Based on the colour differences, the appearance of the parasite can easily be distinguished from the RBC and background regions.

The results obtained after applying the proposed MGCS and MLCS techniques on malaria images are shown in

Figures 4(d)–4(f) and Figures 4(g)–4(i), respectively. Based on the resultant malaria images, the images have become clearer and the contrast of the parasites, infected RBC and background regions has been successfully enhanced. In addition, the enlargement in terms of size for the infected RBC (red circle) which is one of the main malaria characteristics can easily be seen. Here, there are three different sets of minimum and maximum percentage values that have been used to determine the new minimum and maximum RGB values for contrast stretching process. The first set is $\min_p = 1\%$ and $\max_p = 1\%$, the second set is $\min_p = 1\%$ and $\max_p = 10\%$, and the third set is $\min_p = 0.5\%$ and $\max_p = 10\%$. Here, the first, second, and third sets are named as Set I, Set II, and Set III, respectively. For the Set I, a small number of percentage value which is 1 has been used for both \min_p and \max_p in order to access the significance of the proposed MGCS and MLCS techniques on malaria images, compared to the conventional GCS and LCS techniques. Meanwhile, Set II and Set III have used different percentage values for both \min_p and \max_p in order to measure the effect of stretching process for the data that lie on the left and right sides of the histogram.

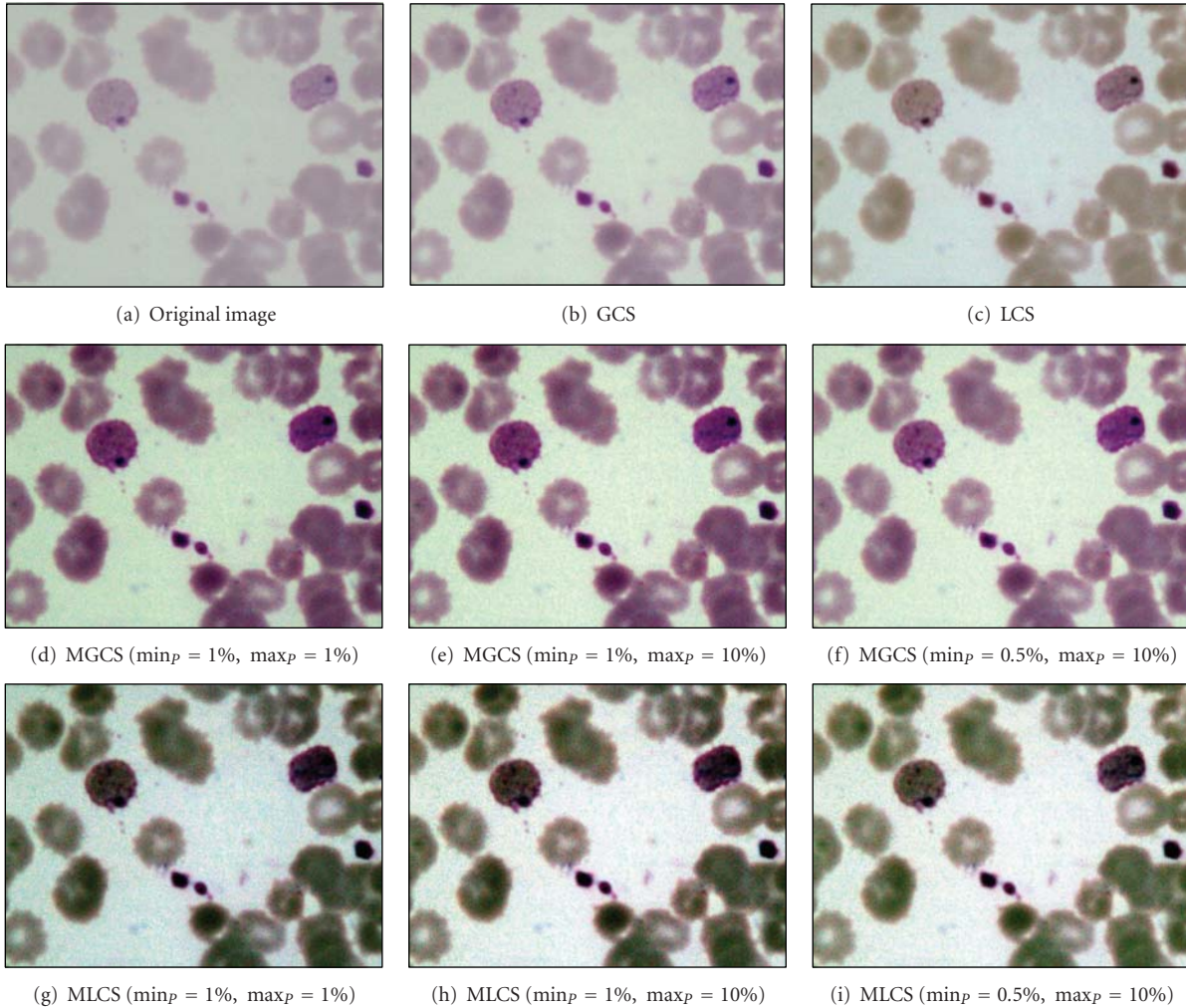


FIGURE 7: Results of contrast enhancement techniques for the normal ring image.

By using these different percentage values for both MGCS and MLCS techniques, changes of contrast inside the resultant malaria images can be easily seen. Figures 4(d) and 4(g) show the resultant images after applying the MGCS and MLCS techniques with the $\min_p = 1\%$ and $\max_p = 1\%$. By applying these values, the narrow range of data in original image will be stretched linearly to a wider range of data so that the dynamic range of the histogram (0 to 255) is fulfilled as shown in Figures 5(d) and 5(g). As a result, the contrast of malaria images has been enhanced compared to the contrast of the original image. Figures 4(e) and 4(h) show the resultant images after applying the MGCS and MLCS techniques with the $\min_p = 1\%$ and $\max_p = 10\%$. Based on the resultant images, the contrast of malaria images has been enhanced and the background region has become brighter compared to the contrast of the original image. By applying the $\max_p = 10\%$, the RGB values of the RBC and background regions have been shifted to the right side of the histogram. Thus, the narrow ranges of data in original image have been stretched to a wider range of data at the right side

of the histogram. Based on the intensity histograms in Figures 5(e) and 5(h), pixels clustered at the right side of the histogram indicate that the resultant images become brighter.

Figures 4(f) and 4(i) show the resultant images after applying the MGCS and MLCS techniques with $\min_p = 0.5\%$ and $\max_p = 10\%$. Based on the resultant images, both techniques have produced colour image with good image contrast compared to the contrast of the original image and the resultant images shown in Figures 4(d) and 4(g). By applying the $\min_p = 0.5\%$, the RGB values of the parasite pixels that lie at the left side of the histogram have been shifted to the right side of the histogram. As a result, the parasite region has become brighter and the presence of malarial pigment inside the parasite can be easily seen. By comparing the three different sets of percentage values, the MGCS and MLCS techniques using Set II and Set III have produced the most acceptable results in enhancing the contrast of malaria images compared to the resultant images provided by Set I. Even though the dynamic range of the histogram has been fulfilled after applying the MGCS and

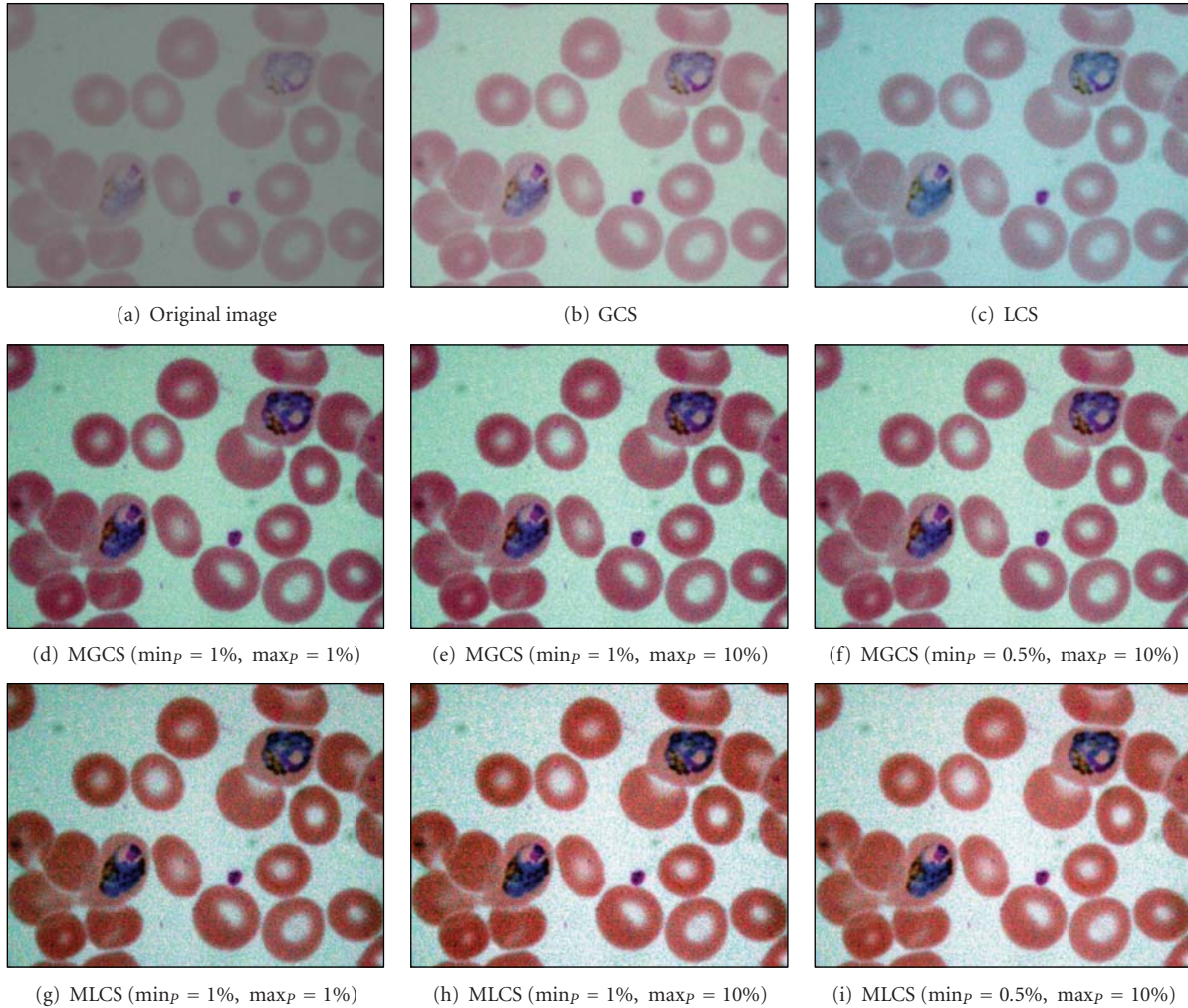


FIGURE 8: Results of contrast enhancement techniques for the underexposed trophozoite image.

MLCS techniques using Set I, the appearance of the parasite and RBC regions are darker compared to the resultant images provided by Set II and Set III.

Figure 6(a) shows the similar original blurred trophozoite image as shown in Figure 4(a). Here, 0.1% density of salt-and-pepper noise has been added to this original image to measure the effect of contrast enhancement technique on noisy image. The results of applying the four contrast enhancement techniques on malaria images are shown in Figures 6(b)–6(i). Based on Figure 6, image (b) shows the result after applying the GCS technique. Based on the resultant image, there is no sign of enhancement in the image. As previously mentioned, the contrast stretching process depends directly on the minimum and maximum values of the RGB inside the malaria image. After adding the salt-and-pepper noise to the image, the minimum and maximum values have been changed. Since the minimum and maximum values are 0 and 255, respectively, there is no enhancement occur which leads to producing the similar original image. The similar effect can also be seen after applying the LCS technique as shown in image (c). Thus,

both GCS and LCS techniques failed to provide the enhanced image if either the minimum value = 0 or maximum value = 255 has been used during the contrast stretching process.

The results obtained after applying the proposed MGCS and MLCS techniques on malaria images are shown in Figures 6(d)–6(f) and Figures 6(g)–6(i), respectively. Based on the resultant malaria images, the images have been simply enhanced by adjusting the minimum and maximum values that lie in a certain percentage of pixels from the total number of pixels in the image. Thus, the contrast of the parasites, infected RBC and background regions has been improved significantly even with the additional of salt-and-pepper noise. The performance of the proposed contrast enhancement techniques has also been tested on other malaria images with three different conditions. The images are called Normal Ring, underexposed trophozoite, normal schizont, blurred gametocyte and Underexposed Gametocyte as shown in Figures 7, 8, 9 and 10, respectively.

Based on the resultant images provided by the four contrast enhancement techniques, GCS technique has not produced satisfactory results due to the slight increase of

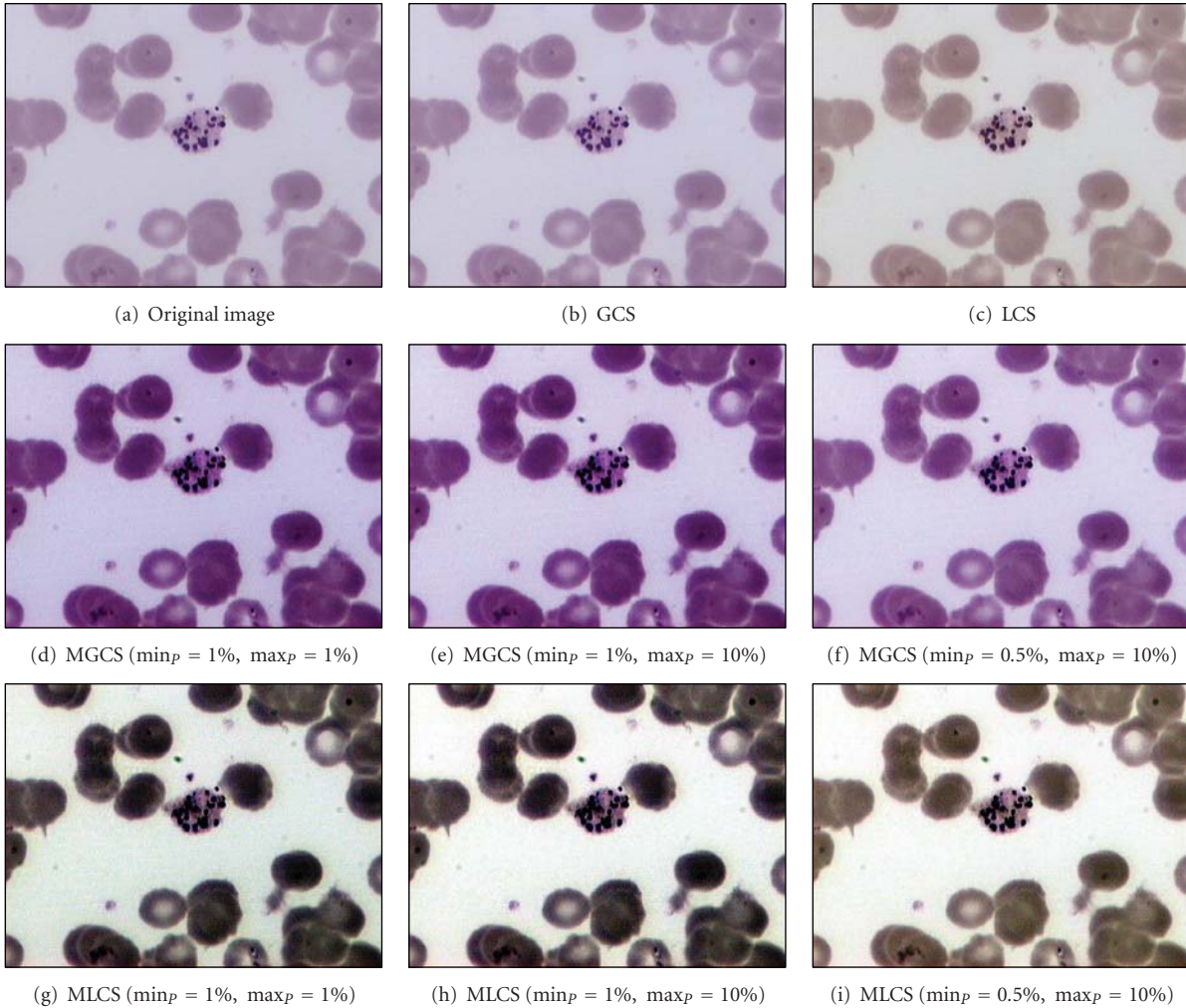


FIGURE 9: Results of contrast enhancement techniques for the normal schizont image.

malaria image contrast. This is mainly because pixels with extreme differences in RGB levels tend to be irregularly scattered in the images, while pixels with the similar RGB levels tend to bunch. Thus, the dynamic adjustment range of contrast enhancement is very limited for the GCS technique but not for the LCS technique. Based on the resultant images, both MGCS and MLCS techniques have produced colour images with good image contrast compared to the conventional GCS and LCS techniques. The previous darker background region has become brighter. Thus, the size and form of the parasites, the size of the RBC, as well as the presence of malarial pigment inside the parasite can be easily seen.

By comparing both techniques in terms of contrast performance, it has been found that the contrast of the image provided by MLCS technique is slightly better compared to the MGCS technique, since the human vision is mainly sensitive to the local contrast. The application of MLCS technique will result in obtaining different colour appearance of the image because every pixel in the image has been mapped according to the local features of the image. Based

on the colour differences, the appearance of the parasite can easily be distinguished from the RBC and background regions. However, this technique has caused a lot of changes in colour for certain malaria images. Based on the resultant images in Figure 7, the colour of the parasite has been changed to dark purple, while the colour of the RBC region has been changed to green after applying the MLCS technique. As a result, the physical appearances of the parasite, RBC and background regions are totally different from the original image. As for the MGCS technique, the overall appearance of images remains mostly unchanged and the enhancement is achieved within the available dynamic range. The images are simply enhanced by adjusting the minimum and maximum values that lie in a certain percentage of pixels, even though every pixel in the image has been mapped in the same way which is independent from the value of surrounding pixels in the image. As a result of applying the MGCS technique, the malaria image becomes clearer and the colour structure does not become disrupted; hence, it can give detailed information about the image.

TABLE 1: The DSM for GCS and MGCS techniques that have been applied on 6 malaria images.

Images	Contrast enhancement techniques	Distribution separation measure (DSM)			
		Red	Green	Blue	Average
Blurred trophozoite	GCS	21	31	15	22.33
	MGCS Set I	47	68	29	48.00
	MGCS Set II	54	77	33	54.67
	MGCS Set III	51	73	32	52.00
Blurred trophozoite with additional salt-and-pepper noise	GCS	5	5	5	5.00
	MGCS Set I	45	66	29	46.67
	MGCS Set II	53	75	33	53.67
	MGCS Set III	49	70	31	50.00
Normal ring	GCS	18	32	18	22.67
	MGCS Set I	39	77	39	51.67
	MGCS Set II	45	89	46	60.00
	MGCS Set III	41	81	42	54.67
Underexposed trophozoite	GCS	27	40	22	29.67
	MGCS Set I	58	82	45	61.67
	MGCS Set II	67	94	51	70.67
	MGCS Set III	61	89	47	65.67
Normal schizont	GCS	6	5	5	5.33
	MGCS Set I	27	25	32	28.00
	MGCS Set II	30	28	24	27.33
	MGCS Set III	28	28	28	28.00
Blurred gametocyte	GCS	28	37	17	27.33
	MGCS Set I	55	72	31	52.67
	MGCS Set II	63	82	35	60.00
	MGCS Set III	58	78	34	56.67

4.2. *Quantitative Analysis.* After the four contrast enhancement techniques have been applied on malaria images, the performance of the proposed contrast enhancement techniques is further evaluated by using the distribution separation measure. Table 1 represents the DSM for GCS and MGCS techniques that have been applied on 6 malaria images, while Table 2 represents the DSM for LCS and MLCS techniques that have been applied on 6 malaria images.

Based on the average RGB results in Table 1, the DSM provided by the MGCS technique using the three different sets is higher compared to the GCS technique, with the value of DSM for all images more than 40 except for the Normal schizont image. The results also show that the MGCS technique using Set II has produced the highest DSM value, followed by the results provided by Set III and Set I. Thus, the MGCS technique based on Set II has been chosen to be the best enhancement technique compared to the GCS and MGCS based on Set I and Set III.

Based on the average RGB results in Table 2, the DSM provided by the MLCS technique is higher compared to the LCS technique, with the value of DSM for all images are more than 40 except for the normal schizont image. The results also show that the MLCS technique using the Set I has produced the highest DSM value, followed by the results provided by Set II and Set III. Thus, the MLCS technique

based on Set I has been chosen to be the best enhancement technique compared to the LCS and MLCS based on Set II and Set III. Based on the results in Tables 1 and 2, both MGCS and MLCS techniques have produced the more promising results compared to the conventional GCS and LCS techniques.

The analysis of DSM for each contrast enhancement technique has also been conducted using the 150 malaria images that have been captured with normal, blurred, and underexposure conditions from different malaria blood slides. Here, MGCS based on Set II and MLCS based on Set I have been chosen for this analysis because each enhancement technique has produced the highest DSM value as shown in Tables 1 and 2, respectively. Figure 11 graphically illustrates the DSM for the four contrast enhancement techniques that have been applied on 150 malaria images. Based on the axis of malaria images, images 1 till 50 are the ranges for normal image, images 51 till 100 are the ranges for underexposed image, while images 101 till 150 are the ranges for blurred image. The DSMs for the four contrast enhancement based on normal, underexposed, blurred and overall malaria images have also been tabulated in Table 3.

By referring to Figures 11(a)–11(c), there are separations of DSM values that can be seen between the four contrast enhancement techniques. Based on the results in Table 3,

TABLE 2: The DSM for LCS and MLCS techniques that have been applied on 6 malaria images.

Images	Contrast enhancement techniques	Distribution separation measure (DSM)			
		Red	Green	Blue	Average
Blurred trophozoite	LCS	37	31	23	30.33
	MLCS Set I	75	65	39	59.67
	MLCS Set II	66	52	20	46.00
	MLCS Set III	60	49	19	42.67
Blurred trophozoite with additional salt-and-pepper noise	LCS	5	5	5	5.00
	MLCS Set I	71	64	39	58.00
	MLCS Set II	64	51	19	44.67
	MLCS Set III	59	46	18	41.00
Normal ring	LCS	23	32	40	31.67
	MLCS Set I	67	79	80	75.33
	MLCS Set II	52	64	64	60.00
	MLCS Set III	46	53	57	52.00
Underexposed trophozoite	LCS	41	40	28	36.33
	MLCS Set I	89	80	58	75.67
	MLCS Set II	85	73	48	68.67
	MLCS Set III	76	67	44	62.33
Normal schizont	LCS	9	8	13	10.00
	MLCS Set I	35	36	33	34.67
	MLCS Set II	13	12	10	11.67
	MLCS Set III	11	9	10	10.00
Blurred gametocyte	LCS	41	41	19	33.67
	MLCS Set I	88	70	37	65.00
	MLCS Set II	84	59	20	54.33
	MLCS Set III	75	55	19	49.67

TABLE 3: The DSM for the four contrast enhancement based on normal, underexposed, blurred, and overall malaria images.

Images	Contrast enhancement techniques	Distribution separation measure (DSM)			
		Red	Green	Blue	Average
50 normal images	GCS	21.84	41.70	17.26	26.93
	LCS	36.92	41.72	45.32	41.32
	MGCS Set II	48.22	89.90	63.62	67.25
	MLCS Set I	83.35	77.40	74.96	78.57
50 underexposed images	GCS	18.84	43.20	17.32	26.45
	LCS	36.38	43.32	36.46	38.72
	MGCS Set II	32.90	80.08	55.92	56.30
	MLCS Set I	67.59	72.22	64.06	67.96
50 blurred images	GCS	19.50	27.34	10.78	19.21
	LCS	34.34	27.80	16.18	26.11
	MGCS Set II	50.36	66.26	19.18	45.27
	MLCS Set I	82.19	62.10	20.68	54.99
Overall 150 images	GCS	20.06	37.41	15.12	24.20
	LCS	35.88	37.61	32.65	35.38
	MGCS Set II	43.83	78.75	46.24	56.27
	MLCS Set I	77.71	70.57	53.23	67.17

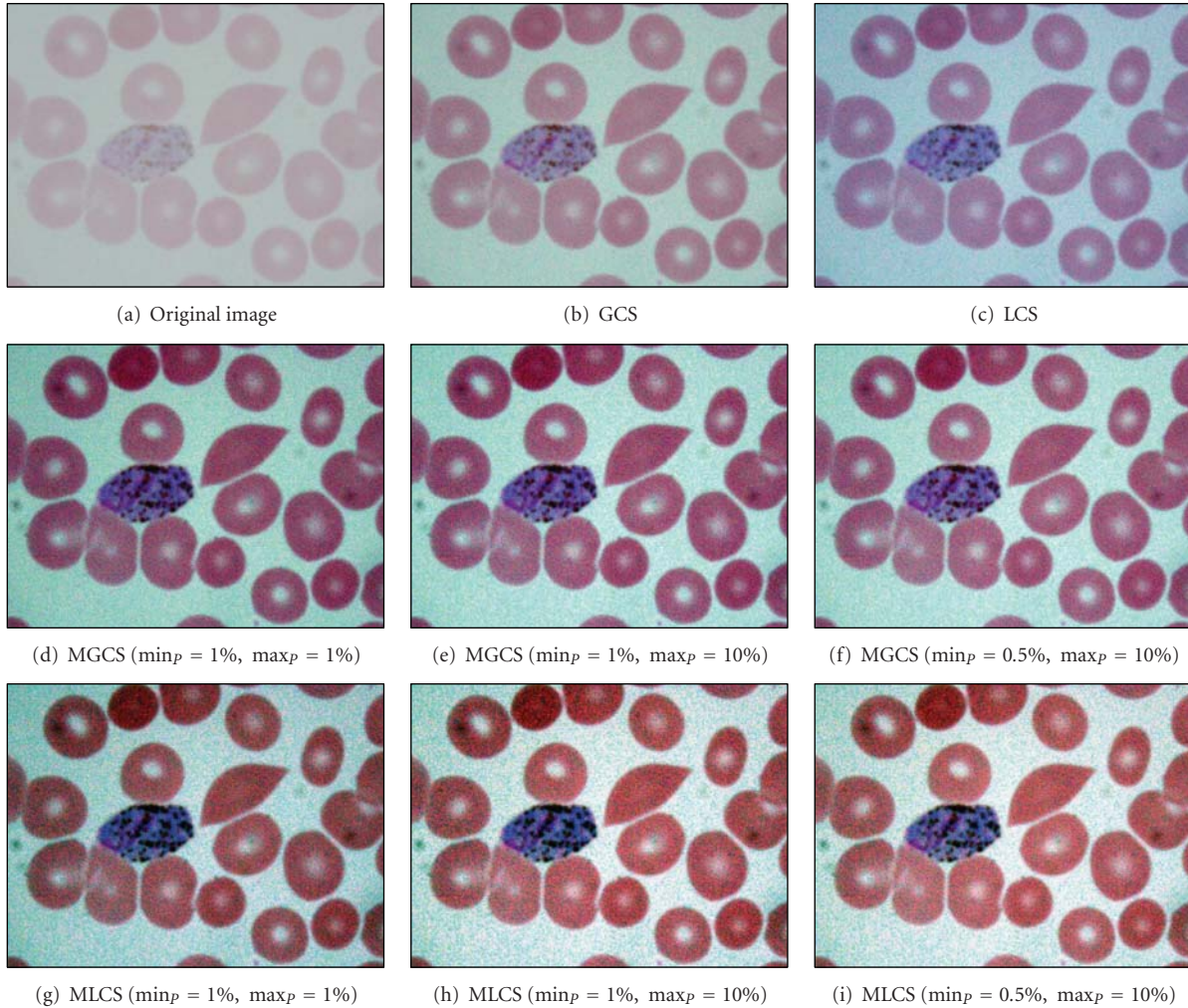


FIGURE 10: Results of contrast enhancement techniques for the blurred gametocyte image.

the MLCS technique has provided the highest DSM value for the red and blue components analyses compared to the other contrast enhancement techniques. Meanwhile, the MGCS technique has provided the highest DSM value for the green component analysis. The results of DSM for the average RGB components are graphically illustrated in Figure 11(d). Based on this analysis, there are separations of DSM values that can be seen between the four contrast enhancement techniques. By calculating the average of DSM using the overall 150 images, MLCS technique has proven to be the best with DSM for the average RGB components of 67.17. This is followed by the MGCS, LCS, and GCS techniques with DSM for the average RGB components of 56.27, 35.38, and 24.20, respectively. Based on the high DSM value provided by the MLCS technique, this result has strongly supported the qualitative findings provided in Section 4.1. The DSMs provided by the three different sets of images have also been compared in order to determine the type of image that can give the best enhancement performance. By comparing the DSM for the average RGB components as shown in Table 3, normal image has produced the highest DSM value, followed by the results provided by the underexposed and

blurred images. Overall, based on the high values of DSM that have been obtained, both MGCS and MLCS techniques have provided good contrast performance compared to the conventional GCS and LCS techniques. These results are strongly supported by the qualitative findings provided in Section 4.1.

5. Conclusions

In this paper, the results of applying the four contrast enhancement techniques namely global, linear, modified global, and modified linear contrast stretching have been presented. Through the experiments using 150 malaria images, the results produced by these four techniques are acceptable in terms of visual quality. The difference between global and linear contrast stretching is the intensity distribution of the image being enhanced. Overall, the proposed MGCS and MLCS techniques have been shown to be good for enhancing the contrast and brightness of the image compared to the conventional GCS and LCS techniques. This statement is strongly supported based on

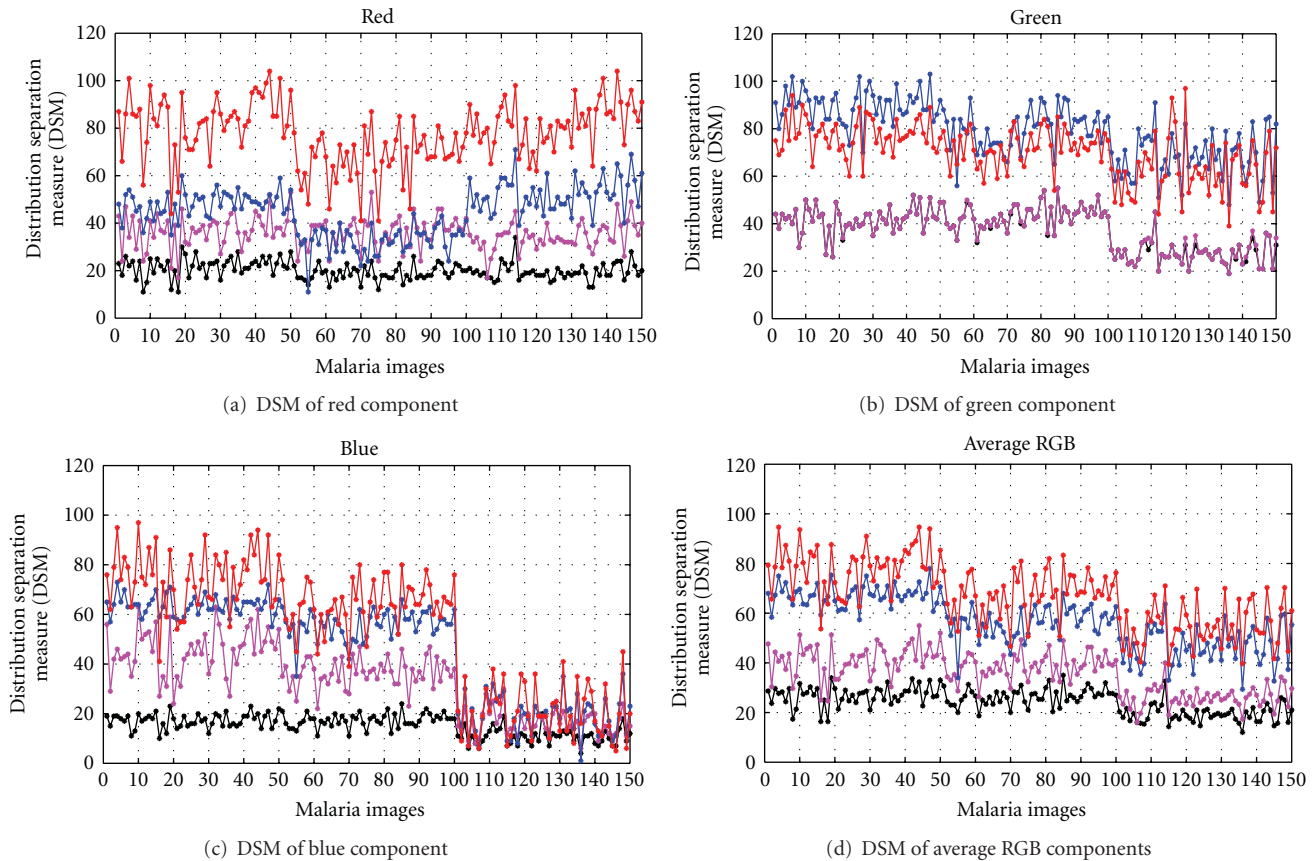


FIGURE 11: The DSM for the four contrast enhancement techniques that have been applied on 150 malaria images.

both qualitative and quantitative findings. Here, the MLCS technique has proven to be the best with DSM for the average RGB components of 67.17. This is followed by the MGCS, LCS, and GCS techniques with DSM for the average RGB components of 56.27, 35.38 and 24.20. Based on the qualitative findings provided in Section 4.1, the contrast of the malaria images that have been captured with normal, blurred, and underexposure conditions from different malaria blood slides has been successfully enhanced. As for the noisy image, it has been shown that both GCS and LCS techniques failed to provide the enhanced image if either the minimum value = 0 or maximum value = 255 has been used during the contrast stretching process. However, the proposed MGCS and MLCS techniques manage to overcome this problem by adjusting the minimum and maximum values that lie in a certain percentage of pixels in the image. By comparing the DSM for the proposed contrast enhancement techniques, it has been proven that the contrast of the image provided by MLCS technique is better compared to the MGCS technique. However, the MGCS technique has also shown to be good in enhancing the contrast of the image by keeping the colour structure of the original image, hence it can preserve as much information as the original. Thus, the results significantly demonstrate the suitability of the proposed contrast enhancement techniques in increasing the contrast of the parasites and the infected RBC so that the resultant images would become useful to microbiologists

for further analysis of the various stages and species of malaria.

Acknowledgments

The authors gratefully acknowledge and thank the team members of malaria research at Universiti Malaysia Perlis (UniMAP) for making this research achievable and Universiti Sains Malaysia (USM) for providing the malaria blood samples and validating the results.

References

- [1] WHO, *Basic Malaria Microscopy, Part I. Learner's Guide*, World Health Organization, 2010.
- [2] N. A. V. Beare, T. E. Taylor, S. P. Harding, S. Lewallen, and M. E. Molyneux, "Malarial retinopathy: a newly established diagnostic sign in severe malaria," *American Journal of Tropical Medicine and Hygiene*, vol. 75, no. 5, pp. 790–797, 2006.
- [3] N. J. White, "Plasmodium knowlesi: the fifth human malaria parasite," *Clinical Infectious Diseases*, vol. 46, no. 2, pp. 172–173, 2008.
- [4] *World Malaria Report 2010*, World Health Organization, Geneva, Switzerland, 2010.
- [5] M. T. Makler, C. J. Palmer, and A. L. Ager, "A review of practical techniques for the diagnosis of malaria," *Annals of Tropical Medicine and Parasitology*, vol. 92, no. 4, pp. 419–433, 1998.

- [6] L. H. Zou, J. Chen, J. Zhang, and N. García, "Malaria cell counting diagnosis within large field of view," in *Proceedings of the International Conference on Digital Image Computing: Techniques and Applications (DICTA '10)*, pp. 172–177, December 2010.
- [7] N. E. Ross, C. J. Pritchard, D. M. Rubin, and A. G. Duse, "Automated image processing method for the diagnosis and classification of malaria on thin blood smears," *Medical & Biological Engineering & Computing*, vol. 44, no. 5, pp. 427–436, 2006.
- [8] K. Mitiku, G. Mengistu, and B. Gelaw, "The reliability of blood film examination for malaria at the peripheral health unit," *The Ethiopian Journal of Health Development*, vol. 17, no. 3, pp. 197–204, 2003.
- [9] B. N. Chatterji and R. N. Murthy, "Adaptive contrast enhancement for colour images," in *Proceedings of the International Conference on Information, Communications and Signal Processing (ICICS '97)*, 2002.
- [10] S. J. Preethi and K. Rajeswari, "Image enhancement techniques for improving the quality of colour and gray scale medical images," *International Journal on Computer Science and Engineering*, pp. 18–23, 2010.
- [11] A. N. Aimi Salihah, M. Y. Mashor, N. H. Harun, and H. Rosline, "Colour image enhancement techniques for acute leukaemia blood cell morphological features," in *Proceedings of the IEEE International Conference on Systems, Man and Cybernetics (SMC '10)*, pp. 3677–3682, October 2010.
- [12] M. D. Saleh, C. Eswaran, and A. Mueen, "An automated blood vessel segmentation algorithm using histogram equalization and automatic threshold selection," *Journal of Digital Imaging*, vol. 24, no. 4, pp. 564–572, 2010.
- [13] H. L. Tong, M. F. A. Fauzi, and S. C. Haw, "Automated hemorrhage slices detection for CT brain images," in *Proceedings of the International Visual Informatics Conference (IVIC '11)*, vol. 7066 of *Lecture Notes in Computer Science*, pp. 268–279, Springer, 2011.
- [14] F. B. Tek, *Computerised diagnosis of malaria [Ph.D. thesis]*, University of Westminster, 2007.
- [15] N. S. M. M. Hanif, M. Y. Mashor, and Z. Mohamed, "Image enhancement and segmentation using dark stretching technique for Plasmodium Falciparum for thick blood smear," in *Proceedings of the IEEE 7th International Colloquium on Signal Processing and Its Applications (CSPA '11)*, pp. 257–260, March 2011.
- [16] DPDx, "Comparison of plasmodium species which cause malaria in humans," 2012, <http://www.dpd.cdc.gov/dpdx/html/malaria.htm>.
- [17] T. Arici and Y. Altunbasak, "Image local contrast enhancement using adaptive non-linear filters," in *Proceedings of the IEEE International Conference on Image Processing (ICIP '06)*, pp. 2881–2884, October 2006.
- [18] K. Matkovic, L. Neumann, A. Neumann, T. Psik, and W. Purgathofer, "Global contrast factor—a new approach to image contrast," in *Proceedings of the Computational Aesthetics in Graphics, Visualization and Imaging Workshop*, pp. 159–168, 2005.
- [19] S. I. Sahidan, M. Y. Mashor, A. S. W. Wahab, Z. Salleh, and H. Jaafar, "Local and global contrast stretching for color contrast enhancement on ziehl-neelsen tissue section slide images," in *Proceedings of the 4th Kuala Lumpur International Conference on Biomedical Engineering*, 2008.
- [20] U. K. Ngah, T. H. Ooi, N. E. A. Khalid, and P. A. Venkatachalam, "The seed based region growing image processing with embedded enhancement techniques," in *Proceeding of the 2nd International Conference on Computers in Industry (ICCI '00)*, 2000.
- [21] S. Singh and R. Al-Mansoori, "Identification of regions of interest in digital mammograms," *Journal of Intelligent Systems*, vol. 10, no. 2, pp. 183–210, 2000.
- [22] S. Singh and K. Bovis, "An evaluation of contrast enhancement techniques for mammographic breast masses," *IEEE Transactions on Information Technology in Biomedicine*, vol. 9, no. 1, pp. 109–119, 2005.